Transactions of the ASME®

Technical Editor, **T. H. OKIISHI (1998)**
Associate Technical Editors
Aeromechanical Interaction
R. E. KIELB (1999)
Gas Turbine (Review Chair)
A. KIDD (1997)
Heat Transfer
M. G. DUNN (1999)
Power
D. LOU (1998)
Turbomachinery
R. A. DELANEY (1998)
A. STRAZISAR (2000)

BOARD ON COMMUNICATIONS
Chairman and Vice-President
R. K. SHAH

OFFICERS OF THE ASME
President, **W. M. PHILLIPS**
Executive Director, **D. L. BELDEN**
Treasurer, **J. A. MASON**

PUBLISHING STAFF
Managing Director, Engineering
CHARLES W. BEARDSLEY
Director, Technical Publishing
PHILIP DI VIETRO
Managing Editor, Technical Publishing
CYNTHIA B. CLARK
Managing Editor, Transactions
CORNELIA MONAHAN
Production Coordinator
VALERIE WINTERS
Production Assistant
MARISOL ANDINO

Transactions of the ASME, Journal of Turbomachinery (ISSN 0889-504X) is published quarterly (Jan., Apr., July, Oct.) for $205.00 per year by The American Society of Mechanical Engineers, 345 East 47th Street, New York, NY 10017. Periodicals postage paid at New York, NY and additional mailing offices. POSTMASTER: Send address changes to Transactions of the ASME, Journal of Turbomachinery, c/o THE AMERICAN SOCIETY OF MECHANICAL ENGINEERS, 22 Law Drive, Box 2300. Fairfield, NJ 07007-2300.
CHANGES OF ADDRESS must be received at Society headquarters seven weeks before they are to be effective. Please send old label and new address.
PRICES: To members, $40.00, annually; to nonmembers, $205.00.
To countries outside the United States and Canada, add $40.00 for surface postage and $60.00 for airmail postage.
STATEMENT from By-Laws. The Society shall not be responsible for statements or opinions advanced in papers or . . . printed in its publications (B7.1, Par. 3).

INDEXED by Applied Mechanics Reviews and Engineering Information, Inc.
Canadian Goods & Services Tax Registration #126148048

Journal of Turbomachinery

Published Quarterly by The American Society of Mechanical Engineers

VOLUME 120 • NUMBER 3 • JULY 1998

TECHNICAL PAPERS

This journal is printed on acid-free paper, which exceeds the ANSI Z39.48-1992 specification for permanence of paper and library materials. ♾ ™

♻ 85% recycled content, including 10% post-consumer fibers.

(Contents continued)

ANNOUNCEMENTS

1997 Best Paper Award—Turbomachinery Committee

A Study of Spike and Modal Stall Phenomena in a Low-Speed Axial Compressor

T. R. Camp
Rolls-Royce plc,
Derby, United Kingdom

I. J. Day
Whittle Laboratory,
University of Cambridge,
Cambridge, United Kingdom

This paper presents a study of stall inception mechanisms in a low-speed axial compressor. Previous work has identified two common flow breakdown sequences, the first associated with a short length-scale disturbance known as a "spike," and the second with a longer length-scale disturbance known as a "modal oscillation." In this paper the physical differences between these two mechanisms are illustrated with detailed measurements. Experimental results are also presented that relate the occurrence of the two stalling mechanisms to the operating conditions of the compressor. It is shown that the stability criteria for the two disturbances are different: Long length-scale disturbances are related to a two-dimensional instability of the whole compression system, while short length-scale disturbances indicate a three-dimensional breakdown of the flow-field associated with high rotor incidence angles. Based on the experimental measurements, a simple model is proposed that explains the type of stall inception pattern observed in a particular compressor. Measurements from a single-stage low-speed compressor and from a multistage high-speed compressor are presented in support of the model.

Introduction and Background

The phenomena of stall and surge in compression systems have been studied almost continuously since the early development of the gas turbine engine. The objective of the work has always been the same, namely to extend the stable operating range of the compressor, but from time to time the immediate motivation for the work has changed. Over the past 20 years the driving problems have included hung stall, inlet distortion, casing treatments and, most recently, the application of active stall control. Active control was first proposed by Epstein et al. in 1986, and since then a significant amount of further research has been done, in both Europe and America. Most of this work can be divided into three categories: theoretical studies of control techniques (Simon et al., 1993; Feulner et al., 1996), the implementation of active control (Paduano et al., 1993; Day, 1993a; Haynes et al., 1994) and detailed studies of stall inception (Garnier et al., 1991; Day, 1993b; Tryfonidis et al., 1995; Hendricks et al., 1993). The work presented in this paper falls into the category of stall inception studies and builds on previous experimental work by Day (1993b).

Experimental work by McDougall et al. (1990) and Day (1993b) confirmed the existence of two different stall inception patterns in low-speed compressors. The first stalling pattern initiates with a short length-scale disturbance, which appears suddenly and develops directly into rotating stall. This type of disturbance, known generally as a "spike" because of its spikelike appearance in the velocity traces, is created by the localized stalling of a particular blade row. Figure 1 illustrates this type of stalling pattern, showing a sharp spike appearing on the velocity traces in an otherwise steady flow field. When the spike first emerges, it is small in circumferential extent and thus propagates quickly around the annulus, usually between 60 and 80 percent of rotor speed. (It is now well established that the fewer blade passages a stall cell occupies the faster it will rotate; Day, 1996). As the spike begins to propagate, it rapidly increases in size and its speed of rotation reduces. A high initial speed of rotation is characteristic of this type of disturbance.

The second type of stall inception pattern, which was predicted theoretically by Moore and Greitzer (1986) before being observed by McDougall et al. (1990), involves the gradual build-up of a long length-scale perturbation, which appears prior to the formation of a finite stall cell. The term "modal oscillation" is used to describe this phenomenon, a first-order mode having a wavelength equal to the circumference of the compressor, and a second-order mode having a wavelength of half the circumference, etc. An example of this phenomenon is given in Fig. 2, which shows a gentle undulation in the velocity traces prior to a gradual transition into rotating stall. In most cases a modal oscillation affects the flow throughout the length of the compressor, although it has recently been found that stage mismatching can limit the disturbance to a particular axial region. The rotational frequency of modal oscillations in low-speed compressors is usually less than 50 percent of rotor speed. (Modes of higher proportional frequencies may occur in high-speed machines, as found by Hendricks et al., 1993.)

The modal oscillation shown in Fig. 2 grows smoothly into a fully developed stall cell. Detailed measurements show that in such cases the low-velocity trough in the modal pattern initiates flow breakdown over a wide sector of the annulus. This results in a broad stall cell, which, because of its size, rotates comparatively slowly, in this case at a speed similar to the fully developed cell. The formation of a broad, slow-moving cell is thought to be associated with flow separation near the hub. In other situations the velocity trough in the modal wave will trigger flow separation in a localized region near the tip of one particular blade row. In such cases the transition from modal oscillation to rotating stall occurs via a spike disturbance, which initially propagates at a speed higher than the mode or the final

Contributed by the International Gas Turbine Institute and presented at the 42nd International Gas Turbine and Aeroengine Congress and Exhibition, Orlando, Florida, June 2–5, 1997. Manuscript received at ASME Headquarters February 1997. Paper No. 97-GT-526. Associate Technical Editor: H. A. Kidd.

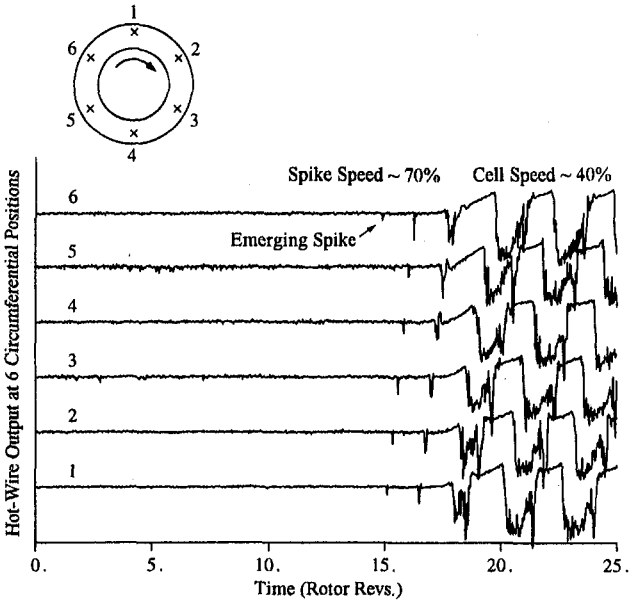

Fig. 1 Example of spike-type stall inception

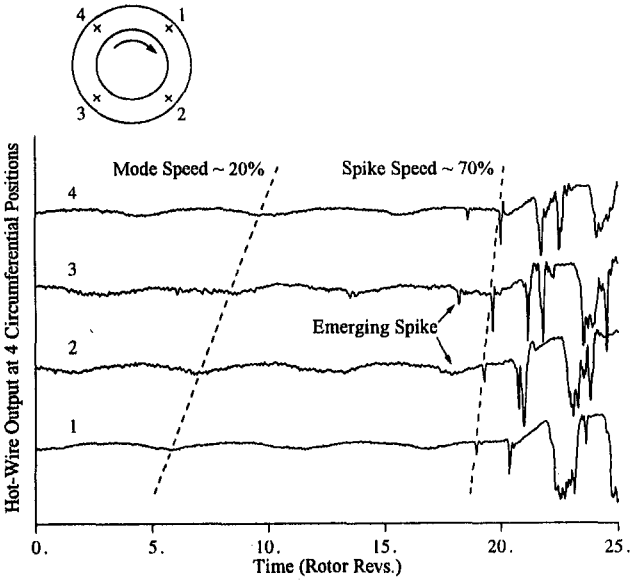

Fig. 3 Example of a spike-type stall cell originating in the trough of a modal velocity perturbation

stall cell. An example of a spike disturbance being initiated by a modal oscillation is given in Fig. 3. A mode can therefore be viewed as an oscillation of the flow-field, which promotes flow breakdown, either at the hub or at the casing, but which is distinct from the actual flow separation, which develops into rotating stall. This concept will be developed further in this paper.

As discussed above, stall in axial compressors is sometimes preceded by modal oscillations, while in other cases it initiates suddenly in the form of a spike. The criteria determining which of the two stalling sequences will occur in a particular compressor have been a topic of much discussion. It was shown by Day (1993b) that either type can occur in the same compressor if the tip clearance is changed. It has since been found that axial stage matching has a more pronounced effect on the stalling pattern than tip clearance. In this paper experiments are reported that identify the operating conditions that promote each of the stalling sequences. Based on these results, a model is proposed that sets out the stability criteria for the two phenomena. Before this is done, however, it is necessary to present some additional information on the physical properties of spikes and modes.

Physical Features of Spikes

When monitoring stall inception patterns using a circumferential array of probes, a spike can be identified by the narrow width of the disturbance (just one or two blade passages) and the high speed at which it rotates. The spike only retains this narrow structure and high rotational speed for a short time, seldom more than half a revolution around the circumference, before it increases in size and its speed decreases. Because the initial flow breakdown process is localized in both circumferential and axial extent, the identification of spikes is made easier if the probes are located near the particular blade row in which the spikes initiate. In many cases spikes remain unidentified, or

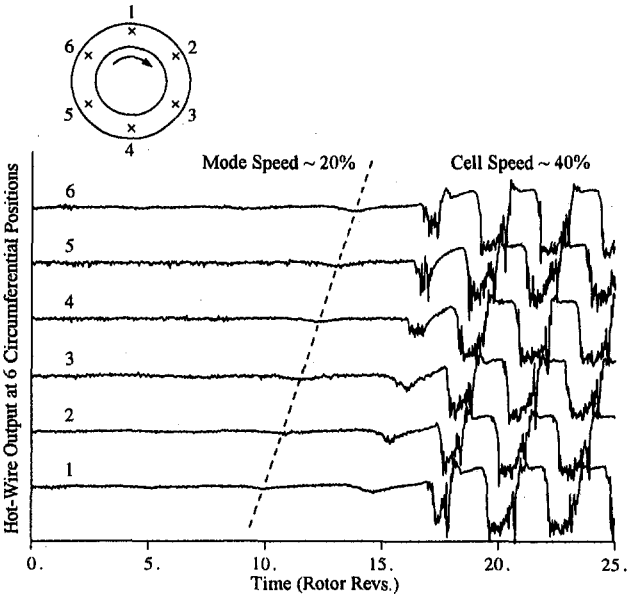

Fig. 2 Example of a modal perturbation preceding stall

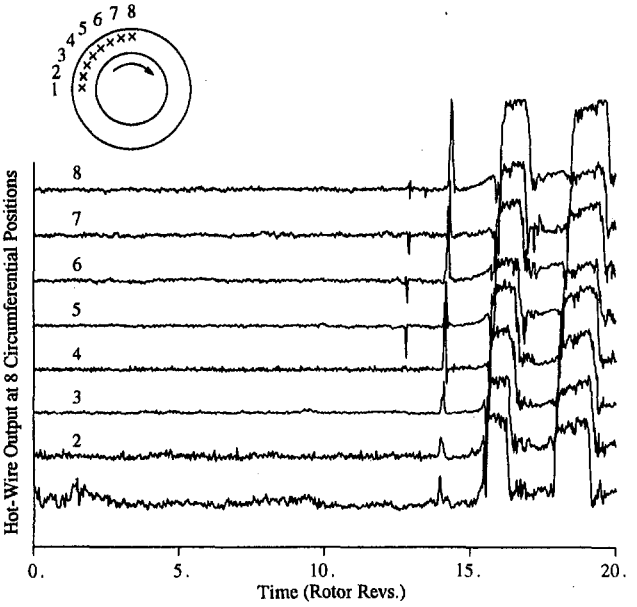

Fig. 4 Tangential velocity measurements showing the abrupt appearance of a spike

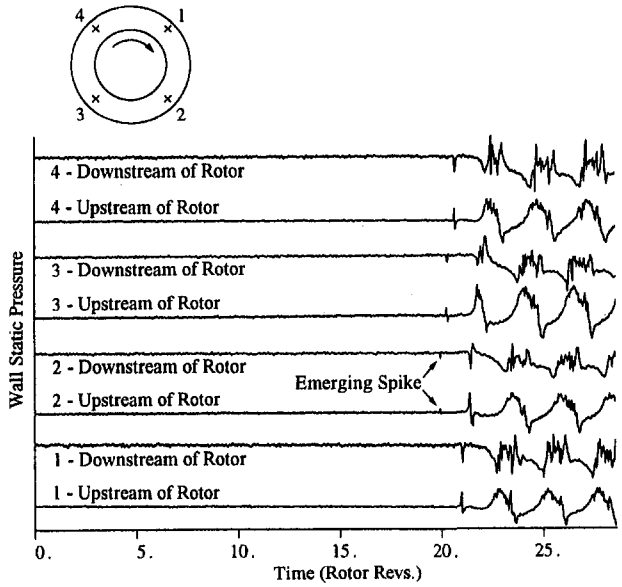

Fig. 5 Wall static measurements showing potential effect of stall cell blockage

are misclassified as modes, because they have originated at a location far removed from the measuring probes and therefore their signature is already broad and slow moving by the time the disturbance is detected.

Experimental work has been performed on the Cambridge four-stage compressor to examine the flow breakdown process associated with spikes. Details of the compressor are given in Appendix 1. Figure 4 shows the tangential velocities measured by an array of eight hot-wire probes positioned a quarter of a chord upstream of the first rotor and separated circumferentially by two blade pitches. The traces show the abrupt nature of the spike formation, the disturbance requiring only two or three blade pitches to become a significant disturbance. The measurements also show that the tangential velocity in the vicinity of the spike, as measured just upstream of the rotor face, is low when the disturbance first appears. From other measurements, such as those in Fig. 1, it is seen that the axial velocity is low in the same region. With low tangential and axial velocities upstream of the disturbance, the flow breakdown region has the appearance of a blockage in the flow-field, with an accompanying upstream stagnation region.

The picture of the spike as a localized blockage originating in one particular blade row is supported by the wall static pressure measurements shown in Fig. 5. These traces were recorded by pressure transducers positioned in axial pairs upstream and downstream of the same rotor row. When the spike first appears near the second pair of probes, the static pressure rises ahead of the disturbance (as it would in a stagnation region) while behind the rotor the pressure falls due to the localized loss of work input. The spike thus grows out of a disturbance that is initially confined to one or two blade passages in one particular blade row. Hot-wire measurements show that the initial flow separation is limited to the tip region of the rotor blades. This is illustrated by the measurements in Fig. 6 for which the probes were positioned alternately near the hub and near the casing. The traces show a drop in axial velocity in the stagnation region ahead of the spike near the rotor tip, and a corresponding increase in velocity near the hub where the flow is diverted under the blockage. The disturbance therefore originates near the blade tips and initially occupies only part of the span.

It has been suggested that spike formation may be related to the instability of the over-tip leakage flow. This point, and the precise details of the flow breakdown in the blade passage, have been examined computationally by Hoying (1996). Over-tip leakage flows also occur in cantilevered stator rows, but no sign of spike stall inception has yet been detected in these blade rows, possibly because of the high reaction of most of the blading in use.

In the Cambridge four-stage compressor, spikes are usually observed in the first rotor row. Experiments on other low-speed compressors having repeating blade geometry in each stage, also show that the first rotor is the most susceptible to spike initiation. It is thought that this occurs because the deviation angle of the flow leaving the inlet guide vanes is approximately constant as stall is approached, whereas the deviation angles from the downstream stator rows increase. Near the point of stall, the first rotor thus operates at a higher incidence than the downstream rotors and therefore it is this row that first succumbs to flow separation. However, spike-type stalling is not confined to the first stage, and can be induced in any of the four stages of the Cambridge compressor by simply restaggering the stator rows. The formation of spikes in the rear stages of high-speed compressors has also been observed, as reported by Day et al. (1998).

Characteristics of Modal Oscillations

In contrast with the sharply defined origins of spike-type disturbances, modal oscillations have no specific origin in time or space and the instant at which they are first detected is largely determined by the sensitivity of the measuring equipment. In most cases modal oscillations appear many revolutions before stall and intensify as the flow rate is reduced. The amplitude of the oscillation usually remains small and seldom exceeds 2 or 3 percent of the free-stream velocity before flow breakdown occurs and stall propagation begins. (However, under certain stage matching conditions, velocity fluctuations of more than 20 percent have been observed.)

In multistage low-speed machines, modal oscillations are usually of equal intensity from the inlet to the exit of the compressor, although variations in stage loading can restrict the perturbation to a particular axial region. An example of this is given in Fig. 7 for the case when a close-coupled screen was positioned upstream of the compressor to simulate a stable group of stages. As shown, modal activity was confined to the front of the compressor in this case. The results in this figure are particularly interesting because they show a spike initiating

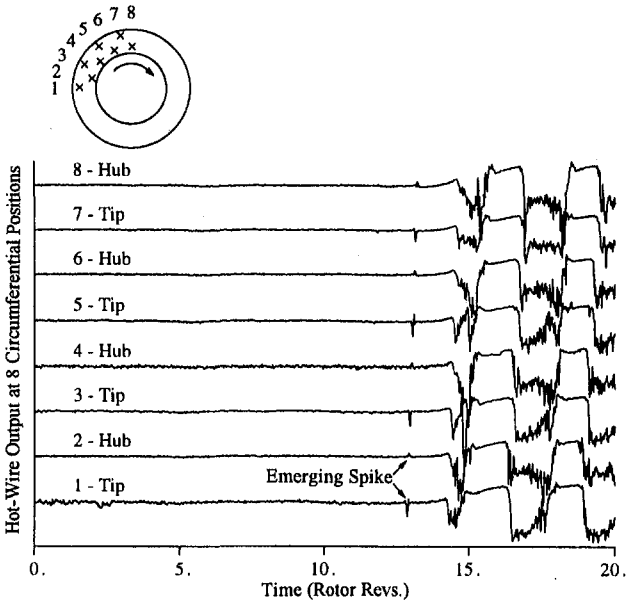

Fig. 6 Hot-wire measurements showing increase in hub velocity owing to spike blockage at the casing

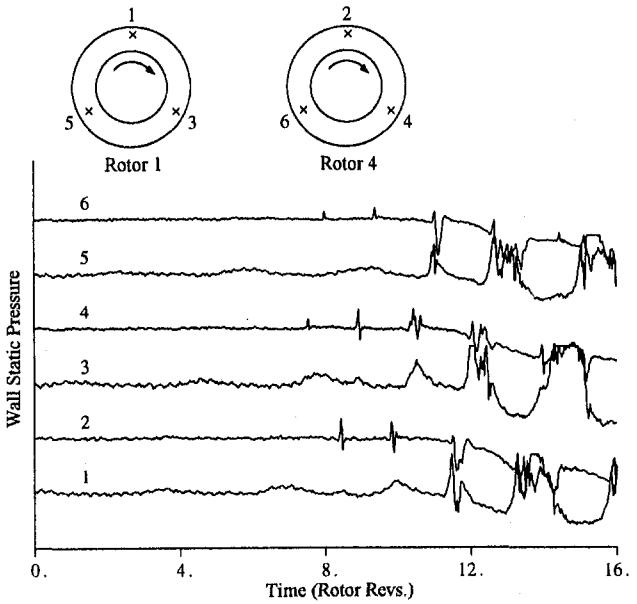

Fig. 7 Static pressure measurements showing modal activity at rotor 1 and spike-type stall initiating in rotor 4

stall from the rear of the compressor independently of the modal activity at the front.

While a spike can be regarded as an embryonic stall cell, which develops continuously into rotating stall, a modal oscillation is not in itself an early form of stall cell. Instead, a mode is an oscillation of the flow-field, which appears close to the peak of the total-to-static pressure rise characteristic, as discussed by Moore and Greitzer (1986). At the peak of the characteristic, some or all of the blade rows are operating close to their stalling limits and hence any modal induced velocity deficit may be sufficient to initiate flow separation, either in the form of a spike, as in Fig. 3, or as a broader stall cell, as shown in Fig. 2.

The observation that modal oscillations occur at the peak of the pressure rise characteristic is illustrated by the example in Fig. 8 where, owing to the presence of a downstream screen, the characteristic has a well-defined peak. In this case, sustained modal activity appears only at the peak of the characteristic and is not present at other flow rates where the slope is non-zero. The lower part of Fig. 8 shows the output from a hot-wire ahead of rotor 1 at three different flow coefficients. At high flow rates the flow field is steady, but at the peak of the characteristic a clear modal perturbation is present, as shown in the center trace. At lower flow coefficients the velocity fluctuation disappears and the flow field is again axisymmetric. Stalling was eventually initiated by a spike at the front of the compressor.

In this discussion we have tried to show that modal perturbations are a particular form of flow instability that occurs when the compressor operating point approaches the peak of the characteristic. A modal perturbation can theoretically develop smoothly into a large nonlinear disturbance, but in most cases its development is interrupted by the appearance of a stall cell. The reason for distinguishing modal activity from the actual flow breakdown process will become clear in the following section where it is shown that stalling occurs when a critical value of blade incidence is exceeded. The velocity fluctuations associated with modes increase the local blade incidence in certain regions of the annulus and therefore the intensity of modal activity required to initiate stall depends on how near or far any of the blade rows in the compressor are from critical incidence. In some situations critical incidence may be exceeded somewhere in the compressor before the peak of the characteristic is reached, in which case stalling, usually of the spike type, will occur before modes have developed.

Axial Matching Experiments

So far it has been established that modes and spikes are different aspects of the stall inception process and that both phenomena can be observed in the same compressor. To investigate the effects of characteristic slope and local blade incidence on the stall inception pattern, a series of experiments was conducted on the Cambridge compressor, making use of its variable stagger IGV and stator rows. Stage pressure rise characteristics and the stalling patterns of the compressor were measured for a large number of settings of the stators and IGVs. The results of two specific experiments are presented below, showing the effect of changing the relative loadings of stage 1 and the group of stages 2–4. This division of the compressor between stage 1 and the remaining downstream stages was made for two reasons. First, it has been observed that the first rotor row in a low-speed multistage compressor of repeating stage design is the most susceptible to flow separation. Second, because the IGV deviation angle is small and the boundary layer at IGV exit is relatively thin, the rotor 1 incidence angle can be controlled more accurately than the incidence onto any of the downstream blade rows.

To measure the stall inception events in these experiments, circumferential arrays of six hot-wire probes were used, following the procedure described by Day (1993b). From the measurements, the presence of modal oscillations prior to stall was determined, either by eye from the shapes of the velocity traces or, in cases which were unclear, by using the spatial Fourier analysis procedure first demonstrated by McDougall et al. (1990).

When measuring the compressor characteristics, it was found that by using the traditional method of recording the flow rate and pressure rise at relatively few throttle positions, the shape

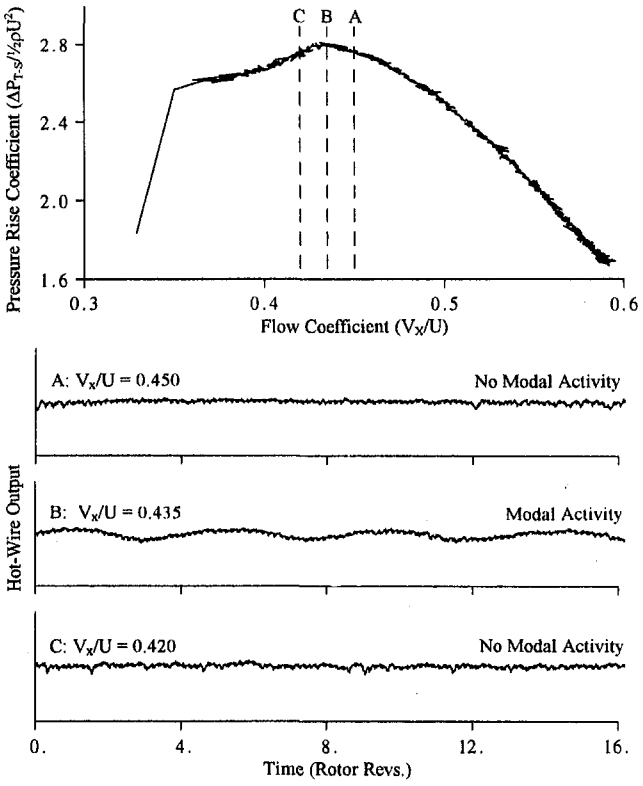

Fig. 8 An example of modal activity that does not lead directly to stall (downstream screen fitted)

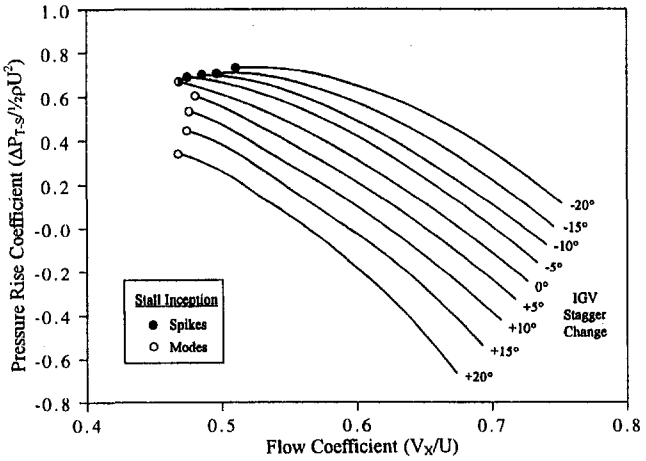

Fig. 9 Stage 1 characteristics as a function of IGV stagger angle

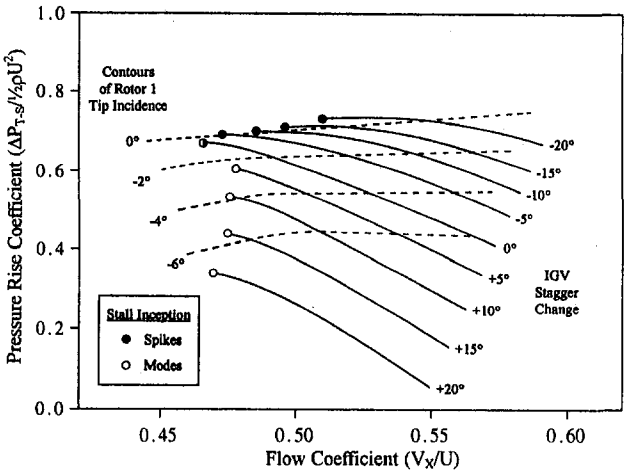

Fig. 11 Enlargement of Fig. 9 showing contours of rotor 1 tip incidence

of the characteristic in the region of the stall point was not sufficiently well defined. To overcome this limitation, an "on-line" data acquisition system was used, which recorded the pressure rise and flow rate of the compressor at every revolution of the rotor. While sampling continuously, the motor-driven throttle valve was closed slowly until the compressor stalled. Using this method, it was possible to record continuous characteristics right up to the instant of stall.

In the first experiment the stalling patterns and stage characteristics were measured for a range of IGV stagger angles while the downstream stators were held fixed at their design settings. The stagger of the IGVs was varied from −20 to +20 deg in steps of 5 deg, relative to their design position. Figure 9 shows the pressure rise characteristics of stage 1 for each stagger setting of the IGVs. The operating points at which the compressor stalled are shown in this figure by circular symbols, an open symbol indicating that modal activity was present at stall onset and a closed symbol indicating that spikes appeared in an axisymmetric flow-field. Figure 10 shows the complementary characteristics of the group of stages 2, 3, and 4, plotted to a larger scale than Fig. 9 in order to distinguish the individual stall points. As expected, the stage 1 characteristics are displaced relative to each other because the inlet flow angle to this stage changed as the IGVs were restaggered. In contrast, the characteristics of stages 2–4 follow a nearly unique curve because stators 2–4 and the inlet flow angle to this group of stages (principally determined by the stagger of stator 1) were held fixed. Figures 9 and 10 show that for the design geometry (IGV stagger of 0 deg) modal oscillations were observed in some cases but not others. When the IGV stagger angles were lower than design (increased rotor 1 incidence) modes did not appear and spikes initiated at rotor 1 in an otherwise steady flow-field. Conversely, for IGV stagger angles greater than design (decreased rotor 1 incidence) stall was always preceded by a clear first-order modal perturbation.

Figure 11 shows enlarged regions of the stage 1 characteristics from Fig. 9, on which contours of rotor 1 tip incidence have been plotted. The method used to estimate rotor tip incidence for this purpose is described in Appendix 2. From these measurements we see that when the compressor stalled via a spike in a clean, non-modal flow-field, the rotor 1 incidence angles at stall were approximately constant. However, when stall was preceded by a modal oscillation, the average rotor 1 incidence angle at the stall point was no longer fixed but covered a range of more negative values. The decision to plot rotor tip incidence in this figure was influenced by the observation that it is at the tip of the rotor blades where stall cells initiate.

Figure 12 shows regions near stall of the total-to-static pressure rise characteristics of the whole compressor as a function of IGV stagger angle. This figure shows that modes appeared prior to stall when the slope of the overall characteristic was zero. When modal oscillations were not present and stall cells grew via spikes from an axisymmetric flow-field, this occurred before the peak of the characteristic was reached, on the negatively sloped region of the characteristic.

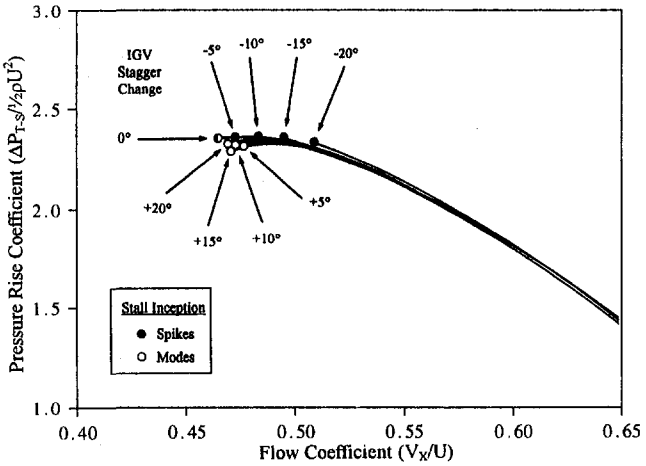

Fig. 10 Stage 2–4 characteristics as a function of IGV stagger angle

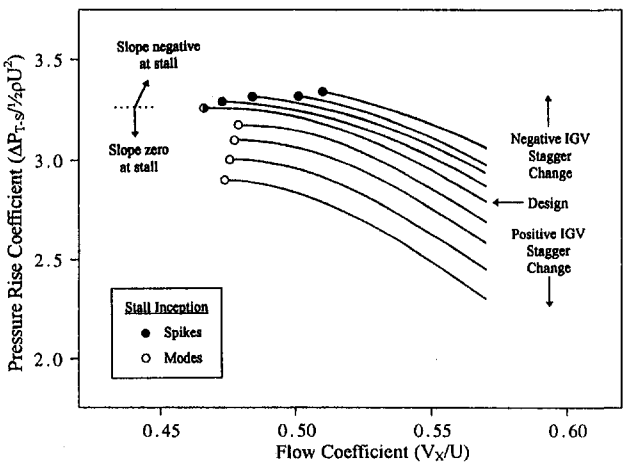

Fig. 12 Stages 1–4 characteristics as a function of IGV stagger angle

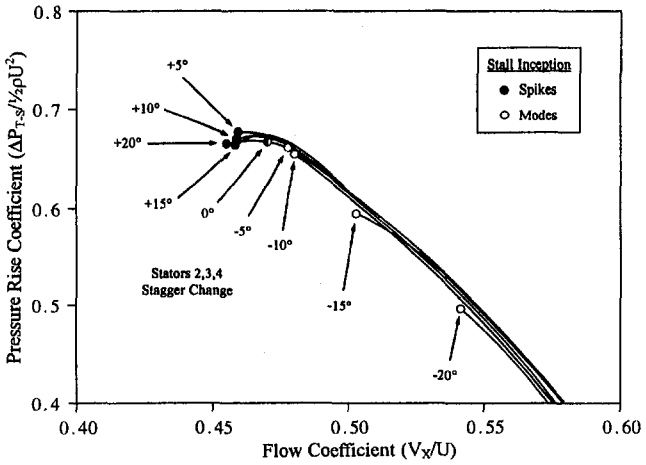

Fig. 13 Stage 1 characteristics as a function of stator 2, 3, and 4 stagger angles

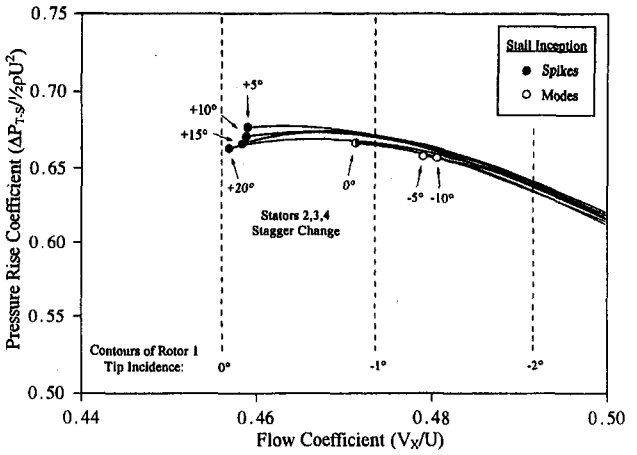

Fig. 15 Enlargement of Fig. 13 showing contours of rotor 1 tip incidence

To check on the generality of these observations, a second experiment was performed in which, rather than changing the flow conditions into the first stage, the geometry of the first stage was held fixed while the conditions in the downstream stages were varied. For this the stagger angles of the IGVs and stator 1 were held at their design settings, while the angles of stators 2, 3, and 4 were changed by equal amounts in steps of 5 deg from −20 to +20 deg relative to their datum positions. The pressure rise characteristics of stage 1 are shown in Fig. 13, while the characteristics of the group of stages 2–4 are shown in Fig. 14. The symbols marking the stall points on these characteristics show that when the stagger angles of stators 2–4 were increased relative to their design setting (increasing the negative slopes of their stage characteristics and thereby increasing the stability of stages 2–4 relative to stage 1) modal oscillations did not occur before stall; instead spike stall cells were initiated at rotor 1. However, when the stagger angles of stators 2–4 were decreased, stages 2–4 became more highly loaded than stage 1 and stall was generally preceded by a modal oscillation. (For stagger changes of −5 and −10 deg, spikes sometimes initiated at rotor 4.)

Figure 15 shows enlarged regions of the stage 1 characteristics overplotted with contours of rotor 1 incidence. Again it can be seen that spikes were initiated in rotor 1 at an approximately constant value of rotor incidence and that when modal behavior appeared before stall this occurred at lower values of average rotor 1 incidence. The value of rotor 1 incidence at which spikes were initiated (about 0 deg) is the same value at which spikes were initiated in the first experiment, as shown in Fig. 11. Figure 16 shows the total-to-static characteristics for the overall compressor near the stall points. Again modal oscillations appeared prior to stall when the slope of the overall pressure rise characteristic was zero or just positive. When the compressor stalled on a negatively sloped region of the characteristic, spike-type stall cells were seen to grow from an axisymmetric flowfield.

Simple Model and Discussion

The low-speed results described above lead to two important observations:

1 When stall is preceded by modal oscillations, the slope of the overall compressor characteristic is zero or slightly positive at the stall point. Alternatively, when stall initiates without a modal oscillation being present, this occurs on a negatively sloped region of the characteristic.

2 When stall is initiated by spike stall cells in rotor 1, this occurs at a limiting value of rotor 1 incidence angle. When stall is preceded by modal oscillations, rotor 1 incidence angles at the stall point are below this limiting value.

From these observations it is possible to propose a simple model to explain why, in some cases, stall is preceded by modal oscillations while in others stall cells grow from an initially

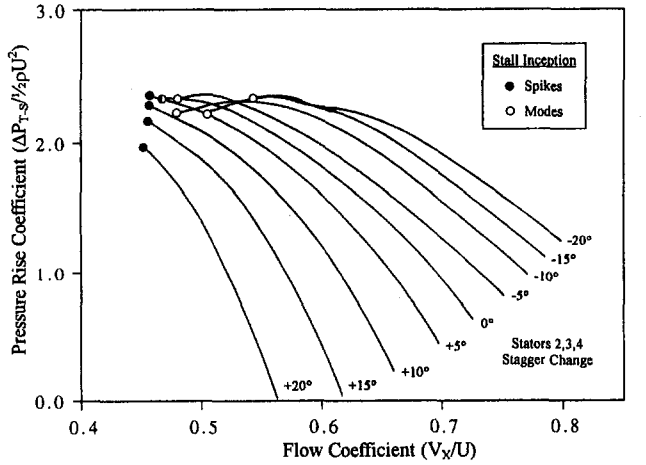

Fig. 14 Stage 2–4 characteristics as a function of stators 2, 3, and 4 stagger angles

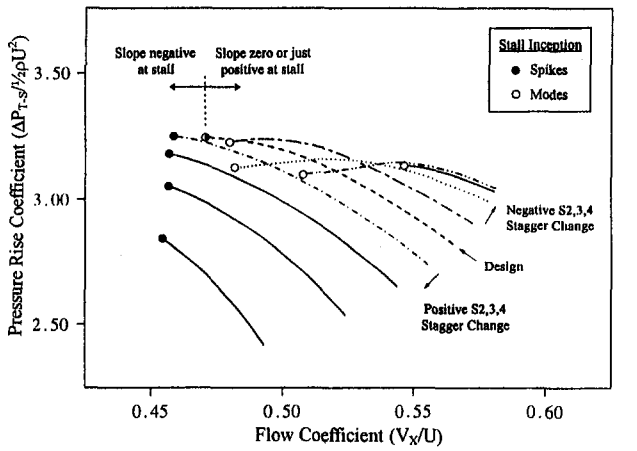

Fig. 16 Stage 1–4 characteristics as a function of stator 2, 3, and 4 stagger angles

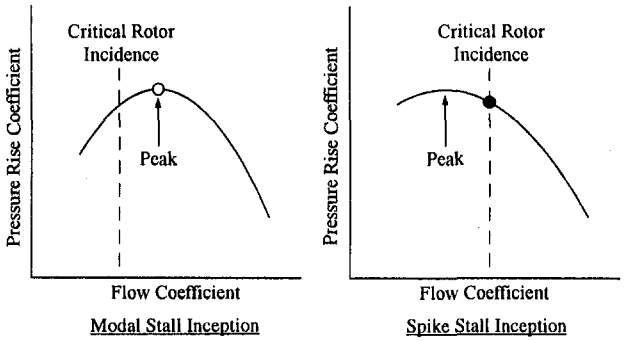

Fig. 17 Diagram illustrating the model

axisymmetric flow-field. The same model explains why some compressors stall at the peak of the characteristic while others stall while the characteristic is still rising. Stated simply, if the peak of the overall characteristic is reached before the critical value of rotor incidence is exceeded, then modal oscillations will occur. If, on the other hand, the critical rotor incidence is exceeded before the peak of the overall characteristic is reached, then spikes will appear in the overloaded rotor before modal activity has had an opportunity to develop. Whichever of these two stability limits is reached first will determine the stalling pattern of the compressor. Figure 17 illustrates these ideas diagramatically.

The general validity of the model is confirmed by Fig. 18, which summarizes the results of tests at various other IGV and stator stagger settings. In these tests the stagger angles of stators 2, 3, and 4 were not constrained to be the same, but were varied independently. The ordinate in Fig. 18 indicates the rotor 1 tip incidence, while the abscissa shows the gradient of the total-to-static pressure rise characteristic at the stall points. Each test symbol indicates whether modal oscillations were observed prior to stall or whether spike-type stall cells grew from a previously axisymmetric flow-field. Of all the measurements taken, the only data to be excluded from Fig. 18 are the few cases where stall was initiated by a spike mechanism at a rotor other than rotor 1. The figure shows that the symbols are grouped according to whether or not modal oscillations appeared before stall. The data points corresponding to stall without modes (spike inception at rotor 1) lie around a line of constant rotor 1 incidence and at positions that indicate negative slopes of the characteristics at stall. In contrast, points corresponding to modal behavior lie close to a line of zero characteristic slope and at rotor incidences below the critical value at which spikes initiate.

Single-Stage Experiments. In the experiments described above, which were conducted in a high hub–tip ratio compressor, the radial distribution of incidence was little affected by changes in stagger setting. There is of course no reason why the occurrence of critical incidence at the rotor tips could not be changed by changes in the twist of the blades or by changes in the radial distribution of the flow. This point has recently been demonstrated in a single-stage compressor where the appearance of modes or spikes was influenced by artificially skewing the flow toward the casing or the hub. A small amount of additional wall blockage was introduced in the vicinity of the stator blades, which had the effect of slightly altering the radial distribution of the flow approaching the rotor. The results show modal activity accompanying a "turned over" characteristic when the flow was diverted to the casing (increased tip velocity and therefore reduced incidence), and clear spikes on a rising characteristic when the flow was diverted to the hub (reduced tip velocity and increased incidence).

High-Speed Compressor Evidence. In a high-speed compressor the axial matching, and hence the rotor incidence, may be changed not only by adjusting variable blade rows but also by changing the shaft speed. If the compressor is well matched at the design speed, then at lower speeds the blading in the front stages will be subject to higher incidence than the rear stages while at higher speeds the blading in the rear stages will experience the highest incidence angles as stall is approached. According to the model discussed above, one would expect different stall inception mechanisms to occur at different speeds. Over a middle range of speeds where the compressor is well matched at the stall point (somewhat lower than the design speed if the design point is some distance from the stall line), stall will be preceded by modal oscillations of the flow-field. At lower speeds modes will not occur because spikes will initiate in the front stages, where the incidence angles are greatest. Likewise at higher speeds we would expect spike-type stalling in the rear stages.

Results from high-speed compressor tests conducted under the BRITE-EURAM Civil Core Compressor Project (Day et al., 1997) show that modal activity is indeed confined to the mid-speed range. Figure 19 shows a set of results from the MTU three-stage compressor studied in this project. At 60 percent speed the compressor stalls with spikes on the first rotor, while at 80 percent speed there is clear modal activity prior to stall. At higher speeds, spike-like behavior was sometimes observed, but owing to the very fast breakdown of the flow-field, the precise initiation mechanism was difficult to classify. Measurements from other compressors in the European project also show a clear trend from spikes to modes as the speed of the compressor is increased from low to medium speeds of rotation. It is interesting to note that the Rolls-Royce Viper compressor tested in the same project yielded modal activity in only a very narrow speed range between 85 and 87 percent. It seems that this occurred because the Viper compressor is relatively long, having eight stages, and therefore it is rare that equal loading on all stages occurs without one stage experiencing higher incidences than the rest.

Influence of Blade Design on Stalling Pattern

As described above, spikes are associated with flow breakdown at the rotor tips and so occur more readily in "tip critical" blading, such as the Cambridge compressor. For the case of blading that is not tip critical, it is thought that the increase in blockage and loss associated with hub corner separation leads to a "turned over" characteristic, which in turn promotes two-dimensional modal behavior. Indeed, the blockage created by separation near the hub tends to divert the flow toward the outer

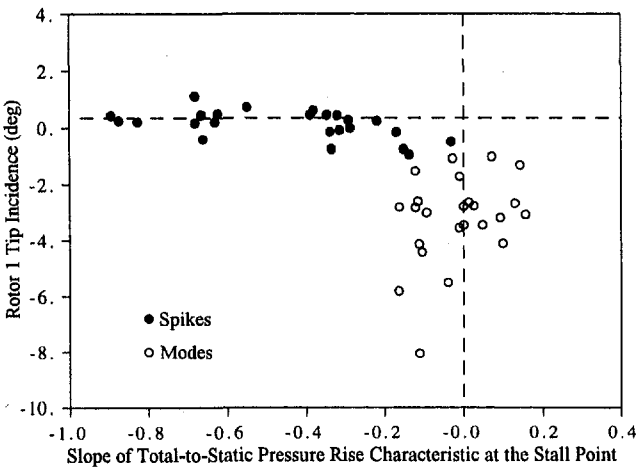

Fig. 18 Stall inception results for many different compressor configurations

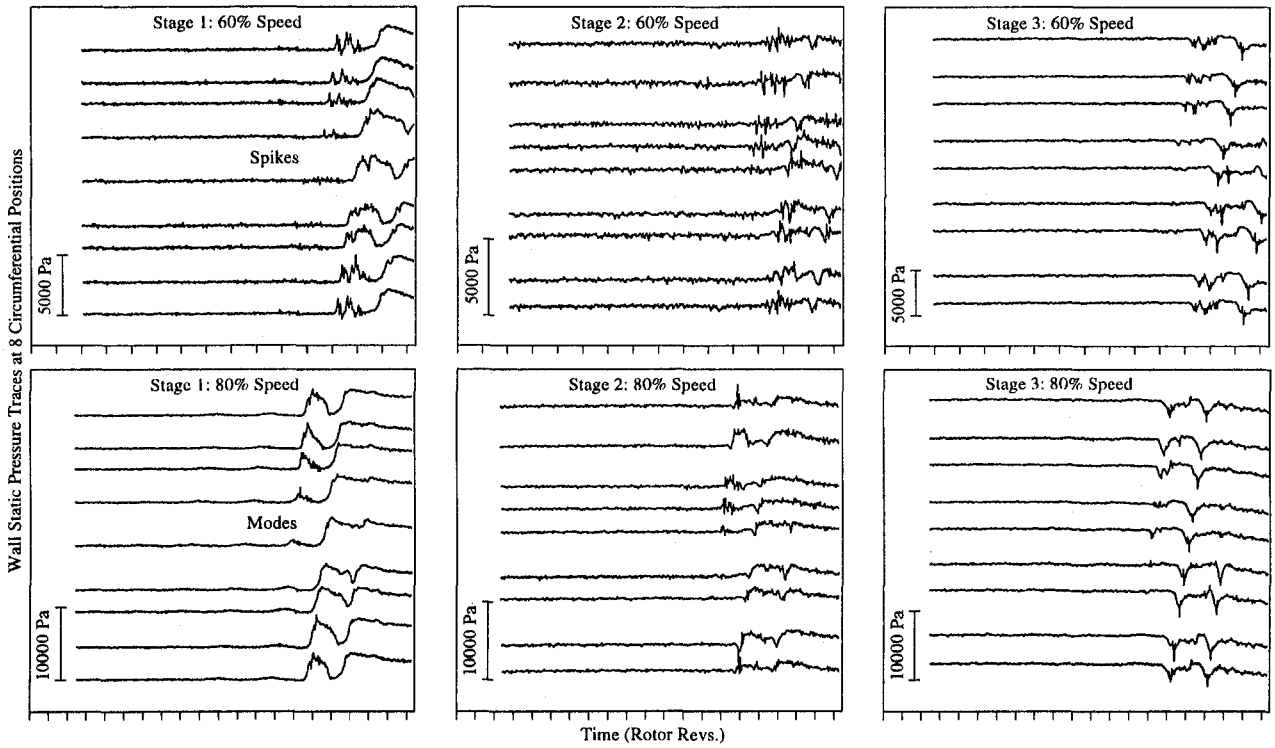

Fig. 19 *Casing static pressure traces from the MTU three-stage compressor showing changes in the stall inception pattern with shaft speed*

casing, thereby reducing rotor tip incidence and suppressing spike formation (as found in the single-stage experiments described above).

To go one step further, in a situation where the characteristic has turned over and modes have developed, the velocity deficit associated with the modes will, when large enough, precipitate flow breakdown and rotating stall. The actual breakdown process will include spikes if, at this stage, the tip is closest to stall, Fig. 3, or will take the form of a broad, slow-moving separation if the hub is the first to separate, as shown in Fig. 2. (The formation of a broad stall cell originating from separated flow at the hub has been reported by McDougall et al., 1990.) This argument does not take into account the contribution of the stator rows to the overall flow and hence to the shape of the characteristic. It has, however, been shown above that corner separations in the stator row at the casing will promote rotor spikes, while separation at the hub will favor the formation of modes.

The view presented here of the relationship between blade design and the stall inception pattern is simplistic and is open to a number of criticisms of detail, but it is consistent with most of our observations from low-speed single-stage and multistage testing.

Conclusions

This paper gives details of the short and long length-scale disturbances that precede stall in low and high-speed compressors. Using the variable geometry features of a four-stage low-speed compressor, we have investigated the situations in which each type of disturbance occurs, and have formulated a descriptive model, which may be used to explain the type of stall inception in a given situation. The generality of this model is supported by results from a single-stage compressor and from multistage high-speed compressors. In detail, the work has shown that:

1 Spike stall inception describes localized flow separation in one particular blade row of the compressor and occurs when a critical incidence is exceeded. This form of stall inception appears to be restricted to the tip region of rotor rows.

2 Modes are a circumferential oscillation of the flow-field occurring at the peak of the total-to-static pressure rise characteristic. When present, a modal oscillation may give rise to local flow conditions in which the incidence onto a particular blade row exceeds the critical value, giving rise to spikes. Alternatively a modal oscillation may give rise to separations in a larger number of blade passages, leading to the formation of a broader, more slowly rotating stall cell. (This type of cell formation is thought to be attributed to flow separation near the hub.) The amplitude to which a modal oscillation will grow before stalling begins depends on how close any particular blade row in the compressor is to being critically overloaded.

3 Modes and spikes may occur in the same compressor, sometimes simultaneously. The stability criteria for each are different: Long length-scale disturbances are related to a two-dimensional instability of the whole compression system, while short length-scale disturbances indicate a three-dimensional breakdown of the flow-field associated with high rotor incidence angles. Tests show that the occurrence of each phenomenon can be influenced by the stage matching, which in turn may be altered by changing blade stagger angles or, in the case of a high-speed compressor, by changing the shaft speed. A change between modes and spikes in a single-stage compressor has also been demonstrated by changing the radial distribution of rotor incidence.

4 A simple model has been proposed, based on the experimental results, which may be used to explain the occurrence of modes or spikes in a given situation. Stated simply, as the compressor flow rate is reduced, if the peak of the overall characteristic is reached before the critical value of rotor incidence is exceeded anywhere in the compressor, then modal oscillations will occur. However, if the critical rotor tip incidence is exceeded before the peak of the overall characteristic is reached then spikes will appear in the overloaded rotor, initiating stall before modal activity has had an opportunity to develop. The model thus explains why some compressors stall at the peak of

the characteristic and why others stall while the characteristic is still rising.

Acknowledgments

The authors would like to acknowledge the support of Rolls-Royce plc, who funded much of this research. We would also like to acknowledge the BRITE-EURAM program and to thank MTU for allowing the publication of the high-speed test data shown in Fig. 19. The suggestions made by several colleagues during the course of the work were very valuable and we would particularly like to thank Prof. N. A. Cumpsty, Prof. E. M. Greitzer, and Dr. D. Wisler.

References

Camp, T. R., 1995, "Aspects of the Off-Design Performance of Axial Flow Compressors," Ph.D. dissertation, Cambridge University Engineering Department.

Day, I. J., 1993a, "Active Suppression of Rotating Stall and Surge in Axial Compressors," ASME JOURNAL OF TURBOMACHINERY, Vol. 115, pp. 40–47.

Day, I. J., 1993b, "Stall Inception in Axial Flow Compressors," ASME JOURNAL OF TURBOMACHINERY, Vol. 115, pp. 1–9.

Day, I. J., 1996, private communication (to be published).

Day, I. J., Breuer, T., Escuret, J. F., and Cherrett, M., 1998, "Stall Inception and the Prospects for Active Control in Four High Speed Compressors," ASME JOURNAL OF TURBOMACHINERY, Vol. 120, in press.

Epstein, A. H., Ffowcs-Williams, J. E., and Greitzer, E. M., 1986, "Active Suppression of Aerodynamic Instabilities in Turbomachines," AIAA *Journal of Propulsion and Power,* Vol. 5, No. 2, pp. 204–211.

Feulner, M. R., Hendricks, G. J., and Paduano, J. D., 1996, "Modeling for Control of Rotating Stall in High-Speed Multistage Axial Compressors," ASME JOURNAL OF TURBOMACHINERY, Vol. 118, pp. 1–10.

Garnier, V. H., Epstein, A. H., and Greitzer, E. M., 1991, "Rotating Waves as a Stall Inception Indication in Axial Compressors," ASME JOURNAL OF TURBOMACHINERY, Vol. 113, pp. 290–301.

Haynes, J. M., Hendricks, G. J., and Epstein, A. H., 1994, "Active Stabilization of Rotating Stall in a Three-Stage Axial Compressor," ASME JOURNAL OF TURBOMACHINERY, Vol. 116, pp. 226–239.

Hendricks, G. J., Bonnaure, L. P., Longley, J. P., Greitzer, E. M., and Epstein, A. H., 1993, "Analysis of Rotating Stall Onset in High Speed Axial Flow Compressors," AIAA Paper No. 93-2233.

Hoying, D. A., 1996, "Blade Passage Flow Structure Effects on Axial Compressor Rotating Stall Inception," Ph.D. Dissertation, Dept. of Aeronautics and Astronautics, M.I.T.

McDougall, N. M., Cumpsty, N. A., and Hynes, T. P., 1990, "Stall Inception in Axial Compressors," ASME JOURNAL OF TURBOMACHINERY, Vol. 112, pp. 116–125.

Moore, F. K., and Greitzer, E. M., 1986, "A Theory of Post-Stall Transients in Axial Compression Systems: Part I—Development of Equations," ASME *Journal of Engineering for Gas Turbines and Power,* Vol. 108, pp. 68–76.

Paduano, J., Epstein, A. H., Valavani, L., Longley, J. P., Greitzer, E. M., and Guenette, G. R., 1993, "Active Control of Rotating Stall in a Low Speed Axial Compressor," ASME JOURNAL OF TURBOMACHINERY, Vol. 115, pp. 48–56.

Simon, J. S., Valavani, L., Epstein, A. H., and Greitzer, E. M., 1993, "Evaluation of Approaches to Active Compressor Surge Stabilisation," ASME JOURNAL OF TURBOMACHINERY, Vol. 115, pp. 57–67.

Tryfonidis, M., Etchevers, O., Paduano, J. D., Epstein, A. H., and Hendricks, G. J., 1995, "Pre-stall Behavior of Several High-Speed Compressors," ASME JOURNAL OF TURBOMACHINERY, Vol. 117, No. 1, pp. 62–80.

APPENDIX 1

Details of the Cambridge Four-Stage Compressor

The multistage compressor used for the low-speed experiments described in this paper was the C106 compressor at the Whittle Laboratory, Cambridge University. This compressor has four identical stages preceded by a lightly loaded row of inlet guide vanes. The stator vanes in this compressor are cantilevered. The hub/casing radius ratio is 0.75 and the speed of rotation is 3000 rpm, giving a maximum Reynolds number of 2×10^5, based on rotor chord. Details of the blading are given in Table 1. The inlet guide vanes and each row of stators are fitted with a variable stagger mechanism, similar to that used in high-speed compressors, which allows these blade rows to be easily restaggered. Further details are given by Camp (1995).

Table 1 Details of the C106 compressor

	IGV	Rotor	Stator
No. of Aerofoils	60	58	60
Mid-Height Chord (mm)	36.0	35.6	36.2
Mid-Height Stagger (deg)	6.5	-44.4	23.1
Mid-Height Camber (deg)	-17.3	17.8	37.6
Mid-Height Solidity	1.55	1.47	1.55
Aspect Ratio	1.76	1.78	1.75
Tip Clearance (% chord)	1.0	1.0	1.0
Axial Gap (% chord)	42	46	45
Reynolds Number	1.04×10^5	2.00×10^5	1.46×10^5
Va / Umid	0.52		
Δho / Umid^2	0.40		
Reaction (%)	68		
Static Pressure Rise Coef.	0.70		
Rotor Tip Mach Number	0.23		

APPENDIX 2

The Calculation of Critical Rotor Incidence

To estimate the values of rotor incidence, contour plotted in Figs. 11 and 15, it was assumed that the IGV deviation angle was constant at its design value and that the axial velocity at the rotor tip was equal to the area-mean axial velocity, calculated over the whole annulus. The increase in rotor incidence due to the casing boundary layer was therefore not accounted for, and thus the incidence values given in these figures underestimate the true rotor tip incidence, but by a relatively constant amount. To check that the restaggering of the IGVs did not cause significant changes to the casing boundary layer or to the IGV deviation, area traverses of a hot-wire probe were performed at the IGV exit plane at operating points near stall for each stagger setting. It was found that the IGV stagger angle had little effect on the thin casing boundary layer at this compressor inlet plane and that the axial velocity profiles remained flat outside the boundary layers. The assumption of a constant IGV deviation angle was also confirmed by the measurements. In summary, the IGV restaggering produced clean changes to the rotor 1 incidence without significant changes to the inlet boundary layers or to the radial distribution of the flow.

In this description of results and in the proposed model, the initiation of stall cells in a previously axisymmetric flow-field (spike stall inception) was linked to a critical value of blade incidence being exceeded. The question arises as to whether blade incidence angle is the most appropriate parameter with which to predict the formation of stall cells. It is unlikely, for example, that the critical value of incidence would be the same for all profile types and all values of camber, space-chord ratio, etc. The formation of stall cells implies separation of the flow from the blade surfaces, endwall or (perhaps more likely) a corner. Therefore it might be thought that a loading parameter, such as diffusion factor, would correlate better with spike formation. It was found, however, that when Fig. 18 was replotted using rotor diffusion factor instead of incidence, the collapse of the datapoints was not as good. Further work is required to clarify which particular measure of blade or endwall loading is the most appropriate guide to spike stall inception.

1997 Best Paper Award—Heat Transfer Committee

The Turbulence That Matters

R. E. Mayle[1]
Fellow ASME

K. Dullenkopf

A. Schulz

Institut für Thermische Strömungsmaschinen, Universität Karlsruhe, Karlsruhe, Germany

A unified expression for the spectrum of turbulence is developed by asymptotically matching known expressions for small and large wave numbers, and a formula for the one-dimensional spectral function, which depends on the turbulence Reynolds number Re_λ, is provided. In addition, formulas relating all the length scales of turbulence are provided. These relations also depend on Reynolds number. The effects of free-stream turbulence on laminar heat transfer and pretransitional flow in gas turbines are re-examined in light of these new expressions using our recent thoughts on an "effective" frequency of turbulence and an "effective" turbulence level. The results of this are that the frequency most effective for laminar heat transfer is about $1.3\ U/2\pi L_e$, where U is the free-stream velocity and L_e is the length scale of the eddies containing the most turbulent energy, and the most effective frequency for producing pretransitional boundary layer fluctuations is about $0.3\ U/2\pi\eta$, where η is Kolmogorov's length scale. In addition, the role of turbulence Reynolds number on stagnation heat transfer and transition is discussed, and new expressions to account for its effect are provided.

Introduction

The aerodynamic performance of a gas turbine and the heat load to its "hot" surfaces are primarily determined by the free-stream pressure gradients and turbulence, as well as by the machine's pressure ratio and turbine inlet temperature. In general, the effects of the latter two are easily taken into account, while those of free-stream pressure gradients are well understood and can be calculated. The effects of free-stream turbulence, on the other hand, are now just beginning to be understood.

Two of its effects are clearly seen in Fig. 1, where the Nusselt number distributions around a typical fore-loaded airfoil for several free-stream turbulence levels are presented (Schulz, 1986). At the leading edge where the highest Nusselt numbers are found, and on the pressure surface ($x/c < 0$) where the highly accelerated boundary layer remains laminar, the main effect of turbulence is to cause a large increase in laminar heat transfer. On the suction surface ($x/c > 0$) where a laminar-to-turbulent transition occurs, the main effect is to cause an earlier onset of transition with its subsequent increase in turbulent heat transfer. Although these are not the only effects of free-stream turbulence in gas turbines, they are important effects and the only two we will presently consider.

We have examined these effects previously (Dullenkopf and Mayle, 1995; Mayle and Schulz, 1997). In our 1995 paper, we focused our attention on how free-stream turbulence affects laminar heat transfer, and developed the concepts of an "effective" frequency[2] and an "effective" turbulence level. In the 1997 paper, we developed a laminar-kinetic-energy equation to calculate the effects of free-stream turbulence on pretransitional laminar flow, and used the effective frequency-and-turbulence-level concepts to obtain the growth of laminar fluctuations in this flow. In both papers it is shown that the effects of free-stream turbulence are intimately connected to its spectral distribution, and not just its integrated level, or its level and integrated length scale, etc., but its full spectrum. In fact, we also showed that the effects of free-stream turbulence depend on the boundary layer thickness as well.

The present paper is our third in this series. Our intent is to examine the role of free-stream turbulence more closely and to present a more coherent picture of its effects than we did before. To accomplish this, we obtain a unified expression for the one-dimensional spectrum of turbulence, which properly accounts for all the scales of turbulence, or in other words, the effect of turbulence Reynolds number.

The paper is divided into several parts. In the first part, we briefly review the effects of free-stream turbulence on stagnation-like heat transfer and pretransitional nonaccelerating laminar flow and discuss the turbulence that matters for each. In the second part, we develop the unified spectral distribution for turbulence and obtain formulas that can be used to predict the effects of free-stream turbulence on heat transfer and transition. Finally, in the last part of the paper, the important role of turbulence Reynolds number is discussed.

Effects of Free-Stream Turbulence

Effect on Heat Transfer. As it turns out (see Mayle and Schulz, 1997), a practical method of treating laminar boundary layers in turbulent free streams is proposed by Lin (1957). Decomposing the velocities and pressure into time-averaged and time-dependent components, he obtained a set of equations very similar to Reynolds' equations for turbulent flow (Schlichting, 1979). The difference between these two sets of equations is the way in which the pressure fluctuations are handled. For laminar boundary layers in a turbulent free stream, the free-stream pressure fluctuations, as well as the mean pressure, are impressed on the flow in the boundary layer, while for turbulent flow they are not.

Following Lin's unsteady-laminar-flow analysis, the time-averaged energy equation for laminar boundary layers in turbulent free streams is

$$\bar{u}\frac{\partial \bar{T}}{\partial x} + \bar{v}\frac{\partial \bar{T}}{\partial y} = \alpha\frac{\partial^2 \bar{T}}{\partial y^2} + \frac{\partial}{\partial y}\left(-\overline{v'T'}\right)$$

which is, not surprisingly, identical to that for turbulent flow.

[1] Professor Emeritus of Mechanical Engineering, Rensselaer Polytechnic Institute, Troy, NY, USA.

[2] Depending on outlook, one may also substitute either the words "effective wave number" or "effective length scale" here.

Contributed by the International Gas Turbine Institute and presented at the 42nd International Gas Turbine and Aeroengine Congress and Exhibition, Orlando, Florida, June 2–5, 1997. Manuscript received at ASME Headquarters February 1997. Paper No. 97-GT-274. Associate Technical Editor: H. A. Kidd.

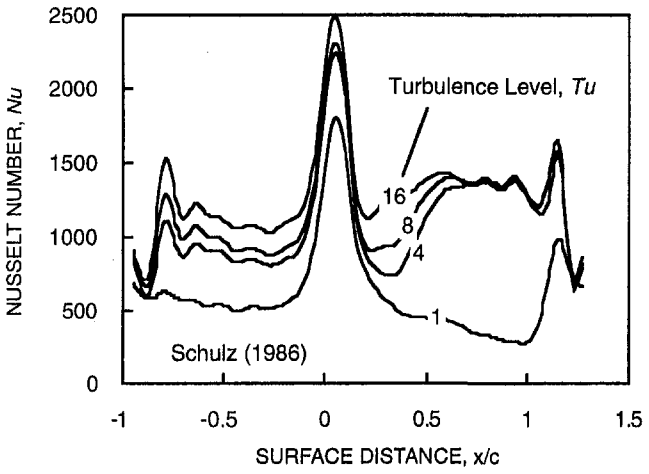

Fig. 1 Effect of free-stream turbulence level on airfoil heat transfer

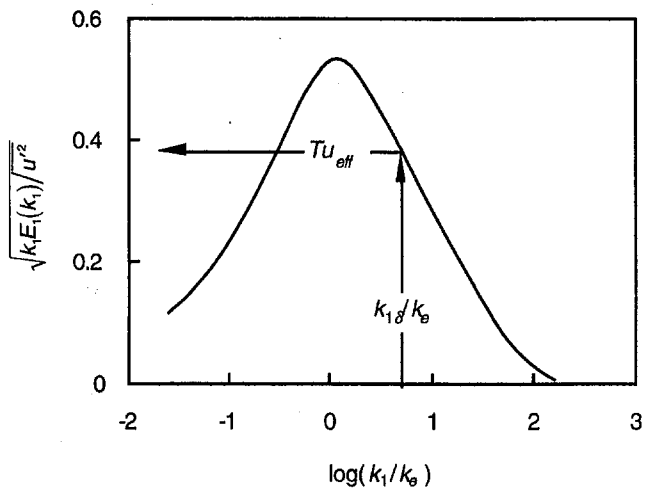

Fig. 2 Spectrum function related to the effective turbulence for heat transfer in a laminar boundary layer

According to the usual notation, the overbars refer to time-averaged quantities, u and v are the velocity components in the streamwise and wall-normal directions, x and y, respectively, T is the temperature, and α is the thermal diffusivity. In this case, however, the quantity $-\overline{v'T'}$ is a heat flux caused by the laminar fluctuations in the boundary layer arising from the turbulence in the free stream.

For stagnation flow, Smith and Kuethe (1966) modeled this heat flux by considering the heat flux turbulent and using an eddy diffusivity proportional to the product of the free-stream turbulence intensity and the distance away from the wall. As a result, they predicted a linear increase in heat transfer with increasing free-stream turbulence level Tu, where $Tu = \sqrt{\overline{u'^2}}/U$, and $\sqrt{\overline{u'^2}}$ is the intensity of the free-stream velocity fluctuation in the direction of the mean velocity U. It is easy to show that the same result would be obtained if the heat flux was considered to be caused by laminar fluctuations. It wasn't until recently, however, after replacing Tu with an effective free-stream turbulence level Tu_{eff}, that their predicted behavior was shown to correlate most of the data, including airfoil data and those for very high turbulence levels (Dullenkopf and Mayle, 1995). (For a consistent analysis of all the data, see Dullenkopf and Mayle, 1994.) The idea of introducing an effective turbulence level was based on the fact that only the turbulence within a small band of frequencies can really affect the boundary layer since any turbulence at higher frequencies will be viscously damped, while that at lower frequencies will appear quasi-steady and have no time-averaged effect.

Considering this last point in more detail, if $E_1(n)$ is the one-dimensional spectral density of turbulence where n is the frequency,[3] and n_δ is a representative frequency of the band most affecting the boundary layer, two of us showed (Dullenkopf and Mayle, 1995) that the effective free-stream turbulence level is given[4] by $\text{Tu}_{\text{eff}} = \sqrt{\overline{u'^2_{\text{eff}}}}/U \propto \sqrt{n_\delta E_1(n_\delta)/U}$. The proportionality factor, which depends directly on the square root of the bandwidth-to-frequency ratio, was supposed constant. In terms of the wave number $k_1 = 2\pi n/U$, and remembering that $E_1(n) = 2\pi E_1(k_1)/U$ (Hinze, 1975), the ratio of effective to integrated turbulence level Tu becomes

$$\frac{Tu_{\text{eff}}}{Tu} \propto \sqrt{\frac{k_{1\delta}E_1(k_{1\delta})}{\overline{u'^2}}} \tag{1}$$

where $k_{1\delta} = 2\pi n_\delta/U$ is the representative wave number of the effective wave number range. The "best" value for $k_{1\delta}$, which was obtained by correlating stagnation heat transfer results (Dullenkopf and Mayle, 1995), is given by $k_{1\delta} \approx 0.11/\delta$.

[3] For readers referring to our previous papers, the following changes in nomenclature have been made: (D&M)—the circular frequency $f \rightarrow n$, the integral length scale $l \rightarrow \Lambda$; (M&S)—the circular instead of the angular frequency ω is used.

[4] Many of the results from our first two papers require some manipulation to obtain those stated in this paper. For the sake of brevity, the details have been omitted. The following result is an example. It is obtained by comparing the first three equations in the section titled "A Simple Model" from D&M (1995).

Nomenclature

$E(k)$ = three-dimensional spectral density, m^3/s^2
$E_1(k_1)$ = one-dimensional spectral density, m^3/s^2
k = kinetic energy of the laminar fluctuations, m^2/s^2; three-dimensional wave number, m^{-1}
k_1 = one-dimensional wave number, m^{-1}
k_d = wave number of energy dissipating eddies, m^{-1}
k_e = wave number of energy containing eddies, m^{-1}
L_e = length scale of the energy containing eddies, m
n = circular frequency, Hz
$\bar{q}$ = time-averaged component of q
q' = fluctuating component of q, $\overline{q'^2} = 0$
$\sqrt{\overline{q'^2}}$ = root-mean-square of q'
Re = Reynolds number
Re_λ = turbulence Reynolds number = $\sqrt{\overline{u'^2}}\,\lambda/\nu$
T = temperature, °C
Tu = free-stream turbulence level = $\sqrt{\overline{u'^2}}/U$
u = velocity component in the x direction, m/s
U = free-stream velocity, m/s
v = velocity component in the y direction, m/s
x = coordinate in the free-stream direction, m
y = coordinate normal to the surface, m
α = thermal diffusivity, m^2/s; Kolmogorov's constant
δ = boundary layer thickness, m
ϵ = dissipation of kinetic energy, m^2/s^3
η = Kolmogorov's length scale, m
λ = viscous dissipation length scale, m
Λ = integral length scale of turbulence, m
ν = kinematic viscosity, m^2/s
ρ = density, kg/m^3
υ = Kolmogorov's velocity scale, m/s

The spectral function on the right-hand-side of Eq. (1) is sketched in Fig. 2. The wave number k_e is that associated with the energy-containing eddies, hence the maximum near unity, or more exactly, as will be shown, at $k_{1\max}/k_e \approx 1.3$. For large turbulence Reynolds numbers $k_e \approx 0.75\Lambda^{-1}$, where Λ is the integral length scale of turbulence. As an example, the effective turbulence level corresponding to a wave number ratio $k_{1\delta}/k_e \approx 0.15\Lambda/\delta$ with $\Lambda/\delta \approx 50$ is also shown. For larger values, corresponding to larger integral length scales or smaller boundary layer thicknesses, Tu_{eff} decreases; for smaller values, Tu_{eff} increases until the maximum effective turbulence level is obtained at $\Lambda/\delta \approx (k_{1\max}/k_e)/0.15 \approx 9$, and then decreases. This is the effect of turbulence length scale on heat transfer we previously described in 1995 (Dullenkopf and Mayle). It is also the effect described much earlier by Yardi and Sukhatme (1978) who measured the effects of turbulence level and length scale on stagnation heat transfer and found a maximum effect when $\Lambda/\delta \approx 10$. Therefore, the turbulence that matters for laminar heat transfer depends not on the measured (integrated) turbulence level, but on the turbulence level corresponding to a band of wave numbers around a wave number selected by the boundary layer, and the maximum effect is obtained for wave numbers in the energy containing range.

Effect on Transition. Transition in a laminar boundary layer begins at the first position along the surface where isolated spots of turbulence (Emmons, 1951) are formed, and as we recently showed (Mayle and Schulz, 1997), the main effect of free-stream turbulence is to generate and amplify the laminar fluctuations in the boundary layer upstream of this position. Where these fluctuations attain a critical value, turbulent spots form and transition begins.

As we showed, the appropriate kinetic energy equation for these pretransitional laminar fluctuations, called the laminar kinetic energy (LKE) equation, is

$$\bar{u}\frac{\partial k}{\partial x} + \bar{v}\frac{\partial k}{\partial y} = \overline{u'\frac{\partial u'_{fs}}{\partial t}} + \nu\frac{\partial^2 k}{\partial y^2} - \epsilon$$

where k is the kinetic energy (not to be confused with the wave number), and ν is the kinematic viscosity. The terms on the right correspond respectively to the production, diffusion, and dissipation of laminar kinetic energy. The production term, shown as the time average of the product of the velocity fluctuations in the boundary layer and the temporal derivative of those in the free stream, is new and arises from taking the average of $u'(dp'/dx)$. Physically, it represents the work done on the fluctuations by the imposed fluctuating pressure forces. Since this term contains u'_{fs}, it provides a direct link between the free-stream turbulence and the fluctuations in the boundary layer. Therefore, these fluctuations are forced and do not arise from any natural instability in the flow.

From dimensional considerations it is easy to see that this term must be proportional to the product of $\sqrt{k}$, which is proportional to $\sqrt{\overline{u'^2}}$, an effective free-stream turbulence intensity $\sqrt{\overline{u'^2_{\text{eff}}}}$, as discussed above, and an effective frequency n_{eff}. Hence, the production term becomes proportional to $n_{\text{eff}}\sqrt{\overline{u'^2_{\text{eff}}}}\sqrt{k}$, of which only the quantity $n_{\text{eff}}\sqrt{\overline{u'^2_{\text{eff}}}}$ reflects the effects of free-stream turbulence. In our last paper (Mayle and Schulz, 1997), this quantity was identified as $C_\omega(U^2/\nu)\sqrt{\overline{u'^2_{fs}}}$ where C_ω is a dimensionless production rate. Replacing n_{eff} with an effective wave number and introducing the spectral density $E_1(k_1)$, using $\sqrt{\overline{u'^2_{\text{eff}}}} = Tu_{\text{eff}}U$ and Eq. (1), one obtains

$$C_\omega \propto \frac{k_{1\text{eff}}\nu}{U}\sqrt{\frac{k_{1\text{eff}}E_1(k_{1\text{eff}})}{\overline{u'^2_{fs}}}} \qquad (2)$$

Since the diffusion and dissipation of laminar kinetic energy are initially small, it is easy to show from the LKE equation,

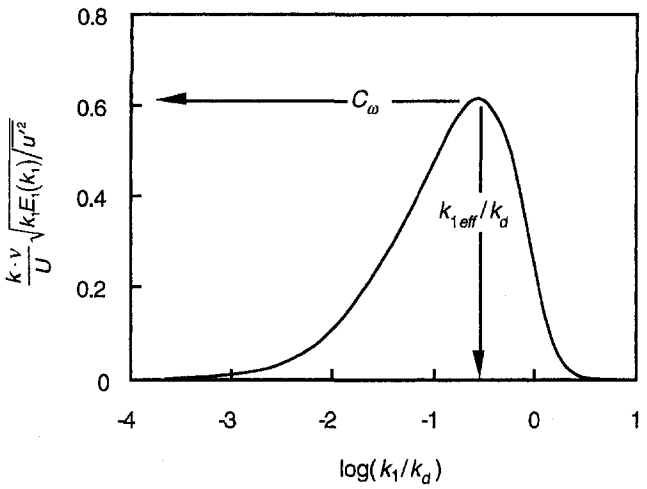

Fig. 3 Spectrum function related to the production of laminar kinetic energy in a laminar boundary layer

with a production term equal to $C_\omega(U^2/\nu)\sqrt{\overline{u'^2_{fs}}}\sqrt{k}$, that $\sqrt{k}$ increases in proportion to C_ω. Therefore, the maximum growth of laminar fluctuations in the boundary layer, leading to the earliest onset of transition, occurs for the value of $k_{1\text{eff}}$ that maximizes C_ω for a given free-stream turbulence level. The appropriate value of C_ω must then be given by

$$C_\omega \propto \left[\frac{k_1\nu}{U}\sqrt{\frac{k_1E_1(k_1)}{\overline{u'^2_{fs}}}}\right]_{\max} \qquad (3)$$

The spectral function on the right-hand-side of Eq. (3) is plotted in Fig. 3 against k_1/k_d, where k_d is the wave number associated with the eddies providing the largest contribution to the dissipation of turbulence. As will be shown, the maximum occurs at $k_1/k_d \approx 0.3$. This provides $k_{1\text{eff}} \approx 0.3\ k_d$, which is nearly the same result we obtained previously using a slightly different approach (Mayle and Schulz, 1997). Therefore, the turbulence that matters for pretransitional laminar flow depends not on the measured turbulence level, but on the turbulence level corresponding to a band of wave numbers near the dissipative range.

The Important Wave Number Ranges. To highlight the important ranges of wave numbers involved, the two previous figures are combined in Fig. 4 using a common abscissa. As

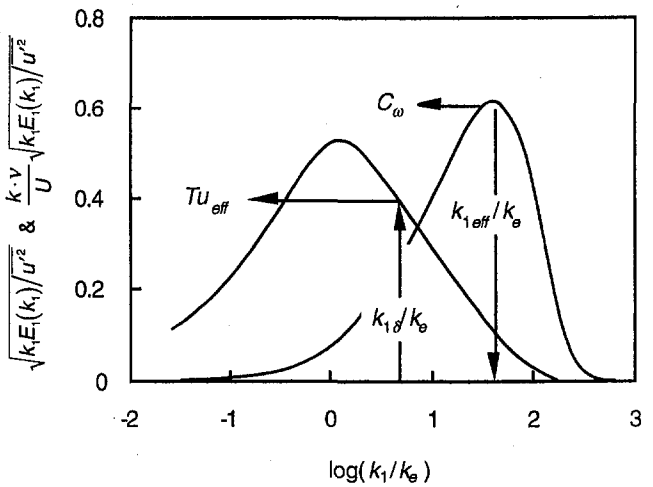

Fig. 4 The different wave number ranges for the effects of turbulence on a laminar boundary layer

seen in this figure, the effective wave number for pretransitional flow is more than one order of magnitude larger than the wave number that provides the maximum effect on laminar heat transfer. This magnitude, which depends on the turbulence Reynolds number, reflects the well-known difference in wave numbers for the energy-containing eddies and those most responsible for dissipation. Using the values previously cited, their ratio becomes $k_{1\text{eff}}/k_{1\max} = 0.25\ k_d/k_e$. For larger Reynolds numbers, the ratio increases.

The curves in this figure have been drawn for a turbulence Reynolds number Re_λ of about 100, where $\mathrm{Re}_\lambda = \sqrt{\overline{u'^2_{fs}}}\,\lambda/\nu$ and λ is Taylor's microscale of turbulence. Typical values for gas turbine engines are about 100 and above, which may be called moderate, with the smaller values found in the airfoils' wakes. These values can easily be attained in experiments using jet-grid-generated turbulence (Thole, 1992). Typical values in experiments with bar-grid-generated turbulence are about 50, which is low for gas turbine application. Large Reynolds numbers as referred to in the literature on turbulence correspond roughly to values > 2000.

A present difficulty, however, is that there is no easy way to account for the effects of turbulence Reynolds number on the spectrum of turbulence. In the following we attempt to provide one.

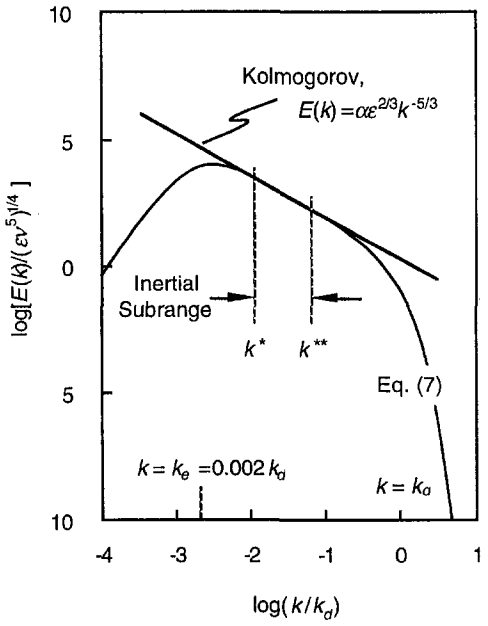

Fig. 5 A unified three-dimensional energy spectrum of turbulence ($\alpha = 1.7$)

A Unified Spectrum of Turbulence

If an inertial subrange exists, where according to Kolmogorov the spectral density varies inversely as the wave number raised to the five-thirds power, it is possible to match von Kármán's (1948) interpolation formula for small wave numbers with Pao's (1965) theoretical expression for large wave numbers to provide a unified three-dimensional energy spectrum for isotropic turbulence. The formula given by von Kármán is

$$E(k) = 2^{17/6}E(k_e)\frac{(k/k_e)^4}{[1 + (k/k_e)^2]^{17/6}} \tag{4}$$

where k is the wave number (actually, the radius vector) in three-dimensional wave number space, and $E(k_e)$ is a function yet to be determined but which for very large turbulence Reynolds numbers is equal to $0.2\ u'^2/k_e$.[5] For $k \ll k_e$, $E(k) \propto k^4$, which matches the behavior for very small wave numbers, while for $k \gg k_e$, $E(k) \approx 2^{17/6}E(k_e)(k/k_e)^{-5/3}$, which matches Kolmogorov's result for the inertial subrange.

For large wave numbers where viscous dissipation is important, the spectrum as determined by Pao is

$$E(k) = \alpha(\epsilon\nu^5)^{1/4}(k/k_d)^{-5/3}\exp(-\tfrac{3}{2}r\alpha(k/k_d)^{4/3}) \tag{5}$$

where $\alpha \cong 1.7$ is Kolmogorov's constant,[6] and ϵ is the rate of dissipation of turbulent kinetic energy. Originally taken as unity by Pao, the quantity r is introduced here to account for the effect of viscosity on the transfer of turbulent energy from one eddy to another and is, therefore, a function of Reynolds number. Since the dissipation of turbulent energy is given by

$$\epsilon = 2\nu\int_0^\infty k^2E(k)dk \tag{6}$$

the wave number k_d corresponds roughly to that where $k^2E(k)$ is maximum. It is also defined as $k_d = 1/\eta$ where $\eta = (\nu^3/\epsilon)^{1/4}$ is Kolmogorov's length scale. For $k \ll k_d$, Eq. (5) becomes $E(k) \approx \alpha(\epsilon\nu^5)^{1/4}(k/k_d)^{-5/3}$, which again corresponds to the behavior for the inertial subrange.

[5] Since free-stream turbulence is only being considered in this section, the subscript "fs" on u' has been dropped.

[6] An average value for a large variety of flows as obtained by Sreenivasan (1995) is $\alpha = 1.62 \pm 0.17$. The value of 1.7 is that found by Pao (1965).

Supposing that an inertial subrange exists, say between k^* and k^{**}, Eqs. (4) and (5) must overlap when $k_e \ll k^* < k^{**} \ll k_d$. Comparing Eqs. (4) and (5) in this region provides $2^{17/6}E(k_e) = \alpha(\epsilon\nu^5)^{1/4}(k_d/k_e)^{5/3}$. Neglecting the error of Eq. (4) at k^* and that of Eq. (5) at k^{**}, which tacitly implies large turbulence Reynolds numbers, Eqs. (4) and (5) may be combined into one unified expression for all wave numbers, namely

$$E(k) = \alpha(\epsilon\nu^5)^{1/4}(k_d/k_e)^{5/3}\frac{(k/k_e)^4\exp[-\frac{3}{2}r\alpha(k/k_d)^{4/3}]}{[1 + (k/k_e)^2]^{17/6}} \tag{7}$$

This expression is plotted in Fig. 5 for $k_e/k_d = 0.002$ (corresponding to $\mathrm{Re}_\lambda \approx 450$). In addition, Kolmogorov's relation and inertial subrange are shown. For $k_e/k_d > 0.01$, corresponding to $\mathrm{Re}_\lambda < 100$, the curve begins to fall below Kolmogorov's relation and less, if any, of it can be said to exhibit an inertial subrange. In spite of this, and remembering that Eq. (7) remains completely valid when an inertial subrange does exist, we propose that it may also be an appropriate interpolation formula when a subrange does not exist. Of course, this remains to be seen.

Using Eq. (7) for $E(k)$, the one-dimensional energy spectrum of turbulence can be obtained from

$$E_1(k_1) = \int_{k_1}^\infty \frac{E(k)}{k}\left(1 - \frac{k_1^2}{k^2}\right)dk \tag{8}$$

In addition, the dissipation can be obtained from Eq. (6), and the integrated mean-square velocity and the integral length scale can be obtained from

$$\overline{u'^2} = \int_0^\infty E_1(k_1)dk_1 \quad \text{and} \quad \Lambda = \frac{\pi}{2\overline{u'^2}}\int_0^\infty \frac{E(k)}{k}dk, \tag{9}$$

respectively. Once ϵ and $\overline{u'^2}$ have been evaluated, the relation between the dissipation and the work done by the energy-containing eddies, namely, $\epsilon = A(u'^2)^{3/2}k_e$, may be evaluated to determine $A = fnc(\mathrm{Re}_\lambda)$. The results of these calculations are given in the appendix where tables of the various integrals and turbulence parameters are presented for $\mathrm{Re}_\lambda = 26$ to 4980. The one-dimensional spectrum, however, was calculated only for $\mathrm{Re}_\lambda = 34$, 106, and 238.

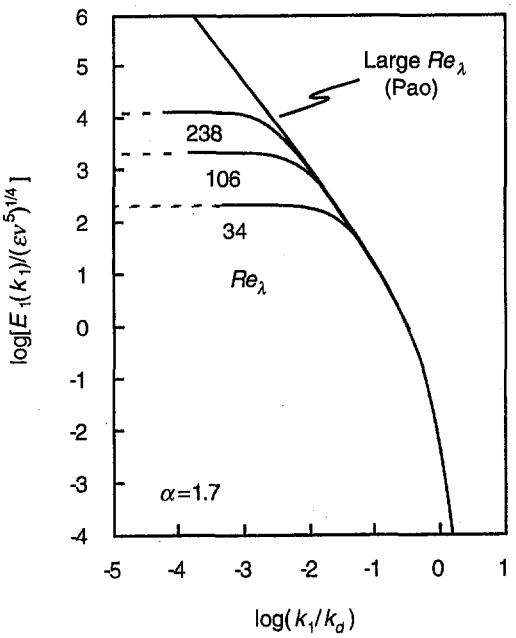

Fig. 6 One-dimensional energy spectrum using the dissipative scales of turbulence

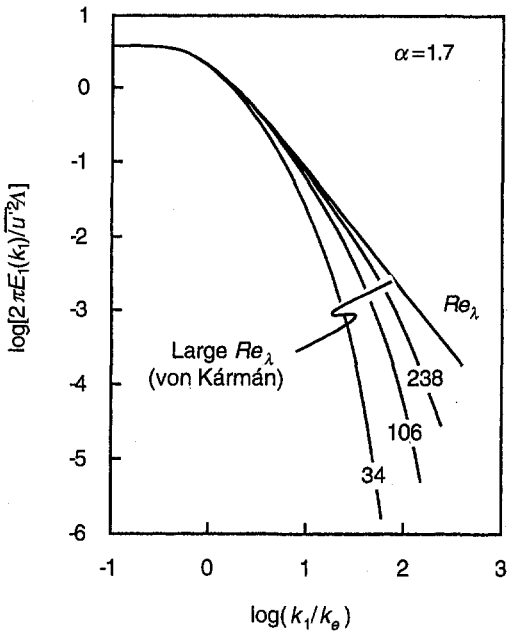

Fig. 8 One-dimensional energy spectrum using the integral scales of turbulence

The results for $E_1(k_1)$ normalized using the dissipative scales of turbulence are plotted in Fig. 6. Pao's result for infinitely large Reynolds numbers is also shown. In this format, the Reynolds number independence of the energy-dissipating eddies (large k_1) is clearly seen. In addition, the increasing amount of energy contained in the large eddies (small k_1) with increasing Reynolds number is also seen. The energy density of the large eddies can be calculated,[7] and is shown in Fig. 7 together with data from experiments on grid turbulence and boundary layers compiled by Chapman (1979). The agreement is good even for small Re_λ, and suggests that the proposed expression for $E(k)$ may be useful even when an inertial subrange does not exist.

Plots of $E_1(k_1)$ normalized using the integral scales of turbulence are presented in Fig. 8. In this format, the viscous effect on the energy-dissipating eddies is easily seen. The result for infinitely large Reynolds numbers is due to von Kármán, namely, $2\pi E_1(k_1)/\overline{u'^2}\Lambda = 4[1 + (k_1/k_e)^2]^{-5/6}$, which is obtained by integrating Eq. (4). According to this expression, it is natural to use Λ rather than $1/k_e$ as the length scale for the ordinate and $1/k_e$ for the abscissa. For large Reynolds numbers, Λ and $1/k_e$ may be freely interchanged as commonly done since $\Lambda k_e \approx 0.74$, a constant. For lower Reynolds numbers, however, the product varies[8] approximately as $0.74\ (1 + 90/\mathrm{Re}_\lambda)^{2/9}$, which produces an increasing rightward shift in the curves of Fig. 8 if Λk_1 rather than k_1/k_e is used for the abscissa. This shift actually produces an overlapping of spectral curves for different Re_λ near $k_1/k_e = 1$, which is commonly found in data plotted this way and worthy to note.

Spectral Function Formulas. Formulas for the spectral function and various other useful relations were obtained by curve fits to the calculated results in the appendix. As mentioned above, the relation between Λ and k_e is approximately given by

$$\Lambda k_e = 0.74(1 + 90/\mathrm{Re}_\lambda)^{2/9} \tag{10}$$

The relations between all the other length scales depend on A. Using the results in Table A2 of the appendix, a good approximation for A is given by

$$A = 0.80(1 + 24/\mathrm{Re}_\lambda) \tag{11}$$

Then the relation between the energy-containing and energy-dissipating eddy scales becomes

$$\frac{k_d}{k_e} = 15^{-3/4} A\ \mathrm{Re}_\lambda^{3/2} = 0.105(1 + 24/\mathrm{Re}_\lambda)\ \mathrm{Re}_\lambda^{3/2} \tag{12}$$

Pao's result for large Re_λ (shown in Fig. 6) is given with good accuracy up to the third moment with respect to k_1 by

$$\frac{E_1(k_1)}{(\epsilon\nu^5)^{1/4}} = \frac{18}{55}\alpha(k_1/k_d)^{-5/3}\exp\left[-\frac{14}{3}(k_1/k_d)\right]; \quad \text{(large } \mathrm{Re}_\lambda\text{)} \tag{13}$$

As noted before, von Kármán's one-dimensional spectral distribution is given by

[7] Noting that the integral for $E_1(k_1)$ with $k_1 = 0$ is identical to the integral for Λ (see Eqs. (8) and (9)), the energy density for these eddies as a function of Re_λ can be determined from values found in Tables A1 and A2 of the appendix.

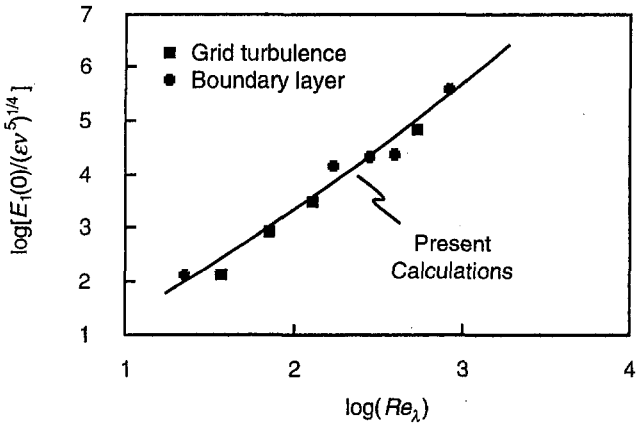

Fig. 7 Calculated values of the energy density at $k_1 = 0$ compared with experimental results

[8] Obtained by a curve fit to the calculated results in Tables A1 and A2.

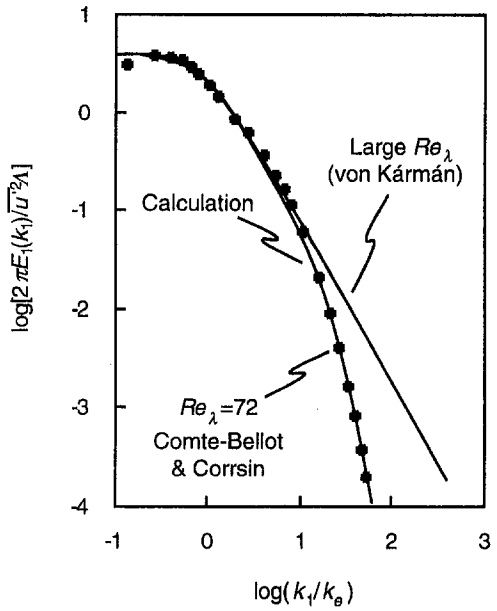

Fig. 9 Calculated and experimental one-dimensional energy spectrums of turbulence

$$\frac{2\pi E_1(k_1)}{\overline{u'^2}\,\Lambda} = \frac{4}{[1 + (k_1/k_e)^2]^{5/6}}; \quad \text{(large Re}_\lambda\text{)} \tag{14}$$

An expression for the complete range of Reynolds numbers, which is also good up to the third moment of accuracy, is

$$\frac{E_1(k_1)}{(\epsilon\nu^5)^{1/4}} = \frac{18}{55}\alpha \frac{r(k_d/k_e)^{5/3}}{1 + r(k_1/k_e)^{5/3}\exp\left[\frac{14}{3}(k_1/k_d)\right]} \tag{15}$$

where a good approximation for r (obtained by fitting the results in Tables A1 and A2 of the appendix) is

$$r = 1 - 15\,\mathrm{Re}_\lambda^{-3/2} \tag{16}$$

An equivalent expression for $E_1(k_1)$ is

$$\frac{2\pi E_1(k_1)}{\overline{u'^2}\Lambda} = \frac{4}{1 + r(k_1/k_e)^{5/3}\exp\left[\frac{14}{3}(k_1/k_d)\right]} \tag{17}$$

Since r approaches unity for large Re_λ, it is readily seen that these expressions reduce to Eqs. (13) and (14) for both small and large wave numbers in the limit of large Reynolds number.

A comparison of Eq. (17) with data for bar-grid-generated isotropic turbulence is shown in Fig. 9. To make the comparison, Eqs. (10), (12), and (16) were also used. The agreement is seen to be very good.

The Role of Turbulence Reynolds Number

The effect of Reynolds number on Tu_{eff}/Tu is shown in Fig. 10 where its spectral functions for Re_λ = 34, 106, and 238 are plotted. The curve for Re_λ = 106 was already used in Fig. 2. As previously mentioned, it corresponds to the lower limit for gas turbine engines and the higher limit found in most bar-grid-generated turbulence experiments.

Clearly, the effect of Re_λ is less pronounced for higher values, where viscous effects are less important, than for the lower. Therefore, once Re_λ is larger than about 200, the results we previously presented (Dullenkopf and Mayle, 1995), which were based on von Kármán's distribution, may be used. Using

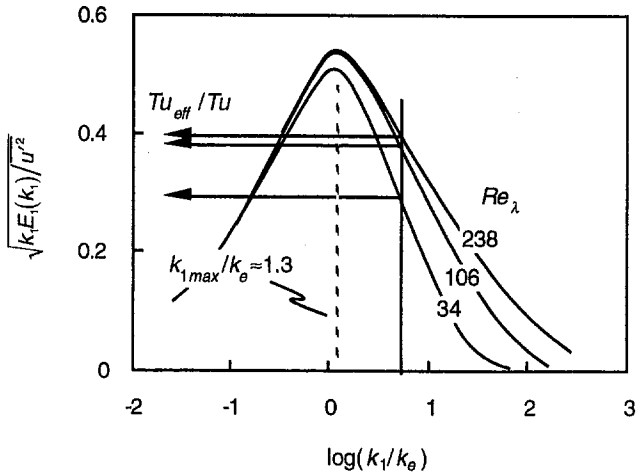

Fig. 10 Effect of Reynolds number on the effective turbulence for heat transfer in a laminar boundary layer

the spectral distribution given by Eq. (17) instead of von Kármán's Eq. (6)[9] of that paper should be replaced with

$$\frac{Tu_{\mathrm{eff}}}{Tu} = 1.29\sqrt{\frac{\Lambda_a(\Lambda k_e)}{1 + 0.01r\Lambda_a^{5/3}\exp[0.29\Lambda_a(k_e/k_d)]}} \tag{18}$$

where $\Lambda_a = \Lambda\sqrt{(a/\nu)}$, and $a = dU/dx$ is the free-stream strain rate.

The effect of Reynolds number on C_ω is shown in Fig. 11. Clearly, the value of C_ω is greatly affected by Re_λ, which underlines the importance of the free-stream turbulence Reynolds number on the production of LKE in pretransitional flow and, consequently, on the onset of transition.

Using Eq. (13), it is easy to show that the maxima occur at $k_{1\mathrm{eff}}/k_d = 0.3$. Substituting this value into Eq. (2) together with $k_d = (\epsilon/\nu^3)^{1/4}$ yields $C_\omega \propto (\epsilon\nu)^{1/2}/U\sqrt{\overline{u_s'^2}}$. By using the various relations between turbulence length and velocity scales (Hinze), many different expressions may be obtained for C_ω. The simplest is $C_\omega \propto \nu/U\Lambda$, which is also easy to evaluate from turbulence decay measurements since $d(\ln Tu)/d\mathrm{Re}x = -5(\nu/U\Lambda)^2$. Evaluating the constant of proportionality using the information presented in Tables 1 and 2 of our previous paper (Mayle and Schulz, 1997), we find

[9] Note that the left-hand side of this equation is equal to Tu_{eff}/Tu.

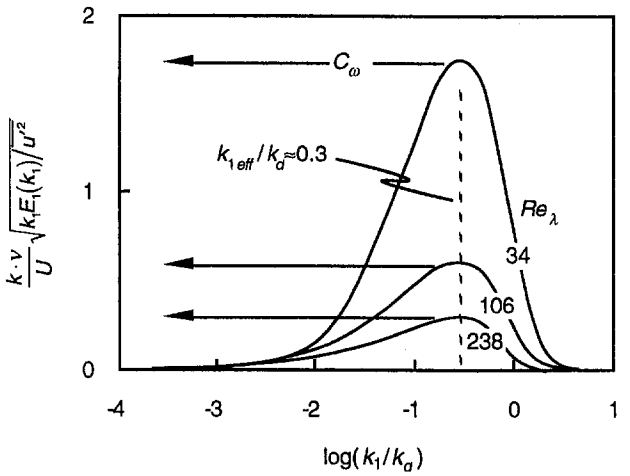

Fig. 11 Effect of Reynolds number on the production of laminar kinetic energy in a laminar boundary layer

$$C_\omega = 0.27\,\frac{\nu}{U\lambda} \tag{19}$$

In our previous paper, we had obtained $C_\omega = 0.07\,(\upsilon/U)^{2/3}(\nu/U\Lambda)^{1/3}$ where $\upsilon = (\epsilon\nu)^{1/4}$ is Kolmogorov's velocity scale. After some rearrangement, this becomes $C_\omega = 0.30\,\nu/U\lambda$, which is nearly the same as that above. Presently, however, we suggest that Eq. (19) be used for the coefficient of the production term in the LKE equation (see subsection above titled "Effect on Transition"). This leads to a new form for the LKE equation:

$$\bar{u}\,\frac{\partial k}{\partial x} + \bar{v}\,\frac{\partial k}{\partial y} = 0.085\,\sqrt{\frac{\epsilon_\infty}{\nu}}\,U\sqrt{k}e^{-y^+/13} + \nu\,\frac{\partial^2 k}{\partial y^2} - \epsilon \tag{20}$$

where $y^+ = yu_\tau/\nu$, $\epsilon = 2\nu k/y^2$ (see Eq. (6), Mayle and Schulz, 1997), and u_τ is the shear velocity.

Conclusions

In this paper, the third in our series concerned with the effects of free-stream turbulence in turbomachines, we have concentrated on the turbulence itself and developed a unified expression for the turbulence spectrum, which can be used, together with the results of our two previous papers, to explain the effects of turbulence on laminar heat transfer and transition from laminar to turbulent flow. The main result of all three papers is that the effects of turbulence can only be explained when the full spectrum of turbulence is known such that the relevant "effective" turbulence levels and frequencies can be determined.

For the complex flows found in turbomachinery, however, this requirement appears almost impossible to satisfy. But from an engineering standpoint, the results of this paper provide a good idea of the turbulence that matters for both laminar heat transfer and transition, and indicate that perhaps the only other quantity needed besides the free-stream turbulence level, if the spectral distribution developed in this paper is accepted, is the turbulence Reynolds number Re_λ (or a Reynolds number based on another turbulence length scale). This conclusion is obtained from the observation that all length scales are related through Re_λ, and if both Tu and Re_λ are known, then λ and all the length scales are known. Of course, the spectral distribution presented in this paper may not apply, but so far we have nothing else.

For the gas turbine designer, the integral length scale of turbulence Λ, rather than the microscale λ, is easier to estimate. In a free stream unaffected by wakes, Λ will be of the same order as the gap in the upstream airfoil row. In the wakes, Λ will be of the same order as the upstream airfoil's trailing edge. From these estimates, a reasonable range of turbulence Reynolds numbers can be obtained and used, together with the results presented in this paper, to project the effects of free-stream turbulence on both heat transfer and aerodynamic performance.

Acknowledgments

The lead author is indebted to Professor S. Wittig for his continuing support. The same author is also grateful to the Sonderforschungsbereich 167, which funded most of this work during the author's 1996 summer stay as a Visiting Professor at the Institut für Thermische Strömungsmaschinen.

References

Batchelor, G. K., 1953, *The Theory of Homogeneous Turbulence,* Cambridge University Press.

Chapman, D. R., 1979, "Computational Aerodynamics Development and Outlook," *AIAA Journal,* Vol. 17, pp. 1293–1313.

Dullenkopf, K., and Mayle, R. E., 1994, "The Effects of Incident Turbulence and Moving Wakes on Laminar Heat Transfer in Gas Turbines," ASME JOURNAL OF TURBOMACHINERY, Vol. 116, pp. 23–28.

Dullenkopf, K., and Mayle, R. E., 1995, "An Account of Free-Stream-Turbulence Length Scale on Laminar Heat Transfer," ASME JOURNAL OF TURBOMACHINERY, Vol. 117, pp. 401–406.

Emmons, H. W., 1951, "The Laminar-Turbulent Transition in a Boundary Layer—Part I," *J. Aero. Sci.,* Vol. 18, pp. 490–498.

Hinze, J. O., 1975, *Turbulence,* McGraw-Hill.

Kármán, T. von, 1948, "Progress in the Statistical Theory of Turbulence," *Proc. Natl. Acad. Science,* Vol. 34, p. 530.

Lin, C. C., 1957, "Motion in the Boundary Layer With a Rapidly Oscillating External Flow," *Proc. 9th Int. Congress Appl. Mech.,* Brussels, 4, pp. 155–167.

Mayle, R. E., and Schulz, A., 1997, "The Path to Predicting Bypass Transition," ASME JOURNAL OF TURBOMACHINERY, Vol. 119, pp. 405–411.

Pao, Y. H., 1965, "Structure of Turbulent Velocity and Scalar Fields at Large Wavenumbers," *Phys. Fluids,* Vol. 8, pp. 1063–1075.

Schlichting, H., 1979, *Boundary-Layer Theory,* McGraw-Hill, New York.

Schulz, A., 1986, "Zum Einfluß hoher Freistromturbulenz, intensiver Kühlung und einer Nachlaufströmung auf den äußeren Wärmeübergang einer konvektiv gekülten Gasturbinenschaufel," Ph.D. Thesis, U. Karlsruhe, Karlsruhe, Germany (also Wittig, S., Schulz, A., Bauer, H. J., and Sill, K. H., 1985, "Effects of Wakes on the Heat Transfer in Gas Turbine Cascades," AGARD CP 390, pp. 6-1–6-13).

Smith, M. C., and Kuethe, A. M., 1966, "Effects of Turbulence on Laminar Skin Friction and Heat Transfer," *Physics of Fluids,* Vol. 9, pp. 2337–2344.

Sreenivasan, K. R., 1995, "On the Universality of the Kolmogorov Constant," *Physics of Fluids,* Vol. 7, pp. 2778–2784.

Thole, K. A., 1992, "High Freestream Turbulence Effects on the Transport of Heat and Momentum," Ph.D. Thesis, University of Texas at Austin.

Yardi, N. R., and Sukhatme, S. P., 1978, "Effect of Turbulence Intensity and Integral Length Scale of a Turbulent Free Stream on Forced Convection Heat Transfer from a Circular Cylinder in Crossflow," *Proc. 6th Int. Heat Transfer Conference,* Toronto, Canada, Vol. 5, FC(b)-29, pp. 347–352.

APPENDIX

With the three-dimensional energy spectral density for isotropic turbulence given as

$$E(k) = \alpha(\epsilon\nu^5)^{1/4}(k_d/k_e)^{5/3}\,\frac{(k/k_e)^4\exp\left[-\frac{3}{2}\,r\alpha(k/k_d)^{4/3}\right]}{[1+(k/k_e)^2]^{17/6}}$$

Eqs. (6), (8), and (9) in the text may be expressed, respectively, as

Table A1 Turbulence spectrum integrals

b	I_ε	I_d/I_ε	I_λ/I_ε	r	$\Lambda k_e/2\pi$
3.0E-2	4.45E+1	2.93E-2	1.30E-2	0.890	0.1671
2.0E-2	6.91E+1	2.05E-2	8.70E-3	0.921	0.1587
7.5E-3	1.94E+2	8.48E-3	3.25E-3	0.970	0.1438
3.4E-3	4.34E+2	4.09E-3	1.48E-3	0.984	0.1359
2.0E-3	7.43E+2	2.47E-3	8.71E-4	0.991	0.1320
8.0E-4	1.87E+3	1.03E-3	3.49E-4	0.996	0.1272
5.0E-4	2.99E+3	6.52E-4	2.18E-4	0.998	0.1256
1.0E-4	1.50E+4	1.34E-4	4.36E-5	0.999	0.1219
3.0E-5	5.00E+4	4.07E-5	1.31E-5	1.000	0.1205

Table A2 Turbulence parameters (α = 1.7)

b	k_d/k_e	A	Re_λ	$(A\Lambda k_e)^{-1}$
3.0E-2	26	1.58	25	0.60
2.0E-2	36	1.39	34	0.72
7.5E-3	77	1.11	66	1.00
3.4E-3	142	0.992	106	1.18
2.0E-3	212	0.941	143	1.28
8.0E-4	423	0.882	237	1.42
5.0E-4	602	0.861	305	1.47
1.0E-4	2020	0.821	705	1.59
3.0E-5	4980	0.807	1300	1.64

Table A3 One-dimensional energy spectrum

	$Re_\lambda = 34$		$Re_\lambda = 106$		$Re_\lambda = 238$	
k_1/k_e	I_E/I_ϵ	$4I_E/I_\Lambda$	I_E/I_ϵ	$4I_E/I_\Lambda$	I_E/I_ϵ	$4I_E/I_\Lambda$
0.0251	8.69E-3	3.99	1.48E-3	4.00	3.49E-4	4.00
0.0398	8.68E-3	3.99	1.48E-3	3.99	3.48E-4	4.00
0.0631	8.66E-3	3.98	1.48E-3	3.99	3.48E-4	3.99
0.100	8.62E-3	3.96	1.47E-3	3.97	3.46E-4	3.97
0.158	8.50E-3	3.91	1.45E-3	3.92	3.42E-4	3.92
0.251	8.23E-3	3.78	1.41E-3	3.80	3.31E-4	3.80
0.398	7.62E-3	3.50	1.31E-3	3.53	3.08E-4	3.54
0.631	6.43E-3	2.96	1.12E-3	3.01	2.63E-4	3.02
1.00	4.65E-3	2.14	8.23E-4	2.22	1.95E-4	2.24
1.58	2.75E-3	1.27	5.08E-4	1.37	1.22E-4	1.40
2.51	1.35E-3	6.23E-1	2.70E-4	7.28E-1	6.56E-5	7.53E-1
3.98	5.70E-4	2.62E-1	1.29E-4	3.48E-1	3.23E-5	3.71E-1
6.31	2.07E-4	9.52E-2	5.76E-5	1.56E-1	1.51E-5	1.74E-1
10.0	6.21E-5	2.86E-2	2.42E-5	6.53E-2	6.88E-6	7.90E-2
15.8	1.42E-5	6.52E-3	9.38E-6	2.53E-2	3.03E-6	3.48E-2
25.1	2.10E-6	9.68E-4	3.24E-6	8.75E-3	1.28E-6	1.47E-2
39.8	1.53E-7	7.01E-5	9.38E-7	2.53E-3	5.08E-7	5.83E-3
63.1	3.36E-9	1.54E-6	2.04E-7	5.51E-4	1.84E-7	2.11E-3
100	9.12E-12	4.19E-9	2.83E-8	7.65E-5	5.71E-8	6.55E-4
158	—	—	1.85E-9	5.00E-6	1.40E-8	1.60E-4
251	—	—	—	—	2.33E-9	2.68E-5

$$\alpha = (k_d/k_e)^{4/3} I_\epsilon^{-1}$$

$$\frac{E_1(k_1)}{(\epsilon\nu^5)^{1/4}} = \frac{1}{2}\alpha(k_d/k_e)^{5/3} I_E = \frac{1}{2}(k_d/k_e)^3 I_E/I_\epsilon$$

$$\frac{\overline{u'^2}}{(\epsilon\nu^5)^{1/4} k_e} = \frac{1}{3}\alpha(k_d/k_e)^{5/3} I_u = \frac{1}{3}(k_d/k_e)^3 I_u/I_\epsilon$$

$$\frac{\overline{u'^2}\,\Lambda}{(\epsilon\nu^5)^{1/4}} = \frac{1}{4}\pi\alpha(k_d/k_e)^{5/3} I_\Lambda = \frac{1}{4}\pi(k_d/k_e)^3 I_\Lambda/I_\epsilon$$

where

$$I_\epsilon = \int_0^\infty \frac{z^{5/2}\exp(-bz^{2/3})}{(1+z)^{17/6}}\,dz,$$

$$I_E = (k_1/k_e)^4 \int_0^\infty \frac{(z-1)\exp[-b(k_1/k_e)^{4/3}z^{2/3}]}{[1+(k_1/k_e)^2 z]^{17/6}}\,dz,$$

$$I_u = \int_0^\infty \frac{z^{3/2}\exp(-bz^{2/3})}{(1+z)^{17/6}}\,dz, \quad I_\Lambda = \int_0^\infty \frac{z\exp(-bz^{2/3})}{(1+z)^{17/6}}\,dz,$$

and

$$b = \tfrac{3}{2} r\alpha(k_e/k_d)^{4/3} = \tfrac{3}{2} r I_\epsilon^{-1}$$

The integrals I_ϵ, I_u, and I_Λ have been evaluated for several values of b and the results tabulated in Table A1. The frequency parameter $n\Lambda/U = (k_1/k_e)(\Lambda k_e/2\pi)$ is often used in spectral plots, so the quantity $\Lambda k_e/2\pi = 3I_\Lambda/8I_u$ is also provided. Note for $b \to 0$, corresponding to large Reynolds numbers, $\Lambda k_e \to 0.75$ as expected. It should also be noted that the results presented in Table A1 are independent of Kolmogorov's constant α.

Once α is chosen, the turbulence parameters $k_d/k_e = (\alpha I_\epsilon)^{3/4}$, $A = (3/\alpha I_u)^{3/2}$, and $\mathrm{Re}_\lambda = (15^{1/2}/3)\alpha^{3/2} I_\epsilon^{1/2} I_u$ can be determined. These quantities have been evaluated using $\alpha = 1.7$ and the results provided in Table A2. The quantity $(A\Lambda k_e)^{-1}$, which is the ratio of the dissipation and integral length scales, is also provided. Experimental values for this quantity typically lie between 1.1 and 1.5. Batchelor (1953) quotes values between 0.8 and 1.3.

The integral $I_E(k_1)$ was evaluated for $b = 0.02$, 0.0034, and 0.0008, which for $\alpha = 1.7$ correspond to $\mathrm{Re}_\lambda = 34$, 106, and 237, respectively. The results of these calculations are presented in Table A3. Since the one-dimensional frequency spectrum $E_1(n)$ is often used, the quantity $UE_1(n)/\overline{u'^2}\Lambda = 2\pi E_1(k_1)/\overline{u'^2}\Lambda = 4I_E/I_\Lambda$ is also given in the table. Note that for $k_1/k_e \to 0$, corresponding to low frequencies, $UE_1(n)/\overline{u'^2}\Lambda \to 4$ as expected. Except for Re_λ, the values given in this table are independent of the value assigned to α. For those interested in performing other calculations, replacing the values of Re_λ with their corresponding values of b from Table A2 makes the whole table independent of α.

1997 Best Paper Award—Structures and Dynamics Committee

A Coupled Mode Analysis of Unsteady Multistage Flows in Turbomachinery

P. D. Silkowski[1]

K. C. Hall
Mem. ASME

Department of Mechanical Engineering and Materials Science,
Duke University,
Durham, NC 27708-0300

A computational method is presented for predicting the unsteady aerodynamic response of a vibrating blade row that is part of a multistage turbomachine. Most current unsteady aerodynamic theories model a single blade row isolated in an infinitely long duct. This assumption neglects the potentially important influence of neighboring blade rows. The present "coupled mode" analysis is an elegant and computationally efficient method for modeling neighboring blade row effects. Using this approach, the coupling between blade rows is modeled using a subset of the so-called spinning modes, i.e., pressure, vorticity, and entropy waves, which propagate between the blade rows. The blade rows themselves are represented by reflection and transmission coefficients. These coefficients describe how spinning modes interact with, and are scattered by, a given blade row. The coefficients can be calculated using any standard isolated blade row model; here we use a linearized full potential flow model together with rapid distortion theory to account for incident vortical gusts. The isolated blade row reflection and transmission coefficients, interrow coupling relationships, and appropriate boundary conditions are all assembled into a small sparse linear system of equations that describes the unsteady multistage flow. A number of numerical examples are presented to validate the method and to demonstrate the profound influence of neighboring blade rows on the aerodynamic damping of a cascade of vibrating airfoils.

1 Introduction

Unsteady fluid motion is essential to gas turbine engine operation. Only through unsteady flow processes can a machine do work on a fluid to increase its total enthalpy. This unsteadiness is provided in compressors and turbines by relative motion of adjacent stators and rotors. Unfortunately, this motion also produces undesirable aeroacoustic and aeroelastic phenomena, i.e., tonal noise and forced blade vibrations induced by rotor/stator interactions. Furthermore, the aeroelastic (flutter) stability of a rotor can be profoundly influenced by the presence of nearby stators and rotors. In this paper, we investigate the aeroelastic stability of a compressor rotor that is part of a larger multistage compressor.

Unsteady aerodynamic theories for use in turbomachinery aeroelastic prediction systems have progressed significantly over the past four decades. Several recent review articles chronicle the development of these theories (Verdon, 1987, 1993; Whitehead, 1987; Marshall and Imregun, 1996). The available theories can be classified roughly into three groups: classical or linear methods, time-linearized theories, and nonlinear time-domain simulations.

In the classical approach, simplifying assumptions are made that reduce the equations governing the unsteady flow to linear constant coefficient equations for the unknown unsteady perturbation flow. For example, the airfoils of the cascade are usually replaced by flat plates, which do not turn the mean flow. These simplified governing equations are then solved analytically or semi-analytically. This approach has been applied to incompressible flows (Whitehead, 1960), subsonic flows (Whitehead, 1970; Smith, 1972), and supersonic flows (Verdon and McCune, 1975; Nagashima and Whitehead, 1977; Adamczyk and Goldstein, 1978).

Using the time-linearized approach, the governing equations are linearized about a nonlinear steady operating condition. The unsteady small-disturbance quantities are assumed to be harmonic in time with frequency ω, i.e., unsteady quantities are proportional to $\exp(j\omega t)$, so that the time derivative $\partial/\partial t$ is replaced by $j\omega$. The resulting linear variable coefficient equations are then discretized on a computational grid using conventional finite element or finite volume techniques and solved numerically. The time-linearized approach is computationally efficient, and has been applied to a range of flow models including the two-dimensional potential equations (Verdon and Caspar, 1982; Whitehead, 1990; Hall, 1993), the two-dimensional Euler equations (Hall and Crawley, 1989; Hall and Clark, 1993; Holmes and Chuang, 1993), the three-dimensional Euler equations (Hall and Lorence, 1993), and the two-dimensional Navier–Stokes equations (Clark and Hall, 1995).

Finally, investigators have developed nonlinear time-domain simulations of unsteady flows in cascades. Using this approach, no simplifying assumptions are made regarding the size of the unsteady disturbance. Instead, the governing fluid dynamic equations, which are nonlinear, are simply marched in time to simulate the unsteady flow. The approach has been applied to the two-dimensional Euler equations (Huff et al., 1991; Giles, 1988a, b; He, 1990) and the three-dimensional Euler equations (Gerolymos, 1993). This approach has the advantage that it is reasonably straightforward to implement, and can model nonlinearities. However, computational times are usually quite large, on the order of two orders of magnitude larger than the time-linearized approach.

[1] Current address: Pratt & Whitney, East Hartford, CT 06108.

Contributed by the International Gas Turbine Institute and presented at the 42nd International Gas Turbine and Aeroengine Congress and Exhibition, Orlando, Florida, June 2–5, 1997. Manuscript received at ASME Headquarters February 1997. Paper No. 97-GT-186. Associate Technical Editor: H. A. Kidd.

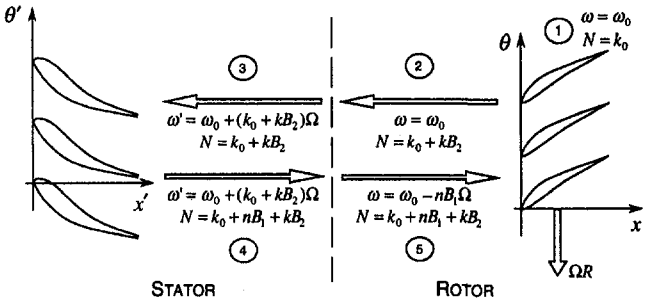

Fig. 1 Kinematics of mode scattering and frequency shifting

Unfortunately, despite many years of development, the accurate and reliable prediction of unsteady aerodynamic forces acting on turbomachinery blades remains elusive. The correlation of theory with experiment is often less than satisfactory (Bölcs and Fransson, 1986), especially when viewed next to the great success investigators have had in predicting steady flows.

We believe there are two main reasons that current theories show poor correlation with experiment, both of which are related to the special physics of unsteady flows. First, most unsteady flow analyses are two-dimensional, or at best quasi-three-dimensional. The unsteady flow is calculated on a two-dimensional axisymmetric streamsheet whose radial thickness varies as a function of axial location. Steady flows are routinely calculated quite accurately using this sort of analysis. However, the unsteady flow equations admit acoustic wave solutions, making the problem inherently three-dimensional since acoustic waves will travel in all directions. Quoting Holmes and Chuang (1993), "There is absolutely no reason to believe that unsteady disturbances will obligingly confine themselves to the [quasi-three-dimensional] mean flow streamsheets! Cases in which [two-dimensional] or [quasi-three-dimensional] unsteady flow codes give accurate results will be relatively rare." Recent work by Hall and Lorence (1993) tends to confirm this hypothesis.

The second main reason for these discrepancies is that nearly all of the current unsteady aerodynamic theories model a single blade row in an infinitely long duct, ignoring potentially important multistage effects. However, unsteady flows are made up of acoustic, vortical, and entropic waves. These waves provide a mechanism for the rotors and stators of multistage machines to communicate with one another. For example, consider the case of a row of vibrating rotor blades (see Fig. 1). The blades will respond aerodynamically, producing acoustic, vortical, and entropic waves that propagate away from the rotor. Some of these waves will then impinge on the neighboring stators. The stators will in turn respond aerodynamically, again producing waves, some of which will impinge upon the original rotor, and so on. In other words, wave behavior makes unsteady flows fundamentally three-dimensional and multistage.

Recently, a number of investigators have studied unsteady multistage flows. The most common approach is to perform a direct simulation. For example, Giles (1988a, b) has time-marched the Euler equations to compute wake/rotor and rotor/stator interactions. For the latter, two computational grids are generated, one for the rotor and one for the stator, with a common interface. The Euler equations are then time marched. At each time step, information at the rotor/stator interface is exchanged, and the position of the rotor is updated. Rai (1989a, b) used a similar technique to study viscous rotor/stator interaction in turbines. One problem with this approach is that many passages of the rotor and stator must be used if the blade counts in the two blade rows are not equal, making the method prohibitively expensive. Rai (1989a, b) simply altered the geometry of one of the blade rows to force the blade counts to be equal, an approach of questionable validity, especially for unsteady flows where the blade counts have a strong influence on the possible tones or frequencies present in the solution. Giles (1988a, b), on the other hand, used an elegant "time-inclining" technique whereby a space–time transformation is made on the governing flow equations, which allows the ratio of blades to be altered, for example from 11:9 to 1:1. Unfortunately, the method has not yet been extended to flows in multiple stages.

A few researchers have modeled multistage flows using frequency domain techniques. Kaji and Okazaki (1970) studied rotor–stator interactions using an acceleration potential technique. They distributed pressure doublets on flat-plate rotor and stator blades. The strengths of the doublets were found by satisfying the no-throughflow condition on the airfoils. However, Kaji and Okazaki assumed the doublet strengths were harmonic in time with a single interblade phase angle in each blade row. In other words, the two blade rows were coupled by a single spinning mode, i.e., acoustic and vortical waves with a single temporal frequency and circumferential wavenumber. Hanson (1992) later applied a similar technique to acoustic problems, using vortex singularities with multiple spinning modes.

Hanson (1993), using an alternative approach suggested by Hall in a 1988 unpublished report, characterized the rotor and stator by reflection and transmission coefficients that describe the response of an isolated blade row to incident vortical or acoustic waves (spinning modes). Hanson used Smith's (1972) method to compute these coefficients. A small set of linear equations can then be assembled that describes how the two blade rows behave when put together into a single stage. Hanson used this method to study the influence of "mode trapping" on the aeroacoustic behavior of a single stage. Buffum (1993) later used a similar technique to investigate the aeroelastic stability of a one and one-half stage compressor. However, Buffum retained only cut-on (superresonant) acoustic modes, and used only a single spinning mode in his model. Concurrently to Hanson's (1993) work, Hall and Silkowski (1997) also developed a coupled mode approach to analyze unsteady flows associated with flutter and forced response of multistage machines composed of flat-plate airfoils, and analyzed machines with as many as three and one-half stages.

In this paper, the coupled mode analysis is extended and applied to the problem of computing the aerodynamic damping of a compressor rotor that is part of a multistage compressor composed of realistic airfoils. That is to say, the blades have camber and thickness, and the blade rows do significant turning of the flow. We show that the aerodynamic damping of a blade row that is part of a multistage machine will, in general, be significantly different from that predicted using an isolated blade row model.

The coupled mode analysis has a number of features that make it desirable for use in aeroelastic and aeroacoustic design and analysis systems. For example, the method is computationally very efficient, especially when compared to conventional time-marching simulations. Furthermore, once a single nominal multistage flow has been computed, certain parametric design studies can be performed with virtually no additional computational expense.

2 Theory

The coupled mode analysis is divided into two parts. First, there is a framework for describing how blade rows interact with one another via so-called spinning modes. In Section 2.1, we describe this framework. Second, a linear or time-linearized unsteady aerodynamic analysis is required to determine reflection and transmission coefficients that characterize the behavior of the individual blade rows. In Section 2.2, we describe the time-linearized theory used in the present investigation, a linearized full potential flow solver along with rapid distortion theory to describe the motion of vorticity through the blade row.

2.1 Coupled Mode Analysis

2.1.1 Kinematics of Mode Scattering and Frequency Shifting. In the present work, we assume that the flow through a multistage compressor or turbine is inviscid, non-heat conducting, and two-dimensional. Therefore, the flow is governed by the nonlinear two-dimensional Euler equations. The state of the flow is completely described by the vector of primitive flow variables $\hat{\mathbf{U}}$ given by

$$\hat{\mathbf{U}}(x, y, t) = \begin{Bmatrix} \hat{\rho}(x, y, t) \\ \hat{U}(x, y, t) \\ \hat{V}(x, y, t) \\ \hat{P}(x, y, t) \end{Bmatrix} \tag{1}$$

where $\hat{\rho}$, $\hat{U}$, $\hat{V}$, and $\hat{P}$ are the density, axial velocity, circumferential velocity, and pressure, respectively, x and y are the axial and circumferential coordinates, and t is time. The angular distance θ is equal to y/R where R is the radius of the annulus.

Consider the single stage shown in Fig. 1 for the case where the airfoils of the rotor vibrate periodically with small amplitude and frequency ω_0. The resulting unsteadiness in the flow is assumed to be small compared to the mean flow. Thus, the flow may be split into a nonlinear mean or steady part plus an unsteady small-perturbation part, i.e.,

$$\hat{\mathbf{U}}(x, y, t) = \mathbf{U}(x, y) + \mathbf{u}(x, y, t) \tag{2}$$

The unsteady flow $\mathbf{u}(x, y, t)$ is described by the linearized Euler equations (Hall and Crawley, 1989)—linear variable coefficient equations whose coefficients depend on the mean flow (see Section 2.2). Thus, unsteady solutions may be superposed. We use this property to decompose the motion of the rotor into a sum of traveling waves, analyze each traveling wave separately, then superpose the resulting solutions. Hence, without loss in generality, we assume that the blades of the rotor vibrate in plunge with frequency ω_0 in a traveling wave with $N = k_0$ nodal diameters. Thus, the plunging velocity of the mth blade is given by

$$\dot{h}(m, t) = \dot{h}_0 \exp[j(\omega_0 t + m\sigma_0)] \tag{3}$$

where

$$\sigma_0 = \frac{2\pi k_0}{B_2} \tag{4}$$

is the interblade phase angle of the motion, $\dot{h}_0$ is the amplitude of the plunging velocity of the reference airfoil, and B_2 is the number of blades in the rotor (blade row number 2).

This traveling wave motion of the blades will give rise to unsteady fluid motion with frequency ω_0, and that also satisfies the complex periodicity condition

$$\mathbf{u}(x, y + G_2, t) = \mathbf{u}(x, y, t) \exp(j\sigma_0) \tag{5}$$

where G_2 is the circumferential spacing between blades on the rotor. Upstream and downstream of the rotor, Eq. (5) can be satisfied with solutions of the form

$$\mathbf{u}(x, \theta, t) = \sum_{k=-\infty}^{\infty} \bar{\mathbf{u}}_k(x) \exp\{j[(k_0 + kB_2)\theta + \omega_0 t]\} \tag{6}$$

where k is a mode order index, which can take on all integer values, and $\bar{\mathbf{u}}_k(x)$ is a vector function to be determined.

In the interrow regions, the mean (time-averaged) flow is uniform, or very nearly so. Thus, the linearized Euler equations reduce to constant coefficient equations. Substituting Eq. (6) into the (constant coefficient) linearized Euler equations, one finds that $\bar{\mathbf{u}}_k(x)$ has exponential behavior, so that

$$\mathbf{u}(x, \theta, t) = \sum_{k=-\infty}^{\infty} \sum_{i=1}^{4} v_{i,k}\mathbf{q}_{i,k} \exp\{j[\alpha_{i,k}x + (k_0 + kB_2)\theta + \omega_0 t]\} \tag{7}$$

In words, the kth spinning mode has N nodal diameters, where $N = k_0 + kB_2$. The spinning mode is composed of four waves with wavenumbers $\alpha_{i,k}$ and eigenvectors $\mathbf{q}_{i,k}$ (Hall and Crawley, 1989). The constant $v_{i,k}$ describes how much of each eigenvector is present in the solution. The four waves correspond to an upstream moving pressure wave, a downstream moving pressure wave, a vorticity wave, and an entropy wave, with wavenumbers given by

$$\alpha_1 = \frac{U(\omega + \beta V) + C\sqrt{(\omega + \beta V)^2 - (C^2 - U^2)\beta^2}}{C^2 - U^2} \tag{8}$$

$$\alpha_2 = \frac{U(\omega + \beta V) - C\sqrt{(\omega + \beta V)^2 - (C^2 - U^2)\beta^2}}{C^2 - U^2} \tag{9}$$

$$\alpha_3 = -\frac{\beta V + \omega}{U} \tag{10}$$

$$\alpha_4 = -\frac{\beta V + \omega}{U} \tag{11}$$

where U and V are the mean flow axial and circumferential velocities, C is the mean speed of sound, and β_k is the circumferential wavenumber equal to σ_k/G_2 with $\sigma_k = \sigma_0 + 2\pi k$. (In Eqs. (8)–(11), the subscript k has been omitted for clarity.) Note that $\alpha_{3,k}$ and $\alpha_{4,k}$ are always real. However, $\alpha_{1,k}$ and $\alpha_{2,k}$ may be real or complex. When the wavenumbers are real, the waves are said to be "superresonant" or "cut-on" and the waves propagate without attenuation; when the wavenumbers are complex, the waves are "subresonant" or "cut-off" and the waves are attenuated as they propagate. The boundary between these two conditions is known as acoustic resonance.

Note that an initial disturbance with k_0 nodal diameters will in general produce a response composed of outgoing waves with an infinite number of nodal diameters, $N = k_0 + kB_2$. This phenomenon is referred to as scattering. Each of these spinning modes, identified by the index k, have the same temporal frequency ω_0 when viewed in the rotor frame of reference. Such a group of spinning modes for a particular blade row will be referred to as a scatter group.

The individual waves (pressure, vorticity, and entropy) of the spinning modes that were created by the rotor vibration will propagate upstream or downstream through the duct, depending on the wavenumber. Some of the upstream traveling pressure waves will impinge on the upstream stator. When viewed in the stator frame of reference, however, the frequency will be shifted. To show this, the coordinates (x, θ) fixed to the moving rotor can be related to the coordinates (x', θ') attached to the stator (see Fig. 1) by the transformation

$$x = x' - \Delta x \tag{12}$$

$$\theta = \theta' - \Delta\theta + \Omega t \tag{13}$$

where Δx is the axial distance between the stator and the rotor, $\Delta\theta$ is an angular location defining the relative clocking of the rotor and stator at time $t = 0$, and Ω is the rotation rate of the rotor. Substitution of Eqs. (12) and (13) into Eq. (7) gives

$$\mathbf{u}(x', \theta', t) = \sum_{k=-\infty}^{\infty} \sum_{i=1}^{4} v_{i,k}\mathbf{q}_{i,k} \exp\{j[\alpha_{i,k}x' + (k_0 + kB_2)\theta' + \omega_k' t]\} \times \exp\{j[-\alpha_{i,k}\Delta x - (k_0 + kB_2)\Delta\theta]\} \tag{14}$$

where $\omega_k' = \omega_0 + (k_0 + kB_2)\Omega$. Note that each of the members of the scatter group experiences a different "Doppler" frequency shift when viewed in the stator frame of reference, with the frequency dependent on the index k associated with the scattering in the rotor frame.

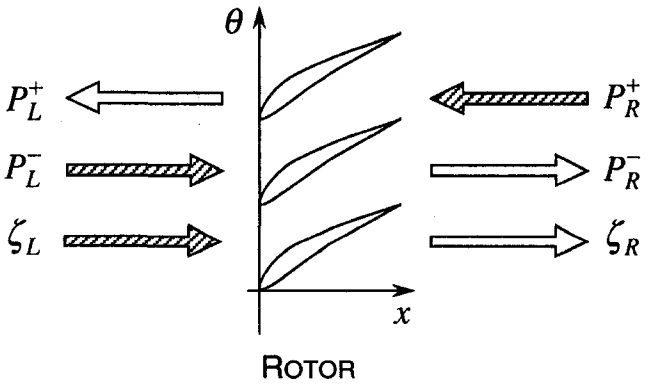

Fig. 2 Incident pressure and vorticity waves (shaded) produce reflected and transmitted pressure and vorticity waves (unshaded)

The upstream traveling waves of this scatter group will impinge on the stator, which in turn will give rise to an unsteady aerodynamic response. Following the same logic outlined for the rotor, the kth spinning mode will produce scattered reflected and transmitted waves with nodal diameters $N = k_0 + nB_1 + kB_2$, where B_1 is the number of stator blades and n takes on all integer values. In the stator frame of reference, these new waves will have frequencies given by

$$\omega_k' = \omega_0 + (k_0 + kB_2)\Omega \tag{15}$$

The reflected waves will impinge on the rotor. When viewed in the rotor frame of reference, however, the frequencies of the waves will again be shifted, so that

$$\omega_n = \omega_0 - nB_1\Omega \tag{16}$$

The waves impinging on the rotor will again produce reflected and transmitted waves, but no new nodal diameters will be produced. Thus, the response of the system to an initial disturbance with nodal diameters $N = k_0$ and frequency ω_0 will contain waves with nodal diameters $N = k_0 + nB_1 + kB_2$ and frequencies given by Eqs. (15) and (16). Note that the frequencies in the stator frame of reference depend on the index k associated with scattering of waves by the rotor, and the frequencies in the rotor frame of reference depend on the index n associated with scattering of waves by the stator.

Finally, for the cases considered in this paper, the mean background flow is subsonic, inviscid, irrotational, and homentropic. Furthermore, the original source of excitation is blade vibration. Under these circumstances, only acoustic and vortical disturbances will be generated, that is, the unsteady flow will also be homentropic. Therefore, for simplicity in the following, entropy waves are omitted. However, for nonhomentropic flows, entropy waves can be included in a straightforward extension of the method described below.

2.1.2 Global System Description. Having outlined the kinematics of mode scattering and frequency shifting in a multistage machine, we next consider in detail the interaction of spinning modes with individual blade rows. The fluid/blade row interaction can be described in terms of incident and outgoing waves (see Fig. 2). We know from the discussion above that incident acoustic and vortical waves (P_R^+, P_L^-, and ζ_L) from a single spinning mode will generate outgoing acoustic and vortical waves (P_R^-, P_L^+, and ζ_R) with all nodal diameters of the scatter group. Here, P^+, P^-, and ζ are the complex magnitudes of acoustic and vortical waves, replacing the less descriptive v_i notation of Eqs. (7) and (14). The "L" and "R" notations signify left (upstream) and right (downstream) sides of the blade row. The "+" and "−" notations signify upstream and downstream traveling waves. Conversely, outgoing waves for a particular nodal diameter are generated by incident waves from every member of the scatter group. Hence, for a rotor, for a specific (n, k) spinning mode,

$$\begin{Bmatrix} P_L^+ \\ P_R^- \\ \zeta_R \end{Bmatrix}_{nk} = \sum_{j=-\infty}^{\infty} \begin{bmatrix} w_{11} & w_{12} & w_{13} \\ w_{21} & w_{22} & w_{23} \\ w_{31} & w_{32} & w_{33} \end{bmatrix}_{nknj} \begin{Bmatrix} P_R^+ \\ P_L^- \\ \zeta_L \end{Bmatrix}_{nj} + \begin{Bmatrix} b_1 \\ b_2 \\ b_3 \end{Bmatrix}_{nk} \tag{17}$$

where the matrix $\mathbf{w}_{nknj}$ is a matrix of reflection and transmission coefficients describing how incident (n, j) waves scatter into outgoing (n, k) waves. The vector $\mathbf{b}_{nk}$ is an an inhomogeneous term arising from the imposition of an external disturbance. For example, $\mathbf{b}_{nk}$ might describe the (n, k) waves generated by a prescribed traveling wave blade motion with frequency ω_0 and k_0 nodal diameters. The reflection/transmission matrix $\mathbf{w}_{nknj}$ and the inhomogeneous vector $\mathbf{b}_{nk}$ are obtained using classical or time-linearized unsteady aerodynamic theories (see Section 2.2).

It will be convenient to rearrange Eq. (17) in terms of fluid waves on the left (upstream) side and right (downstream) side of the blade row instead of incident and outgoing waves. Rearranging Eq. (17) gives

$$\sum_{j=-\infty}^{\infty} [\mathbf{A}_{nknj}^i \mathbf{v}_{L,nj}^i + \mathbf{B}_{nknj}^i \mathbf{v}_{R,nj}^i] = \mathbf{b}_{nk}^i \tag{18}$$

where i is the blade row number,

$$\mathbf{v}_{L,nj}^i = \begin{Bmatrix} P_L^+ \\ P_L^- \\ \zeta_L \end{Bmatrix}_{nj}^i, \quad \mathbf{v}_{R,nj}^i = \begin{Bmatrix} P_R^+ \\ P_R^- \\ \zeta_R \end{Bmatrix}_{nj}^i \tag{19}$$

and

$$\mathbf{A}_{nknj}^i = \begin{bmatrix} \delta_{jk} & -w_{12} & -w_{13} \\ 0 & -w_{22} & -w_{23} \\ 0 & -w_{32} & -w_{33} \end{bmatrix}_{nknj}^i \tag{20}$$

$$\mathbf{B}_{nknj}^i = \begin{bmatrix} -w_{11} & 0 & 0 \\ -w_{21} & \delta_{jk} & 0 \\ -w_{31} & 0 & \delta_{jk} \end{bmatrix}_{nknj}^i \tag{21}$$

where δ_{jk} is the Krönecker delta function. A similar set of equations can be developed for the stator.

Next, a set of equations is required to model the coupling provided by the spinning modes in the interrow region. For the stator/rotor example shown in Fig. 1, a wave leaving the rotor is equivalent to a wave entering the stator. Said another way, the $\mathbf{v}_R$ quantities of the stator must be related to the $\mathbf{v}_L$ quantities of the rotor. Therefore,

$$\mathbf{E}_{nk}\mathbf{v}_{R,nk}^1 + \mathbf{v}_{L,nk}^2 = 0 \tag{22}$$

with

$$\mathbf{E}_{nk} = \begin{bmatrix} -e^{j\alpha_{1,nk}\Delta x} & 0 & 0 \\ 0 & -e^{j\alpha_{2,nk}\Delta x} & 0 \\ 0 & 0 & -e^{j\alpha_{3,nk}\Delta x} \end{bmatrix} \tag{23}$$

where for simplicity the clocking index $\Delta\theta$ is taken to be zero. Note that Eqs. (22) and (23) are based on the assumption that the time-averaged mean flow is uniform at some axial location between the blade rows, a condition that may be only approximately satisfied for very closely spaced blade rows.

Finally, one must specify any acoustic or vortical waves which originate upstream or downstream of the multistage machine. For the two blade row problem,

$$\mathbf{C}\mathbf{v}_{L,nk}^1 + \mathbf{D}\mathbf{v}_{R,nk}^2 = \mathbf{d}_{nk} \tag{24}$$

where

$$\mathbf{C} = \begin{bmatrix} 0 & 0 & 0 \\ 0 & 1 & 0 \\ 0 & 0 & 1 \end{bmatrix}, \mathbf{D} = \begin{bmatrix} 1 & 0 & 0 \\ 0 & 0 & 0 \\ 0 & 0 & 0 \end{bmatrix} \tag{25}$$

and $\mathbf{d}_{nk}$ is a vector containing the complex magnitudes of the incoming pressure and vorticity disturbances. For the flutter problem, $\mathbf{d}_{nk}$ is set to zero.

Equations (18), (22), and (24) can be assembled into a small sparse matrix equation of the form given by Eq. (26). Shown is the form of the matrix equation when the modes $(n, k) = (0, 0), (0, 1), (1, 0)$, and $(1, 1)$ are used for a single stage. Note that the system of equations is truncated. In principle, an infinite set of spinning modes must be included in the model to obtain the exact solution. In practice, however, only a few of the many possible modes are needed to obtain solutions with engineering accuracy. Also note the nonzero off-diagonal superblocks in Eq. (26). These are a result of mode scattering.

$$\left[\begin{array}{cccc|cccc|cccc|cccc}
\mathbf{A}^1_{0000}\,\mathbf{B}^1_{0000} & & & & & & & & \mathbf{A}^1_{0010}\,\mathbf{B}^1_{0010} & & & & & & & \\
\mathbf{E}_{00} & \mathbf{I} & & & & & & & & & & & & & & \\
 & & \mathbf{A}^2_{0000}\,\mathbf{B}^2_{0000} & & & & \mathbf{A}^2_{0001}\,\mathbf{B}^2_{0001} & & & & & & & & & & & \\
\mathbf{C} & & & \mathbf{D} & & & & & & & & & & & & \\
\hline
 & & & & \mathbf{A}^1_{0101}\,\mathbf{B}^1_{0101} & & & & & & & & \mathbf{A}^1_{0111}\,\mathbf{B}^1_{0111} & & & \\
 & & & & \mathbf{E}_{01} & \mathbf{I} & & & & & & & & & & \\
 & & \mathbf{A}^2_{0100}\,\mathbf{B}^2_{0100} & & & & \mathbf{A}^2_{0101}\,\mathbf{B}^2_{0101} & & & & & & & & & & & \\
 & & & & \mathbf{C} & & & \mathbf{D} & & & & & & & & \\
\hline
\mathbf{A}^1_{1000}\,\mathbf{B}^1_{1000} & & & & & & & & \mathbf{A}^1_{1010}\,\mathbf{B}^1_{1010} & & & & & & & \\
 & & & & & & & & \mathbf{E}_{10} & \mathbf{I} & & & & & & \\
 & & & & & & & & & & \mathbf{A}^2_{1010}\,\mathbf{B}^2_{1010} & & & & \mathbf{A}^2_{1011}\,\mathbf{B}^2_{1011} & \\
 & & & & & & & & \mathbf{C} & & & \mathbf{D} & & & & \\
\hline
 & & & & \mathbf{A}^1_{1101}\,\mathbf{B}^1_{1101} & & & & & & & & \mathbf{A}^1_{1111}\,\mathbf{B}^1_{1111} & & & \\
 & & & & & & & & & & & & \mathbf{E}_{11} & \mathbf{I} & & \\
 & & & & & & & & & & \mathbf{A}^2_{1110}\,\mathbf{B}^2_{1110} & & & & \mathbf{A}^2_{1111}\,\mathbf{B}^2_{1111} & \\
 & & & & & & & & & & & & \mathbf{C} & & & \mathbf{D}
\end{array}\right]
\left[\begin{array}{c} \mathbf{v}^1_{L,00} \\ \mathbf{v}^1_{R,00} \\ \mathbf{v}^2_{L,00} \\ \mathbf{v}^2_{R,00} \\ \hline \mathbf{v}^1_{L,01} \\ \mathbf{v}^1_{R,01} \\ \mathbf{v}^2_{L,01} \\ \mathbf{v}^2_{R,01} \\ \hline \mathbf{v}^1_{L,10} \\ \mathbf{v}^1_{R,10} \\ \mathbf{v}^2_{L,10} \\ \mathbf{v}^2_{R,10} \\ \hline \mathbf{v}^1_{L,11} \\ \mathbf{v}^1_{R,11} \\ \mathbf{v}^2_{L,11} \\ \mathbf{v}^2_{R,11} \end{array}\right]
=
\left[\begin{array}{c} \mathbf{b}^1_{00} \\ \mathbf{0} \\ \mathbf{b}^2_{00} \\ \mathbf{d}_{00} \\ \hline \mathbf{b}^1_{01} \\ \mathbf{0} \\ \mathbf{b}^2_{01} \\ \mathbf{d}_{01} \\ \hline \mathbf{b}^1_{10} \\ \mathbf{0} \\ \mathbf{b}^2_{10} \\ \mathbf{d}_{10} \\ \hline \mathbf{b}^1_{11} \\ \mathbf{0} \\ \mathbf{b}^2_{11} \\ \mathbf{d}_{11} \end{array}\right] \tag{26}$$

Although presented for a single stage, this analysis easily generalizes to multiple stages. Consider a multistage machine with M blade rows. The number of blades in each blade row is $B_1, B_2, B_3, \ldots, B_M$, with rotors having even indices. If the original disturbance has n_0 nodal diameters and frequency ω_0 in the rotating frame of reference, then the resulting unsteady flow will contain spinning modes with N nodal diameters where

$$N = n_0 + \sum_{i=1}^{M} n_i B_i \tag{27}$$

with each n_i taking on all integer values. The corresponding frequencies of the spinning modes in the stationary frame are

$$\omega'_{n_2,n_4,n_6,\ldots} = \omega_0 + \Omega\left(n_0 + \sum_{i\ \text{even}} n_i B_i\right) \tag{28}$$

Similarly, in the rotating frame, the frequencies of the spinning modes are given by

$$\omega_{n_1,n_3,n_5,\ldots} = \omega_0 - \Omega \sum_{i\ \text{odd}} n_i B_i \tag{29}$$

2.2 Unsteady Aerodynamic Blade Row Model. The coupled mode analysis outlined above provides a flexible framework for solving unsteady flow problems in multistage compressors and turbines. In this section, the unsteady aerodynamic theory used to compute the unsteady flow in individual blade rows is summarized.

2.2.1 Rapid Distortion Theory. To begin, we assume that the flow is two-dimensional, inviscid, and homentropic, with constant total pressure P_T and total density ρ_T. Thus, the pressure $\hat{p}$ and density $\hat{\rho}$ are related through the condition

$$\frac{\hat{p}}{P_T} = \left(\frac{\hat{\rho}}{\rho_T}\right)^{\gamma} \tag{30}$$

where γ is the ratio of specific heats.

The unsteady flow is, in general, rotational. For convenience, we split the flow into a sum of irrotational (potential) and rotational (vortical) parts, so that

$$\mathbf{V}(x, y, t) = \nabla\hat{\Phi}(x, y, t) + \hat{\mathbf{V}}^R(x, y, t) \tag{31}$$

where $\hat{\Phi}(x, y, t)$ is a scalar velocity potential, and all the vorticity in the flow is contained in the rotational velocity $\hat{\mathbf{V}}^R(x, y, t)$. Furthermore, the unsteadiness in the flow is assumed to be small compared to the mean flow. Thus, we further split the flow into a mean or steady part, plus an unsteady small-disturbance part, which is harmonic in time. It is assumed that the mean background flow is irrotational, but the unsteady flow may be rotational. Hence, the potential $\nabla\hat{\Phi}(x, y, t)$ and the rotational velocity $\hat{\mathbf{V}}^R(x, y, t)$ may be expressed as

$$\hat{\Phi}(x, y, t) = \Phi(x, y) + \phi(x, y)e^{j\omega t} \tag{32}$$

$$\hat{\mathbf{V}}^R(x, y, t) = \mathbf{v}^R(x, y)e^{j\omega t} \tag{33}$$

where $\Phi(x, y)$ is the mean flow potential, and $\phi(x, y)$, and $\mathbf{v}^R(x, y)$ are the complex amplitudes of the small-disturbance potential and rotational velocities, respectively.

Integrating the conservation of momentum equation, one finds that the steady pressure is given by the steady Bernoulli equation

$$P = P_T\left[1 - \frac{\gamma - 1}{2C_T^2}(\nabla\Phi)^2\right]^{\gamma/(\gamma-1)} \tag{34}$$

where $C_T^2 = \gamma P_T/\rho_T$. In general, the unsteady pressure is a

function of both the perturbation potential ϕ and perturbation rotational velocity $\mathbf{v}^R$. Note, however, that the splitting given by Eqs. (31)–(33) is not unique. It is useful to constrain this splitting so that the perturbation pressure p is independent of the rotational velocity. In this case, integrating the unsteady momentum equation, one finds that the perturbation pressure is given by the linearized unsteady Bernoulli equation

$$p = -\bar{\rho}\frac{D_\phi}{Dt} = -\bar{\rho}\left(\frac{\partial\phi}{\partial t} + \nabla\Phi\cdot\nabla\phi\right) \tag{35}$$

where $\bar{\rho}$ is the mean flow density.

Next, Eqs. (30)–(35) are substituted into the continuity equation. Collecting terms of zeroth order and first order in the perturbation flow quantities, one obtains the mean flow and linearized unsteady flow equations. The steady flow is governed by the nonlinear full potential equation, given by

$$\nabla^2\Phi = \frac{1}{C^2}\left[\frac{1}{2}\nabla\Phi\cdot\nabla(\nabla\Phi)^2\right] \tag{36}$$

where C is the steady flow speed of sound given by

$$C^2 = C_T^2\left[1 - \frac{\gamma-1}{2C_T^2}(\nabla\Phi)^2\right] \tag{37}$$

Note that the full potential equation is nonlinear in the unknown potential Φ.

Similarly, the time-linearized equations describing the unsteady flow—the linearized Euler equations for homentropic flow—are

$$\frac{D\mathbf{v}^R}{Dt} + (\mathbf{v}^R\cdot\nabla)\nabla\Phi = 0 \tag{38}$$

$$\frac{D}{Dt}\left(\frac{1}{C^2}\frac{D\phi}{Dt}\right) - \frac{1}{\bar{\rho}}\nabla\cdot(\bar{\rho}\nabla\phi) = \frac{1}{\bar{\rho}}\nabla\cdot(\bar{\rho}\mathbf{v}^R) \tag{39}$$

Equation (38) describes the convection and distortion of the rotational velocity $\mathbf{v}^R$. Equation (39) is the usual linearized potential equation, but with a source term on the right-hand side to account for the fact that the rotational velocity $\mathbf{v}^R$ does not necessarily satisfy mass continuity. Note that Eqs. (38) and (39) are sequentially coupled, that is, one can first solve Eq. (38) for $\mathbf{v}^R$, then solve Eq. (39) for ϕ.

Goldstein (1978) showed that, remarkably, the rotational velocity may be expressed analytically in terms of the steady flow stream function Ψ and Lighthill's (1956) drift function Δ. The drift function Δ is essentially the time required for a fluid particle to convect from a reference point on a streamline to another point on the same streamline. Following Goldstein (1978) and Atassi and Grzedzinski (1989),

$$\mathbf{v}^R = [c_1(\Psi)\nabla\Delta + c_2(\Psi)\nabla\Psi]\exp[j(K_1\Delta + K_2\Psi)] \tag{40}$$

where K_1 and K_2 are essentially wavenumbers, and are related algebraically to the axial and circumferential wavenumbers α and β. The functions c_1 and c_2 determine the amplitude of vorticity coming into the cascade. Goldstein's (1978) original formulation is singular for airfoils with stagnation points. Atassi and Grzedzinski (1989) later removed this singularity by a judicious choice of $c_1(\Psi)$ and $c_2(\Psi)$. Hall and Verdon (1991) and Lorence and Hall (1996) later used this modified formulation to compute unsteady flows in cascades.

2.2.2 Numerical Solution of the Steady Flow Field. The steady flow potential equation, Eq. (36), is solved numerically using a nonlinear variational finite element solver developed by Hall (1993). The computational grid used in this study is an **H**-grid composed of quadrilateral cells. Four-node isoparametric finite elements are used to discretize Bateman's (1930) variational principle for compressible flow. The resulting discretized equations take the form

$$\mathbf{N}(\mathbf{\Phi}, \mathbf{X}) = \mathbf{0} \tag{41}$$

where $\mathbf{N}$ is a vector of nonlinear functions, $\mathbf{\Phi}$ is a vector containing the nodal values of the steady potential Φ, and $\mathbf{X}$ is a vector containing the x and y coordinates of each node of the grid.

Because the unsteady rotational velocity $\mathbf{v}^R$ is fundamentally dependent on the drift and stream functions, it is convenient to perform our numerical calculations on a streamline computational grid. However, one cannot know the position of streamlines *a priori*. Therefore, we must generate the computational grid as part of the steady solution procedure. We use a modified elliptic grid generation technique originally proposed by Thompson et al. (1977), but modified to ensure that the resulting streamwise grid lines are true streamlines. When discretized, the grid equations are of the form

$$\mathbf{M}(\mathbf{\Phi}, \mathbf{X}) = \mathbf{0} \tag{42}$$

where $\mathbf{M}$ is a vector of nonlinear grid generation equations, two for each node of the grid.

Equations (41) and (42) are solved simultaneously using Newton iteration to determine the steady velocity potential $\mathbf{\Phi}$ and the grid geometry $\mathbf{X}$. Typically, about four Newton iterations are required to obtained a converged steady solution. A trivial computation is then required to compute the stream function Ψ and drift function Δ at each node of the grid. For typical problems using a 129×33 computational grid, the steady solution procedure requires on the order of 25 minutes of computer time per blade row using a Silicon Graphics Indigo (R4400) workstation.

2.2.3 Numerical Solution of the Unsteady Flow Field. Next, the small disturbance unsteady flow equations are discretized. First, for vortical gust problems, the rotational velocity $\mathbf{v}^R$ is computed analytically at the nodes of the computational grid using Eq. (40). Then, Eq. (39) is discretized using a variational finite element technique developed by Hall (1993). The finite element code has a number of important features. For instance, complex periodicity, Eq. (5), is imposed, allowing the computational domain to be reduced to a single blade passage, thereby reducing the computational effort required to compute flows with nonzero interblade phase angles. Also, to prevent spurious reflections of acoustic and vortical waves, numerically exact nonreflecting boundary conditions are applied at the far-field boundaries of the computational domain. Finally, for aerodynamic damping calculations, a deforming computational grid, which conforms to the motion of the airfoil, is used to improve the accuracy of the scheme.

When assembled, the discretized equations governing the unsteady small disturbance flow have the form

$$[\mathbf{A}]\{\phi\} = \{\mathbf{b}\} \tag{43}$$

where $\mathbf{A}$ is a sparse complex matrix, which is a function of the frequency ω and interblade phase angle σ. The vector $\mathbf{b}$ arises from the imposition of an external disturbance, e.g., an incident acoustic wave or a prescribed blade motion. Note that the number of unknowns in Eq. (43) is about one-third that in Eqs. (41) and (42) since no grid generation equations must be solved for the unsteady flow problem. The matrix $\mathbf{A}$ is factored into a product of upper and lower triangular matrices (LU factorization). In this way, the unsteady solution for several different external disturbances at the same interblade phase angle and frequency (different $\mathbf{b}$'s) can be computed very efficiently, each requiring just one forward and one backward matrix substitution. Typically, the reflection/transmission coefficients for a single scatter group can be computed in less than one minute.

Table 1 Cascade parameters for Configuration C, a one and one-half stage compressor composed of flat-plate airfoils

Station or Row	0	1	2	3
Type of Blade Row	—	Stator	Rotor	Stator
Number of Blades, B	—	3	4	5
Chord	—	1.261	1.0	0.820
Circumferential Gap, G	—	1.067	0.8	0.64
Stagger Angle, Θ (deg)	—	37.5	–60.0	37.5
Axial Gap, Δx	—	0.125	0.125	—
V_{rel}	1.000	1.000	1.000	1.000
V_{abs}	0.630	0.630	0.630	0.630
M	0.0	0.0	0.0	0.0
Flow Angle, α_{rel} (deg)	–60.0	–60.0	–60.0	–60.0
Flow Angle, α_{abs} (deg)	37.5	37.5	37.5	37.5
Static Density, $\bar{\rho}$	1.000	1.000	1.000	1.000

This description of the numerical model used to compute the steady and unsteady aerodynamic characteristics of the individual blade rows is, because of space limitations, quite terse. The interested reader is referred to Hall (1993), Lorence and Hall (1996), and Silkowski (1996) for additional details on the method, and also numerical examples used to validate the method.

3 Results

In this section, we consider the unsteady aerodynamic response of a compressor rotor is part of a multistage compressor. In particular, we consider two geometries. The first, Configuration C, is a one and one-half stage compressor whose airfoils are flat plates, which do no steady turning. The second, Configuration D, is a two and one-half stage section of a two-dimensional compressor with "real" blades, i.e., the blades have thickness and camber and do steady turning.

3.1 Multistage Configuration C. To validate the coupled mode analysis, we first consider a one and one-half stage compressor composed of flat plate airfoils, which do no steady turning. The geometry for this multistage machine is given in Table 1. In particular, the ratio of blades in the three blade rows is 3:4:5, and the axial gap between blade rows is quite small, approximately 12.5 percent of the blade chord. Note that lengths have been nondimensionalized by the aerodynamic chord c of the rotor blades, velocities by the relative inflow velocity to the rotor, and pressures by the quantity $\bar{\rho}V_{\text{rel}}^2$.

The airfoils of the rotor (the middle blade row) are prescribed to vibrate in plunge with a reduced frequency ω_0 of 0.5 and an interblade phase angle σ_0 of 90 deg. The unsteady aerodynamic response was then computed in two ways. First, we applied the present coupled mode analysis described in this paper, but with Whitehead's (1987) LINSUB code used to compute the reflection/transmission coefficients of the individual blade rows. LINSUB was used here because it is essentially exact. Thus, any errors will be due to the coupled mode analysis itself, and not truncation error of the aerodynamic code. To couple the blade rows, we used 1, 11, and 27 spinning modes. The mode order indices associated with these spinning modes are shown in Table 2. For the 11-mode case, for example, we used the first 11 modes in the table. The selection of spinning modes used is somewhat of an art. Generally, spinning modes are selected that have a relatively small number of nodal diameters, since these low-order modes tend to be cut-on or are weakly cut-off. Also used are some spinning modes, which may have a larger number of nodal diameters, but are members of the fundamental mode's scatter group, and also provide a kinematic connection between the fundamental and low-order spinning modes.

We also used an incompressible time-marching vortex-lattice code developed by Silkowski (1996) to compute the unsteady lift acting on the compressor blades. Using this approach, the blades and wakes of the cascades are modeled by vortex elements. At the quarter-chord of each element is placed a discrete vortex. At the three-quarter-chord of each element on the airfoils is a collocation point. To start the calculation, the strengths of all the vortex elements are set to zero. Then, at each time step, the strengths of the vortex elements on the airfoils are selected so that the no-throughflow condition is satisfied. The strength of the first vortex element in the wake of each airfoil is chosen so as to satisfy Kelvin's theorem, i.e., the circulation about a fixed set of fluid particles is constant. The vorticity in the remainder of the wake is simply convected with the mean flow velocity. After each time step, the position of the rotor is incremented, and the entire process is repeated. For this example, we divided each airfoil of the three blade rows into 80, 40, and 52 vortex elements, respectively. At this resolution, the resulting unsteady lift computation was found to be element converged, that is, the unsteady lift is nearly identical to that predicted using half as many elements per airfoil.

Shown in Fig. 3 is the computed unsteady lift acting on the three blade rows as a function of time. These results were computed using the coupled mode analysis with 1, 11, and 27 spinning modes. (The 27-mode solution is nearly identical to the 11-mode solution, and is omitted from the figure for clarity.) Also shown is the unsteady lift calculated using the vortex-lattice time-domain simulation. Here the lift is nondimensionalized by $\bar{\rho}V\dot{h}_0 c$, where $\bar{\rho}$ is the mean static density, V is the mean flow velocity as viewed in the blade row's frame of reference, c is the chord of the airfoils in the specified row, and $\dot{h}_0$ is the amplitude of plunging of the rotor blades.

After the initial transients associated with the start-up of the vortex-lattice simulation have subsided, the agreement between the vortex-lattice simulation and the coupled mode analysis is quite good, especially for the 11- and 27-mode cases. The minor discrepancies are seen to have a high frequency content. The agreement is not exact because only a finite number of the infinite number of spinning modes that participate in the solution have been included in the coupled mode model. Nevertheless, even the one-mode case shows the correct low-frequency behavior (this frequency corresponds to the original blade vibration frequency). These results demonstrate several important points.

Table 2 Indices of spinning modes used for coupled mode analysis of multistage compressors: $N = n_1B_1 + n_2B_2 + n_3B_3$

Mode	(n_1, n_2, n_3)	Mode	(n_1, n_2, n_3)
1	(0, 0, 0)	14	(–1,–2,+1)
2	(0,–1, 0)	15	(+1,–2, 0)
3	(–1, 0, 0)	16	(–1,+1,–1)
4	(0,+1,–1)	17	(0,+2, 0)
5	(+1,–1, 0)	18	(0,–2,+1)
6	(0, 0,–1)	19	(+1, 0,–1)
7	(–1,+1, 0)	20	(–1,+2,–1)
8	(0,–1,+1)	21	(+1,–2,+1)
9	(+1, 0, 0)	22	(–1, 0,+1)
10	(0,+1, 0)	23	(0,+2,–1)
11	(0, 0,+1)	24	(+1,–1,+1)
12	(–1, 0,–1)	25	(–1,+2, 0)
13	(0,–2, 0)	26	(+1,+2,–1)
		27	(+1, 0,+1)

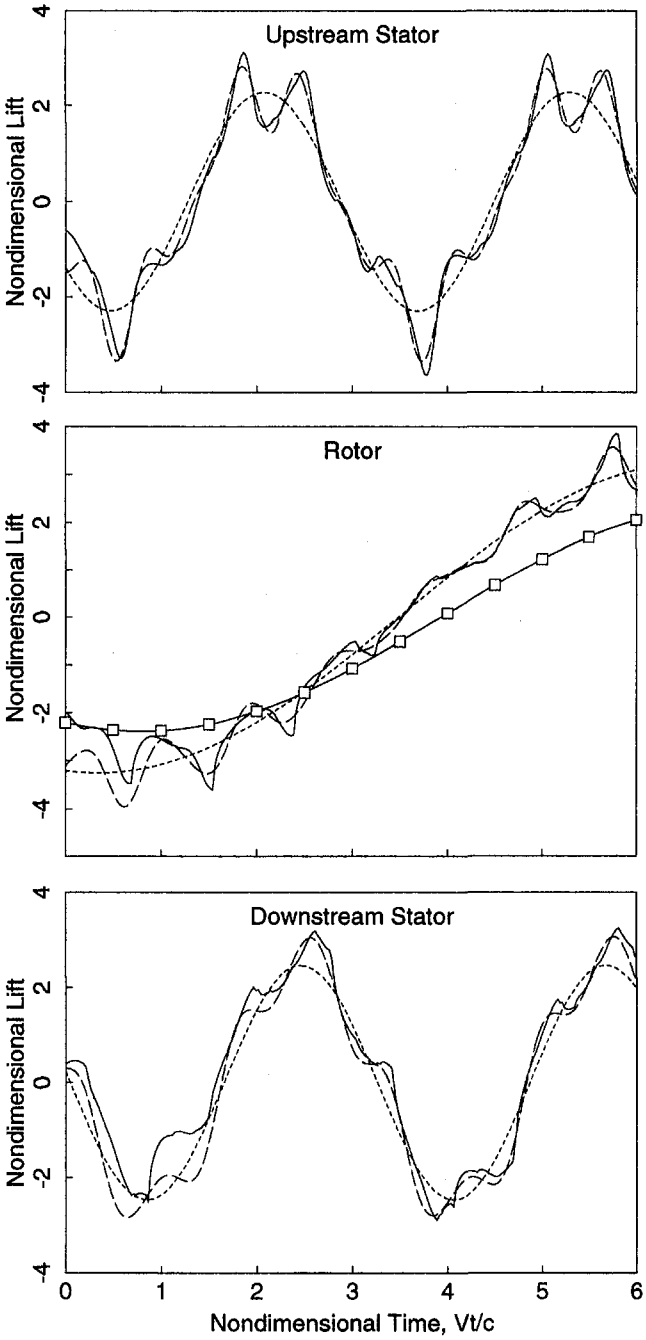

Fig. 3 Unsteady lift histories on the reference airfoils of Configuration C (stator/rotor/stator). Rotor blades vibrate in plunge with $\sigma_0 = 90$ deg, $\omega_0 = 0.5$. ——□——, uncoupled; - - - - -, 1 mode; – – –, 11 modes; ——, vortex-lattice code.

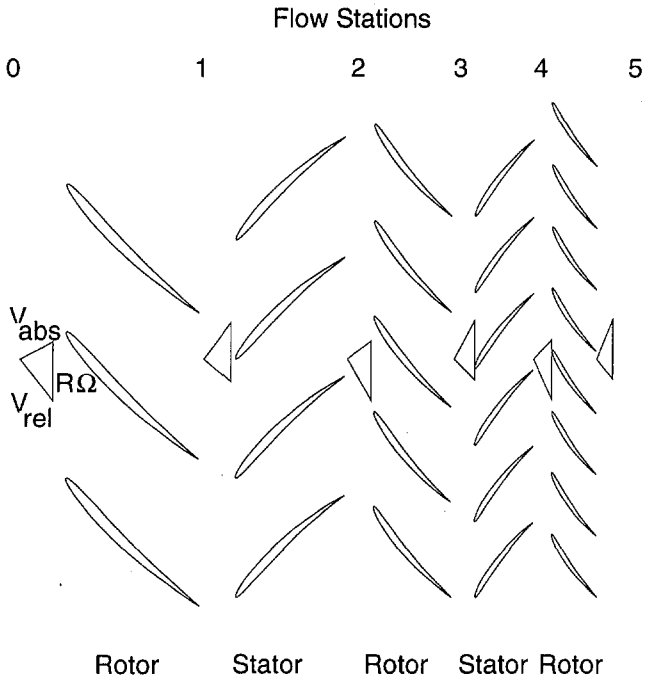

Fig. 4 Configuration D, a two-dimensional, two and one-half stage compressor with rows of NACA four digit series airfoils

First, a small number of the infinite set of possible spinning modes provide most of the coupling between the blade rows. Second, the coupled mode analysis exhibits mode convergence. As more spinning modes are included in the model, the solution converges to the exact solution. Third, if one is interested in the response at the original excitation frequency, e.g., for aerodynamic damping calculations, then engineering accuracy results may be obtained with as few as one spinning mode. Fourth, and finally, the unsteady aerodynamic response of the rotor to blade vibration is significantly altered by the presence of neighboring blade rows.

3.2 Multistage Configuration D. Having validated the coupled mode analysis for incompressible flows, we next consider compressible flows in the two and one-half stage compressor section shown in Fig. 4, denoted here as Configuration D. The airfoils of each blade row of the compressor are NACA four digit series airfoils. In most instances, we will calculate the unsteady flow through the middle three blade rows of this configuration (one and one-half stages). Later, the first and last blade rows will be included to create a full two and one-half stage machine. As shown in Fig. 4, the blade rows are closely spaced, as is typical in modern compressors. The specific geometry for the compressor is given in Table 3. As before, lengths have been nondimensionalized by the aerodynamic chord c of the rotor blades of the middle rotor, velocities by the relative inflow velocity V_{rel} at Station 2, and pressures by the quantity $\bar{p}V^2_{\text{rel}}$ at Station 2.

Shown in Fig. 5 is the computed steady pressure distribution on the surface of the blades of the middle blade row. The grid used for this calculation was an **H**-grid with 129 × 33 grid points (129 nodes in the streamwise direction, and 33 nodes in the normal direction). This same grid resolution was used to compute the steady and unsteady flow solutions in all the blade

Table 3 Cascade parameters for Configuration D, a two and one-half stage compressor composed of NACA four digit series airfoils

Station or Row	0	1	2	3	4	5
Type of Blade Row	—	Rotor	Stator	Rotor	Stator	Rotor
Number of Blades, B	—	26	32	40	50	62
NACA 4-Digit Airfoil	—	(3.5)506	(4.5)506	(4.5)506	(4.5)506	(4.5)506
Chord	—	1.539	1.25	1.0	0.8	0.645
Circumferential Gap, G	—	1.231	1.0	0.8	0.64	0.516
Axial Gap, Δx	—	0.31	0.25	0.20	0.16	—
V_{rel}	1.112	0.744	1.000	0.609	0.919	0.531
V_{abs}	0.780	0.959	0.630	0.926	0.562	0.906
M_{rel}	0.829	0.535	0.700	0.414	0.609	0.344
M_{abs}	0.581	0.689	0.441	0.629	0.373	0.586
Flow Angle, α_{rel} (deg)	–52.0	–40.0	–60.0	–45.0	–65.5	–50.5
Flow Angle, α_{abs} (deg)	28.6	53.5	37.5	62.3	47.3	68.1
Stagger Angle, Θ (deg)	—	–44	43	–49.5	52	–55
Static Pressure, P	0.939	1.213	1.458	1.797	2.131	2.524
Total Pressure, $P_{\text{T,rel}}$	1.473	1.473	2.022	2.022	2.739	2.739
Total Pressure, $P_{\text{T,abs}}$	1.180	1.666	1.666	2.346	2.346	3.185

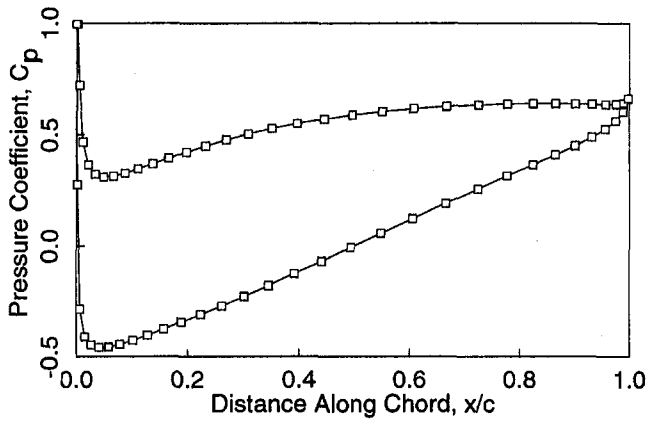

Fig. 5 Steady pressure distribution on surface of airfoils of middle rotor of Configuration D compressor at design condition

rows. For the cases considered in this paper, the flow throughout the multistage compressor is entirely subsonic.

The first unsteady example considered for Configuration D is an aerodynamic damping calculation where the middle three blade rows (one and one-half stages) are retained in the model. The blades of the middle rotor are prescribed to vibrate in plunge normal to the blade chord with a reduced frequency ω_0 of 0.5 for a range of interblade phase angles σ_0. The unsteady aerodynamic response was computed using the coupled mode analysis with 0, 1, 11, and 27 spinning modes (see Table 2). The 0-mode case corresponds to an isolated blade row (no interrow coupling).

Figure 6 shows the computed unsteady pressure on the surface of the reference blade of the rotor for the case where a single mode is used to couple the three blade rows. Also shown is the pressure distribution for the uncoupled case. Here, the pressure is nondimensionalized by $\bar{p}V\dot{h}_0$, where $\bar{p}$ and V are the mean static density and flow velocity as viewed in the rotor's frame of reference, and $\dot{h}_0$ is the amplitude of the plunging velocity of the reference blade of the rotor. Using this nondimensionalization, it is the real part of the unsteady pressure that contributes to aerodynamic damping. Note that the coupled and uncoupled pressure distributions differ substantially. In this case, the damping of the rotor in the presence of the neighboring stators is much larger than the damping of the same rotor isolated in an infinitely long duct.

One can integrate the unsteady pressure distribution on the surface of the airfoil to obtain the unsteady lift. Figure 7 shows the real and imaginary part of the computed unsteady lift. In general, the unsteady lift will contain many frequencies due to the scattering of modes and subsequent shifting of frequencies. However, we have plotted only the component of the lift that has the same frequency and interblade phase angle as the blade motion since this is the only part that does modal work on the vibrating airfoils, and hence is the only part that contributes to aerodynamic damping. The unsteady lift is nondimensionalized by $\bar{p}V_{\text{rel}}\dot{h}_0 c$ where the steady flow quantities are taken to be those at Station 2, c is the chord of the middle rotor, and $\dot{h}_0$ is the amplitude of the plunging velocity of the reference rotor blade. Using this nondimensionalization, the aerodynamic damping is negative whenever the real part of the lift is greater than zero.

For small interblade phase angles, the presence of the stators has had an aeroelastically destabilizing effect on the rotor. In other regions, for example near an interblade phase angle σ_0 of 60 deg, the isolated blade row calculation seriously underpredicts the aerodynamic damping. This is an important result. *The aerodynamic damping of a blade row that is part of a multistage machine can be significantly different from that predicted using an isolated blade row model.*

The results shown in Fig. 7 demonstrate that the Coupled Mode Method displays mode convergence, i.e., as the number of spinning modes in the model is increased, the computed unsteady lift converges to a fixed value. Furthermore, only a relatively small number of spinning modes need to be retained to obtain good estimates of the aerodynamic damping. In fact, for this example, engineering accuracy is achieved with just one mode.

Another interesting feature of Fig. 7 is that the coupled unsteady aerodynamic damping curves have numerous slope discontinuities, whereas the uncoupled aerodynamic damping curve has just four. For the uncoupled (isolated blade row) case, these discontinuities correspond to the four interblade phase angles at which duct modes are cut on (acoustic resonances) upstream and downstream of the blade row for the prescribed blade vibration frequency. For the coupled case, many more acoustic resonance points appear. These new resonance points appear for at least three reasons. First, there are now multiple frequencies and nodal diameters present in the response owing to frequency shifting and mode scattering. Thus, there will be new sets of acoustic resonances for each discrete frequency in the response. Second, even if a specific mode is not at a resonance condition, if any member of that mode's scatter group passes through a resonance, all of the transmission/reflection coefficients of all the modes in the scatter group will change abruptly. Third, each blade row does mean turning of the flow, causing each of the interrow flow regions to have different properties, including acoustic resonance points. The acoustic resonance points of the one and one-half stage compressor are identified with vertical lines in Fig. 7. Overall, the

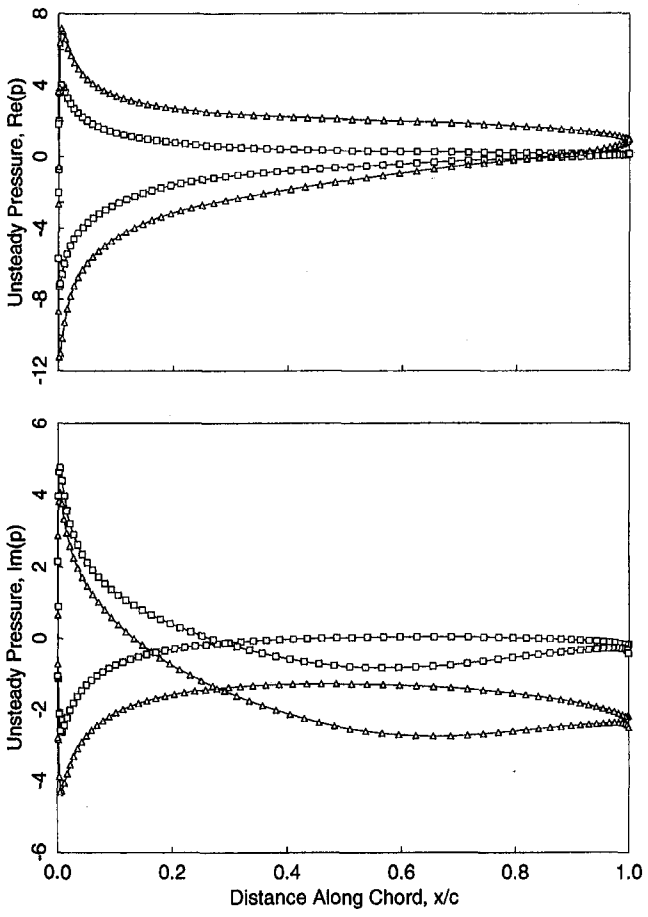

Fig. 6 Fundamental harmonic of unsteady surface pressure on reference airfoil of middle rotor of Configuration D. Three blade row case, plunging excitation with (σ_0, ω_0) = (60 deg, 0.5). -□-, uncoupled; —△—, one mode coupling.

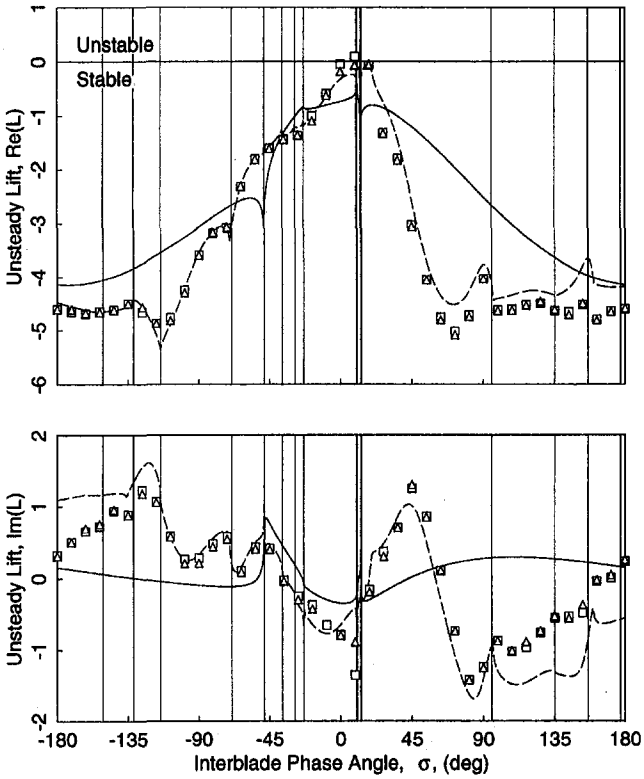

Fig. 7 Fundamental harmonic of unsteady lift acting on reference airfoil of middle rotor of Configuration D. Three blade row case, plunging excitation with $\omega_0 = 0.5$. ———, uncoupled; – – –, 1 mode; □, 11 modes; △, 27 modes.

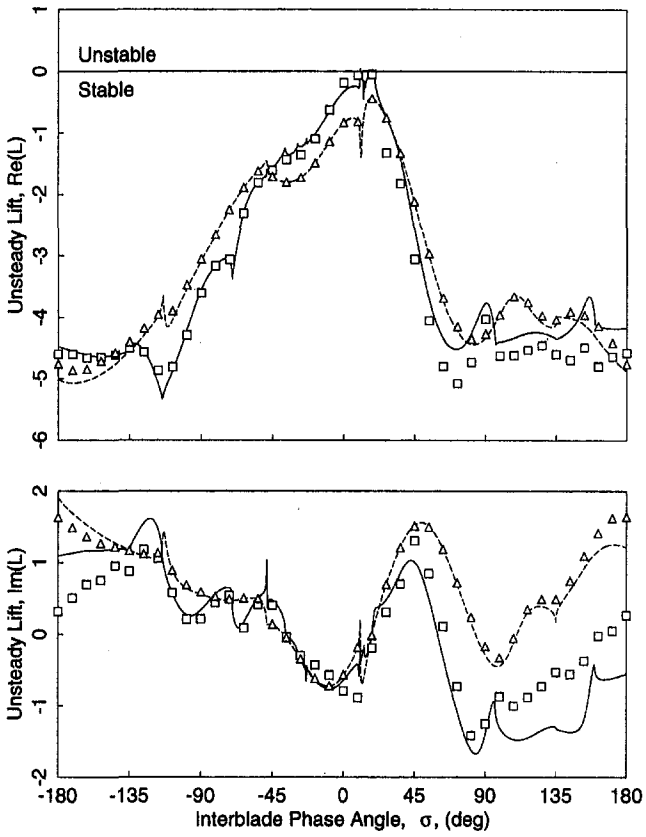

Fig. 8 Fundamental harmonic of unsteady lift acting on reference airfoil of middle rotor of one and one-half stage compressor. Three blade row case, plunging excitation with $\omega_0 = 0.5$. Configuration D: ———, 1 mode; □, 27 modes. equivalent flat-plate compressor: – – –, 1 mode; △, 27 modes.

agreement between the actual (vertical lines) and computed (slope discontinuities) resonance points is quite good. The lack of agreement at some of the higher interblade phase angles may be due to a lack of grid resolution required to analyze spinning modes with high frequencies and short wavelengths. This problem is not a deficiency of the coupled mode analysis, but rather truncation error associated the individual blade row flow solver (this problem also occurs with time-marching codes).

Next, to determine the relative importance of multistage effects compared to real blade effects (camber, thickness, etc.), we defined an "equivalent flat-plate compressor." This compressor is similar to Configuration D, except that the airfoils in each row have been replaced with flat plates with the same aerodynamic chord. The equivalent flat-plate compressor does no work on the fluid. Thus, the mean flow is uniform with flow properties equal to those at Station 2 (the inlet conditions to the reference rotor) of Configuration D. Finally, the stagger angles of the blades are adjusted to be aligned with the relative mean flow in each blade row. Shown in Fig. 8 is the computed unsteady lift for Configuration D and the Equivalent Flat-Plate Compressor for plunging motion of the middle rotor blade with a reduced frequency ω_0 of 0.5. As expected, the unsteady lifts for these two configurations differ somewhat. However, the differences are smaller than the differences between the coupled and uncoupled solutions of Configuration D (see Fig. 7). In other words, *multistage effects can have a larger impact on aerodynamic damping than real blade effects.*

If multistage effects can indeed influence the aerodynamic damping of a rotor, as suggested by the previous results, then it may be possible to use the axial spacing between blade rows as a passive means for improving the aeroelastic performance of a rotor. Figure 9 shows the real part of the unsteady lift for Configuration D due to plunging motion of the middle rotor as before, but for several values of axial spacing between the rotor and the neighboring stators (these results were computed using one mode coupling). As the axial gaps are varied, the unsteady lift (aerodynamic damping) takes on a wide range of values.

Finally, we consider the influence of blade rows beyond the two neighboring stators. For this final example, we include the upstream and downstream rotors of Configuration D. Figure 10 shows the computed unsteady lift where all five blade rows have been modeled (we also show the isolated blade row model and the previous three blade row model for comparison).

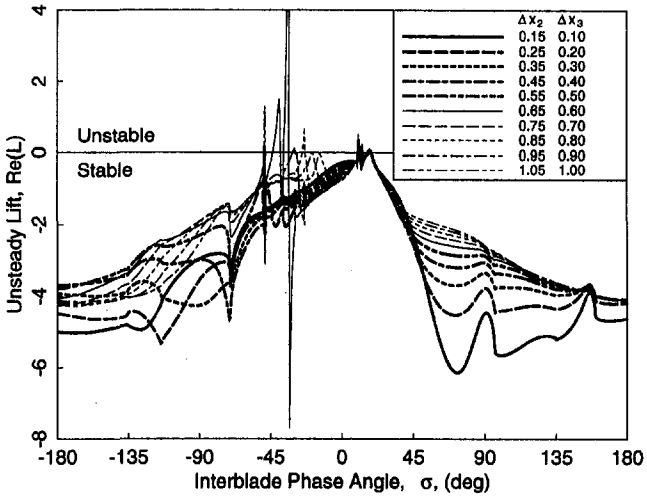

Fig. 9 Fundamental harmonic of unsteady lift acting on reference airfoil of middle rotor of Configuration D for various axial spacings between blade rows. Three blade row case, plunging excitation with $\omega_0 = 0.5$.

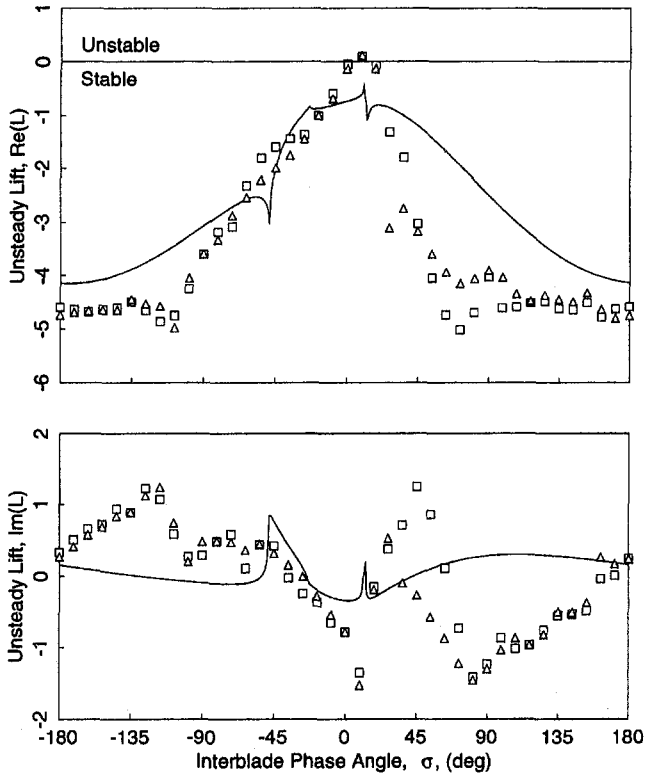

Fig. 10 Fundamental harmonic of unsteady lift acting on reference airfoil of middle rotor of Configuration D for plunging excitation with $\omega_0 = 0.5$. ———, uncoupled; △, three blade rows; □, five blade rows.

Eleven spinning modes were used to couple the blade rows. Over most of the interblade phase angle range, the three and five blade row solutions are nearly the same. For interblade phase angles between about 20 and 100 deg, however, the addition of the outer two rotors has a modest influence on the aerodynamic damping of the middle rotor. Nevertheless, the nearest two stators clearly have the strongest influence on the unsteady aerodynamic behavior of the rotor. Hall and Silkowski (1997) have shown that additional blade rows (beyond five) have very little influence on the unsteady lift on the middle rotor. The physical explanation for this is that vortical and acoustic waves tend to be diminished as they travel from one blade row to the next. This is because transmission and reflection coefficients are usually less than unity. Furthermore, many of the acoustic waves are cut-off.

3.3 Computational Requirements. The computational time t_{cpu} required to solve a series of unsteady multistage problems can be approximated by

$$t_{\text{cpu}} \approx M \cdot (t_s + M_p M_m t_u) \tag{44}$$

where M is the number of blade rows, M_m is the number of spinning modes used in the multistage calculations, M_p is the number of original interblade phase angles σ_0 and/or frequencies ω_0 considered, t_s is the computational time required to compute the steady flow in a single blade row, and t_u is the computational time required to compute the unsteady response of a single blade row to unsteady excitations of a single spinning mode. As an example, consider the results shown in Fig. 7 computed using 11 spinning modes ($M_m = 11$). For this example $M = 3$ and $M_p = 41$. Using a Silicon Graphics Indigo (R4400) workstation, we found that $t_s = 1475$ s and $t_u = 51$ s. Thus, to generate all 11 spinning mode results shown in Fig. 7 required approximately 20.4 h of CPU time.

4 Summary and Conclusions

In this paper, we have presented a coupled mode analysis—a technique for calculating the unsteady aerodynamic response of a blade row which is embedded in a multistage machine. Using this approach, the problem is first subdivided into a number of simpler problems, that is, finding the response of the individual blade rows in isolation at a number of frequencies and interblade phase angles. These individual solutions are then used to form a fairly small sparse matrix equation that describes the unsteady aerodynamic response of the multistage machine.

Based on the numerical results computed to date, we can make the following conclusions and observations:

1 The aerodynamic damping of a blade row that is part of a multistage machine can be significantly different from that predicted using an isolated blade row model. This is an important result since virtually all unsteady aerodynamic theories currently used in industry assume that the blade row can be modeled as isolated in an infinitely long duct.

2 A good estimate of the aerodynamic damping can be obtained using just a few spinning modes in the model. In fact, most of the unsteady aerodynamic coupling between blade rows occurs in the fundamental spinning mode, that is, the spinning mode associated with the original disturbance. Scattered modes are relatively less important.

3 For a typical compressor geometry, multistage effects can have a larger impact on aerodynamic damping than real blade effects. (This may not be true in the case of turbine blades, where the turning is much larger.) Given the state of the art in unsteady aerodynamic theories, this suggests that more effort should be devoted to understanding multistage physics.

4 The two neighboring stator blade rows adjacent to a rotor have the strongest influence on the unsteady aerodynamic response of the rotor. The next nearest blade rows are less important, but can still have a modest influence.

5 The coupled mode analysis is computationally very efficient. For example, to compute the aerodynamic damping of a rotor embedded in a one and one-half stage compressor section (Configuration D) at a single reduced frequency and interblade phase angle using a single spinning mode required just 153 s of CPU time on a Silicon Graphics Indigo (R4400) workstation.

6 The coupled mode analysis is flexible and well-suited for certain parametric design studies. For example, once the reflection/transmission coefficients have been calculated for each of the blade rows of a given multistage machine, it is very inexpensive to recompute the aerodynamic damping for a range of axial or circumferential spacings between blade rows, or to compute the response to an incident wake instead of a prescribed blade vibration. Furthermore, because of the modular nature of the method, if a single blade row of a multistage machine is redesigned, one need only recompute the reflection/transmission coefficients for the redesigned blade row, and then solve the small global matrix equation. Conventional time-marching simulations, on the other hand, would require a completely new computation of the entire multistage machine for any variation in geometry or excitation.

7 It may be possible to use the multistage influence on aerodynamic damping to good effect. For instance, it may be possible in some cases to increase the aerodynamic damping of a rotor by altering the axial spacing between adjacent blade rows.

Finally, we would comment that while the analysis presented in this paper has been entirely two-dimensional, we expect that multistage effects will strongly influence unsteady flows in real turbomachines, which are fundamentally three-dimensional. Indeed, unlike steady flows, which can to a good approximation be computed using two-dimensional isolated blade row techniques, accurate predictions of unsteady flows will likely require a three-dimensional multistage analysis. The authors are currently

extending the present coupled mode analysis to three-dimensional flows.

Acknowledgments

This material is based upon work supported by the National Science Foundation under Grant No. CTS-9157908. The government has certain rights in this material. The authors would like to thank Dr. Christopher B. Lorence for his help in developing the linearized potential/rapid distortion theory model used in this study, and Dr. Donald B. Hanson for many helpful discussions on mode coupling.

References

Adamczyk, J. J., and Goldstein, M. E., 1978, "Unsteady Flow in a Supersonic Cascade With Subsonic Leading Edge Locus," *AIAA Journal,* Vol. 16, No. 12, pp. 1248–1254.

Atassi, H. M., and Grzedzinski, J., 1989, "Unsteady Disturbances of Streaming Motions Around Bodies," *Journal of Fluid Mechanics,* Vol. 209, Dec., pp. 385–403.

Bateman, H., 1930, "Irrotational Motion of a Compressible Fluid," *Proc. National Academy of Sciences,* Vol. 16, pp. 816–825.

Bölcs, A., and Fransson, T. H., 1986, "Aeroelasticity in Turbomachines. Comparison of Theoretical and Experimental Cascade Results," AFOSR-TR-0605, Air Force Office of Scientific Research, Washington, DC.

Buffum, D. H., 1993, "Blade Row Interaction Effects on Flutter and Forced Response," AIAA Paper No. 93-2084.

Clark, W. S., and Hall, K. C., 1995, "A Numerical Model of the Onset of Stall Flutter in Cascades," ASME Paper No. 95-GT-377.

Gerolymos, G. A., 1993, "Advances in the Numerical Integration of the Three-Dimensional Euler Equations in Vibrating Cascades," ASME JOURNAL OF TURBOMACHINERY, Vol. 115, pp. 781–790.

Giles, M. B., 1988a, "Calculation of Unsteady Wake/Rotor Interaction," *AIAA Journal of Propulsion,* Vol. 4, No. 4, pp. 356–362.

Giles, M. B., 1988b, "Stator/Rotor Interaction in a Transonic Turbine," AIAA Paper No. 88-3093.

Goldstein, M. E., 1978, "Unsteady Vortical and Entropic Distortions of Potential Flows Round Arbitrary Obstacles," *Journal of Fluid Mechanics,* Vol. 93, Part 3, pp. 433–468.

Hall, K. C., 1993, "Deforming Grid Variational Principle for Unsteady Small Disturbance Flows in Cascades," *AIAA Journal,* Vol. 31, No. 5, pp. 891–900.

Hall, K. C., and Clark, W. S., 1993, "Linearized Euler Prediction of Unsteady Aerodynamic Loads in Cascades," *AIAA Journal,* Vol. 31, No. 3, pp. 540–550.

Hall, K. C., and Crawley, E. F., 1989, "Calculation of Unsteady Flows in Turbomachinery Using the Linearized Euler Equations," *AIAA Journal,* Vol. 27, No. 6, pp. 777–787.

Hall, K. C., and Lorence, C. B., 1993, "Calculation of Three-Dimensional Unsteady Flows in Turbomachinery Using the Linearized Harmonic Euler Equations," ASME JOURNAL OF TURBOMACHINERY, Vol. 115, No. 4, pp. 800–809.

Hall, K. C., and Silkowski, P. D., 1997, "The Influence of Neighboring Blade Rows on the Unsteady Aerodynamic Response of Cascades," ASME JOURNAL OF TURBOMACHINERY, Vol. 119, pp. 85–93.

Hall, K. C., and Verdon, J. M., 1991, "Gust Response Analysis for Cascades Operating in Nonuniform Mean Flows," *AIAA Journal,* Vol. 29, No. 9, pp. 1463–1471.

Hanson, D. B., 1992, "Unsteady Coupled Cascade Theory Applied to the Rotor/Stator Interaction Noise Problem," DGLR/AIAA Paper No. 92-02-084.

Hanson, D. B., 1993, "Mode Trapping in Coupled 2D Cascades—Acoustic and Aerodynamic Results," AIAA Paper NO. 93-4417.

He, L., 1990, "An Euler Solution for Unsteady Flows Around Oscillating Blades," ASME JOURNAL OF TURBOMACHINERY, Vol. 112, pp. 714–722.

Holmes, D. G., and Chuang, H. A., 1993, "2D Linearized Harmonic Euler Flow Analysis for Flutter and Forced Response," *Unsteady Aerodynamics, Aeroacoustics, and Aeroelasticity of Turbomachines and Propellers,* H. M. Atassi, ed., Springer-Verlag, New York [Originally presented 1991].

Huff, D. L., Swafford, T. W., and Reddy, T. S. R., 1991, "Euler Flow Predictions for an Oscillating Cascade Using a High Resolution Wave-Split Scheme," ASME Paper No. 91-GT-198.

Kaji, S., and Okazaki, T., 1970, "Generation of Sound by Rotor-Stator Interaction," *Journal of Sound and Vibration,* Vol. 13, No. 3, pp. 281–307.

Lighthill, M. J., 1956, "Drift," *Journal of Fluid Mechanics,* Vol. 1, May, pp. 31–53.

Lorence, C. B., and Hall, K. C., 1996, "Sensitivity Analysis of the Aeroacoustic Response of Turbomachinery Blade Rows," *AIAA Journal,* Vol. 34, No. 8, pp. 1545–1554.

Marshall, J. G., and Imregun, M., 1996, "A Review of Aeroelasticity Methods With Emphasis on Turbomachinery Applications," *Journal Fluids and Structures,* Vol. 10, No. 3, pp. 237–267.

Nagashima, T., and Whitehead, D. S., 1977, "Linearized Supersonic Unsteady Flow in Cascades," Reports and Memoranda No. 3711, Aeronautical Research Council, London.

Rai, M. M., 1989a, "Three-Dimensional Navier–Stokes Simulations of Turbine Rotor–Stator Interaction, Part I—Methodology," *Journal of Propulsion and Power,* Vol. 5, No. 3, pp. 305–311.

Rai, M. M., 1989b, "Three-Dimensional Navier–Stokes Simulations of Turbine Rotor–Stator Interaction, Part II—Results," *Journal of Propulsion and Power,* Vol. 5, No. 3, pp. 312–319.

Silkowski, P. D., 1996, "A Coupled Mode Method for Multistage Aeroelastic and Aeroacoustic Analysis of Turbomachinery," Ph.D. Thesis, Duke University, Durham, NC.

Smith, S. N., 1972, "Discrete Frequency Sound Generation in Axial Flow Turbomachines," Reports and Memoranda No. 3709, Aeronautical Research Council, London.

Thompson, J. F., Thames, F. C., and Mastin, C. W., 1977, "A Code for Numerical Generation of Boundary-Fitted Curvilinear Coordinate Systems on Fields Containing Any Number of Arbitrary Two-Dimensional Bodies," *Journal of Computational Physics,* Vol. 24, No. 3, pp. 274–302.

Verdon, J. M., 1987, "Linearized Unsteady Aerodynamic Theory," in: *AGARD Manual on Aeroelasticity in Axial Flow Turbomachines, Vol. 1, Unsteady Turbomachinery Aerodynamics* (AGARD-AG-298), M. F. Platzer and F. O. Carta, eds., Neuilly sur Seine, France, Ch. 2.

Verdon, J. M., 1993, "Review of Unsteady Aerodynamic Methods for Turbomachinery Aeroelastic and Aeroacoustic Applications," *AIAA Journal,* Vol. 31, No. 2, pp. 235–250.

Verdon, J. M., and Caspar, J. R., 1982, "Development of a Linear Unsteady Aerodynamic Analysis for Finite-Deflection Subsonic Cascades," *AIAA Journal,* Vol. 20, No. 9, pp. 1259–1267.

Verdon, J. M., and McCune, J. E., 1975, "Unsteady Supersonic Cascade in Subsonic Axial Flow," *AIAA Journal,* Vol. 13, No. 2, pp. 193–201.

Whitehead, D. S., 1960, "Force and Moment Coefficients for Vibrating Aerofoils in Cascade," Reports and Memoranda No. 3254, Aeronautical Research Council, London.

Whitehead, D. S., 1970, "Vibration and Sound Generation in a Cascade of Flat Plates in Subsonic Flow," Reports and Memoranda No. 3685, Aeronautical Research Council, London.

Whitehead, D. S., 1987, "Classical Two-Dimensional Methods," in: *AGARD Manual on Aeroelasticity in Axial Flow Turbomachines, Vol. 1, Unsteady Turbomachinery Aerodynamics* (AGARD-AG-298), M. F. Platzer and F. O. Carta, eds., Neuilly sur Seine, France, Ch. 3.

Whitehead, D. S., 1990, "A Finite Element Solution of Unsteady Two-Dimensional Flow in Cascades," *International Journal for Numerical Methods in Fluids,* Vol. 10, No. 1, pp. 13–34.

1997 Best Paper Award—Education Committee

A Three-Dimensional Turbine Engine Analysis Compressor Code (TEACC) for Steady-State Inlet Distortion

A. Hale
Sverdrup Technology, Inc., AEDC Group,
Arnold Engineering Development Center,
Arnold Air Force Base, TN 37389-6001

W. O'Brien
Mechanical Engineering Department Head,
Virginia Polytechnic Institute and
State University,
Blacksburg, VA 24061-0139

The direct approach of modeling the flow between all blade passages for each blade row in the compressor is too computationally intensive for practical design and analysis investigations with inlet distortion. Therefore a new simulation tool called the Turbine Engine Analysis Compressor Code (TEACC) has been developed. TEACC solves the compressible, time-dependent, three-dimensional Euler equations modified to include turbomachinery source terms, which represent the effect of the blades. The source terms are calculated for each blade row by the application of a streamline curvature code. TEACC was validated against experimental data from the transonic NASA rotor, Rotor 1B, for a clean inlet and for an inlet distortion produced by a 90-deg, one-per-revolution distortion screen. TEACC revealed that strong swirl produced by the rotor caused the compressor to increase in loading in the direction of rotor rotation through the distorted region and decrease in loading circumferentially away from the distorted region.

Introduction

Modern high-performance military aircraft are subjected to rapid flight maneuvers, which place great operational demands on their air-breathing gas turbine engines. One component of the engine that is particularly sensitive to the fluid dynamic transients that result from rapid aircraft maneuvers is the compressor. The compressor should operate in a stable manner during all aspects of flight. However, rapid flight transients cause the inlet to produce a highly distorted total pressure flow field to the compressor inlet. High distortion levels may cause the compressor to surge at high rotational speeds or slip into rotating stall at lower rotational speeds (AIR-1419, 1983). Since total pressure distortion is the primary reason for reaching the engine stability limit, its effects on system performance and operability need to be understood.

Distortion imposed on a circumferentially swirling flow was shown by Greitzer and Strand (1978) to have a three-dimensional nature, which is fundamental to the development of both inlets and compressors. Design or analysis engineers are interested in understanding the details of the flow field to determine the effects of inlet total pressure distortion on the compressor. One way to quantify the effects of distortion is to test for that effect in a ground test facility. Currently, the inlet and engine are tested separately. Typically, the aircraft fuselage is too big to fit in a wind tunnel. A forebody simulator is used in conjunction with the inlet to characterize its flow field. The forebody simulator is designed to produce a flow field at the inlet reference plane (IRP) similar to the flow field produced by the aircraft (Fig. 1).

Screens are constructed to capture the most severe dynamic patterns produced by the inlet and are then placed in front of the engine to measure the loss of stall margin produced by the steady-state inlet distortion (AIR-1419, 1983). However, it is expensive to instrument a compressor and perform the necessary number of tests to understand the compressor flow field adequately. Therefore, numerical simulations have been developed to support the testing community.

Parallel compressor theory has been used successfully to develop an understanding of compressor performance with inlet distortion. Parallel compressor theory models the compressor with multiple circumferential segments and a uniform exit back boundary condition. Parallel compressor theory is restricted to simple inlet distortion patterns and is consistently conservative at estimating the stability limit. Investigators have made extensive modifications to parallel compressor theory through modeling techniques to account for the transfer of mass, momentum, and energy transfer between segments (Korn, 1974; Steenken, 1983; Mazzawy, 1977; Longley and Greitzer, 1992; Kimzey, 1977; Shahrokhi, 1995). 3D simulations have recently been developed that automatically account for the transfer of conservation properties (Billet et al., 1988; Tan, 1996). However, these investigations have been restricted to incompressible flow or low-speed compression systems. There is still a need to develop a three-dimensional compression system to investigate the effects of complex inlet distortion on a high-speed compression system.

Therefore, a numerical simulation of inlet distortion has been developed and is called the Turbine Engine Analysis Compressor Code (TEACC). TEACC is a direct extension of previous work by the author (Hale et al., 1994) and solves the compressible three-dimensional Euler equations over a finite-volume grid domain through each blade row. The Euler equations are modified to include turbomachinery source terms, which model the effect of the blades. The turbomachinery source terms are bleed, blade forces in the three Cartesian directions, and shaft work. The source terms are calculated for each circumferential grid section of each blade row by the application of a streamline curvature code. A methodology was developed for distributing

Contributed by the International Gas Turbine Institute and presented at the 42nd International Gas Turbine and Aeroengine Congress and Exhibition, Orlando, Florida, June 2–5, 1997. Manuscript received at ASME Headquarters February 1997. Paper No. 97-GT-124. Associate Technical Editor: H. A. Kidd.

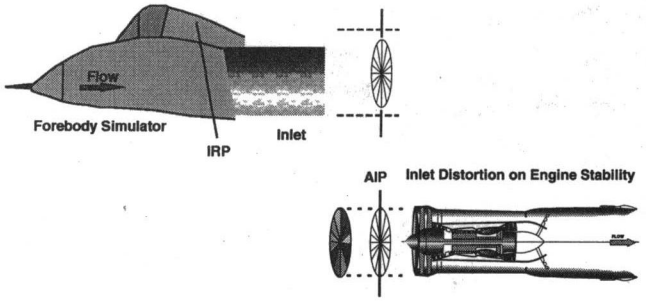

Fig. 1 Engine screen developed to duplicate distortion

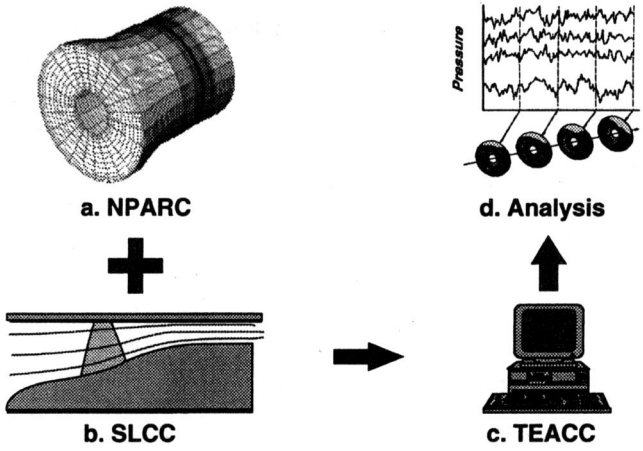

Fig. 2 Overall TEACC methodology

the turbomachinery source terms axially, radially, and circumferentially through the bladed region.

Overall Approach to TEACC

The overall TEACC development methodology is conceptually presented in Fig. 2. A general purpose three-dimensional flow simulation computer code (NPARC, Cooper and Sirbaugh, 1989) is modified to accept turbomachinery source terms by semi-actuator disk theory. These turbomachinery source terms are calculated using a streamline curvature code (SLCC, Hearsey, 1970). TEACC is constructed by combining the technology of solving the Euler equations (NPARC) modified to include source terms and the technology of calculating the source terms (SLCC) to produce a time-dependent turbomachinery simulation with the capability of analyzing inlet distortion.

Governing Equations. The governing equations used in TEACC are developed by applying the conservation of mass, momentum, and energy. In turbomachinery flows, the viscous effects predominate mostly along the wall, making accurate simulation of the flow field away from the wall possible by using the Euler equations with turbomachinery source terms (Longley and Greitzer, 1992). The equations of fluid motion using the thermally and calorically perfect ideal gas assumption with turbomachinery source terms are:

$$\frac{\partial \mathbf{Q}}{\partial t} + \frac{\partial \mathbf{E}}{\partial x} + \frac{\partial \mathbf{F}}{\partial y} + \frac{\partial \mathbf{G}}{\partial z} = \mathbf{S}$$

$$e_t = e + \frac{1}{2}V^2 \quad \mathbf{Q} = \begin{bmatrix} \rho \\ \rho u \\ \rho v \\ \rho w \\ \rho e_t \end{bmatrix} ; \quad \mathbf{E} = \begin{bmatrix} \rho u \\ \rho u^2 + P \\ \rho uv \\ \rho uw \\ \rho e_t + Pu \end{bmatrix}$$

$$\mathbf{F} = \begin{bmatrix} \rho v \\ \rho vu \\ \rho v^2 + P \\ \rho vw \\ (\rho e_t + P)v \end{bmatrix} ; \quad \mathbf{G} = \begin{bmatrix} \rho w \\ \rho wu \\ \rho wv \\ \rho w^2 + P \\ (\rho e_t + P)w \end{bmatrix} ; \quad \mathbf{S} = \begin{bmatrix} S_{\dot{m}} \\ S_{Fx} \\ S_{Fy} \\ S_{Fz} \\ S_{\dot{SW}} \end{bmatrix}$$

The volumetric turbomachinery source terms are: (1) bleed per volume, (2) forces in the x, y, and z directions per volume, and (3) rate of shaft work per volume. The techniques for calculating these source terms from the SLCC are developed later in this paper.

TEACC Boundary Conditions. The time-dependent Euler equations with source terms define a hyperbolic in time and an elliptic in space system of equations requiring a full set of boundary conditions specified at all boundaries. The boundary conditions used with NPARC are explicit. The inflow boundary condition is based on reference plane characteristics, and the total pressure and total temperature at the inlet are specified. Inlet flow directions are assumed to be normal to the boundary. The exit boundary condition is a variable static pressure capable of supporting the exit profile of strong swirl. The exit static pressure is calculated by specifying a single value and imposing the static pressure profile of the adjacent upstream station on the exit. The wall boundary conditions are assumed to be slip wall; the normal velocity components are set equal to zero at the solid walls. A rotationally periodic (wrap-around) boundary condition is used in the circumferential direction, where the circumferential seam of the grid was overlapped by one circumferential segment.

Nomenclature

c_p = constant-pressure specific heat
$\mathbf{E}, \mathbf{F}, \mathbf{G}$ = flux vectors
e = internal energy and kinetic energy per mass
F = component of force
$\mathbf{F}$ = force
$\dot{m}$ = rate of mass flow
P = pressure
$\mathbf{Q}$ = conservation variables
R = ideal gas constant
Residual = vector representing the value of the explicit part of the implicit discretized conservation equations
r = radial direction
S = component of the source vector
$\mathbf{S}$ = source vector
$\dot{SW}$ = rate of shaft work
T = temperature
u = velocity in the x direction
V = component of velocity
$\mathbf{V}$ = velocity
$\forall$ = volume
v = velocity in the y direction
w = velocity in the z direction
x, y, z = Cartesian right-handed coordinate directions

Subscripts

b = bleed
t = total

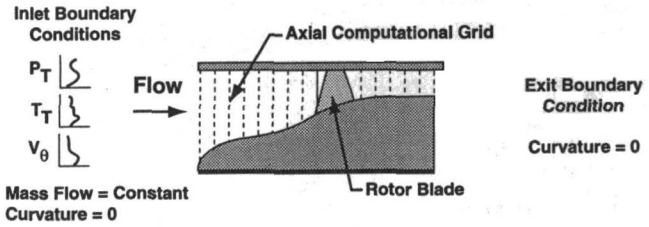

Fig. 3 Original SLCC with overall geometry

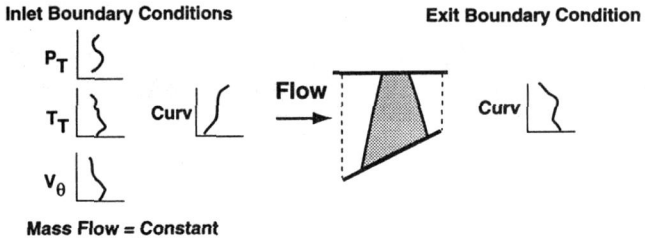

Fig. 4 Modifications to SLCC for calculating source terms

TEACC Solution Procedure. TEACC's and NPARC's solution procedures are the same, solving the governing equations with the Beam and Warming approximate factorization algorithm (Beam, 1976) to obtain a flow-field solution. These equations are consistently discretized with central differences to produce an implicit algorithm. The governing equations were cast in strong conservation form to keep global conservation, even if strong shocks are present. The technique of Pulliam and Steger (1980) to implement the Beam and Warming implicit algorithm was incorporated to diagonalize the implicit matrices, requiring a pentadiagonal solver. Since this is a central difference algorithm, artificial dissipation is included for stability. NPARC uses the Jameson-style (Jameson et al., 1981) improved shock-capturing artificial dissipation. TEACC, as well as NPARC, uses the time-stepping method to achieve steady state. There are two criteria used to verify TEACC's convergence to steady state. First, the L2 norm of the residual is dropped to machine zero, defined as:

$$\|\mathbf{Residual}\|_2 = \sqrt{\left(\sum_{q=1,n} \mathbf{Residual}_q^2\right)};$$

n = number of nodes. The second criterion used to verify TEACC's convergence to steady state is to monitor key variables of interest and verify they no longer vary as TEACC continues to iterate.

Turbomachinery Source Terms

Three-dimensional blade force and rate of shaft work terms are supplied by a streamline curvature code (SLCC). The SLCC is based on a radial redistribution of blade force and shaft work producing an "axisymmetric flow with swirl" in the form of streamlines. Necessary inputs include overall geometry, blade geometry, and loss and deviation correlations. These correlations are obtained from experimental data. A typical SLCC grid illustrated in Fig. 3 extends far upstream and far downstream of the compressor.

Axial stations are chosen to include the inlet and exit of the blades and other convenient stations to allow a proper resolution of the flow field. Boundary conditions are required around the computational domain, with the outer casing and inner centerbody treated as streamlines. The boundary conditions are inlet total pressure, inlet total temperature, and inlet swirl angle with curvature set equal to zero at both the inlet and exit. A particular operating point is established by specifying the rotor speed and overall mass flow.

The radial momentum equation was developed from the Euler equations by assuming that entropy and enthalpy do not change along streamlines except as prescribed across the blades by the loss and deviation correlations. The set of conservation equations are simplified by replacing the axial momentum and the energy equation with $\Delta S = 0$ and $\Delta H = 0$. The remaining two equations, continuity and radial momentum, are solved simultaneously at each axial station.

Modifications of the SLCC Technique. For the TEACC simulation to be responsive to the local change in total pressure due to inlet distortion and capable of modeling transients, the SLCC must be restricted to a small axial region on either side of the blades. Since the SLCC is a subsonic flow solver, it needs a full set of boundary conditions around its domain. The SLCC boundary conditions of inlet and exit curvature, overall mass flow, swirl angle, total temperature, and total pressure are calculated from the TEACC flow field. Figure 4 is included to show the truncated grid in which the SLCC is restricted to operate.

Although the boundary conditions are of the same type in this new mode of operation as they were before the grid was truncated to the blades, they are now more complicated since they are no longer uniform but a function of the time-dependent TEACC flow field around the blades.

The boundary conditions for the modified SLCC technique are outlined below for the computational domain specified in Fig. 4. Inlet and exit curvature provided by the three-dimensional integrator are calculated from a circumferential projection of the flow field onto a circumferential slice (axial–radial plane). This is effectively the same as calculating streamline curvature from only the axial and radial velocity components of the three-dimensional transient velocity flow field. Curvature is calculated as a function of local velocity and acceleration. Overall mass flow rate as a boundary condition to the SLCC is calculated from the three-dimensional flow field just upstream of the bladed region by the integration of mass for each circumferential segment. The mass flow rate of each circumferential segment is summed together to calculate overall mass flow. A radial distribution of swirl angle is calculated from the TEACC solution at the blade inlet and defined as the arc-tangent of tangential velocity divided by axial velocity. The total temperature and total pressure at the inlet are calculated by using the conservation variables, ideal gas relations, and the compressible form of the stagnation definitions at the inlet of each control volume.

Technique to Calculate Turbomachinery Source Terms. The source term calculations are performed after the SLCC converges to a steady-state solution through the bladed region. The technique for calculating turbomachinery source terms uses control volumes within the bladed region and applies steady-

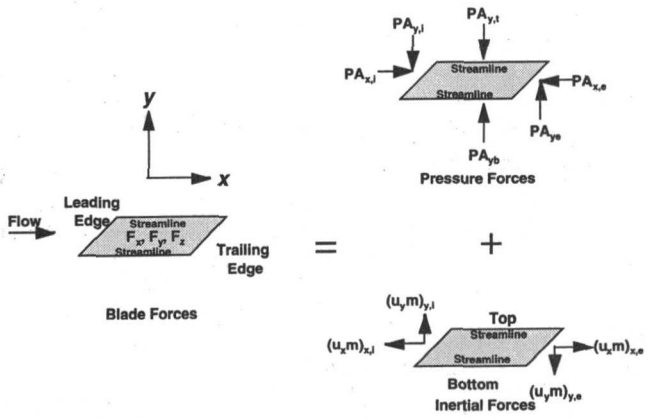

Fig. 5 Turbomachinery blade force calculations

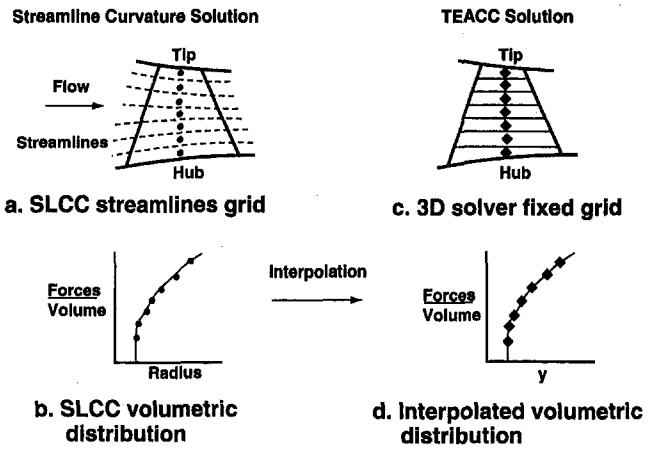

Fig. 6 Interpolation of radial distribution of source terms

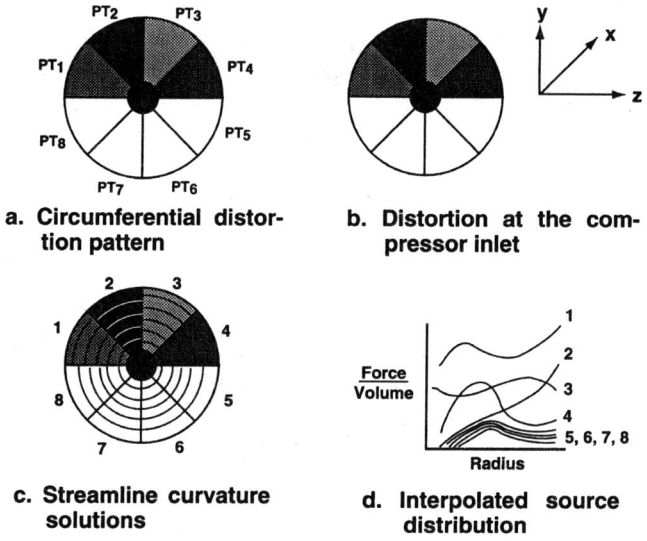

Fig. 7 Circumferential distribution of source terms

state conservation laws across each control volume. Since the conservation of angular momentum is maintained in the axisymmetric solution of the SLCC, a radial distribution of circumferential velocity vectors are produced. Cartesian control volumes are constructed over a circumferential segment of the bladed region from streamlines and overall blade geometry with velocities and pressures known on all surfaces from streamline calculations. A simplifying assumption that the top and bottom surfaces of each control volume are streamsurfaces is incorporated since mass, momentum, and energy do not cross a streamsurface. The turbomachinery forces are calculated from a control volume analysis and the streamsurface assumption by the pressure area forces and the inertial forces (Fig. 5).

Methodology to Implement Source Terms Into TEACC

With the TEACC-supplied boundary conditions, the SLCC produces an axisymmetric solution through the bladed region in the form of streamsurfaces, which are constructed into control volumes to calculate turbomachinery source terms. A methodology for distributing the sources radially, circumferentially, and axially through the grid packed region through the blade was developed.

Radial Interpolation of Turbomachinery Source Terms. To implement these source terms into TEACC, a radial interpolation technique was derived. A radial distribution of sources is constructed by selecting the radius at the center of each SLCC source control volume (Fig. 6(a)). This radius is nondimensionalized by the radial extent of the inner and outer casing in the axial center of the blade (Fig. 6(b)).

A spline is used to interpolate these source terms to TEACC along a single circumferential segment of the bladed region. A radial distribution of TEACC control volumes is defined through the bladed region using the existing grid structure as shown in Fig. 6(c). The radius is nondimensionalized by the radial extent of the inner and outer casing in the middle of the bladed region. A radial distribution of TEACC source terms is acquired by interpolating the fixed TEACC volume centers onto the function of sources developed earlier from the SLCC as shown in Fig. 6(d).

Circumferential Distribution of Turbomachinery Source Terms. The circumferential distributions of turbomachinery source terms are calculated by a direct application of the SLCC in each circumferential grid segment. For a distorted inlet upstream of the compressor, a circumferential inlet distortion is imposed on the system, as in Fig. 7(a). This distortion affects the adjacent flow field, and Fig. 7(b) shows that this circumferential distortion, ignoring viscous effects, will persist up to the compressor inlet (Longley and Greitzer, 1992). The compressor's performance will be affected by this distortion, causing a nonuniform circumferential flow field. The modeling technique for acquiring a circumferential distribution of turbomachinery source terms applies the SLCC separately at each circumferential segment, as shown in Fig. 7(c). The SLCC is sensitive to the changing demands to the flow field because it acquires its boundary conditions immediately upstream and downstream of each circumferential segment. Therefore, the SLCC interpolates a new radial distribution of turbomachinery source terms, sensitive to the changing flow field for each circumferential segment as shown in Fig. 7(d). With a more complex inlet distortion pattern, the number of circumferential segments would be increased to maintain the high fidelity of the TEACC simulation.

Axial Distribution of Turbomachinery Source Terms. The grid was packed through the bladed region to reduce the numerical error from strong flow gradients. This method means a great deal of freedom exists in how the sources should be distributed through the bladed region. The sources are distributed conservatively through the bladed region by requiring that the sum of the sources distributed through the NPARC grid must equal the sum of the sources developed in the SLCC. A simple technique to investigate this problem was incorporated by using a weighting function, which could take on a variety of linear shapes. However, a uniform weighting function was found to be the most robust.

Validation Results

Rotor 1B (Seyler and Gostelow, 1967) was chosen as the validation vehicle because it offered simplicity in the number of stages (one blade row), and it represented a compression system with a thorough analysis of clean and distorted inlet.

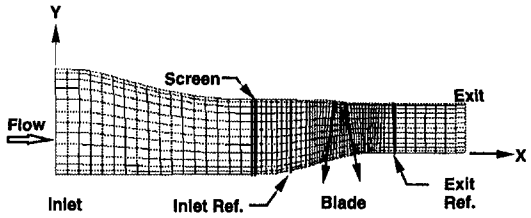

Fig. 8 Axial-radial view of three-dimensional grid modeling Rotor 1B and test facility

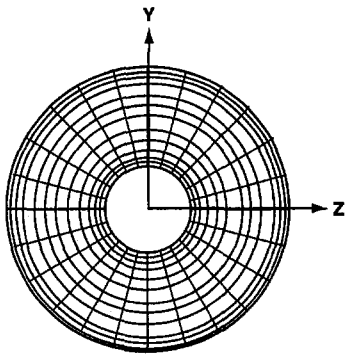

Fig. 9 Radial-circumferential view of three-dimensional grid for Rotor 1B

Rotor 1B is a high-performance transonic rotor similar to those found in modern high-speed aircraft. The rotor was designed with a multiple circular-arc blade shape, which was applied over the top 40 percent of the blade while a double circular-arc construction was employed for the bottom 60 percent of the blade. With a hub-to-tip ratio at the rotor inlet of 0.5, the blade sections were long enough to require a midspan damper to maintain structural integrity during operation. Rotor 1B consisted of 44 blades, producing a moderate solidity of 1.3 at the rotor tip.

Grid Development. TEACC requires a fixed three-dimensional grid on which to resolve the conservation equations. A grid of 69 × 13 × 26 was constructed to model Rotor 1B, where the inlet and exit of the blade were defined as slanting lines in Fig. 8. The grid was constructed with vertical grid lines in the vicinity of the screen to model the experimental distortion screen properly. Grid lines were smoothly packed to reduce numerical losses through the bladed region where the flow was known to have strong gradients. A radial-circumferential view of this base grid is presented in Fig. 9, where a cylindrical right-handed coordinate system has been used with uniform circumferential segments. An integer number of grid segments was constructed to conveniently model a 90-deg, one-per-revolution inlet distortion. Each segment was 15 deg in circumferential extent with a total of 24 segments within a circle (6 segments in each quadrant).

A grid density investigation was conducted by doubling the grid independently in each direction. This study revealed that the radial distribution of the flow field was unaffected by the increase in grid density. However, the error in overall total pressure ratio and efficiency was roughly halved by doubling the grid in the circumferential direction. This improvement was found to be directly related to halving the error in cross-sectional area and mass flow by doubling the circumferential grid.

Clean Inlet Validation of TEACC

TEACC was tailored to simulate Rotor 1B by calibrating the streamline curvature code (SLCC) used to calculate the turbomachinery source terms. The calibration was done by specifying a radial distribution of loss and exit relative flow angle from experimental data as a function of corrected mass flow and by specifying a radial distribution of blockage as a function of corrected mass flow.

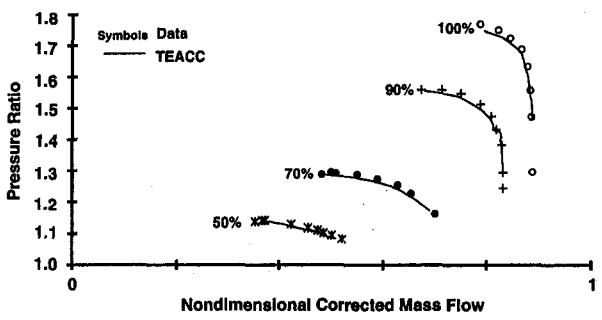

Fig. 10 Clean inlet, overall pressure ratio compared with experimental data

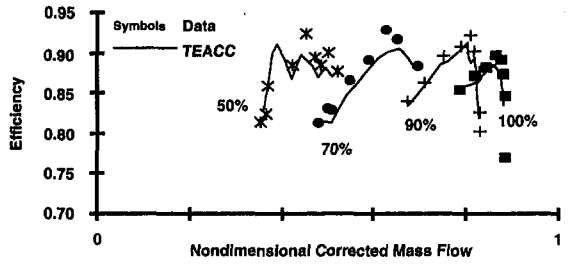

Fig. 11 Clean inlet, efficiency compared to experimental data

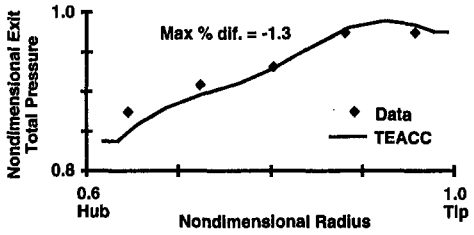

Fig. 12 Clean inlet, exit total pressure on the 100 percent speedline

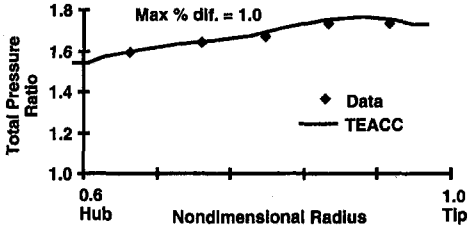

Fig. 13 Clean inlet, total temperature ratio on the 100 percent speedline

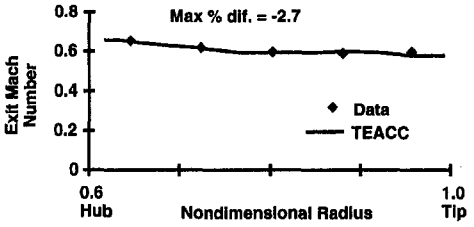

Fig. 14 Clean inlet, exit Mach number on the 100 percent speedline

Calculated overall total pressure map of Rotor 1B with a clean inlet is presented in Fig. 10 and compared with experimental data. Four corrected speeds (50, 70, 90, and 100 percent) were available for comparison, with symbols presented for the experimental data and lines for the TEACC solution. In an overall sense, there is good comparison between TEACC and data. The maximum percent difference in total pressure ratio is less than 1 percent difference for each characteristic.

TEACC's overall efficiency calculations for Rotor 1B are compared with experimental data in Fig. 11. The overall shape and character compare well with the experimental data. Each efficiency curve has a peak value, which TEACC fails to reach, causing a maximum percent difference (for all speeds) between TEACC and experimental data of −2.9 percent occurring at the 50 percent corrected speedline.

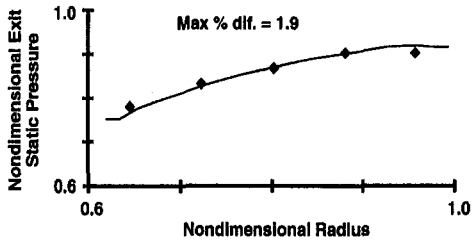

Fig. 15 Clean inlet, exit static pressure on the 100-percent speedline

Radial Comparison of TEACC With Data (Clean Inlet). A radial comparison was made with exit total pressure and total pressure ratio as presented in Figs. 12 and 13 for the 100 percent speed point near the design throttle line. The overall shape is quite complicated for total pressure, increasing from hub to tip with the hub calculations deviating the most from experimental data by −1.3 percent. The tip and overall shape are in good agreement with the experimental data. The total pressure ratio is compared with data in Fig. 13, where a wide radial range in total pressure ratio can be seen. There is good agreement (1.0 percent difference) between TEACC and the experimental data. The exit static pressure and exit Mach number consistently support the strong distribution in total pressure ratio. As shown in Figs. 14 and 15, the exit Mach number and the exit static pressure are in good agreement with the experimental data, and the exit Mach number is fairly uniform. The exit static pressure varied consistently with the exit total pressure. The largest difference for both exit Mach number and exit static pressure with experimental data is at the tip, where Mach number is underpredicted by 2.7 percent and static pressure is overpredicted by 1.9 percent. The SLCC operates in the relative reference frame where the relative Mach number was observed to be transonic. The TEACC simulation remains in the absolute reference frame where Mach number remained subsonic (Fig. 14).

Distorted Inflow Validation of TEACC

Rotor 1B was tested with an inlet screen to quantify the effects of inlet flow distortion on its performance. Because the distortion data provided with Rotor 1B were based on a 90-deg, one-per-revolution screen, a simulation of the screen was used in the TEACC simulation. For this study, TEACC was compared at three different corrected speedlines for a distorted inlet. A single distortion point on the 100 percent speedline was investigated in great detail because radial and circumferential data were available. Overall performance of the distorted compressor is compared to experimental data as well as radial and circumferential distributions.

Distortion Screen Modeling. To model the distortion screen, the porous wall boundary condition (Cooper, K., Jones, R., and Kincade, B., "NPARC Porous Wall Boundary Conditions," private communication and notes, May 1991; Pinker, 1967) was used. The boundary condition is semi-empirical in

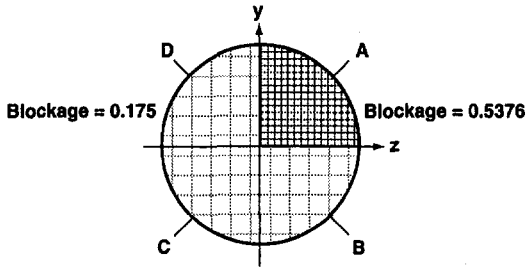

Fig. 16 Screen location and labeling

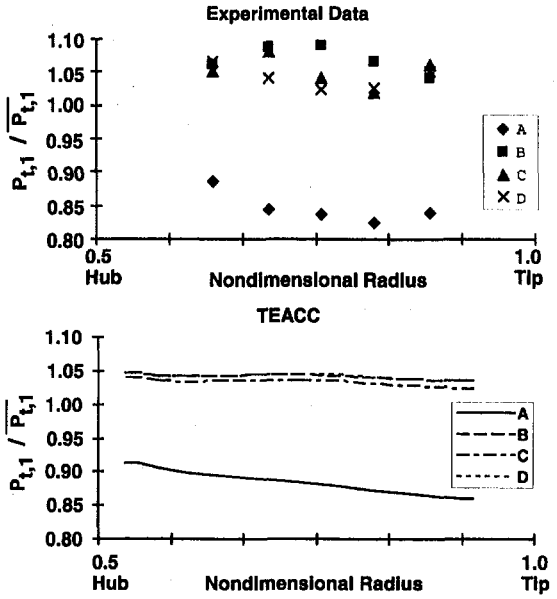

Fig. 17 Inlet total pressure distortion produced by the screen simulation at 100 percent corrected speed

that experimental data have been taken across a variety of screens to establish a loss in total pressure as a function of Mach number, porosity, and Reynolds number. The value of total pressure at the exit of the screen was calculated from the continuity, energy equations (total enthalpy equal to a constant), and an empirical pressure loss coefficient. This general technique to simulate the effect of a distortion screen was incorporated for all inlet distortion calculations.

A single screen with a 90-deg, one-per-revolution pattern was designed to give a classical circumferential inlet total pressure inlet distortion to Rotor 1B. At the 100 percent speed, the experimental data showed that the screen produced a total pressure loss of 15 percent from the clean inlet, which was duplicated for the TEACC simulation. Investigations were conducted through the middle of the four circumferential quadrants where the experimental data were taken. The screen was located in quadrant A (Fig. 16). The compressor rotates clockwise, causing air to swirl in the direction of increasing quadrant letter (A, B, C, and D).

Illustrated in Fig. 17 are the radial characteristics of the distortion screen simulation and comparison to experimental results with experimental data in Fig. 17(*a*) and TEACC results in Fig. 17(*b*). The character of the flow field behind the screen has certainly been captured, with Quadrant A (90-deg distortion) clearly separated from the other three quadrants. The individual pressure drops for Quadrants B–D calculated by the screen simulator are clustered together and represent the mean of the data in these quadrants. Not enough experimental data

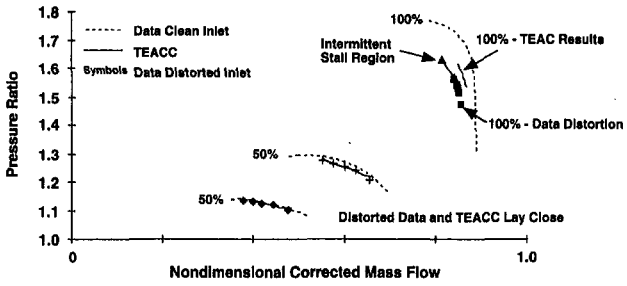

Fig. 18 Distorted inlet, overall performance map with total pressure ratio at 100 percent corrected speed

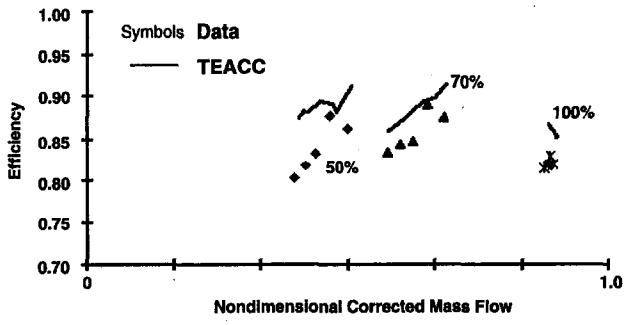

Fig. 19 Distorted inlet, overall performance map with efficiency

were available to explain the scatter in the experimental data adequately for Quadrants B–D. A possible explanation, however, is that the scatter is a result of unsteadiness in the flow field upstream of the distortion screen.

Overall Rotor 1B Performance Comparison (Distorted Inlet). An overall total pressure ratio performance map for Rotor 1B is presented in Fig. 18 for three corrected speeds of 50, 70, and 100 percent. The clean speedlines are presented to give a proper orientation of the distorted data, with stall depicted for each speedline at its lowest corrected mass flow rate. A conservative, but simple, stalling criterion was imposed on the TEACC simulation. When any one of the circumferential segments acquired a corrected mass flow that exceeded stall for the clean inlet, the compressor was considered stalled. Likewise, the TEACC simulation was halted when any one of the circumferential segments exceeded the clean inlet data on the choked end of the speedlines. These two restrictions define the distortion calculation limits presented for each speed in Fig. 18.

For the two low-speed cases, the clean and distorted data lay close together. The extent in corrected mass flow rate is about the same for the simulation and the experimental distortion data. The maximum percent difference between TEACC results and experimental data at the lower speeds was approximately 2 percent. The 100 percent speed is more interesting because the experimental data presented a region where the compressor intermittently stalled or remained stable with the imposed inlet distortion screen. The TEACC simulation predicted the corrected mass flow rate differently from reported experimental data by a maximum of 3 percent. The TEACC simulation maps out a range of corrected mass flow, which includes approximately the middle of the intermittent stall region.

Overall efficiency is compared to experimental data in Fig. 19. In all cases TEACC predicts an efficiency that is higher than reported experimental data. The maximum percent difference between TEACC and the experimental data is located near the stall or choked portion of each corrected speed. The maximum percent difference between TEACC results and data are 6.9, 4.5, and 5.9 percent difference for 50, 70, and 100 percent speeds, respectively.

Radial Comparison of Compressor With Experimental Data (Distorted Inlet). This investigation now turns to an examination of TEACC results compared to experimental data behind the compressor. Exit total pressure (defined by the ratio of exit total pressure over the average screen inlet total pressure) versus compressor radius is plotted with experimental data in Fig. 20(a) and TEACC results in Fig. 20(b). Pressure ratio is characterized by a division between Quadrant A and the other three quadrants. TEACC does a good job of matching the character of the exit total pressure in Quadrant A with experimental data. TEACC results agree with the experimental data in the general character of the other three quadrants and identifies Quadrant B with the largest exit total pressure. The experimental data also confirm the TEACC results and show that exit total pressure decreases steadily from Quadrant B to Quadrant D. Although the shapes of the other three quadrants are moving in the correct direction, the extent and scatter with pressure ratio are missing. The TEACC results in Quadrant A compare well with the experimental data, except for the hub point, which causes the maximum percent difference with pressure ratio equal to 6.15 percent. TEACC results compared to experimental data are too low for Quadrant B (6.82 percent) and too high for Quadrants C (5.86 percent) and D (8.64 percent). The highest maximum percent difference is within 8.7 percent in Quadrant D.

The final comparison with experimental data is also behind the compressor (same reference location as exit total pressure). The ratio of total temperature at the compressor exit divided by the average total temperature at the screen inlet is compared to experimental data with data presented in Fig. 21(a) and TEACC results in Fig. 21(b). Quadrant A is again characterized as having a greater slope than the other three quadrants, and TEACC does a good job identifying this overall flow character. TEACC correctly identifies that, in the nondistorted region, the exit total temperature was the highest in Quadrant B, with the other quadrants decreasing in value from Quadrants B–D. TEACC's calculations for the total temperature at the compressor exit have a greater spread in Quadrants B–D than for the exit total pressure. Comparisons also show that the hub of Quadrant A is not as steep a slope as the experimental data, but the tip matches the data very well. Quadrants C and D match the data well, within 1.81 percent and 2.19 percent, respectively, and even Quadrant B matches the data well, except at a single tip point. The largest percent difference of TEACC with experimental data for exit total temperature is 6.60 percent.

Effect of Swirl on the Compressor Performance With Inlet Distortion

The circumferential velocity within the flow field caused by the high-rotor-speed compressor blade is a direct result of the compressor blade doing work on the flow. The blade causes a strong circumferential velocity, which establishes the location of the largest static and total pressure regions. The compressor exit total pressure is presented in Fig. 22. Notice that the highest value in total pressure is not in the center of the distorted region,

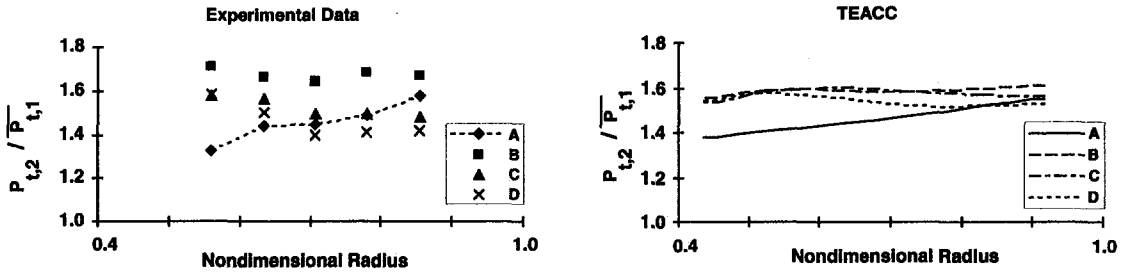

Fig. 20 Distorted inlet, exit total pressure on 100 percent speedline

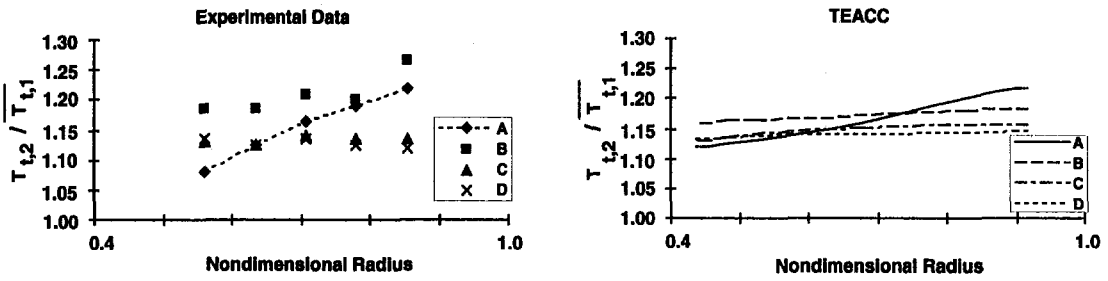

Fig. 21 Distorted inlet, exit total temperature on 100 percent speedline

but has shifted clockwise and has its largest value near the tip. Displayed in Fig. 23 is exit total temperature, where it has shifted clockwise but is not as pronounced as the exit total pressure. Figure 24 presents the static pressure, which resembles that of the previously presented total pressure. The highest static pressure is close to the interface of Quadrants A and B. The velocity vectors can be converted to streamlines, which show the strong effect of swirl downstream of the compressor.

The streamlines are shown in Fig. 25. A schematic of the distortion screen is presented to indicate inlet distortion (Fig. 25(*a*)); Quadrant A is defined in the middle of the distorted region and Segment Ð is chosen to represent a segment just before the rotor begins to sweep through the distortion in Quadrant D. An important distinction is that Quadrant A is in the distorted region, and Segment Ð is in the undistorted region.

Fig. 22 Exit total pressure distribution produced by 90 deg, one-per-revolution screen on the 100 percent speedline

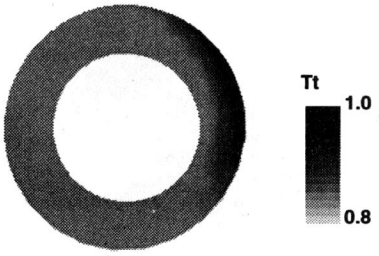

Fig. 23 Exit total temperature distribution produced by 90 deg, one-per-revolution screen on the 100 percent speedline

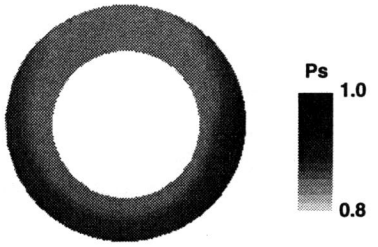

Fig. 24 Exit static pressure distribution produced by 90 deg, one-per-revolution screen on the 100 percent speedline

The upper right-hand picture in Fig. 25(*b*) shows in simple terms how Quadrant A and Segment Ð behave on the compressor map. First, Segment Ð operates in the clean inlet region of the compressor, producing a pressure ratio with a high corrected mass flow, but Quadrant A operates through the distorted screen where the total pressure in front of the compressor is low, causing a reduction in corrected mass flow. Quadrant A operates higher on the compressor map closer to stall, which means that approximately 75 percent of the compressor operates near choke while 25 percent of the compressor operates near stall. The portion of the compressor operating behind the distortion produces more work than any other part of the compressor.

The streamlines in the bottom view of Fig. 25(*c*) tell more about the compressor operation. Segment Ð describes the streamlines to the right of the distorted region while the blade turns the flow strongly toward and behind the distorted region. The streamlines through the middle of the distorted region are represented by Quadrant A. Again, the compressor strongly swirls the flow, but the total pressure increase through the distorted region is greater than that of Segment Ð. The flow field at the compressor exit is convected clockwise by the swirling flow to an adjacent part of the compressor, and the streamlines in Segment Ð show that the lower total pressure fluid is convected behind the compressor in the distorted region. This is a further indication of the clockwise transport of total pressure attributable to the swirling flow, and an indication that the total pressure behind the compressor is not uniform, but increasing in the direction of flow rotation. The performance increase that begins at the distorted region increases the static pressure behind the compressor and convects total temperature and total pressure with the flow to an adjacent point behind the compressor. This action causes the adjacent point to further backpressure the compressor in this region, subsequently increasing its perfor-

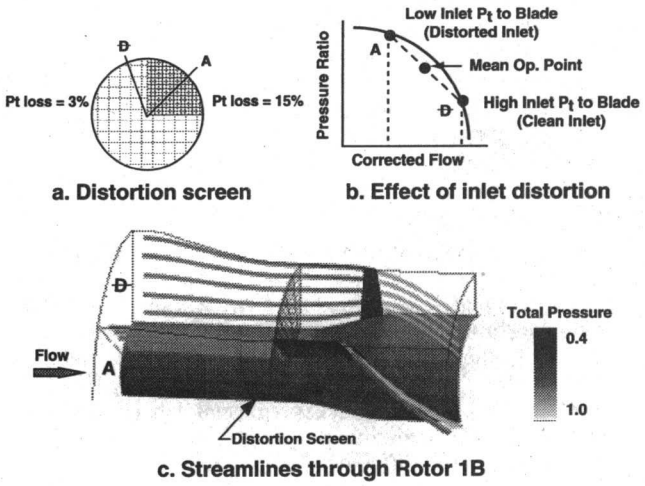

Fig. 25 Streamlines showing pressure convected with the flow on the 100 percent speedline with inlet distortion

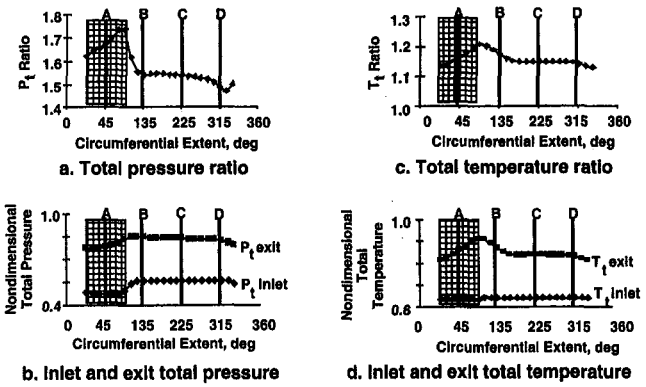

Fig. 26 Circumferential transport of total pressure and total temperature on 100 percent speedline

mance and moving that region closer to stall. This increase implies that the swirl will cause the strongest backpressuring of the distorted region to be transported clockwise behind the adjacent nondistorted region (intersection of Quadrants A and B), increasing performance in this region and producing the largest total pressure found anywhere in the compressor, as shown in Fig. 22. Therefore, the total pressure increases clockwise through the distorted region.

The transport of total pressure and total temperature clockwise through the compressor can be viewed in a slightly different way through Fig. 26. Here, a radial mass-weighted average of total pressure and total temperature is presented versus the circumferential extent at the upstream and downstream reference locations. Inlet total pressure (Fig. 26(b)) to the compressor can be observed to have two different uniform regions, one behind the distortion screen (Quadrant A) and a higher value through the other three quadrants. The compressor exit total pressure increases steadily through the distorted region, with its highest value at the beginning of Quadrant B. The ratio of total pressure (Fig. 26(a)) also increases steadily in a clockwise direction through the distorted region, due to the compressor transportation of total pressure clockwise through the distorted region. This increases the static pressure behind an adjacent portion of the compressor in the clockwise direction, backpressuring this portion of the compressor and producing a performance increase. This increased performance shows itself as an increase in total pressure ratio.

A similar story can be constructed with total temperature at the compressor inlet and exit. The inlet total temperature to the compressor remains uniform in the presence of the screen, as shown in Fig. 26(d). The exit total temperature, like the exit total pressure, steadily increases clockwise through the distorted region. This means the total temperature ratio in Fig. 26(c) also increases through the distorted region. Total temperature ratio, just like total pressure ratio, reaches its largest value at the interface of Quadrant A and Quadrant B because of the swirl effect through the distorted region.

Summary/Conclusions

TEACC has been developed to model inlet distortion through the use of semi-actuator disk theory. This technique allows efficient computational grids that provide a practical solution for inlet distortion problems. TEACC was constructed by developing a methodology to merge two proven technologies, NPARC and a SLCC, into a single turbomachinery simulation.

TEACC's predictions with experimental data (Rotor 1B) for a clean inlet compared within 1 percent for total pressure ratio and within 3 percent difference for efficiency. A radial comparison of TEACC with experimental data also produced good results.

The distortion was produced with a 90 deg, one-per-revolution screen simulated by a boundary condition provided by NPARC. TEACC simulated Rotor 1B over three speedlines and produced a total pressure ratio that compared within 3 percent of experimental data and an efficiency that compared within 7 percent difference of experimental data.

A radial comparison of TEACC results to experimental data revealed that TEACC models the overall character of the compressor well and does a particularly good job of predicting the magnitude and shape of exit total temperature and exit total pressure in the distorted region (Quadrant A).

A detailed investigation of the compressor flow field was conducted to evaluate the effects of the distortion screen simulation and to compare these results with experimental data. The study revealed that strong swirl convects total temperature and total pressure with the flow in the direction of rotor rotation. This increase in total pressure produced an increase in static pressure in an adjacent part of the compressor that backpressured the compressor, producing an increase in performance. Therefore, the greatest total pressure is produced in transition from distorted to undistorted flow regions.

The TEACC development effort to simulate Rotor 1B with inlet distortion has been very successful. The TEACC technique was developed for a single rotor and is expected to be immediately expandable to multiple blade rows. TEACC is immediately recognized as a time-dependent solution technique that can be extended to investigate surge and rotating stall instabilities. TEACC is an ideal environment to investigate inlet compatibility issues with the inlet and the compressor tightly coupled.

Acknowledgments

The research reported herein was performed by the Arnold Engineering Development Center (AEDC), Air Force Materiel Command. Work and analysis for this research were performed by personnel of Virginia Polytechnic Institute and State University and by personnel of Sverdrup Technology, Inc., AEDC Group, technical services contractor for AEDC. Further reproduction is authorized to satisfy needs of the U. S. Government.

References

Billet, G., Huard, J., Chevalier, P., and Laval, P., 1988, "Experimental and Numerical Study of the Response of an Axial Compressor to Distorted Inlet Flow," ASME *Journal of Fluids Engineering,* Vol. 110, pp. 355–360.

Cooper, G. K., and Sirbaugh, J. R., 1989, "PARC Code: Theory and Usage," AEDC-TR-89-15, Dec.

Greitzer, E. M., and Strand, T., 1978, "Asymmetric Swirling Flows in Turbomachine Annuli," ASME Paper No. 78-GT-109.

Hale, A. A., Davis, M. W., Jr., and Kneile, K. R., 1994, "Turbine Engine Analysis Compressor Code: TEACC, Part I: Technical Approach and Steady Results," AIAA Paper No. 94-0148.

Hearsey, R. M., 1970, "HT0300—A Computer Program for the Design and Analysis of Axial Turbomachinery," Cambridge, MA, Mar.

Jameson, A., Schmidt, W., and Turkel, E., 1981, "Numerical Solutions of the Euler Equations by Finite Volume Methods Using Runge–Kutta Time-Stepping Schemes," AIAA Paper No. 81-1259.

Kimzey, W. F., 1977, "An Analysis of the Influence of Some External Disturbances on the Aerodynamic Stability of Turbine Engine Axial Flow Fans and Compressors," AEDC-TR-77-80, Aug.

Longley, J. P., and Greitzer, E. M., 1992, "Inlet Distortion Effects in Aircraft Propulsion System Integration," AGARD-LS-183. Advisory Group for Aerospace Research & Development Lecture Series, May.

Mazzawy, R. S., 1977, "Multiple Segment Parallel Compressor Model for Circumferential Flow Distortion," ASME *Journal of Engineering for Power,* Vol. 99, pp. 288–296.

Pulliam, T. H., and Steger, J. L., 1980, "Implicit Finite-Difference Simulations of Three Dimensional Compressible Flow," *AIAA Journal,* Vol. 18, No. 2, pp. 159–167.

Seyler, D. R., and Gostelow, J. P., 1967, "Single Stage Experimental Evaluation of High Mach Number Compressor Rotor Blading: Part 2—Performance of Rotor 1B," NASA-CR-54582, Sept.

Shahrokhi, K. A., 1995, "Application of Modified Dynamic Compression System Model to a Low-Aspect Ratio Fan: Effects of Inlet Distortion," MS Thesis, Mechanical Engineering, Vanderbilt University, Nashville, TN.

Steenken, W. G., 1983, "Modeling Compression Component Stability Characteristics—Effects of Inlet Distortion and Fan Bypass Duct Disturbances," AGARD-CP-324, Advisory Group for Aerospace Research & Development Conference Proceedings, Feb.

Active Stabilization of Axial Compressors With Circumferential Inlet Distortion

C. M. van Schalkwyk
Scientific Systems Co., Inc.,
Woburn, MA 01801

J. D. Paduano

E. M. Greitzer

A. H. Epstein

Department of Aeronautics and Astronautics,
Massachusetts Institute of Technology,
Cambridge, MA 02139

This paper describes the first experimental validation of transfer function modeling and active stabilization for axial compressors with circumferential inlet distortion. The inlet distortion experiments were carried out in a three-stage low-speed compressor. Theory–experiment comparisons of steady performance, unsteady stall precursor, and forced response (transfer function) data were all used to assess a control-theoretic version of the Hynes–Greitzer distorted flow model. The tests showed good agreement between theory and data and demonstrated that a priori predictions, based on geometry and steady-state performance data, can be used to design control laws that stabilize rotating stall with inlet distortion. Based on these results, active feedback control has been used to stabilize the inlet distortion induced instability associated with rotating stall onset. The stabilization allowed stall-free operation to be extended below the natural (distorted flow) stall point by up to 3.7 percent for a 0.8 dynamic head distortion. For a 1.9 dynamic head distortion, 40 percent of the mass flow range lost due to inlet distortion was regained through active control. The paper elucidates the difficulties associated with active control with distortion, and introduces a new control law that addresses many of these challenges.

1 Introduction and Problem Definition

The detrimental impact of distortion on compressor stability is well documented, both qualitatively and quantitatively [18, 13]. Stall and surge safety margins can be severely degraded by inlet separation and other sources of inlet flow nonuniformity. As such, a substantial percentage of the stall margin built into a compressor design specifically addresses the effects of inlet distortion. Further, especially in military engines, distorted flow is typically the situation under which instability is encountered.

The concept of active stabilization to improve compressor operating range has received wide attention (see, for instance, [4, 5]), but a key question is whether improvements in operating range can be obtained by active stabilization in the presence of inlet distortion. Prior to this study, active stabilization of rotating stall has been demonstrated exclusively under "clean" inlet flow conditions—that is, steady-state operation of the compressor with circumferentially uniform flow.

Circumferential distortion creates a nonaxisymmetric flow field in the compressor that fundamentally changes the nature of the control problem to be addressed. The nonuniform medium through which prestall waves travel causes more complex wave dynamics than in undistorted flow, because circumferential sinusoids are no longer eigenmodes of the flow in the compressor annulus. The implication for control is that the system can no longer be viewed as a parallel interconnection of single-input single-output (SISO) systems (decoupling of sinusoidal eigenmodes) as in past rotating stall research, such as that of Paduano et al. [17] and Haynes et al. [7]. With distortion the system is inherently multiple-input multiple-output (MIMO).

Two related techniques will be brought to bear on control of compressors with inlet distortion in this paper. The first is modeling of the unsteady compression system behavior, which began with the work of Moore [15] and Moore and Greitzer [16]. In these papers, hydrodynamic stability models for rotating stall in compressors without distortion were derived. Based on this work, Longley [11], Hynes and Greitzer [8], and Chue et al. [2] extended the model to the case with inlet distortion, and showed that many of the experimental features of distortion were captured by the method. We have further extended this model to include the effects introduced by Haynes et al. [7], as well as forcing, and developed a state-space model for actuated compression systems with inlet distortion.

The second set of methods we will apply are those of system identification and control theory. By incorporating high-bandwidth, distributed actuation into an experimental compressor, we are able to assess the fluid dynamic model more rigorously than has been possible in the past. We will capitalize on the measurements of Haynes et al. [7] to build a predictive model of the effects of distortion, and verify this model through system identification. We will then investigate the effectiveness of various control schemes to stabilize rotating stall and increase the compressor stable operating range with distortion.

The paper is organized as follows. After briefly reviewing the effects of inlet distortion and describing the experimental setup, we verify our extension of the model of [8] against a detailed set of steady-state, unsteady, and input-output data. Second, we elucidate the main features of the active stabilization problem when distortion is present. Finally, we demonstrate that active stabilization can be achieved with distortion, and quantify the gains attained in our experiment.

2 Compressor Response to Small Perturbations

The basic tenet of the work described here is that instability and subsequent growth of small perturbation traveling waves lead to fully developed rotating stall. We thus briefly describe compression system response to these small perturbations.

2.1 Uniform Flow. We start with a conceptual description of the compression system without distortion. Figure 1 shows the compressor annulus unwrapped into a two-dimensional setting, as is valid for compressors with high hub-to-tip radius ratio. The compressor is modeled as a high-solidity semi-actuator disk. The flow in the upstream duct is considered irrotational, and the flow in the downstream duct is rotational but

Contributed by the International Gas Turbine Institute and presented at the 42nd International Gas Turbine and Aeroengine Congress and Exhibition, Orlando, Florida, June 2–5, 1997. Manuscript received at ASME Headquarters February 1997. Paper No. 97-GT-279. Associate Technical Editor: H. A. Kidd.

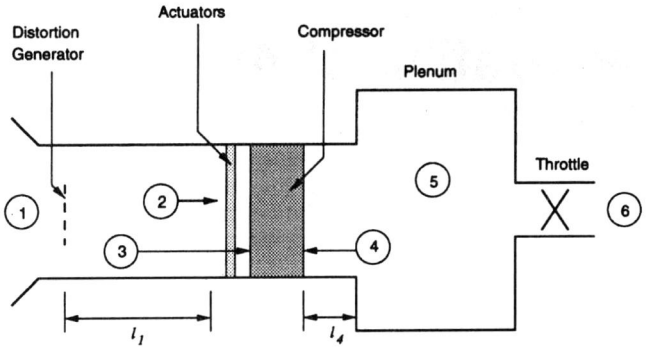

Fig. 1 Schematic of compressor flow field

linearized (see Lavrich [10] for experimental justification of these assumptions). There is a plenum downstream of the compressor, but the dynamics associated with the plenum do not interact with the (linearized) rotating stall dynamics if there is no inlet distortion. A detailed description of the analysis for uniform flow can be found in Haynes et al. [7].

The flow variables at the compressor face can be expressed as Fourier series. For example, the axial velocity coefficient ϕ at the compressor face is given by

$$\phi(\theta, t) = \sum_{n=-\infty}^{\infty} \tilde{\phi}_n(t) e^{in\theta} \tag{1}$$

where ϕ is the axial velocity divided by the wheel speed c_x/u_w, θ is the angle around the annulus, t is time, and $(\tilde{\ })$ denotes the Fourier coefficients. If the flow far upstream is uniform, there is no coupling of waves of different harmonic number. In this situation Moore [14] has derived a simple relationship that holds *independently* for each of the Fourier coefficients of the unsteady perturbations:

$$\frac{2}{|n|}\frac{\partial \tilde{\phi}_n}{\partial t} = \frac{d\psi_c}{d\phi}\delta\tilde{\phi}_n - in\lambda\delta\tilde{\phi}_n - \mu\frac{\partial \tilde{\phi}_n}{\partial t}, \quad n \neq 0. \tag{2}$$

In Eq. (2) $d\psi_c/d\phi$ is the slope of the compressor total-to-static pressure rise characteristic, $\delta\tilde{\phi}_n$ is the nth harmonic of the perturbation $\delta\phi(\theta) = \phi(\theta) - \phi_{ss}$, with ϕ_{ss} the steady-state flow, and λ and μ are parameters that quantify the inertia in the blade row passages. The left-hand side of the equation captures the impedance characteristics of the flow fields upstream and downstream of the compressor face (see Moore [15] or Longley [12] for a full derivation). The important thing to note is that the slope of the pressure rise characteristic, $d\psi_c/d\phi$ in Eq. (2), is uniform around the annulus of the compressor, so that $(d\psi_c/d\phi)\,\delta\tilde{\phi}_n$ affects only the nth harmonic, and there is no coupling between circumferential harmonics.

2.2 Inlet Distortion. When inlet distortion is present, the picture is quite different. The compressor time mean pressure rise and axial velocity are nonuniform in θ. The nonuniform velocity field, which now needs to be computed, is the background environment in which the small unsteady disturbances that lead to instability propagate.

Hynes and Greitzer [8] derived the following description of distorted flow in a compressor, which must be satisfied by the steady-state axial velocity coefficient at the compressor face:

$$\psi_p - \psi_{\text{dist}}(\theta) = \psi_c(\phi_{ss}) - \lambda\frac{\partial \phi_{ss}}{\partial \theta}. \tag{3}$$

This is the nonlinear condition satisfied by the steady-state velocity field $\phi_{ss}(\theta)$ at the compressor face. ψ_p is the plenum pressure, which is set by the throttle constant k_t and mean compressor flow ($\psi_p = \frac{1}{2}k_t\bar{\phi}^2$). ψ_{dist} is the total pressure distortion, determined by the loss through a screen or otherwise specified. Note that the linearized compressor characteristic in Eq. (2) is replaced here by the nonlinear compressor characteristic $\psi_c(\phi)$.

Because the steady flow pattern $\phi_{ss}(\theta)$ that satisfies Eq. (3) is not circumferentially uniform, $d\psi_c/d\phi$ is also a function of θ. When distortion is present, the equation describing small perturbation dynamics (Eq. (2)) is modified as follows:

$$\frac{2}{|n|}\frac{\partial \tilde{\phi}_n}{\partial t} = \left\{\frac{d\psi_c}{d\phi}(\theta) \times \delta\phi(\theta)\right\}_n - in\lambda\delta\tilde{\phi}_n - \mu\frac{\partial \tilde{\phi}_n}{\partial t}, \quad n \neq 0. \tag{4}$$

In Eq. (4) $\{\cdot\}_n$ evaluates the nth harmonic of the product in brackets, which is evaluated at each θ in the spatial domain. In [8] this term was given as a convolution sum; it involves *all* of the harmonics of both $d\psi_c/d\phi$ and $\delta\phi$. The central point and the essential difference from the uniform flow situation is that *the Fourier harmonics are coupled through the interaction of* $(d\psi_c/d\phi)$ *and* $\delta\phi$, *which are both functions of* θ. The eigenmodes of the system, i.e., the perturbations that grow into rotating stall, are no longer sinusoidal in θ, and the modal control approach described in Paduano et al. [17] and Haynes et al. [7] for uniform background flow becomes difficult.

We will have more to say about the control problem with distortion in a later section; here it suffices to give a pictorial example and a qualitative description of the behavior. Figure 2 defines the magnitude and extent of a square total pressure inlet distortion introduced far upstream of the compressor. Using Eq. (3) and knowing the geometry and uniform flow pressure rise capability of the compressor, we can solve for the steady-state velocity profile at the compressor face, as shown in Fig. 3. The least stable eigenmode of the dynamic system described by coupling Eq. (4) and the plenum response is pictured in Fig. 4. Several realizations of the wave as it travels around the

Nomenclature

DF = distributed feedback
HF = harmonic feedback
HFC = harmonic feedback with cross coupling
IGV = inlet guide vanes
LQG = linear quadratic Gaussian
MIMO = multi-input multi-output
PSD = power density spectrum
rms = root mean squared
SISO = single-input single-output
XHG = extended Hynes–Greitzer model
b = chord
b_G = "B" parameter
β = spatial phase shift of DF controller
c_x = axial velocity
δ = perturbation
γ = inlet guide vane deflection
k_t = throttle constant
l = duct length
ϕ = flow coefficient
ψ_c = compressor inlet-total to exit-static pressure rise
ρ = density of air
θ = angle around annulus
r = reaction
$\bar{r}$ = mean radius
t = time
τ_f = time constant
u = velocity
μ = fluid inertia
ω_r = rotor frequency
x_m = upstream sensor location

Subscripts

a = actuator inlet guide vane
i = inlet guide vane, ideal
r = rotor
s = stator
w = wheel

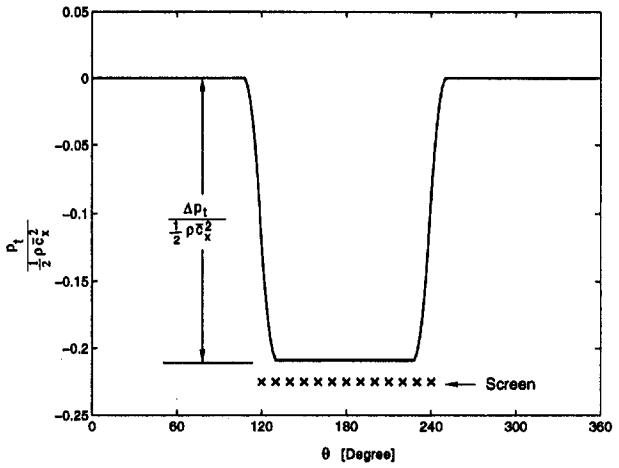

Fig. 2 Distortion magnitude and extent

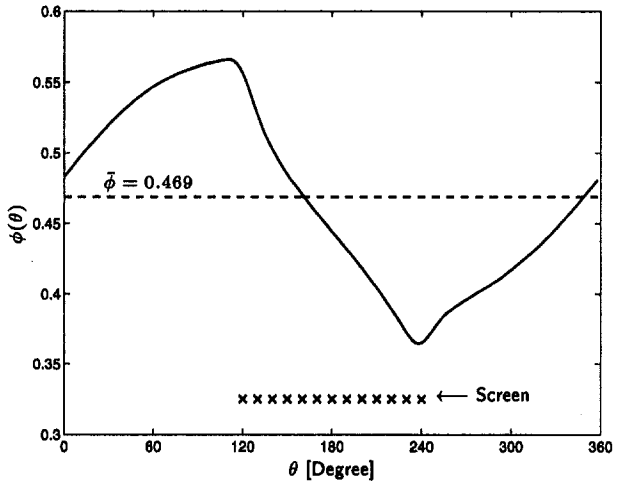

Fig. 3 Computed compressor inlet steady-state axial velocity profile for the distortion shown in Fig. 2

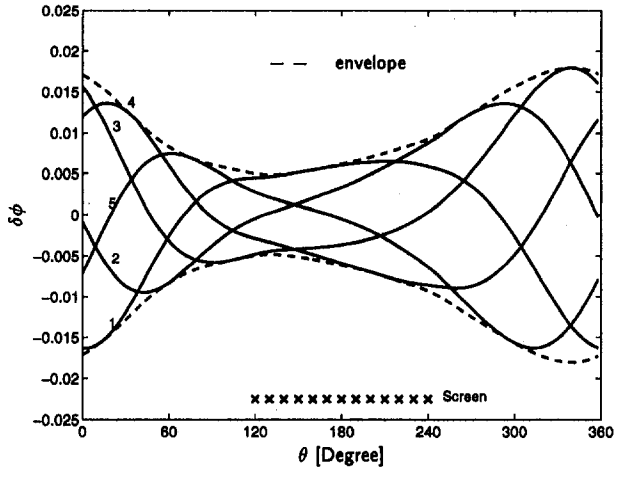

Fig. 4 Neutrally stable eigenmode associated with the background distorted flow given in Fig. 3. Numbers denote the eigenmode at different points in time. Velocity scale is arbitrary.

compressor annulus are shown, with the eigenmode pictured for the mass flow at which it is neutrally stable. For uniform inlet flow, this picture would be a first harmonic sinusoid translating around the annulus, but we now see a wave shape, which changes as it travels around the annulus. The modeling, identification, and stabilization through active control of this and other complex eigenmodes are the subject of this paper.

3 Experimental Design and Setup

The MIT three-stage low-speed (tip Mach number = 0.2) active control research compressor was modified to study inlet distortion by adding an inlet duct extension and distortion ring. Figure 5 shows, from left to right, the following elements of the rig: (1) the distortion ring, which is designed so that the distortion screen can be slowly rotated to enable high spatial resolution distortion measurements; (2) the inlet duct extension, which was incorporated to decouple the potential flow effects of the distortion screen and the compressor; (3) the inlet guide vanes; (4) the 12 servo-controlled guide vanes, which are driven by independent computer-controlled servomotors—the incidence of these vanes can be commanded at a bandwidth of approximately 100 Hz (2.5 times rotor frequency); and (5) the three stages of the compressor.

Table 1 gives nondimensionalized parameters describing this system; these parameters were measured by Haynes [6, 7], and were used to develop *a priori* models for the system with inlet distortion. The parameters required for the model are divided into three categories in Table 1: geometric parameters, measured pressure rise characteristics, and two additional parameters determined by Haynes, reaction r and characteristic time constant τ_f associated with loss generation. The theoretical value of τ_f is between 1 and 2. The actual value was determined from system identification results (see Haynes et al. [7] and Van Schalkwyk [20]). Varying the value from $\tau_f = 1$ to $\tau_f = 2$ does not significantly affect our predictions.

The distortion screens were designed to represent "worst case" distortions encountered in practice [18]. A circumferential extent (see Fig. 2) of 120 deg was used for both distortion screens tested. The first screen imposed a distortion magnitude (also defined in Fig. 2) of 0.8 dynamic head, that is,

$$\frac{\Delta p_t}{\frac{1}{2}\rho \bar{c}_x^2} = 0.8 \tag{5}$$

where $\bar{c}_x$ is the mean axial velocity, Δp_t is the drop in total pressure across the screen, and ρ is the air density. Because the effect on stalling flow coefficient and peak pressure rise due to this distortion was relatively small, a second screen, which imposed a 1.9 dynamic head distortion, was also tested.

A parameter often used to assess the severity of inlet distortion is the DC(60) descriptor (see Williams [21]) defined by

$$\mathrm{DC}(60) = \frac{\bar{p}_t|_{360°} - \bar{p}_t|_{\text{worst } 60°}}{\frac{1}{2}\rho \bar{c}_x^2} \tag{6}$$

where the overbar indicates average over the specified range of angles. For an idealized case with uniform inlet static pressure, DC(60) = 1 corresponds to zero-velocity flow in a 60 deg sector of the annulus, i.e., very poor inlet aerodynamics (Williams [21]). Experiments by Aulehla and Schmitz [1] on the Tornado showed $0.15 \le \mathrm{DC}(60) \le 0.55$ as the angle of attack is varied over the range 3 to 35 deg. At the respective stalling flow coefficients, the 0.8 and 1.9 dynamic head distortions correspond to DC(60) = 0.53 and DC(60) = 1.31, respectively, so that these are severe in terms of practical situations.

4 Model Assessment

In this section we compare predictions of the extended Hynes–Greitzer model to three types of experimental data. First, steady-state performance is compared to that predicted by the model. Second, the unsteady behavior of prestall waves is

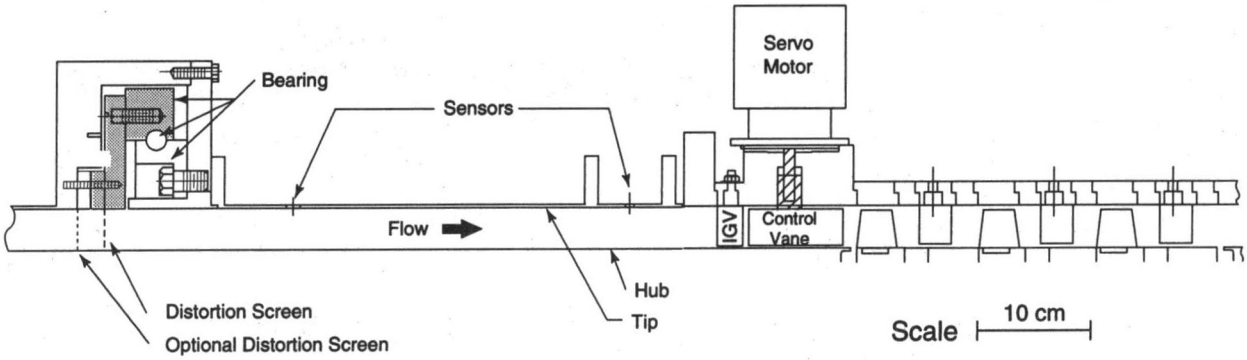

Fig. 5 Experimental setup/distortion generator

studied and compared to predictions. These two comparisons have been done before, most notably by Longley [11]. The third set of comparisons, however, are more informative as regards dynamic response, and these have not been performed before. These are comparisons of the transfer functions between control guide vane deflection waves and measured waves of axial velocity in the compressor. The comparisons tested the full range of frequencies, spatial harmonics, and input-output characteristics modeled.

4.1 Steady-State Performance With Inlet Distortion. The first comparison is the steady-state predicted velocity profile. The velocity profile at the compressor face for the 1.9 dynamic head distortion has been given in Fig. 3. The hot-wire measurements are taken approximately 0.6 rotor radii upstream of the compressor face, and at this location the velocity profile is much different (see Van Schalkwyk [20]). Figure 6 gives the velocity profile and static pressure distribution at the hot-wire measurement station, as well as the experimental data. The features of the measured velocity profile are captured by the model, although they are somewhat more pronounced in the model. The differences are primarily caused by the assumption that the total pressure deficit introduced by the distortion screen convects downstream without changing shape. In reality, some flow redistribution occurs, narrowing the distortion. The static pressure nonuniformity induced by the compressor ($p - \bar{p}$) is well captured.

Table 1 Three-stage compressor model parameters

Geometric parameters (see list of symbols for definitions). Hub-to-tip ratio = 0.88.

$\lambda = \mu_r = 0.679$	$\mu_s = 0.334$
$\mu_a = 0.286$	$\mu_i = 0.071$
$b_r = 0.118$	$b_s = 0.108$
$l_1 = 2.992$	$l_4 = 1.529$
$b_G = 0.163$	$x_m = -0.6$
$\bar{r} = 286$ mm	

Pressure rise characteristics (Haynes [6, 7]).

(*a*) Pressure rise characteristic

$$\psi_c = -10.07\phi^2 + 9.4306\phi - 1.1849$$

(*b*) Ideal (no loss) pressure rise characteristic

$$\psi_i = -15.5341\phi^3 + 24.1238\phi^2 - 15.0262\phi + 4.6951$$

(*c*) Pressure rise sensitivity with respect to control vane deflection

$$\frac{d\psi_c}{d\gamma} = 2.8880\phi^2 - 3.6550\phi + 0.8251$$

Other parameters.

Reaction $r = 0.75$ $\tau_f = 1.5$

The velocity profiles can be used to compute the pressure rise delivered by the compressor at any flow coefficient and thus to generate speed lines with distortion. Figure 7 shows the measured and predicted compressor characteristics for 0.8 and 1.9 dynamic head distortions. The 1.9 dynamic head distortion reduces the operating range by 4.3 percent and the compressor pressure rise by 8 percent.

Figure 7 also shows the uniform inlet data and the polynomial curve fit given in Table 1 and used as one of the model inputs. Both measured and predicted characteristics are terminated at the "no control" stall point. To determine the stall point using the model, an eigenvalue analysis is performed at each flow coefficient; the minimum flow coefficient for which all eigenvalues are stable is taken as the stall point.

Note how well the Hynes–Greitzer model predicts degradation in stall margin for a 0.8 dynamic head distortion. This prediction capability is by itself a valuable feature of the model. For a 1.9 dynamic head distortion, the model is less accurate. One reason may be that the compressor characteristic is steeper than predicted at flow coefficients below stall. This part of the compressor characteristic cannot be measured, so the potential error tends to increase with larger distortions, which access lower flow coefficients over part of the annulus (as shown, for example, in Fig. 3).

4.2 Unsteady Behavior at Stall Inception (Unforced). It is instructive to examine the unforced unsteady behavior for two reasons. First, it shows how theory-to-experiment comparisons can be made even for unforced experiments [11]. Second,

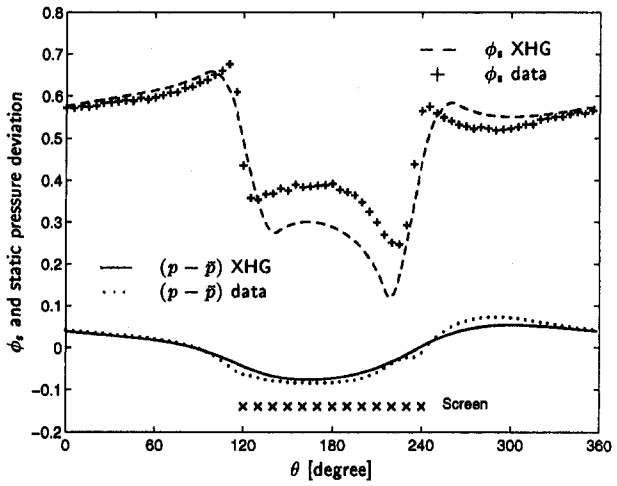

Fig. 6 Steady-state velocity profiles and static pressure deviations at 0.6 radii upstream of the compressor face, $\bar{\phi} = 0.5$, 1.9 dynamic head distortion. Pressure is in units of $(p - \bar{p})/(\frac{1}{2}\rho u_w^2)$.

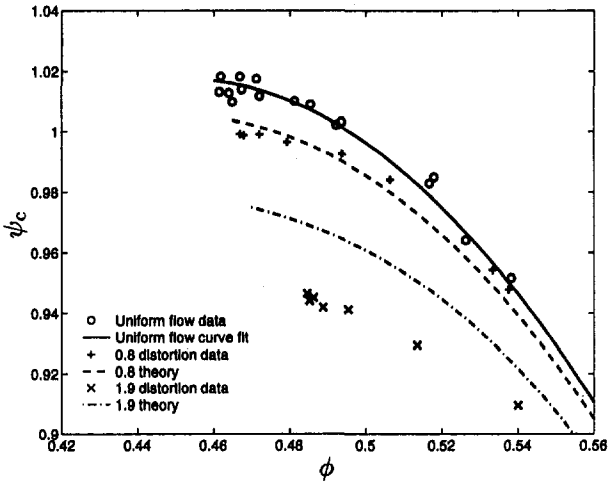

Fig. 7 Compressor performance lines with uniform flow, 0.8 and 1.9 mean dynamic head distortions

however, we can see the shortcomings associated with measuring system dynamics in the noisy compressor environment without a known forcing input.

Figure 8 gives the spectrum of the zeroth and first spatial Fourier coefficient immediately prior to stall for the 1.9 dynamic head distortion. Three features can be noted in these spectra. First, the most unstable eigenvalue, represented by the resonant peak at roughly 0.42 of the rotor frequency, resonates in both the zeroth and the first spatial Fourier coefficient. Coupling into the second and third spatial harmonic is also predicted and measured; but the fact that the zeroth spatial harmonic also participates in the mode is particularly important. This coupling of surge-type and rotating stall-type perturbations makes surge-type dynamics important in determining compressor stability. Chue et al. [2] noted this effect, and showed that when this resonance occurs compressor stability degrades.

The second feature of note in Fig. 8 is the peak at negative frequency at the frequency magnitude of the eigenvalue. As described in Tryfonidis et al. [19], this indicates that the spatial wave is oscillating in amplitude as it rotates around the annulus. The graphs in Fig. 9 show why this occurs. As the spatial wave encounters the region of high flow and negative compressor slope $d\psi_c/d\phi$ (stabilizing), the amplitude of the wave decreases. In the region where the slope is positive (destabilizing),

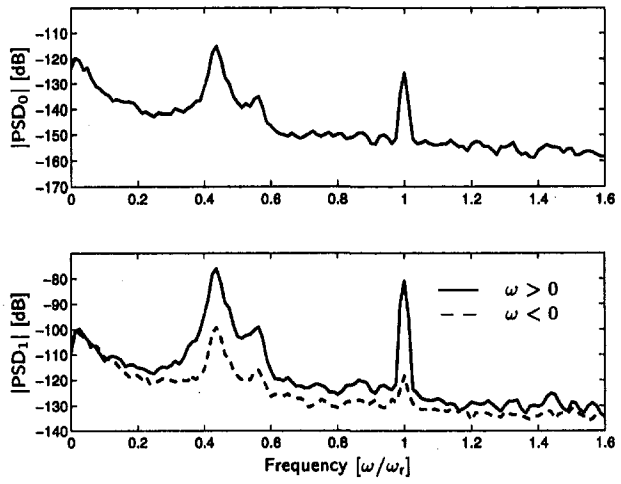

Fig. 8 PSDs of $\delta\dot{\phi}_0$ (top) and $\delta\dot{\phi}_1$ (bottom). The PSDs at positive and negative frequencies are shown by the solid and dashed lines in the bottom figure respectively; 1.9 dynamic head distortion.

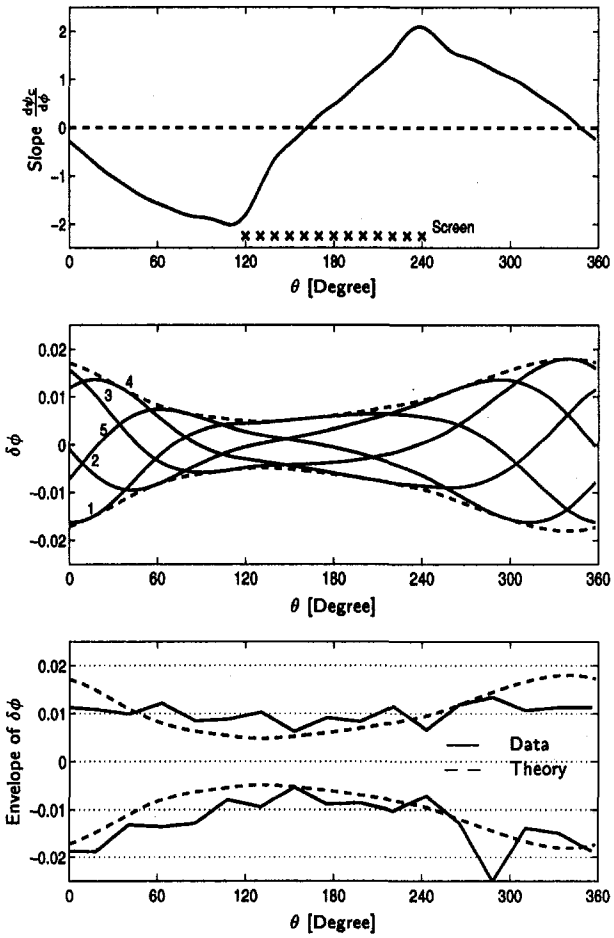

Fig. 9 Slope ($d\psi_c/d\phi$) (top), axial velocity perturbation at different points in time (middle), and analytical and measured rms of velocity perturbations around the annulus (bottom). The rms values of the perturbations are shown for $\delta\phi > 0$ and $\delta\phi < 0$. The rms values obtained from the different hot-wires were connected by straight lines to show the trend. 1.9 dynamic head distortion, at neutral stability point.

the wave grows. This occurs once per revolution of the wave and the resulting pulsation shows up as a negative frequency component in the spectrum. The peak of the envelope occurs approximately where the slope changes sign from positive to negative.

Figure 9 also shows the experimental envelope of rms axial velocity fluctuation, and compares this to the rms amplitudes given by the model. Qualitative agreement is obtained between experimental and theoretical results, but the data are quite noisy.

The third observation in Fig. 8 is the large peak at rotor shaft frequency and the smaller peak at 0.58 of the rotor frequency. The peak at one rotor revolution is not predicted by the model and we associate it with a nonuniformity of the rotor blade geometry. This peak is observed in uniform flow but is more pronounced in the presence of distortion. The peak at 0.58 indicates interaction between the first mode and the rotor shaft frequency disturbance ($0.58 = 1 - 0.42$). There is also a small peak at $1.42 = 1 + 0.42$ in the PSD of the first harmonic (bottom graph of Fig. 8). The interaction between the first mode and the rotor frequency is also not predicted by the model; this type of behavior is characteristic of nonlinear systems.

4.3 Input-Output Behavior of the Actuated Compressor (Forced). A more complete comparison of model and data can be obtained by performing *forced-response experiments.* These allow the linearized dynamics to be examined as functions of both spatial and temporal frequency. Eigenvalues can be identified as the peaks in the transfer functions, and cross-

coupling between spatial harmonics can be quantified. The transfer function information can also be used for design of control laws.

A brief explanation of the input-output system is in order. The 12 control vane deflections represent a "wave" of actuation, which forces the compressor unsteady aerodynamics. This wave can be decomposed into spatial Fourier coefficients, just as the axial velocity was decomposed in Eq. (1)

$$\delta\gamma(\theta, t) = \sum_{n=-3}^{3} \delta\tilde{\gamma}_n(t) e^{in\theta} \tag{7}$$

where $\delta\gamma$ is the deflection from the mean position, measured in radians. Actuation of the zeroth, first, second, and third Fourier coefficient can be introduced and the responses of $\delta\tilde{\phi}_n$ ($n = 0, 1, 2, 3$) can be measured. Thus there are 16 transfer functions that can be measured and compared to the theory. Transfer functions are identified using sinusoidal excitation at discrete frequencies, to improve the signal-to-noise ratio. A full MIMO transfer function estimate is made at each frequency, regardless of whether distortion is present. See Van Schalkwyk [20] for further details on the system identification procedures.

Figure 10 gives a representative subset of the 16 identified transfer functions for a mass flow coefficient of $\bar{\phi} = 0.5$. This is approximately 17 percent above the stalling flow coefficient so that we expect the system to exhibit behavior that is well damped. Results for both uniform flow and inlet distortion are shown. Actuating the nth harmonic $\delta\tilde{\gamma}_n$ and measuring the mth harmonic $\delta\tilde{\phi}_m$ is denoted by $\delta\tilde{\gamma}_n \rightarrow \delta\tilde{\phi}_m$. In Fig. 10 $|\cdot|$ and arg $(\cdot)$ indicate the magnitude and phase of a transfer function, respectively.

Peaks in the transfer function magnitudes indicate lightly damped modes at which the system will tend to resonate. The magnitude of the measured transfer function from $\delta\tilde{\gamma}_1 \rightarrow \delta\tilde{\phi}_1$ has a small peak at approximately 0.38 ω_r while the theory gives the peak at 0.40 ω_r. The corresponding eigenvalue in the uniform flow transfer function is highly damped (although an eigenvalue is still present as indicated in the phase plot). This shows that at the same flow coefficient, distortion causes a significant decrease in damping. The peak at 0.38 ω_r is visible in the magnitude of the distorted flow $\delta\tilde{\gamma}_0 \rightarrow \delta\tilde{\phi}_0$ transfer function, indicating that the zeroth harmonic is also present in the first eigenmode.

Valleys in the transfer functions indicate zeros close to the $i\omega$-axis. A zero is visible in the transfer function $\delta\tilde{\gamma}_1 \rightarrow \delta\tilde{\phi}_1$. The minimum values of the measured and theoretical transfer function magnitudes occur at 0.93 ω_r and 1.03 ω_r, respectively (with distortion). However, for this transfer function the measured and calculated phases change abruptly[1] to within 0.05 ω_r, and we conclude that the frequency of the zero is given accurately by the model.

Theoretically, with no distortion, all coupling transfer functions (for instance, $\delta\tilde{\gamma}_2 \rightarrow \delta\tilde{\phi}_1$) are zero. The experimental results with uniform flow (see Fig. 10 for the $\delta\tilde{\gamma}_1 \rightarrow \delta\tilde{\phi}_0$ and $\delta\tilde{\gamma}_2 \rightarrow \delta\tilde{\phi}_1$ results) show that the cross transfer functions remain at very low levels (roughly 20 dB below the distorted flow results) and show no coherent magnitude or phase behavior. This implies that the cross-coupling is a feature of a linear fluid system with a nonuniform mean flow rather than an effect of nonlinearity. For the 1.9 dynamic head distortion, the amplitude of $\delta\tilde{\gamma}_2 \rightarrow \delta\tilde{\phi}_1$ is almost as large as the direct transfer function $\delta\tilde{\gamma}_1 \rightarrow \delta\tilde{\phi}_1$. Thus substantial coupling occurs between spatial harmonics, including the zeroth, so the harmonic-by-harmonic feedback control method that has been applied to undistorted cases may not be effective in distorted flow.

Finally, Fig. 11 shows the predictive capability of the model across the entire operating range where transfer functions can be measured. Here, the evolution of the $\delta\tilde{\gamma}_1 \rightarrow \delta\tilde{\phi}_1$ transfer function from very stable to slightly unstable is shown. Once again the main features of the response are well captured. The eigenvalue and zero frequencies of the real system increase in frequency with respect to the model as flow coefficient is reduced, and the zero is less stable than the theory says. Nevertheless, the dynamics have been represented well enough for control purposes.

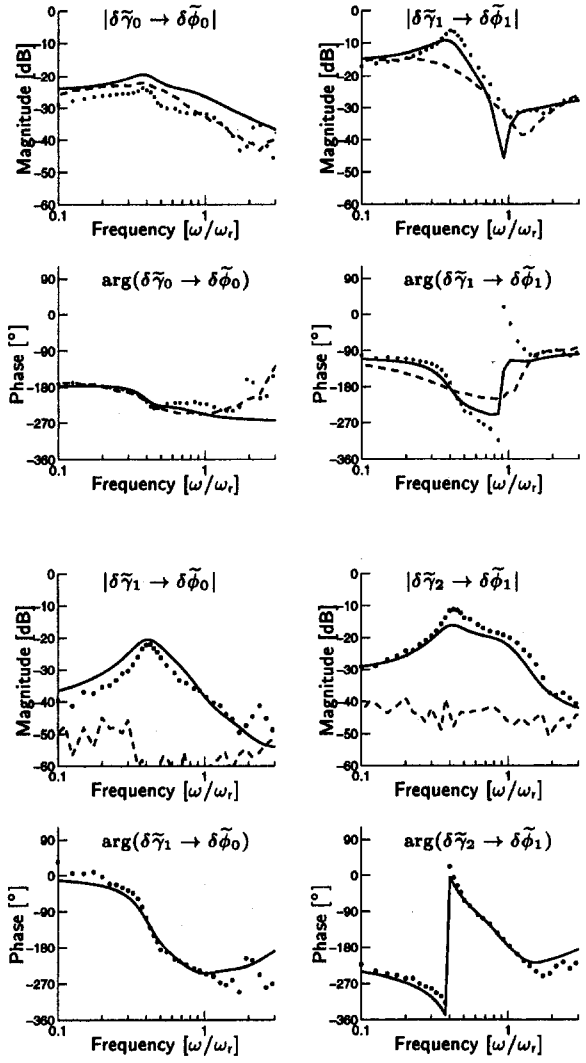

Fig. 10 Transfer functions $\bar{\phi}$ = 0.500, 1.9 dynamic head distortion. —— = theory, distorted flow; · · · = experiment, distorted flow; - - - = experiment, uniform flow.

5 Features of the Control Problem With Distortion

The experimental results shown above provide a backdrop for describing active stabilization with distorted flow, particularly the challenges that exist compared to undistorted flow. There are several features of the distorted flow control problem that need to be addressed.

One of these, the coupling between spatial harmonics, has already been mentioned. In uniform flow each spatial harmonic is an eigenmode, and evolves according to a single eigenvalue equation. With distortion, however, each spatial harmonic participates in more than one eigenmode. A corollary is that commanding a given spatial harmonic in guide vane deflection affects many other spatial harmonics; the system is fully coupled and multi-input multi-output. Feedback laws must therefore account for all spatial harmonics, including the zeroth order

[1] Abrupt phase changes in either the positive or negative direction, as in the $\delta\tilde{\gamma}_1 \rightarrow \delta\tilde{\phi}_1$ transfer function, indicate a zero near the $i\omega$ axis. Slight errors in the position of such zeros cause reversal in direction of the abrupt phase change.

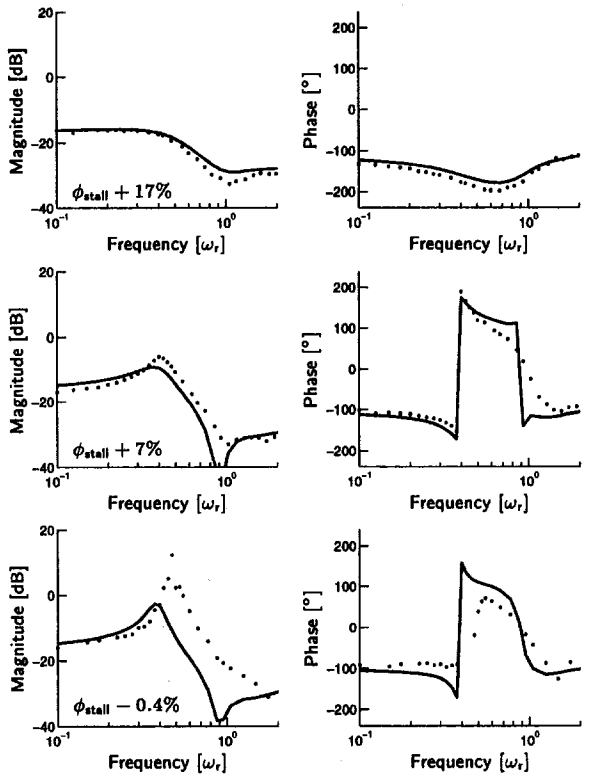

Fig. 11 $\delta\tilde{\gamma}_1 \rightarrow \delta\tilde{\phi}_1$ **transfer function at three different flow coefficients, 1.9 dynamic head distortion. Magnitude and phase are shown on the left and right, respectively.** —— = **theory,** · · · = **experiment.**

(surge-type) disturbance, simultaneously rather than one at a time.

Another feature of distorted flow is that the poles and zeros become unstable more abruptly as a function of flow coefficient compared to uniform flow. This is because much of the compressor is experiencing flow values well below the values at which uniform inlet flow would be unstable and the local flow is strongly destabilized in this region. The most unstable pole and zero as a function of distortion extent are shown in Fig. 12, based on results of the model described earlier. We see that the pole is unstable (positive real part) over a large range of distortion extents.

Also shown in Fig. 12 is the zero location associated with the multi-input multi-output transfer function. This zero has a

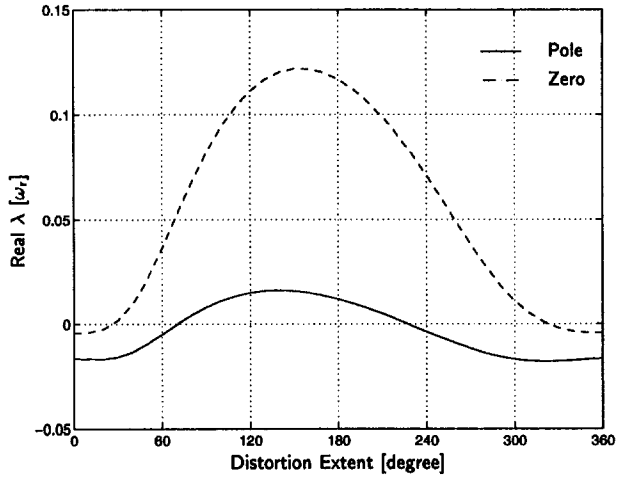

Fig. 12 Effect of distortion extent on the most unstable pole and dominant zero, $\bar{\phi}$ = **0.465, 1.9 dynamic head distortion. Results from model.**

Table 2 Stable operating range increase of various control laws, 0.8 dynamic head distortion

Type of Control	Range increase, percent
Linear Quadratic Gaussian	1.5
Cross-coupled harmonic feedback	3.0
SISO harmonic feedback	2.2
Distributed feedback	3.7

positive real part, and is known as a "nonminimum phase zero." Such zeros severely degrade the ability of feedback control to stabilize the system [3]. Although this zero location depends on the choice and placement of actuators and sensors, the main issue is that for the actuator/sensor configuration used here distortion degrades the control problem.

Distortion also appears to have an impact on the background noise level in the compressor, perhaps due to the part of the annulus operating at positive slope amplifying random fluctuations in the flow. Whatever the cause, the rms of random axial velocity fluctuations with 1.9 dynamic head distortion are about twice those in uniform flow. Increased noise levels cause the actuators to work harder than they otherwise would, and make determining the location and size of unstable waves more difficult. They also increase the likelihood of nonlinear events, which are not accounted for in the control law design procedure.

The final feature of the control problem with inlet distortion is its spatial character. With uniform flow, the circumferential orientation of the compressor is arbitrary and control laws do not depend on orientation with θ. Inlet distortion creates a definite spatial orientation so that a control policy different from that used in uniform flow may be necessary. Distortion control laws must account for both the orientation of the disturbance wave *and* the orientation of the inlet distortion. Further, a control law that depends on the distortion profile must maintain some "robustness" to its orientation and shape, because these typically are not well known.

6 Control Law Design and Implementation

The results of the model-to-data comparisons imply that a first-cut control law can be designed based on the physical description provided by the model. A control law was thus designed using the Linear Quadratic Gaussian (LQG) design approach [9]. This approach was successful at stabilizing rotating stall, but because of the inherent lack of robustness in such control law designs, performance was poor. The mass flow operating range extension afforded by LQG control was 1.1 percent, or 26 percent of the operating range lost due to a 1.9 dynamic head distortion. For a 0.8 dynamic head distortion the LQG controller increased the stable flow range 1.5 percent below the open loop undistorted flow stall point.

The primary drawback of an LQG control law (or any direct model-based control law) is sensitivity—one must know the circumferential location, magnitude, and extent of the inlet distortion before a control law can be enacted. The LQG controller maintained its performance for an 80 deg range of distortion locations but outside this range, the control law actually destabilized the system.

One therefore expects a trade-off between range extension and insensitivity to distortion location. Table 2 lists the control laws tested in order of sensitivity to distortion location. The poor performance of LQG control reflects its sensitivity to other modeling errors as well.

The next control law shown is the SISO harmonic feedback (HF) controller experimentally optimized by Haynes [7], with additional cross-feed channels introduced to account for coupling between harmonics. This controller will be referred to as harmonic feedback plus coupling (HFC). Figure 13 gives a functional block diagram as well as numerical values for the

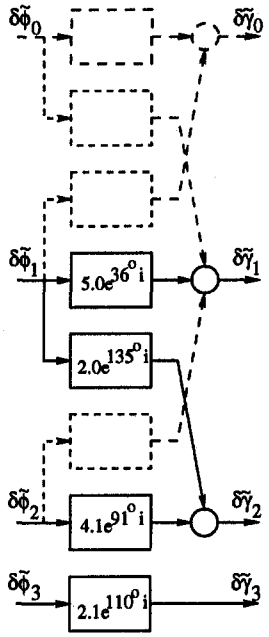

Fig. 13 Cross-coupled harmonic feedback control law. Cross coupling between harmonics that did not lower the stalling flow coefficient are shown with dashed lines.

control scheme used. The cross-feed channels introduce coupling with a spatial orientation. This control law is thus also sensitive to distortion location, although it might be considered less sensitive than LQG control because fewer cross-feeds exist than in the LQG controller.

To arrive at the HFC gains in Fig. 13, a procedure similar to that employed by Haynes was used. Gains are initially chosen to be as high as possible without saturating the system. Then the phases are chosen by experimentally testing the range extension afforded by each choice of phase. The feedback paths are added sequentially, and each one is optimized with the preceding gains fixed. Experience and additional experiments govern the order that feedback paths are added. In this case the direct gains are optimized first, followed by the cross-feed gains. Attempts were made at optimization of several other cross-feed channels, but no additional range extension was provided by these. Final gain adjustments are made after the phase optimization.

This controller's performance can be compared to the original SISO harmonic feedback controller designed by Haynes [7], which would be represented by Fig. 13 with all cross-feed channels set to zero. This control law is completely insensitive to distortion location but, because it does not account for coupling, is not as effective as the cross-coupled control law (see Table 2).

The final control law, termed distributed feedback (DF), measured the entire shape of the disturbance $\delta\phi(\theta)$, and fed back a rotated and amplified version of it to the actuators (see Fig. 14). The specific formulation was

$$\delta\gamma(\theta) = k\delta\phi(\theta - \beta) \tag{8}$$

where the gain k and rotation angle β are design variables.

Table 2 Stable operating range increase of various control laws, 0.8 dynamic head distortion

Type of Control	Range increase, percent
Linear Quadratic Gaussian	1.5
Cross-coupled harmonic feedback	3.0
SISO harmonic feedback	2.2
Distributed feedback	3.7

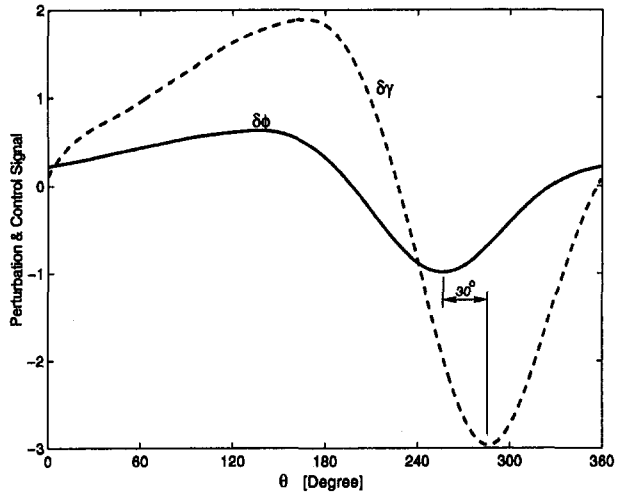

Fig. 14 Distributed feedback control signal for a typical velocity perturbation. Gain k = 3, spatial phase shift β = 30 deg.

These variables are optimized in the same fashion as the gains and phases in the HFC control law: Gain is fixed by saturation considerations, and stalling mass flow reduction is then tested for a complete sequence of β's. This is followed by gain adjustment tests at the optimized β.

The gain tuning procedure is less tedious than the HFC procedure because only two parameters need to be optimized. This control law has several other advantages. It is a fixed rather than dynamic controller, thus simply implemented. It is insensitive to the location of the distortion. According to simulation studies, it is also insensitive to the type of distortion introduced. This control law performed as well or better than any other control law tested.

Figure 15 summarizes the range extensions obtained with the different controllers for the 0.8 and 1.9 dynamic head distortions. The uniform flow stall flow coefficient (without control) is indicated by the dashed line. The lowest flow coefficient at which Haynes [7] stabilized this compressor in uniform flow ($\phi = 0.42$) is also indicated. For the 0.8 dynamic head distortion the range extension was approximately 43 percent of the extension obtained for uniform flow.

The effectiveness of the DF controller is also characterized by comparing the open and closed-loop PSDs of the zeroth and

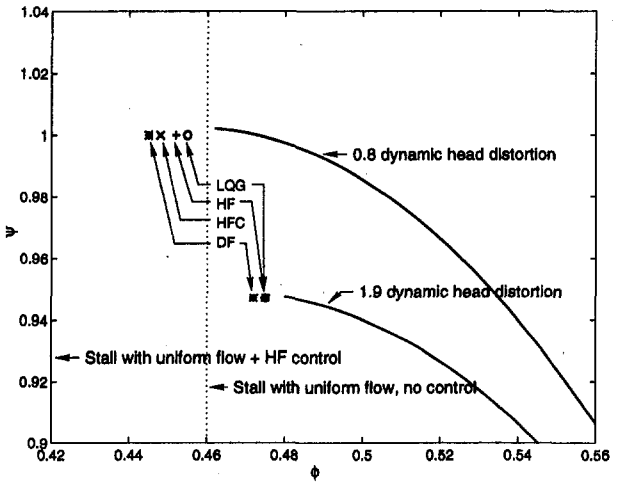

Fig. 15 Measured compressor performance for 0.8 and 1.9 dynamic head distortions and various control laws (note: no HFC results exist for 1.9 dynamic head distortion). Each symbol represents the minimum flow coefficient obtained using the indicated control law.

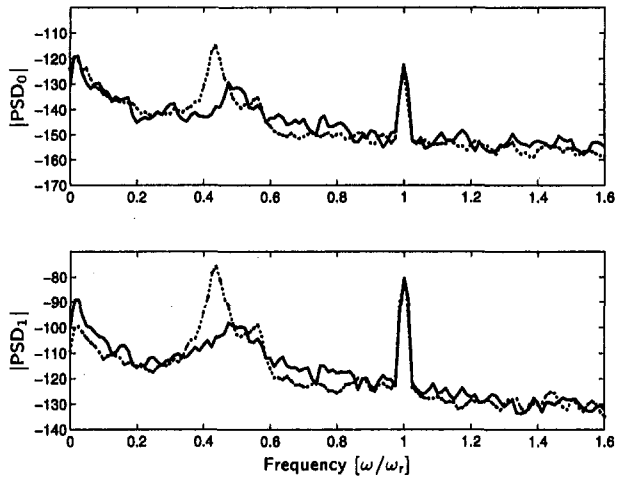

Fig. 16 PSDs immediately prior to stall inception, with and without control. · · · = open-loop PSD, —— = closed-loop PSD for DF controller, 0.8 dynamic head distortion.

first harmonics in Fig. 16. Both PSDs were taken immediately prior to stall, to show the prestall behavior of the system. Thus the closed-loop PSDs are at a lower flow coefficient. Even at this more unstable condition, the DF controller suppressed the zeroth and first harmonics of the first mode by approximately 15 and 23 dB, respectively.

The distributed feedback controller was both the best performer and the most insensitive to distortion type and location. Because the measured shape of the perturbation is used, this control law takes into account cross-feed effects while remaining insensitive to distortion location. The structure is also compatible with nonlinear behavior; as perturbations become larger and more localized, the control law responds accordingly.

7 Summary and Conclusions

The experiments reported in this paper represent the first systematic attempt to apply system identification and control theory to a compressor with circumferential inlet distortion. The behavior of such a dynamic system is qualitatively different from that of compressors in uniform flow and thus requires a different control strategy and approach.

Active control has been demonstrated to stabilize rotating stall with inlet distortion, extending the stable operating range of the compressor. Using our validated model, we can also show that the distributed feedback (DF) controller is insensitive to both the size and location of the distortion. Of course, our study is limited to two-dimensional distortions, the system is incompressible, and the surge dynamics are relatively stable in this system. Also, the effects of rotating or otherwise unsteady distortions, which may be significant, were not considered.

Based on theory-experiment comparisons of (*i*) distortion profiles, (*ii*) compressor characteristics, (*iii*) unforced transients, (*iv*) eigenvalues, (*v*) transfer functions, and (*vi*) the effect of stabilizing control, the extended Hynes–Greitzer distortion model was found to be adequate to both describe phenomenology and to design control laws. Thus a tool exists for investigating extensions and different implementations. The predictions of the model were found to be accurate enough to allow working LQG control laws to be successfully implemented.

Other control laws, however, were found to have better performance. In particular, a new distributed feedback control law was introduced that achieves the best overall performance, extending the stable operating range by 3.7 percent for a worst case, practical distortion (DC(60) = 0.53). Using this control law, approximately 40 percent of the operating range lost due to a 1.9 dynamic head (DC(60) = 1.31) total pressure distortion was regained using active control.

Much extension of this technology is required to impact a real system. For instance, additional research is required to understand the physical limitations that determine maximum range extension. In addition, robustness to distortion as a (possibly three-dimensional) unsteady disturbance, the effects of lightly damped surge dynamics, and implementation in a high-speed compressor must all be addressed. The results here indicate that the modeling and control concepts used are valuable for addressing these issues.

Acknowledgments

This work was conducted under AFOSR Grant No. F49620-93-1-0032, Dr. James McMichael technical manager, and ONR Grant No. N00014-91-J-1575, Dr. Eric Hendricks technical monitor. This support is gratefully acknowledged. We also acknowledge the help of Dr. J. P. Longley and Mr. Y. F. Gong at different stages in this research.

References

1 F. Aulehla and D. M. Schmitz, "New Trends in Intake/Engine Compatibility Assessment," in: *AGARD-CP-400: Engine Response to Distorted Inflow Conditions,* Mar. 1987.

2 R. Chue, T. P. Hynes, E. M. Greitzer, C. S. Tan, and J. P. Longley, "Calculation of Inlet Distortion Induced Compressor Flow Field Instability," *International Journal of Heat and Fluid Flow,* 10(3):211–233, Sept. 1986.

3 J. S. Freudenberg and D. P. Looze, "Right Half Plane Poles and Zeros and Design Tradeoffs in Feedback Systems," *IEEE Transactions on Automatic Control,* 30(6), June 1985.

4 E. M. Greitzer, A. H. Epstein, G. R. Guenette, D. L. Gysling, J. Haynes, G. J. Hendricks, J. D. Paduano, J. S. Simon, and L. Valavani, "Dynamic Control of Aerodynamic Instabilities in Gas Turbine Engines," *Steady and Transient Performance Prediction of Gas Turbine Engines, AGARD-LS-183,* pp. 8-1–8-21, May 1992.

5 G. Gu, S. Banda, and A. Sparks, "An Overview of Rotating Stall and Surge Control for Axial Flow Compressors," Technical report, Wright-Patterson, Nov. 1995; private communication.

6 J. M. Haynes, "Active Control of Rotating Stall in a Three-Stage Axial Compressor," Master's thesis, Department of Aeronautics and Astronautics, MIT, 1993.

7 J. M. Haynes, G. J. Hendricks, and A. H. Epstein, "Active Stabilization of Rotating Stall in a Three-Stage Axial Compressor," ASME JOURNAL OF TURBOMACHINE, 116:226–239, 1994.

8 T. P. Hynes and E. M. Greitzer, "A Method for Assessing Effects of Circumferential Flow Distortion on Compressor Stability," ASME JOURNAL OF TURBOMACHINERY, 109:371–379, July 1987.

9 H. Kwakernaak and R. Sivan, *Linear Optimal Control Systems,* Wiley-Interscience, 1972.

10 P. L. Lavrich, "Time Resolved Measurements of Rotating Stall in Axial Flow Compressors," PhD thesis, Department of Aeronautics and Astronautics, MIT, Aug. 1988; also available as Gas Turbine Lab Report #194.

11 J. P. Longley, "Inlet Distortion and Compressor Stability," PhD thesis, Trinity College, Cambridge University, 1988.

12 J. P. Longley, "A Review of Nonsteady Flow Models for Compressor Stability," ASME JOURNAL OF TURBOMACHINERY, 116:202–215, Apr. 1994.

13 J. P. Longley and E. M. Greitzer, "Inlet Distortion Effects in Aircraft Propulsion System Integration," *Steady and Transient Performance Prediction of Gas Turbine Engines,* AGARD-LS-183, pp. 6-1–6-18, May 1992.

14 F. K. Moore, "A Theory of Rotating Stall of Multistage Axial Compressors: Part I—Small Disturbances," ASME *Journal of Engineering for Gas Turbines and Power,* 106:313–320, Apr. 1984.

15 F. K. Moore, "A Theory of Rotating Stall of Multistage Axial Compressors: Part II—Finite Disturbances," ASME *Journal of Engineering for Gas Turbines and Power,* 106:321–326, Apr. 1984.

16 F. K. Moore and E. M. Greitzer, "A Theory of Post-Stall Transients in Axial Compressors: Part I—Development of the Equations," ASME *Journal of Engineering for Gas Turbines and Power,* 108:68–76, 1986.

17 J. D. Paduano, A. H. Epstein, L. Valavani, J. P. Longley, E. M. Greitzer, and G. R. Guenette, "Active Control of Rotating Stall in a Low-Speed Axial Compressors," ASME JOURNAL OF TURBOMACHINERY, 115:48–56, Jan. 1993.

18 C. Reid, "The Response of Axial Flow Compressors to Intake Flow Distortion," ASME Paper No. 69-GT-29, 1969.

19 M. Tryfonidis, O. Etchevers, J. D. Paduano, A. E. Epstein, and G. J. Hendricks, "Pre-stall Behavior of Several High-Speed Compressors," ASME JOURNAL OF TURBOMACHINERY, Vol. 117, 1995, pp. 62–80.

20 C. M. van Schalkwyk, "Active Control of Rotating Stall With Inlet Distortion," PhD thesis, Department of Aeronautics and Astronautics, MIT, June 1996; also available as Gas Turbine Lab Report #222.

21 D. D. Williams, "Engine Compatibility," Technical report, Rolls-Royce PLC, May 1991.

Integrated Control of Rotating Stall and Surge in High-Speed Multistage Compression Systems

K. M. Eveker[1]
United Technologies Pratt & Whitney,
East Hartford, CT 02123

D. L. Gysling
United Technologies Research Center,
East Hartford, CT 02123

C. N. Nett
United Technologies Pratt & Whitney,
East Hartford, CT 02123

O. P. Sharma
United Technologies Pratt & Whitney,
East Hartford, CT 02123

Aeroengines operate in regimes for which both rotating stall and surge impose low-flow operability limits. Thus, active control strategies designed to enhance operability of aeroengines must address both rotating stall and surge as well as their interaction. In this paper, a previously developed nonlinear control strategy that achieves simultaneous active control of rotating stall and surge is applied to a high-speed three-stage axial flow compression system with operating parameters representative of modern aeroengines. The controller is experimentally validated for two compressor builds and its robustness to radial distortion assessed. For actuation, the control strategy utilizes an annulus-averaged bleed valve with bandwidth on the order of the rotor frequency. For sensing, measurements of the circumferential asymmetry and annulus-averaged unsteadiness of the flow through the compressor are used. Experimental validation of simultaneous control of rotating stall and surge in a high-speed environment with minimal sensing and actuation requirements is viewed as another important step toward applying active control to enhance operability of compression systems in modern aeroengines.

Introduction

Rotating stall and surge impose fundamental limits on the low-flow operating range of compressors. Surge is characterized by violent oscillations in the annulus-averaged flow throughout the compression system. Rotating stall is a two-dimensional or three-dimensional disturbance localized to the compressor and characterized by regions of reduced or reversed flow that rotate around the annulus of the compressor [11–13]. In recent years, there has been much work on improving compression system operability using active control [1–6, 9, 10, 14–17, 19–21]. Nearly all of these previous works addressed rotating stall or surge independently; either controlling rotating stall in an axial flow machine in operating regimes incapable of surge, or controlling surge in centrifugal compression system for which rotating stall dynamics were inconsequential. These efforts have been successful in enhancing the stability of such compression systems in laboratory environments.

This paper focuses on enhancing operability of a compression system containing a replica of the rear three stages of a modern high-pressure compressor operating at representative Mach and Reynolds numbers. As such, this work extends previously reported efforts to actively control rotating stall and surge in a low-speed environment into the high speed environment. The compression system parameters are such that the baseline compression system exhibits surge at high-speed operation and rotating stall at part-speed operation when throttled beyond the surge/stall line on the compressor pressure ratio versus corrected flow performance map. The strong interaction between rotating stall and surge present in this compression system is indicative of that found in modern aeroengines. Thus, to enhance low-flow operability substantively, any control strategy must address rotating stall and surge simultaneously.

Scope

The goal of this research was to demonstrate integrated control of rotating stall and surge in a high-speed, multistage compression system, which demonstrated the strong interaction between the annulus averaged compression system dynamics (surge) and the nonaxisymmetric compression system dynamics (rotating stall). The open-loop compression system dynamics were characterized and the effect of the stability enhancing control strategy studied. The robustness of the control strategy to variations in compressor builds and inlet radial total pressure distortion was assessed. No attempt was made to use flightworthy hardware.

Control Strategy

The framework of nonlinear control strategy utilized in this paper to provide integrated control of rotating stall and surge is developed in [8]. The control law is given as follows:

$$K_T = K_{Tnom} + K_{RS} \cdot A^2 + K_{\mathrm{SUR}} \cdot \dot{\Phi}$$

where K_T denotes the throttle area of the compression system, K_{Tnom} denotes the nominal position of the throttle, A denotes the level of asymmetry in the compressor flowfield, $\dot{\Phi}$ denotes the time rate of change of the annulus-averaged flow through the compressor, and K_{RS} and K_{SUR} are controller gains associated with the two terms of the controller.

As described in [8], this control strategy achieves operability benefits by modifying the nonlinear compression system dynamics. The benefits are best illustrated by comparing bifurcation diagrams of the compression system with and without the control strategy. Figure 1 shows the bifurcation diagrams for a typical uncontrolled compression system generated using a three-state Moore–Greitzer model. The throttle area parameter, K_T, determines the throttle characteristic and sets the operating point of the compression system. Therefore, it is a natural choice to parameterize the bifurcation diagrams. The set of bifurcation diagrams shows the level of flow asymmetry, the annulus-averaged mass flow, and compressor discharge pressure as a func-

[1] Current address: Institute for Defense Analyses, Alexandria, VA 22311.

Contributed by the International Gas Turbine Institute and presented at the 42nd International Gas Turbine and Aeroengine Congress and Exhibition, Orlando, Florida, June 2–5, 1997. Manuscript received at ASME Headquarters February 1997. Paper No. 97-GT-352. Associate Technical Editor: H. A. Kidd.

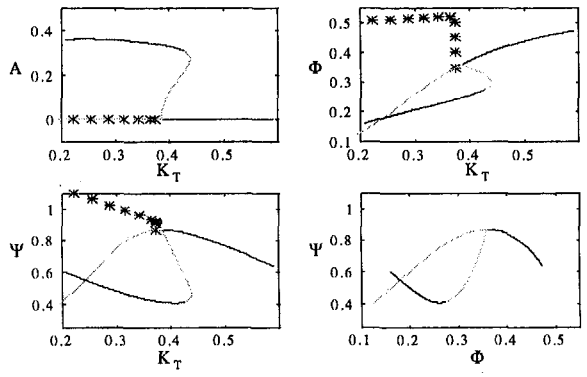

Fig. 1 Uncontrolled bifurcation diagrams, high *B* parameter

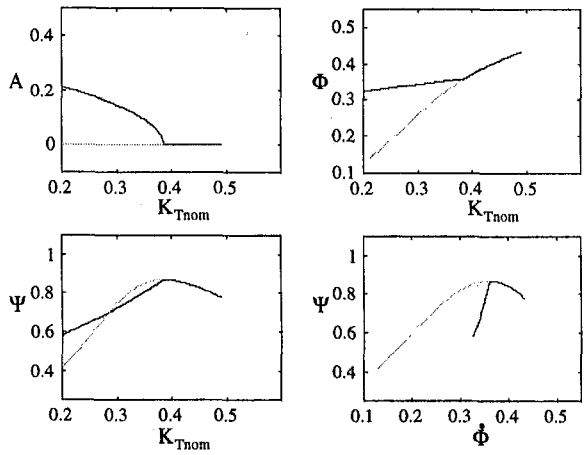

Fig. 2 Integrated R.S./surge controlled bifurcation diagrams, high *B*-parameter

tion of the throttle parameter. A fourth plot showing compressor discharge pressure versus annulus-averaged flow coefficient as the throttle parameter is varied is also presented.

In these diagrams, a black line indicates a locus of (linearly) stable equilibrium points, a gray line indicates a locus of unstable equilibrium points, and *'s indicate the maximum value that the state variable attains along a (linearly) stable periodic orbit.

In these diagrams, the condition of rotating stall corresponds to a linearly stable equilibrium point, whereas surge corresponds to a stable periodic orbit. For throttle areas greater than a critical value, the flow is axisymmetric, and the pressure rise, Ψ, is given by the axisymmetric flow characteristic. As the throttle area is decreased, the flow coefficient decreases monotonically and the pressure approaches its peak value. As the throttle area corresponding to the linear stability boundary is reached, the system exhibits either rotating stall or surge, depending on how the system was perturbed.

If the compressor enters fully developed rotating stall, there is a large increase in flow asymmetry and an associated reduction in annulus-averaged pressure rise and mass flow. As the throttle area is further decreased, the compressor remains in large-amplitude, performance-limiting rotating stall. Hysteresis is exhibited when the throttle is increased from a value corresponding to a condition of rotating stall to a value corresponding to axisymmetric flow. As the throttle area is increased, the system remains in rotating stall for throttle values larger than the throttle values at which the system previously entered rotating stall. The subcritical nature [18] of the loss of stability and the associated hysteresis significantly increases the deleterious effect of rotating stall on aeroengine operability [2].

If the compression system is perturbed in a manner that results in surge, the system exhibits periodic oscillations in mass flow and pressure rise. For the system behavior shown in Fig. 1, the flow remains axisymmetric while the system exhibits stable periodic oscillations.

Implementing the control strategy described above yields the bifurcation diagrams shown in Fig. 2. As shown, surge is eliminated, and the hard, subcritical bifurcation associated with open-loop rotating stall is transformed into a soft, supercritical bifurcation without hysteresis. In the controlled system, as the main throttle area is decreased beyond that associated with the linear stability boundary, the level of asymmetry gradually increases, and the pressure rise and flow gradually decrease. The enhanced operability provided by this control strategy can be inferred by viewing the throttle area as composed of a fixed throttle area as set by the nominal operating line of a compression system and a disturbance throttle that accounts for disturbances that tend to throttle the compression system towards stall. By eliminating the large drop in pressure rise and flow and the hysteresis behavior, this strategy rejects disturbances that would otherwise cause the compression system to enter surge or performance limiting rotating stall. Thus, this control strategy ensures robust operability by desensitizing the compression system to disturbances.

It should be pointed out that practical implementation of this controller would be very difficult due to the noise associated with differentiating a measurement of the compressor mass flow. Crucial to successful implementation of the integrated controller is an appropriate estimation scheme for the time rate of change of compressor mass flow. Such a scheme was used in the experimental work presented here. Details of this approach will become available with the release of [7].

Experimental Validation

Experimental validation of the integrated rotating stall/surge control scheme was first performed successfully on the UTRC 3 stage low-speed rig [8]. In this section, results are presented from application of this control scheme to the three-stage high-speed compressor operating in the UTRC Closed Circuit Compressor Facility shown in Fig. 3.

This experimental validation of integrated rotating stall/surge control scheme is believed to be the first successful demonstration of active compressor stability control on full-scale engine hardware operating at representative speeds and pressure ratios. The geometry for the second of the three stages is given in Table 1 and is intended to be indicative of the other two stages. Compression system parameters are given in Table 2.

To evaluate the robustness of the control scheme, a second, lower reaction configuration was investigated. To interrogate

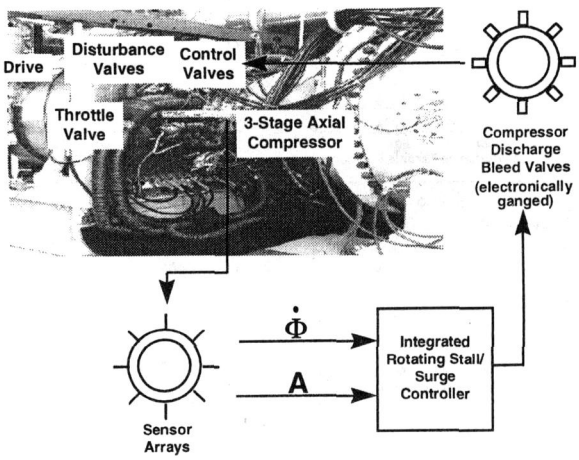

Fig. 3 RS3 compression system diagram

Table 1 Stage two compressor geometry

Parameter	Rotor	Stator
Chord (in.)	1.1	1.0
Aspect ratio	1.5	1.6
Baseline stagger angle (deg)	38	64
High-reaction stagger angle (deg)	33	74
Solidity	0.9	1.1

Table 2 Compression system design parameters

Compression system parameter	Value
Hub/tip radius ratio	0.9
Mean radius (in.)	12.7
Corrected flow (lb/sec)	22
Overall pressure ratio	1.5
Number of stages	3
Wheel speed (rpm)	0 to 6400

robustness further, the control scheme was evaluated in the presence of radial distortion screens installed at the compressor inlet. As will be shown, the performance of the operability-enhancing control scheme was insensitive to the described variations in system parameters.

Axially and circumferentially distributed time-resolved pressure measurements were recorded throughout the compression system. The pressure measurements were acquired at bandwidths of roughly ten times the rotor frequency. Steady-state measurements of compressor performance were also recorded. An array of eight, electronically ganged, high-bandwidth bleed valves were mounted at the compressor discharge to serve as the annulus averaged actuator for the active control strategy. Another array of four high-bandwidth bleed valves were mounted in the discharge plenum to impose impulsive disturbances on the compression system. Each valve is capable of discharging up to 1.5 percent of design compressor mass flow. The valves had a small signal bandwidth of approximately 600 Hz and full open/full close bandwidth of approximately 80 Hz. Since this is a closed-circuit compressor facility, the bleed air was reintroduced into the compressor flow loop downstream of the main throttle valve.

Bifurcation diagrams similar to those described in Fig. 1 were experimentally recorded from the RS3 rig. The bifurcation diagrams for the high-reaction configuration operating at 75 percent speed are shown in Fig. 4.

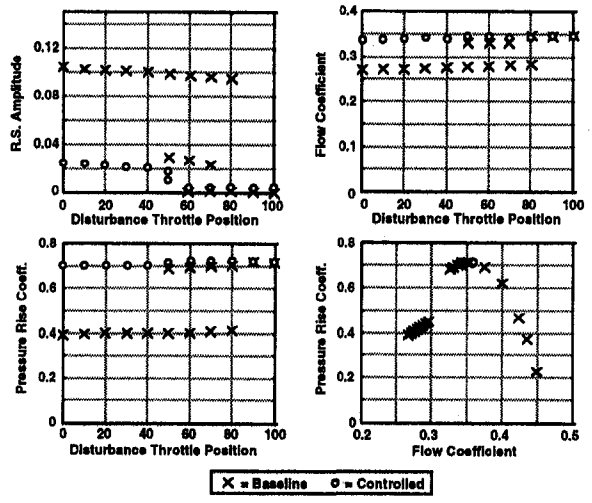

Fig. 4 High reaction, 75 percent speed experimental bifurcation diagrams

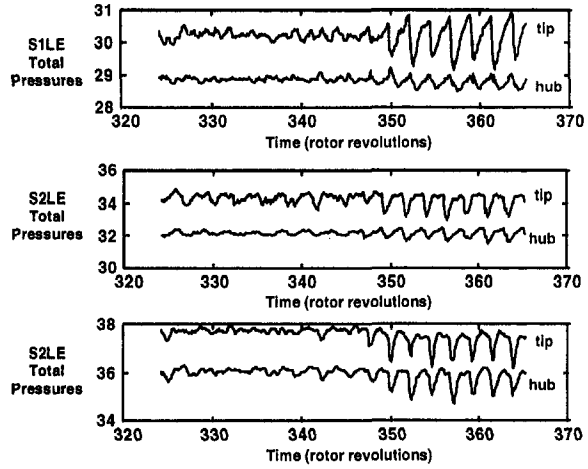

Fig. 5 High reaction, 75 percent speed mini-stall part-span behavior

Note that since these bifurcation diagrams are obtained experimentally, only stable equilibria and periodic orbits can be measured. Bifurcation diagrams are shown for the compression system without feedback control (×) and for the compression system with the integrated rotating stall/surge control strategy (○).

At 75 percent speed, the uncontrolled compression system did not exhibit surge. The bifurcation diagrams for such a system are qualitatively consistent with bifurcation diagrams predicted from the model shown in Fig. 1, however, without the periodic orbits. As can be seen in Fig. 4, with the exception of the details in the region very close to the stall inception point, this is essentially the case. As shown, the system enters large-amplitude rotating stall via a hard, subcritical, loss of stability and the system exhibits hysteresis. However, near the inception region, there is another branch of stable, relatively low-amplitude, rotating stall equilibria present in this system. This condition is termed "mini-stall," and upon further investigation of this condition it was found to involve stall cells with significant radial variations, as evidenced by the differences in the hub and tip total pressure signals at various stages in the compressor shown in Fig. 5. The mini-stall results in a slight reduction in the overall pressure ratio of the compressor. As shown in Fig. 6, the pressure rise reduction is confined to the third stage of the compressor. The bifurcation diagrams also indicate that there is hysteresis associated with the mini-stall, similar to that demonstrated by the full-span rotating stall. This phenomenon is not exhibited by the present form of the Moore–Greitzer model. Since the integrated rotating stall/surge controller was devel-

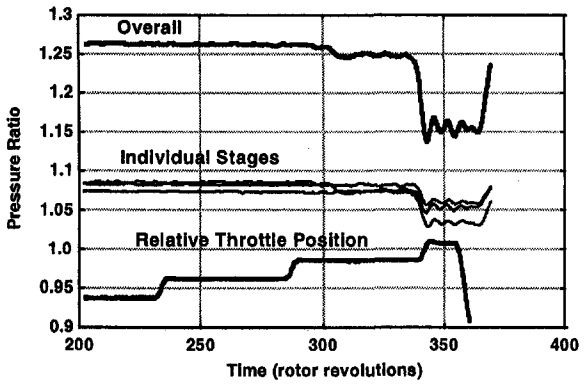

Fig. 6 High reaction, 75 percent speed mini-stall pressure ratio behavior

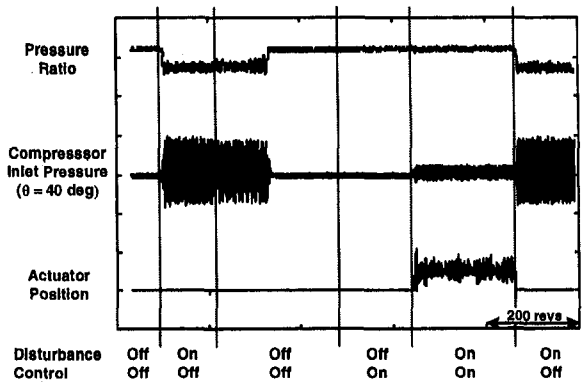

Fig. 7 High reaction, 75 percent speed experimental time traces

oped using this model, it was uncertain how the presence of mini-stall in the uncontrolled compression system would affect control system performance.

As shown in Fig. 4, with the integrated rotating stall/surge controller activated, the system exhibits reduced amplitude rotating stall when throttled beyond the peak of the flow versus pressure rise characteristic. The decrease in pressure rise associated with this rotating stall is significantly reduced relative to the full span rotating stall and is less than that associated with the mini-stall condition observed in the open loop system. In addition, the hysteresis associated with both the full-span rotating stall and the mini-stall has been eliminated. Remarkably, the controlled system behaves as predicted against the model despite the presence of the mini-stall phenomena. This provides an indication that this is a robust controller.

In addition to the bifurcation diagrams, time histories are useful in demonstrating the disturbance rejecting capability of this control strategy. Figure 7 shows time histories of (1) compressor pressure rise coefficient, (2) normalized static pressure at the compressor inlet at a fixed circumferential position, and (3) control actuator position for a disturbance scenario designed to illustrate the effect of the stability enhancing control strategy.

The traces begin with the system operating at a stable axisymmetric equilibrium point with the controller deactivated. A disturbance is then introduced to the system (i.e., the disturbance throttle is closed), throttling the system beyond the stability limit. The compression system enters performance limiting, large-amplitude rotating stall. The plenum pressure settles to a steady-state value, roughly 40 percent less than the peak pressure. The unsteadiness of the compressor inlet pressure at a single circumferential position indicates the presence of large-amplitude flow asymmetry (rotating stall) within the compressor. The disturbance is then removed, the system returns to stable axisymmetric operation after a delay of approximately 100 rotor revolutions, indicating that the disturbance step size barely clears the hysteresis loop of the rotating stall. The controller is then activated, and the system is subjected to the same disturbance, resulting in the compressor entering significantly reduced amplitude rotating stall, with a significantly reduced penalty in compressor pressure rise. The controller is then deactivated, and the system returns to large-amplitude rotating stall.

As shown in the time traces, the bleed valve maintains a nonzero offset when the system is subjected to disturbances that would cause the uncontrolled compression system to stall and/or surge. Although the level of this offset scales with the level of stability-threatening disturbances acting on the system, the controller is not merely avoiding the phenomenon by increasing throttle area to compensate for the disturbance. The controller is modifying the system dynamics resulting in operation at a point that could not be achieved without the feedback introduced by the control strategy.

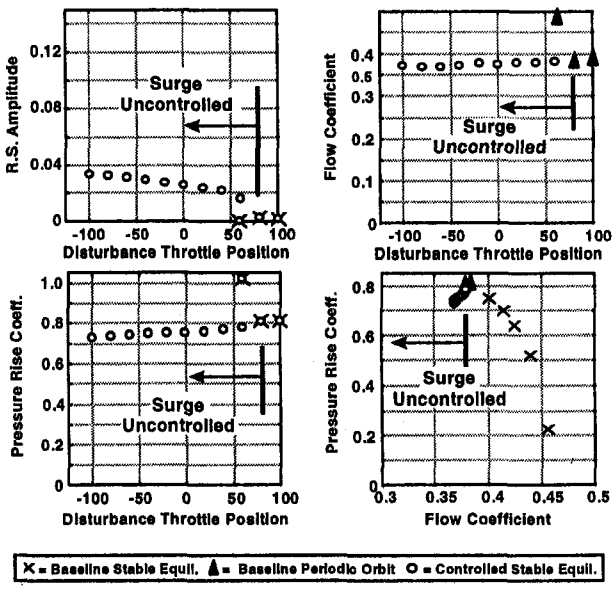

Fig. 8 High reaction, 100 percent speed experimental bifurcation diagrams

To study the effect of this control strategy in a compression system exhibiting open loop surge, the controller was also tested for this configuration operating at 100 percent speed. Experimentally measured bifurcation diagrams from the RS3 rig, high-reaction configuration operating at 100 percent speed are shown in Fig. 8. Once again, bifurcation diagrams are shown for the compression system without feedback control (x, Δ) and for the compression system with the integrated rotating stall/surge control strategy ($\circ$). The maximum values of the variables achieved during the surge limit cycle are denoted by an Δ. However, due to the violent nature of the surge oscillations, rig safety issues prevented the full mapping of the locus of periodic orbits (surge). Thus, the uncontrolled bifurcation diagrams consist of the locus of stable, axisymmetric equilibria and the surge limit cycle encountered immediately beyond the stability boundary. The bifurcation diagrams for the controlled system look identical to those for the controlled system bifurcation diagrams operating at 75 percent speed. Thus, in addition transforming the nature of the bifurcation, the control strategy eliminated surge.

A further demonstration of integrated control of rotating stall and surge in the high reaction configuration of the RS3 rig at 100 percent speed is given by the time traces in Fig. 9.

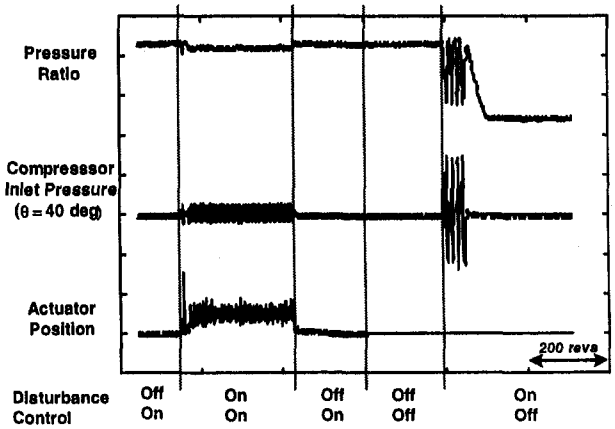

Fig. 9 High reaction, 100 percent speed experimental time traces

In this case, the time traces begin with the system operating at a stable axisymmetric equilibrium point with the controller activated. A disturbance is then introduced to the system that throttles the system beyond the stability limit, and the system enters a reduced amplitude rotating stall, maintaining 96 percent of peak compressor pressure rise. When the disturbance is removed, the system returns to stable axisymmetric operation. Next, the controller is deactivated, and the same disturbance is introduced once again, pushing the system into a surge limit cycle and activating the rig safety systems.

To establish the robustness of the integrated rotating stall/surge controller to variations in compressor aerodynamics, a lower reaction configuration was evaluated. Experimentally measured bifurcation diagrams from the RS3 rig, low-reaction configuration operating at 75 percent speed are shown in Fig. 10 for the system with and without control.

As shown, this build does not exhibit the mini-stall phenomenon in the uncontrolled system, and the compression system does not exhibit surge at this speed. Thus, the bifurcation diagrams are consistent with those predicted by the Moore–Greitzer model when surge limit cycles are not present. With the integrated rotating stall/surge controller activated, it is evident that the operability enhancement provided by this control strategy is achieved for this lower reaction configuration as well. At 100 percent speed for the low reaction configuration, comparable results to those for the high-reaction configuration at 100 percent speed are also achievable. The comparable results achieved with the integrated rotating stall/surge controller for these two configurations speaks directly to robustness of this control strategy. This is further illustrated by the fact that the three-dimensional mini-stall phenomena, which was not considered in the design of this control strategy, is present without control in one configuration and not in the other. Upon further investigation of data from part-span probes, it was found that with the controller activated in both the high and low-reaction configurations, the low-amplitude rotating stall achieved by the controller did involve three-dimensional part-span behaviors. Thus, the controller was able to achieve operation of the compressor in a condition of very low-amplitude mini-stall regardless of whether the compressor exhibited similar phenomena without control.

A final test of the robustness of the integrated rotating stall/surge controller was performed by introducing a radial inlet distortion screen in front of the low-reaction compressor configuration to simulate the effect of deterioration of the compressor and determine how the integrated rotating stall/surge controller performs in the presence of this disturbance. Figure 11 shows the experimentally measured compressor performance map for four situations with the low reaction configuration at 100 percent speed: (Δ) uncontrolled and undeteriorated, (×) uncontrolled and deteriorated, (○) controlled and undeteriorated; and (+) controlled and deteriorated.

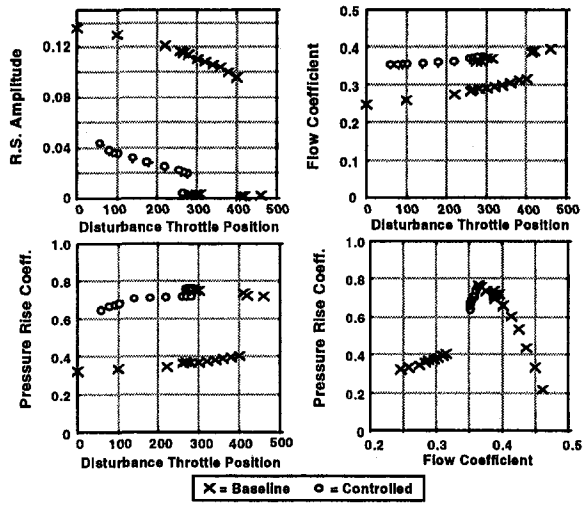

Fig. 10 Low reaction, 75 percent speed experimental bifurcation diagrams

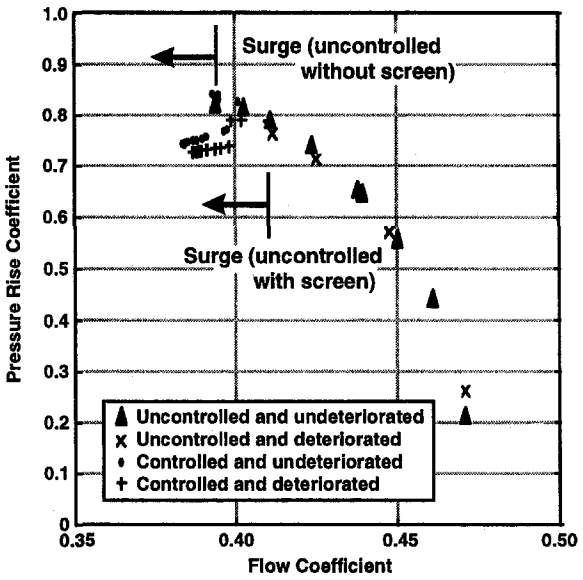

Fig. 11 Low-reaction, 100 percent speed deterioration effects

As can be seen, without control the undeteriorated compressor stalls at a lower flow and higher pressure ratio than the deteriorated compressor as would be expected. With the integrated rotating stall/surge controller, when the undeteriorated compressor reaches the uncontrolled stall point, it falls into a low-amplitude rotating stall (as opposed to surge) with a small drop in pressure ratio, and a measurable operating range increase in terms of flow coefficient is achieved. With control on the deteriorated compressor, the operating range in terms of flow coefficient of the compressor is increased both before and after the systems enters low-amplitude rotating stall with its associated small drop in pressure ratio. Furthermore, when the performance characteristics of the undeteriorated and deteriorated compressors with control are compared, it can be seen that they are very similar, unlike the case without control, and the controller seems to have desensitized the operability characteristics of the compressor to the presence of deterioration in the compressor.

Conclusions

A previously developed nonlinear control strategy that achieves simultaneous active control of rotating stall and surge was experimentally validated on a high-speed three-stage axial flow compression system with operating parameters representative of modern aeroengines. The controller was experimentally validated for two compressor builds, showing significant operability benefits for both configurations. Furthermore, these benefits were not reduced by the presence of an unmodeled reduced amplitude rotating stall condition. The robustness of this controller was also demonstrated by introducing a radial distortion screen at the inlet of the compressor. The controller was shown to desensitize the operability characteristics of the compressor to the presence of radial distortion. The validation of the integrated rotating stall/surge control scheme on full-scale engine hardware operating at representative speeds and pressure ratios is believed to be a significant step toward utilizing active control to achieve operability enhancement in modern aeroengines.

Acknowledgments

The authors would like acknowledge the many people who contributed to this research, with a special thanks to: Mike Carey, Gavin Hendricks, Phil Lavrich, Mark Myers, Dan Pfau, Jayant Sabnis, Bill Sisson, Karen Teerlinck, and Jim Wilkinson.

References

1 O. O. Badmus, S. Chowdhury, K. M. Eveker, and C. N. Nett, "Control-oriented high-frequency turbomachinery modeling: Single-stage compression system ID model," ASME JOURNAL OF TURBOMACHINERY, Vol. 117, 1995, pp. 47–61.

2 O. O. Badmus, S. Chowdhury, K. M. Eveker, C. N. Nett, and C. J. Rivera, "A simplified approach for control of rotating stall, Parts I and II," AIAA Paper No. 93-2229 and 93-2234, 1993.

3 O. O. Badmus, C. N. Nett, and F. J. Schork, "An integrated full-range surge control/rotating stall avoidance compressor control system," *Proc. of the 1991 American Control Conference,* June 1991.

4 I. J. Day, "Active suppression of rotating stall and surge in axial compressors," ASME JOURNAL OF TURBOMACHINERY, Vol. 115, No. 1., 1993.

5 A. H. Epstein, J. E. Ffowcs-Williams, and E. M. Greitzer, "Active suppression of aerodynamic instabilities in turbomachines," *J. Propulsion and Power,* 5(2):204–211, 1989.

6 K. M. Eveker and C. N. Nett, "Control of compression system surge and rotating stall: A laboratory-based "hands-on" introduction," *Proc. 1993 American Control Conference,* June 1993.

7 K. M. Eveker, D. L. Gysling, C. N. Nett, and H. O. Wang, "Rotating Stall and Surge Control," U. S. Patent Application, U. S. Serial Number 08355763, 1994.

8 K. M. Eveker, D. L. Gysling, C. N. Nett, and O. P. Sharma, "Integrated Control of Rotating Stall and Surge in Aeroengines," *Proc. 1995 SPIE Conference on Sensing, Actuation, and Control in Aeropropulsion,* Apr. 1995.

9 J. E. Ffowcs-Williams and W. R. Graham, "Engine demonstration of active surge control," ASME Paper No. 90-GT-224, 1990.

10 J. E. Ffowcs-Williams and X. Y. Huang, "Active stabilization of compressor surge," *J. Fluid Mech.,* 204:245–262, July 1989.

11 E. M. Greitzer, "Review—axial compressor stall phenomena," ASME *Journal of Fluids Engineering,* 102:134–151, 1980.

12 E. M. Greitzer, "The stability of pumping systems—The 1980 Freeman Scholar Lecture," ASME *Journal of Fluids Engineering,* 103:193–242, 1981.

13 E. M. Greitzer, "Surge and Rotating Stall in Axial Flow Compressors," ASME *Journal of Engineering for Power,* Vol. 98, 1976.

14 D. L. Gysling, J. Dugundji, A. H. Epstein, and E. M. Greitzer, "Dynamic control of centrifugal compressor surge using tailored structures," ASME JOURNAL OF TURBOMACHINERY, Vol. 113, 1991, pp. 710–712.

15 D. L. Gysling and E. M. Greitzer, "Dynamics Control of Rotating Stall in Axial Flow Compressors Using Aeromechanical Feedback," ASME JOURNAL OF TURBOMACHINERY, Vol. 117, 1995, pp. 307–319.

16 L. Harris and H. Spang III, "Compressor modeling and active control of stall/surge," *Proc. 1991 American Control Conference,* 1991.

17 D. C. Liaw and E. H. Abed, "Stability analysis and control of rotating stall," *Proc. 2nd IFAC Nonlinear Control Systems Design Symposium,* June 1992.

18 A. I. Mees, "A plain man's guide to bifurcations," *IEEE Transactions on Circuits and Systems,* CAS-30:512–517, No. 8, 1983.

19 J. P. Paduano, A. H. Epstein, L. Valavani, J., P. Longley, E. M. Greitzer, and G. R. Guennette, "Active Control of Rotating Stall in a Low Speed Compressor," ASME JOURNAL OF TURBOMACHINERY, Vol. 115, 1993, pp. 48–56.

20 J. E. Pinsley, G. R. Guenette, A. H. Epstein and E. M. Greitzer, "Active stabilization of centrifugal compressor surge," ASME JOURNAL OF TURBOMACHINERY, Vol. 113, 1991, pp. 723–732.

21 J. S. Simon and L. Valavani, "A Lyapunov based nonlinear control scheme for stabilizing a basic compression system using a close-coupled valve," *Proc. 1991 American Control Conference,* 1991.

ERRATA

To the paper "Heat Transfer Measurements to a Gas Turbine Cooling Passage With Inclined Ribs," by Z. Wang, P. T. Ireland, S. T. Kohler, and J. W. Chew, published in the January 1998 issue of the ASME JOURNAL OF TURBOMACHINERY, Vol. 120, pp. 63–69:

Equation (7) was printed incorrectly in the paper. The correct version appears below:

$$\frac{T(0, t) - T_o}{T_g - T_o} = 1 + h\left(\frac{\exp(a^2t)\ \text{erfc}\ (a\sqrt{t})}{\beta a(a - b)} + \frac{\exp(b^2t)\ \text{erfc}\ (b\sqrt{t})}{\beta b(b - a)}\right) \tag{7}$$

Also note that in Eq. (6), $\frac{hl}{2k_c} << 1$ and has been eliminated.

Comparison Between Complete Hilbert Transform and Simplified Solutions of the Moore Rotating Stall Model

G. L. Arnulfi
University of Udine,
Dipartimento di Energetica e Macchine,
Udine, Italy

F. L. Ghiglino

A. F. Massardo
Mem. ASME

University of Genova,
Istituto di Macchine e Sistemi Energetici,
Genova, Italy

The main objective of this work is the analysis and the comparison between different methods utilized to solve the Moore rotating stall model. To date only simplified relations between the axial flow perturbation g and the transverse one h have been utilized and presented in literature, such as $h' = -g$ or the truncated Fourier series. On the contrary, in this paper the accurate relation given by the Hilbert Transform is utilized, and to improve the numerical stability of the method, a new expression of the first derivative of transverse flow coefficient perturbation is proposed and utilized. A complete and detailed comparison between the results of the simplified methods and the solution proposed here is presented. This comparison is extended to a wide range of geometric and physical compressor parameters, and it allows the accuracy of simplified approaches to be tested. Finally, a correlative approach estimating overall rotating stall effects based on the complete solution proposed here is presented. It allows rotating stall influence to be quickly and easily taken into account in several axial compressor areas (design, optimization, active control, etc.).

Introduction

The importance of the simulation of rotating stall and the evaluation of the influence of that phenomenon on multistage axial compressors performance are well known and have been studied by several authors (e.g., Greitzer, 1976; Moore, 1984; Day, 1993; Cumpsty and Greitzer, 1982). In literature various models are proposed to model rotating stall phenomenon, but the Moore model seems to provide the most complete approach; it allows the shape of the stall cell, the propagation speed, and the actual performance curve to be determined, and it only deals with compressor data that can be easily obtained.

In literature only simplified solutions of this model have been presented. The most commonly used relation correlating the axial g and transverse h flow perturbations is $h' = -g$ proposed by Moore (1984), while some authors utilize a truncated form of the corresponding Fourier series (McCaughan, 1989).

In this work, the solution of the rotating stall model proposed by Moore is carried out utilizing the complete set of equations without additional simplifying hypotheses for the relationship between h and g. In this way the complete Hilbert transform of the perturbations is taken into account in the method presented here. To improve the stability and the reliability of the proposed solution, a new expression for the first derivative of transverse flow perturbation (h') has been proposed and extensively utilized.

Based on the method described here, a complete in-depth comparison between the accurate and the simplified results is made for a wide range of compressor configurations. In this way, the accuracy of the different simplified relations is clearly stated.

Since the resolution of the Moore model including Hilbert transform is time consuming, the results of the accurate calculation have been utilized to develop a new correlative approach for the evaluation of the overall effects of rotating stall: propagation speed F and alterations δ of the compressor axisymmetric performance curve. The correlation, which is, in most cases, as accurate as traditional simplified models, might be useful when quick a response is needed, such as in the compressor control field or compressor design optimization problem.

Contributed by the International Gas Turbine Institute and presented at the 41st International Gas Turbine and Aeroengine Congress and Exhibition, Birmingham, United Kingdom, June 10–13, 1996. Manuscript received at ASME Headquarters February 1996. Paper No. 96-GT-140. Associate Technical Editor: J. N. Shinn.

Mathematical and Numerical Model

In this study, we adopt the mathematical approach to model rotating stall proposed by Moore (1984); Moore introduced four main hypotheses to get the final form of his model:

1 incompressible flow through the compressor,
2 irrotational flow in the inlet duct;
3 negligible radial effects in the flow;
4 negligible losses at the IGV entrance, due to the flow angular disturbance present at the inlet.

Moreover rotating stall is studied in a moving frame, rotating with the stall cell; in this way the rotating stall in the turbomachine is steady.

The final equations representing rotating stall are:

$$\delta = [\psi(\varphi) - \psi(\Phi)] - \lambda \cdot g'(\vartheta) + e \cdot F \cdot h(\vartheta) \qquad (1)$$

where

$$\delta = \Psi(\Phi) - \psi(\Phi) \quad \text{and} \quad \lambda = s/2 - F(s + v);$$

$$h(\vartheta) = -\frac{1}{\pi} \int_{-\infty}^{+\infty} \frac{g(\xi)}{\vartheta - \xi} \, d\xi \qquad (2)$$

Equation (1) represents the sum of pressure rise contribution of every component of the compressor (i.e., inlet duct, inlet guide vanes, stages, etc.), and Eq. (2) gives the relation existing between the axial flow perturbation g and the transverse one h (Takata and Nagano, 1972). In addition, it is imposed that the mean value of g and h must be zero. In this way δ is the unknown to calculate, e, s and v are fixed parameters, and F, g, and h are variables to iterate.

In Eq. (1) the axisymmetric characteristic curve ψ is present; this curve represents the compressor characteristic in the ab-

sence of rotating stall for every mass-flow condition. As suggested by Moore (1984), the axisymmetric characteristic can be obtained in an experimental way by utilizing high-loss screens at the inlet and outlet of the turbomachine to eliminate flow distortion. In this study, the S-shaped cubic curve proposed by Koff and Greitzer (1984) is utilized.

Equation (1) is usually derived with respect to the circumferential coordinate ϑ:

$$0 = \left.\frac{d\psi}{d\varphi}\right|_{\Phi+g} \cdot g'(\vartheta) - \lambda \cdot g''(\vartheta) + e \cdot F \cdot h'(\vartheta) \qquad (3)$$

Since g and h for physical reasons are periodic functions, Eq. (2) can be written as

$$h(\vartheta) = -\frac{1}{\pi}\int_0^{2\pi} \frac{dg(\xi)}{d\xi} \ln\left|\sin\frac{\xi-\vartheta}{2}\right| d\xi \qquad (4)$$

The use of Eq. (4) can be cumbersome, so many proposals for simplified forms of g–h relation were made. Starting from the potential of the flow perturbation developed as a Fourier series (note that the potential exists since the flow is irrotational and incompressible upstream)

$$P(x, \vartheta) = \sum_{n=1}^{+\infty} \frac{1}{n} e^{nx}(a_n \sin n\vartheta + b_n \cos n\vartheta) \qquad (5a)$$

g and h are obtained as

$$g(\vartheta) = \left.\frac{\partial P}{\partial x}\right|_{x=0} = \sum_{n=1}^{+\infty} (a_n \sin n\vartheta + b_n \cos n\vartheta) \qquad (5b)$$

$$h(\vartheta) = \left.\frac{\partial P}{\partial \vartheta}\right|_{x=0} = \sum_{n=1}^{+\infty} (a_n \cos n\vartheta - b_n \sin n\vartheta) \qquad (5c)$$

Many authors use Eqs. (5b) and (5c) truncated at the nth term to calculate the rotating stall phenomenon.

Moore himself proposed a simplified relation for his model:

$$h'(\vartheta) = -g(\vartheta) \qquad (6)$$

Equation (6) is equivalent to Eq. (4) only if g is a purely harmonic function. Equation (6) is true for the first terms of Fourier series (Eq. (5)), but it can also relate functions that are not necessarily truncated Fourier series (Moore, 1984, p. 328, Fig. 2). In this paper for the simplified solution g is not obtained by Eq. (5) with $n = 1$.

Here the complete Hilbert transform relation is used to avoid the approximation given by Eqs. (5a), (5b), and (6), but in Eq. (3) the first derivative of h is needed:

$$h'(\vartheta) = \frac{dh(\vartheta)}{d\vartheta} = -\frac{1}{\pi}\frac{d}{d\vartheta}\left(\int_0^{2\pi} \frac{dg(\xi)}{d\xi} \ln\left|\sin\frac{\xi-\vartheta}{2}\right| d\xi\right) \qquad (7)$$

In this form h' is numerically difficult to treat; in fact in some zones the integral function presents very steep slopes, and so the derivative shows singular values. To avoid the influence of the singular point a new expression for h' is obtained by substitution in Eq. (7) of:

$$\eta = \frac{\vartheta-\xi}{2} \quad G(\vartheta - 2\eta) = \frac{dg(\xi)}{d\xi} \qquad (8)$$

and dividing into two parts the integral to avoid the singular value of the integrand function for $\xi = \vartheta$

$$h'(\vartheta) = -\frac{1}{\pi}\left[-2\frac{d}{d\vartheta}\int_{\vartheta/2}^{\vartheta/2-\pi} G(\vartheta - 2\eta) \ln|\sin\eta|\, d\eta\right] \qquad (9a)$$

$$h'(\vartheta) \cong -\frac{1}{\pi}\left\{2\frac{d}{d\vartheta}\left[\int_{\vartheta/2-\pi}^{-\epsilon} G(\vartheta - 2\eta) \ln|\sin\eta|\, d\eta + \int_{\epsilon}^{\vartheta/2} G(\vartheta - 2\eta) \ln|\sin\eta|\, d\eta\right]\right\} \qquad (9b)$$

and since the integrand functions in Eq. (9b) are bounded and continuous, and ϵ is so small that the neglected areas are nearly zero, letting

$$J(\eta, \vartheta) = G(\vartheta - 2\eta) \ln|\sin\eta| \qquad (10)$$

Eq. (9b) becomes

$$h'(\vartheta) = -\frac{1}{\pi}\left\{2\left[\int_{\vartheta/2-\pi}^{-\epsilon} \frac{\partial J}{\partial \vartheta}\, d\eta - \frac{1}{2} J\left(\frac{\vartheta}{2} - \pi, \vartheta\right) + \int_{\epsilon}^{\vartheta/2} \frac{\partial J}{\partial \vartheta}\, d\eta + \frac{1}{2} J\left(\frac{\vartheta}{2}, \vartheta\right)\right]\right\} \qquad (11)$$

Since the function J is periodic of period 2π, if only one stall cell exists; substituting again Eq. (8) and Eq. (10) into Eq. (11) one obtains:

$$h'(\vartheta) = -\frac{1}{\pi}\left(\int_0^{2\pi} \frac{d^2 g(\xi)}{d\xi^2} \ln\left|\sin\frac{\xi-\vartheta}{2}\right| d\xi\right) \qquad (12)$$

The second derivative of the axial perturbation g is calculated

Nomenclature

A = amplitude of harmonics
AR = compressor characteristic aspect ratio
E = energy coefficient
e = exit duct lag parameter
F = stall propagation speed and wheel speed ratio
f = frequency
g = axial flow coefficient perturbation $= \varphi - \Phi$
h = transverse flow coefficient perturbation
N = number of results
P = flow perturbation potential
R = regression coefficient
s = compressor stages lag parameter
v = guide vanes lag parameter
x = axial coordinate
δ = difference real/axisymmetric compressor curve
ϑ = circumferential coordinate
λ = overall lag parameter
Φ = average flow coefficient
φ = flow coefficient
Ψ = pressure coefficient
ψ = axisymmetric pressure coefficient

Superscripts and subscripts

a = accurate solution
c = correlative model
n = number of harmonics
p = compressor characteristic peak point
s = simplified solution
v = compressor characteristic valley point
0 = referred to standard condition
$'$ = ϑ derivative
$*$ = normalized with respect to peak-to-valley value
$**$ = normalized with respect to mean g^2 value

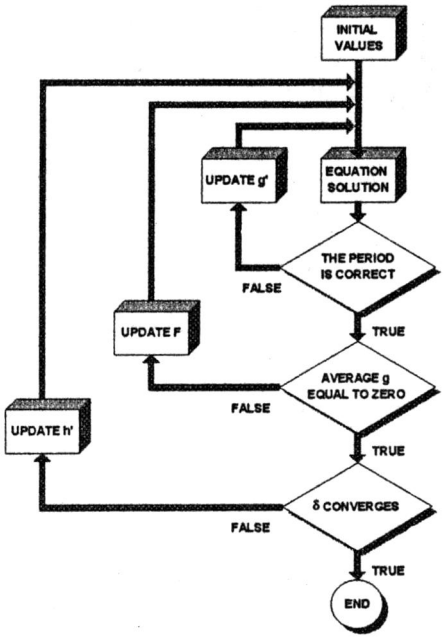

Fig. 1 Flow chart of the accurate model

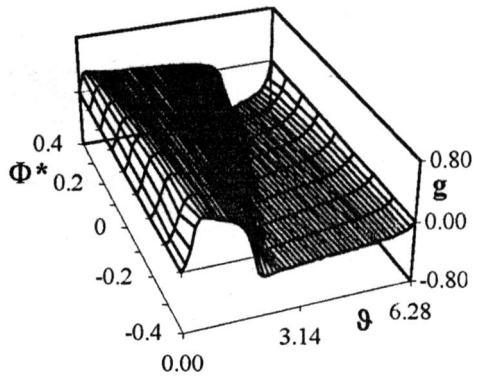

Fig. 2(*a*) Influence of Φ* and ϑ on *g* behavior obtained with accurate solution

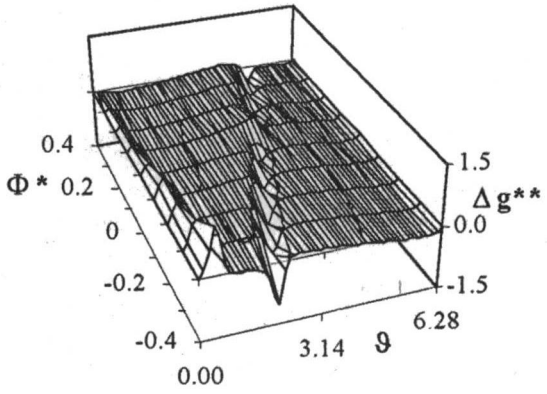

Fig. 2(*b*) Influence of Φ* and ϑ on the normalized difference of *g* function (accurate and simplified solution)

from the previous iteration; the first one utilizes the Moore simplified relation (Eq. (6)), as suggested by Saju (1985). Utilizing Eq. (12), h' presents a continuous behavior without singular values, increasing the convergence speed of the solution.

Numerically the problem is the solution of a nonlinear second-order ordinary differential equation (a boundary value one), solved by a shooting method, using an explicit fourth-order Runge–Kutta solver with Simpson constants and variable step.

The flow chart of the accurate solution code is shown in Fig. 1. The inner loop controls the period value changing g' at $\vartheta = 0$ by the bisection method (periodicity is intrinsic with the definition of g). The second loop checks whether the integral of g is nearly zero; if not, the value of the stall cell speed propagation F is changed by the secant method. The external loop controls the value of δ (difference between the real and the axisymmetric compressor characteristic): h' is updated by the recursive method until the differences of δ values of the last two calculations are inside a prescribed tolerance.

The accurate solution is obtained by starting from the simplified one; this implies that some numerical problems can arise in the internal loop if the exact value of the period is not quickly reached, because of matching difficulties with the simplified solution which is, for one stall cell, a periodic function of period 2π. These numerical problems grow for high characteristic aspect ratio AR (see Eq. (17)).

The code, written in Fortran language, runs on a Pentium 90 PC, and it takes about 20 seconds to get the simplified solution and 100 times more for the complete one.

Discussion of Results

Utilizing the model described and the code developed, the behavior of axial multistage compressors, operating under rotating stall conditions, is evaluated. The lag parameters are evaluated with the method given by Hynes et al. (1985), while the axisymmetric curve and the mass flow rate are normalized to make possible an easy comparison among different compressors in the following way:

$$\Phi^* = \frac{\Phi - 0.5\cdot(\Phi_p + \Phi_v)}{\Phi_p - \Phi_v}; \quad \Psi^* = \frac{\Psi - 0.5\cdot(\psi_p + \psi_v)}{\psi_p - \psi_v} \tag{13}$$

All the flow and characteristic coefficients are calculated both with the simplified Moore relation (Eq. (6)) and with the accurate one (Eq. (4)) given by the Hilbert transform. This allows a quick comparison in every flow condition to be obtained.

The first comparison between the two methods is carried out for the axial flow perturbation in Fig. 2, where the configuration of the considered turbomachine is shown in Table 1 (standard configuration). The trend of g versus Φ^* and ϑ is shown in Fig. 2(a), while the difference between the accurate and simplified solutions is shown in Fig. 2(b).

In this way, it is easy to understand how accurate the simplified method is. The gap between the two solutions for g is normalized with respect to a sort of "mean" axial perturbation coefficient

$$\sqrt{2E} = \sqrt{\overline{g^2}} \tag{14}$$

where E is the energy related to the stall cell and is defined as:

$$E = \frac{1}{4\pi}\int_0^{2\pi} g^2(\vartheta)\,d\vartheta \tag{15}$$

and

$$\Delta g^{**}(\vartheta) = \frac{g_a(\vartheta) - g_s(\vartheta)}{\sqrt{2E}} \tag{16a}$$

As shown in Fig. 2, Δg^{**} is not large, except near the peaks (maximum and minimum) of the g function where the variation is approximately 100 percent. This is not negligible, especially

Table 1 Standard compressor parameters

Φp-Φv	AR	v	s	e
0.45	0.7	0.15	1.4	1.75

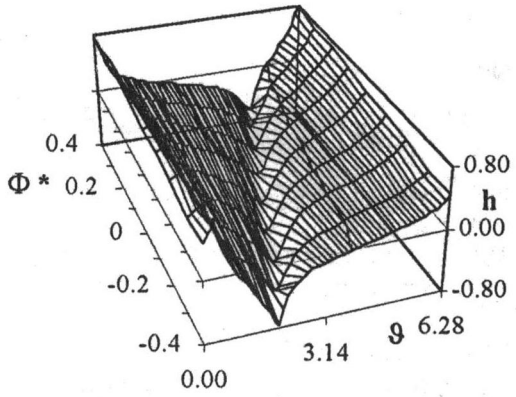

Fig. 3(*a*) Influence of Φ^* and ϑ on h behavior obtained with accurate solution

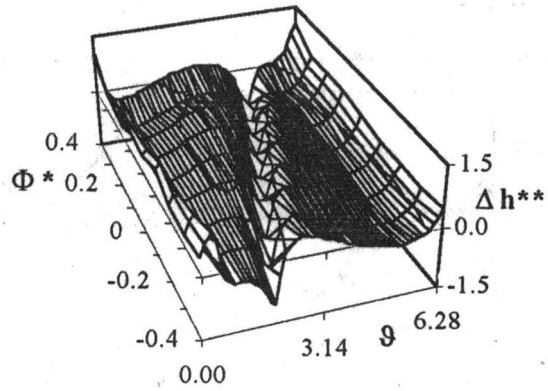

Fig. 3(*b*) Influence of Φ^* and ϑ on the normalized difference of h function (accurate and simplified solution)

for the zone where g is minimum, in fact there is the possibility of falling in a back-flow zone, while the underestimated values given by the Moore simplification do not represent this flow behavior, as already discussed by Arnulfi et al. (1995).

The same analysis is done for the transverse flow perturbation shown in Fig. 3(*a*) and the difference between the two solutions shown in Fig. 3(*b*). Again the error is normalized as before and now one obtains:

$$\Delta h^{**}(\vartheta) = \frac{h_a(\vartheta) - h_s(\vartheta)}{\sqrt{2E}} \qquad (16b)$$

In this case the gap between the two solutions is large for every operating condition and, since h gives information about the stall cell propagation around the annulus and the way in which flow goes in and out from the stall condition, this is not a negligible detail.

To complete this first part of the comparison, the behavior of the energy related to the stall cell changing with the mass flow rate Φ^* is shown in Fig. 4. Both the simplified and the

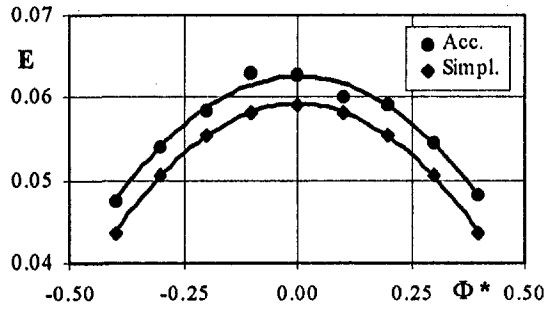

Fig. 4 Comparison between simplified and accurate stall cell energy

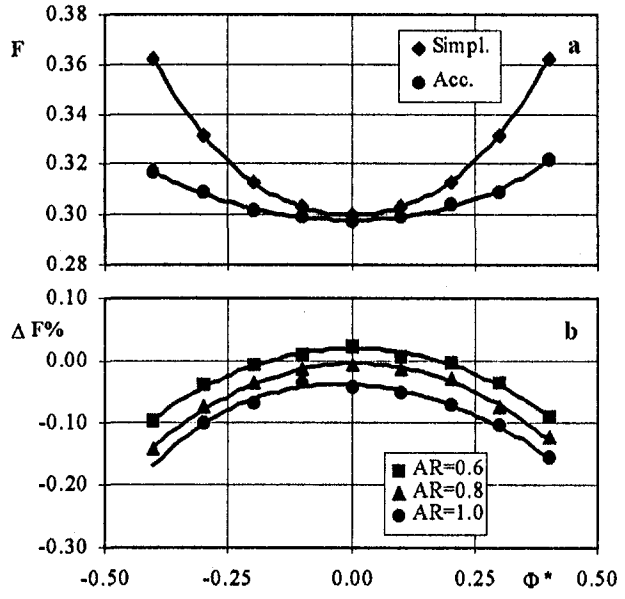

Fig. 5 Comparison between simplified and accurate stall cell speed: (*a*) standard condition; (*b*) AR influence

accurate solution present the same trend: in fact, as expected, this energy decreases as the compressor approaches stable operating or back flow conditions, where the stall cell vanishes. On the contrary, the simplified solution underestimates the accurate values with an error of about 7 percent, that is why the stall cell shape calculated by the Moore relation $h' = -g$ is smoother than the shape calculated by the Hilbert transform, as shown in Fig. 2.

The comparison is then carried out on the overall characteristic of rotating stall. The nondimensional propagation speed of the stall cell versus Φ^* for the two methods is shown in Fig. 5(*a*), one can see that the stall cell moves, around the annulus, more quickly as it approaches nearer and nearer to the negative slope legs of the characteristic ($\Phi^* \cong \pm 0.5$). Moreover, the curve obtained by the Moore relation overestimates the one obtained by the Hilbert transform.

The difference between the accurate and the simplified solution, normalized with respect to the accurate one, is shown in Fig. 5(*b*) for several aspect ratio values AR, defined as:

$$AR = \frac{\Psi_p - \Psi_v}{\Phi_p - \Phi_v} \qquad (17)$$

The parameter AR is representative of the compressor curve steepness, so when AR grows, the compressor characteristic becomes steeper. One can see that the gap for F between the two solutions increases as AR increases and as one approaches the recovery or back flow zone; this gap can reach 15 percent and more.

The behavior of the coefficient δ^*, the difference between the stalled and the axisymmetric characteristic, is reported in Fig. 6(*a*). δ^* is a decreasing function with Φ^*, becoming negative for positive values of Φ^*; this means that the stalled curve is always less steep than the axisymmetric one.

The difference between the two analyzed methods is shown in Fig. 6(*b*) for different AR values. It is clear that the simplified solution overestimates the accurate one for every mass flow rate; this difference increases as the compressor goes toward stable or back flow condition, while it decreases for high values of the AR parameter.

Since the coefficient δ^* is referred to the overall outlet conditions of the compressor, it is important to know the influence of the single parts of the machine and the influence of the two methods of solution during the calculation. So the contributions

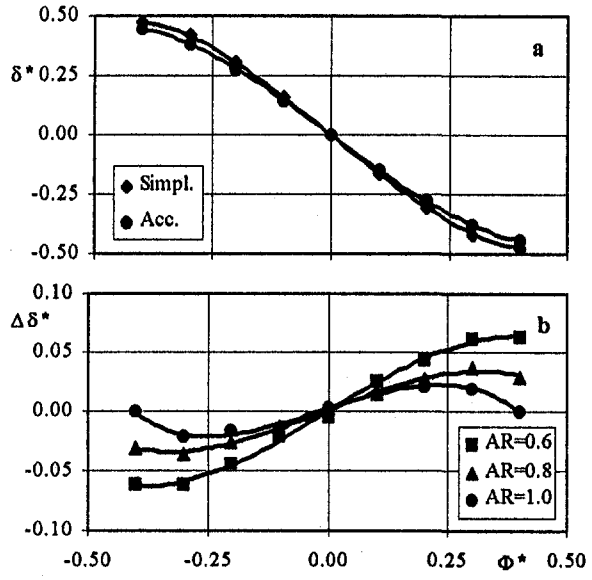

Fig. 6 Comparison between simplified and accurate δ^* values: (*a*) standard condition; (*b*) AR influence

of the single compressor components for pressure rise, for three different values of Φ^*, are shown in Fig. 7. One can observe that through the inlet duct there is a pressure drop due to flow acceleration and pressure losses, except for the circumferential stalled portion where the pressure of course does not decrease. The IGV also shows a slight pressure drop, but within two narrow zones there is a pressure rise due to the crossing of the entrance plane of the IGV and due to inertial effects, a function of h^2. The compressor stages of course provide a pressure increase except for the stalled blades that cannot operate well. Finally, in the outlet duct the circumferential pressure trend is governed by the boundary conditions: stage outlet and downstream plenum conditions. The pressure rise of the single compressor components calculated by the Hilbert transform is shown in Fig. 7(a), while the ones calculated by the simplified relation are shown in Fig. 7(b).

The results obtained by the two methods have the same qualitative trend, but there are strong differences for the maximum and minimum values, and the corresponding gradient of the pressure functions; this kind of behavior was already shown by g and h in Figs. 2 and 3. For this reason, using the simplified approach, information on sudden pressure drops or pressure increases along ϑ could be lost, as can be observed for all the components here analyzed and especially for the inlet duct and the compressor stages.

A parametric analysis of the overall characteristic of the rotating stall phenomenon is carried out and shown in Fig. 8 to complete the study on the accurate solution. One can see in Fig. 8(b) and 8(c) that propagation speed is quite sensitive to stage and exit duct geometry. In fact F increases as s increases and e decreases, and slightly decreases when the IGV lag parameter v grows (Fig. 8(a)). The characteristic curve of the compressor (represented by gap δ^*) and the cell shape (represented by the energy E) are not influenced by the lag parameters, but a slight change, if the exit geometry varies (e), is noted (Fig. 8(c)).

FFT Analysis. Many authors utilize a truncated form of the Fourier series of g and h (see Eq. 5(b) and Eq. 5(c)) to calculate the rotating stall effects. For this reason an FFT analysis of the accurate results is made, then a comparison between g and h calculated by the Hilbert transform and g and h calculated using the first 10, 15, and 20 harmonics obtained by the FFT analysis, is carried out. This comparison is shown in Fig. 9 for two different mass flow rate conditions, the gap is normalized in the same way as Fig. 2(b) and 3(b), but this time

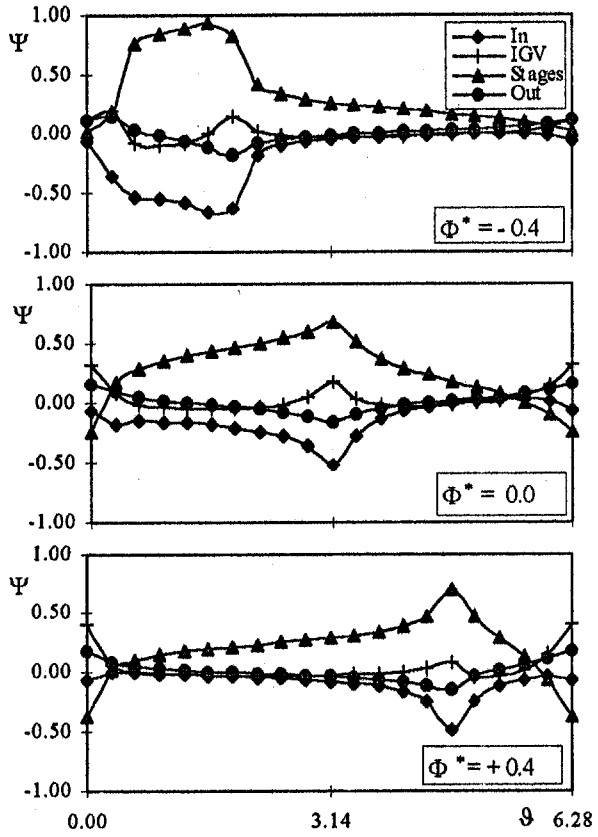

Fig. 7(*a*) Pressure rise of the single components obtained by the accurate method (standard condition)

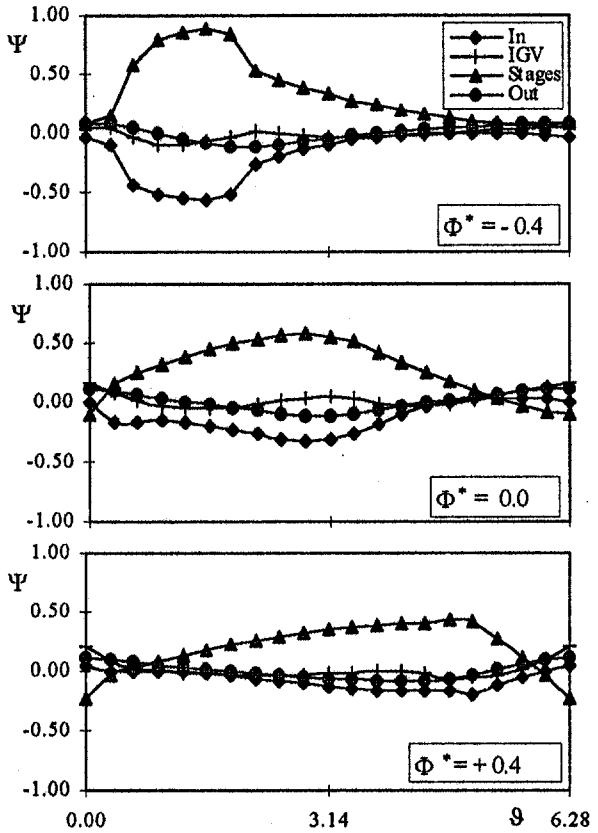

Fig. 7(*b*) Pressure rise of the single components obtained by the simplified method (standard condition)

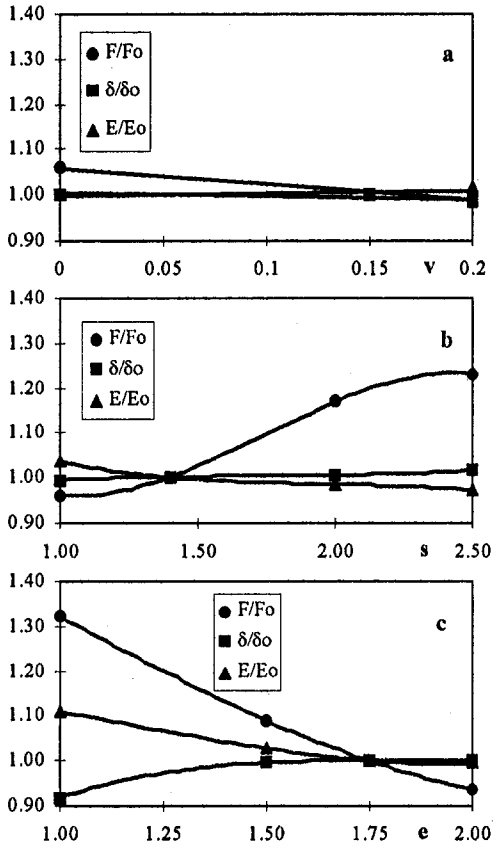

Fig. 8 Parametric analysis ($\Phi^* = -0.2$): (*a*) influence of IGV lag parameter; (*b*) influence of stages lag parameter; (*c*) influence of outlet duct parameter

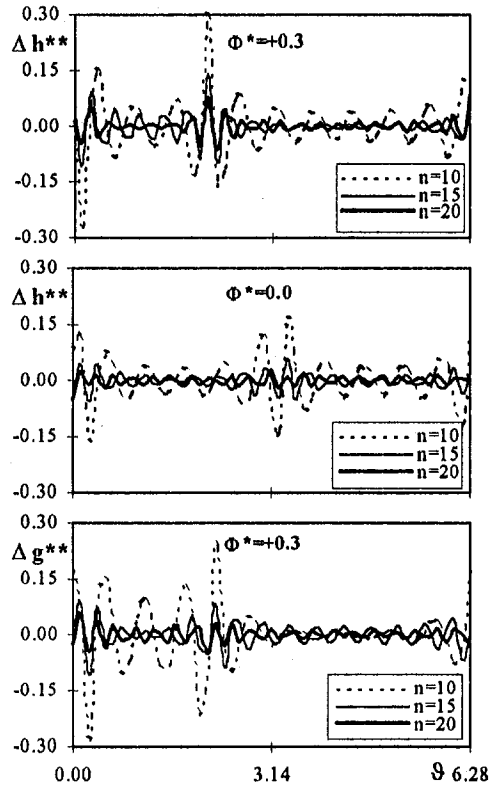

Fig. 9 Comparison for *g* and *h* obtained by accurate and truncated solutions (*n* = harmonics number)

$$\Delta g^{**}(\vartheta) = \frac{g_a(\vartheta) - g_n(\vartheta)}{\sqrt{2E}},$$

$$\Delta h^{**}(\vartheta) = \frac{h_a(\vartheta) - h_n(\vartheta)}{\sqrt{2E}} \tag{18}$$

where n is the number of harmonics.

Considering less than 10 harmonics, agreement with the complete solution is too poor still, the gap being of the order of magnitude of the mean g coefficient (over 30 percent), and it needs more than 20 harmonics to differ less than 5 percent, even in the simplest case of h, for $\Phi^* = 0.0$.

The FFT analysis is then carried out changing the parameter AR and the lag parameters v, s, and e, to obtain a complete comparison with the methods utilising the truncated Fourier series (Fig. 10). An FFT analysis is also carried out for the simplified solution to show the lack of accuracy introduced with respect to the accurate one (Fig. 11). It is important to remember that the simplified solution has been obtained by the Moore relation (Eq. (6)), but not as truncated Fourier series. As shown in Fig. 10, for the accurate solution, since h is the Hilbert transform of g, their spectra coincide (equal frequency and amplitude, only phase differs), while (Fig. 11) two different spectra are obtained by the simplified solution. At $\Phi^* = 0.0$ only odd harmonics occur and their amplitude smoothly decreases down to zero, close to $\frac{1}{30}$ of a revolution. The closer negative slope characteristic lags, the more complex the spectra are, with even harmonics too and irregular amplitude trends. This is not surprising because of the stall cell shape behavior (Arnulfi et al., 1995), but unfortunately, from the stall recovery point of view, the high Φ^* zone is the most interesting. By varying characteristic shape (AR) and lag parameters (v, s, and e) no qualitative changes occur in the spectra, but amplitudes are slightly different. Comparison with the simplified solution shows a rather good agreement as to g, being responsible for stall cell shape, but a very poor one as to h, being related to local propagation speed.

A Time-Effective Model

The resolution of the rotating stall model including the Hilbert transform is CPU-time expensive, while in some applications, such as active compressor control or optimization problems for compressor design, a quicker and not iterative procedure should be necessary. For this reason, using the accurate method presented in this paper, a new correlative approach for the overall compressor performance (pressure coefficient and propagation speed) is obtained and described by the relations:

$$\delta^* = f_1(\Phi^*, AR, e, s, v) \tag{19a}$$

$$F = f_2(\Phi^*, AR, e, s, v) \tag{19b}$$

and in this case the equations are:

$$\delta^* = K_1\Phi^* + K_3\Phi^{*3} \tag{20a}$$

$$F = K_0 + K_2\Phi^{*2} + K_4\Phi^{*4} \tag{20b}$$

where

$$K_j = K_{j0} + K_{j1}v + K_{j2}s + K_{j3}e + K_{j4}AR \tag{20c}$$

for $j = 0 \div 4$.

Their numerical values are shown in Table 2.

The constants have been obtained by a least-squares method, based on the results of the accurate model code.

This correlative approach should be used in the following range:

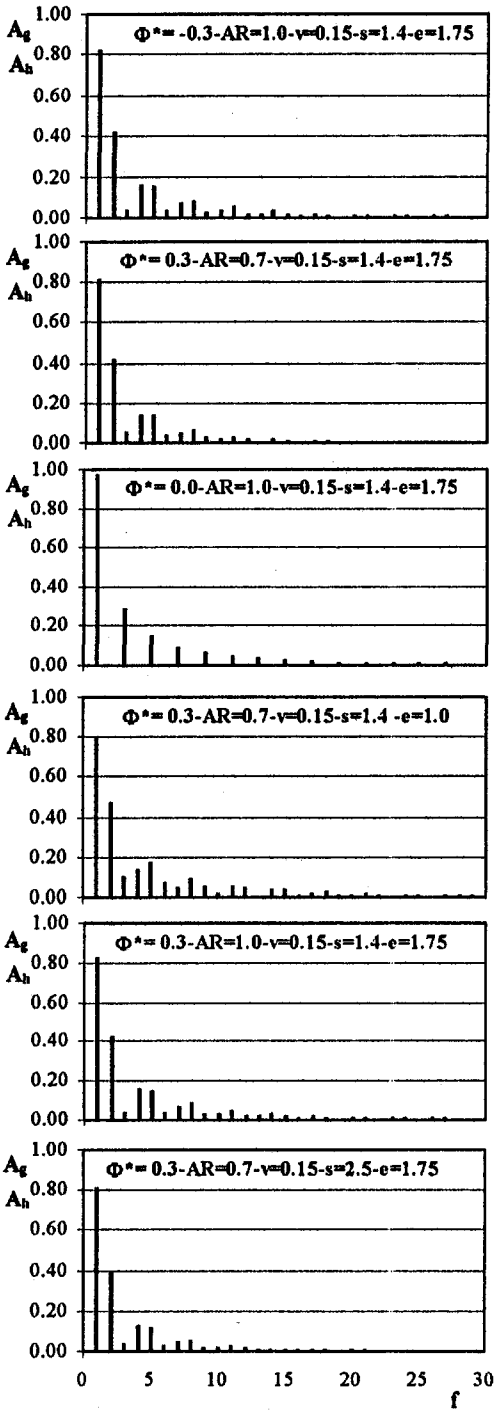

Fig. 10 FFT analysis of the accurate solution at different flow rate and geometric parameters

$$-0.4 < \Phi^* < +0.4 \qquad +0.5 < AR < +1.0$$

$$+1.0 < e < +2.0 \qquad +1.0 < s < +2.5$$

$$+0.0 < v < +0.2$$

Since one can easily estimate axisymmetric characteristic and lag parameters (Hynes et al., 1985), immediately these equations give an approximate value of δ^* and F for every compressor operating in any stalled condition. As one can see in Fig. 12, the estimation is good (the regression coefficients, defined in Eq. (21), are $R(\delta^*) = 0.020$ and $R(F) = 0.005$) and, above all, not worse than that obtained by traditional simplified methods.

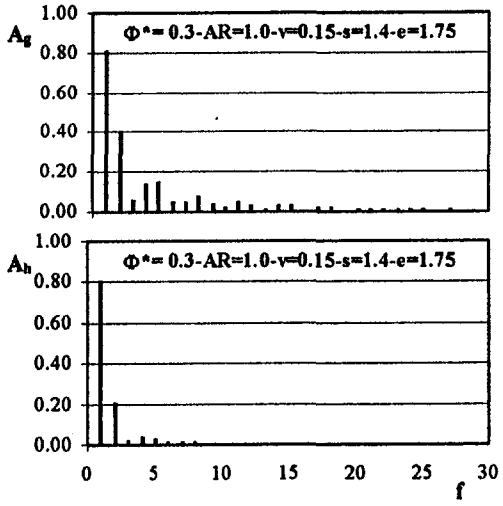

Fig. 11 FFT analysis of the simplified solution (standard condition)

Table 2 Coefficients of correlation

K_{00}= 0.340	K_{01}= - 0.105	K_{02}= 0.050	K_{03}= - 0.103	K_{04}= 0.103
K_{10}= - 2.011	K_{11}= 0.062	K_{12}= - 0.034	K_{13}= 0.220	K_{14}= 0.263
K_{20}= - 0.213	K_{21}= 1.355	K_{22}= 0.032	K_{23}= - 0.082	K_{24}= 0.367
K_{30}= 19.040	K_{31}= 0.838	K_{32}= 0.014	K_{33}= - 9.182	K_{34}= - 1.209
K_{40}= 2.863	K_{41}= - 13.27	K_{42}= - 0.549	K_{43}= 1.555	K_{44}= - 3.932

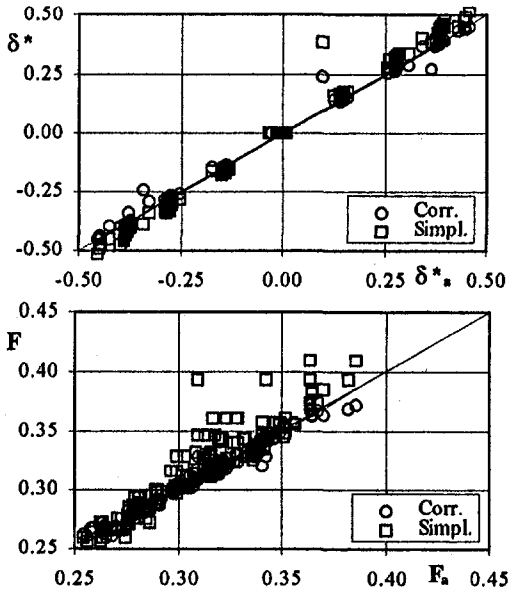

Fig. 12 Comparison between accurate, simplified (Eq. (6)) and correlative (Eqs. (17) and (18)) approaches

$$R(y) = \sqrt{\frac{\sum_{i=1}^{N} [y_a - y_c]_i^2}{N - 1}} \tag{21}$$

Conclusions

Rotating stall was modeled as proposed by Moore, by utilizing the complete Hilbert transform relation between the axial flow perturbation g and the transverse one h.

A full comparison between the data given by the accurate model and the ones given by the simplified relation was made. The main results of this comparison are:

- the axial perturbations obtained by the two models are quite similar, except near peak values, while the transverse flow perturbation shows a large difference (Figs. 2, 3);
- the energy coefficient E calculated by the simplified model underestimates the energy related to the stall cell given by the accurate one (Fig. 4);
- δ^* and F calculated by the simplified solution always overestimate the ones calculated by the Hilbert transform (Figs. 5, 6);
- the single component pressure rise contribution calculated by the two models shows a similar trend, but the simplified relation does not capture the sudden pressure drops well (Fig. 7);
- from a FFT analysis it turns out that more harmonics are needed to represent the flow perturbation as the mass flow rate approaches recovery or back flow conditions (Fig. 10);
- only a slight change in the amplitudes is produced by varying the aspect ratio values AR and the lag parameters v, s, and e (Fig. 10).

Finally a new analytical formulation for δ^* and F has been proposed, utilizing the data given by the accurate model. In this way a quick and easy response on overall rotating stall effects is obtained (Fig. 12).

Acknowledgments

This research was supported by MURST (Italian Ministry of University and Research—40 percent funds and 60 percent funds).

The authors wish to thank the reviewers for their valuable suggestions.

References

Arnulfi, G. L., Ghiglino, F. L., and Massardo, A. F., 1995, "A Complete Solution of Non-linear Equations for Rotating Stall in Axial Multistage Compressors," *Proc. 2nd International Conference on Pumps and Fans,* Beijing, People's Republic of China, Oct. 17–20.

Cumpsty, N. A., and Greitzer, E. M., 1982, "A Simple Model for Compressor Stall Cell Propagation," ASME *Journal of Engineering for Power,* Vol. 104, pp. 170–176.

Day, I. J., 1993, "Stall Inception in Axial Flow Compressors," ASME JOURNAL OF TURBOMACHINERY, Vol. 115, pp. 1–9.

Greitzer, E. M., 1976, "Surge and Rotating Stall in Axial Flow Compressors," ASME *Journal of Engineering for Power,* Vol. 98, pp. 190–217.

Hynes, T. P., Chue, R., Greitzer, E. M., and Tan, C. S., 1985, "Calculations of Inlet Distortion Induced Compressor Flowfield Instability," *AGARD Conference Proceedings No. 400.*

Koff, S. G., and Greitzer, E. M., 1984, "Stalled Flow Performance for Axial Compressors: Axisymmetric Characteristic," ASME Paper No. 84-GT-93.

McCaughan, F. E., 1989, "Numerical Results for Axial Flow Compressor Instability," ASME JOURNAL OF TURBOMACHINERY, Vol. 111, pp. 434–441.

Moore, F. K., 1984, "A Theory of Rotating Stall of Multistage Axial Compressors," ASME *Journal of Engineering for Gas Turbines and Power,* Vol. 106, pp. 313–336.

Saju, T. J., 1985, "Effect of Compressor Parameters on Rotating Stall," MSc Thesis, Cornell University, Ithaca, NY.

Takata, H., and Nagano, S., 1972, "Non-linear Analysis of Rotating Stall," ASME *Journal of Engineering for Power,* Vol. 94, pp. 279–293.

Comparison of Sweep and Dihedral Effects on Compressor Cascade Performance

T. Sasaki
Heavy Apparatus Engineering Laboratory,
Toshiba Corporation,
2-4 Suehiro-cho, Tsurumi-ku,
Yokohama, Kanagawa, 230 Japan

F. Breugelmans
Turbomachinery Department,
von Karman Institute for Fluid Dynamics,
Chaussée de Waterloo, 72,
B-1640 Rhode-St-Genèse, Belgium

The influence of two stacking lines, namely sweep and dihedral, has been investigated in a linear compressor cascade. Both types of blade considered are symmetric about midspan and consist of a straight central section with either swept or dihedral sections toward the endwalls. Two types of experiment have been carried out. First, a parametric study was performed by changing both the magnitude and the extent of the sweep or dihedral. In the case of swept blades, those with forward sweep (SWF), for which the stacking line is swept in the upstream direction toward the endwall, were found to have better performance than backward-swept blades. Subsequently, four sets of SWFs were compared. In the case of dihedral blades, it is well known that the dihedral is advantageous when the angle between the suction surface and the endwall is obtuse, i.e., positive dihedral. Thus, four sets of positive dihedral blades (DHP) were compared. In both SWF and DHP blades, those configurations that have better efficiency than straight blades were determined. Second, detailed three-dimensional measurements inside the blade passage were performed in the cases that showed the best performance in the parametric study. Both SWF and DHP showed significant effects on the flowfield. In the SWF case, a vortex, which has the opposite sense to the passage vortex, was observed in the forward portion inside the blade passage. This vortex supplies high-energy fluid to the endwall region and reduces the corner stall. The secondary flow is greatly reduced. In the DHP, the blade loading was reduced at the endwall and increased at the midspan. Reduction of the corner stall and the secondary flow was also observed.

Introduction

Over the years, enormous efforts have been devoted to improving the efficiency of gas turbines. One way is to increase the "thermodynamic cycle" efficiency by increasing both the turbine inlet temperature and the pressure ratio. Another way is to increase efficiency in each component, i.e., the compressor and the turbine. Because two-dimensional airfoil losses have already been greatly reduced with state-of-the-art technology, it is necessary to minimize endwall losses to achieve further efficiency improvement.

Many attempts have been made to reduce endwall losses, as follows. Breugelmans et al. [1] clarified the positive effect of the "dihedral" in a linear compressor cascade when the suction/endwall corner lies on the obtuse side. Weingold et al. [2] investigated bowed stators in a three-stage compressor, which have dihedral on both endwalls, and reported a 1 percent increase in overall efficiency and an elimination of corner stall. The beneficial effects of dihedral in turbine cases were also reported by Harrison [3] and Wang et al. [4], among others. "Dihedral" has begun to be used in "real turbines" these days as "lean" blades. "Endbends" might be one of the most popular techniques employed in compressors to reduce endwall losses. Wisler [6] showed the beneficial effect of endbends, which increase camber angle at the endwall and align the camber line with the secondary flow. Robinson [5] reported that endbends can reduce the separation at a suction/endwall corner. Tweedt et al. [7] investigated the effect of "leading-edge" sweep using a two-stage compressor and showed that it can be beneficial when it is used with a stationary endwall (a casing or a shroud) but detrimental with a running hub clearance. Doerffer and Amecke [8] demonstrated that a streamwise endwall "fence" could reduce the spanwise extent of the secondary flow and could change the spanwise loss distribution significantly.

The present paper aims to contribute to improved understanding of endwall loss control and concentrates on clarifying the effect of blade stacking lines on the endwall loss in a linear compressor cascade. First, a parametric study was performed by using different stacking lines: one straight blade (STR), four forward-swept blades (SWF), one backward-swept blade (SWB) and four positive dihedral blades (DHP). Second, detailed three-dimensional measurements were carried out in the configurations that showed the best performance in each of two parametric studies (considering respectively sweep and dihedral). The difference of loss improvement mechanism between the sweep and the dihedral is discussed.

Experimental Setup

Wind Tunnel and Cascade Configuration. The experimental rig is the low-speed cascade wind tunnel "C-1" at the von Karman Institute. It is a continuous flow facility of a blow-down type with a rectangular test section of 127 × 500 mm. A large centrifugal blower pumps air into the settling chamber, which is equipped with screens. A large convergent nozzle guides the flow into the rectangular duct and then toward the test section. The inlet velocity can be controlled by a variable speed D.C. motor. The airfoil used in this study is a controlled diffusion blade (CDB), which was designed by Sanger [9] and investigated by the Naval Postgraduate school in the USA [10]. This airfoil was chosen because it was proved to have better "two-dimensional" efficiency than conventional airfoils such as the NACA series; thus, the endwall loss seems to become relatively larger and the effect of the stacking line is expected to be more apparent. The original design has a chord length of

Contributed by the International Gas Turbine Institute and presented at the 42nd International Gas Turbine and Aeroengine Congress and Exhibition, Orlando, Florida, June 2–5, 1997. Manuscript received at ASME Headquarters February 1997. Paper No. 97-GT-2. Associate Technical Editor: H. A. Kidd.

Table 1 Cascade configuration

chord length	100 mm	$\alpha_{design,in}$	39.0 deg.
number of blades	9	stagger	14.4 deg.
leading edge radius	0.9% chord	solidity	1.67
max. thickness	7 % chord	aspect ratio	1.27

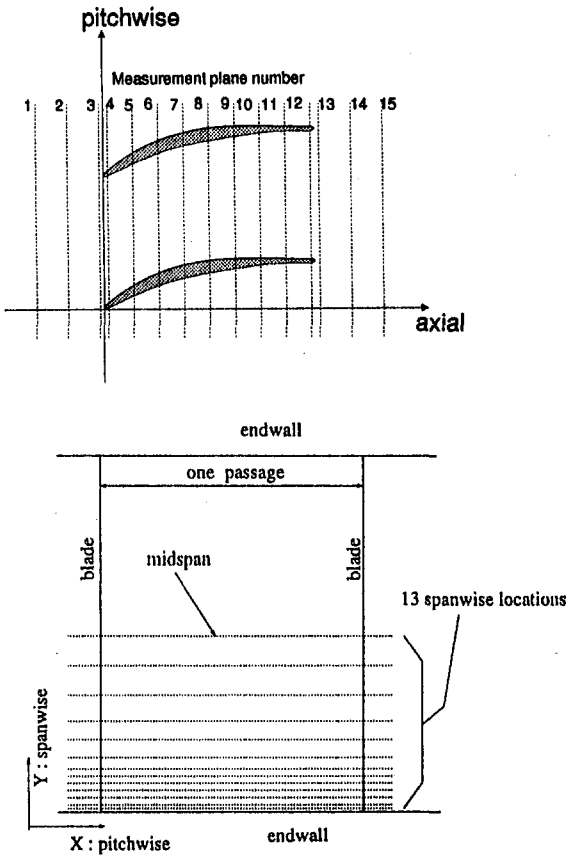

Fig. 1 Location of measurement planes

5 in. (127 mm). However, it was scaled down to 100 mm in this experiment for manufacturing convenience and also to increase the aspect ratio, which is restricted by the tunnel width. Its specifications are given in Table 1.

Probe, Traverse, and Data Reduction. A four-hole directional pressure probe was used in this study. This pressure probe consists of four small pipes. The diameter of each pipe is 0.6 mm/0.4 mm (outer and inner, respectively) and the resultant head size is 1.8 mm × 1.2 mm. The data were taken at 15 different axial planes, as seen in Fig. 1. At each axial plane, traverses at 13 spanwise locations were performed in the pitchwise direction. The data were taken at intervals of 1 mm.

Total pressure loss coefficients are calculated with respect to the pitchwise-averaged flow condition of the midspan at the inlet. Using the averaging procedure, three pressure loss coefficients are defined as follows:

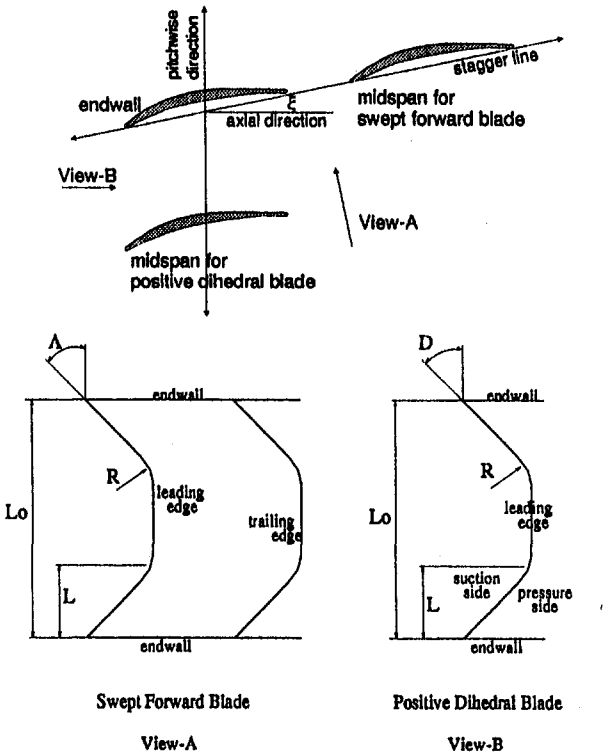

Fig. 2 Test blade configuration

Local total-pressure loss coefficient:

$$\omega = \frac{\bar{P}_{t,MS1} - P_t}{\bar{q}_{MS1}} \tag{1}$$

Pitchwise-averaged total-pressure loss coefficient:

$$\bar{\omega} = \frac{\bar{P}_{t,MS1} - \bar{P}_t}{\bar{q}_{MS1}} \tag{2}$$

Overall total-pressure loss coefficient:

$$\bar{\bar{\omega}} = \frac{\bar{\bar{P}}_{t,MS1} - \bar{\bar{P}}_t}{\bar{\bar{q}}_{MS1}} \tag{3}$$

The uncertainty levels in this experiment were estimated at the Reynolds number of 350,000 with a 95 percent confidence level as follows:

Angle; ± 0.7 deg

Total pressure coefficient; ± 0.15 percent

Parametric Study

Measurement Conditions. In this parametric study, the effects of two stacking lines, namely sweep and dihedral, are investigated. The blades examined are symmetric about the midspan and consist of a straight central portion with either swept or dihedral portions toward the endwalls (Fig. 2). The airfoil

Nomenclature

D = dihedral angle
L = length of sweep or dihedral portion
L_0 = blade height
P_t = total pressure
V = velocity
q = dynamic head
α = flow angle measured from axial line
Λ = sweep angle
ρ = static density
ω = total pressure loss coefficient

Subscripts

t = total
$MS1$ = midspan at inlet plane

Superscripts

$-$ = pitchwise mass average
$=$ = overall mass average (pitch and spanwise)

Table 2 Test cases in swept blade parametric study

Case	Sweep Angle Λ	Sweep Depth L/L_0	Direction
SWB(30,2/6)	-30deg	2/6	Backward
SWF(30,1/6)	30deg	1/6	Forward
SWF(30,2/6)	30deg	2/6	Forward
SWF(15,1/6)	15deg	1/6	Forward
SWF(15,2/6)	15deg	2/6	Forward

Table 3 Test cases in dihedral blade parametric study

Case	Dihedral Angle D	Dihedral Depth L/L_0	Direction
DHP(30,1/6)	30deg	1/6	Positive
DHP(30,2/6)	30deg	2/6	Positive
DHP(15,1/6)	15deg	1/6	Positive
DHP(15,2/6)	15deg	2/6	Positive

Table 4 Measurement condition

Inlet Reynolds Number	Inlet Setting Angle degree	Incidence
350,000	31	Highly Negative
350,000	33	
350,000	37	Near Design
350,000	40	
350,000	43	Highly Positive

shape at each span height is kept the same and also parallel to the endwalls so that only the effect of the stacking line is determined. The values in Table 1 are kept constant. As is seen from their definition, sweep and dihedral are independent only when the stagger angle is zero, i.e., when the stagger line is parallel to an axial line. In other cases, they are always dependent. In the present study, they can be considered nearly independent because of the small stagger angle.

The configurations tested are summarized in Tables 2 and 3. Because the thickness of the inlet boundary layer (shown later) is approximately $\frac{1}{6}$ of the span height, the depths of sweep and dihedral are chosen as $\frac{1}{6}$ and $\frac{2}{6}$. In this parametric study, the downstream traversing was carried out only at 30 mm from the trailing edge (plane 15 in Fig. 1). Data were taken at 13 spanwise locations at every millimeter. For each configuration, five inlet flow conditions were examined (Table 4). Also, oil-flow visualizations were performed using a mixture of oil and TiO_2 powder.

Overall Performance. In this section, the overall loss for each configuration is compared. Because of its definition, even the overall total pressure loss coefficient at the inlet plane has a certain value (not zero) due to the presence of the endwall boundary layer. The typical inlet boundary layer profile is shown in Fig. 3.

In order to evaluate the actual generation of the loss along the passage, an overall net loss at each axial plane is defined as follows:

$$\bar{\omega}_{\text{NET}} = \bar{\omega}_{\text{each axial plane}} - \bar{\omega}_{\text{inlet}} \quad (4)$$

Swept Blades. First, a comparison between a forward-swept blade, SWF(30, $\frac{2}{6}$), and a backward-swept blade, SWB(30, $\frac{2}{6}$), was carried out to determine the advantageous sweep direction. The result of the oil-flow visualization (Fig. 4) shows that the corner stall at the suction surface endwall in SWF(30, $\frac{2}{6}$) is much smaller than that of SWB(30, $\frac{2}{6}$). It is understood that SWF(30, $\frac{2}{6}$) has the effect of delaying the onset of the corner

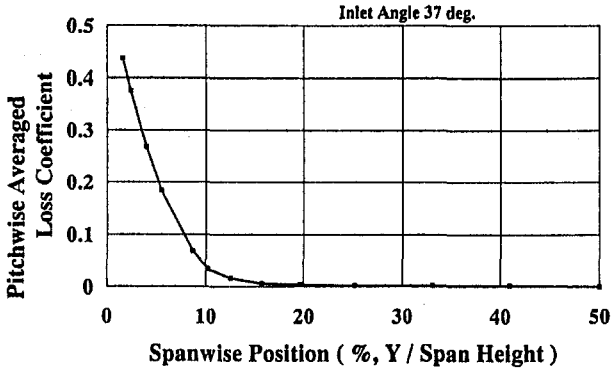

Fig. 3 Typical inlet boundary layer profile (axial plane 1)

stall while SWB(30, $\frac{2}{6}$) does the opposite. Also in the performance measurement by the pressure probe, SWF(30, $\frac{2}{6}$) showed much better performance than SWB(30, $\frac{2}{6}$) at all the incidences tested.

Second, three additional configurations of only forward-swept blades (Table 2) were tested in order to determine the sensitivity of the sweep angle and the sweep depth. The results of all the swept blades are shown in Fig. 5. All of the "forward" swept blades show lower losses than the straight blades in the smaller incidence region; however, they give almost the same or higher loss in the larger incidence region. On the other hand, the "backward" swept blades always give higher losses than all the rest.

The minimum losses for each configuration are shown in Fig. 6. SWF(30, 2/6) shows the smallest loss while SWF(15, $\frac{1}{6}$)

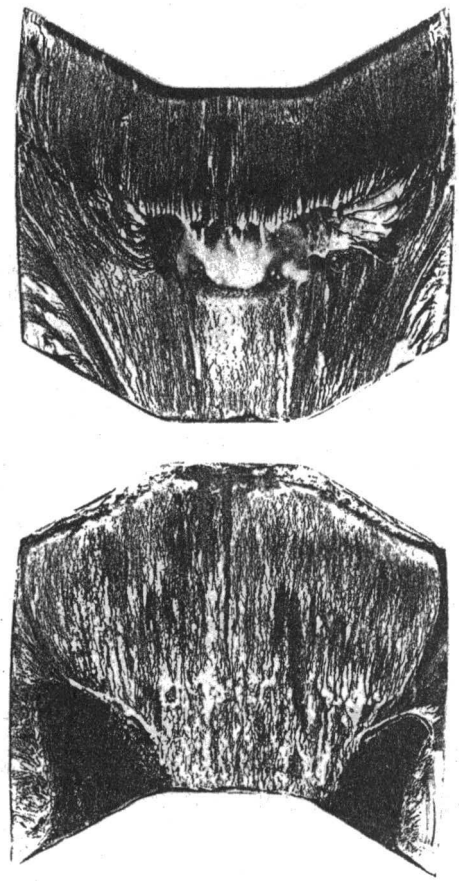

Fig. 4 Oil flow visualization of SWF and SWB at negative incidence

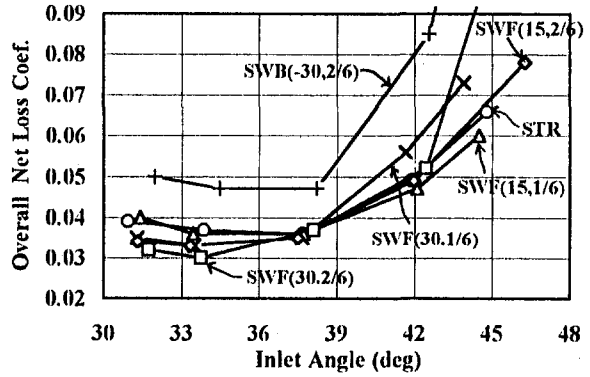

Fig. 5 Net losses in swept blades

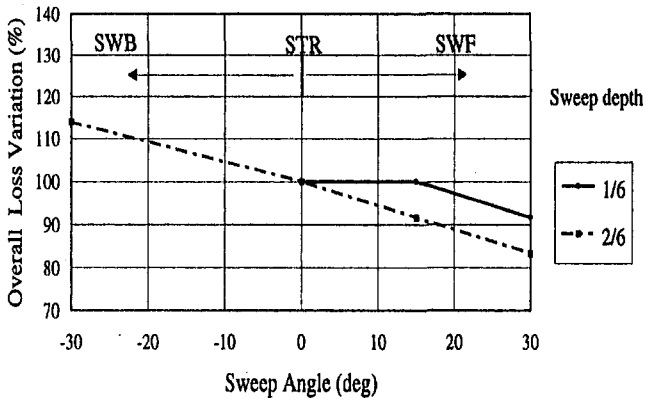

Fig. 6 Loss improvement in swept blades

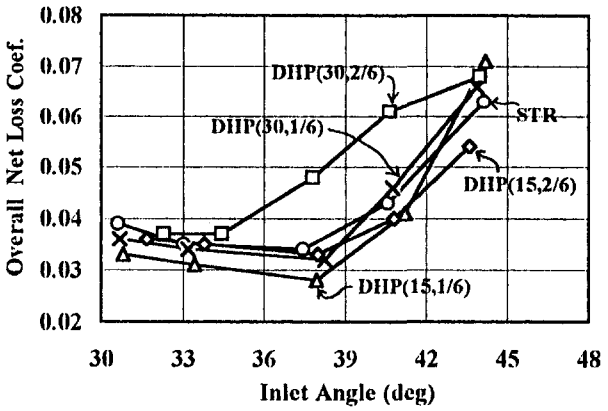

Fig. 7 Net losses in dihedral blades

has no effect. SWF(30, $\frac{1}{6}$) and SWF(15, $\frac{2}{6}$) show almost the same improvement. Within the range tested, the sweep angle has a linear effect on loss variation. Further efficiency improvement seems to be obtained if the sweep angle or the sweep depth is increased more, although efficiency deterioration is expected in the higher incidence region as seen in Fig. 5.

Dihedral Blades. It is well known that dihedral is advantageous when the angle between the suction surface and the endwall is obtuse, i.e., positive dihedral. Thus, four sets of positive dihedral blades were examined (Table 3). The results for all the configurations are shown in Fig. 7. DHP (30, $\frac{2}{6}$), which has the largest dihedral angle and depth, gives the highest losses. The rest are better or equal to the straight blades. The loss deterioration in the higher incidence region, which is observed in forward-swept blades, is not clearly seen in dihedral blades.

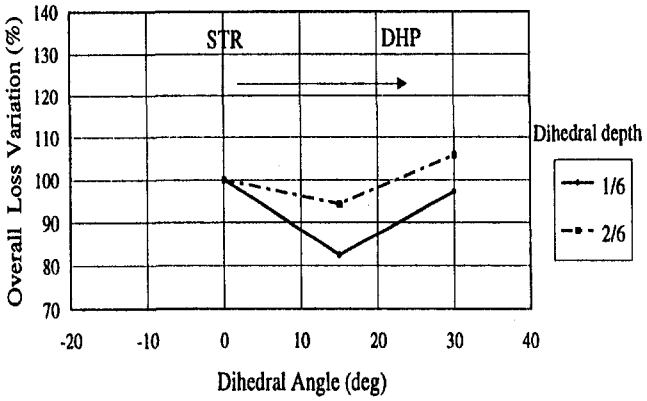

Fig. 8 Loss improvement in dihedral blades

The minimum losses for each configuration are shown in Fig. 8. In both dihedral depths of $\frac{1}{6}$ and $\frac{2}{6}$, a dihedral angle of 15 deg gives the minimum value. DHP(15, $\frac{1}{6}$), which has the least dihedral angle and depth, gives the best results of about 20 percent loss reduction. This improvement is almost the same amount as that achieved by the forward-swept blade, which, in contrast, has the largest swept angle and depth. A loss sensitivity to stacking line variation is much higher in DHP than in SWF.

Pitchwise-Averaged Parameters. In this section, spanwise loss distributions in swept and dihedral blades are compared. In order to determine the improvement or deterioration of pitchwise-averaged losses with respect to straight blades at the particular span height position, a loss improvement factor, $\Delta\bar{\omega}$, is defined as follows:

$$\Delta\bar{\omega} = \frac{(\bar{\omega} - \bar{\omega}_{\text{straight blade}})_{\text{each span height}}}{\bar{\omega}_{\text{NET,straight blades}}} \quad (5)$$

Figures 9 and 10 show the loss improvement factors of swept blades and dihedral blades near the design incidence. All of the SWFs show smaller losses at the endwall and at the span height from 8 to 20 percent while they show larger losses near the midspan. The backward-swept blade, SWB(30, $\frac{2}{6}$) shows the opposite effect to SWFs except at the endwall. The trends in DHPs are very different from those in SWFs. All the DHPs show lower losses from the endwall to 15 percent span height and more losses in the rest of the span height positions. Depending on the magnitude of dihedral angles, the curves near the endwall are divided into two groups: large loss improvement with dihedral angle of 30 deg and mild loss improvement with 15 deg. This

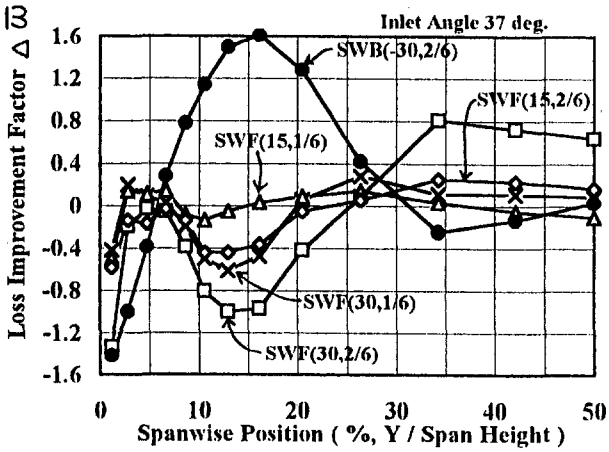

Fig. 9 Loss improvement factor for SWF

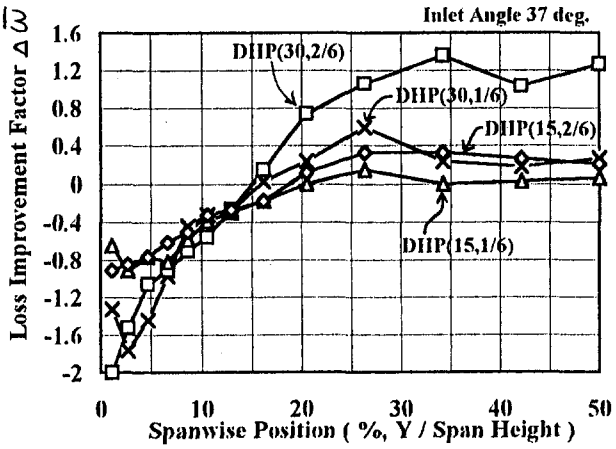

Fig. 10 Loss improvement factor for DHP

implies that the flow behavior near the endwall is influenced only by the dihedral angle, not by its depth (spanwise extent).

In the case of negative incidences, for both SWF and DHP, only the beneficial effects near the endwall remain and losses near the midspan do not increase. Consequently, both configurations result in reduced losses. On the other hand, in the case of the positive incidence, loss deterioration around the midspan becomes dominant. Especially in SWF, loss improvement near the endwall is hardly seen.

Detailed Measurement Inside Blades

Measurement Condition. Detailed pressure probe measurements were carried out for STR, SWF, and DHP. Both SWF and DHP are the configurations that showed the smallest losses in their respective parametric studies. The SWF has a swept angle of 30 deg and a depth of $\frac{2}{6}$. The DHP has a dihedral angle of 15 deg and a depth of $\frac{1}{6}$. The data were taken at 15 different axial planes, as seen in Fig. 1. At each axial plane, traverses at 13 spanwise locations were performed every 1 mm. The inlet Reynolds number and the inlet setting angle are fixed to 350,000 and 37 deg, respectively for each configuration (cf. Table 4).

Flow Structure

Loss Distribution. The contours of the total pressure loss coefficient are compared at 98 percent chord (Fig. 11), which is 2 mm upstream from the trailing edge. SWF does not have a loss core at the suction/endwall corner as seen in STR, although the boundary layer on the suction surface is thicker than STR. DHP has a loss core but its size is smaller than that of STR. The boundary layer of DHP on the suction surface is somewhat thicker than STR. The endwall boundary layer of each of the three stackings becomes thinner near the pressure surface due to the secondary motion, but the case in DHP is the most apparent.

Secondary Vectors. The secondary vectors are compared at 26 percent axial chord plane (Fig. 12). The traces of vectors are also shown in these figures. These are not real streamlines but just loci of two-dimensional vectors, which ignore the axial components; however, they are useful for visualizing the flow patterns.

In the case of STR, the so-called passage vortex, which is the consequence of the inlet boundary layer and the flow deflection in the passage, is already clearly formed at the 26 percent axial chord plane, probably because the airfoil used here is a front-loading type. This vortex continues to develop up to the exit of the passage.

In the case of SWF, a large counterclockwise vortex, which has the opposite sense to the passage vortex, is seen in the forward portion of the passage. This vortex is already found even at the 2 percent axial chord plane. Its scale becomes largest at the 26 percent plane (Fig. 12) and then gets weaker. At the 50 percent plane, it almost disappears and, instead, a weak passage vortex is formed near the endwall. This passage vortex does not develop as in STR and results in high spanwise flow at the 98 percent plane (Fig. 13); spanwise flow toward the midspan near the suction surface and toward the endwall near the pressure surface.

In the case of DHP, the same trend as for STR is observed, but the center of the passage vortex is closer to the suction surface and the vortex shape is deformed.

Flow Pattern on the Suction Surface and the Endwall. A comparison of the flow vectors near the suction surface is shown in Fig. 14. Again, the traces shown on the figures are loci of two-dimensional vectors, not the streamlines.

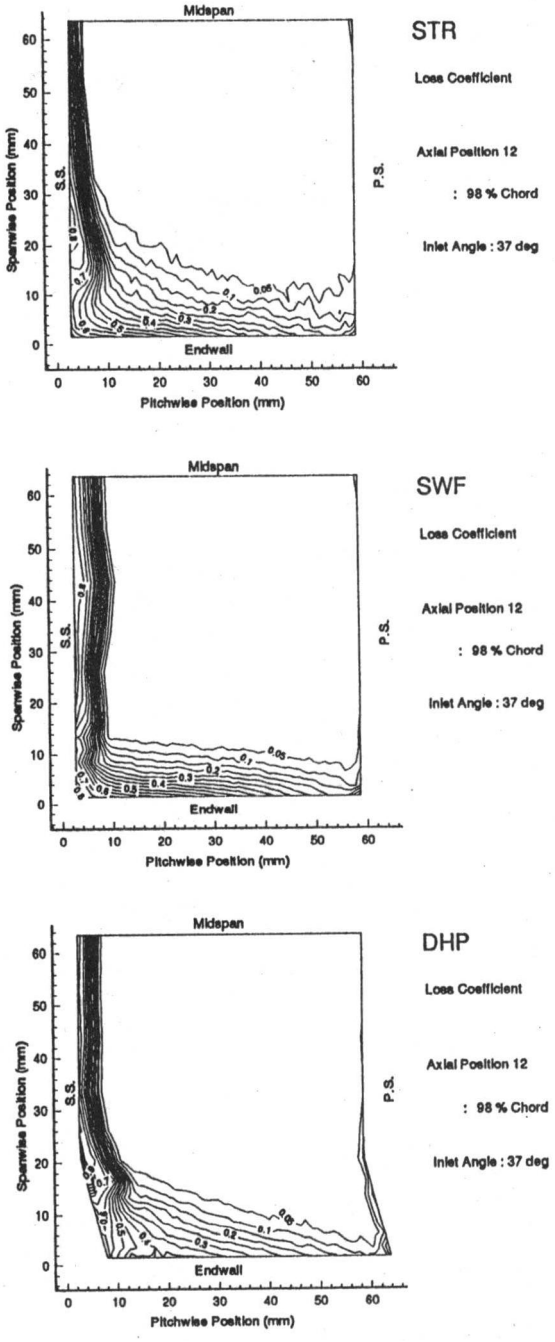

Fig. 11 Loss contour at 98 percent axial chord plane

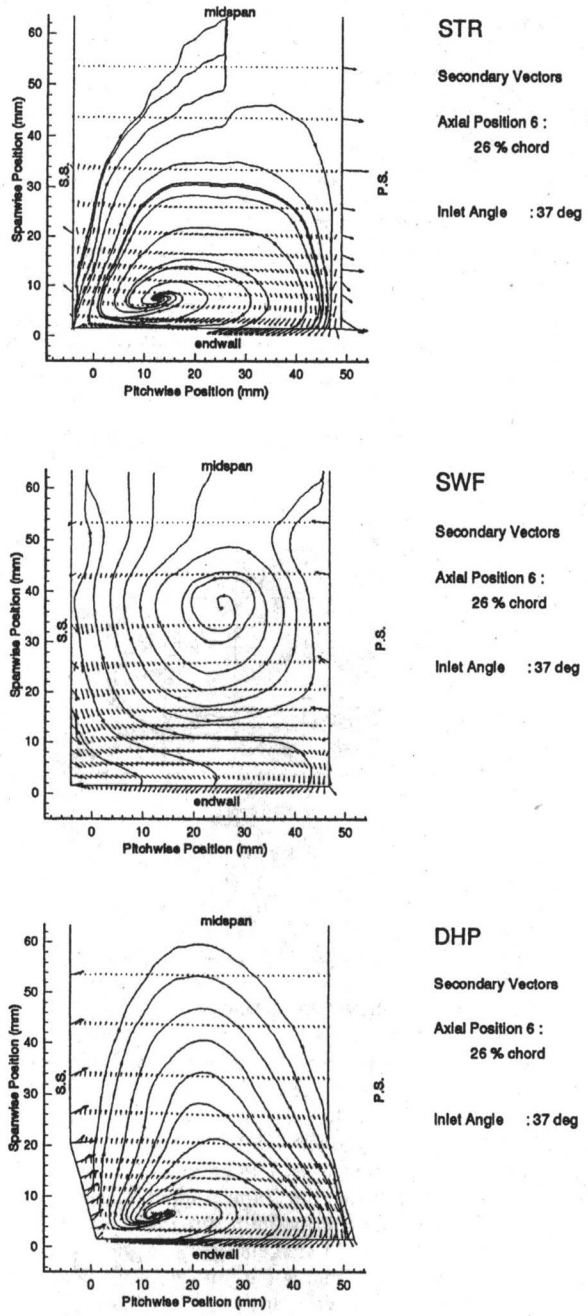

Fig. 12 Comparison of secondary velocity vector at 26 percent axial chord plane

The corner-stall lines are clearly seen in each type of stacking. The extent of the corner stall at the trailing edge is almost the same for the three stacking lines, although the location where the corner stall occurs at the endwall is different. The locations of the onset of the corner stall are at about 30 mm from the leading edge in STR and at about 50 mm in SWF and DHP. Apparently, SWF and DHP have the effect of delaying the onset of corner stall.

At the plane 3.6 mm from the suction surface (not shown), the effect of the corner stall is still observed clearly in STR but is hardly seen in SWF and DHP. This implies that the corner stall in SWF and DHP is thinner in the pitchwise direction than that in STR.

Static Pressure Distribution and Blade Loading. The static pressure distribution near the blade surface, i.e., blade loading, is compared at the midspan and near the endwall in Fig. 15.

In the case of SWF, the suction peak moves upstream at the midspan and downstream near the endwall compared to that of STR. Also, the static pressure on the pressure surface becomes slightly larger at the midspan and smaller near the endwall. Consequently, at the midspan, SWF has higher loading in the forward portion of the passage and less loading in the aft portion. The loading at the endwall has the opposite trend. Also, the adverse pressure gradient at the midspan is larger in SWF than in STR. This larger adverse pressure gradient results in the separation identified by a "flattening" of the static pressure seen from the axial position of 70 mm to the trailing edge. The flow visualization results verified this separation, too. This is probably one of the reasons for the higher loss around the midspan observed in the loss contour (Fig. 11).

In the case of DHP, the loading distribution changes in a different way. At the midspan, the peak suction pressure becomes smaller, although its position does not change. The blade loading becomes larger almost over the full passage. At the endwall, the suction peak pressure becomes larger while its position again does not change and thus the blade loading becomes smaller. This phenomenon, i.e., high loading at the midspan and less loading at the endwall, is commonly reported in both compressors and turbines [1, 3].

The comparison of the local diffusion factor is shown in Fig. 16. The local diffusion factor is defined as follows:

$$\text{L.D.F.} = \left[\frac{v_{\max} - v_{\text{exit}}}{v_{\max}}\right]_{\text{each span height}} \tag{6}$$

Compared to STR, SWF has higher diffusion factors near the midspan, lower values from around 10 mm to 25 mm span height, and again higher values in the vicinity of the endwall. This trend clearly corresponds to the difference of the loss pattern observed along the suction surface (Fig. 11). In the case of DHP, diffusion factors are higher near the midspan, almost the same as STR from about 5 mm to 30 mm span height and lower at the endwall. This trend is also seen in the loss pattern.

The spanwise static-pressure distributions near the suction surface are compared in Fig. 17. At the 14 percent axial position, the spanwise pressure gradient of both SWF and DHP is smaller than that of STR near the endwall. This might delay the onset of the corner stall. At the 38 percent axial position, SWF shows a relatively flat distribution because the suction peak moves upstream at midspan and downstream near the endwall. DHP clearly shows the higher loading at the midspan and lower loading near the endwall, which results in a larger spanwise pressure gradient.

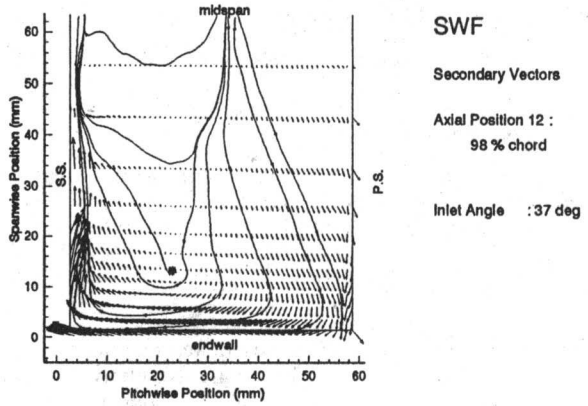

Fig. 13 Secondary velocity vector of SWF at 98 percent axial chord plane

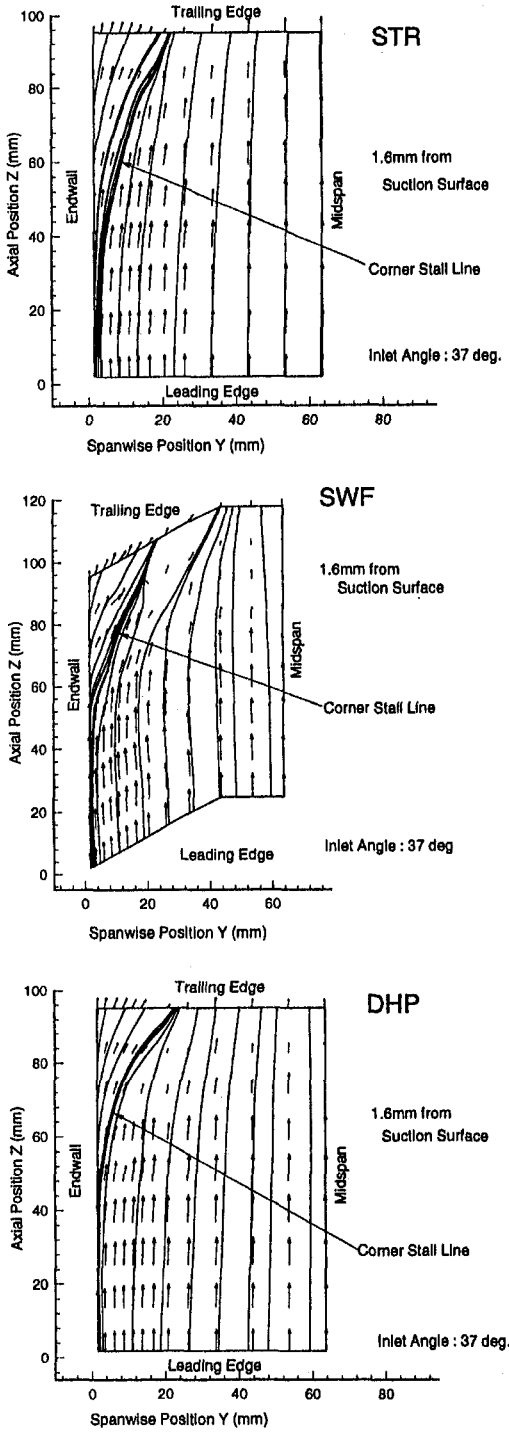

Fig. 14 Flow patterns near suction surface

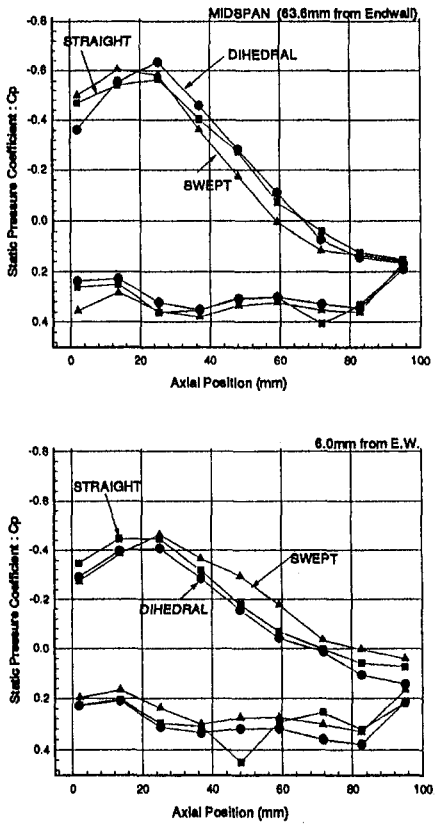

Fig. 15 Blade loading

Averaged Parameters

Loss Evolution. In order to determine a real change of pitchwise-averaged loss at the particular span height position, a net loss at each span height is defined as follows:

$$\bar{\omega}_{\mathrm{NET}} = \frac{(\bar{\omega}_{\text{each axial plane}} - \bar{\omega}_{\text{inlet}})_{\text{each span height}}}{\bar{\bar{\omega}}_{\mathrm{NET}}} \tag{7}$$

It should be mentioned that, in this representation, values on streamlines are not followed. The value $\bar{\omega}_{\mathrm{NET}}$ only shows the difference between the inlet and certain axial position, thus, the difference can come from any of the following: convection, diffusion or loss generation.

The evolution of the net losses, $\bar{\omega}_{\mathrm{NET}}$, are compared at three different span height positions with the overall net losses, $\bar{\bar{\omega}}_{\mathrm{NET}}$ (dotted line), in Figs. 18, 19, and 20.

In the case of STR, the overall net loss, $\bar{\omega}_{\mathrm{NET}}$, increases more than the midspan loss, $\bar{\omega}_{\mathrm{NET,50\%\ span}}$, inside the blade passage as commonly expected. However, the difference rapidly decreases downstream of the trailing edge, which implies that high spanwise mixing occurs. The loss at the endwall, $\bar{\omega}_{\mathrm{NET,1\%\ span}}$, increases rapidly until 30 percent axial position, where the onset of corner stall is seen in flow vectors (Fig. 14), then decreases gradually. This suggests that the corner stall enhances the spanwise transport of the low-energy fluid from the endwall towards the midspan. The loss at 11 percent span height, $\bar{\omega}_{\mathrm{NET,11\%\ span}}$, increases much more than that at the midspan (50 percent span height) and forms the loss core at the suction/endwall corner.

In the case of SWF (Fig. 19), the loss evolution pattern inside the blade passage is almost the same as the net loss

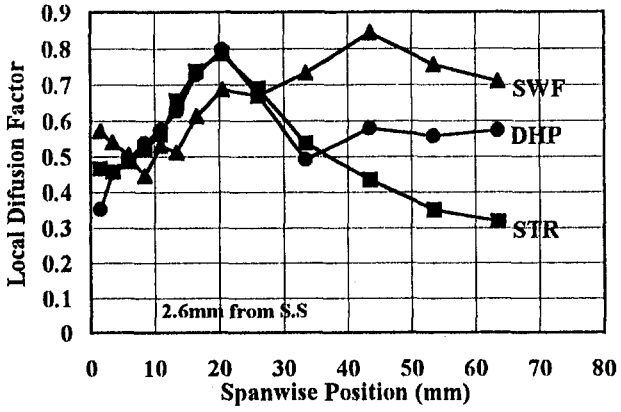

Fig. 16 Local diffusion factor

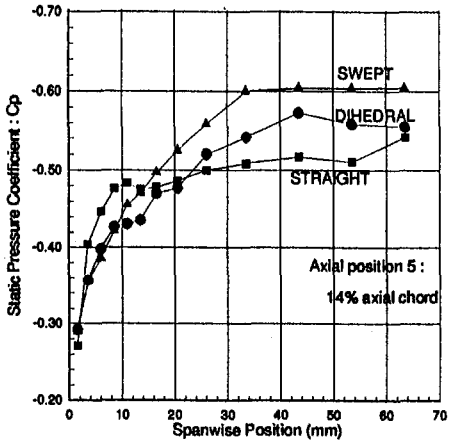

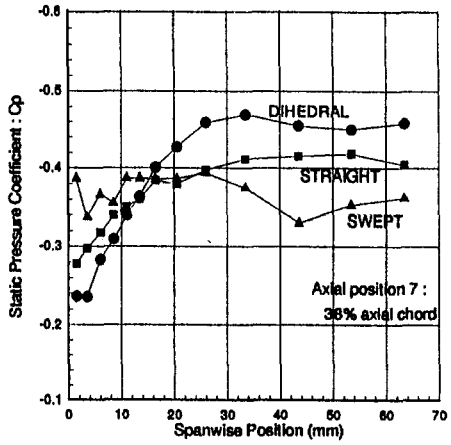

Fig. 17 Spanwise static pressure distribution on suction surface

($\bar{\omega}_{NET}$) from the midspan ($\bar{\omega}_{NET,50\%\ span}$) to the 11 percent span height ($\bar{\omega}_{NET,11\%\ span}$). Each of them increases mainly in the forward portion of the blade passage. After the trailing edge, the midspan loss becomes much larger than the overall net loss probably due to the separation on the suction surface and the convection of low energy fluid from the endwall region. The rapid increase of the loss at the endwall ($\bar{\omega}_{NET,1\%\ span}$), which is observed in the case of STR, does not occur here. The counterclockwise vortex observed in the forward portion of the passage (Fig. 12) seems to supply high energy fluid to the endwall region. From 80 percent axial position, the loss near the endwall

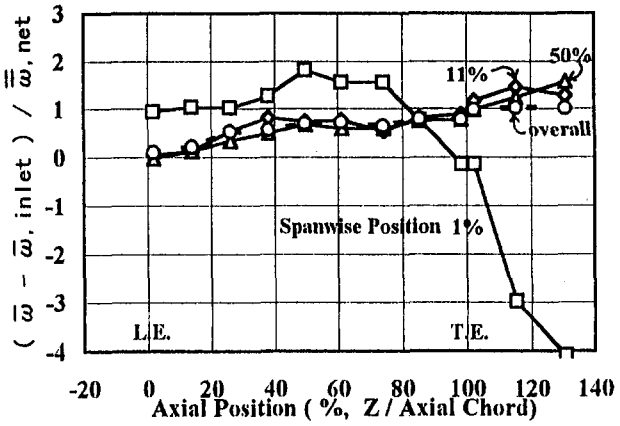

Fig. 19 Axial distribution of overall loss and loss at three spanwise positions for SWF

($\bar{\omega}_{NET,1\%\ span}$) decreases sharply. This is probably due to the large spanwise flow near the suction surface in the aft portion of the blade passage (Fig. 13).

In the case of DHP (Fig. 20), the loss evolution pattern is very similar to STR but there are still some differences. The loss at the midspan suddenly increases around 70 percent axial position while it increases gradually inside the passage in the case of STR. This is probably because of the high loading at the midspan in DHP observed in the static pressure distribution. The difference worth mentioning is that the position, from which $\bar{\omega}_{NET,1\%\ span}$ begins to decrease, moves to 50 percent axial position (30 percent in STR), which again corresponds to the onset of corner stall in DHP as in STR.

Mass Flow Distribution. Because the flowfield considered is incompressible, the mass flow rate is proportional to an axial velocity. In order to compare the mass flow distribution at the different axial planes, where the mean axial velocity is different due to the change of the passage area, a mass flow rate is defined as follows:

$$\dot{m} = \frac{\bar{v}_{axial}}{\bar{\bar{v}}_{axial}} \tag{8}$$

The axial evolution of the mass flow rate at two different spanwise positions, one at the midspan and another at 3.5 mm from the endwall, is shown in Fig. 21. Also the spanwise distribution of the mass flow rate is compared at 98 percent axial plane and 131 percent axial plane in Figs. 22 and 23.

In the case of SWF, the mass flow rate is larger near the endwall and smaller at the midspan than STR inside the passage

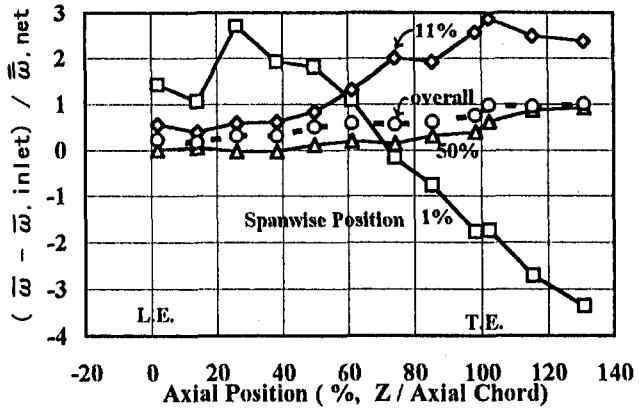

Fig. 18 Axial distribution of overall loss and loss at three spanwise positions for STR

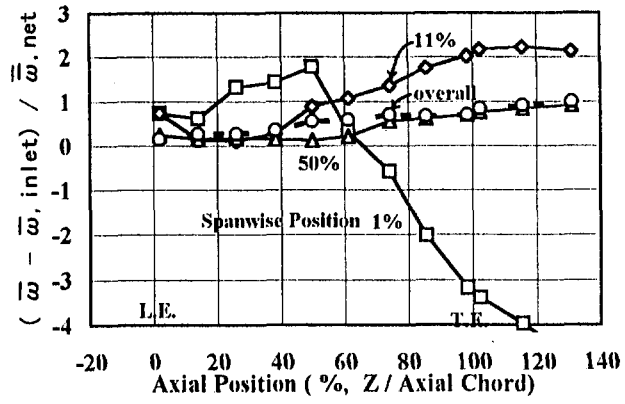

Fig. 20 Axial distribution of overall loss and loss at three spanwise positions for DHP

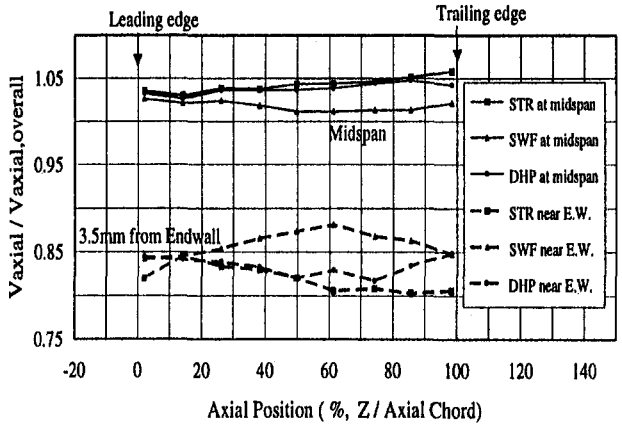

Fig. 21 Axial variation of mass flow rate distribution

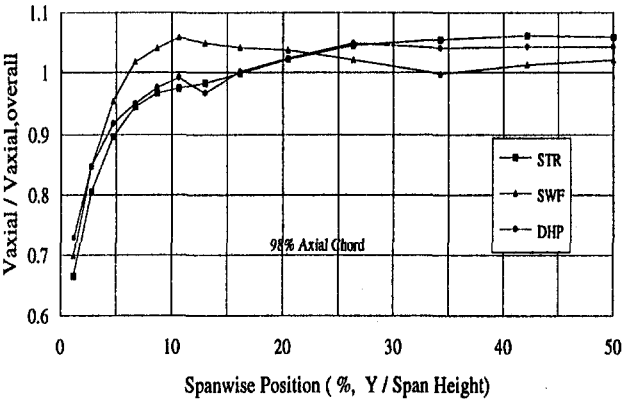

Fig. 22 Spanwise distribution of mass flow rate at 98 percent axial plane

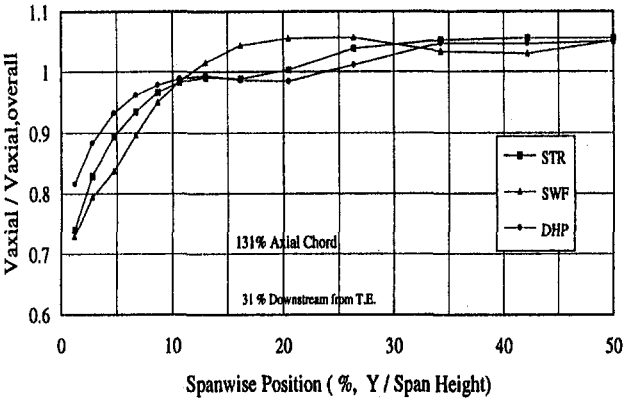

Fig. 23 Spanwise distribution of mass flow rate at 131 percent axial plane

(Fig. 21). After the trailing edge, the high mass flow region around 10 percent span height moves toward midspan (Fig. 23). In other words, SWF causes a high flow rate near the endwall in the forward portion of the passage due to the counterclockwise vortex and decreases the flow rate again in the aft portion of the passage due to the high spanwise flow near the suction surface.

In the case of DHP, the trend in the forward portion of the passage is the same as that for STR. However, the flow rate near the endwall increases gradually after 50 percent axial position (Fig. 21). Subsequently, DHP has the most uniform mass flow distribution at 131 percent axial position (Fig. 23).

Discussion

Both in SWF and DHP, performance improvement is obtained by the balance between beneficial and negative effects. In this section, these two effects are discussed.

Loss Improvement Mechanism in SWF. The beneficial effects for SWF are attributed to the delay of the onset of corner stall and its reduced pitchwise expansion from the suction surface. Both of them are identified by the flow pattern seen from flow vectors and the flow visualization results.

The delay of the onset of the corner stall is mainly due to two phenomena. One is the vortex observed in the forward portion of the passage and has the opposite sense to the passage vortex. This vortex supplies high-energy fluid into the suction/endwall corner and energizes the endwall boundary layer. The other is the lower spanwise pressure gradient near the endwall with which the flow can attach to the wall longer than for STR.

The reduced pitchwise expansion of the corner stall is probably the result of high spanwise flow toward the midspan in the aft portion of the passage. This flow sweeps the low-energy fluid toward the midspan, prevents accumulation of it and keeps the stall size small.

The vortex mentioned above is not the same as the one commonly seen on a delta-wing because the sense of the rotation is opposite and a leading edge separation, which is observed on the delta-wing, was not found from the flow visualization of SWF.

The negative effects are twofold. One is the larger adverse pressure gradient on the suction surface at the midspan, which results in the separation at about 70 percent of the axial chord. Another is the high spanwise flow, which, on the contrary, has a beneficial effect at the endwall. Near the midspan, the low-energy flow from the endwall region enlarges the midspan separation.

Near the design incidence, where the detailed measurement was carried out, these two effects balance and the overall loss becomes almost the same as STR. However, at negative incidence, the midspan separation does not occur (identified by flow visualization), only the beneficial effects hold and, consequently, SWF has better efficiency than STR. In the high positive incidence, the midspan separation becomes so dominant that the loss of SWF becomes worse.

Loss Improvement Mechanism in DHP. The main feature in DHP is the unloading near the endwall and the overloading around the midspan. Both effects are identified by static pressure and local diffusion factor distributions.

Although the beneficial effects of DHP come from the same phenomena as SWF, i.e., the delay of the corner stall and less pitchwise expansion, the way they are achieved is different. At the endwall, the inclination of the blade force by the dihedral increases the pressure level, reduces the velocity level (and mass flow rate), and reduces the loading there. Because of this unloading at the endwall, the onset of the corner stall is delayed and secondary flows on the endwall decrease. Also, the low-energy fluid near the endwall moves toward the midspan because of the larger spanwise pressure gradient. Probably, this avoids an accumulation of low-energy fluid and prevents the expansion of the corner stall.

A main negative effect is the increased loading at the midspan, which results in higher airfoil loss. Also, the movement of low-energy fluid from the endwall mentioned above makes the midspan loss worse.

In the case of DHP, loss improvement is achieved over wider range of incidences than SWF. This is because the loss deterioration at the midspan is smaller than SWF and DHP can keep better balance between the gain at the endwall and the loss at the midspan.

Conclusion

We have carried out a parametric study of two stacking lines, namely, sweep and dihedral, using pressure measurements at the downstream plane of the cascades and flow visualizations on the blade surface and the endwall. Both types of blades considered are symmetric about the midspan and consist of a straight central portion with either swept or dihedral portions towards the endwalls.

Also, detailed three-dimensional flowfield measurements inside the blade passage were performed in the cases that showed the best performance in each of the parametric study for swept blades or dihedral blades.

The following conclusions have been drawn:

- The parametric study determined the configurations that reduce overall losses by about 20 percent in both swept blades and dihedral blades. Also, the advantageous direction of the sweep is proved to be forward, the stacking line being more upstream at the endwall than the midspan.
- Detailed flowfield measurements inside the blade passage clarified that both sweep and dihedral have beneficial effects and negative effects at the same time and loss improvement depends on their balance.
- The forward-swept blades form a vortex in the forward portion of the passage, which has the opposite sense of rotation to the passage vortex. This vortex seems to supply high-energy fluid to the suction/endwall corner and to delay the onset of corner stall.
- The forward swept blades change the pressure field and create a larger adverse pressure gradient on the suction surface around the midspan. This causes a separation and high losses. Also, the forward-swept blades create large spanwise flows toward the midspan on the suction surface at the aft portion of the passage. Because of these, losses near the endwall reduce but losses around the midspan increase.
- In the positive dihedral blades, unloading near the endwall and overloading near the midspan were observed. Unloading near the endwall delays the onset of the corner stall while overloading around the midspan increases the airfoil loss.
- The somewhat larger spanwise pressure gradient on the suction surface created by dihedral prevents an accumulation of low-energy fluid near the endwall; however, it worsens midspan losses by the convection of the low-energy fluid from the endwall.
- The positive dihedral blades are effective over a wider range of incidence angles than swept blades.

References

1 Breugelmans, F. A. E., Carels, Y., and Demuth, M., 1984, "Influence of Dihedral on the Secondary Flow in a Two-Dimensional Compressor Cascade," ASME *Journal of Engineering for Gas Turbine and Power,* Vol. 106, pp. 578–584.

2 Weingold, H. D., Neubert, R. J., Behlke, R. F., and Potter, G. E., 1995, "Reduction of Compressor Stator Endwall Losses Through the Use of Bowed Stators," ASME Paper No. 95-GT-380.

3 Harrison, S., 1992, "The Influence of Blade Lean on Turbine Losses," ASME JOURNAL OF TURBOMACHINERY, Vol. 114, pp. 185–190.

4 Wang, Z., Han, W., and Xu, W., 1991, "The Effect of Blade Curving on Flow Characteristics in Rectangular Turbine Stator Cascades With Different Incidences," ASME Paper No. 91-GT-60.

5 Robinson, C. J., Northall, J. D., and McFarlane, C. W. R., 1989, "Measurement and Calculation of the Three-Dimensional Flow in Axial Compressor Stators, With and Without Endbends," ASME Paper No. 89-GT-6.

6 D. C. Wisler, 1985, "Loss Reduction in Axial-Flow Compressors Through Low-Speed Model Testing," ASME *Journal of Engineering for Gas Turbine and Power,* Vol. 107, pp. 354–363.

7 Tweedt, D. L., Okiishi, T. H., and Hathaway, M. D., 1986, "Stator Endwall Leading-Edge Sweep and Hub Shroud Influence on Compressor Performance," ASME JOURNAL OF TURBOMACHINERY, Vol. 108, pp. 224–232.

8 Doerffer, P. P., and Amecke, J., 1994, "Secondary Flow Control and Streamwise Vortices Formation," ASME Paper No. 94-GT-376.

9 Sanger, N. L., 1983, "The Use of Optimization Techniques to Design-Controlled Diffusion Compressor Blading," ASME *Journal of Engineering of Power,* Vol. 105, pp. 256–263.

10 Sanger, N. L., and Shreeve, R. P., 1986, "Comparison of the Calculated and Experimental Cascade Performance for Controlled-Diffusion Compressor Stator Blading," ASME JOURNAL OF TURBOMACHINERY, Vol. 108, pp. 42–50.

DISCUSSION

J. M. M. Place[1] and N. A. Cumpsty[2]

Accurate data obtained in nonsimple cascades offer opportunities for testing our understanding of how flow behaves in three dimensions. They also provide cases for testing CFD. The present results are to be welcomed.

We ourselves have encountered difficulty with the terminology that describes different blade stacking lines because sweep and dihedral have distinct aerodynamic effects. It is convenient to reserve the meaning of dihedral to be lean at right angles to the sweep so the translation producing it is normal to the stagger line. As the authors point out, the DHP blade, described in the paper as having "dihedral," actually has aft sweep as well as dihedral. Since Breugelmans et al. (1984) were so careful in their definitions, this much less rigorous usage seems paradoxical. It would seem more logical, as well as more desirable, to describe the DHP blades as having "tangential lean," which includes both true dihedral and sweep.

In our research we have made some effort to explain the effects of sweep and dihedral (Place, 1997). Most of this has been carried out using three-dimensional Navier–Stokes solvers, but some insight can be obtained using a lifting line or bound vortex representation of the blades. When the blade is swept or leaned, the lifting line is assumed in these simplified treatments to move by the same amount. The circulation of the bound vorticity inclined into the wall induces velocities, as does the image vortex of equal magnitude. Over the forward part of the blade, the forward sweep induces flow near the suction surface toward the endwall and induces flow near the pressure surface away from the endwall. These changes to the spanwise flow oppose the classical secondary flow created by turning the incoming endwall boundary layer within the blade passage, and therefore reduce the cross-passage flow of endwall fluid toward the suction surface. This effect can be discerned in Fig. 12, where the flow is toward the suction surface in the straight blade and toward the pressure surface in the forward-swept blade. Aft sweep will tend to add to the classical secondary flow and there is then more loss and blockage buildup on the suction surface.

Sweep has other effects on the end-wall flow, which may be explained by trying to match the curved meridional streamline pattern on an infinite-span blade (which approximates the behavior near midspan) with the straight meridional streamlines near the endwalls. Forward sweep leads to dilation of the meridional streamtube near the endwall ahead of the leading edge followed by a contraction and then again a dilation further downstream. The sequence leads to a corresponding acceleration, deceleration, and acceleration of the endwall flow relative to that for unswept blades; the consequence is usually lower endwall loss. Aft sweep has the opposite effects and leads to an increase in endwall loss.

Dihedral, on the other hand, causes the bound vortex and its image to induce velocities more or less parallel to the primary flow. If the dihedral is positive, so that the suction surface makes an obtuse angle with the endwall, the induced velocities tend to reduce the velocity peak on the suction surface, which reduces the diffusion near the suction surface-endwall corner.

[1] Rolls Royce plc, P.O. Box 31, Derby DE24 8BJ United Kingdom.

[2] Whittle Laboratory, University of Cambridge, Madingley Road, Cambridge, CB3 ODY United Kingdom.

Conclusion

We have carried out a parametric study of two stacking lines, namely, sweep and dihedral, using pressure measurements at the downstream plane of the cascades and flow visualizations on the blade surface and the endwall. Both types of blades considered are symmetric about the midspan and consist of a straight central portion with either swept or dihedral portions towards the endwalls.

Also, detailed three-dimensional flowfield measurements inside the blade passage were performed in the cases that showed the best performance in each of the parametric study for swept blades or dihedral blades.

The following conclusions have been drawn:

- The parametric study determined the configurations that reduce overall losses by about 20 percent in both swept blades and dihedral blades. Also, the advantageous direction of the sweep is proved to be forward, the stacking line being more upstream at the endwall than the midspan.
- Detailed flowfield measurements inside the blade passage clarified that both sweep and dihedral have beneficial effects and negative effects at the same time and loss improvement depends on their balance.
- The forward-swept blades form a vortex in the forward portion of the passage, which has the opposite sense of rotation to the passage vortex. This vortex seems to supply high-energy fluid to the suction/endwall corner and to delay the onset of corner stall.
- The forward swept blades change the pressure field and create a larger adverse pressure gradient on the suction surface around the midspan. This causes a separation and high losses. Also, the forward-swept blades create large spanwise flows toward the midspan on the suction surface at the aft portion of the passage. Because of these, losses near the endwall reduce but losses around the midspan increase.
- In the positive dihedral blades, unloading near the endwall and overloading near the midspan were observed. Unloading near the endwall delays the onset of the corner stall while overloading around the midspan increases the airfoil loss.
- The somewhat larger spanwise pressure gradient on the suction surface created by dihedral prevents an accumulation of low-energy fluid near the endwall; however, it worsens midspan losses by the convection of the low-energy fluid from the endwall.
- The positive dihedral blades are effective over a wider range of incidence angles than swept blades.

References

1 Breugelmans, F. A. E., Carels, Y., and Demuth, M., 1984, "Influence of Dihedral on the Secondary Flow in a Two-Dimensional Compressor Cascade," ASME *Journal of Engineering for Gas Turbine and Power,* Vol. 106, pp. 578–584.

2 Weingold, H. D., Neubert, R. J., Behlke, R. F., and Potter, G. E., 1995, "Reduction of Compressor Stator Endwall Losses Through the Use of Bowed Stators," ASME Paper No. 95-GT-380.

3 Harrison, S., 1992, "The Influence of Blade Lean on Turbine Losses," ASME JOURNAL OF TURBOMACHINERY, Vol. 114, pp. 185–190.

4 Wang, Z., Han, W., and Xu, W., 1991, "The Effect of Blade Curving on Flow Characteristics in Rectangular Turbine Stator Cascades With Different Incidences," ASME Paper No. 91-GT-60.

5 Robinson, C. J., Northall, J. D., and McFarlane, C. W. R., 1989, "Measurement and Calculation of the Three-Dimensional Flow in Axial Compressor Stators, With and Without Endbends," ASME Paper No. 89-GT-6.

6 D. C. Wisler, 1985, "Loss Reduction in Axial-Flow Compressors Through Low-Speed Model Testing," ASME *Journal of Engineering for Gas Turbine and Power,* Vol. 107, pp. 354–363.

7 Tweedt, D. L., Okiishi, T. H., and Hathaway, M. D., 1986, "Stator Endwall Leading-Edge Sweep and Hub Shroud Influence on Compressor Performance," ASME JOURNAL OF TURBOMACHINERY, Vol. 108, pp. 224–232.

8 Doerffer, P. P., and Amecke, J., 1994, "Secondary Flow Control and Streamwise Vortices Formation," ASME Paper No. 94-GT-376.

9 Sanger, N. L., 1983, "The Use of Optimization Techniques to Design-Controlled Diffusion Compressor Blading," ASME *Journal of Engineering of Power,* Vol. 105, pp. 256–263.

10 Sanger, N. L., and Shreeve, R. P., 1986, "Comparison of the Calculated and Experimental Cascade Performance for Controlled-Diffusion Compressor Stator Blading," ASME JOURNAL OF TURBOMACHINERY, Vol. 108, pp. 42–50.

DISCUSSION

J. M. M. Place[1] and N. A. Cumpsty[2]

Accurate data obtained in nonsimple cascades offer opportunities for testing our understanding of how flow behaves in three dimensions. They also provide cases for testing CFD. The present results are to be welcomed.

We ourselves have encountered difficulty with the terminology that describes different blade stacking lines because sweep and dihedral have distinct aerodynamic effects. It is convenient to reserve the meaning of dihedral to be lean at right angles to the sweep so the translation producing it is normal to the stagger line. As the authors point out, the DHP blade, described in the paper as having "dihedral," actually has aft sweep as well as dihedral. Since Breugelmans et al. (1984) were so careful in their definitions, this much less rigorous usage seems paradoxical. It would seem more logical, as well as more desirable, to describe the DHP blades as having "tangential lean," which includes both true dihedral and sweep.

In our research we have made some effort to explain the effects of sweep and dihedral (Place, 1997). Most of this has been carried out using three-dimensional Navier–Stokes solvers, but some insight can be obtained using a lifting line or bound vortex representation of the blades. When the blade is swept or leaned, the lifting line is assumed in these simplified treatments to move by the same amount. The circulation of the bound vorticity inclined into the wall induces velocities, as does the image vortex of equal magnitude. Over the forward part of the blade, the forward sweep induces flow near the suction surface toward the endwall and induces flow near the pressure surface away from the endwall. These changes to the spanwise flow oppose the classical secondary flow created by turning the incoming endwall boundary layer within the blade passage, and therefore reduce the cross-passage flow of endwall fluid toward the suction surface. This effect can be discerned in Fig. 12, where the flow is toward the suction surface in the straight blade and toward the pressure surface in the forward-swept blade. Aft sweep will tend to add to the classical secondary flow and there is then more loss and blockage buildup on the suction surface.

Sweep has other effects on the end-wall flow, which may be explained by trying to match the curved meridional streamline pattern on an infinite-span blade (which approximates the behavior near midspan) with the straight meridional streamlines near the endwalls. Forward sweep leads to dilation of the meridional streamtube near the endwall ahead of the leading edge followed by a contraction and then again a dilation further downstream. The sequence leads to a corresponding acceleration, deceleration, and acceleration of the endwall flow relative to that for unswept blades; the consequence is usually lower endwall loss. Aft sweep has the opposite effects and leads to an increase in endwall loss.

Dihedral, on the other hand, causes the bound vortex and its image to induce velocities more or less parallel to the primary flow. If the dihedral is positive, so that the suction surface makes an obtuse angle with the endwall, the induced velocities tend to reduce the velocity peak on the suction surface, which reduces the diffusion near the suction surface-endwall corner.

[1] Rolls Royce plc, P.O. Box 31, Derby DE24 8BJ United Kingdom.

[2] Whittle Laboratory, University of Cambridge, Madingley Road, Cambridge, CB3 ODY United Kingdom.

Dihedral generally has only a small effect on cross-passage flow. Although positive dihedral reduces the cross-passage pressure gradient, the net effect on cross-passage flow can be small, because positive dihedral also reduces the throughflow velocity near the wall. This can be seen in Fig. 11, where the "twist" of the loss contours near the endwall (a measure of the cross-passage flow) for the blade with dihedral is similar to that of the straight blade. (In fact, the twist is slightly greater for the DHP blade, which is probably a result of the aft sweep produced by the tangential lean.)

These arguments about sweep and dihedral are based on the lifting-line vortex model, which is an oversimplification. In the first place, the use of a single bound vortex is a poor representation of blades that are long in the chordwise sense compared with the thickness of the endwall boundary layer or the spanwise extent of dihedral or sweep. Furthermore, the effect of stacking-line geometry changes on the pressure distribution of the blades is not as assumed above, but the suction and the pressure peaks move less than the blade sections move. Most obviously in the case of sweep, the isobars tend to remain comparatively straight across the span, so the blade sections tend to move relative to the isobars. A proper treatment requires full three-dimensional calculation methods, and arguments such as these that consider a bound vortex are intended only to give a plausible explanation rather than a complete description. One can, however, use such the simplified methods to recognize that the low loss of the forward-swept blade is not due to the vortex observed in the forward part of the passage, but to the bound vorticity inducing velocities that oppose the classical secondary flow.

It should also be noted that an aerofoil profile section (such as the NACA series), which is an optimum in a two-dimensional flow, will not form the optimum in a three-dimensional flow, or one where lean and sweep has been introduced. The appropriate blades will have their profile (camber, stagger, and thickness distributions) tailored to the flow and geometry.

There are two further points that the authors may be able to deal with before the paper is published in the ASME JOURNAL OF TURBOMACHINERY. There is some confusion in our minds between Figs. 15 and 16. In Fig. 16 the swept-forward blade has the highest diffusion factor at midspan, but in Fig. 15 it would appear to be the blade with dihedral, which has the largest suction surface diffusion. It might also be mentioned that our experience has shown that the highest level of blade loading is not to be expected at midspan, but where the sweep or dihedral blend into the straight section. Finally, the arrows in Figs. 11 and 12 are too small in some places and there is a need for an arrow to be shown that gives the free-stream velocity magnitude.

References

Breugelmans, F. A. H., Carels, Y., and Demuth, M., 1984, "Influence of Dihedral on the Secondary Flow in a Two-Dimensional Compressor Cascade," ASME *Journal of Engineering for Gas Turbines and Power*, Vol. 106, pp. 578–584.

Place, J. M. M., 1997, "Three-Dimensional Flow in Core Compressors," PhD Dissertation, University of Cambridge.

Authors' Closure

The authors would like to thank Dr. Place and Professor Cumpsty for their detailed discussion. The following closure is prepared for the discussion:

1 According to Smith et al. (1963), "Blades are said to have sweep when the flow direction is not perpendicular to the spanwise direction," and we did not want our "dihedral blades" to have this feature. On the other hand, sweep inevitably introduces some extent of dihedral. And, as we have pointed out in our paper, sweep and dihedral are purely independent only when the stagger angle is zero. In this geometric sense, the authors agree that it is more logical to describe our DHP blades as "tangential-lean blades." Also in this sense, we might say that sweep has "stagger-wise lean."

2 We simply described the experimental results that the vortex in the forward part of SWF rotates in the direction opposite to that the passage vortex. In the aft part of SWF, the passage vortex is weakened. This result does not contradict the lifting-line vortex model in the discussion. Also we would like to emphasize the effect of delaying the onset of corner stall by the flow behavior observed in the forward part of SWF.

3 With respect to the experience of Dr. Place and Professor Cumpsty that the highest level of loading is expected where sweep or dihedral blends into straight section, our results also showed the same feature as shown in Fig. 16 (Local Diffusion Factor). SWF has a sweep portion of 42 mm and DHP has dihedral portion of 21 mm. Both of them show the highest values there.

Reference

Leroy, H., Smith, J. R., and Hsuan, Yeh, 1963, "Sweep and Dihedral Effects in Axial-Flow Turbomachinery," ASME *Journal of Basic Engineering*, Vol. 85, pp. 401–416.

Dihedral generally has only a small effect on cross-passage flow. Although positive dihedral reduces the cross-passage pressure gradient, the net effect on cross-passage flow can be small, because positive dihedral also reduces the throughflow velocity near the wall. This can be seen in Fig. 11, where the "twist" of the loss contours near the endwall (a measure of the cross-passage flow) for the blade with dihedral is similar to that of the straight blade. (In fact, the twist is slightly greater for the DHP blade, which is probably a result of the aft sweep produced by the tangential lean.)

These arguments about sweep and dihedral are based on the lifting-line vortex model, which is an oversimplification. In the first place, the use of a single bound vortex is a poor representation of blades that are long in the chordwise sense compared with the thickness of the endwall boundary layer or the spanwise extent of dihedral or sweep. Furthermore, the effect of stacking-line geometry changes on the pressure distribution of the blades is not as assumed above, but the suction and the pressure peaks move less than the blade sections move. Most obviously in the case of sweep, the isobars tend to remain comparatively straight across the span, so the blade sections tend to move relative to the isobars. A proper treatment requires full three-dimensional calculation methods, and arguments such as these that consider a bound vortex are intended only to give a plausible explanation rather than a complete description. One can, however, use such the simplified methods to recognize that the low loss of the forward-swept blade is not due to the vortex observed in the forward part of the passage, but to the bound vorticity inducing velocities that oppose the classical secondary flow.

It should also be noted that an aerofoil profile section (such as the NACA series), which is an optimum in a two-dimensional flow, will not form the optimum in a three-dimensional flow, or one where lean and sweep has been introduced. The appropriate blades will have their profile (camber, stagger, and thickness distributions) tailored to the flow and geometry.

There are two further points that the authors may be able to deal with before the paper is published in the ASME JOURNAL OF TURBOMACHINERY. There is some confusion in our minds between Figs. 15 and 16. In Fig. 16 the swept-forward blade has the highest diffusion factor at midspan, but in Fig. 15 it would appear to be the blade with dihedral, which has the largest suction surface diffusion. It might also be mentioned that our experience has shown that the highest level of blade loading is not to be expected at midspan, but where the sweep or dihedral blend into the straight section. Finally, the arrows in Figs. 11 and 12 are too small in some places and there is a need for an arrow to be shown that gives the free-stream velocity magnitude.

References

Breugelmans, F. A. H., Carels, Y., and Demuth, M., 1984, "Influence of Dihedral on the Secondary Flow in a Two-Dimensional Compressor Cascade," ASME *Journal of Engineering for Gas Turbines and Power*, Vol. 106, pp. 578–584.

Place, J. M. M., 1997, "Three-Dimensional Flow in Core Compressors," PhD Dissertation, University of Cambridge.

Authors' Closure

The authors would like to thank Dr. Place and Professor Cumpsty for their detailed discussion. The following closure is prepared for the discussion:

1 According to Smith et al. (1963), "Blades are said to have sweep when the flow direction is not perpendicular to the spanwise direction," and we did not want our "dihedral blades" to have this feature. On the other hand, sweep inevitably introduces some extent of dihedral. And, as we have pointed out in our paper, sweep and dihedral are purely independent only when the stagger angle is zero. In this geometric sense, the authors agree that it is more logical to describe our DHP blades as "tangential-lean blades." Also in this sense, we might say that sweep has "stagger-wise lean."

2 We simply described the experimental results that the vortex in the forward part of SWF rotates in the direction opposite to that the passage vortex. In the aft part of SWF, the passage vortex is weakened. This result does not contradict the lifting-line vortex model in the discussion. Also we would like to emphasize the effect of delaying the onset of corner stall by the flow behavior observed in the forward part of SWF.

3 With respect to the experience of Dr. Place and Professor Cumpsty that the highest level of loading is expected where sweep or dihedral blends into straight section, our results also showed the same feature as shown in Fig. 16 (Local Diffusion Factor). SWF has a sweep portion of 42 mm and DHP has dihedral portion of 21 mm. Both of them show the highest values there.

Reference

Leroy, H., Smith, J. R., and Hsuan, Yeh, 1963, "Sweep and Dihedral Effects in Axial-Flow Turbomachinery," ASME *Journal of Basic Engineering*, Vol. 85, pp. 401–416.

Blockage Development in a Transonic, Axial Compressor Rotor

K. L. Suder
NASA-Lewis Research Center,
Cleveland, OH 44135

A detailed experimental investigation to understand and quantify the development of blockage in the flow field of a transonic, axial flow compressor rotor (NASA Rotor 37) has been undertaken. Detailed laser anemometer measurements were acquired upstream, within, and downstream of a transonic, axial compressor rotor operating at 100, 85, 80, and 60 percent of design speed, which provided inlet relative Mach numbers at the blade tip of 1.48, 1.26, 1.18, and 0.89, respectively. The impact of the shock on the blockage development, pertaining to both the shock/boundary layer interactions and the shock/tip clearance flow interactions, is discussed. The results indicate that for this rotor the blockage in the endwall region is 2–3 times that of the core flow region, and the blockage in the core flow region more than doubles when the shock strength is sufficient to separate the suction surface boundary layer.

Introduction

Based on the work of Koch and Smith (1976), and Koch (1981), it is clear that there is a relationship between the blockage (defined as the effective reduction in flow area) in a turbomachine and the losses, pressure rise, and flow range of that turbomachine. For example, Smith (1970) correlated the casing boundary layer displacement thickness to the static pressure rise and efficiency from a number of low-speed multistage compressor tests. Furthermore, Smith demonstrated that for low-speed axial compressors the endwall boundary layer thickness is directly related to (1) the blade-to-blade passage width, (2) the aerodynamic loading level, and (3) the tip clearance. Smith never used the term blockage, but his work clearly demonstrates the direct relationship of the blockage to the pressure rise and losses in the endwall region of low-speed compressors. In this investigation both endwall blockage and the blockage generated by the blade surface boundary layers will be evaluated. It will be shown that the blockage resulting from the blade boundary layers is sensitive to the inlet Mach number level, especially at high Mach number conditions for which the shock may induce boundary layer separation, thereby changing the blockage level and its spanwise distribution.

A methodology to quantify the endwall blockage generated within the blade row by the tip clearance flow was developed by Khalid (1994). His results were based on three-dimensional Navier–Stokes computations of the flowfields in a low-speed stator, low-speed rotor, and a transonic fan with several values of tip clearance height. His results indicated that the loss in total pressure in the endwall region resulted from the interaction of the leakage flow and passage flows and that the vortical structure associated with the clearance vortex was not a major factor in generating the endwall blockage. Khalid developed a correlation between the endwall blockage and the aerodynamic loading on the blade, which indicated there is a limiting value of the loading. In this paper we use experimental data and variations on Khalid's methodology to evaluate the blockage in both the endwall and core flow regions of a high-speed, highly loaded compressor rotor. The assumptions made and calculation procedure used in this paper to estimate blockage are described in the data analysis section.

One may question the need to quantify blockage from experimental measurements with the advent of three-dimensional Navier–Stokes flow solvers. However, it has been demonstrated that state-of-the-art computational fluid dynamic (CFD) codes are unable to predict the performance and flowfield characteristics of NASA Rotor 37 accurately. CFD simulations of Rotor 37 generated for the ASME "blind test case study" as well as additional simulations of Rotor 37 generally predict a higher total pressure and total temperature rise across the rotor as compared to the experimental data (see Chima, 1996; Dalbert and Wiss, 1995; Denton, 1996; Shabbir et al., 1996; Suder, 1996). In addition, the shapes of the radial distributions of total temperature and pressure from the CFD simulations were very much different from that of the experimental data. These discrepancies between the data and CFD and the differences among the various CFD solutions are in part attributed to the inability of the CFD to predict the blockage accurately and to the sensitivity of the rotor's performance to slight changes in blockage. Further evidence that the CFD has difficulty in accurately predicting the blockage in NASA Rotor 37 can be found in the results of Suder and Celestina (1996) who studied the interaction between the shock and tip clearance flow. Their results indicated that their CFD simulation predicted the features and trends of the endwall flow field but underpredicted the radial penetration of the tip clearance flow. It was surmised that the CFD was underpredicting the blockage in the endwall region. In this paper we will quantify the blockage development resulting from the shock/tip clearance flow interactions and the shock/blade surface boundary layer interactions and relate the blockage to the performance characteristics of the rotor.

To illustrate the impact of the blockage on the performance characteristics of the rotor in this investigation using only the experimental data, the measured and ideal pressure rise and adiabatic efficiency characteristics for this test compressor operating at design speed are plotted in Fig. 1. The mass flow is normalized by the choking mass flow of 20.93 kg/s. The ideal pressure ratio was calculated by using the isentropic relation and the actual work input. The shock loss was calculated using a normal shock with an inlet Mach number of 1.4. In a transonic/supersonic compressor the shock is the primary source of pressure rise, and though the losses are considerable across the shock, it is shown in Fig. 1 that the shock is an efficient compressor. These results are consistent with the findings of Wood et al. (1986). The remaining losses such as those due to blade boundary layers, blade wakes, secondary flows, and tip clear-

Contributed by the International Gas Turbine Institute and presented at the 42nd International Gas Turbine and Aeroengine Congress and Exhibition, Orlando, Florida, June 2–5, 1997. Manuscript received at ASME Headquarters February 1997. Paper No. 97-GT-394. Associate Technical Editor: H. A. Kidd.

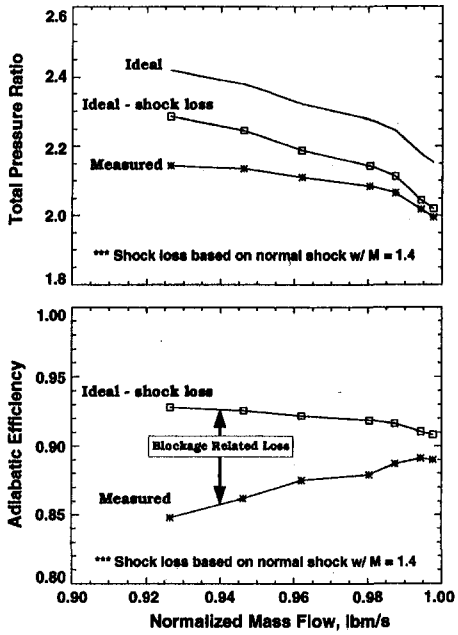

Fig. 1 Estimation of blockage related losses and their impact on performance

ance flows are indicative of a blockage to the flow, and they will be referred to as the "blockage-related losses." It is evident that for this rotor the blockage has a considerable impact on the performance, and there is much potential for gains in machine performance if we can understand the blockage development and optimize the design to minimize the blockage related losses.

Therefore, the intent of this work is to quantify the level of blockage and to explain and verify with experimental evidence the flow mechanisms responsible for the development of blockage in a transonic, axial compressor rotor operating at design and off-design conditions. Previous research in this area has either been performed using computational methods to calculate the flowfield or experimental measurements acquired downstream of the compressor—generally for low-speed machines operating at design conditions. In this investigation detailed laser anemometer measurements acquired upstream, within, and downstream of a transonic, axial compressor rotor operating at design and off-design conditions are used to investigate blockage development. At design speed where the rotor shock is present, data are presented and analysis performed at two operating conditions to show the blockage development within and downstream of the rotor blade row. Inside the blade row the blockage is evaluated ahead of the rotor passage shock, downstream of the rotor passage shock, and near the trailing edge of the blade row. This analysis is performed in the core flow area as well as in the casing endwall region. Blockage is also evaluated for two part-speed conditions for which (1) the rotor passage shock is much weaker than that at design speed and (2) there is no rotor passage shock.

Test Equipment and Procedure

Facility and Test Rotor. The experiment was performed in the single-stage transonic compressor facility at the NASA Lewis Research Center. A detailed description of the facility is given by Urasek and Janetzke (1972). The test compressor was designed as an inlet stage for an eight-stage 20:1 pressure ratio advanced core compressor and is designated as NASA Stage 37. For this experiment NASA Rotor 37 was tested in isolation to avoid the interaction effects generated by the presence of an upstream inlet guide vane or downstream stator blade row. (Note that this test configuration of NASA Rotor 37 was that used as the test vehicle for the ASME sponsored CFD test case exercise. The results of this exercise were presented at the 1994 ASME IGTI turbomachinery conference and are discussed by Denton, 1996.) The rotor design pressure ratio is 2.106 at a mass flow of 20.19 kg/s. The inlet Mach number is 1.13 at the hub and 1.48 at the tip at the design tip speed of 454 m/s. The rotor aspect ratio is 1.19 and the hub/tip radius ratio is 0.70. Details of the rotor aerodynamic design were reported by Reid and Moore (1978). Overall aerodynamic performance of the stage was reported by Moore and Reid (1980).

Aerodynamic Probe Measurements. The performance characteristics of the rotor are determined from aerodynamic probes, which are surveyed radially approximately one chord upstream of the rotor and two chords downstream of the rotor. The probe measurements are corrected for Mach number and streamline slope based on a calibration of each probe used and on the design streamline slope. All measurements are corrected to NACA standard-day sea-level conditions at the rotor inlet. Radial distributions of total temperature are mass averaged across the annulus. Radial distributions of total pressure are energy averaged by converting them to their enthalpy equivalents and then mass averaging them across the annulus. The details of these calculations are described by Suder (1996). The measurement uncertainties are: massflow, ± 0.3 kg/s; flow angle, ± 1.0 deg; total pressure, ± 0.01 N/cm^2; total temperature, ± 0.6 K.

Laser Anemometer System and Measurements. Detailed flow field measurements are acquired with a two-color fringe-type laser anemometer system, which is configured to simultaneously acquire the tangential and axial velocity components. Measurements are acquired along the 30, 50, 70, 90, and 95 percent span streamsurfaces and several cross-channel planes upstream and downstream of the rotor. A full description of the laser anemometer system, seeding system, data acquisition, and reduction procedure is given in Suder (1996). The uncertainties in the laser anemometer velocity and flow angle measurements are estimated as 1 percent and 0.5 deg, respectively.

All laser anemometer results presented are based on the velocity distribution across an averaged blade passage, which is calculated by ensemble-averaging the measurements acquired in each individual blade passage. The relative Mach number is calculated from the relative velocity and the local speed of sound at each point in the flow field using the procedure discussed by Strazisar et al. (1989).

Nomenclature

A = area, m^2
B = blockage (1 = effective flow area/geometric flow area)
H = shape factor = δ^*/θ
M_{rel} = relative Mach number
N = rotation speed of rotor, rpm
NB = number of rotor blades = 36
P = total pressure, N/m^2
P_{ref} = standard day total pressure = 101,325 N/m^2
r = radius, cm
T_{ref} = standard day total temperature = 288.2 K
T_s = static temperature, K
u = local velocity, m/s
y = distance normal from a surface, cm
δ = boundary layer thickness, cm
δ^* = boundary layer displacement thickness, cm
θ = boundary layer or wake momentum thickness, cm
ρ = density, kg/m^3

Table 1 Variation of inlet relative Mach number and rotor tip clearance for tested rotor wheel speeds

% Design Speed	M_{rel} at Hub	M_{rel} at Tip	Tip Clearance, mm (% rotor tip chord)
60	0.68	0.89	0.58 (1.0)
80	0.90	1.18	0.50 (0.9)
85	0.96	1.26	N/A
100	1.13	1.48	0.40 (0.7)

Experimental Procedure. The majority of the data were acquired for the rotor operating at design speed conditions. However, to evaluate the effect of the inlet Mach number on the rotor performance and blockage development, data were also acquired at part speed conditions. The inlet relative Mach numbers and measured tip clearance for each rotor wheel speed are provided in Table 1.

The performance characteristics at 60, 80, and 100 percent of design speed, based on the aerodynamic probe surveys, are plotted in Fig. 2. Detailed laser anemometer surveys were performed at one throttle valve setting each for the data acquired at 60, 80, and 85 percent of rotor design speed. At design speed the LFA data were acquired at three throttle valve positions and are denoted max flow, high flow, and low flow in reference to the amount of mass flow through the rotor. The circled data points in Fig. 2 indicate the high flow operating conditions where the detailed laser anemometer surveys were acquired. These conditions represent a nearly constant incidence angle to the rotor at 60, 80, and 100 percent of design speed.

Data Analysis: Quantification of Blockage

Blockage is defined as an effective reduction in flow area and is represented by:

$$B = \left[1 - \left(\frac{\text{effective area}}{\text{geometric area}}\right)\right] = 1 - \frac{\left(A - \int \delta^* dr\right)}{A} \quad (1)$$

where A is the total area and δ^* is the integral of the velocity-density deficit across the rotor passage. The integral of the velocity-density deficit is defined at each radial measurement location by

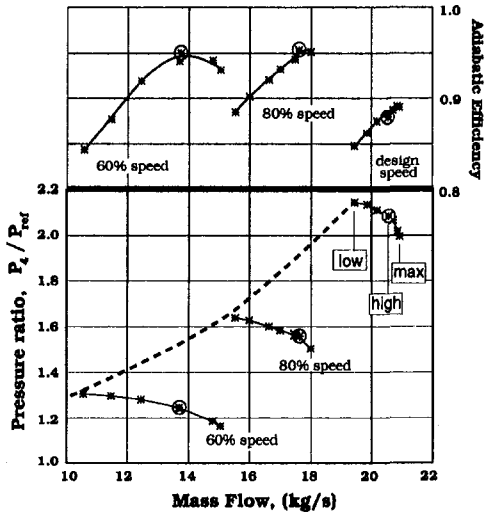

Fig. 2 Overall performance characteristics

$$\delta^*(r) = \int_{\theta=0}^{2\pi/NB} \left(1 - \frac{\rho u}{(\rho u)_{\text{inviscid}}}\right) r d\theta \quad (2)$$

and is analogous to the displacement thickness from boundary layer theory. (δ^* will be referred to as the displacement thickness throughout the text.) The difficulty in evaluating δ^* arises in determining the inviscid velocity and density inside a compressor, in which the flow is compressible and not uniform across the passage. Since the density is not measured by the laser anemometer system, an approximation of the displacement thickness inside the blade row is evaluated by neglecting the variation of density within the defect region, i.e., it is assumed that $\rho = \rho_{\text{inviscid}}$, and the displacement thickness is estimated by:

$$\delta^*(r) = \int_{\theta=0}^{2\pi/NB} \left(1 - \frac{u}{u_{\text{inviscid}}}\right) r d\theta \quad (3)$$

Downstream of the blade it is assumed that the static pressure is constant within the defect region and is equal to the value at the edge of the defect region. Assuming uniform static pressure in the defect region in conjunction with the ideal gas law, the displacement thickness downstream of the blade is estimated by:

$$\delta^*_{\text{downstream}}(r) = \int_{\theta=0}^{2\pi/NB} \left(1 - \frac{T_{s,\text{inviscid}} \cdot u}{T_s \cdot u_{\text{inviscid}}}\right) r d\theta \quad (4)$$

The displacement thickness downstream of the blade has been evaluated using both Eqs. (3) and (4). Comparing these calculations to those from CFD results indicate that using Eq. (4) is appropriate to account for the density variations in the defect region. (The analysis code used in the present study was used by Suder and Celestina (1996), and it solves the Reynolds-averaged form of the Navier–Stokes equations developed by Adamczyk et al. (1989).) In order to assess the impact of the density variations in the defect region on the blockage calculations, this same CFD simulation was used to calculate the blockage using both the density-velocity defect (Eq. (2)) and the velocity defect alone (Eq. (3)). These calculations (though not shown herein) indicate the region of velocity defect is in phase with density defect, therefore the shape of the curve depicting the radial distribution of blockage is the same whether or not density is included in the calculation of displacement thickness. However, the inclusion of density variations in the blockage calculation does increase the overall level of blockage, and for this case the difference in blockage was only 0.8 percent of the flow area. Also, note that CFD users can calculate the blockage using the same procedure used herein to compare their results to the data. In summary, the values of blockage calculated downstream of the rotor using only the measured velocity distributions are believed to be within 10 percent of those calculated with density variations included, which is sufficient to establish trends and evaluate the regions of the flowfield that dominate the generation of blockage.

Quantification of Blockage Downstream of the Rotor Blade Row. Downstream of the rotor blade row, blockage is evaluated at a given axial location by calculating the displacement thickness for each radial location at which data were measured. An example illustrating the method used is presented in Fig. 3.

1 Identify the area over which to evaluate the blockage. Figure 3(*a*) is a cross-channel plot of the axial velocity contours at approximately 15 percent rotor chord downstream of the rotor trailing edge. The data were ensemble and passage averaged and were then duplicated across two rotor pitches in the circumferential direction for clarity. In this example the data were

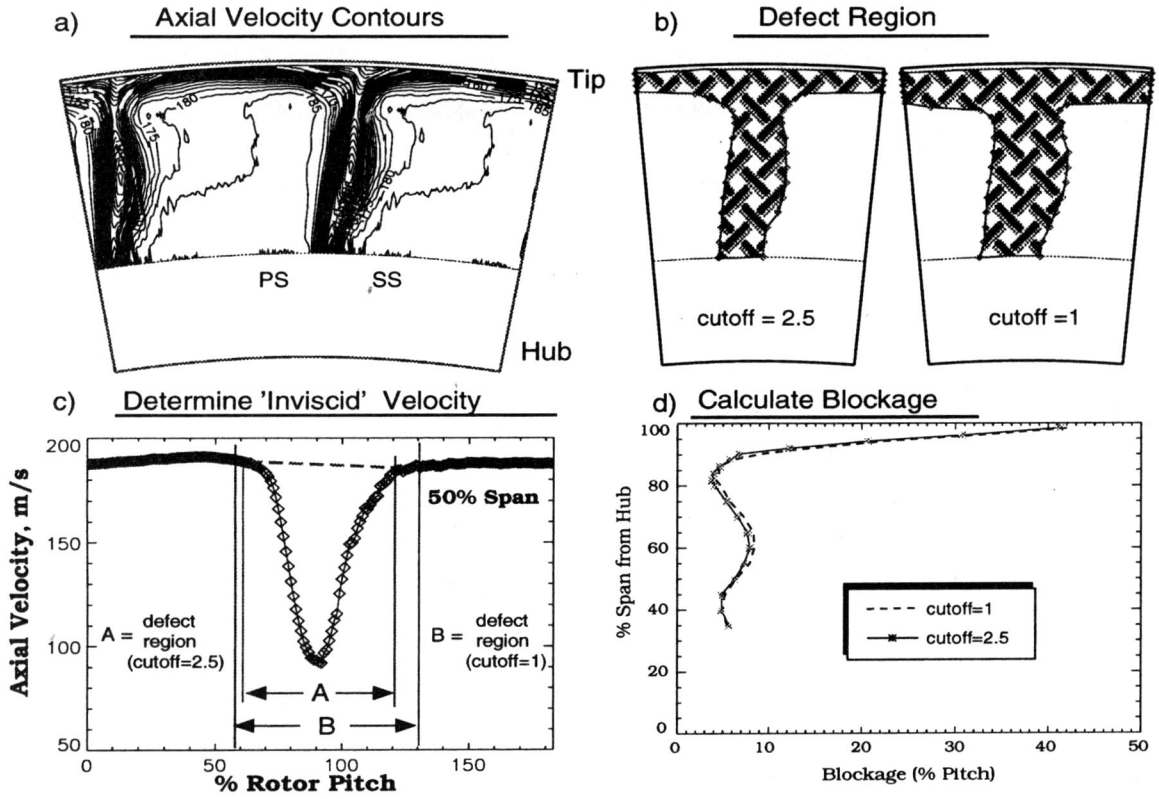

Fig. 3 Procedure to calculate blockage downstream of the blade row

acquired from 35 to 98 percent of span from the rotor hub. The axial velocity contours are shown for increments of 5 m/s and the velocity deficit due to the rotor wake and endwall flow is clearly identifiable.

2 *Identify the velocity defect region.* The defect region is determined by taking the gradient of the axial velocity in the radial and circumferential directions and applying a cutoff value:

$$\text{Defect Region:} \quad \text{where} \left|\frac{\partial u}{\partial r}\right| + \left|\frac{\partial u}{\partial (r\theta)}\right| \geq (\text{cutoff}) \quad (5)$$

The cutoff value is influenced by the radial spacing of the measurements and the velocity gradients within the flowfield. In this investigation the radial spacing of the measurements was identical for each survey. However, the velocity gradients within the flowfield varied with operating condition and a different cutoff value was subjectively selected for each case. Although the determination of this cutoff value is arbitrary, its choice does not significantly impact the evaluation of the displacement thickness for two reasons. First, the velocity gradients decrease significantly with distance from the center of the defect region to the outer edges of the defect region. Second, outside of the defect region, the velocity gradients are less than those within the defect region, as is evident from the velocity contours in Fig. 3(*a*). The sensitivity of the defect region size to the cutoff value is shown in Fig. 3(*b*), where the defect region has been roughly centered on the plot. A comparison of the axial velocity contours in Fig. 3(*a*) to the defect region in Fig. 3(*b*) illustrates that this method of determining the defect region is reasonable.

3 *Determine the "inviscid" velocity at each measurement location.* Outside of the defect region the "inviscid" velocity is set equal to the local velocity. In the core flow region (the region in which the velocity defect no longer encompasses the entire circumference), the inviscid velocity across the defect region is linearly extrapolated from the velocity distribution in the circumferential direction outside of the defect region. This is shown schematically in Fig. 3(*c*), which includes the distribution of axial velocity at 50 percent span and the location of the defect region. The dashed line indicates the estimated "inviscid" velocity distribution, which would be present if there were no viscous effects. Since the variation in the velocity between the pressure surface and the suction surface side of the wake is small in comparison to the velocity deficit within the wake, the calculation of the displacement thickness is insensitive to the estimation of the inviscid velocity. This process breaks down in the endwall region where the velocity defect encompasses the entire circumference. Therefore, in the endwall defect region the inviscid velocity is extrapolated in the radial direction from the velocity distribution outside of the defect region.

4 *Calculate the blockage at each radial measurement location.* The blockage was calculated in a two-dimensional sense in that the displacement thickness is calculated at each radial measurement location and divided by the circumferential distance corresponding to the rotor pitch at that radial location. The results, presented in Fig. 3(*d*), indicate that the blockage is not a strong function of the cutoff value. The radial distribution of the blockage is identical in shape for both values of the cutoff and the maximum difference in the blocked area is about 0.8 percent of blade pitch. For all cases used in this investigation, the cutoff value ranged between 2 s^{-1} and 3 s^{-1}. Note that the resulting radial distribution of blockage is consistent with the measured velocity field. For example, the local increase in blockage centered around 60 percent span coincides with the increased wake width identified in Fig. 3(*a*).

Quantification of Blockage Within the Rotor. Within the rotor the boundary layer is thick enough to enable acquisition of measurements within the outer region of the boundary layer. For example, the relative velocity across a rotor pitch at approxi-

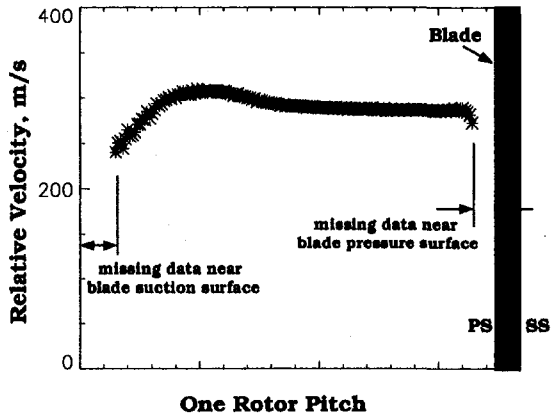

Fig. 4 Pitchwise relative velocity distribution at 85 percent chord, 70 percent span for the rotor operating at design speed low flow condition

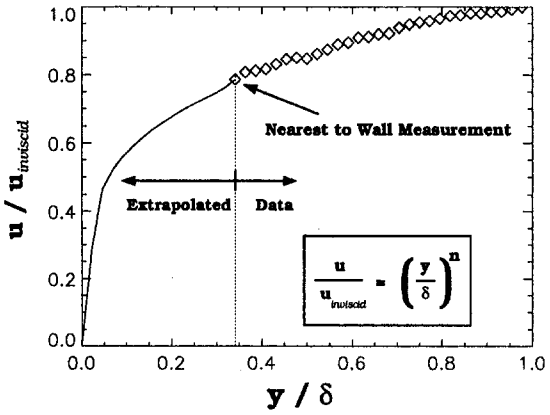

Fig. 5 Sample calculation showing estimation of boundary layer parameters

mately 85 percent rotor chord and 70 percent rotor span is plotted in Fig. 4. The left-hand side of the plot represents the suction surface of a rotor blade and the next blade is shaded on the right-hand side of the plot. There are no data within about 8 percent of pitch from the suction surface and about 5 percent of pitch from the pressure surface. Clearly, the suction surface boundary layer contributes substantially more to the blockage development as compared to the pressure surface boundary layer. In order to estimate the velocities within the inner region of the boundary layer where the data are missing and hence calculate the blockage, the following steps were taken:

1 Identify the edge of the boundary layer in a manner similar to that described in the previous section for finding the edges of the wake.
2 Fit a power law velocity distribution to the data in the outer region of the boundary layer by determining the value of the exponent n for:

$$\frac{u}{u_{\text{inviscid}}} = \left(\frac{y}{\delta}\right)^n \tag{6}$$

3 Use the power law fit to estimate the values of the velocity within the inner region of the boundary layer where no data was acquired.
4 Calculate the displacement and momentum thicknesses using the measured and estimated velocities within the boundary layer. The resulting shape factor is compared to the theoretical value of the shape factor H, where $H = 2n + 1$ (Schlichting, 1979), to assess the "goodness" of the power law fit described in item 2.
5 Calculate the blockage. To obtain a dimensionless blockage the displacement thickness is normalized by the rotor gap (the distance corresponding to one rotor pitch minus the blade thickness).

The result of this calculation procedure for the suction surface boundary layer shown in Fig. 4 is presented in Fig. 5. The shape factor calculated from the data is 1.55 versus the theoretical value of 1.48, which was based on the power law velocity distribution. The fact that the value for the shape factor is reasonable for a turbulent boundary layer in an adverse pressure gradient and that the shape factor from the idealized power law velocity distribution differs by about 5 percent from the measured data indicate that approximating the velocity profile with a power law is a reasonable approach. In Fig. 6, the calculated boundary layer parameters for the low flow design speed condition at 70 percent span are plotted in relation to the blade geometry. Note that at each axial measurement location the boundary layer parameters are calculated independently, yet as a group they appear well-behaved. In the following section these procedures will be used to calculate the blockage development within the blade row.

Results and Discussion of Blockage Estimations

The objective in this section is to quantify the blockage generated in a transonic compressor rotor operating at design and part speed conditions. The rotor flow field is arbitrarily divided into the core-flow region and the endwall region. Suder and Celestina (1996) reported that the radial extent of influence of the tip clearance flows was limited to the outer 15–20 percent span for this rotor. Therefore, the endwall region (primarily the tip region for our discussions) is defined as the outer 15–20 percent span. Similarly, the core-flow region, which is defined as the region outside of the influence of the tip clearance flows and endwall boundary layers, encompasses the 20–80 percent span region of the compressor flowpath. The blockage in the core flow region will be quantified both downstream and within the rotor blade row where the data is of sufficient detail. In the endwall region, where the flow gradients are large in the radial, circumferential, and axial directions, there are not sufficient data in the radial direction to assess the blockage within the blade row. Therefore, the endwall blockage will be quantified downstream of the rotor only, and the results will be compared to Khalid's correlation (Khalid, 1994) of blockage parameter versus loading parameter.

Downstream Blockage Calculations. At the trailing edge of the blade the boundary layers from the pressure and suction surface merge to form the rotor wake. In the near-wake region, there is significant momentum exchange and mixing between

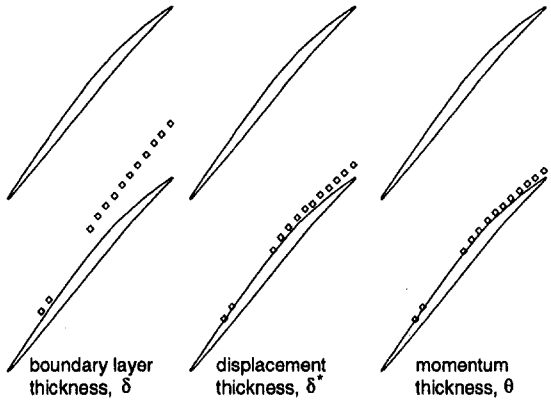

Fig. 6 Development of the boundary layer thickness parameters, δ, δ^*, and θ for the low flow, design speed condition at 70 percent span

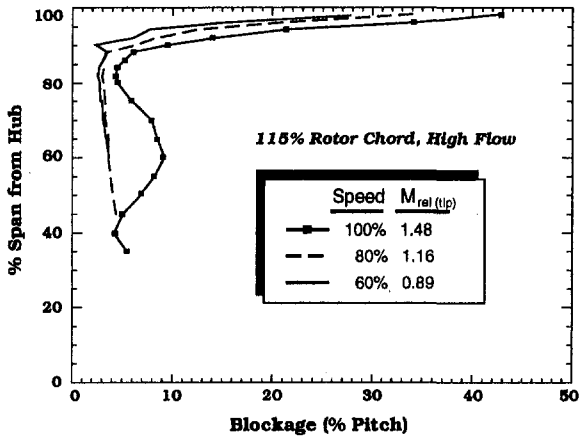

Fig. 7 Radial distribution of blockage at 60, 80, and 100 percent speed

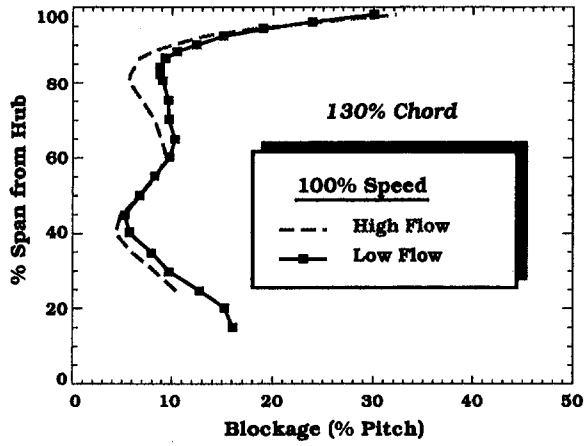

Fig. 8 Radial distribution of blockage at 130 percent chord and 100 percent speed for the low flow and high flow conditions

the two blade surface boundary layers. The streamwise extent of this near wake mixing region was determined by Suder (1996). In the present investigation, the blockage is evaluated downstream of this mixing region. At design speed conditions the blockage will be evaluated at 130 percent chord. At part-speed conditions there are insufficient data at 130 percent chord and the blockage will be evaluated at 115 percent chord. For the high flow condition at 100 percent speed the blockage distribution at 115 percent chord is nearly identical to that at 130 percent chord; therefore using either of these two locations is considered appropriate.

Comparison of Results at 100, 80, and 60 percent Rotor Speed. The impact of the inlet relative Mach number on the blockage development is illustrated in Fig. 7, where the radial distributions of blockage are plotted for the rotor operating at mass flows that maintain nearly the same flow incidence angle. These operating conditions are near peak efficiency and correspond to the circled conditions in Fig. 2. The symbols for the design speed results indicate the measurement radii. These same measurement locations were used at 60 and 80 percent speed, but the symbols were omitted for clarity. For part-speed conditions the following observations are noteworthy:

1 Blockage in the endwall region is much larger than the core region.
2 Blockage in the endwall region is slightly higher for the 80 percent speed case as compared to the 60 percent speed case. Although the casing boundary layer is thicker and the tip clearance height is greater at 60 percent speed, the blockage generated by the tip clearance flow is larger at 80 percent speed due to (1) the higher blade loading, which results in more flow through the tip clearance gap, and (2) the interaction of the tip clearance vortex with the passage shock.
3 Blockage in the core region is nearly identical at 60 and 80 percent speed, which implies the blockage due to the blade wake is nearly identical at 60 and 80 percent speed.
4 The radial distribution of blockage in the core region is nearly constant with span.

Similarly, for the design speed data consider the following:

1 Blockage is significantly larger in the endwall region as compared to the core region.
2 Blockage in the endwall region is much larger at design speed than part speed conditions. The increase in blockage from part-speed to design-speed conditions is attributed to the increase in rotor tip clearance flow and the additional blockage resulting from the stronger interaction between the shock and the clearance flow.
3 The radial distribution of blockage in the core region is no longer constant with radius and the level is much larger than it was at part speed. Clearly, the blockage due to the rotor wakes at design speed is significantly larger in comparison to that of the wakes at part-speed conditions.

Comparisons of Design Speed Results at High and Low Flow. The impact of varying the loading while maintaining a nearly constant inlet relative Mach number on blockage development is illustrated in Fig. 8, where the radial distributions of blockage for the high and low flow conditions are plotted. The measurements at the high flow condition were acquired with the same resolution in the radial direction as that indicated by the symbols at the low flow condition. As the loading is increased from the high flow to low flow condition, the overall blockage increases as expected. However, the increase in blockage is not uniform across the span. From Fig. 8 it is evident that the blockage increase primarily occurs from 60–90 percent span and below 40 percent span. It is also interesting to note that the shape of the curve representing the radial distribution of blockage is similar for the high and low flow conditions at design speed and very much different from that at part-speed conditions.

Summary of Blockage Results Downstream of the Blade Row. Table 2 summarizes the blockage calculations downstream of the blade row. The last two columns of this table were generated by performing an integration of the radial distribution of the blockage in the core flow and endwall regions. For example, the average blockage in the endwall region is evaluated by:

$$B|_{r_1-r_2} = \frac{\int_{r_1}^{r_2} \delta^*(r)\,dr}{\pi(r_2^2 - r_1^2)/NB} \tag{7}$$

where r_1 and r_2 indicate the radii over which the blockage is

Table 2 Summary of integrated blockage results downstream of the rotor

% Design-Speed	Flow Rate	Endwall Defect Region (% span)	Endwall Blockage (% area)	Core Flow Blockage (% area)
100	High	84 - 98	17	8
100	Low	84 - 98	18	10
80	High	86 - 98	14	4
60	High	86 - 98	10	4

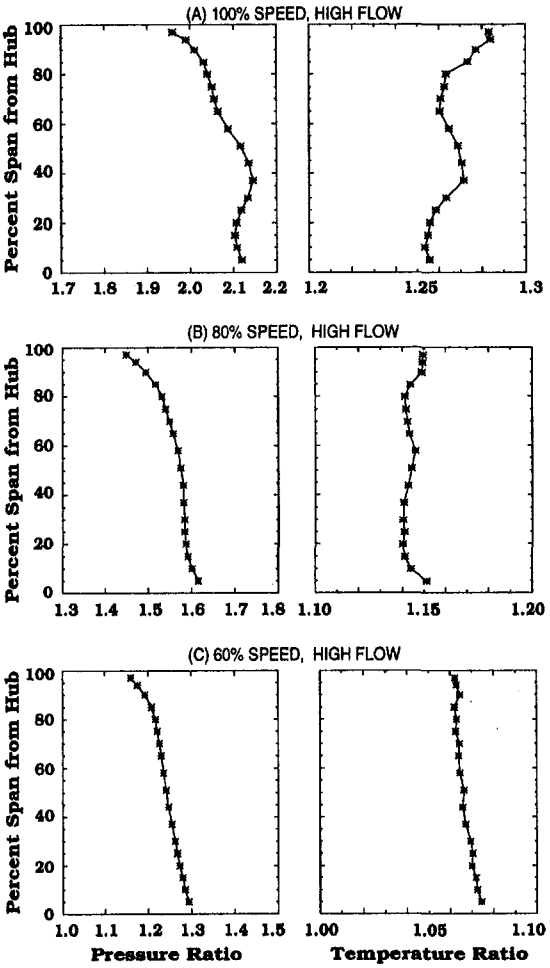

Fig. 9 Radial distributions of the overall performance characteristics at (*a*) 100 percent speed, (*b*) 80 percent speed, and (c) 60 percent speed for the rotor operating along a throttle line

evaluated and in this case are representative of the endwall defect region. From Table 2 it is evident that the integrated average of the blockage in the endwall defect region increases as the increase in pressure difference across the blade tips increases with rotational speed. Also, the blockage in the core flow region at design speed is approximately double that at part speed conditions. In the next section the flow physics responsible for these trends in blockage development will be discussed.

Relating Blockage to Rotor Flow Physics. In this section we will verify that the radial distributions of blockage depicted in Figs. 7 and 8 are related to the flow physics of the rotor. Specifically, the sensitivity of blockage to the shock strength and its interaction with the blade surface boundary layer and the rotor tip clearance flows will be demonstrated using experimental data. First, the relationship between the radial distribution of blockage to the pressure and temperature distribution will be discussed.

Impact of Blockage on Performance. The radial distribution of total pressure ratio and total temperature ratio for the rotor operating conditions corresponding to the circled data points in Fig. 2 are presented in Fig. 9. The data are plotted on different scales but with the same sensitivity so comparisons could be made between operating conditions. The shape of the radial distribution of total temperature ratio and total pressure ratio is similar at 60 and 80 percent speed and very much different from that at design speed, which is consistent with the distributions of blockage plotted in Fig. 7. In the core flow region, an increase in blockage results in an acceleration of the flow and a reduction of the work input. Therefore, an increase in blockage results in a reduction of core-flow temperature rise to the fluid and conversely, a decrease in blockage results in an increase of core-flow temperature rise. For example, at design speed the blockage dips to a local minimum at 40 percent span, which is compatible with a local increase in the total pressure and total temperature, i.e., less blockage implies more work input and therefore more pressure rise. Similarly, at part-speed conditions the pressure ratio and temperature ratio from 20 to 80 percent span varies linearly across the passage and the distributions of adiabatic efficiency (not shown) are nearly equal, which is consistent with the linear and nearly uniform distributions of blockage in the core flow region. In addition, the reduced levels of adiabatic efficiency at design speed (as compared to part speed conditions—see Fig. 2) is in agreement with the increase in blockage across the span at design speed relative to that at part-speed conditions. Therefore, the blockage, as calculated herein, is not only consistent with the overall performance characteristics, but it also is consistent with the radial distributions of pressure and temperature.

Endwall Region: Impact of Shock/Vortex Interaction. In this section it will be shown that the increase in blockage in the endwall, as depicted in Figs. 7 and 8, is directly related to the blockage associated with the tip clearance flow and the additional blockage resulting from the interaction of the tip leakage flow with the passage shock. A detailed discussion of the endwall flow physics for this rotor is presented in Suder and Celestina (1996), and therefore only a brief discussion of their results that pertain to blockage development is included herein.

A description of the blade-to-blade flow field along the 95 percent span streamsurface is depicted by contours of the relative Mach number for the rotor operating at design speed high flow and low flow conditions in Fig. 10. Note that the tip clearance height within which the clearance vortex originates is approximately 0.5 percent of span. Therefore, the Mach contours in Fig. 10 at 95 percent span indicate the influence of the tip clearance flow that lies below the actual tip clearance region. As the rotor back pressure is increased (from high flow to low flow condition) the Mach contours at midpitch and 20 percent of rotor chord become more distorted due to a strengthening of the interaction between the clearance vortex and the passage shock. Downstream of the shock/vortex interaction, a region of low relative Mach number exists due to the blockage generated by the diffusion inherent to the vortex passing through the steep pressure gradient associated with the shock. The data indicate that the low Mach number fluid within the diffused vortex migrates toward the pressure surface and merges with the rotor wake. Using the location of the lowest Mach number to indicate the "heart" of the blockage region and the level to represent the severity, it is evident that the blockage becomes more severe and is located farther upstream as the rotor backpressure is increased from the high flow to the low flow operating conditions.

A comparison of the endwall flowfield at 80 percent speed to that at design speed indicates a similar path of the vortex trajectory. Likewise, the interaction between the clearance vortex and the shock occurs near 20 percent chord and midpitch, and downstream of the shock vortex interaction resides a region of low Mach number fluid, which migrates toward the pressure surface and merges with the rotor wake. In summary, at 80 percent speed the blockage generated by the shock/vortex interaction is consistent with the design speed results at a reduced shock strength. Similarly, at 60 percent speed, in the absence of the shock, the blockage in the endwall region decreases with decreased loading. These results are in agreement with Khalid's (1994) correlation of endwall blockage versus loading.

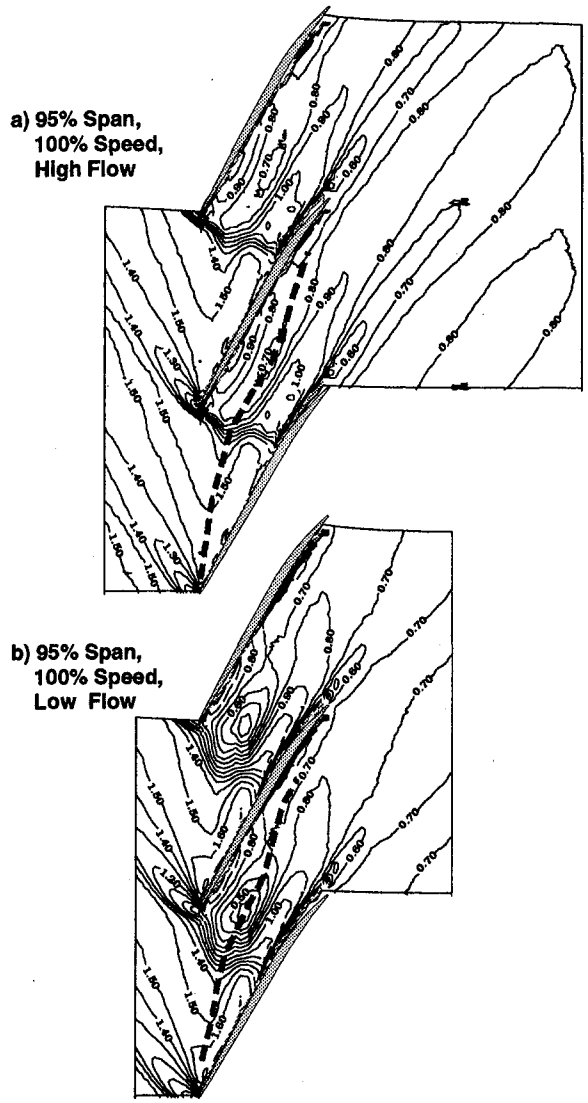

Fig. 10 Contours of the relative Mach number in a blade-to-blade view along the 95 percent streamsurface for design speed (where -- - - indicates trajectory of tip leakage vortex)

Comparison With Khalid's Correlation. Khalid (1994) evaluated the blockage in the endwall region from CFD solutions of a low-speed stator, low-speed rotor, and a transonic fan using several values of tip clearance heights. He developed nondimensional parameters representing the endwall blockage and aerodynamic blade loading and showed that the results from all of his computations were well correlated. The blockage parameter can be summarized as:

$$\frac{\text{blocked area in the endwall}}{\text{leakage flow area}} * \frac{\Delta P \text{ in throughflow direction}}{\Delta P \text{ across blade tip}} \quad (8)$$

where the second term is the ratio of the pressure difference that drives the mainflow through the passage to the pressure difference that drives the leakage flow through the clearance height. The loading parameter is the ratio of the relative dynamic head integrated over the defect region in the endwall to the inlet relative dynamic head evaluated at the radial reference location corresponding to two times the clearance height from the endwall. Khalid's results illustrate the increase in the endwall blockage with increased loading and indicate that there is a limiting value of the loading parameter.

For this investigation the data acquired downstream of the blade row were normalized in a manner analogous to Khalid's blockage and loading parameters and the results are presented in Fig. 11 where the values for NASA rotor 37 are denoted by the flagged solid circles and all other symbols represent results from Khalid's computations. The general trend of the correlation is preserved in that the data exhibit the increase in endwall blockage with loading and are in agreement with Khalid's limiting value for the loading parameter. In conclusion, the increase in the endwall blockage, as determined from the experimental measurements and indicated in Figs. 7 and 8, is consistent with an increase in blade loading.

Core Flow Region: Influence of Shock/Boundary Layer Interaction. The blade to blade flow field at 70 percent span for the rotor operating at design speed and low flow condition is presented in terms of measured relative Mach number contours in Fig. 12. Figure 12(b) features a blowup of the leading edge region of Fig. 12(a). The shock forms in the front of the blade and is detached. Downstream of the shock in front of the leading edge the flow is subsonic and there is a rapid acceleration around the leading edge of the blade on the suction surface. The flow continues to accelerate on the suction surface until it encounters the shock from the adjacent blade. The shock strength is reasonable for a nearly normal shock as indicated by an upstream Mach number of 1.4–1.45 and a downstream Mach number of 0.7–0.8. (At an upstream Mach number of 1.4 a normal shock results in a post-shock Mach number of 0.74.) Also shown in Fig. 12(b) is the interaction region between the rotor passage shock and the suction surface boundary layer. Since the boundary layer fluid cannot sustain the steep pressure gradient resulting from a nearly normal shock, the flow field adjusts and the shock becomes more oblique near the blade surface, thereby forming a lambda (λ) shock. Downstream of the lambda shock is evidence of a thickening of the blade suction surface boundary layer. Downstream of the shock and especially near the trailing edge it is evident that the suction surface boundary layer is considerably thicker than the pressure surface boundary layer.

The impact on blockage due to reducing the strength of the passage shock is best illustrated by comparing the rotor wakes at 100 and 80 percent speed at the high flow condition, as shown in Fig. 13. The inlet relative Mach number at 70 percent span has decreased from 1.4 at design speed to 1.1 at 80 percent speed. It is evident that decreasing the shock strength from 100 percent speed to 80 percent speed at the high flow condition results in a significant change in the boundary layer development and the blockage associated with the rotor wake.

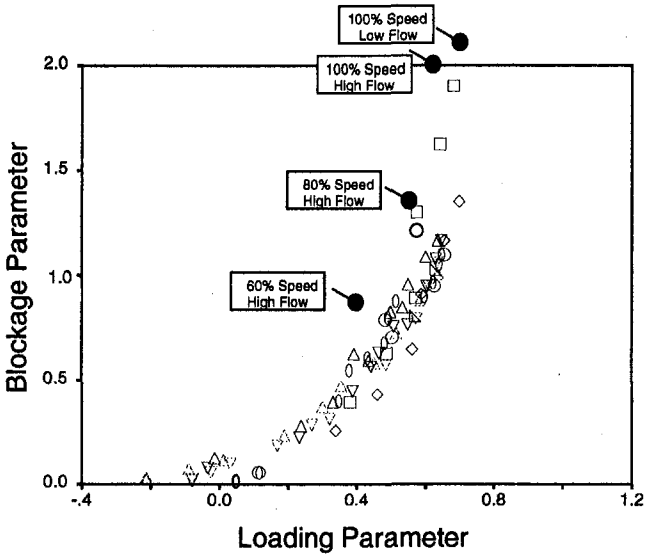

Fig. 11 Comparison of NASA rotor 37 data to Khalid's correlation of loading versus endwall blockage

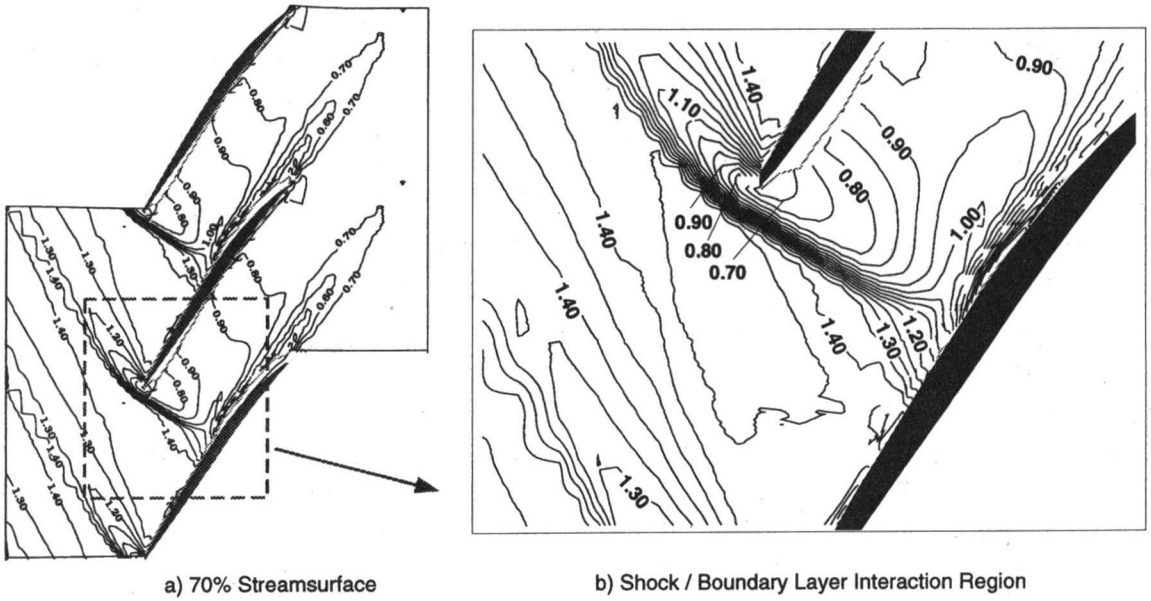

Fig. 12 Contours of measured relative Mach number along the 70 percent span streamsurface for the rotor operating at design speed and low-flow condition

Likewise, a comparison of the rotor wakes at 80 and 60 percent speed (not shown here) indicates the width and depth of the rotor wakes are nearly identical in character and much reduced in comparison to design speed. This indicates that the shock/boundary layer interaction was sufficient to thicken the suction surface boundary layer at design speed but not by a measurable amount below 80 percent speed. Therefore, the difference in the blockage between the design speed and part speed conditions in the core flow region, shown in Fig. 7, is due to the additional blockage generated by the stronger shock/boundary layer interaction on the blade suction surface at design speed.

Blockage Development Within the Rotor Passage. It has been shown that the increased blockage in the core flow region at design speed is associated with the additional blockage resulting from the shock/boundary layer interaction. The question is how much of the blockage is due to the shock boundary layer interaction itself and how much results from diffusing a thicker boundary layer downstream of the shock boundary layer interaction region. In order to answer these questions, we will investigate the blockage development within the rotor passage.

The blockage on the blade suction surface was calculated on the 70 percent span streamsurface for the rotor operating at design speed low flow condition, and these results are presented in Fig. 14. The region of the shock boundary layer interaction is identified by the region denoted "lambda shock region." In this region there is strong evidence to suggest the presence of a lambda shock (see Fig. 12), and it was quite difficult to define the edge of the boundary layer. It is evident that the increase in blockage that occurs across the shock, for which blockage increases by a factor of 10, is much more significant than the blockage increase due to diffusion downstream of the shock, for which blockage increases by a factor of 1.5–2. Therefore, the shock/boundary layer interaction dominates the generation of blockage in the core flow region. This same development of blockage was evident at other spans as well. A relevant question is whether the shock/boundary layer interaction is sufficient to separate the blade surface boundary layer.

Results from wind tunnel tests on flat plate turbulent boundary layers will be used to determine if the suction surface boundary layer is separated. Using separation criteria deduced from flat plate results is justified because the geometry and the flow over the first part of the blade suction surface of the airfoil section at 70 percent span resembles that of a flat plate geometry and flow structure. The suction surface angles indicate very little turning over the front part of the airfoil prior to the shock impingement on the suction surface. In addition, the distribution

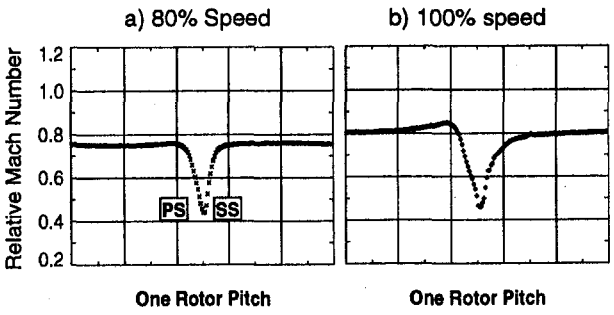

Fig. 13 Relative Mach number distributions on the 70 percent span streamsurface for the rotor operating near peak efficiency

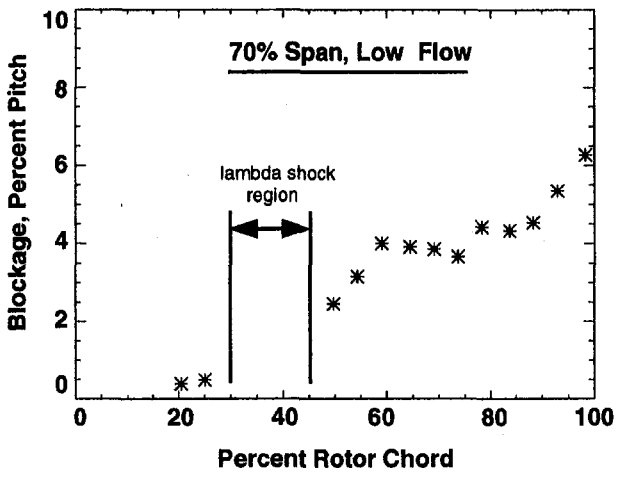

Fig. 14 Blockage development on the blade suction surface at 70 percent span for low-flow condition at design speed

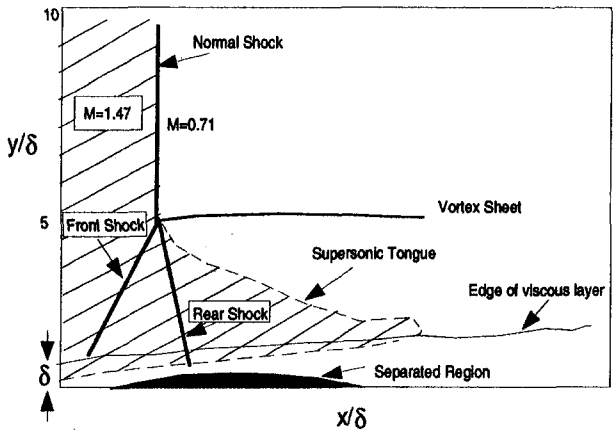

Fig. 15 Seddon's model depicting the boundary layer separation due to a normal two-dimensional shock wave

of the relative Mach number near the blade surface indicates a nearly zero velocity gradient prior to the shock impingement on the suction surface.

Seddon's model (1960) depicting the boundary layer separation due to a normal two-dimensional shock wave is presented in Fig. 15. The normal shock is bifurcated into a classical lambda (λ) shape close to the surface. The front leg of the lambda shock is formed in response to the separation bubble and directs the flow away from the surface. The rear leg of the lambda shock deflects the flow back into the mainflow direction. A vortex sheet is shed downstream of the bifurcation point due to the entropy differences of the flow region behind the normal shock and the two oblique shocks. For the rotor geometry in question, the Reynolds number based on chord is about 1.8×10^6 and the boundary layer thickness ahead of the shock is approximately 4 percent of pitch. Therefore, it is anticipated that the separated region, if it exists, is much too small to measure. However, according to Seddon's model the lambda shock structure extends to a distance from the wall that is five times the boundary layer thickness and measurements were acquired in this region. In order to assess whether the severity of the shock/boundary layer interaction is sufficient to cause a separation, the data were examined for evidence of the flow angle changes inherent to a lambda shock where the front oblique shock turns the flow away from the surface and the second or rear oblique shock redirects the flow in the mainflow direction. Alber et al. (1973) has shown that the boundary layer is separated if the flow undergoes a deflection angle greater than 6.6 deg.

The flow deviation from the blade surface angle is plotted for the high flow and low flow conditions at design speed in Fig. 16. The flow in general follows the pressure surface, whereas on the suction surface there are regions where the flow deviates from the blade surface angle. Near midchord there are regions of increasing and decreasing deviation, which suggest flow turning through the front and rear legs of a lambda shock. At the low-flow condition there is an increase in the suction surface deviation angle from 35 to 45 percent chord followed by a decrease in the deviation from 45 to 50 percent chord. This region from 35 to 50 percent chord corresponds to the region of the shock influence on the blade suction surface as depicted in the blade surface Mach number distributions in Fig. 12 and the blockage distribution in Fig. 14. Similarly, at the high flow there is an increase in the deviation from 45 to 55 percent chord and a subsequent decrease in deviation from 55 to 65 percent chord, which also corresponds to the region of the shock influence on the blade suction surface. These changes in the flow deflection are near the value of 6.6 deg required for boundary layer separation. Unfortunately the data near the blade surface are not sufficient in detail to detect the size of the separation. Similar results (not shown) were found for the 30 and 50 percent span streamsurfaces at design speed high and low-flow operating conditions.

Results at Part-Speed Conditions. Attempts to calculate the blockage development inside the blade for the data at part-speed conditions were unsuccessful because the thickness of the boundary layer downstream of the shock was much reduced at part speed and the data were not of sufficient quality to evaluate the boundary layer displacement and momentum thicknesses. However, there was sufficient data to deduce the edge of the boundary layer, and therefore the deviation from the blade surface angles was evaluated. The results for 85 percent speed and 80 percent speed conditions are presented in Fig. 17. Except for the last 20 percent of blade chord on the suction surface, it is evident that the flow follows the blade surfaces. At 85 percent speed there is evidence of an increase and decrease in deviation from 45 to 55 percent chord, which corresponds to the location of the shock impingement and influence on the blade suction surface. However, the flow deflection is less than three degrees and according to Alber et al. (1973) is not sufficient to indicate a separation. In contrast, at 80 percent speed there is no evidence of the increase and decrease in deviation due to a lambda shock. Therefore, based on the distribution of the deviation from the blade surface angles, it is concluded that the shock is not of sufficient strength to separate the blade suction surface boundary layer at 80 and 85 percent speed.

Variation of Blockage With Span at Design Speed. It is reasonable to ask why the radial distribution of blockage varies so unpredictably across the span at design speed. One would suspect that if the additional blockage, relative to that at part-speed conditions, results from the shock-induced boundary layer separation, then the blockage would increase with increasing inlet relative Mach number, and therefore, the blockage would merely increase with span. However, the blade camber decreases with span such that at the lower spans the camber results in a flow acceleration along the suction surface of the blade.

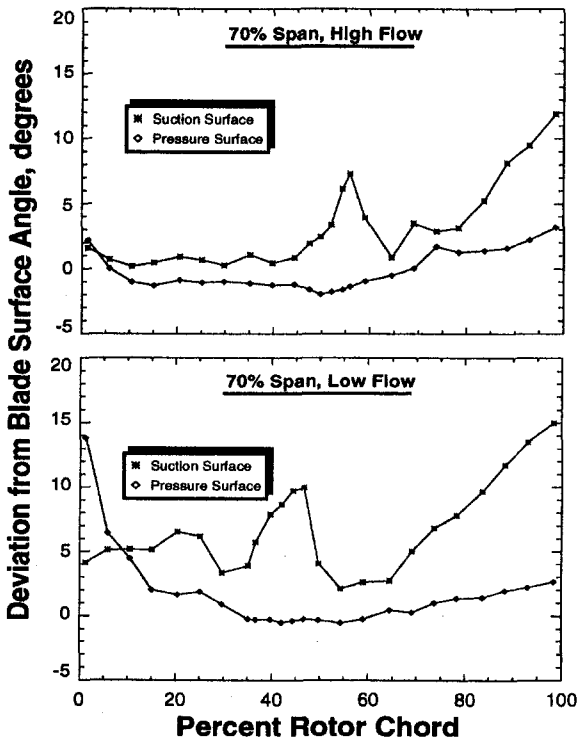

Fig. 16 Deviation from blade surface angles on the 70 percent span streamsurface at high flow and low flow conditions at design speed

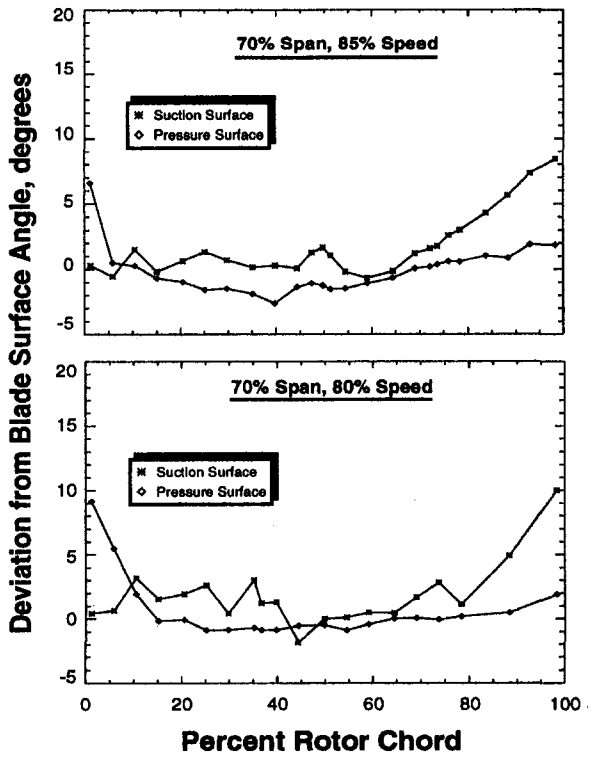

Fig. 17 Deviation from blade surface angles on the 70 percent span streamsurface at 85 percent speed and 80 percent speed

The preshock Mach number at lower spans is therefore comparable to that at the higher blade spans. To determine the spanwise variation in shock strength, the Mach number normal to the flow was estimated from measured Mach numbers and flow angles upstream and downstream of the shock as prescribed in detail by Suder (1996). The results indicated that the normal Mach number ranged from 1.3–1.4 for the design speed cases at all measured spans and was less than 1.3 (max of 1.27 at 85 percent speed) for all part-speed cases. From wind tunnel tests (Nussdorfer, 1956; Atkin and Squire, 1992; Alber et al., 1993; Chriss et al., 1987) it has been shown that the pressure rise associated with a normal shock Mach number of around 1.3 is required to separate the boundary layer. Therefore deducing from the level of the estimated normal Mach number and the plots of deviation from the blade suction surface, the shock strength is sufficient to separate the boundary layer over much if not all of the blade span at design speed.

The blockage generated by the shock/boundary layer interaction is a function of the shock strength, location of where the shock impinges on the blade suction surface, the boundary layer thickness prior to the shock, and the pressure gradient downstream of the shock/boundary layer interaction region (see Griepentrog, 1972; Ackeret et al., 1947; Liepmann, 1946; Pearcy, 1959). When the shock separates the boundary layer, the blockage is quite sensitive to these effects, and it is much less sensitive when the boundary layer is not separated, as is evident in Fig. 7. Unfortunately, the data are not sufficient to describe accurately: (1) the boundary layer characteristics upstream of the shock impingement on the suction surface where the boundary layer is very thin, (2) the details of the flow within the shock/boundary layer interaction region and therefore the size of the separation, and (3) the radial migration that results within the low-momentum and/or separated regions. However, the data do indicate the boundary layer is separated at 30, 50, and 70 percent span at design speed, and therefore, the variation in blockage in the core flow region at design speed may be attributed to the spanwise variation of shock strength, size and location of the separation, blade suction surface curvature, and the pressure gradient to which the boundary layer is subjected.

To illustrate that the spanwise variation of blockage is directly related to the details of the blade boundary layer characteristics and shock/boundary layer interaction process, in the absence of detailed data in the shock/boundary layer interaction region, the blockage was evaluated using the results from two CFD simulations. The two simulations employed an identical algorithm and computational grid, and the only difference between the simulations was the turbulence model used. One computation used a modified Baldwin–Lomax turbulence model (Celestina, 1997; Adamczyk et al., 1989) and the second computation used a modified two-equation turbulence model as described by Shabbir et al. (1996). The radial distribution of blockage was evaluated using the same calculation procedure as described in the data analysis section, and a comparison of the CFD results with the data is presented in Fig. 18. From this figure it is evident that the blockage levels calculated using the two-equation turbulence model are very much different from those using the Baldwin–Lomax turbulence model, and the two-equation model identifies a local increase in blockage from 40 to 80 percent span in agreement with the data. Further interrogation of the CFD simulations indicated that this local increase in blockage from the two-equation model is primarily due to additional low-momentum fluid on the blade suction surface, which results from the shock/boundary layer interaction. In summary, the point of this discussion is not to compare the two turbulence models, but rather to demonstrate that (1) the spanwise variation in the blockage at 130 percent chord is primarily attributed to the spanwise variation in the blockage resulting from the shock/boundary layer interaction process within the blade passage, and (2) predicting the boundary layer characteristics and fluid mechanic details of the shock/boundary layer interaction is paramount to predict the blockage and therefore the performance of this rotor accurately.

Concluding Remarks

A detailed experimental investigation to understand and quantify the development of blockage in the flow field of a transonic axial flow compressor rotor has been undertaken. Comparisons of the blockage development at 60, 80, and 100 percent speed at a constant incidence angle provided a means to evaluate the effect of variations of the inlet Mach number on the blockage development. Data acquired at design speed at varying rotor exit pressures provided a means to evaluate the sensitivity of blockage to changes in shock structure at a nearly constant inlet Mach number.

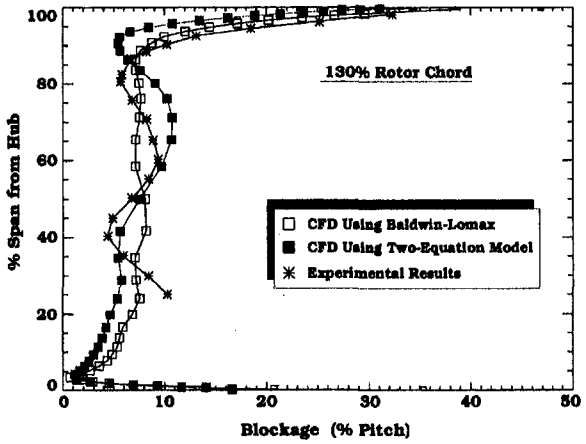

Fig. 18 Radial blockage distribution at 130 percent chord for design speed and high flow condition—comparison between data and two CFD simulations

The conclusions of this investigation regarding the development of blockage in a transonic axial compressor are:

1 The radial distribution of the blockage was consistent with the radial distribution of the pressure and temperature rise across the rotor. For example, in the core-flow region a local increase in blockage coincided with a local decrease in the temperature and pressure rise and conversely, a region of reduced blockage coincided with a region of increased pressure and temperature rise.

2 Blockage in the endwall region was 2–3 times greater than that in the core flow region. The increase in blockage near the endwall is primarily attributed to the tip clearance flow and the shock/tip leakage vortex interaction. In addition, the blockage in the endwall region increases with blade loading in agreement with Khalid's (1994) correlation of endwall blockage versus aerodynamic blade loading.

3 In the core flow region at design speed conditions the blockage is more than double that at part-speed conditions for the same incidence. This increase in blockage at design speed occurs because the shock/boundary layer interaction induces separation of the blade suction surface boundary layer.

It is clear that the performance of the rotor used in this investigation is very sensitive to changes in blockage and that the blockage related losses account for a significant amount of the total loss. It is believed that this sensitivity results from the high loading levels, high Mach numbers and tight choke area margin (A/A^* of 1.03–1.05) associated with this rotor. The sensitivity of the rotor performance to changes in blockage at design speed accompanied with the fact that the shock is of sufficient strength to separate the boundary layer provides a challenge to computational fluid dynamics codes used for design and analysis. As the design trends move to higher blade loadings and rotational speeds, the shock strengths and flow phenomena reported herein will be more prevalent. Therefore, in order to optimize the design of compressors with high loading levels and tip speeds comparable to or in excess of the compressor rotor used in this investigation, it is paramount to be able to predict and/or model the blockage in order to predict the rotor flowfield and performance accurately.

Acknowledgments

The author wishes to acknowledge the efforts of Dr. Tony Strazisar, Mr. Jerry Wood, and Dr. John Adamczyk of NASA Lewis Research Center for their guidance not only in the writing of this paper, but also for the many helpful discussions throughout the course of this work. I am also grateful to Dr. Ed Greitzer of Massachusetts Institute of Technology, Dr. Nick Cumpsty of Whittle Labs at Cambridge University, Dr. Frank Marble, Professor Emeritus from California Technology Institute, and Dr. Eli Reshotko from Case Western Reserve University for their helpful comments and suggestions. The author also would like to thank Mr. Mark Celestina of NYMA Inc. and Dr. Aamir Shabbir of Institute for Computational Mechanics in Propulsion for providing their computational results of NASA Rotor 37.

References

Ackeret, J., Feldmann, F., and Rott, N., 1947, "Investigation of Compression Shocks and Boundary Layers in Gases Moving at High Speed," NACA TM 1113.

Adamczyk, J., Celestina, M., Beach, T., and Barnett, M., 1989, "Simulation of Three-Dimensional Viscous Flow Within a Multistage Turbine," ASME JOURNAL OF TURBOMACHINERY, Vol. 112, pp. 370–376.

Alber, I., Bacon, J., Masson, B., and D. J., C., 1973, "An Experimental Investigation of Turbulent Transonic Viscious-Inviscid Interactions," *AIAA Journal,* Vol. 11, No. 5, pp. 620–627.

Atkin, C., and Squire, L., 1992, "A Study of the Interaction of a Normal Shock Wave With a Turbulent Boundary Layer at Mach Numbers Between 1.3 and 1.5," *European Journal Mechanics B/Fluids,* Vol. 11, No. 1.

Celestina, M., 1997, Personal communication—Provided computational results for NASA Rotor 37.

Chima, R., 1998, "Calculation of Tip Clearance Effects in a Transonic Compressor Rotor," ASME JOURNAL OF TURBOMACHINERY, Vol. 120, pp. 131–140; Also NASA TM 107216.

Chriss, R., Keith, T., Hingst, W., Strazisar, A., and Porro, A., 1987, "An LDA Investigation of Three-Dimensional Normal Shock-Boundary Layer Interactions in a Corner," Paper No. AIAA-87-1369.

Dalbert, P., and Wiss, D., 1995, "Numerical Transonic Flow Field Predictions for NASA Compressor Rotor 37," ASME Paper No. 95-GT-326.

Denton, J., 1996, "Lessons Learned From Rotor 37," presented at the Third International Symposium on Experimental and Computational Aerothermodynamics of Internal Flows (ISAIF).

Griepentrog, H., 1972, "Shock Wave Boundary Layer Interaction in Cascades," *AGARDograph No. 164, Boundary Layer Effects in Turbomachines,* J. Surugue, ed., pp. 443–456.

Khalid, S., 1994, "The Effects of Tip Clearance on Axial Compressor Pressure Rise," Ph.D. Dissertation, Massachusetts Institute of Technology.

Koch, C., 1981, "Stalling Pressure Rise Capability of Axial Flow Compressor Stages," ASME *Journal of Engineering for Power,* Vol. 103, pp. 645–656.

Koch, C., and Smith, L., 1976, "Loss Sources and Magnitudes in Axial-Flow Compressors," ASME *Journal of Engineering for Power,* Vol. 98, pp. 411–424.

Liepmann, H., 1946, "The Interaction Between Boundary Layer and Shock Waves in Transonic Flow," *Journal of Aeron. Sciences,* Vol. 13, No. 12.

Moore, R., and Reid, L., 1980, "Performance of Single-Stage Axial-Flow Transonic Compressor With Rotor and Stator Aspect Ratios of 1.19 and 1.26, Respectively, and With Design Pressure Ratio of 2.05," NASA TP 1659.

Nussdorfer, T., 1956, "Some Observations of Shock-Induced Turbulent Separation on Supersonic Diffusers," NACA RM E51 L26.

Pearcey, H., 1959, "Some Effects of Shock Induced Separation of Turbulent Boundary Layers in Transonic Flow Past Aerofoils," A.R.C. R&M, No. 3108.

Reid, L., and Moore, R., 1978, "Design and Overall Performance of Four Highly Loaded, High-Speed Inlet Stages for an Advanced High-Pressure Ratio Core Compressor," NASA TP 1337.

Schlichting, H., 1979, *Boundary-Layer Theory,* 7th ed., McGraw-Hill.

Seddon, J., 1960, "Flow Produced by Interaction of a Turbulent Boundary Layer With a Normal Shock Wave of Strength Sufficient to Cause Separation," *Brit. Aero. Res. Council Report and Memo No. 3502.*

Shabbir, A., Zhu, J., and Celestina, M., 1996, "Assessment of Three Turbulence Models in a Compressor Rotor," ASME Paper No. 96-GT-198.

Smith, J. L. H., 1970, "Casing Boundary Layers in Multistage Axial-Flow Compressors," *Flow Research on Blading,* A. L. S. Dzung, ed., Elsevier, pp. 275–304.

Strazisar, A., Wood, J., Hathaway, M., and Suder, K., 1989, "Laser Anemometer Measurements in a Transonic Axial-Flow Fan Rotor," NASA TP 2879.

Suder, K., and Celestina, M., 1996, "Experimental and Computational Investigation of the Tip Clearance Flow in a Transonic Axial Compressor Rotor," ASME JOURNAL OF TURBOMACHINERY, Vol. 118, pp. 218–229.

Suder, K. L., 1996, "Experimental Investigation of the Flow Field in a Transonic, Axial Flow Compressor With Respect to the Development of Blockage and Loss," Ph.D. Dissertation, Case Western Reserve University: also NASA TM 107310.

Urasek, D., and Janetzke, D., 1972, "Performance of Tandem-Bladed Transonic Compressor Rotor With Rotor Tip Speed of 1375 Feet per Second," NASA TM X-2484.

Wood, J., Strazisar, A., and Simonyi, P., 1986, "Shock Structure Measured in a Transonic Fan Using Laser Anemometry," *AGARD CP-401: Transonic and Supersonic Phenomena in Turbomachines.*

Experimental Investigation of Stepped Tip Gap Effects on the Performance of a Transonic Axial-Flow Compressor Rotor

D. W. Thompson
Mem. ASME

P. I. King
Mem. ASME

Department of Aeronautics and Astronautics,
Air Force Institute of Technology,
Wright-Patterson AFB, OH 45433

D. C. Rabe
Compressor Research Facility,
Wright Laboratories,
Wright-Patterson AFB, OH 45433
Mem. ASME

The effects of stepped-tip gaps and clearance levels on the performance of a transonic axial-flow compressor rotor were experimentally determined. A two-stage compressor with no inlet guide vanes was tested in a modern transonic compressor research facility. The first-stage rotor was unswept and was tested for an optimum tip clearance with variations in stepped gaps machined into the casing near the aft tip region of the rotor. Nine casing geometries were investigated consisting of three step profiles at each of three clearance levels. For small and intermediate clearances, stepped tip gaps were found to improve pressure ratio, efficiency, and flow range for most operating conditions. At 100 percent design rotor speed, stepped tip gaps produced a doubling of mass flow range with as much as a 2.0 percent increase in mass flow and a 1.5 percent improvement in efficiency. This study provides guidelines for engineers to improve compressor performance for an existing design by applying an optimum casing profile.

Introduction

A current initiative guiding the research of jet engine components is the Integrated High Performance Turbine Engine Technology (IHPTET) program (Grier, 1995; Valenti, 1995). This joint venture between US government and industry began in 1988, and it calls for doubling the thrust-to-weight ratio of 1987 turbine engine technology by the year 2003. A logical approach for doubling the thrust-to-weight ratio of an engine is to reduce its weight by half while maintaining the same amount of thrust. Since the compressor comprises most of the mass of an engine, steps to reduce the number of stages and the number of blades per stage are evident objectives. However, the compressor must still deliver the same mass flow with the same pressure rise as its larger counterpart; its work requirements are unchanged. Therefore, the smaller compressor becomes highly loaded, with associated physical limitations and flow phenomena.

The most detrimental effects to highly loaded transonic compressor performance are losses associated with the rotor tip region; therefore, much research has been devoted to the understanding and elimination of losses in this area. Losses in the form of flow separation, stall, and reduced rotor work efficiency are the result of flow blockage created by the interaction of tip region flows. Despite efforts to eliminate blockage, it will always remain as a consequence of flow physics. Therefore, the main focus of this study was to relocate the blockage to benefit compressor performance. This simple objective was achieved by simple means when the flow features of the tip region were identified and understood.

The flowfield in the tip region of axial-flow compressors has been studied for decades. The flow is a three-dimensional phenomenon comprised of the complex interactions between the tip-leakage vortex, the turbulent endwall and blade boundary layers, and often times shock waves distorted by radial and rotational effects. Suder and Celestina (1996), Puterbaugh (1994), Puterbaugh and Brendel (1995), Cybyk et al. (1995), and Sellin et al. (1993) provide detailed characterization of these flow structures and their interactions.

The rotor tip clearance is a major factor controlling the level of interaction of the various flow phenomena in the tip region, but loss effects also extend beyond that region. Large pockets of low-energy fluid are created by the interacting flows (Suder and Celestina, 1996); a large zone of blockage, which alters the flow throughout the rotor cavity (Dring and Joslyn, 1986, 1987) is created as the tip-leakage vortex passes through the leading edge shock (Suder and Celestina, 1996; Sellin et al., 1993). The shock–vortex interaction creates curvature in the shock with a weakened localized pressure gradient and shock-induced growth of the tip-leakage vortex. Thus, a pronounced area of low-velocity fluid exists immediately downstream of the interaction as the shock-expanded vortex continues to grow circumferentially and radially as it moves through the passage. For mass continuity, the low-velocity fluid near the tip displaces the main flow in the passage. Altered flow often creates greater adverse pressure gradients, which lead to flow separation and stall of rotor blades.

Flow separation and overall performance are interrelated. Blade loading and mass flow range are limited by stall, an advanced case of flow separation; efficiency is also degraded by partial flow separation. If separation can be mitigated or controlled, compressor performance and work capacity will improve. Therefore, tip gap effects on blockage, flow separation, and performance merit detailed examination. This paper focuses on tip gap geometry and its effects on compressor rotor performance; in particular, it qualifies the conditions for which an optimum tip gap geometry, if one exists, can be identified.

The issue of the existence of an optimum tip gap for transonic rotors has been marked with conflicting data. Some research (Moore, 1982; Copenhaver et al., 1996) indicates the optimum gap to be the minimum possible (zero would be best), while other experiments (Wennerstrom, 1984; Freeman, 1985) have found a nonzero clearance to give the best performance. The explanation for these seemingly contradictory results requires examination of an extensive database. Unfortunately, the experimental database exploring this topic is small and often disjointed or is a secondary byproduct of results from other research of

Contributed by the International Gas Turbine Institute and presented at the 42nd International Gas Turbine and Aeroengine Congress and Exhibition, Orlando, Florida, June 2–5, 1997. Manuscript received at ASME Headquarters February 1997. Paper No. 97-GT-7. Associate Technical Editor: H. A. Kidd.

transonic flow. The large database from low-speed two-dimensional cascade tests gives little assistance since cascade data lack radial flow effects and, with rare exception (Peter and King, 1996; Yaras and Sjolander, 1992a, b), the moving wall effects that complicate the tip gap flow. Transonic flows are much more complicated than low-speed flows; shock waves are distorted by radial flow and moving wall effects. An adequate accounting for these effects requires transonic flows to be studied in rotating machinery for which the existing data set is small.

Theoretical approaches have often been used to explore the effects of variations in tip clearance. Numerous studies (Adamczyk et al., 1993; Basson and Lakshminarayana, 1995; Chen et al., 1991; Crook et al., 1993; Hah, 1986; Hall et al., 1994; Kunz et al., 1993) have aided the evolution of computational fluid dynamic (CFD) models, but because of the limited experimental data set to validate these simulations, it is not clear that all the necessary factors for accurate modeling have been included. Therefore, the experimental data available in the open literature need to be expanded to encompass a wider variety of transonic rotors and operating conditions; specifically, additional testing is needed to address and generalize the problem of an optimum tip gap for transonic rotors.

Despite the disparity of existing tests, consistent trends can be extracted and explained. In particular, as the tip gap increases, the stall-to-choke mass flow range increases, but the range is shifted to a lower mass flow on the same speed line (e.g., Wennerstrom, 1984). Conservation of mass and a knowledge of shock–vortex interaction mentioned earlier can help explain this shift.

With an increased tip gap over the axial length of the rotor, the size and strength of the tip-leakage vortex is increased, thereby creating a larger zone of low-energy fluid downstream of the shock-vortex interaction (Puterbaugh, 1994). This larger pocket of low-energy air produces a larger region of blockage to the flow. The larger blockage effectively reduces the area of the channel, causing the high-energy mainstream flow to be diverted around the low-energy blockage. To satisfy continuity, the essentially inviscid mainstream flow must accelerate to a greater velocity. This process affects the choking limit; if the main flow is nearly sonic (i.e., near the choked mass flow limit) prior to the tip clearance increase, the increased tip gap will cause the mainstream flow to accelerate to sonic velocity and create shock waves that choke the passage near the blade trailing edge. Therefore, choking will occur at a lesser mass flow for the larger tip clearance.

Increased tip gap also lowers the stall limit mass flow. Since the mainstream axial velocity increases with greater tip gap as discussed in the previous paragraph, the incident air angle of the rotor (with no inlet guide vanes) decreases for the main portion of the span. Recall that when the rotor speed is fixed, stall requires a decrease in mass flow from the normal operating point. If the flow is near stall prior to the gap increase, an increased gap requires a further decrease in mass flow to attain the incident air angle at which stall occurs. Thus, increasing the tip gap causes the rotor to stall at a lesser mass flow for a given speed. Therefore, the entire mass flow range of the stage shifts to a lesser mass flow with increased tip gap.

From simple observation, blockage is not always a bad thing. Blockage can have a beneficial sealing effect near the rotor blade tips, an effect the authors call an "aerodynamic seal." The blockage produced by the interactions in the tip region creates zones of low-velocity fluid that divert the main flow away from this area. By removing air from the tip region, additional tip region losses are averted, and rotor work efficiency is increased. Some tip losses are unavoidable in achieving this diversion effect.

For a compressor designed for the optimum tip clearance, there is just sufficient interaction and blockage to seal the endwall aerodynamically. Furthermore, though this sealing yields apparently the best efficiency and pressure rise, a more optimum casing geometry with even greater performance improvements may exist. Thus, if thoroughly understood, the interactions can be further tailored to provide the desired tip sealing without adversely affecting the passage throughflow area. Stepped tip gaps are the logical approach for tailoring the interactions to achieve these goals.

Since the tip-leakage vortex impacts the adjacent blade pressure surface (Suder and Celestina, 1996; Cybyk et al., 1995), a larger tip gap near the point of impact may alter the path and extent of the blockage. Opening the channel should create a path of lesser resistance for the flow by providing more throughflow area to relieve the blockage. As the flow is drawn into the increased area, it will entrain the vortex blocking the flow. Entrainment of the blockage results from the viscous interaction of two fluids at different velocities (White, 1991). A free shear layer exists in the region between these two flow velocities, and in this region, some of the low-velocity fluid accelerates to merge with the higher speed main flow. The intensity of free shear interaction is a function of the fluid viscosity and the velocity defect between the main flow and the blockage. Since the fluid in the outer fringe of the blockage is accelerating, the extent of the blockage normal to the flow is lessened, and the zone of acceleration results in the blockage being swept with the flow. The low-velocity blockage entrained by the flow thereby elongates the vortex and draws the vortex closer to the annulus casing. The primary flow going through the increased clearance will thus include the low-energy fluid of the blockage, and the blockage will be smaller in radial extent, thereby creating a larger flow area for the compressor. This increased flow area should shift the mass flow range to one with a higher mass flow while maintaining the larger flow range associated with an optimum tip gap.

The placement and size of the stepped tip gap is crucial. It is desirable to reduce the extent of the blockage without excessive mass leakage through the increased clearance. With a modification of the casing in the region where the vortex impacts the trailing edge of the adjacent blade, we can achieve the desired effect of entraining the blockage into the gap to create an aerodynamic seal. For the rotor used in these experiments, at peak efficiency operation, the vortex center impacts the adjacent blade at approximately 90 percent axial chord (Russler et al., 1995), and for near-stall operation, the impact zone on the pressure surface of the adjacent blade is centered approximately at 70 percent axial chord. To ensure these zones are encompassed, initial tests had stepped tip gaps in the region of 80 and 60 percent axial chord.

Objectives

As a result of the discussion in the previous paragraphs, the objectives of this research were to:

1. Expand the experimental data available in the open literature for transonic axial-flow compressor rotors.
2. Determine an optimum tip clearance and its effects on performance.
3. Determine the effects of stepped tip gaps on performance.
4. Identify key geometric bounds and candidates deserving additional study and optimization for future numerical and analytical models.
5. Provide guidance to compressor designers that will aid the IHPTET program goal of doubling thrust-to-weight ratio of turbojet engines.

Test Facility and Instrumentation

This series of tests was conducted in a transonic compressor research facility described by Reitz (1996) and an informational pamphlet (WL/POTX, 1995). This highly automated facility is capable of mapping the performance parameters of a full-

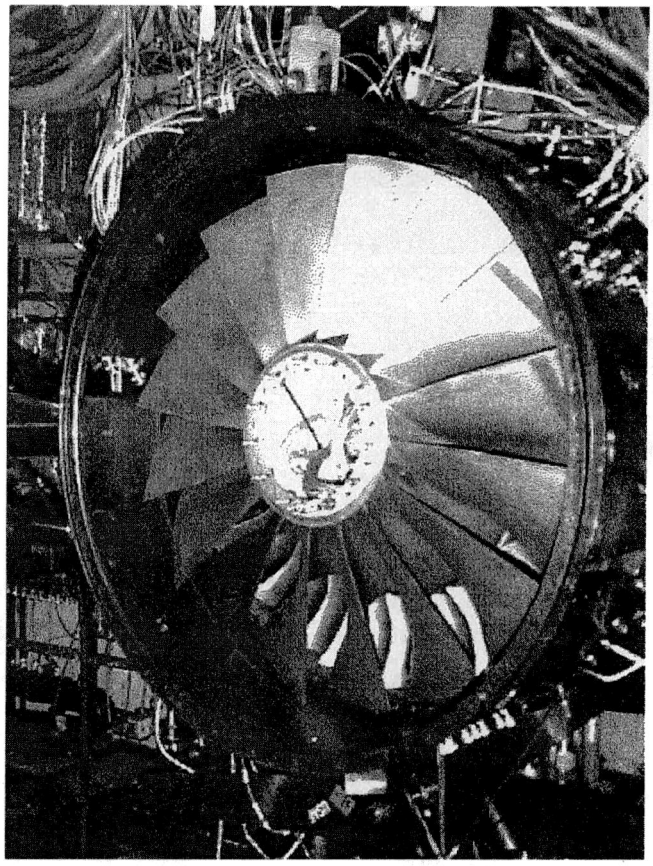

Fig. 1 First-stage transonic rotor

scale compressor throughout its operating regime and will accommodate hardware to extract specific flowfield measurements during a test. Details relating exclusively to this series of tests are described in the following sections.

Compressor and First-Stage Rotor. The research facility was configured to test an unswept transonic two-stage axial-flow research compressor (Russler et al., 1995). The first-stage rotor (Fig. 1), with key parameters listed in Table 1, was tested without inlet guide vanes. The outer casing (Fig. 2) was removed, modified, and replaced each run without disturbing the rotor.

Casing Configurations. Nine casing configurations comprised of three step profiles at each of three clearance levels were tested in this series. The rotor annulus casing was machined to provide the sequence of geometries shown in Fig. 3. The clearance levels were designed to encompass the zones that previous research (Wennerstrom, 1984; Freeman, 1985; Copenhaver et al., 1996) had indicated for an optimum tip clearance. The depth of each step corresponded to the subsequent desired clearance level. Locating the steps at 58 and 86 percent axial chord eased integration with hardware constraints of the research facility.

Table 1 Rotor geometric parameters

Parameter	Value
Number of Blades	16
Rotor Tip Radius (cm)	35.24
Blade Tip True Chord (cm)	20.79
Blade Tip Axial Chord (cm)	10.56
Hub-to-tip Ratio at Leading Edge	0.33
Hub-to-tip Ratio at Trailing Edge	0.62
Tip Solidity (true chord / pitch)	1.50
Design Rotational Speed (RPM)	13288
Design Mass Flow [100% RPM, STP] (kg/sec)	71.66

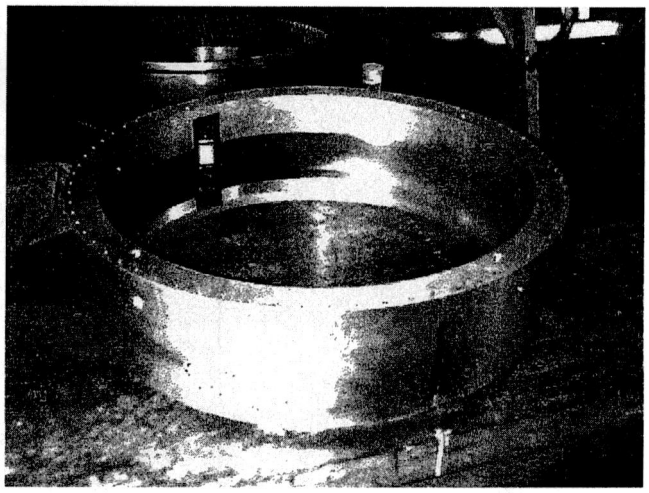

Fig. 2 First-stage rotor casing

Instrumentation. A rotor's performance is usually measured in terms of its pressure ratio, efficiency, and mass flow. Since rotor tip clearance influences these values, the tip gap size must also be quantifiable for the various operating conditions and casing configurations. To attain these quantities, the following instrumentation was used.

Performance Measures. Performance quantities were derived from total pressure and total temperature measurements upstream of the rotor leading edge and downstream of the trailing edge. The upstream total temperature was the average from 49 thermocouples located in the airflow stilling chamber. Two radial rakes of five total pressure probes each mounted in the compressor's straight inlet duct provided the average total pressure of the upstream air. To measure the downstream variables, sensors were mounted on the leading edges of three first-stage stator vanes positioned approximately 120 deg apart; each vane had pairs of collocated total pressure and temperature sensors spanning seven radial positions extending over the range from 10 to 94 percent span. The sensors were aligned with the stator vane leading edge angle, which followed a predefined schedule as a function of rotor speed. This same schedule was used for each test. Static pressure sensors in the inlet bellmouth provided the input for mass flow computation; consistency was verified by a comparison of the calculated bellmouth mass flow with the mass flow derived from the inlet pressure rakes and the downstream venturi. The mass flows presented in this paper were corrected for temperature and pressure. Mass flow through the compressor was controlled with a discharge throttling valve set by the facility operator.

Clearance Measurement. The nonrotating tip clearances were verified before each run using gaged shims. Also, during each test, electrical capacitance proximity probes measured the running tip clearances near the leading and trailing edges of the rotor. The compiled tip gap data for the test series is shown in Fig. 3.

Results

For each casing configuration, performance data were collected as the rotor was tested throughout the mass flow range at each of 100, 95, 90, and 85 percent corrected design speeds (corrected for nonstandard inlet total temperature). A variation of the tip clearance and the use of stepped tip gaps generated

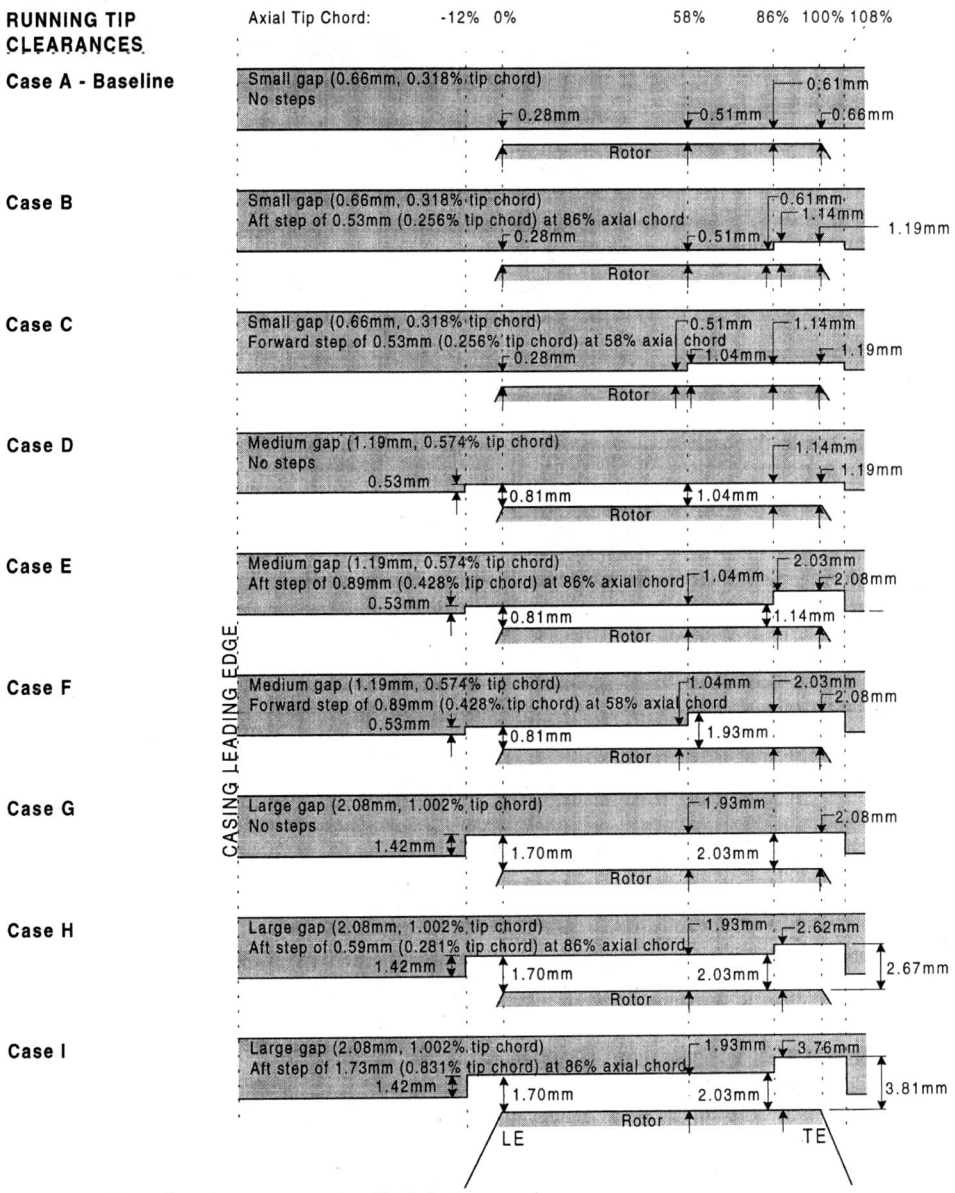

Notes: 1. All running clearances are for 100% design speed.
2. Clearances increase approximately linearly at 0.03mm per 5% decrease in rotor speed in the range from 100% to 85% RPM.

Fig. 3 Rotor casing geometry

marked differences in rotor performance. Generally, while varying clearance levels produced large differences in performance, the inclusion of stepped-tip gaps produced new performance improvements.

Effect of Tip Clearance on Stall Margin. To calculate the effects on stall margin, the stall line for each configuration was first determined from a least-squares linear-fit through the four stall conditions corresponding to each rotor speed (Fig. 4). From such a line, the stalling pressure ratio at any mass flow can be determined. The stall margin for each configuration was calculated as the ratio of the difference between the curve-fitted stall pressure ratio and pressure ratio at peak efficiency to the pressure ratio at peak efficiency.

The effect of clearance on stall margin can be seen in Fig. 5. At 100 percent speed, stall margin tended to increase with increased tip gap; however, for the 85 percent speed condition, stall margin decreased with increased clearance. A transition between these opposing extremes occurred for rotor speeds of 90 and 95 percent, giving mixed results for stall margin.

Effect of Tip Clearance on Pressure Ratio. For all rotor speeds, the small clearance yielded the greatest pressure ratio; pressure ratio decreased with increased (no step) tip gap (Fig. 4). As seen in Figs. 6(a–d), the pressure ratio in the outer half of span decreased with increased clearance, whereas it increased nearer the hub. This shift is due to blockage created in the tip region, which diverts the main flow to the inner span creating greater throughflow and work nearer the hub.

Effect of Tip Clearance on Efficiency. Efficiency also tended to decrease with increased clearance, with a significant decrease occurring for the large (1.002 percent tip chord) tip gap (Fig. 4). Differences in efficiency were minimal between the small (0.318 percent tip chord) and medium (0.574 percent tip chord) gaps, with the medium gap giving slightly improved efficiency in the lower mass flow region near stall for each speed line. As seen in Figs. 6(a–d), efficiency in the outer portion of span decreased with larger tip gap and was essentially unchanged for the inner span. Thus, it is the outer span region that contributes most to changes in overall efficiency.

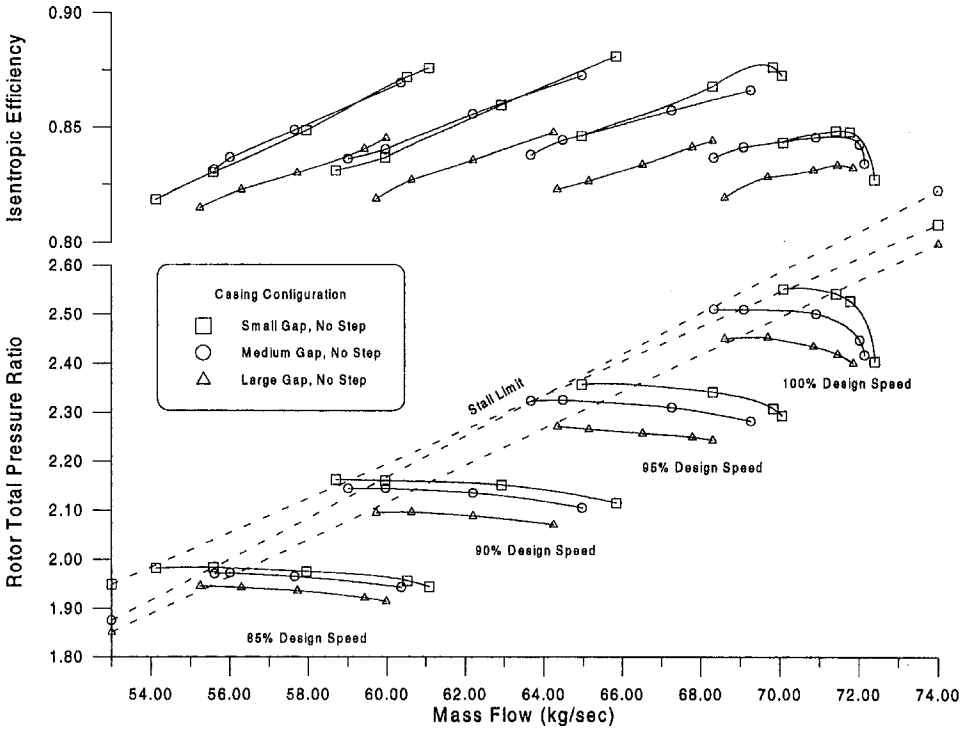

Fig. 4 Rotor map of unstepped clearance level (no steps) configurations

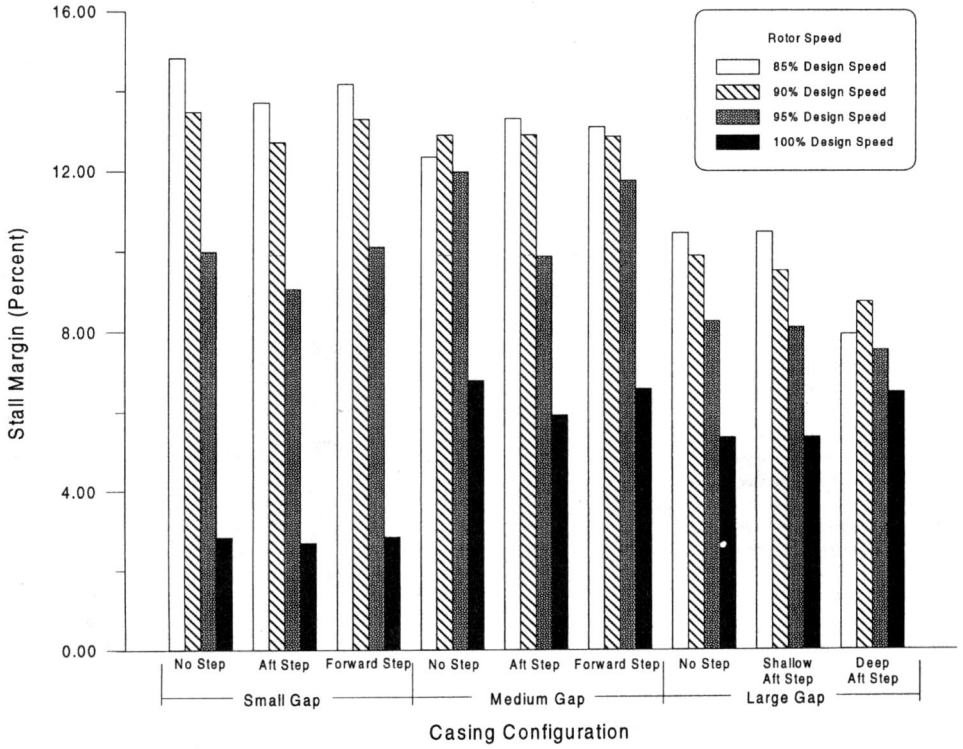

Fig. 5 Stall margin for casing configurations and speeds

Effect of Tip Clearance on Mass Flow Range. For rotor speeds of 90 percent or less, mass flow range decreased with increased tip gap (Fig. 4). For the 100 percent speed line, larger clearances gave increased flow range, with the medium clearance producing the largest gain. At the slower 95 percent speed, the medium clearance also yielded increased mass flow range over the small gap, but the large gap resulted in a significant loss of flow range. In all cases, the maximum mass flow attainable was reduced with increasing clearance. These results indicate the optimum tip gap to maximize flow range for high speed operation resides in an intermediate running clearance range between 0.318 and 1.002 percent tip chord; for the slower speeds, the smallest tip gap possible optimizes mass flow range. It should be noted that a maximized mass flow range does not

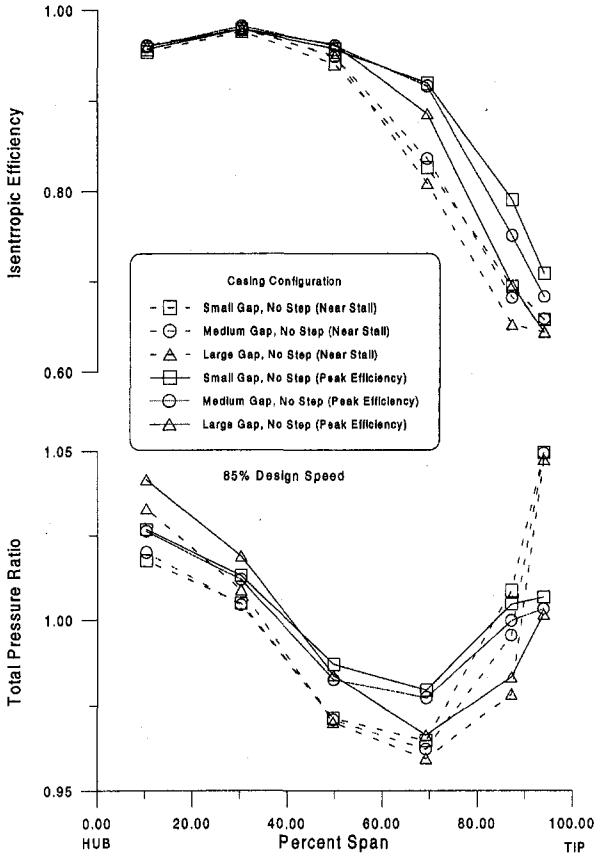

Fig. 6(*a*) Clearance effects on spanwise rotor performance for 85 percent design speed

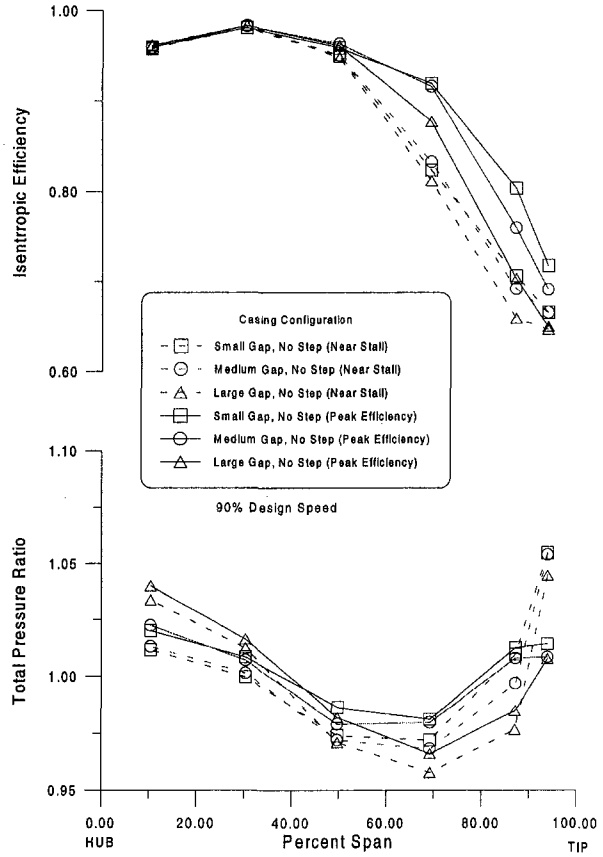

Fig. 6(*b*) Clearance effects on spanwise rotor performance for 90 percent design speed

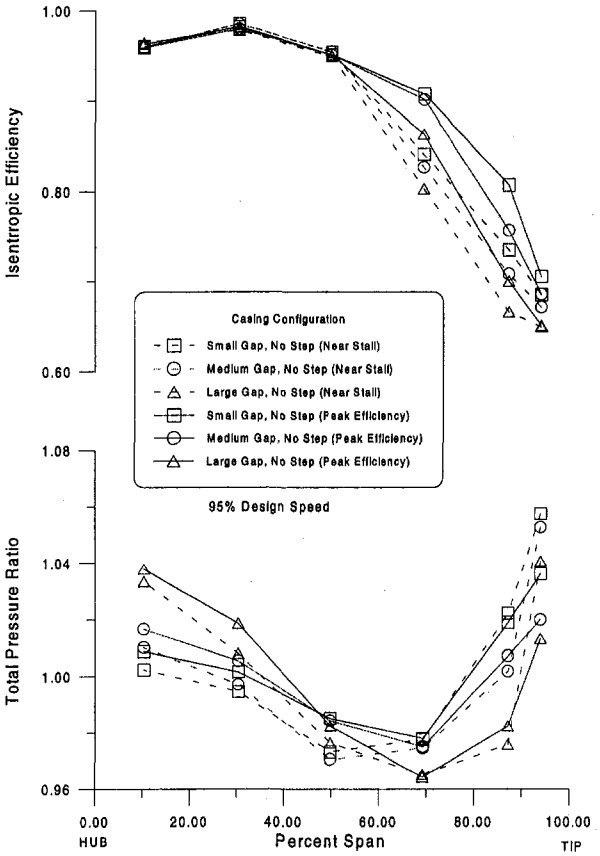

Fig. 6(*c*) Clearance effects on spanwise rotor performance for 95 percent design speed

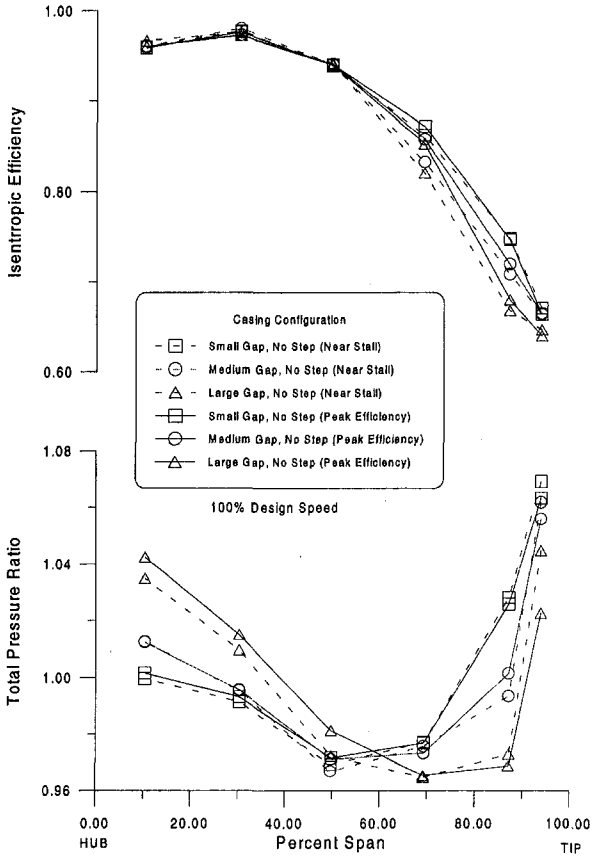

Fig. 6(*d*) Clearance effects on spanwise rotor performance for 100 percent design speed

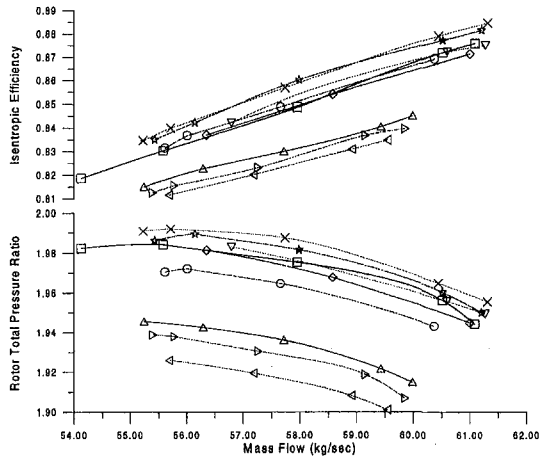

Fig. 7(*a*) Rotor map for 85 percent design speed

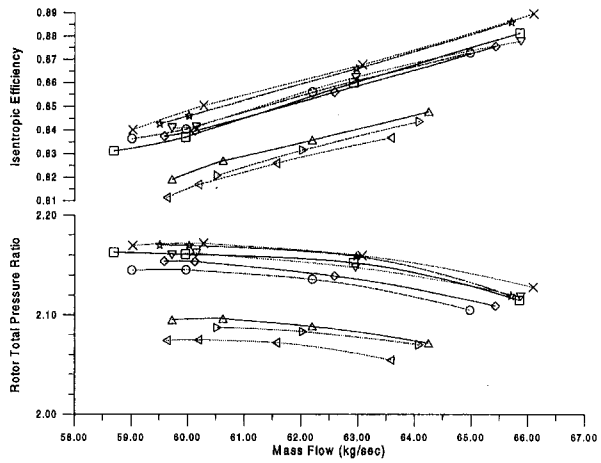

Fig. 7(*b*) Rotor map for 90 percent design speed

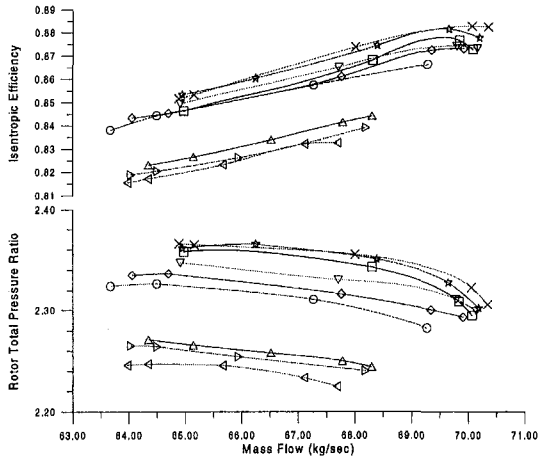

Fig. 7(*c*) Rotor map for 95 percent design speed

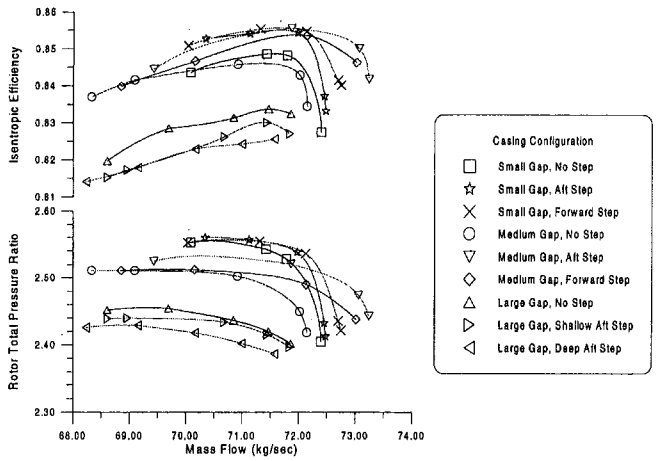

Fig. 7(*d*) Rotor map for 100 percent design speed

necessarily coincide with the condition for maximum mass flow capability.

Effect of Stepped Tip Gap on Stall Margin. No significant changes in stall margin were noticed with the use of stepped tip gaps (Fig. 5). Any differences are within the error introduced by the definition of the stall line—a least-squares linear-fit through the four stall conditions corresponding to each rotor speed.

Effect of Stepped Tip Gap on Pressure Ratio. The effects of stepped tip gaps on rotor performance are seen in Figs. 7(*a–d*). Supplementing Fig. 4, these segmented rotor maps provide detailed comparisons by speed for all configurations tested.

The inclusion of stepped tip gaps with the small and medium clearances gave increased pressure ratio throughout the mass flow range for all rotor speeds (Figs. 7*a*, 7*b*, 7*c*, 7*d*); furthermore, the small clearance with forward step location gave the greatest pressure ratio of all cases tested. However, for the largest tip clearance level of 1.002 percent tip chord, pressure ratio decreased throughout the mass flow range for all rotor speeds. More importantly, the axial location of the step giving the greatest improvement depended mainly on the clearance level. For the small clearance level of 0.318 percent tip chord, the forward step of 0.256 percent tip chord at 58 percent axial chord produced the greatest improvement. This relation held true for all speeds except in the low mass flow range at 100 percent design speed (Fig. 7(*d*)). For the medium clearance level of 0.574 percent tip chord, the aft step at 86 percent axial chord clearly produced the better pressure ratio throughout the mass flow range. As evidenced in Figs. 8(*a–d*), pressure ratio decreased in the outer 40 percent of span when stepped gaps were used, but this loss was countered with improved performance in the inner 60 percent of span to produce an average gain in pressure ratio across the span.

Only the aft step location was tested for the large clearance level (1.002 percent tip chord). Unlike for the small and medium clearances, a stepped gap for the large clearance degraded pressure ratio throughout mass flow range. A deeper step (0.831 percent tip chord) at this clearance caused an even greater degradation of pressure ratio. The authors feel it is doubtful that any step for this larger clearance will improve performance.

Effect of Stepped Tip Gap on Efficiency. As with pressure ratio, efficiency tended to increase when stepped gaps were employed for the small and medium clearance levels but tended to decrease for the large clearance level. Again, for the small clearance level, the forward step at 58 percent axial chord gave the largest increase in efficiency throughout the mass flow range for all rotor speeds tested (Figs. 7(*a*, 7*b*, 7*c*, 7*d*)). For the medium clearance level, though minimal changes in efficiency occurred for 90 and 85 percent design speeds, at 95 and 100 percent speeds, stepped tip gaps produced significant gains in efficiency throughout the mass flow range, with the greatest change occurring for the aft step at 85 percent axial chord. As seen in Figs. 8(*a–d*), stepped gaps increased efficiency across the entire span for those cases that showed an overall efficiency improvement. Again, as with pressure ratio, efficiency decreased when stepped tip gaps were used with the large clear-

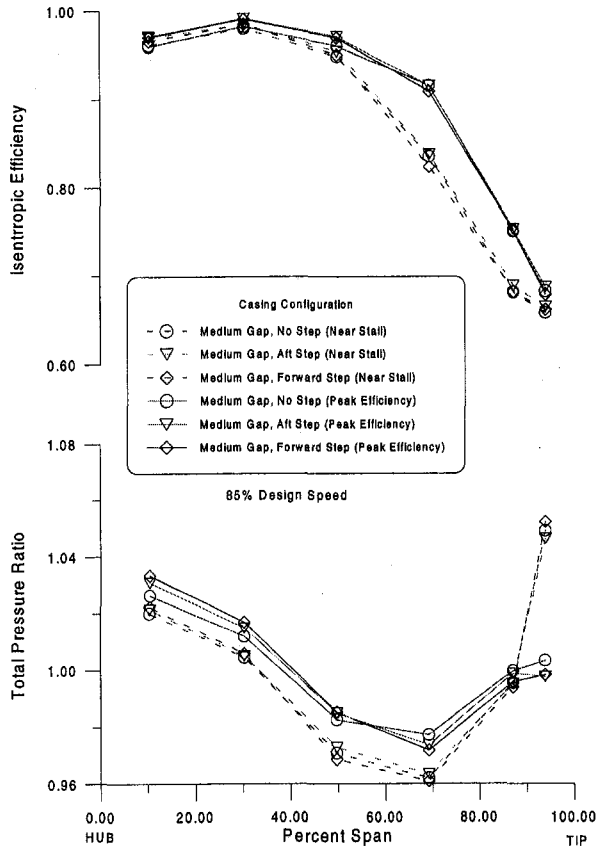

Fig. 8(*a*) Stepped tip gap effects on spanwise rotor performance for 85 percent design speed and medium clearance level

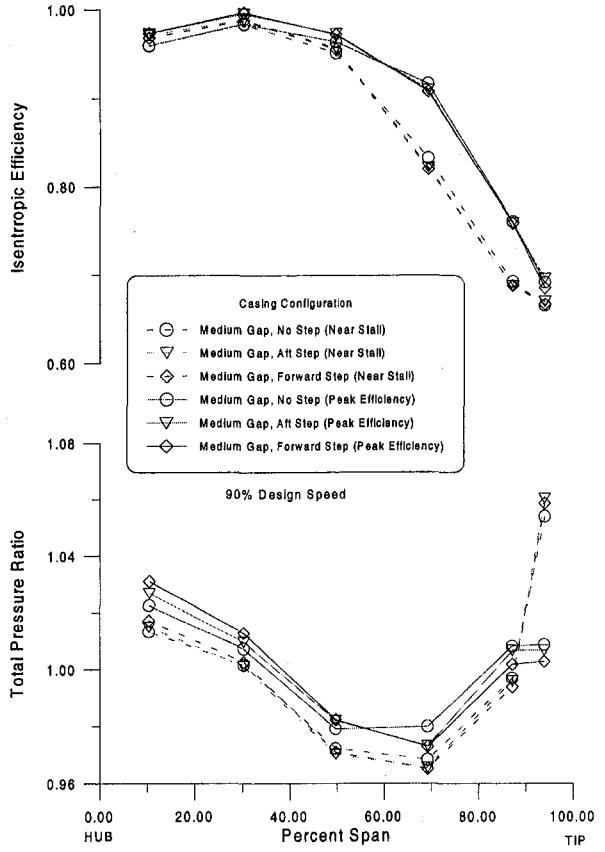

Fig. 8(*b*) Stepped tip gap effects on spanwise rotor performance for 90 percent design speed and medium clearance level

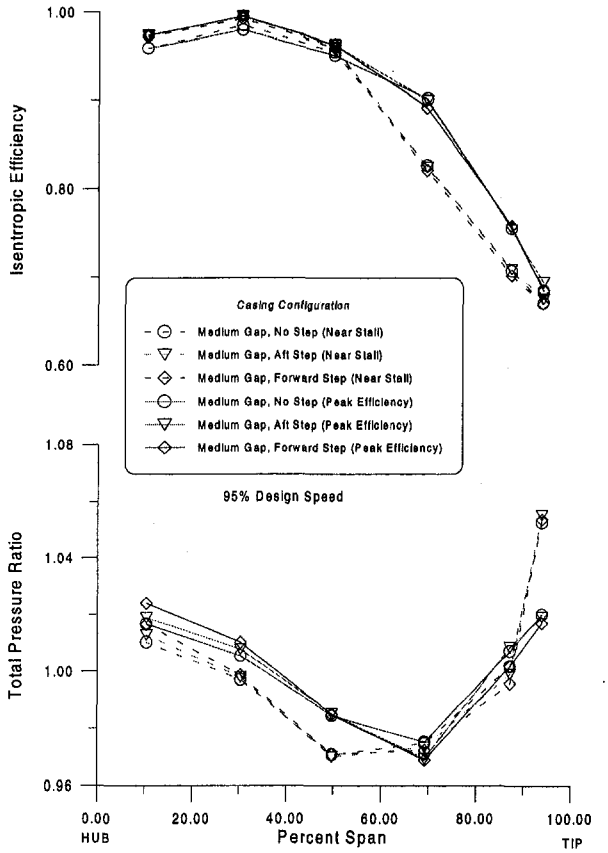

Fig. 8(*c*) Stepped tip gap effects on spanwise rotor performance for 95 percent design speed and medium clearance level

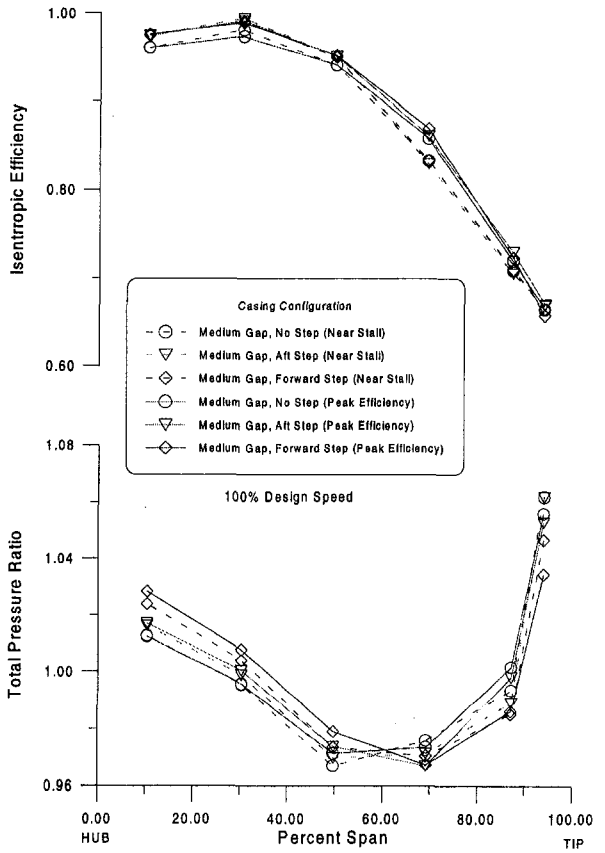

Fig. 8(*d*) Stepped tip gap effects on spanwise rotor performance for 100 percent design speed and medium clearance level

ance level at all rotor speeds, with the deeper step being the worst.

Effect of Stepped Tip Gap on Mass Flow Range. The effects of stepped tip gaps on mass flow range are summarized in Figs. 7(*a–d*). With the small clearance, mass flow range improvement was only achieved at the two faster rotor speeds by using stepped gaps, with the best results occurring for the forward step location. With the medium clearance level, flow range improvement was increased at all speeds by using a stepped gap. The forward step location gave improvement for the two fastest rotor speeds, and the aft step gave improvement for the two slowest speeds tested. With the large clearance level, there were no significant improvements in mass flow range at any speed or aft step depth; in most cases, the mass flow range decreased.

The effects of stepped tip gaps on the upper limit of mass flow are also seen in Figs. 7(*a–d*). Only for the medium gap did significant increases occur in the upper limit mass flow for all conditions; for the small and large gaps, only minor increases or decreases occurred with stepped gaps. Moreover, the configuration yielding the greatest mass flow capability for all rotor speeds was the medium clearance level with aft axial step location. In summary, only the medium gap yielded increases in both mass flow range and mass flow capability by using steps.

Discussion and Conclusions

Tradeoffs exist when optimizing performance measures based purely on clearance level. The tip gap that yields the greatest pressure ratio and efficiency is not necessarily the gap giving the largest flow range, mass flow capability, and stall margin. As a result, one performance measure is optimized at the expense of others, or a compromise is made of all measures to achieve a best all-around performance. These results suggest one cannot claim an overall optimum tip gap exists based on one performance measure alone, and any optimum gap may change with operating conditions.

The results of this series of tests indicate that the tip region flowfield of a transonic axial-flow rotor can be controlled with judicious choice of clearance level and a stepped tip gap. Moreover, changes to this flowfield can improve rotor performance in many instances. Although purely increased tip clearance typically harms performance by introducing more blockage, an increased tip clearance uniquely paired with a stepped gap can actually improve performance by offsetting the undesirable effects of increased clearance. In essence, the blockage created by the increased clearance is used to minimize tip region losses and maximize core passage performance—the authors choose to call this process an "aerodynamic seal" of the tip region, a process that was described in the introduction. This seal can be created by entraining the blockage produced by the upstream flow interaction into the tip gap of an adjacent blade; a stepped tip gap in the aft portion of the blade chord will accomplish this action. (A complementary computational analysis which will aid in clarifying the underlying physical processes is in progress.) The range of clearance levels for which the aerodynamic sealing process is achievable lies between 0.318 and 1.002 percent tip chord. Furthermore, the results shown in Figs. 7(*a–d*) indicate that for any clearance within this range, a unique axial location of stepped tip gap exists to achieve improved performance. The optimum stepped tip gap size and location will depend on the specific compressor rotor, its application, and operating conditions. The best depth of the stepped tip gap requires further study, as do the effects of the sharpness of the step cut into the casing wall. Also, any practical applications must include the effects of material erosion occurring in normal operation. Further research efforts by the authors to determine the optimum relationships are underway.

A summary of specific conclusions relating to the objectives of this research follows:

1 The optimum tip gap depends on the performance measure optimized. To maximize efficiency and pressure ratio, an unstepped tip gap should be the narrowest possible; pressure ratio and efficiency decrease with increased clearance. However, the optimum tip clearance to maximize mass flow range and stall margin falls between 0.318 and 1.002 percent tip chord. Thus, the designer must choose the best compromise to optimize overall rotor performance. However, when stepped tip gaps are employed, further performance increases are possible.

2 Stepped tip gaps benefit some or all measures of rotor performance. For tip clearances less than 1.002 percent tip chord, stepped tip gaps yield improved pressure ratio, efficiency, and flow range over the straight casing profile for many operating conditions. A small clearance level (0.318 percent tip chord) with forward (58 percent axial chord) stepped tip gap, Case C in Fig. 3, and a medium clearance level (0.574 percent tip chord) with aft (86 percent axial chord) stepped tip gap, Case E in Fig. 3, yielded the best improvement of performance measures of the configurations tested.

3 The optimum axial location of the stepped tip gap moves aft as clearance level increases, with the largest clearance level (1.002 percent tip chord) not needing a step; additional study is needed to determine a functional pairing. Studies should focus on clearance levels between 0.318 and 1.002 percent tip chord.

4 An optimum paired combination of clearance level and stepped tip gap may exist. If mass flow range and maximum mass flow capability are important to the designer, the best candidate is an intermediate clearance level with a stepped tip gap located toward the rotor trailing edge. If efficiency and pressure ratio are most important, the small gap with forward step is the best candidate.

In closing, stepped tip gaps improve compressor performance. Using stepped tip gaps in future designs will aid the IHPTET program in accomplishing its goal of doubling thrust-to-weight ratio of turbojet engines.

Acknowledgments

This research was the result of a cooperative effort between the Air Force Institute of Technology and the USAF Wright Laboratories Compressor Research Facility (CRF). The authors wish to acknowledge the teamwork and talents of the management, engineers, and technicians at the CRF who were vital to the data collection effort. The authors also wish to thank Carl Williams, Pat Russler, David Engler, Chuck Greer, and the entire CRF support team of the Battelle Memorial Institute for significant contributions in software development for reducing and analyzing the experimental data.

References

Adamczyk, J. J., Celestina, M. L., and Greitzer, E. M., 1993, "The Role of Tip Clearance in High-Speed Fan Stall," ASME JOURNAL OF TURBOMACHINERY, Vol. 115, pp. 29–39.

Basson, A., and Lakshminarayana, B., 1995, "Numerical Simulation of Tip Clearance Effects in Turbomachinery," ASME JOURNAL OF TURBOMACHINERY, Vol. 117, pp. 348–359.

Chen, G. T., Greitzer, E. M., Tan, C. S., and Marble, F. E., 1991, "Similarity Analysis of Compressor Tip Clearance Flow Structure," ASME JOURNAL OF TURBOMACHINERY, Vol. 113, pp. 260–271.

Copenhaver, W. W., Mayhew, E. R., and Hah, C., 1996, "The Effect of Tip Clearance on a Swept Transonic Compressor Rotor," ASME JOURNAL OF TURBOMACHINERY, Vol. 118, pp. 230–239.

Crook, A. J., Greitzer, E. M., Tan, C. S., and Adamczyk, J. J., 1993, "Numerical Simulation of Compressor Endwall Casing Treatment Flow Phenomena," ASME JOURNAL OF TURBOMACHINERY, Vol. 115, pp. 501–512.

Cybyk, B. Z., Rabe, D. C., Russler, P. M., and Hah, C., 1995, "Characterization of the First-Stage Rotor in a Two-Stage Transonic Compressor," AIAA Paper No. 95-2460.

Dring, R. P., and Joslyn, H. D., 1986, "Through-Flow Modeling of Axial Turbomachinery," ASME *Journal of Engineering for Gas Turbines and Power*, Vol. 108, pp. 246–253.

Dring, R. P., and Joslyn, H. D., 1987, "Throughflow Analysis of a Multistage Compressor Operating at Near-Stall Conditions," ASME JOURNAL OF TURBOMACHINERY, Vol. 109, pp. 483–491.

Freeman, C., 1985, "Effect of Tip Clearance on Compressor Stability and Engine Performance," *Von Karman Institute Lecture Series on Tip Clearance Effects in Axial Turbomachines,* Apr. 15–19.

Grier, P., 1995, "At the Aeronautical Frontier," *Air Force Magazine,* Vol. 78, No. 1, pp. 22–28.

Hah, C., 1986, "A Numerical Modeling of Endwall and Tip Clearance Flow of an Isolated Compressor Rotor," ASME *Journal of Engineering for Gas Turbines and Power,* Vol. 108, pp. 15–21.

Hall, E. J., Crook, A. J., and Delaney, R. A., 1994, "Aerodynamic Analysis of Compressor Casing Treatment With a 3-D Navier–Stokes Solver," AIAA Paper No. 94-2796.

Hill, P. P., and Peterson, C. R., 1992, *Mechanics and Thermodynamics of Propulsion,* 2nd ed., Addison-Wesley.

Kunz, R. F., Lakshminarayana, B., and Basson, A. H., 1993, "Investigation of Tip Clearance Phenomena in an Axial Compressor Cascade Using Euler and Navier–Stokes Procedures," ASME JOURNAL OF TURBOMACHINERY, Vol. 115, pp. 453–467.

Moore, R. D., 1982, "Rotor Tip Clearance Effects on Overall and Blade-Element Performance of Axial-Flow Transonic Fan Stage," NASA TP-2049.

Peter, L. J., and King, P. I., 1996, "Moving Endwall Effects on Passage Losses in Compressor Cascade," AIAA Paper No. 96-2653.

Puterbaugh, S. L., 1994, "Tip Clearance Flow-Shock Interaction in an Advanced, Transonic, Axial-Flow Compressor Rotor," PhD dissertation, University of Dayton, Dayton, OH, Dec.

Puterbaugh, S. L., and Brendel, M., 1995, "Tip Clearance Flow-Shock Interaction in a Transonic Compressor Rotor," AIAA Paper No. 95-2459.

Reitz, M. D., 1996, *Compressor Research Facility Database User's Guide,* WL/POTX, Wright-Patterson AFB, OH 45433.

Russler, P. M., Rabe, D. C., Cybyk, B. Z., and Hah, C., 1995, "Tip Flow Fields in a Low Aspect Ratio Transonic Compressor," ASME Paper No. 95-GT-89.

Russler, P. M., 1995, "Acquisition and Reduction of Rotor Tip Static Pressure Transducer Data From a Low Aspect Ratio Transonic Fan," Battelle Memorial Institute, Dayton, OH, Wright Laboratory Technical Report WL-TR-95-2022.

Sellin, M. D., Puterbaugh, S. L., and Copenhaver, W. W., 1993, "Tip Shock Structures in Transonic Compressor Rotors," AIAA Paper No. 93-1869.

Society of Automotive Engineers, Aerospace Council Division, Technical Committee S-16, 1983, *Inlet Total-Pressure-Distortion Considerations for Gas-Turbine Engines,* Publishers Choice Book Mfg., Inc., Mars, PA, Aerospace Information Report 1419.

Suder, K. L., and Celestina, M. L., 1996, "Experimental and Computational Investigation of the Tip Clearance Flow in a Transonic Axial Compressor Rotor," ASME JOURNAL OF TURBOMACHINERY, Vol. 118, pp. 218–229.

Valenti, M., 1995, "Upgrading Jet Turbine Technology," *Mechanical Engineering,* Vol. 117, No. 12, Dec., pp. 56–60.

Wennerstrom, A. J., 1984, "Experimental Study of a High Through-Flow Transonic Axial Compressor Stage," ASME *Journal of Engineering for Gas Turbines and Power,* Vol. 106, pp. 552–560.

White, F. M., 1991, *Viscous Fluid Flow,* 2nd ed., McGraw-Hill.

WL/POTX Pamphlet, 1995, *Compressor Research Facility,* Aero Propulsion and Power Directorate, Wright Laboratory, Wright-Patterson AFB, OH 45433.

Yaras, M. I., and Sjolander, S. A., 1992a, "Effects of Simulated Rotation on Tip Leakage in a Planar Cascade of Turbine Blades: Part I—Tip Gap Flow," ASME JOURNAL OF TURBOMACHINERY, Vol. 114, pp. 652–659.

Yaras, M. I., and Sjolander, S. A., 1992b, "Effects of Simulated Rotation on Tip Leakage in a Planar Cascade of Turbine Blades: Part II—Downstream Flow Field and Blade Loading," ASME JOURNAL OF TURBOMACHINERY, Vol. 114, pp. 660–667.

The Performance of a Centrifugal Compressor With High Inlet Prewhirl

A. Whitfield
Department of Mechanical Engineering,
University of Bath,
Bath, United Kingdom

A. H. Abdullah
Department of Mechanical Engineering,
University Technologi Malaysia,
Johore Baharu, Malaysia

The performance requirements of centrifugal compressors usually include a broad operating range between surge and choke. This becomes increasingly difficult to achieve as increased pressure ratio is demanded. In order to suppress the tendency to surge and extend the operating range at low flow rates, inlet swirl is often considered through the application of inlet guide vanes. To generate high inlet swirl angles efficiently, an inlet volute has been applied as the swirl generator, and a variable geometry design developed in order to provide zero swirl. The variable geometry approach can be applied to increase the swirl progressively or to switch rapidly from zero swirl to maximum swirl. The variable geometry volute and the swirl conditions generated are described. The performance of a small centrifugal compressor is presented for a wide range of inlet swirl angles. In addition to the basic performance characteristics of the compressor, the onsets of flow reversals at impeller inlet are presented, together with the development of pressure pulsations, in the inlet and discharge ducts, through to full surge. The flow rate at which surge occurred was shown, by the shift of the peak pressure condition and by the measurement of the pressure pulsations, to be reduced by over 40 percent.

Introduction

A general requirement for a centrifugal compressor is that it should provide a high pressure ratio with good efficiency together with a broad operating range. This requirement can be applied to most applications, be it for small gas turbines, turbochargers, or process compressors. With developments in both compressor and user technologies there is a demand for increased pressure ratio per stage, without sacrifice of efficiency or operating range. Yet as pressure ratio is increased, both efficiency and operating range are inexorably reduced. The requirement for a broad operating range stems from the need for the compressor to match the operating range of the component for which the compressed gas is supplied. The compressor must supply the engine air demand over a wide range of speeds and loads. A process compressor must meet the demand for a wide range of flow rates and possible variations in the composition of the gas being compressed. Compressor operating range is limited at high flow rates by choking and at low flow rates by surge. Prolonged operation in the surge region cannot be tolerated as it can lead to an interruption of the process that the gas supply is supporting, and possible mechanical failure. For many applications, a broad operating range between choke and surge is of such importance that efficiency levels are often sacrificed for flow range through the general adoption of the vaneless diffuser, rather than the more efficient vaned diffuser. A simple criterion for the onset of surge is that it commences at the peak of the pressure ratio/mass flow characteristic, the positive gradient part of the curve defining the unstable operating region of the compressor. While it may be possible to operate with a positive sloping characteristic prior to full surge, it is generally an unstable region in which surge can be triggered by any externally imposed disturbance. The most commonly adopted design feature applied to ensure a rising pressure ratio mass flow characteristic is that of backward swept blades at impeller discharge. The larger the degree of backward sweep, the greater the negative slope of the ideal characteristic. The application of the backward-swept impeller has played a dominant role in the development of compressors with a broad operating range and high efficiency. The adoption of a backward-swept impeller not only leads to a stable rising pressure ratio characteristic, but also reduces the magnitude of the impeller discharge Mach number with consequent benefits for the efficiency of both the impeller and the following diffuser system. When increased rotational speed is undesirable, pressure ratio can be increased through a reduction in the blade discharge backsweep, but this will lead to a reduction in the operating range. To remedy this variable geometry, techniques can be considered where, in the case of inlet swirl, fixed impeller blade backsweep is traded for variable geometry components. The natural areas for the application of variable geometry devices are the regions immediately upstream and downstream of the impeller. Inlet guide vanes, which generate a swirling flow in the direction of rotation of the impeller, enhance the underlying stability by developing a rising characteristic similar to that obtained with a backswept impeller. This approach has been extensively investigated, e.g., Steinke and Crouse (1967), and Rodgers (1977, 1990), for small gas turbines, Whitfield et al. (1975) for turbochargers, and Simon et al. (1987) and Williams (1989) for process compressors. Rodgers obtained a significant shift of the surge line to reduced flow rates through the application of a 40 deg swirl angle, while Williams had to apply 60 deg of swirl to obtain a similar beneficial shift of the surge line. The application by Rodgers was at a pressure ratio of 5 to 1, while that of Williams was at only 1.7 to 1. Application of the Euler equation leads to the familiar expression for compressor pressure ratio as

$$P_R^{(\gamma-1)/\gamma} = 1 + \frac{\gamma - 1}{a_{o1}^2}\eta_s(U_2C_{u2} - U_1C_{u1})$$

As the flow rate is reduced toward surge, the tangential component of velocity at impeller discharge increases and approaches the blade speed U_2. At inlet the tangential component of velocity approaches zero and large swirl angles are necessary to generate a significant tangential component of velocity at near-surge flow rates. Inlet guide vanes are usually straight uncambered vanes in order to generate zero swirl, and when

Contributed by the International Gas Turbine Institute and presented at the 42nd International Gas Turbine and Aeroengine Congress and Exhibition, Orlando, Florida, June 2–5, 1997. Manuscript received at ASME Headquarters February 1997. Paper No. 97-GT-182. Associate Technical Editor: H. A. Kidd.

aligned to give large swirl angles are inefficient, due to large incidence angles, and shed wakes into the impeller passage. Cambered guide vanes designed to generate a specified swirl angle cannot be oriented to provide zero swirl. With this in mind a volute swirl generator, based on that commonly used for radial inflow turbines, was used to develop the high swirl angles. Variable geometry techniques were investigated to vary the swirl angle from zero through to full swirl.

Experimental Test Facility

All tests were performed with a small turbocharger compressor with an axial inlet, a radial vaneless diffuser and volute collector. The basic geometry of the impeller is given in Table 1.

Table 1 Impeller dimensions

Inducer hub radius (mm)	10.5
Inducer tip radius (mm)	31.0
Impeller discharge radius (mm)	50.0
Impeller discharge blade height (mm)	5.0
Inducer inlet tip blade angle (deg)	50.0
Impeller discharge backsweep angle (deg)	7.0

The design and basic performance of the impeller were given by Whitfield et al. (1993). The impeller was designed for a pressure ratio of 3.6:1 at an impeller speed of 98,000 rpm. The application of 25 deg of prewhirl was considered from the outset. As a consequence the impeller backsweep was only 7 deg, and the inducer blade angle at the tip was selected as −50 deg to correspond with the minimum relative Mach number condition; see Whitfield et al. (1993).

The compressor air supply was drawn from the laboratory and discharged to the atmosphere, external to the test cell, through the laboratory exhaust system. The compressor air flow rate was regulated by a stepper-motor-controlled throttle valve. Through the stepper motor control the valve could be set at any repeatable position and the air flow rate closely regulated. The basic compressor performance was measured through the application of platinum resistance thermometers and static pressure taps at compressor inlet and discharge, together with a flow metering orifice downstream of the compressor. In addition a three-hole yaw probe was traversed across the inlet duct to measure both the inlet stagnation pressure and the inlet swirl angle. Pressure transducers were located in the compressor inlet and discharge ducts to monitor the development of flow unsteadiness. A rapid response thermocouple was also positioned 10 mm upstream of the impeller leading edge, and at a radius ratio (r_s) of 0.8 (radius of 25 mm). This provided an indication of the onset of flow reversal at the impeller inducer tip radius.

The design of the variable geometry volute swirl generator was based on a radial inflow turbine volute and fabricated with a simple rectangular cross section. The design procedure was

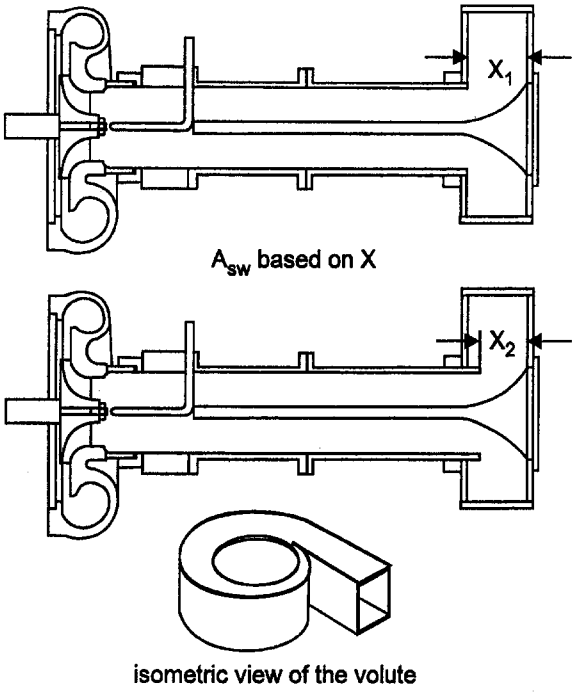

Fig. 1(*a*) Variable volute swirl generator, volute A

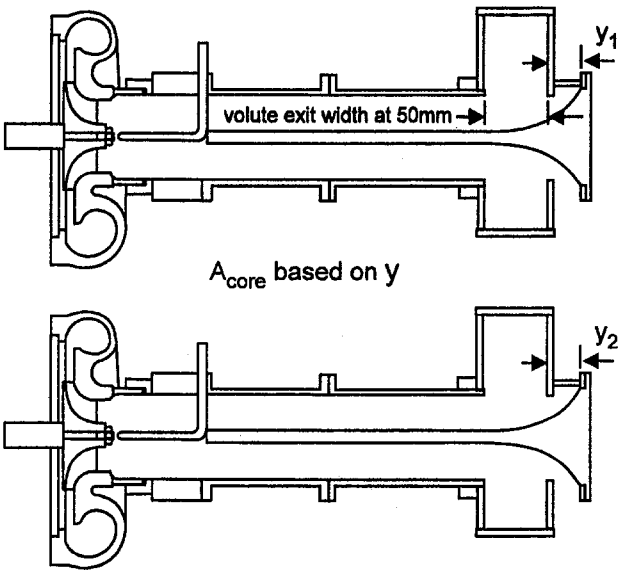

Fig. 1(*b*) Volute with variable core flow, volute B

Nomenclature

A_{core} = area for core flow
A_E = area of entry duct
A_{SW} = area of volute discharge
a_{o1} = speed of sound at inlet total temperature
C_{U1} = tangential component of velocity at impeller inlet
C_{U2} = tangential component of velocity at impeller exit
I = incidence; relative air angle − blade angle at inducer tip
$\dot{m}$ = mass flow rate
P_R = pressure ratio
PSD = power spectral density = V^2/Hz
r_s = radius/inducer tip radius
T_{ui} = temperature 10 mm upstream of the impeller
T_{amb} = ambient temperature
U = impeller blade velocity
X = volute discharge passage width, Fig. 1(*a*)
Y = axial passage width for core flow, Fig. 1(*b*)
γ = ratio of specific heats
ΔP = total pressure drop, cm of water
η_s = stage isentropic efficiency

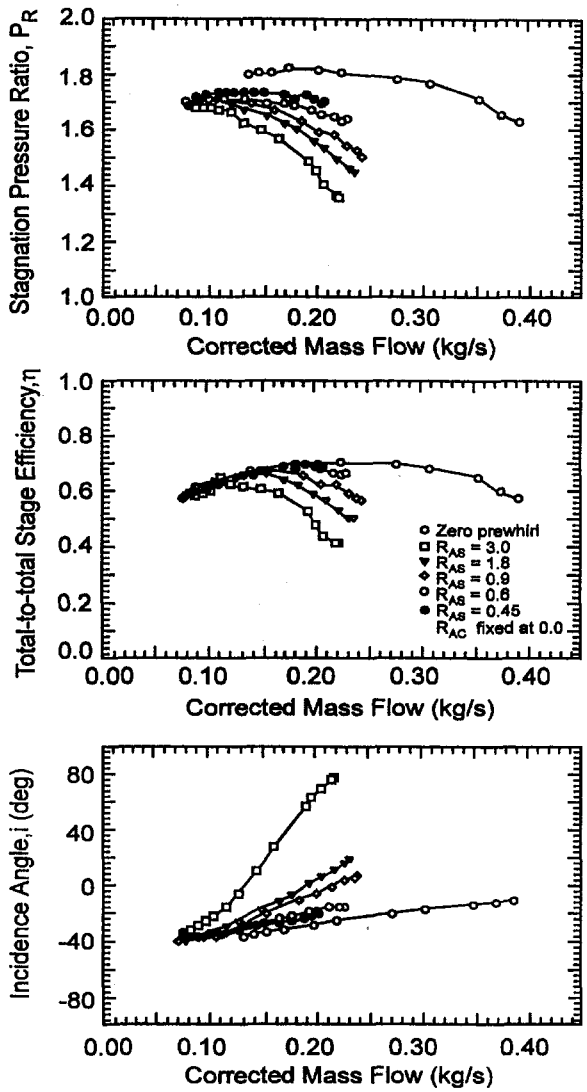

Fig. 2 Compressor performance with varying swirl, volute A

described by Whitfield and Mohd Noor (1994). Two approaches were used to vary the swirl. For volute A the exit width (X) was varied, see Fig. 1(a), while with volute B a nonswirling core flow was introduced by retracting the center body, see Fig. 1(b). The core flow was varied by changing the radial entry width (y) between the center body and volute casing. For volute A the swirl flow area ratio, R_{AS}, is given as the ratio of the area at volute exit, A_{SW} (based on X Fig. 1(a)), to the area of the inlet duct, A_E, at the measurement station

$$R_{AS} = A_{SW}/A_E$$

Similarly for volute B the core flow is given as the area ratio

$$R_{AC} = A_{\text{core}}/A_E$$

where A_{core} is the area of the opening (based on y, Fig. 1(b)) through which the core flow entered the inlet duct.

Presentation and Discussion of Results

All tests were conducted at an impeller speed of 60,000 rpm as it provided a satisfactory pressure ratio for the tests and was the maximum speed that could be tested with cold air driving the turbine. This made it possible to measure the inlet swirl conditions by hand with a yaw probe.

Performance Characteristics. The basic performance characteristics of pressure ratio, efficiency, and derived incidence angle are presented as a function of corrected mass flow rate in Figs. 2 and 3 for volutes A and B, respectively. In each case the performance with a completely swirl-free inlet is presented for comparison purposes. For volute A the exit width was varied between its full opening of 50 mm (a swirl flow area ratio, R_{AS}, of 3.0) and 7.5 mm (a swirl flow area ratio, R_{AS}, of 0.45). As the swirl flow area ratio was reduced from 3.0 to 0.45, the swirl angle at impeller inlet decreased from 67 to 25 deg. With zero swirl the peak pressure ratio occurred at a mass flow rate of 0.17 kg/s, and violent surge at a flow rate of 0.14 kg/s. With maximum swirl the peak pressure ratio was shifted to a flow rate of less than 0.1 kg/s, a reduction in minimum flow rate in excess of 40 percent, and violent surge was not obtained over the flow range tested. At high flow rates, however, the efficiency and pressure ratio decreased rapidly due

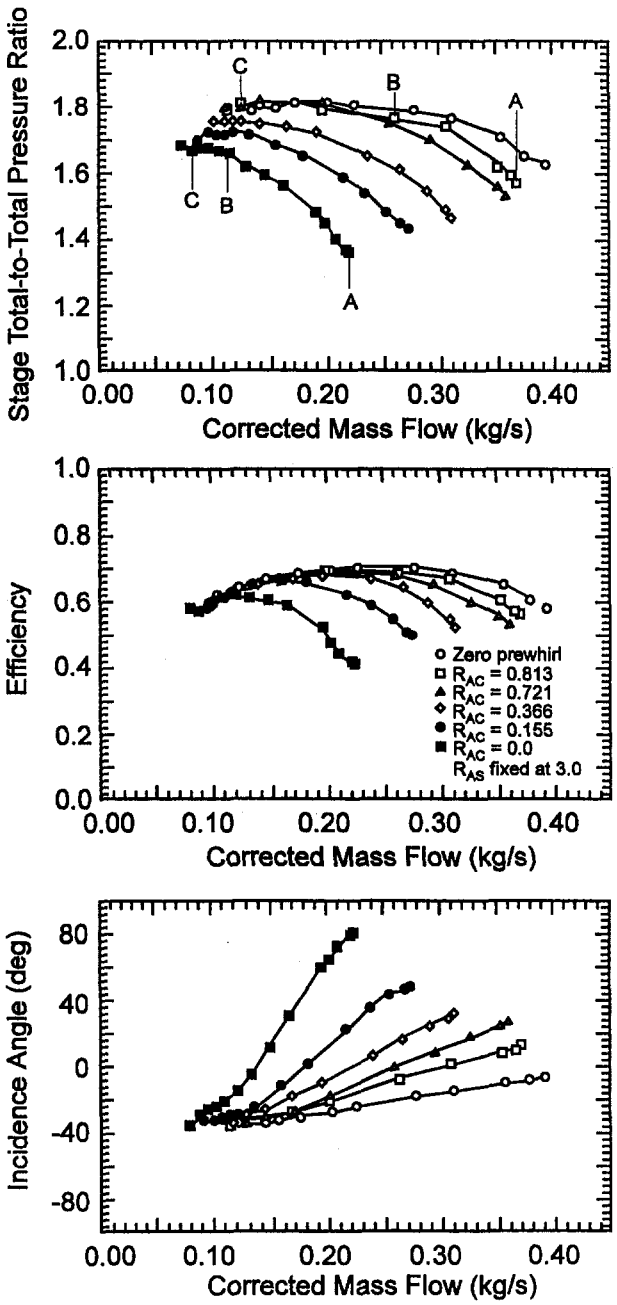

Fig. 3 Compressor performance with varying core flow, volute B

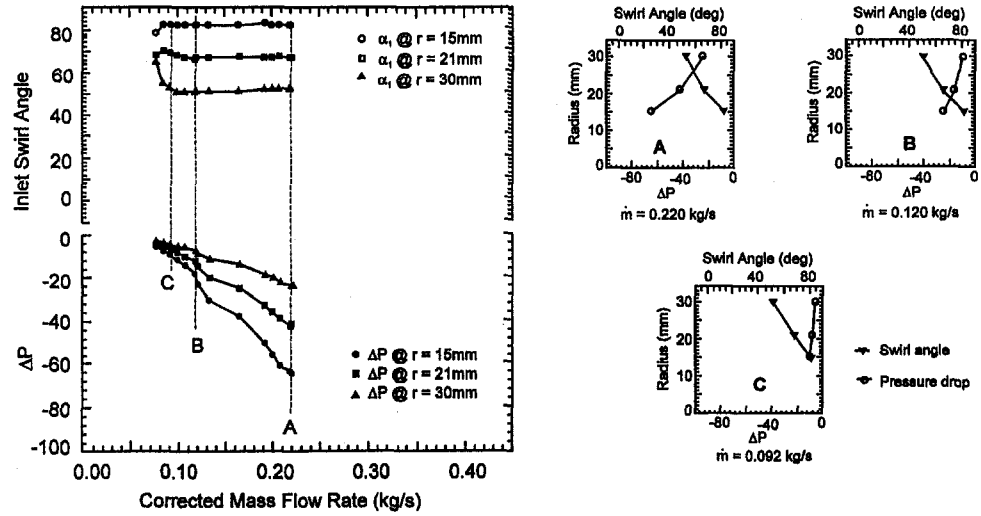

Fig. 4 Volute B inlet flow conditions, no core flow

to the sharp increase in impeller incidence angle. Also by varying the volute flow area not only was the magnitude of swirl reduced, but also the flow rate, and it was not possible with this variable geometry configuration alone to obtain zero swirl at high flow rates.

For volute B a nonswirling core flow was introduced by withdrawing the center core; the radial entry passage was increased from zero to 20 mm, giving a maximum core flow area ratio of 0.813. The basic performance with volute B is shown in Fig. 3. Here a full range of swirl has been obtained and the performance approached that with zero swirl as the core flow area was increased. For the maximum core flow area ratio tested, the mean swirl angle was of the order of 15 deg at high flow rates and 10 deg at low flow rates. The variation of swirl angle with flow rate, and the variation with radius in the inlet duct (at selected flow rates, points A, B, and C in Fig. 3) is shown in Figs. 4 and 5 for volute B. For maximum swirl, Fig. 4, the swirl angle was inversely proportional to the radius, as would be expected for a free vortex. The swirl angle did not vary significantly with flow rate; measured magnitudes at the lowest flow rates were probably influenced by reverse flow from the impeller. With maximum core flow, Fig. 5, the variation of flow angle with radius resembles that expected from a forced vortex, and the flow angle decreased slightly with flow rate. That is, the core flow was dominant and became more dominant as the flow rate was reduced.

Also shown in Figs. 4 and 5 is the measured stagnation pressure relative to the atmosphere; this gives the stagnation pressure drop, ΔP, across the swirl generator. With maximum swirl, the stagnation pressure drop was high at high flow rates and decreased with flow rate. There was also a large radial stagnation pressure gradient at high flow rates. As high swirl would not be applied at high flow rates, the stagnation pressure drop is not important until the flow rate is of the order of that indicated by condition B. Application of maximum core flow, Fig. 5, led to a significant reduction in stagnation pressure loss at high flow rates, and there was little variation with radius. Clearly the mixing of the core and swirl flow has not given rise to large pressure loss, nor a radial variation.

Similar swirl measurements for volute A showed a free-vortex-type distribution at all flow rates. However, due to space limitations, these results are not included as the full flow range could not be covered.

Development of Reverse Flow and Flow Pulsations. The detailed development of flow reversal at impeller inlet was monitored through: (1) a temperature probe located at a radius ratio, r_s, of 0.8 and 10 mm upstream of the inducer leading edge, and (2) by pressure transducers in the inlet and discharge ducts.

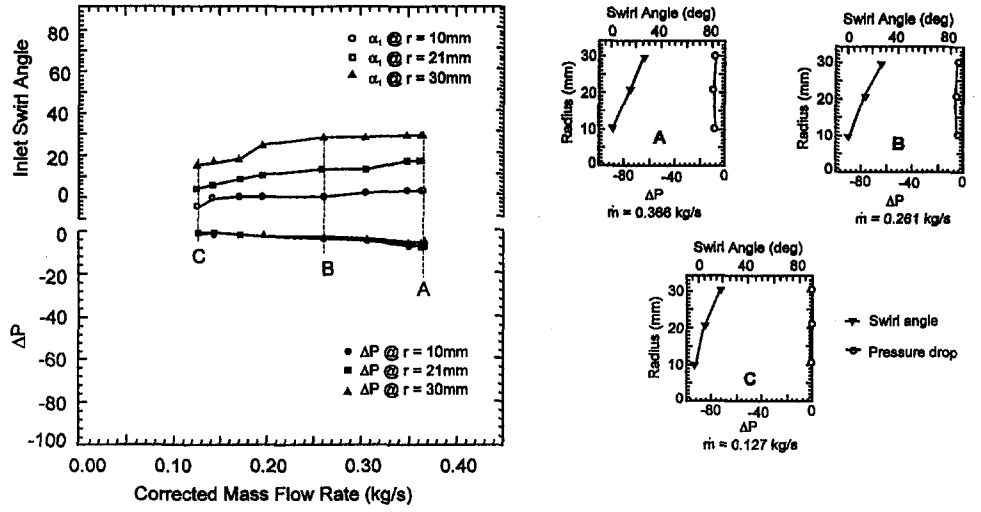

Fig. 5 Volute B inlet flow conditions, core flow area ratio 0.813

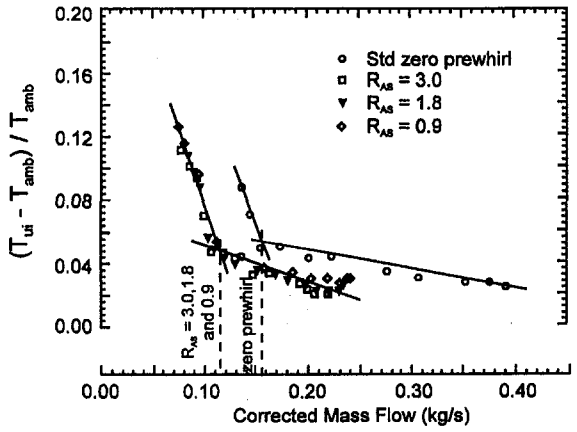

Fig. 6 Inlet temperature rise due to backflow, volute A

The inlet temperature is presented as a temperature difference, $T_{ui} - T_{amb}$, normalized by the ambient temperature, T_{amb}. The temperature difference measured with the standard zero swirl configuration is compared with that obtained with inlet volutes A and B in Figs. 6 and 7, respectively. As the mass flow rate was reduced, the inlet temperature difference initially increased very gradually. A flow rate was then reached where the temperature difference increased rapidly, indicating a backflow of high-temperature air from the impeller.

For the standard zero swirl configuration, the critical mass flow rate at which this change in slope occurred was 0.16 kg/s (this is close to the peak pressure ratio flow rate). Performance with the swirl generator volute A moved this critical mass flow rate to approximately 0.12 kg/s. In this case results are shown for three volute geometries, and it is difficult to discern a significant change in the inlet temperature characteristic with volute geometry.

By varying the inlet core flow, volute B, the effect of volute geometry on the inlet temperature profile is quite clear, Fig. 7. Again, for clarity, three volute configurations are compared with the standard zero swirl case. By progressively reducing the magnitude of the core flow, and increasing the swirl flow, the critical mass flow rate at which the inlet temperature increased was moved to reduced magnitudes. With full volute swirling flow the critical mass flow rate was of the order of 0.11 kg/s, a 33 percent reduction relative to that obtained with zero swirl.

This indication of the onset of reverse flow at impeller inlet did not coincide with the peak pressure ratio flow rate, or with full surge as shown by the pressure transducers in the inlet and discharge ducts, Figs. 8, 9, and 10. The pressure signals are presented in time and frequency domains. The time domain

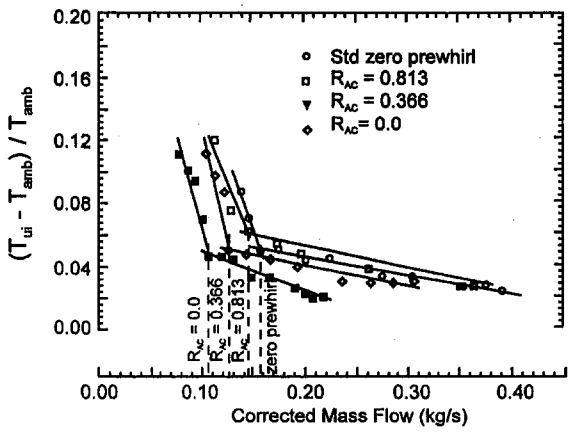

Fig. 7 Inlet temperature rise due to backflow, volute B

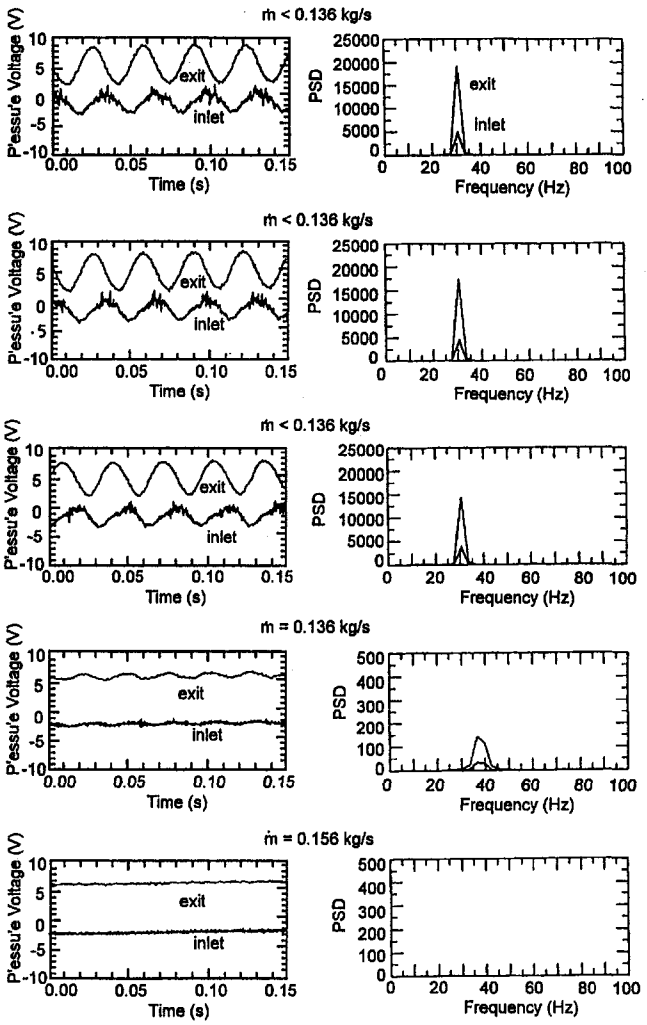

Fig. 8 Development of pressure pulsations, zero prewhirl

signal represents the voltage from the transducer, while the frequency domain was obtained through a Fast Fourier Transform of the pressure signal.

The development of pressure pulsations as the mass flow rate was reduced for the standard zero prewhirl configuration is shown in Fig. 8. Pressure traces at the peak efficiency flow rate were similar to those at high flow rate, and this continued until the mass flow rate was reduced to 0.136 kg/s. At this flow rate, a sinusoidal fluctuation developed with a frequency of 37 Hz. Further throttling of the mass flow rate pushed the compressor operation into full surge with distinctive pressure pulsations at a frequency of 30 Hz. This is approximately the Helmholtz resonance frequency of the ducting.

With maximum inlet swirl, volute B with zero core flow, the distinctive surge pulsations were not obtained for flow rates down to 0.077 kg/s, Fig. 9. With a flow rate of 0.085 kg/s analysis of the pressure signals indicated two main frequencies of 79 and 46 Hz. A similar pressure trace was obtained at the reduced flow rate of 0.077 kg/s; however, the dominant frequencies were reduced to 49 and 40 Hz. Further reduction of the mass flow rate led to a pressure pulsation with a dominant frequency of 40 Hz. This final pressure trace is similar to that shown with zero swirl at a flow rate of 0.136 kg/s, Fig. 8; further reduction in mass flow rate was not attempted as the compressor operation was noisy.

Reducing the inlet swirl by increasing the core flow area ratio to 0.366 led to the development of pressure pulsations with reducing flow rate as shown in Fig. 10. In this case an initial

disturbance was obtained at a flow rate of 0.12 kg/s, and this developed until a clear surge (with a frequency of 30 Hz) was obtained at a flow rate of approximately 0.1 kg/s.

The pressure transducers have been used to detect the onset of surge pressure pulsations only. The apparent modification of the relative strength of the inlet and discharge pulsation as swirl was introduced needs further investigation. This requires accurate calibration of the transducers to provide pressure measurements rather than output voltage.

Conclusions

Application of high inlet swirl through the use of a volute swirl generator has led to the suppression of surge. Surge suppression was indicated by: (*i*) a shift of the peak pressure ratio to reduced flow rates, and (*ii*) by measured pressure pulsations in the inlet and discharge ducts. In addition temperature measurements close to the impeller inducer showed that local flow reversals were also suppressed. Surge pressure pulsations were not detected at the lowest flow rate tested when full swirl was generated by the volute; however, compressor operation become noisy.

At high flow rates, inlet swirl cannot be used, as it leads to large impeller incidence angles and reduced efficiency. A well-designed volute will generate high swirl efficiently; however, a variable-geometry arrangement has to be deployed in order to obtain zero swirl at high flow rates. From the investigations conducted here, a variable core flow proved to be effective. The variable geometry concept is relatively simple with few moving parts, compared to a variable vane arrangement, and it could be readily developed so that the volute flow could be reduced to zero as the core flow is increased. The simplest mode of operation would be an on/off device with the compressor operating with full core flow, zero swirl, until the peak pressure ratio point is reached; whereupon the core flow could be sealed and the full volute flow obtained in order to extend the operating range. The volute design could then be sized to carry the low flow rates only. This application of an on/off device would lead to a stepped reduction in both pressure ratio and efficiency when full swirl is introduced.

The major disadvantage with this arrangement is the need to have a dual inlet. While this is practically possible for a compressor drawing air from the atmosphere, there may be installation restraints which would have to be addressed. For a process compressor, or a boost compressor in a gas pipeline, such a dual inlet would have additional design and installation difficulties.

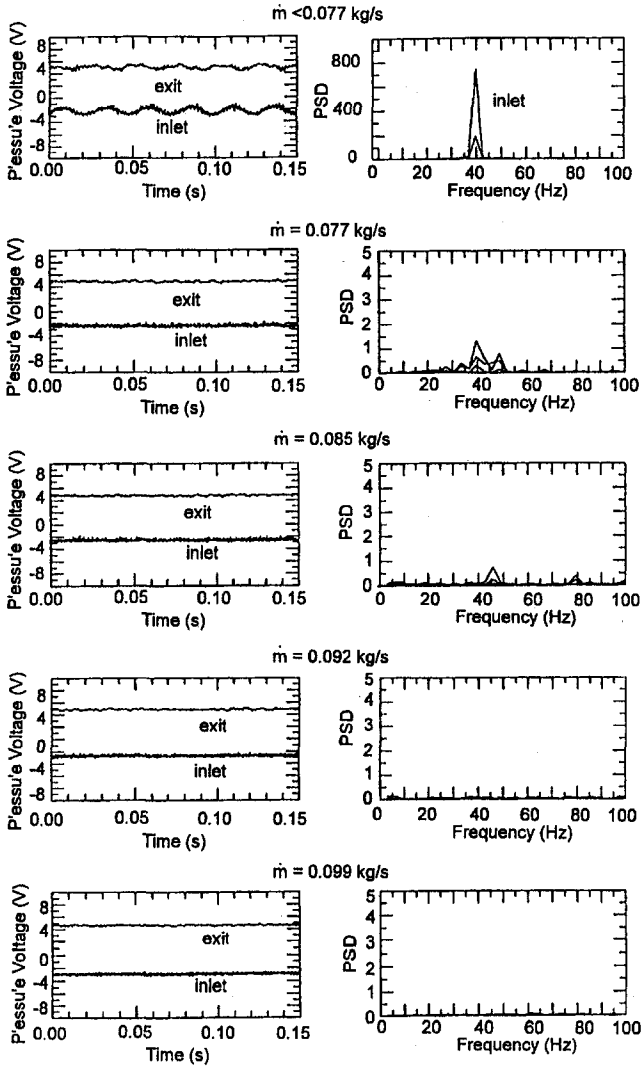

Fig. 9 Development of pressure pulsations, volute B no core flow

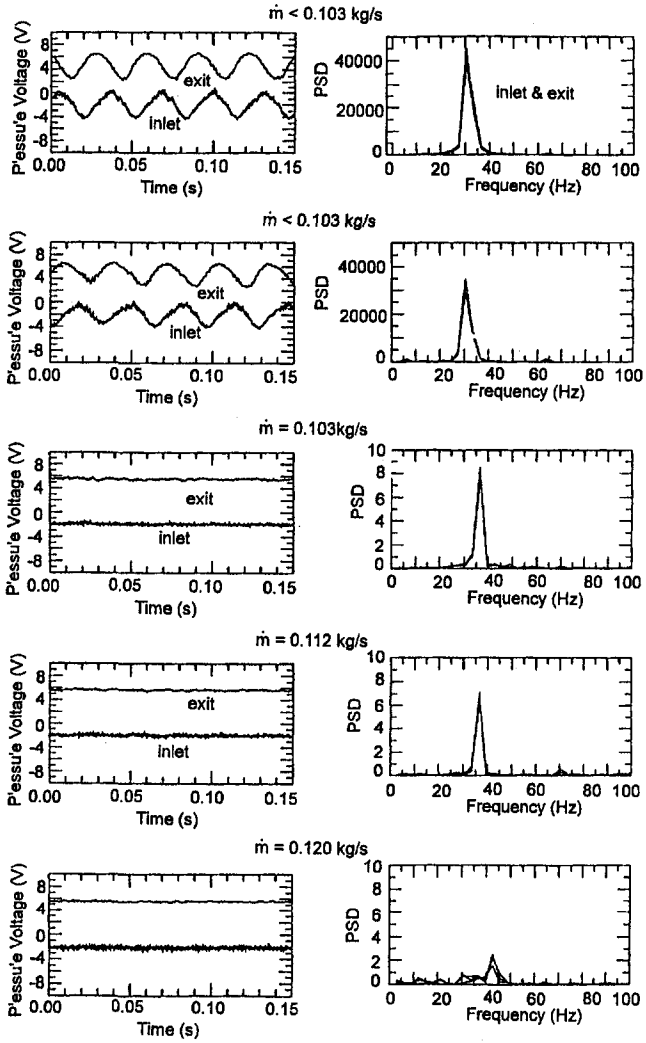

Fig. 10 Development of pressure pulsations, volute B core flow area ratio 0.366

References

Rodgers, C., 1977, "Impeller stalling as influenced by diffusion limitations," ASME *Journal of Fluids Engineering*, Vol. 99, p. 84.

Rodgers, C., 1990, "Centrifugal compressor inlet guide vanes for increased surge margin," ASME Paper No. 90-GT-158.

Simon, H., et al., 1987, "Improvements in the performance characteristics of single-stage and multistage centrifugal compressors by simultaneous adjustments of inlet guide vanes and diffuser vanes," ASME JOURNAL OF TURBOMACHINERY, Vol. 109, p. 41.

Steinke, R. J., and Crouse, J. E., 1967, "Preliminary analysis of the effectiveness of variable geometry guide vanes to control rotor-inlet flow conditions," NASA TN-D 3823.

Whitfield, A., et al., 1975, "Experimental and theoretical performance of a radial flow turbocharger compressor with inlet prewhirl," *Proc. I. Mech. E,* Vol. 189, p. 177.

Whitfield, A., Doyle, M. D. C., and Firth, M. R., 1993, "Design and performance of a high-pressure ratio turbocharger compressor. Part 1: Design considerations. Part 2: Experimental performance," *Proc. I. Mech. E,* Vol. 207, p. 115.

Whitfield, A., and Mohd Noor, A. B., 1994, "Design and performance of vaneless volutes for radial inflow turbines. Part 1. Non-dimensional conceptual design considerations," *Proc. I. Mech. E J. Power and Energy,* Part A, Vol. 208, pp. 199–211.

Williams, P. R., 1989, "An examination of the methods used to vary the output of centrifugal compressors with particular reference to part-load efficiency," *Proc. I. Mech. E Euro Conf. Developments in Industrial Compressors,* p. 37.

Aerothermal Performance Measurements and Analysis of a Two-Dimensional High Turning Rotor Blade

T. Arts
von Karman Institute for Fluid Dynamics,
Rhode St. Genèse, Belgium

J.-M. Duboue
SNECMA,
Centre de Villaroche, France

G. Rollin
SNECMA,
Centre de Villaroche, France

The purpose of this contribution is to report on the aerothermal performance measurements and calculations carried out around a high-pressure gas turbine rotor blade profile mounted in a two-dimensional linear cascade arrangement. The measurements were performed in the CT-2 facility of the von Karman Institute, allowing a correct simulation of the operating conditions encountered in modern aero-engines. Independent variations of exit Mach (0.8–1.3) and Reynolds numbers (5×10^5–2×10^6), free-stream turbulence (1–6 percent) and incidence angle (−14–+11 deg) provided the definition of a detailed data base of test results. The measured quantities were the blade velocity and convective heat transfer coefficient distributions. The first objective of the paper is to open and analyze this data base, which is one of those used at SNECMA for validation purposes. The paper shows the degree of maturity and reliability SNECMA-ONERA Navier–Stokes solvers have now reached for daily use in turbine airfoil design and analysis.

Introduction

CFD tools represent a significant source of improvement in the design process of SNECMA turbines, leading to higher performances, cost and cycle savings, as well as to lower associated risks. Today, most of the blade-to-blade CFD calculations used in the turbine design and analysis methodology are carried out with quasi-three-dimensional and three-dimensional Navier–Stokes codes; the last Euler solver presently in use is applied to get the three-dimensional unsteady aeromechanical blade forced response due to wake excitation. These codes have been developed at ONERA and adapted for turbomachinery and integration applications at SNECMA; they compute compressible flows with finite volume and time marching techniques applied on multiblock structured grids.

The quasi-three-dimensional Navier–Stokes code "COLIBRI" is able to give accurate aerodynamic (velocity field, losses, angles) and heat transfer predictions for uncooled or cooled turbines operating in steady or unsteady conditions (Vuillez and Veuillot, 1990; Petot and Fourmaux, 1992; Chanez et al., 1993; D'Hoop et al., 1996). The three-dimensional Navier–Stokes code "CANARI" provides precise aerodynamic and heat transfer solutions for uncooled, film cooled, unshrouded, or multistage turbines running in steady or unsteady conditions (Petot and Fourmaux, 1992; Heider and Arts, 1994; Fougères and Heider, 1994; Heider et al., 1993; Billonnet et al., 1995).

An important, even essential, step in the development of these numerical tools remains their validation procedure. Accurate and reliable test cases have to be developed for this purpose. Besides the classical flat plates or bump channels, geometries representative of modern airfoil design should be considered as well. Considerable efforts were therefore devoted at the von Karman Institute (Sieverding, 1973, 1982; Arts et al., 1989; Arts, 1994) as well as in other laboratories around the world; a detailed review of these test cases has been provided by Simoneau and Simon (1993).

Contributed by the International Gas Turbine Institute and presented at the 42nd International Gas Turbine and Aeroengine Congress and Exhibition, Orlando, Florida, June 2–5, 1997. Manuscript received at ASME Headquarters February 1997. Paper No. 97-GT-120. Associate Technical Editor: H. A. Kidd.

The first objective of the paper is to present the data base obtained from uncooled measurements around the two-dimensional RS1S rotor blade profile of SNECMA. Independent variations of Mach and Reynolds numbers as well as of free-stream turbulence intensity and inlet incidence are reported and analyzed. These results are presented in terms of blade velocity and convective heat transfer distributions. The second objective is to demonstrate the degree of reliability and maturity the Navier–Stokes solvers used at SNECMA have now reached for day-to-day application in turbine airfoil design and analysis.

Model Description

The airfoil investigated in the present contribution was designed by SNECMA (RS1S profile). It is a two-dimensional rotor blade characterized by a turning of about 119 deg, and design values of the exit isentropic Mach and Reynolds numbers respectively equal to 1.11 and 1.0075×10^6. Its geometry is plotted in Fig. 1; a summary of the manufacturing coordinates is provided in Table 1. This airfoil was mounted in a linear cascade arrangement; six blades (i.e., five passages) were used. The third (counted from the top) profile was instrumented either for static pressure or heat flux measurements.

The main geometric characteristics of the blade and the cascade are summarized here:

c : 35.906 mm
g/c : 0.7607
h/c : 1.393
γ : 58.38 deg (from tangential direction)
α_1 : 53.36 deg (from axial direction)
α_2 : ≈ -65 deg (from axial direction)

The cascade model was manufactured at a scale 2:1.

The test matrix is based on variations of exit isentropic Mach (0.8–1.3) and Reynolds (5×10^5–2×10^6) numbers, inlet free-stream turbulence intensity (1–6 percent) and inlet incidence (−14–+11 deg). Because of paper length constraints, only some representative results will be presented here. The complete data base, including the detailed geometry, is nevertheless available upon simple request.

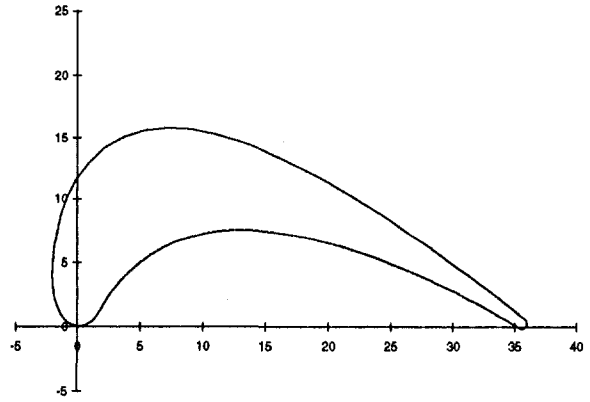

Fig. 1 Geometry of the two-dimensional RS1S rotor blade

Table 1 RS1S rotor blade coordinates

x (mm)	y(mm)	x (mm)	y(mm)	x (mm)	y(mm)
0.000	0.000	28.102	6.179	25.035	4.904
-0.248	0.031	30.299	4.642	22.561	5.787
-0.746	0.251	32.144	3.310	19.924	6.553
-1.378	0.933	33.630	2.218	17.180	7.146
-1.852	2.208	34.758	1.380	14.395	7.481
-2.031	4.007	35.542	0.783	11.655	7.469
-1.883	6.248	35.969	0.362	9.079	7.007
-1.297	8.839	35.949	0.076	6.806	6.123
-0.063	11.597	35.868	-0.052	4.940	4.937
2.119	14.103	35.697	-0.177	3.513	3.620
5.345	15.592	35.284	-0.062	2.489	2.335
9.077	15.687	34.660	0.297	1.760	1.230
12.791	14.748	33.762	0.797	1.154	0.440
16.320	13.242	32.572	1.432	0.575	0.082
19.643	11.490	31.090	2.188	0.183	0.008
22.739	9.668	29.327	3.046	0.000	0.000
25.573	7.876	27.300	3.967		

Facility and Instrumentation

The measurements were performed in one of the two Isentropic Light Piston Compression Tube facilities of the von Karman Institute, namely, the linear cascade wind tunnel CT-2. Its description and operating principles, derived from the initial development of Schultz, Jones and co-workers about 2 decades ago (Jones et al., 1973; Schultz et al., 1978), have been described by Richards (1980). The definite advantage of this facility is to provide an independent selection of Mach and Reynolds numbers as well as of gas-to-wall temperature ratio. Air is used as working fluid. The typical test duration is about 500 ms.

Free-stream total pressure and temperature, static pressure, and turbulence intensity were quantified at $\frac{1}{2}\ C_{ax}$ (measured along the axial direction) upstream of the leading edge plane. Static pressure taps were installed at $\frac{1}{3}\ C_{ax}$ (also measured along the axial direction) downstream of the trailing edge plane. These taps covered almost 2.5 pitches in order to define the exit Mach number and to qualify the downstream periodicity. The latter was proved to be fully acceptable. The blade Mach number distributions were determined by means of 27 static pressure taps distributed at midheight around one of the profiles in the cascade.

The forced convection heat flux distribution at the wall was determined by means of a transient technique. Platinum thin film gages, painted at midheight onto one of the profiles made of machinable ceramic, provided the local time-dependent temperature history. The local wall heat flux was then obtained from the solution of the unsteady conduction equation in a semi-infinite body. An electrical analogy was used for this purpose (Schultz and Jones, 1973). The convective heat transfer coefficient h used in this contribution is defined as the ratio of the measured wall heat flux and the difference between the total free-stream and the local wall temperatures:

$$h = \frac{\dot{q}_w}{T_{01} - T_w}$$

It is also worthwhile to mention that the present results describe some kind of spanwise averaged behavior as the heat flux gages were about 20 mm long.

More details about these measurement procedures have been presented by Arts et al. (1990).

Measurement Uncertainty

The uncertainty on the measured quantities was carefully evaluated and led to the following error bars, based on a 20:1 confidence interval. The uncertainty on pressure was of the order of ±0.5 percent, on gas temperature of the order of ±1.5 K, and on the heat transfer coefficient of the order of ±5 percent. The repeatability of the results was verified and proved to remain within 0.5 and 1 percent, respectively for the velocity and heat transfer measurements (Arts et al., 1990).

Velocity Distributions: Measurements and Analysis

Blade isentropic Mach number distributions have been obtained for various inlet incidences and loadings from local static pressure measurements, referred to the upstream total pressure. The instrumented airfoil was equipped with 27 taps along suction (15) and pressure (12) sides. The influence of inlet turbulence intensity and free-stream Reynolds number has not been considered. All tests were performed for an upstream total temperature of the order of 415–420 K and an exit static pressure almost equal to the atmospheric value. The results are presented in terms of isentropic Mach number distribution in function of a coordinate measured along suction and pressure surface wetted length.

A first series of measurements was conducted to verify the influence of inlet incidence. The latter was varied between −14 deg and +11 deg while maintaining the exit Mach number at a constant value of about 1.10. A sample of these results is presented in Fig. 2. As might have been expected, the airfoil is quite sensitive to this parameter. An early transition of the suction side boundary layer most probably occurs at positive inci-

Nomenclature

c = chord
g = pitch
h = forced convection heat transfer coefficient or blade height
I = incidence angle
M = Mach number
q = forced convection heat flux
Re = Reynolds number
s = coordinate along profile
T = temperature
Tu = turbulence intensity
α = flow angle
γ = stagger angle

Subscripts

1 = inlet
2 = exit
ax = axial
is = isentropic condition
∞ = free-stream condition
w = wall

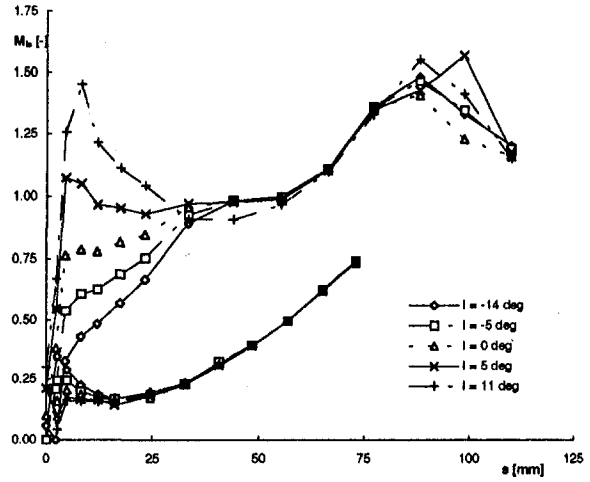

Fig. 2 Measured velocity distributions: influence of I

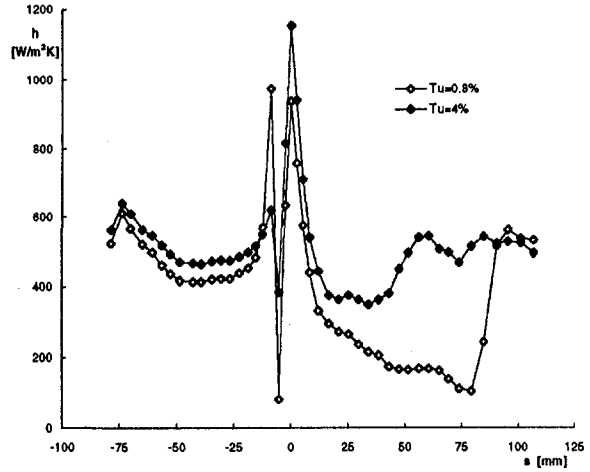

Fig. 4 Measured heat transfer distributions: influence of Tu_∞ ($I = -5$ deg, $M_{2,is} = 1.12$, $Re_{2,is} = 1.04 \times 10^6$)

dence, whereas the acceleration is much more continuous at negative incidence, favoring the development of a laminar boundary layer. The existence of a velocity peak, decreasing from negative to positive incidences, on the front part of the pressure side also definitely influences the local boundary layer development. A detailed analysis of these results finally led to the decision to set the nominal incidence at −5 deg. The main reason was to control the position of the stagnation point, as the same cascade had to be used later on with a leading edge film cooling configuration.

The influence of exit Mach number is shown in Fig. 3. These results were obtained at the nominal incidence of −5 deg. The velocity peak is clearly present on the pressure side. As will be shown in the next section, the flow regime and the different rates of acceleration along the rear part of the suction side also influence the boundary layer development.

Convective Heat Transfer Distributions: Measurements and Analysis

Blade convective heat flux measurements were conducted for different values of Mach and Reynolds numbers, free-stream turbulence intensity, and inlet incidence. Local heat transfer data were obtained by means of 45 platinum thin film thermometers painted on a machinable ceramic airfoil. All tests were performed for an upstream total temperature of about 415–420 K. The results are presented in terms of convective heat transfer coefficient distributions in function of a coordinate measured along suction (positive values) and pressure (negative values) surface wetted length.

The effect of turbulence intensity is shown in Fig. 4. These tests were conducted at $I = -5$ deg, $M_{2,is} = 1.12$, $Re_{2,is} = 1.04 \times 10^6$. The increase of laminar heating with turbulence intensity is clearly observed in the leading edge area and along the first (laminar) part of the suction side. At $Tu_\infty = 0.8$ percent, the suction side boundary layer clearly remains laminar until $s \approx 80$ mm. The transition is induced by the impingement of the shock on the blade surface. At $Tu_\infty = 4$ percent, the transition is triggered farther upstream ($s \approx 35$ mm); it is well correlated with the change in the free-stream acceleration rate (Fig. 3). The footprint of the shock is also clearly seen and is preceded by a decrease of the heat transfer coefficient; the latter is attributed to the reacceleration of the flow (40 mm $< s <$ 80 mm). The existence of a small recirculation bubble at the beginning of the pressure surface, due to the velocity peak identified in the preceding section, is proven by the strong heat transfer coefficient variation, indicating the separation and reattachment of the flow. The amplitude of this variation is strongly reduced for increasing values of turbulence intensity.

The influence of free-stream Reynolds number is presented in Fig. 5. The corresponding flow conditions were $I = -5$ deg, $M_{2,is} = 1.12$, $Tu_\infty = 4$ percent, and $Re_{2,is} = 0.54$, 1.05, and 1.84 $\times 10^6$. As expected, the overall heat transfer coefficient level increases with Reynolds number. At the lowest value, the suc-

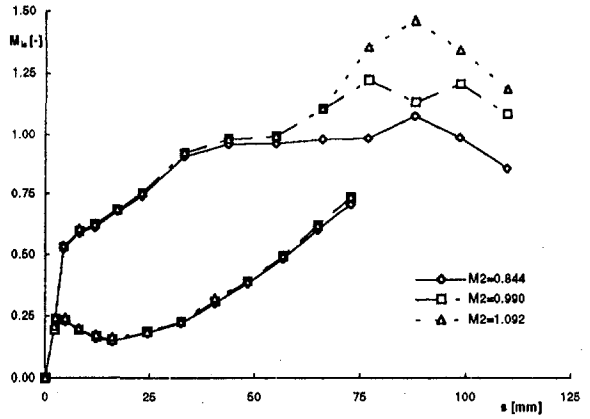

Fig. 3 Measured velocity distributions: influence of $M_{2,is}$

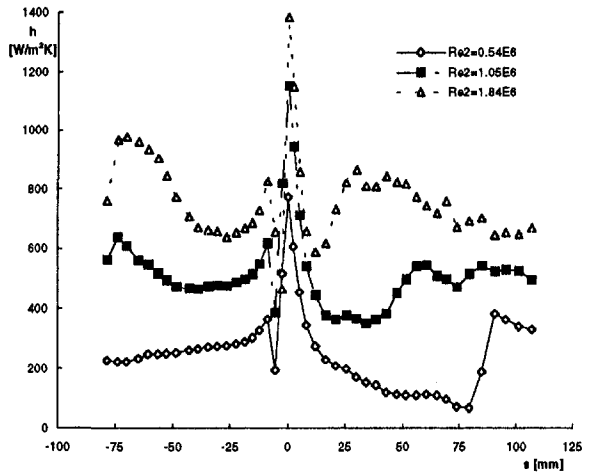

Fig. 5 Measured heat transfer distributions: influence of $Re_{2,is}$ ($I = -5$ deg, $M_{2,is} = 1.12$, $Tu_\infty = 4$ percent)

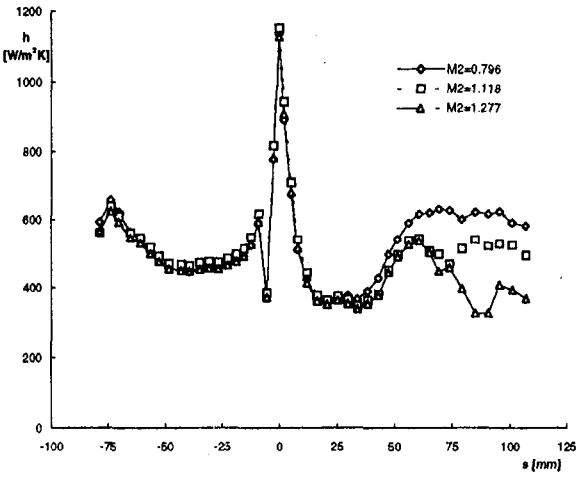

Fig. 6 Measured heat transfer distributions: influence of $M_{2,is}$ ($I = -5$ deg, $Tu_\infty = 4$ percent, $Re_{2,is} = 1.05 \times 10^6$)

tion side boundary layer remains laminar until the impingement of the shock ($s \approx 80$ mm). At the two highest values, the transition is again triggered by the change in acceleration rate, i.e., around 35 and 10 mm, respectively, for the medium and highest value of $Re_{2,is}$. These locations correlate very well with the two major variations observed in the acceleration rate (Fig. 3). The stabilizing effect of the favorable pressure gradient measured between $s = 40$ and 80 mm justifies the decrease of heat transfer until the location of the shock/wall interaction. Along the pressure side, the boundary layer gradually varies from a fully laminar to a fully turbulent state. The importance of the separation bubble is not a function of Reynolds number.

Figure 6 demonstrates the effect of the free-stream Mach number distribution. The flow conditions were set as follows: $I = -5$ deg, $Tu_\infty = 4$ percent, $Re_{2,is} = 1.05 \times 10^6$ and $M_{2,is} = 0.796$, 1.118, and 1.277. The pressure side distributions are similar. Along the suction side, the transition is triggered at $s \approx 35$ mm in the three cases. The major differences are observed in the development of the turbulent boundary layer along the rear part of the airfoil. Because of the shock/boundary layer interaction, it grows much faster in the transonic and supersonic regimes. In the last case, the effect of the acceleration is perfectly visible.

Finally, the influence of the inlet incidence is shown in Fig. 7. The flow conditions correspond to $Tu_\infty = 4$ percent, $Re_{2,is} = 1.06 \times 10^6$, $M_{2,is} = 1.12$, and $I = -14$, -5, and $+5$ deg. An important separation bubble is observed along the pressure side at $I = -14$ deg, whereas the suction side boundary layer undergoes an almost immediate transition at $I = +5$ deg. Both phenomena are well explained by the corresponding velocity distribution (Fig. 2). The overall distributions can again be justified by the arguments developed in the three preceding paragraphs.

Numerical Predictions

Two Navier–Stokes solvers have been applied to compute the Mach number and heat transfer distributions around this two-dimensional rotor blade. The first one is the commonly used, basic quasi-three-dimensional code "COLIBRI" using a Runge–Kutta cell-vertex scheme with a mixing-length turbulence model, while the second one is the latest version of the three-dimensional code "CANARI" using a Runge–Kutta cell-centered scheme with a $k-\epsilon$ turbulence model.

Solvers. Several cell-vertex and cell-centered integration schemes are used in these codes, depending on the application: a one or two-step Lax–Wendroff–Ni scheme or a Jameson-type space discretization combined with a four-step Runge–Kutta time integration scheme. The convergence is accelerated by local time stepping and implicit residual smoothing techniques, allowing higher CFL numbers to be applied. Second and fourth-order Jameson artificial dissipation is also included. Two types of low-Reynolds-number turbulence models are available when running these codes: an algebraic mixing-length model formulated by Michel (Michel et al., 1969) and a two-equation $k-\epsilon$ model formulated by Jones and Launder (Jones and Launder, 1973; Liamis and Lebret, 1995; Moreau and Mauffret, 1996).

Transition Modeling. As the quasi-three-dimensional Navier–Stokes code uses a mixing-lenth model, the transition onset locations on suction and pressure sides are imposed; the eddy viscosity is modified in the transitional zone by an intermittency factor, as recommended by Abu-Ghannam and Shaw (1980). The transition is "free" in the three-dimensional code using the $k-\epsilon$ model, and is triggered by the numerical procedure.

Mesh. The computational domain is divided into three subdomains. Each domain supports a structured grid, leading to a H-O-H mesh type. The **O**-mesh wrapped around the airfoil is built with an automatic dual algebraic-optimization process in order to obtain better orthogonality and regularity of the grid cells. The mesh of the RS1S blade is shown in Fig. 8; the total number of grid points is equal to 26,500, distributed as follows: **H**-mesh upstream (13×49), **O**-mesh (301×65), **H**-mesh downstream (129×49). The thickness of the cell adjacent to the surface is fixed at 1 μm and the ratio by which the cell size increases normal to the wall is 1.12; these values allow to get $y^+ < 1$ in most of the configurations.

Boundary Conditions. The total pressure, total temperature, and flow angle are imposed at inlet while the dual static pressure/nonreflection condition is used in the exit plane, depending on the flow regime (subsonic/transonic). For the $k-\epsilon$ model, inlet values of $\rho \cdot k$ (turbulent kinetic energy) and $\rho \cdot \epsilon$ (dissipation rate) are calculated from the external turbulence intensity. No-slip and isothermal boundary conditions are imposed at the wall. The corresponding heat transfer coefficient was defined in the section "Facility-Instrumentation."

Computational Results and Analysis. The Mach number distributions calculated by the quasi-three-dimensional code COLIBRI and the three-dimensional code CANARI are very close to each other (Figs. 9 and 10; $I = -5$ deg, $M_{2,is} = 0.844$ and 1.092). When comparing them to the measured results, the agreement is rather good along the pressure side. Along the suction side, both codes have some difficulties into predicting the real shock structure. Moreover, for the positive incidence

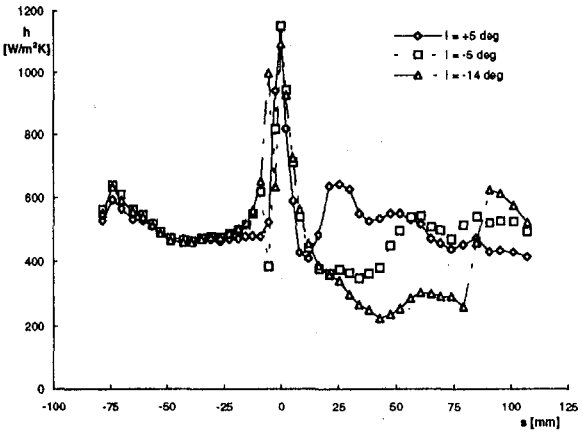

Fig. 7 Measured heat transfer distributions: influence of I ($Tu_\infty = 4$ percent, $Re_{2,is} = 1.06 \times 10^6$, $M_{2,is} = 1.12$)

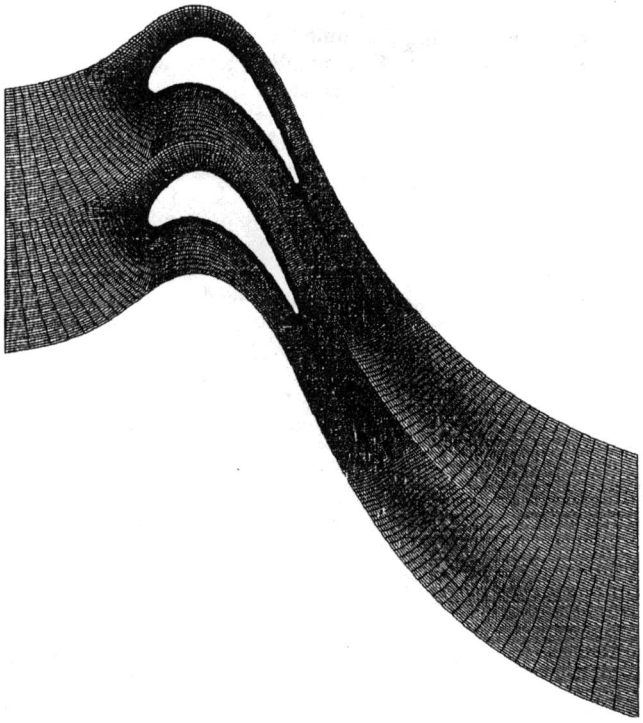

Fig. 8 Computational mesh of the RS1S blade

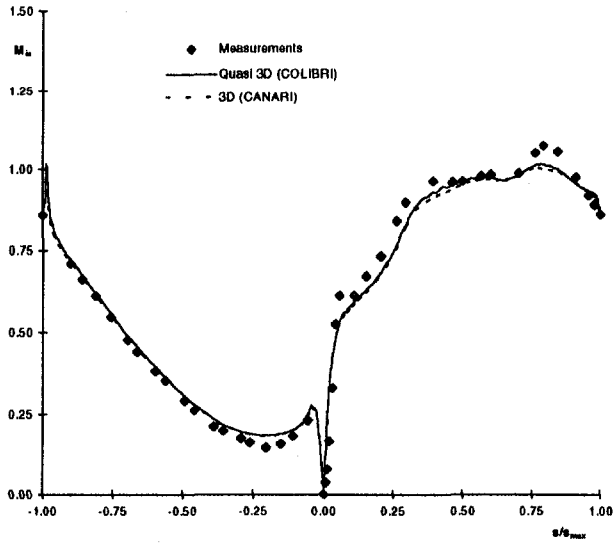

Fig. 9 Computed velocity distributions ($I = -5$ deg, $M_{2,is} = 0.844$)

test case (Fig. 11; $I = +5$ deg, $M_{2,is} = 1.088$), it seems that the real inlet flow angle is more tangential than the one specified in the code. It has to be noticed that all the calculations were performed by slightly (a few percent) adjusting the exit static pressure in order to obtain the best possible correspondence with the measured blade velocity distributions.

The calculated pressure side heat transfer coefficient distribution agrees fairly well with the experimental results at nominal incidence. Figures 12 and 13 present the results calculated respectively for subsonic ($I = -5$ deg, $Tu = 4$ percent, $Re_{2,is} = 0.97 \times 10^6$, $M_{2,is} = 0.796$) and transonic ($I = -5$ deg, $Tu = 4$ percent, $Re_{2,is} = 1.07 \times 10^6$, $M_{2,is} = 1.132$) exit flow conditions. The separation buble close to the leading edge is only predicted by the $k-\epsilon$ model. With a positive incidence (Fig. 14—$I = +5$ deg, $Tu = 4$ percent, $Re_{2,is} = 1.07 \times 10^6$, $M_{2,is} =$

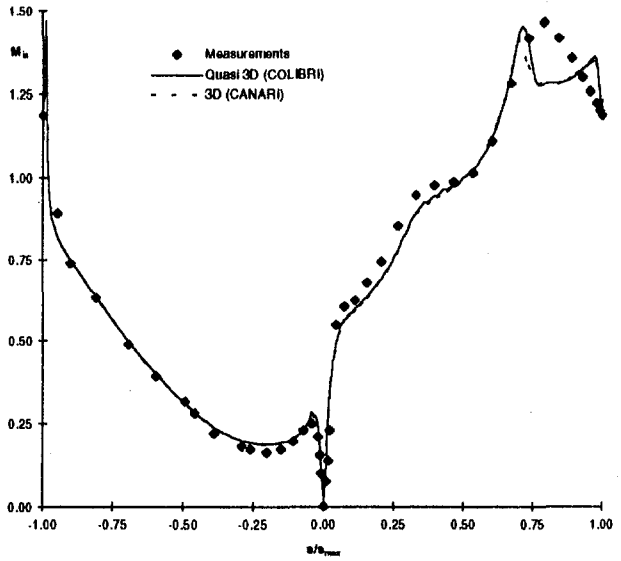

Fig. 10 Computed velocity distributions ($I = -5$ deg, $M_{2,is} = 1.092$)

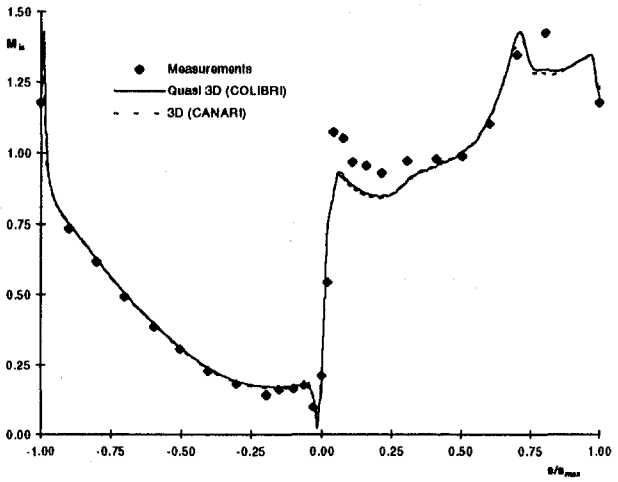

Fig. 11 Computed velocity distributions ($I = 5$ deg, $M_{2,is} = 1.088$)

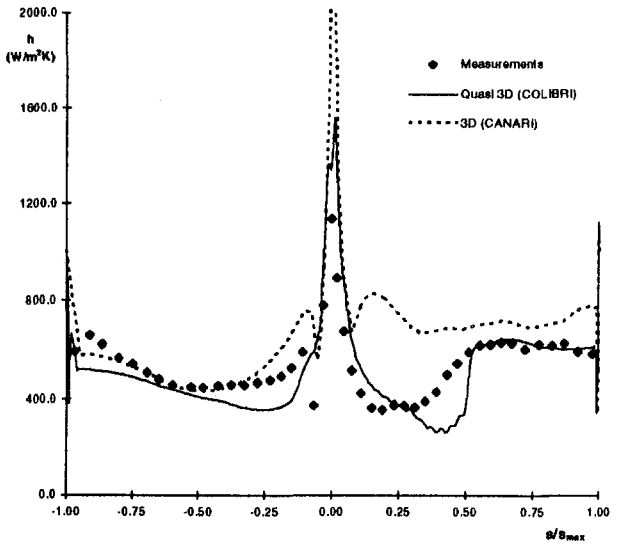

Fig. 12 Computed heat transfer distributions ($I = -5$ deg, $Tu_\infty = 4$ percent, $Re_{2,is} = 0.97\ 10^6$, $M_{2,is} = 0.796$)

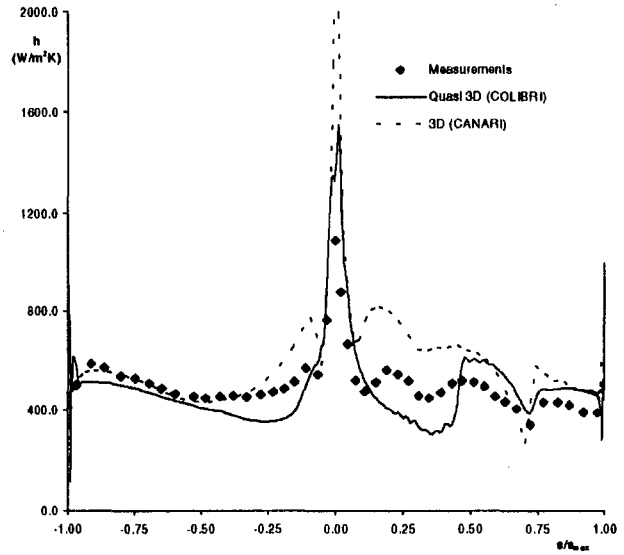

Fig. 13 Computed heat transfer distributions ($I = -5$ deg, $Tu_\infty = 4$ percent, $Re_{2,is} = 1.07 \times 10^6$, $M_{2,is} = 1.132$)

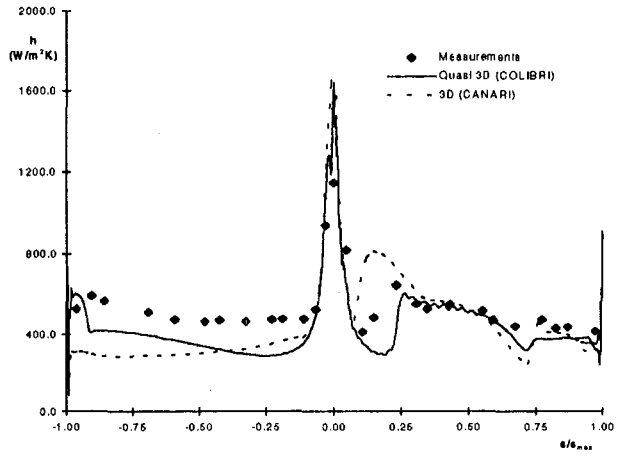

Fig. 14 Computed heat transfer distributions ($I = 5$ deg, $Tu_\infty = 4$ percent, $Re_{2,is} = 1.07 \times 10^6$, $M_{2,is} = 1.124$)

1.124) the difference between calculations and measurements increases; this may eventually be due to nonnegligible secondary flows encountered at this regime. When looking at the suction side heat transfer predictions (Figs. 12, 13, and 14), the lack of imposed transition associated with the $k-\epsilon$ model penalizes the CANARI code; the transition imposed in the COLIBRI code at the first acceleration change in the velocity distribution provides a better prediction than in the three-dimensional CANARI code. When the transitional regime extends over a large portion of the suction surface (Fig. 13), the $k-\epsilon$ heat transfer prediction better agrees with the measured distribution.

Summary and Conclusions

Detailed blade velocity and convective heat transfer measurements have been performed around the two-dimensional RS1S rotor blade designed at SNECMA. This experimental investigation was performed in one of the VKI Isentropic Compression Tube facilities, allowing a correct simulation of modern aeroengine operating conditions. The analysis of the data includes the effect of Mach and Reynolds numbers, free-stream turbulence intensity, and inlet incidence. It has clearly been shown that velocity and heat transfer data correlate very well to define the onset of laminar to turbulent transition.

Both quasi-three-dimensional (COLIBRI) and full three-dimensional (CANARI) Navier–Stokes solvers were used at SNECMA to predict the measured performances. The proper choice of the turbulence model (algebraic or two equations) remains a key point to reproduce the measured flow features. The reliability and maturity of both codes in routine use for design and analysis of turbomachinery airfoils have been demonstrated.

Acknowledgments

The authors gratefully acknowledge SNECMA for the financial support of this investigation as well as for the permission to publish the present results. The contribution of Mrs. L. Demons and Miss V. Guibert in preparing and running the numerical simulations is also acknowledged.

References

Abu-Ghannam, B. J., and Shaw, R., 1980, "Natural transition of boundary layers—The effect of turbulence, pressure gradient, and flow history," *J. Mechanical Engineering Science,* Vol. 22, No. 5, pp. 213–228.

Arts, T., Lambert de Rouvroit, M., and Sieverding, C. H., 1989, "Contribution to the workshop on two-dimensional inviscid and viscous turbomachinery flow calculation," *Numerical Methods for Flows in Turbomachinery,* VKI Lecture Series 1989-06.

Arts, T., Lambert de Rouvroit, M., and Rutherford, A. W., 1990, "Aero-thermal investigation of a highly loaded transonic linear turbine guide vane cascade," VKI Technical Note 174.

Arts, T., 1994, "Test case No 2: highly loaded transonic and film cooled linear turbine guide vane cascade LS94," *Numerical Methods for Flow Calculations in Turbomachines,* VKI Lecture Series 1994-06.

Billonnet, G., Fourmaux, A., Huard, J., and Occhionigro, A., 1995, "Utilisation de calculs 2.5D et 3D d'écoulements instationnaires pour le choix de l'instrumentation d'un banc d'essai de turbine," 85th PEP-AGARD Loss and Unsteady Flows in Turbomachines, Derby, UK.

Chanez, Ph., Petot, B., and Jourdren, Ch., 1993, "Viscous Analysis of High Pressure Inlet Guide Vane Flow including Cooling Injections," AIAA Paper No. 93-1798.

D'Hoop, E., Duboué, J.-M., and Chanez Ph., 1996, "Aerothermal Turbine Test Analysis using a Quasi-3D Navier-Stokes Code," Eccomas Conference, Paris.

Fougères, J.-M., and Heider, R., 1994, "Three-Dimensional Navier–Stokes Prediction of Heat Transfer with Film Cooling," ASME Paper No. 94-GT-14.

Heider, R., Duboué, J.-M., Petot, B., Billonnet, G., Couaillier, V., and Liamis, N., 1993, "Three-Dimensional Analysis of Turbine Rotor Flow including Tip Clearance," ASME Paper No. 93-GT-111.

Heider, R., and Arts, T., 1994, "Aerodynamic and Thermal Performance of a Three Dimensional Annular Transonic Nozzle Guide Vane (Parts I and II)," AIAA Paper No. 94-2930.

Jones, T. V., Schultz, D. L., Hendley, A. D., 1973, "On the Flow in an Isentropic Free Piston Tunnel," ARC R&M 3731.

Jones, W. P., and Launder, B. E., 1973, "The calculation of low-Reynolds-number phenomena with a two-equation model of turbulence," *Int. J. Heat Mass Transfer,* Vol. 16, No 3, pp. 1119–1130.

Liamis, N., and Lebret, Y., 1995, "Implantation of a Low Reynolds k-ϵ Turbulence Model in a 3D Navier–Stokes Solver for Turbomachinery Flows," AIAA Paper No. 95-2335.

Michel, R., Quemard, C., and Durand, R., 1969, "Application d'un schéma de longueur de mélange à l'étude des couches limites turbulentes d'équilibre," ONERA NT 154.

Moreau, S., and Mauffret, T., 1996, "Numerical Simulations of Afterbody Flowfield with Two-Equation Turbulence Models," AIAA Paper No. 96-0570.

Petot, B., and Fourmaux, A., 1992, "Validation of Viscous and Inviscid Computational Methods around Axial Flow Turbine Blades," Eccomas Conference, Brussels.

Richards, B. E., 1980, "Heat transfer measurements related to hot turbine components in the von Karman Institute Hot Cascade Tunnel," *Testing and Measurement Techniques in Heat Transfer and Combustion,* AGARD CP 281.

Schultz, D. L., and Jones, T. V., 1973, "Heat transfer measurements in short duration hypersonic facilities," AGARDograph 165.

Schultz, D. L., Jones, T. V., Oldfield, M. L. G., Daniels, L. C., 1978, "A new transient facility for the measurement of heat transfer rates," *High Temperature Problems in Gas Turbine Engines,* AGARD CP 229.

Sieverding, C. H., 1973, "Sample calculations—Turbine tests," *Transonic Flows in Turbomachinery,* VKI Lecture Series 59.

Sieverding, C. H., 1982, "Workshop on two-dimensional and three-dimensional flow calculations in turbine bladings," *Numerical Methods for Flows in Turbomachinery Bladings,* VKI Lecture Series 1982-07.

Simoneau, R. J., and Simon, F. F., 1993, "Progress towards understanding and predicting heat transfer in the turbine gas path," *Int. J. Heat Fluid Flow,* Vol. 14, No. 2, pp. 106–128.

Vuillez, Ch., and Veuillot, J.-P., 1990, "Quasi-3D Viscous Flow Computations in Subsonic and Transonic Turbomachinery Bladings," AIAA Paper No. 90-2126.

A Numerical Study of Flutter in a Transonic Fan

K. Isomura
Ishikawajima-Harima Heavy Industries Co. Ltd.,
Aero-engine and Space Operations,
Mizuho-machi Tokyo, Japan

M. B. Giles
Oxford University Computing Lab,
Parks Road,
Oxford, OX1 3QD United Kingdom

The bending mode flutter of a modern transonic fan has been studied using a quasi-three-dimensional viscous unsteady CFD code. The type of flutter in this research is that of a highly loaded blade with a tip relative Mach number just above unity, commonly referred to as transonic stall flutter. This type of flutter is often encountered in modern wide chord fans without a part span shroud. The CFD simulation uses an upwinding scheme with Roe's third-order flux differencing, and Johnson and King's turbulence model with the later modification due to Johnson and Coakley. A dynamic transition point model is developed using the e" method and Schubauer and Klebanoff's experimental data. The calculations of the flow in this fan reveal that the source of the flutter of IHI transonic fan is an oscillation of the passage shock, rather than a stall. As the blade loading increases, the passage shock moves forward. Just before the passage shock unstarts, the stability of the passage shock decreases, and a small blade vibration causes the shock to oscillate with a large amplitude between unstarted and started positions. The dominant component of the blade excitation force is due to the foot of the oscillating passage shock on the blade pressure surface.

Introduction

One of the most important requirements for jet engines for modern civil transport aircraft is high fuel efficiency at high-subsonic cruising speeds. This requirement results in high bypass-ratio transonic fans, which have very thin and flat blade sections. Such blades with low camber angle are more vulnerable to flow separation at high flow incidence angles than conventional low-speed blade sections. In a typical compressor/fan, the incidence increases as the speed is reduced through the operating line. Hence, separation is more likely to be encountered in a transonic fan at a part-speed operating point. When separation occurs, the blade can experience stall flutter under certain conditions, shown as the cross-hatched region-I and region-Ia in Fig. 1. Region-I is categorized as subsonic/transonic stall flutter, but the mechanism of the transonic stall flutter is not well understood yet. It is not even clear whether stall is actually responsible for this flutter. What we do know about this type of flutter we encountered in an in-house rig test is that the structural mode of oscillation is bending, whereas classical stall flutter is predominantly in a torsional mode (a study by Sisto [2] shows less likelihood of classical stall flutter in a bending mode). Some reports point out the possibility of shock wave oscillation being involved [3, 4], but why the shock oscillation occurs is still unknown. Since higher loading is desirable to achieve higher efficiency with less weight, engine designers often encounter stall flutter in prototype rigs. When they encounter stall flutter in transonic fan, solutions to the problem often greatly affect the performance by reducing the efficiency or increasing the weight. Therefore, a better understanding of the flutter itself is needed in order to handle this problem with less penalty.

Because of the difficulty in observing and modeling the behavior of separated flow, there has been less research on stall flutter than on flutter with attached flow. Sisto [2] predicted stall flutter by solving differential equations for blade vibration with aerodynamic forces, derived from subsonic static cascade experiments, used as an exciting force. He treated the effect of stall by modeling the dynamic force coefficient as a polynomial function of incidence angle. In his calculation, he showed that the blades oscillating in a torsional mode will exhibit large unsteadiness, but that in a bending mode they may not flutter. Yashima and Tanaka [5] introduced a leading edge separation model into a potential flow calculation. The modeled separation area was extended far downstream. The match with experimental data was only qualitative. Chi [6] performed a calculation with a small perturbation equation and a separation model initiating from a certain fixed point on the blade suction surface. The matching of the reduced frequency for the largest negative damping was excellent but the magnitude of damping was not. Sisto et al. [7] adapted a vortex method used by Spalart [8] in a rotating stall calculation to the stall flutter case. They were very successful in simulating the evolution of separation, but these calculations were for low subsonic stall flutter in a torsional mode. None of them treated viscous or compressibility effects, including shock waves.

For bending mode stall flutter of a transonic fan, Stargardter [3] of Pratt & Whitney performed thorough flutter measurements in a transonic fan rig and pointed out the possibility of the shock wave oscillation contributing to the flutter. The flutter occurred only at conditions at which shock waves existed; however, he could not find any evidence of the exciting aerodynamic force from the pressure measurements. Szechenyi [4] of ONERA performed two-dimensional wind tunnel experiments for cases in which a shock wave is attached to the leading edge of the blade, and found the shock wave oscillation was a dominant contribution to the blade excitation. However, the experiment with a detached shock wave was not successful because it was too difficult to achieve a pitchwise periodic condition in the cascade.

Since cascade tests of unsteady transonic flow are extremely difficult and costly, and numerical simulations are a very useful and practical tool to study this phenomena, we decided to investigate the flutter mechanism using a numerical simulation. Joubert [9] of SNECMA performed an unsteady quasi-three-dimensional Euler calculation, and showed that the shock oscillation is indeed a source of blade excitation. Since this was an Euler calculation, the shock oscillation was entirely due to the change of the potential field due to the given blade oscillations and the effect of the shock/boundary layer interaction was not included. Thus, he could show the possibility of the instability being caused by the shock movement due to potential effects, but did not show whether it is the most important mechanism

Contributed by the International Gas Turbine Institute and presented at the 42nd International Gas Turbine and Aeroengine Congress and Exhibition, Orlando, Florida, June 2–5, 1997. Manuscript received at ASME Headquarters February 1997. Paper No. 97-GT-235. Associate Technical Editor: H. A. Kidd.

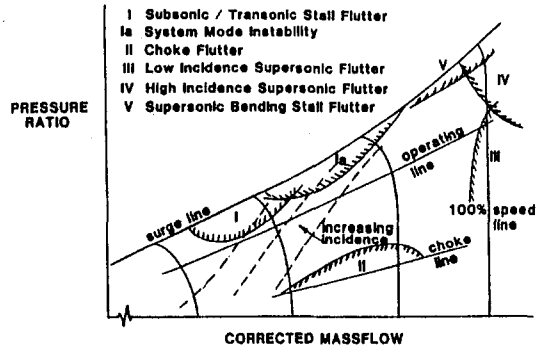

Fig. 1 Typical axial compressor/fan characteristic map (from Sisto [1])

for the transonic flutter. In a transonic fan with a strong shock wave in the flowfield, shock/boundary layer interaction may play an important role, and therefore we decided to use a viscous algorithm for the numerical simulations to find whether viscous effect is important. In addition, the unsteady shock structure in transonic fans is extremely sensitive to the blade design, and the design philosophy of the SNECMA blade looked very different from that of IHI blades. Therefore, it is possible the flutter mechanism of the IHI fan blade is different from that studied by Joubert.

Objectives

The objective of the present study is to reveal the detailed mechanisms behind the transonic high-loading flutter observed in a IHI transonic fan rig at part speed. Some specific questions to be answered in this research are:

1 Is this flutter due to stall?
2 Does the shock wave play an important role?

Since cascade tests in the transonic regime are difficult to perform, and numerical simulations allow us to study the effect of various aerodynamic parameters one at a time, these questions will be addressed by a numerical simulation. It must be emphasized in using the computational fluid dynamic code that the code should be thoroughly validated so that we can have confidence that the output of the computation corresponds closely to the real flow in the fan.

Numerical Approach

The flow physics to be simulated in the numerical calculations include shock movement, shock/boundary layer interaction, and boundary layer separation. Accordingly, the Navier–Stokes equations are used, and to simulate these phenomena accurately, the details of the numerical scheme, turbulence model, transition model, computational grid, and boundary conditions are all important.

Due to the lack of sufficient computational resources to perform fully three-dimensional calculations, the quasi-three-dimensional thin-shear-layer Navier–Stokes equations are used. The numerical scheme uses a second-order discretization of the unsteady terms. The viscous fluxes are discretized by second-order central differences. The inviscid fluxes are approximated by an upwinding Alternating Direction Implicit (ADI) scheme formulated by Giles [10] with Roe's third-order flux differencing [11]. This provides sharp resolution of the passage shocks.

One-dimensional, unsteady, nonreflecting boundary conditions are applied at inflow and outflow boundaries to suppress nonphysical wave reflections. The basic equations used in the code were formulated by Giles [12]. Two-dimensional nonreflecting boundary conditions are not used because they are known to show great benefit only in steady flow calculations [13].

For the turbulence model, Johnson and King's one-half equation [14] is used with the later correction from Johnson and Coakley [15] because of its capability to simulate shock/boundary-layer interaction in two dimensional calculations. The transition model is the e^n method [16], but using the envelope of the Orr–Sommerfeld spatial amplification curves to simplify the calculations. The use of the e^n method in transonic flow in which shock–boundary layer interaction exists can be justified because this method shows good results in transonic flow calculations of airfoils [17]. The e^n method gives the turbulent transition point in a quasi-steady sense, but will not correctly simulate the unsteady motion of the transition point. Physically, the transition point could move upstream abruptly when a new transition occurs upstream of the current transition point, but it won't instantly disappear and therefore a transition point cannot move downstream abruptly. This limited downstream movement of the transition point is modeled using an experimental observation of Schubauer and Klebanoff [18] in 1956. They generated a turbulent spot by an electric spark, and observed how the spot evolves. From the data, the maximum velocity of the transition point moving downstream can be modeled as $0.5 \times U_e$, where U_e is the boundary layer edge velocity. In our CFD calculations, this maximum velocity is used to move the transition point whenever the standard e^n method predicts a larger downstream movement.

The computational grid consists of **C**-type grids around each blade, with grid density 223 and 60 in the ξ and η directions, respectively. The grids are connected at midpassage to form a multipassage calculation domain. The number of passages is chosen so that the unsteady flows on the upper and lower periodic boundaries are in phase, allowing simple periodic boundary conditions to be used. The grids move with the blade on the blade surface and are stationary at inflow, outflow, and side boundaries. The motion of the rest of the grid is obtained by linear interpolation. The details of the code and the grid are documented in [19].

The code has been validated thoroughly by a series of calculations [19]. Only the final test case is shown here. This test, an oscillating transonic compressor cascade flow, is configuration No. 7 Case-9 in the standard configuration data set compiled by Bölcs and Fransson [20]. The original data were taken in the Detroit Diesel Allison rectilinear air test facility under the sponsorship of NASA Lewis Research Center [21]. The blades have a multiple circular arc (MCA) profile. The blades oscillate

Nomenclature

a_{in} = inflow sound velocity
C = chord
C_p = pressure coefficient
f = frequency, Hz
K = reduced frequency $\equiv \pi fC/U_{in}$
p = pressure
p_a = half-amplitude of the pressure
t = time
U_{in} = inflow relative velocity, m/s
U_e = boundary layer edge velocity, m/s
u_n = velocity of the blade motion normal to the surface
x = Cartesian coordinate axis in blade chord direction
x_a = half-amplitude of the blade bending oscillation
η = curvilinear coordinate axis of **C**-grid approximately normal to the blade surface
θ = phase advance of the unsteady pressure from the blade oscillation
ξ = curvilinear coordinate axis of **C**-grid along the blade surface
ρ_{in} = inflow density
σ = interblade phase angle

in pitching mode around the half-chord point at a reduced frequency based on the half-chord of $K = \pi fC/U = 0.44$. A detached shock wave impinges on the suction surface near the trailing edge of the blade and a mild trailing edge separation is observed behind the shock foot. The interblade phase angle is 0 deg and the amplitude of the blade oscillation is 0.1157 deg.

The steady calculation was performed first. Since the axial velocity density ratio (AVDR) is not supplied in the test data, it was adjusted to match the known shock position. The resulting AVDR matched that reported by Starken and Schreiber [22] of DFVLR as test case E/CA-4.

The amplitude and phase distribution of the unsteady pressure on the blade are shown in Fig. 2. The calculated results match the cascade data well. Although a discrepancy is seen in the phase behind the shock foot on the suction surface and in the amplitude on the pressure surface, the amplitude and phase of the unsteady pressure upstream of the shock foot and the phase on the pressure surface show a good match. The chordwise amplitude of the shock oscillation also shows a good match. Together with other test cases not reported here [?], this validates the code as a plausible tool to simulate quasi-three-dimensional unsteady transonic flow.

The Importance of the Transition Point Model

Downstream motion of the transition point is modeled in the code using the experimental results reported by Schubauer and Klebanoff [18] as explained previously. Since Ekaterrinaris and Platzer [23] reported that the unsteady blade aerodynamic excitation was not predicted by the calculation with fixed transition point, it is worth checking the effect of the current transition point motion model on the blade excitation.

Three unsteady calculations with (1) the current transition point motion model, (2) the current model with the e^n method alone, with no downstream motion limiter, and (3) a fixed transition point, are compared to see the effect of the moving transition point model. The input data correspond to a near-flutter condition taken from a IHI research fan rig test. Details of the IHI research fan are presented in a later section.

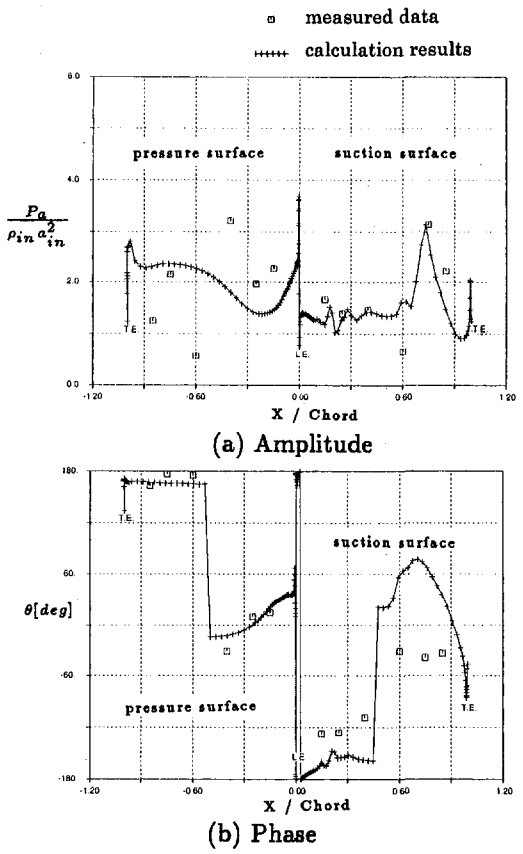

Fig. 2 Blade surface unsteady pressure distribution. Standard configuration #7, σ = 0 deg.

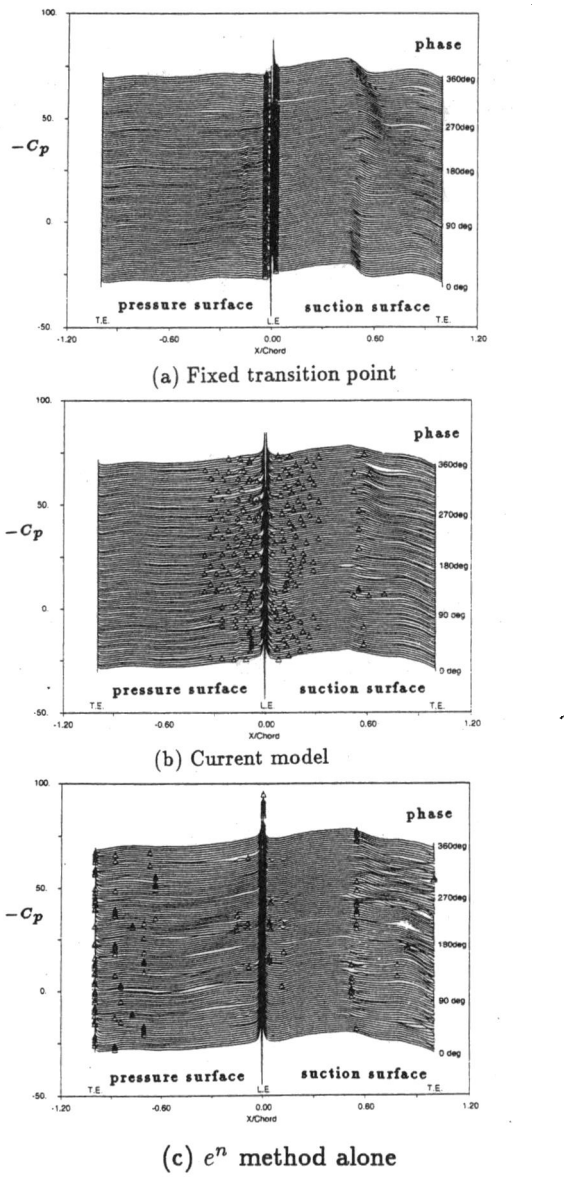

Fig. 3 Effect of the transition point model on the timewise blade surface pressure distribution

The motion of the transition point during a cycle of the blade oscillation for each of the three calculations is shown in Fig. 3. The triangles in the figures are the transition points. For the current model, periodic downstream movement of the transition points is seen, whereas for the case with the e^n method on its own, a larger scatter of transition points is seen and the transition points are located farther downstream than in the other cases. The average location of the transition points differs greatly from the most upstream location calculated. In unsteady calculations, the e^n method does not give a stable transition location, and therefore it is important to have a model for the downstream motion of the transition points to simulate the unsteady behavior of the transition point better, even if the model is quite simple.

A large difference is also seen in the blade surface aerodynamic work distribution in Fig. 4. The ordinate of the figure is the normalized time-averaged blade surface work distribution, which is defined as $(1/2\pi) \oint pu_n dt = (\frac{1}{2}) p_a x_a \sin\theta$, where p is

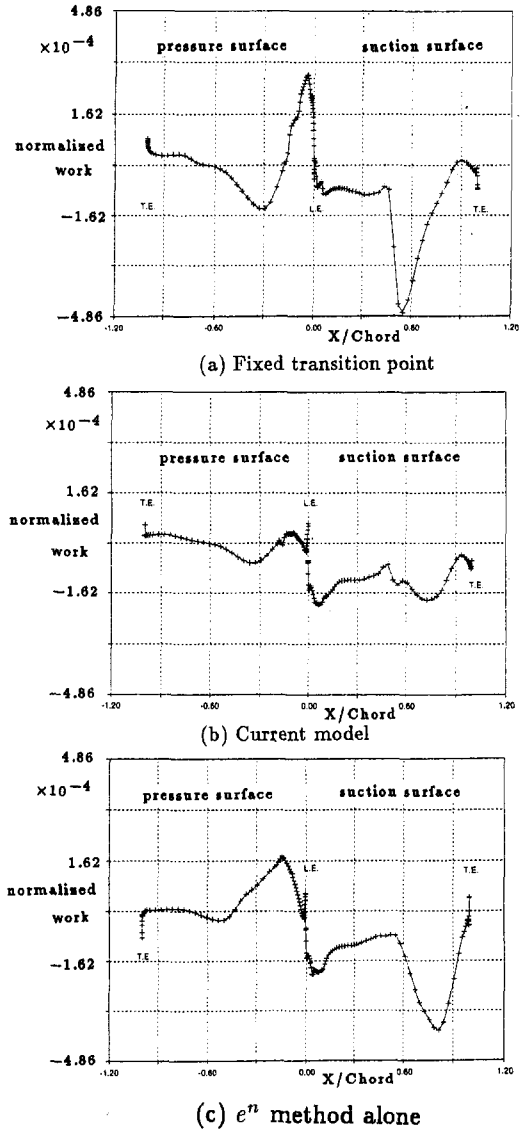

Fig. 4 Effect of the transition point model on the blade surface work distribution

the blade surface pressure, u_n is the blade surface normal velocity, p_a and x_a are the amplitudes of the first harmonics of the unsteady pressure and blade oscillation, and θ is the phase difference between the two. The value is normalized by the inflow density and the cube of the inflow sound velocity. Positive work corresponds to blade excitation, while negative work corresponds to blade damping. In the figure, not only the location of the shock waves, but also the location of the blade exciting work are different. Therefore, the limiting of the downstream motion of the transition point plays an important role and should be used in unsteady calculations.

IHI Transonic Fan Rig and Calculation Conditions

The numerical flutter investigation is based on data provided by IHI Co. Ltd. The data are taken from an in-house research transonic fan rig. The rig has a fan stage with 22 wide-chord snubberless multiple curvature arc (MCA) type blades. Its tip relative Mach number is over 1.4 at the design point. The solidity at the tip is approximately 0.8, the aspect ratio is approximately 2, and the hub/tip ratio is approximately 0.3 at the leading edge. The detail of the fan rig is described in [19]. The fan experienced flutter at midspeed high-pressure-ratio condi-

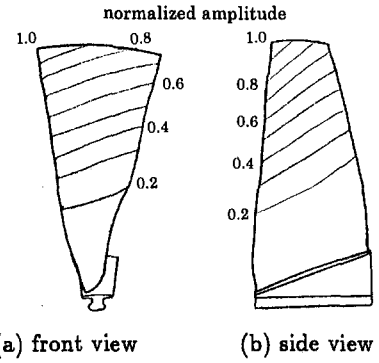

Fig. 5 IHI transonic fan blade and its first flex mode shape

tions during rig tests. The blades oscillated predominantly in the heaving motion. The fan blade is shown in Fig. 5 with the blade displacement contour of the first flex mode superposed on it. The displacement is normalized by the maximum displacement, which is at the leading edge of the tip. It is seen from the figure that the first flex mode has a dominant heaving motion component, with pitching motion amplitude at the leading edge less than 20 percent of that of heaving. The rate of motion and pitching motion is approximately constant over the outer half of the span, which justifies the typical section approach for this flutter. The blade oscillated at a reduced frequency $K = \pi fC/U = 0.22$ with interblade phase angle -32.7 deg corresponding to a two nodal diameter counterrotating mode. Numerical simulations are performed at both near-flutter and in-flutter conditions. The aerodynamic input data for the near-flutter conditions are obtained from throughflow calculations using data measured in the rig test. The input data for in-flutter and deep-in-flutter condition calculations are obtained by extrapolating the throughflow calculation results from the points with no flutter, because aerodynamic data cannot be measured during flutter. The instability boundary measured in the rig test and the points used for the calculations are shown in Fig. 6. 79 percent speed is chosen for the simulation calculations. The most critical point for the flutter is located at a lower speed, but a three-dimensional interaction between the tip leakage vortices and the detaching shock wave is anticipated because the tip relative Mach number is just about unity at the most critical point. In addition, the repeatability of the flutter boundary was observed to be better at 79 percent speed. Following a typical section approach, quasi-three-dimensional calculations are performed for the conditions at 85 percent span. This is the spanwise position for which the relative Mach number just exceeds unity. This spanwise position is selected because the flutter first appeared at the fan speed for which the tip relative Mach number just exceeded unity, suggesting that near-sonic conditions are

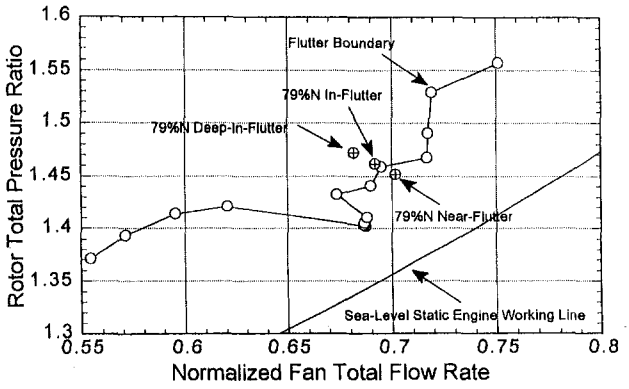

Fig. 6 The operating points of the simulation calculations

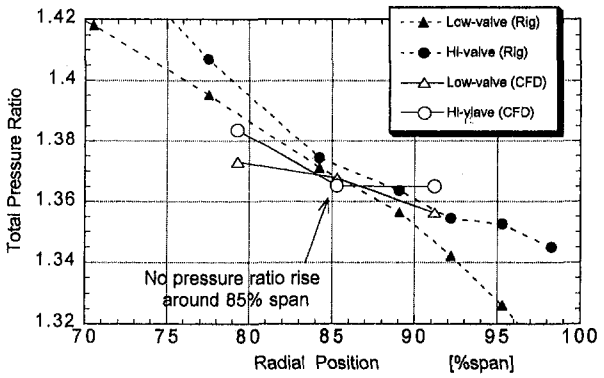

Fig. 7 Fan pressure ratio distribution calculated by quasi-three-dimensional code

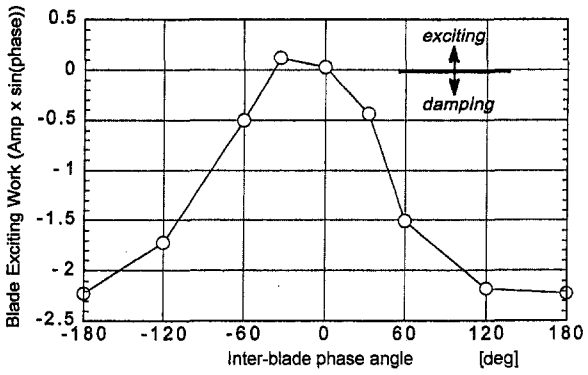

Fig. 9 The effect of the interblade phase angle on aerodynamic blade exciting work

an important ingredient for this type of flutter. At near-flutter, in-flutter, and deep-in-flutter conditions, the inflow Mach numbers are 1.018, 1.012, 1.006 and the static pressure ratios are 1.30, 1.32, 1.34, at this spanwise position, respectively.

The use of a quasi-three-dimensional code is checked by steady flow calculations around a spanwise position for which the rig test results show no pressure rise by closing the exit valve. The AVDRs are calculated by throughflow calculations using measured data as input. The result is shown in Fig. 7. The calculations show qualitatively good agreement with the rig data, justifying the use of a quasi-three-dimensional code to simulate the losses in this transonic fan. The pressure contour at the spanwise position at which no total pressure ratio rise was seen shows that the unsteady separation at the shock foot due to a shock boundary-layer interaction is the primary source of the loss (Fig. 8).

For the flutter simulations, the blades oscillate in a pure bending mode with reduced frequency $K = \pi fC/U = 0.22$. The amplitude of the oscillation is chosen to be 4.5 percent of the pitch, which corresponds to the amplitude observed during the flutter in the rig test.

Effect of Interblade Phase Angle

Unsteady calculations at various interblade phase angles are performed to see whether the interblade phase angle that yields the minimum stability in the calculations matches that observed in the rig test, and to see what aerodynamic mechanism is responsible for the minimum stability at this interblade phase angle.

Figure 9 shows the variation of the aerodynamic blade exciting work against the interblade phase angle at the "in-flutter" condition. The blade excitation is calculated to be the largest (smallest damping force) at the interblade phase angle −32.7 deg. This result agrees with the observation in the rig test.

Figure 10 shows the contributions to the aerodynamic work on the blade surface from five regions, the shock-foot and downstream of the shock foot on both the suction and pressure surfaces, and upstream of the shock foot on the suction surface. It can be seen from this figure that for most values of interblade phase angle, the largest contributions come from the two feet of the shock, and that these work approximately in opposition. Thus, it is the balance between these two works that defines the stability of the blade section. In particular, the dominant source of aerodynamic work input at the interblade phase angle −32.7 deg is the shock foot on the pressure surface.

Now that we recognize that the balance between the unsteady forces exerted by the two shock feet controls the aerodynamic stability of the blade section, the mechanisms that vary the strength of the two shock feet are investigated. Figure 11(a, b) shows the variation of the amplitude and the phase of the unsteady pressure at the two shock feet. The amplitude of the shock foot on the suction surface is always larger than that on the pressure surface, but the difference between the two amplitudes stays approximately the same, so the variation in the amplitude is not responsible for the variation in the aerodynamic work. Instead, it is the phase that is responsible for the variation in the work input with interblade phase angle, as shown in Fig. 11(b).

The separation region behind the shock foot on the suction surface, which is marked as "S.S. downstream" in Fig. 10, has a negative (damping) work component at all the interblade phase angles. Therefore, this flutter cannot be described as a stall flutter. The source of the blade excitation is not a stall, but the unsteady shock foot of the passage shock near the blade's leading edge on the pressure surface.

Effect of Fan Pressure Ratio

Calculations perturbing the rotor static pressure ratio are performed to investigate the effect of the pressure ratio. The pres-

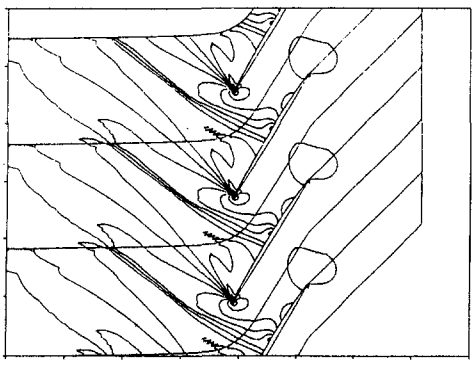

Fig. 8 Pressure contour at 85 percent span high valve condition

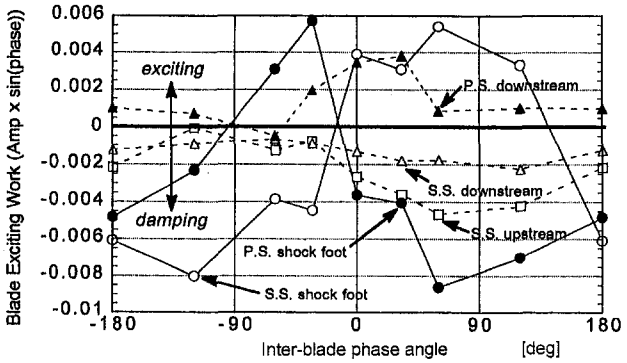

Fig. 10 Effect of interblade phase angle on components of aerodynamic work

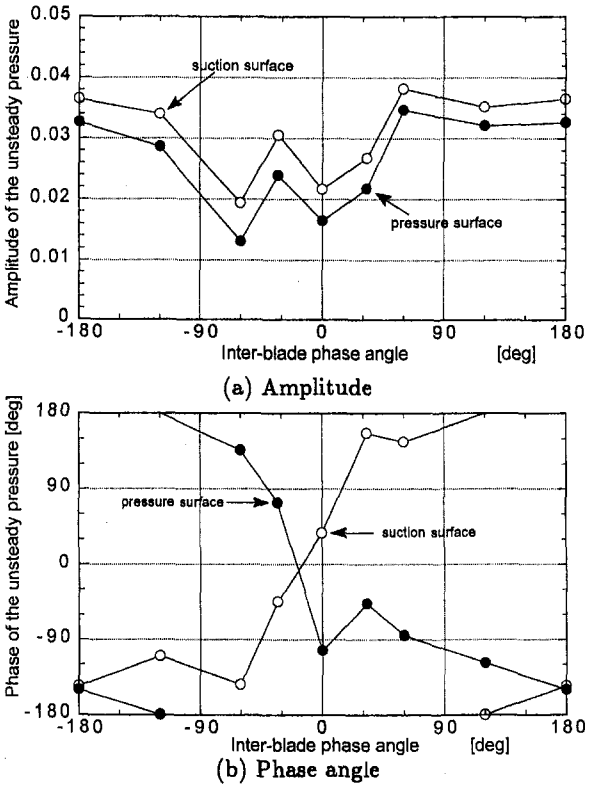

Fig. 11 Effect of interblade phase angle on amplitude and phase of unsteady blade surface pressure at shock feet

sure ratio is perturbed along the constant speed line in the fan characteristic map shown in Fig. 6. Therefore the inflow angle and the inflow Mach number are also perturbed accordingly. The idea is to investigate the effect of the blade loading through one parameter, the pressure ratio. The static pressure ratios are chosen to be around the point at which the shock wave just unstarts, i.e., 1.32. The interblade phase angle is taken to be −32.7 deg.

The result of the calculations is shown in Fig. 12. The figure shows that the aerodynamic instability appears at the static pressure ratio 1.32, and the unsteady pressure is working as a blade exciting force only in the vicinity of this pressure ratio. This agrees with the observation in the rig test that at some fan speeds the flutter subsided by further closing the exit valve. At most fan speeds, the exit valve could not be further closed because of the limit on fan vibration amplitude for safe operation, so it could not be checked if this observation is true at all fan speeds.

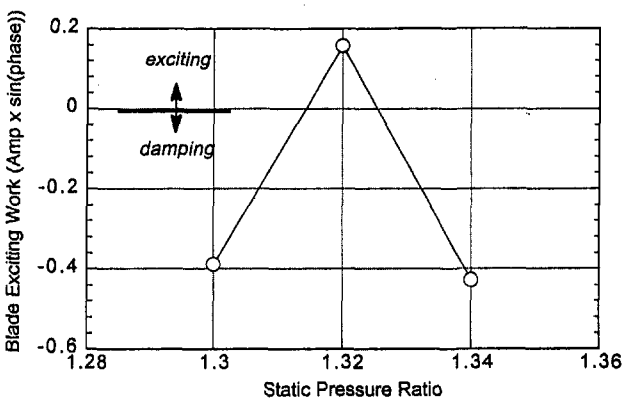

Fig. 12 Aerodynamic stability change due to the pressure ratio

The details of the unsteady blade surface pressures are seen qualitatively in a timewise surface pressure distribution in Fig. 13. In the case of pressure ratio 1.30, a shock foot is visible on each surface, but the shock oscillation is less on the pressure surface. At pressure ratio 1.32, large shock oscillations are seen on both the suction and pressure surfaces. In the case of pressure ratio 1.34, the shock wave is detached and the shock foot on the pressure surface has almost disappeared.

Figure 14 shows the blade surface work distributions for the three pressure ratios. These distributions show that the shock foot on the suction surface works to damp a blade oscillation, and the passage shock foot on the pressure surface works to excite a blade in the whole range of calculated pressure ratios. It is a balance between these two unsteady aerodynamic works

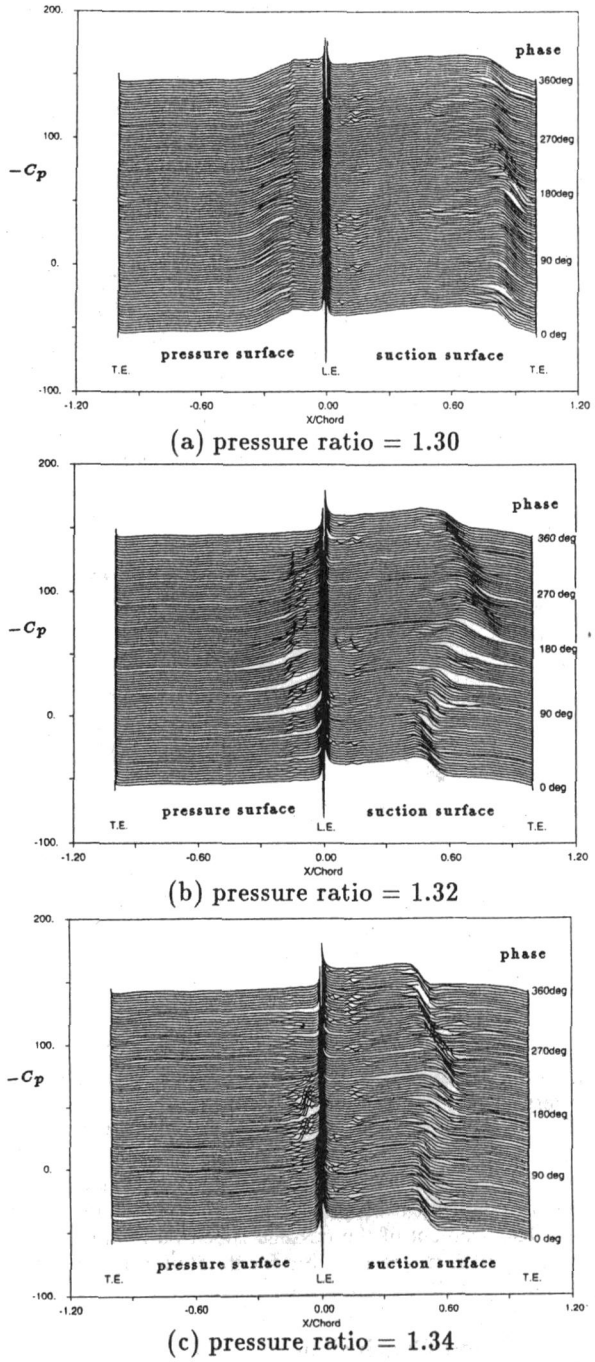

Fig. 13 Timewise blade surface pressure distribution (interblade phase angle −32.7 deg)

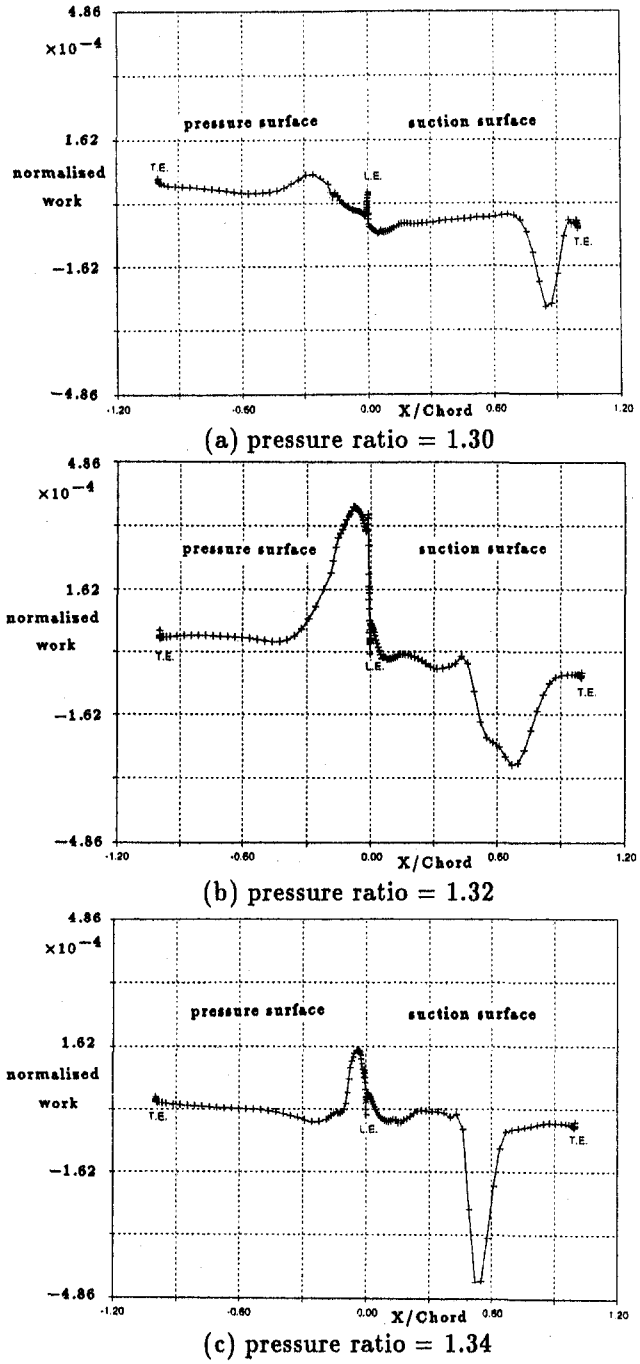

Fig. 14 Blade surface aerodynamic work distribution (interblade phase angle −32.7 deg)

that determines the stability of the blade section. The displacement of the passage shock foot on the pressure surface becomes very large when the shock is between the started and the unstarted positions, and this exerts the dominant blade exciting work.

In each of these cases, no blade exciting work due to stall is detected. Hence, the aerodynamic instability can only be caused by the displacement of the passage shock on the pressure surface, and stall is not responsible for the flutter of the IHI transonic fan rig at 86 percent span.

Summary and Conclusions

1 A quasi-three-dimensional viscous unsteady code has been developed to calculate the blade-to-blade flow in a modern transonic fan with shock waves. The code has been validated by a series of calculations so that the result of calculations can be trusted to represent physically correct phenomena.

2 The importance of properly modeling the motion of transition points in unsteady calculations has been shown. In steady calculations, the e^n method is sufficient to model the transition point, but in unsteady calculations it has been shown that a model that simulates the streamwise shedding of the transition point is needed.

3 The ability to use a quasi-three-dimensional code for simulating the unsteady blade-to-blade flow in modern transonic fan has been demonstrated. The calculation using a "typical section" approach showed that the largest aerodynamic instability occurred at the same interblade phase angle as seen in the flutter of the rig test. Also, the calculation confirmed that positive blade-exciting aerodynamic work input appears at the boundary condition taken from the rig data for which the flutter occurred.

4 The flutter observed in the IHI fan rig was found to be not a flutter due to stall, but a flutter due to shock oscillation. While the shock oscillation produces the dominant aerodynamic excitation, the separation behind the shock foot was found to produce an aerodynamic damping effect.

5 The shock wave has been found to play an important role in this flutter.

   (*a*) The key mechanism of the transonic fan flutter lies in the oscillation of the shock wave as it detaches. At a pressure ratio close to the value at which the shock wave detaches, the stability of the shock wave decreases, and minor blade oscillations cause the shock wave to oscillate between started and unstarted positions. At such a condition, the unsteady blade surface pressure on the pressure surface generated by the foot of the passage shock wave becomes a dominant source of aerodynamic excitation.

   (*b*) The unsteady blade surface pressure at the shock foot on the suction surface has a damping effect when the flutter occurred.

   (*c*) Flutter due to the shock oscillation occurs at conditions near the shock unstarting point. This kind of flutter will not occur when the shock wave is fully detached.

   (*d*) Since a fan operating at a tip relative Mach number over unity always has a spanwise position, which the shock wave detaches, transonic fans can have an aerodynamically unstable radius whenever the tip relative Mach number exceeds unity.

Recommendations for Future Work

1 A study of the effect of blade design parameters, such as the camber angle, stagger angle, and the curvature of the blade passage between the unstarted and started shock positions, is suggested to develop a method of designing a transonic fan that is less susceptible to high loading flutter.

2 The significance of three-dimensional effects, such as unsteady passage contraction, end-wall boundary layers, tip-clearance vortices, and spanwise slanted shock waves needs to be checked by full three-dimensional calculations.

References

1 F. Sisto, *AGARD Manual on Aeroelasticity in Axial-Flow Turbomachines*, AGARDograph No. 298, Vol. 1, Unsteady Turbomachinery Aerodynamics, Chap. 7, Stall Flutter, AGARD, 1987.

2 F. Sisto, "Stall-flutter in cascades," *Journal of the Aeronautical Science,* 20(9):598–604, Sept. 1953.

3 H. Stargardter, "Subsonic/transonic stall flutter study," NASA CR-165256, June 1979.

4 E. Szechenyi, *AGARD Manual on Aeroelasticity in Axial-Flow Turbomachines,* AGARDograph No. 298, Vol. 1, Unsteady Turbomachinery Aerodynamics, Chap. 10, Understanding Fan Blade Flutter Through Linear Cascade Aeroelastic Testing, AGARD, 1987.

5 S. Yashima and H. Tanaka, "Torsional flutter in stalled cascade," ASME Paper No. 77-GT-72, Mar. 1977.

6 M. R. Chi, "Unsteady aerodynamics in stalled cascade and stall flutter prediction," ASME Paper No. 80-C2/Aero-1, Aug. 1980.

7 F. Sisto, W. Wu, S. Thangam, and S. Jonnavithula, "Computational aerodynamics of oscillating cascades with the evolution of stall," *AIAA Journal,* 27(4):462–471, Apr. 1989.

8 P. R. Spalart, "Two recent extensions of the vortex method," Paper No. AIAA-84-0343, Jan. 1984.

9 H. Joubert, "Supersonic flutter in axial flow compressors," *Unsteady Aerodynamics of Turbomachines and Propellers,* Sept. 1984.

10 M. B. Giles, "A numerical method for the calculation of unsteady flow in turbomachinery," M.I.T. GTL Report No. 205, May 1991.

11 P. L. Roe, *Characteristic-Based Schemes for the Euler Equations,* Vol. 18, ARF, 1986, pp. 337–365.

12 M. B. Giles, "Numerical methods for unsteady turbomachinery flow," M.I.T. CFDL-TR-89-3, Apr. 1989.

13 M. B. Giles, "Non-reflecting boundary conditions for Euler equation calculations," *AIAA Journal,* 28(12), Dec. 1990.

14 D. A. Johnson and L. S. King, "A mathematically simple turbulence closure model for attached and separated turbulent boundary layers," Paper No. AIAA-84-0175, Jan. 1984.

15 D. A. Johnson and T. J. Coakley, "Improvements to a nonequilibrium algebraic turbulence model," *AIAA Journal,* 28(11):2000–2003, Nov. 1990.

16 F. M. White, *Viscous Fluid Flow,* McGraw-Hill, 1974.

17 M. Drela and M. B. Giles, "Viscous-inviscid analysis of transonic and low Reynolds number airfoils," *AIAA Journal,* 25(10):1347–1355, Oct. 1987.

18 G. B. Schubauer and P. S. Klebanoff, "Contributions on the mechanics of boundary-layer transition," NACA Rep. 1289, 1956.

19 K. Isomura, "A numerical investigation of a flutter in a transonic fan," MIT Ph.D. Thesis, June 1996.

20 A. Bölcs and T. H. Fransson, eds., *Aeroelasticity in Turbomachines, Comparison of Theoretical and Experimental Cascade Results, Communication du Laboratoire de Thermique Appliquée et de Turbomachines,* No. 13, Chap. 7, Seventh Standard Configuration, École Polytechnique Fédérale de Lausanne, 1986.

21 R. E. Riffel and M. D. Rothrock, "Experimental determination of unsteady blade element aerodynamics in cascades; torsional mode final report," NASA CR-159831, 1980.

22 H. Starken and H. A. Schreiber, *Test Cases for Computation of Internal Flows in Aero Engine Components,* AGARD-AR-275, Chap. V.4 Test Case E/CA-4: Low supersonic compressor cascade MCA, AGARD, 1990.

23 J. A. Ekaterrinaris and M. F. Platzer, "Progress in the analysis of blade stall flutter," in: *Proc. 7th International Symposium of Unsteady Aerodynamics and Aeroacoustics in Turbomachines,* Elsevier, 1994, pp. 287–302.

Computation of Unsteady Flows Around Oscillating Blades Using Linear and Nonlinear Harmonic Euler Methods

W. Ning

L. He

School of Engineering,
University of Durham,
Durham, DH1 3LE, United Kingdom

A quasi-three-dimensional time-linearized Euler method has been developed to compute unsteady flows around oscillating blades. In the baseline method, unsteady flow is decomposed into a steady flow plus a linear harmonically varying unsteady flow. Both the steady flow equations and the unsteady perturbation equations are solved using a pseudo-time-marching method. Based upon this method, a novel nonlinear harmonic Euler method has been developed. Due to the nonlinearity of the aerodynamic governing equations, time-averaging generates extra "unsteady stress" terms. These nonlinear effects are included by a strongly coupled approach between the perturbation equations and the time-averaged equations. Numerical results demonstrate that nonlinear effects are very effectively modeled by the nonlinear harmonic method.

Introduction

Currently, there are two distinct approaches for solving unsteady turbomachinery flows: the nonlinear time-marching approach and the time-linearized approach. Generally, the time-linearized methods are much more efficient than the nonlinear time-marching approach, while the time-marching approach should be more applicable to complex flow conditions than the time-linearized approach.

Time-linearized approaches have been widely used in turbomachinery aeroelastic analyses because of their high computational efficiency. In these methods, a linear perturbation is superimposed on a steady solution. The earlier time-linearized methods have been developed based upon the potential flow assumption, with notable contributions from Verdon and Caspar (1984) and Whitehead (1982). Because of the assumption of potential flow, these methods may not be appropriate for transonic flows with strong shock discontinuities. Recently, the development of time-linearized Euler methods is very active. A notable example is the work by Hall and Crawley (1987). One important issue on the time-linearized Euler methods is the treatment of shock waves. Lindquist and Giles (1991) show that the unsteady shock load can be accurately modeled using a linearized Euler analysis, provided that the scheme is conservative and shock is sufficiently smeared. The shock-capturing technique is also used in the time-linearized Euler methods (Hall et al., 1994) to predict transonic unsteady cascade flows.

Although time-linearized Euler methods meet the need of turbomachinery designers for efficient unsteady aerodynamic response predictions, their validity is limited by the linear assumption. It is desirable to develop a method that has a high computational efficiency like the conventional time-linearized method, and can account for nonlinear effects like the nonlinear time-marching method. This is the major objective of present work. To meet this objective, the present study is initiated with the development of a quasi-three-dimensional time-linearized Euler method called the Linear Harmonic method. On the basis of the linear harmonic method, a novel nonlinear harmonic method has been developed. In this method, a time-averaged flow field is used as the basis for the harmonic perturbations. Due to the nonlinearity of flow equations, time-averaging generates extra "unsteady stress" terms in time-averaged equations. These extra terms are evaluated from the solution of the unsteady perturbation equations, while the coefficients of the perturbation equations are evaluated from the solution of the time-averaged equations. A strongly coupled method is used to integrate both the time-averaged equations and the perturbation equations simultaneously in time.

Contributed by the International Gas Turbine Institute and presented at the 42nd International Gas Turbine and Aeroengine Congress and Exhibition, Orlando, Florida, June 2–5, 1997. Manuscript received at ASME Headquarters February 1997. Paper No. 97-GT-229. Associate Technical Editor: H. A. Kidd.

Methodology

Governing Equations. The integral form of the quasi-three-dimensional unsteady Euler equations over a moving finite area ΔA is

$$\frac{\partial}{\partial t}\iint_{\Delta A} U dA + \oint_S [Fdy + Gdx] = \iint_{\Delta A} S dA \quad (1)$$

where

$$U = h\begin{pmatrix} \rho \\ \rho u \\ r\rho v \\ \rho e \end{pmatrix} \quad F = h\begin{pmatrix} \rho u - \rho u_g \\ \rho uu + P - \rho uu_g \\ r(\rho uv - \rho vu_g) \\ (\rho e + P)u - \rho eu_g \end{pmatrix}$$

$$G = h\begin{pmatrix} \rho v - \rho v_g \\ \rho uv - \rho uv_g \\ r(\rho vv + P - \rho vv_g) \\ (\rho e + P)v - \rho ev_g \end{pmatrix} \quad S = \begin{pmatrix} 0 \\ P\dfrac{\partial h}{\partial x} \\ 0 \\ 0 \end{pmatrix}$$

To complete the system of equations, a state equation of an ideal gas is used to define the pressure P. The quasi-three-dimensional effect is introduced by allowing specified variations of radius r and streamtube height h in the axial direction. u_g and v_g are the grid velocities, used to accommodate the motion of the mesh due to the blade rotation and vibrations.

Linear Harmonic Method. If the temporal or spatial change of a flow variable is very small compared to the steady value, Eq. (1) can be linearized. Assume that the flow field can

be divided into two parts: a "steady" flow plus a small harmonic perturbation part, i.e.,

$$U = \bar{U} + \tilde{U}e^{-i\omega t} \tag{2}$$

Here the $\tilde{U}$ is the vector of complex amplitudes of the perturbation conservation variables. Similar perturbation series exist for the remaining fluxes F, G, and the vector of source terms S. Meanwhile, the grid is also assumed to undergo a small harmonic deformation about its steady position.

We substitute the perturbation series for the conservation variables, flux vectors, source term and grid velocities into the integral form of the nonlinear Euler equation. Collecting the zero and first-order terms, Eq. (1) can be divided into two parts, i.e., the steady and the linearized unsteady Euler equations. The steady equation is given by

$$\oint_S [\bar{\bar{F}}dy + \bar{\bar{G}}dx] = \iint_{\Delta A} \bar{\bar{S}}dA \tag{3}$$

The linearized Euler equation is

$$\oint_S [\bar{F}d\tilde{y} + \bar{\bar{G}}d\tilde{x} + \tilde{F}dy + \tilde{G}dx] = i\omega \iint_{\Delta A} \tilde{U}dA + i\omega \iint_{\Delta A} \bar{U}d\tilde{A} + \iint_{\Delta A} \bar{\bar{S}}d\tilde{A} + \iint_{\Delta A} \tilde{S}dA \tag{4}$$

Note that all the parameters in Eq. (4) are only space dependent. The coefficients of this equation depend on the solutions of the steady Eq. (3), so Eq. (3) must be first solved before solving the linearized amplitude equation. This steady equation is solved by using a conventional finite volume time-marching method.

The linearized Euler Eq. (4) is solved by using the pseudo-time technique originally proposed by Ni and Sisto (1976). Using this method, the perturbation conservation variables $\tilde{U}$ are assumed to be functions of both space and time, so that Eq. (4) becomes

$$\frac{\partial}{\partial t}\iint_{\Delta A} \tilde{U}dA + \oint_S [\bar{F}d\tilde{y} + \bar{\bar{G}}d\tilde{x} + \tilde{F}dy + \tilde{G}dx] = i\omega \iint_{\Delta A} \tilde{U}dA + i\omega \iint_{\Delta A} \bar{U}d\tilde{A} + \iint_{\Delta A} \bar{\bar{S}}d\tilde{A} + \iint_{\Delta A} \tilde{S}dA \tag{5}$$

Now Eq. (5) is hyperbolic in time. As time advances, U reaches a steady-state value so that the first term of Eq. (5) goes to zero and the solution to Eq. (4) is recovered. The advantage of this method is that any well-developed time-marching schemes can be used to solve the linearized Euler equations. Furthermore, since only a "steady-state" solution is desired, the local time-stepping and multiple-grid techniques can be used to speed convergence of the computation.

The spatial discretization for both Eq. (3) and Eq. (5) is made by using the cell-vertex finite volume scheme. The temporal integration is performed by using the four-stage Runge–Kutta scheme. A combination of second and fourth difference smoothing is used to capture shock waves.

By contrast to the nonlinear time-marching method in which the flow equation is solved in the time domain, the linear perturbation equation for the unsteady amplitude is solved in a frequency domain. In this time-linearized Euler method, solving an unsteady flow problem is now effectively equivalent to solving two steady problems (Eqs. (3) and (4)).

Nonlinear Harmonic Method. In order to include nonlinear effects, a novel nonlinear harmonic method has been developed based on the linear harmonic method. In this approach, a simple but significant change is that a time-averaged (instead of a steady) flow field is used as the basis for the harmonic perturbations. Due to nonlinearity of the flow equations, the time-averaging generates extra terms in time-averaged flow equations, which can account for the nonlinear effects of unsteadiness on the time-averaged flow (He, 1996).

We assume that the flow field is composed of two parts: a "time-averaged" flow plus a small perturbation, e.g.,

$$U = \bar{U} + \tilde{U} \tag{6}$$

Here the $\bar{U}$ is the vector of the time-averaged conservative variables. $\tilde{U}$ is the vector of perturbation conservative variables. Similar perturbation series exist for the flux F, G, and the source term vector S.

Substituting Eq. (6) into the original governing Eq. (1), the time-averaged form of Eq. (1) can be given as:

$$\oint_S [\bar{F}dy + \bar{G}dx + \overline{\tilde{F}d\tilde{x}} + \overline{\tilde{G}d\tilde{y}}] = \iint_{\Delta A} (\bar{S}dA + \bar{\tilde{S}}d\tilde{A}) \tag{7}$$

The time-averaged forms of fluxes F and G are as follows:

$$\bar{F} = h\begin{bmatrix} \overline{\rho u} - \overline{\rho u}_g \\ \bar{u}(\overline{\rho u} - \overline{\rho u}_g) + \bar{P} + \overline{(\rho\tilde{u})\tilde{u}} - \overline{(\rho\tilde{u}_g)\tilde{u}} \\ r[\bar{v}(\overline{\rho u} - \overline{\rho u}_g) + \overline{(\rho\tilde{u})\tilde{v}} - \overline{(\rho\tilde{u}_g)\tilde{v}}] \\ \bar{H}(\overline{\rho u} - \overline{\rho u}_g) + \bar{P}\bar{u}_g + \overline{\tilde{H}(\rho\tilde{u})} + \overline{\tilde{P}\tilde{u}_g} - \overline{\tilde{H}(\rho\tilde{u}_g)} \end{bmatrix}$$

$$\bar{G} = h\begin{bmatrix} \overline{\rho v} - \overline{\rho v}_g \\ \bar{u}(\overline{\rho v} - \overline{\rho v}_g) + \overline{(\rho\tilde{v})\tilde{u}} - \overline{(\rho\tilde{v}_g)\tilde{u}} \\ r[\bar{v}(\overline{\rho v} - \overline{\rho v}_g) + \bar{P} + \overline{(\rho\tilde{v})\tilde{v}} - \overline{(\rho\tilde{v}_g)\tilde{v}}] \\ \bar{H}(\overline{\rho v} - \overline{\rho v}_g) + \bar{P}\bar{v}_g + \overline{\tilde{H}(\rho\tilde{v})} + \overline{\tilde{P}\tilde{v}_g} - \overline{\tilde{H}(\rho\tilde{v}_g)} \end{bmatrix}$$

Comparison between the time-averaged equation and the steady flow Eq. (1) has shown that: (1) Regardless of the effects of moving grid, the mass continuity equation remains unchanged, i.e., the time-averaged mass flow at the inlet and outlet of a flow domain should be conserved; (2) due to nonlinearity of the momentum and energy equations, time averaging generates extra terms in these equations. These extra terms are similar to the turbulence (Reynolds) stress terms, so we call these extra terms "unsteady stress" terms.

The unsteady perturbations can be obtained by solving the first-order perturbation equation. Assuming all the perturbations also

Nomenclature

A = computation cell area; amplitude; channel height
C_p = pressure coefficient
e = internal energy
F, G = Euler equation flux vectors
H = enthalpy
h = streamtube height
k = reduced frequency
M = Mach number
P, p = pressure
r = radius
S = Euler equation source term vector
t = time
U = conservative variable vector
u, v = Cartesian components of velocities
u_g, v_g = grid moving velocities
x, y = Cartesian coordinates
θ = stagger angle
ρ = density
σ = interblade phase angle
ϕ = relative phase angle
ω = angular frequency

Superscripts

u = upper surface of blade
l = lower surface of blade
$-$ = time-averaged quantity
$=$ = steady quantity
$\sim$ = perturbation; perturbation amplitude

change in harmonic modes, the form of the first-order perturbation equation is the same as the linearized Euler Eq. (4):

$$\oint_S [\bar{F}d\tilde{y} + \bar{G}d\tilde{x} + \tilde{F}d\bar{y} + \tilde{G}d\bar{x}] = i\omega \iint_{\Delta A} \tilde{U}\overline{dA} + i\omega \iint_{\Delta A} \bar{U}d\tilde{A} + \iint_{\Delta A} \bar{S}d\tilde{A} + \iint_{\Delta A} \tilde{S}\overline{dA} \quad (8)$$

In the time-averaged equation, the "unsteady stress" terms need some extra relationships to be closed. For a periodically unsteady flow, the unsteady stress terms can be directly evaluated in terms of the phase and amplitude of the perturbations. For example, $\tilde{u}$ and $\tilde{v}$ are two unsteady quantities changing in the harmonic form; the time averaging of $\overline{\tilde{u}\tilde{v}}$ over one oscillating period is

$$\overline{\tilde{u}\tilde{v}} = \tfrac{1}{2}A_u A_v \cos(\phi_{vu}) \quad (9)$$

where A_u and A_v are the amplitudes of the $\tilde{u}$ and $\tilde{v}$, and ϕ_{vu} is the relative phase angle between $\tilde{u}$ and $\tilde{v}$.

The extra terms in Eq. (7) are evaluated from the solution of the first-order perturbation Eq. (8), while the coefficients of the perturbation equation are evaluated from the solution of the time-averaged Eq. (7). The coupling procedure between these two equations can be very important in terms of convergence and accuracy, especially when the nonlinearity is strong. The key point is that the solving of these two equations should be carried out without any hierarchy. In order to cope with this strong interaction between the time-averaged Eq. (7) and the first-order unsteady perturbation Eq. (8), two sets of equations are integrated simultaneously in a strongly coupled manner by using the four-stage Runge–Kutta time-marching scheme, as in the aerodynamic and structure coupling solution (He, 1994). The temporal integration of this coupled system is illustrated in Fig. 1. In this method, the time-averaged flow field is one part of the solution.

Boundary Conditions. For the solutions of steady and time-averaging flows through a single blade passage, a direct repeating periodic condition can be applied at both the upper and lower periodic boundaries. In the solving of unsteady perturbation equations, the direct periodicity does not exist. For the blade flutter problems, adjacent blades usually vibrate with a constant phase angle difference σ (interblade phase angle). The phase-shifted periodic boundary condition must be implemented along the upper and the lower periodic boundaries as follows:

$$\tilde{U}^u = \tilde{U}^l e^{-i\sigma} \quad (10)$$

$\tilde{U}^u$ and $\tilde{U}^l$ are the perturbation conservation variables on the upper and lower periodic boundaries, respectively.

On the blade surface, because the grid moves with the blade, zero flux is applied across the finite volume boundaries on the solid surface, while for the energy equation, work terms done by pressure due to the surface movement must be retained. At the inlet and outlet boundaries, in order to prevent spurious reflections of outgoing waves back into the computational domain, the exact two-dimensional unsteady nonreflecting boundary condition for single frequency (Giles, 1990) is implemented.

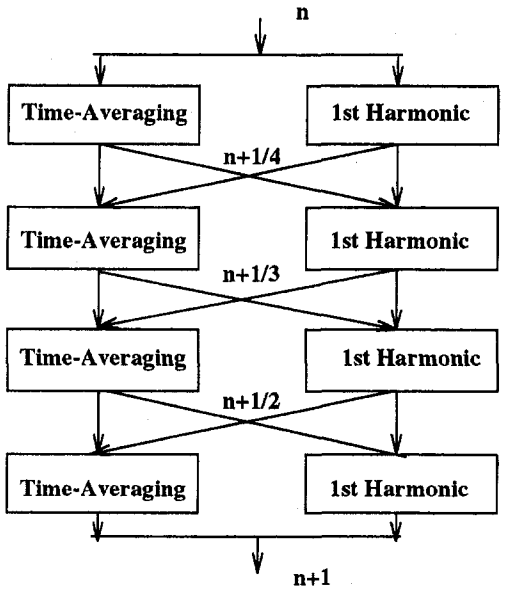

Fig. 1 Temporal integration of nonlinear harmonic method

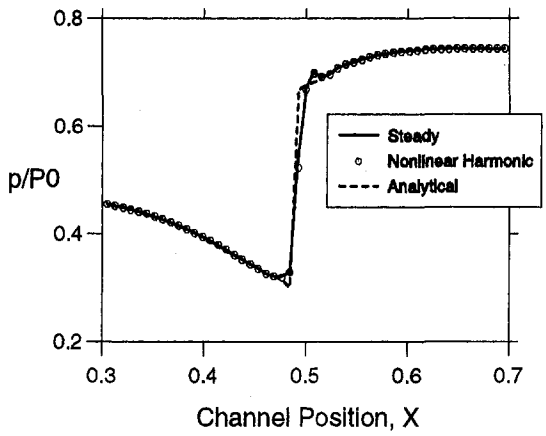

Fig. 2 Steady and time-averaged pressure in channel

Results

Transonic Unsteady Channel Flow. This case is calculated to demonstrate the ability of both of the linear and nonlinear harmonic methods to model the shock impulse due to the shock moving. Consider a transonic flow through a diverging channel. The ratio between exit back pressure and inflow total pressure P_0 is 0.7422, the inlet Mach number is 1.093. On Fig. 2, the solid line is the computational steady pressure (p/P_0) distribution given by the nonlinear steady Euler solver on a 129 × 10 node mesh. Meanwhile, the steady pressure distribution given by one-dimensional analytical method is also presented in Fig. 2. It can be seen that the shock wave is just slightly smeared in the nonlinear steady Euler solution.

In this numerical test, the unsteady flows induced by an unsteady perturbation of the back pressure with a reduced frequency, $k = 0.63$ (based on the upstream velocity and A_{inlet}), have been computed by both the linear and nonlinear harmonic methods. First, the amplitude of the back-pressure variation (A_{mp}) is specified to be 1 percent of p_{exit}. The marks on Fig. 2 are the time-averaged pressure distribution generated by the nonlinear harmonic method. Because the back pressure amplitude is small, the time-averaged flow field is almost the same as the steady flow field, as shown in Fig. 4. The unsteady pressure coefficient (here $\tilde{C}_p = \tilde{p}/(p_{\text{exit}} * A_{mp})$) distributions are shown on Fig. 3. The unsteady pressure distribution calculated by the nonlinear harmonic method is almost identical to those by the linear harmonic method. The results obtained by a nonlinear time-marching method (He, 1990) are also presented on Fig. 3. The comparison among these three methods is very good, although the shock impulse predicted by the linear and nonlinear harmonic methods is slightly higher than that by the nonlinear time-marching method.

Then the amplitude of the back pressure variation is increased to 7 percent of the p_{exit}. The shock moves in a bigger region in

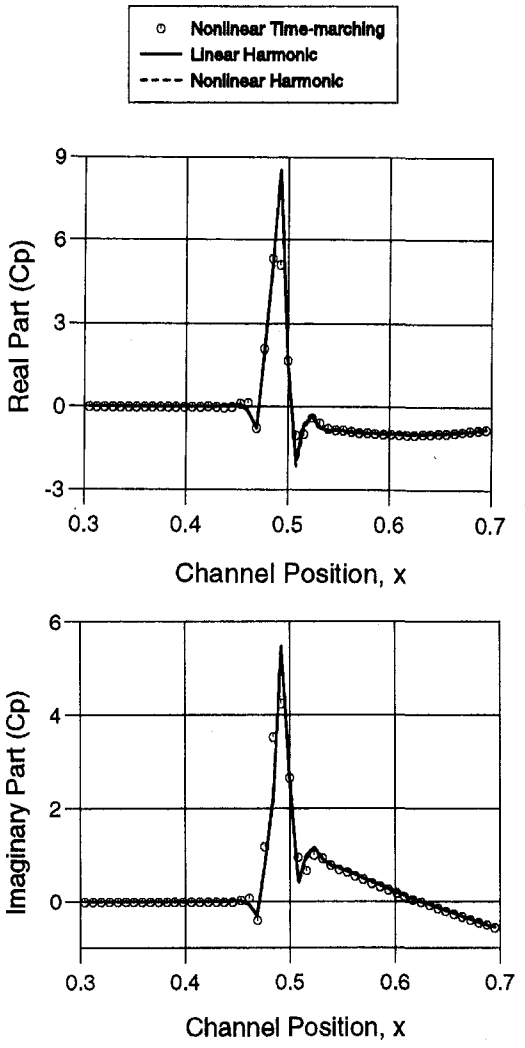

Fig. 3 Unsteady pressure distribution in channel

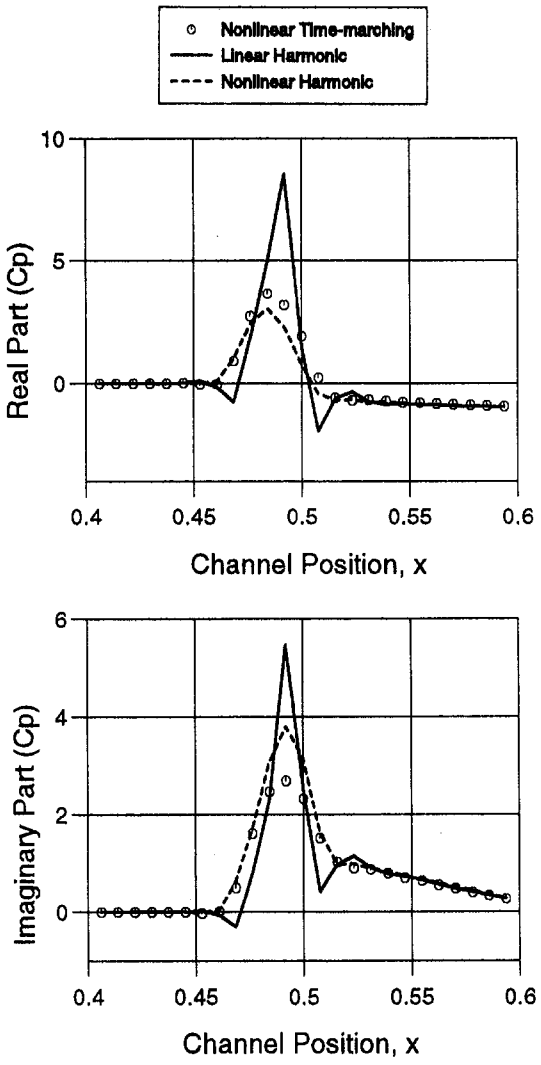

Fig. 4 Unsteady pressure distribution in channel

the channel, and the nonlinear effects are now relatively stronger. The unsteady pressure distributions are shown in Fig. 4. Because of the strong nonlinear effects, the linear harmonic method cannot correctly predict the unsteady flow. The unsteady pressure impulse around the shock wave generated by the linear method is much narrower and higher than the results by the nonlinear time-marching method. However, the results can be greatly improved by using the nonlinear harmonic method as shown in Fig. 4. The steady and time-averaged pressure distributions obtained by these three approaches are shown in Fig. 5. It can be seen that in this case, the time-averaging flow field is quite different from the steady flow field because of strong nonlinear effects. The shock moves over a large region, and the time-averaged shock wave is physically smeared by the unsteadiness. The time-averaged pressure distribution generated by the nonlinear harmonic method agrees very well with that by the nonlinear time-marching method.

Tenth Standard Configuration. A numerical test has been carried out to compute the transonic unsteady flows around an oscillating cascade. The cascade, known as the Tenth Standard Configuration, has a stagger angle, 45 deg and a gap/chord ratio, of unity. The airfoils of this cascade have a NACA 0006 thickness distribution slightly modified so that the trailing edge is wedged. A transonic steady flow considered here occurs at inlet free-stream Mach number 0.8 and flow angle 58 deg. The unsteady flows are excited by the airfoils plunging with an interblade phase angle of −90 deg and a reduced frequency of 1.287 (based on the upstream velocity and blade chord).

First, the steady flow is computed by the nonlinear steady Euler solver with an **H**-grid of 109 × 37. The isentropic Mach number distribution on the airfoil surface is presented in Fig. 6. There is a transonic patch around the leading edge on the

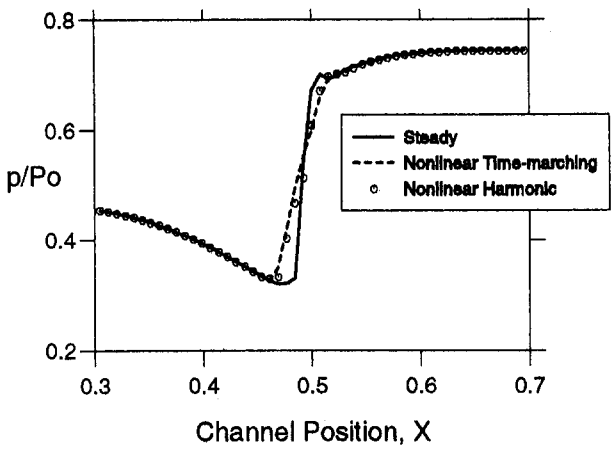

Fig. 5 Steady and time-averaged pressure in channel

suction surface with a maximum Mach number of about 1.29. Then the unsteady flows are computed by both the linear harmonic and nonlinear harmonic methods. The time-averaged isentropic Mach number distribution by the nonlinear harmonic method is also demonstrated in the Fig. 6. It can be seen that time-averaged shock wave is just slightly smeared by the unsteadiness, and positions of steady and time-averaged shock waves are almost the same. This implies that the nonlinear effects are not strong. The unsteady pressure distributions measured by both linear and nonlinear harmonic methods are shown in Fig. 7. These calculated results are compared with those from a nonlinear time-marching method (Huff and Reddy, 1989). The comparison among these three methods is very good. Compared to the linear harmonic method, the unsteady computation results are slightly improved by the nonlinear harmonic method.

Supersonic Compressor Cascade. In order to validate both the linear and nonlinear harmonic methods further, the unsteady flows around an oscillating supersonic cascade are computed by these two methods. This supersonic cascade has a stagger angle, 61.55 deg, and an inlet Mach number of 1.05. In this numerical test, the two pressure ratios (p_b/P_0) are specified to give the different shock wave positions, where p_b is the back static pressure, P_0 is the inlet total pressure. The unsteady flows are induced by the blades vibrating in a bending mode with an interblade phase angle of 180 deg and a reduced frequency of about 1. The vibrating amplitude is 1 percent chord. All the unsteady calculation results by the linear and nonlinear harmonic methods are compared with the results generated by a nonlinear time-marching Euler solver (He, 1990).

In the first calculation, a lower pressure ratio (0.64) is given, a strong normal shock wave exists around the trailing edge on the suction surface. The steady flow calculation results are shown in Fig. 8. Then the unsteady flow is computed by the linear, nonlinear harmonic, and the nonlinear time-marching methods, respectively. The time-averaged isentropic Mach number generated by the nonlinear harmonic method is also presented in the Fig. 8. In this case, the steady flow field is almost the same as the time-averaged flow field, just the shock wave is slightly smeared by the nonlinear effects. This implies that the shock wave is very stable at this position and the nonlinearity is small. The unsteady pressure distributions on blade surfaces by these three methods are shown in Fig. 9. The comparison among these methods is quite good.

Then the back pressure is increased to a higher value (0.68) to push the shock wave upstream and a transonic patch is formed around the leading edge of the suction surface. The steady isentropic Mach number distribution found by the steady Euler solver is presented in Fig. 10. The time-averaged isentropic Mach numbers generated by both the nonlinear harmonic and nonlinear time-marching methods are plotted on Fig. 10. It can be seen that the time-averaged shock wave is at the upstream

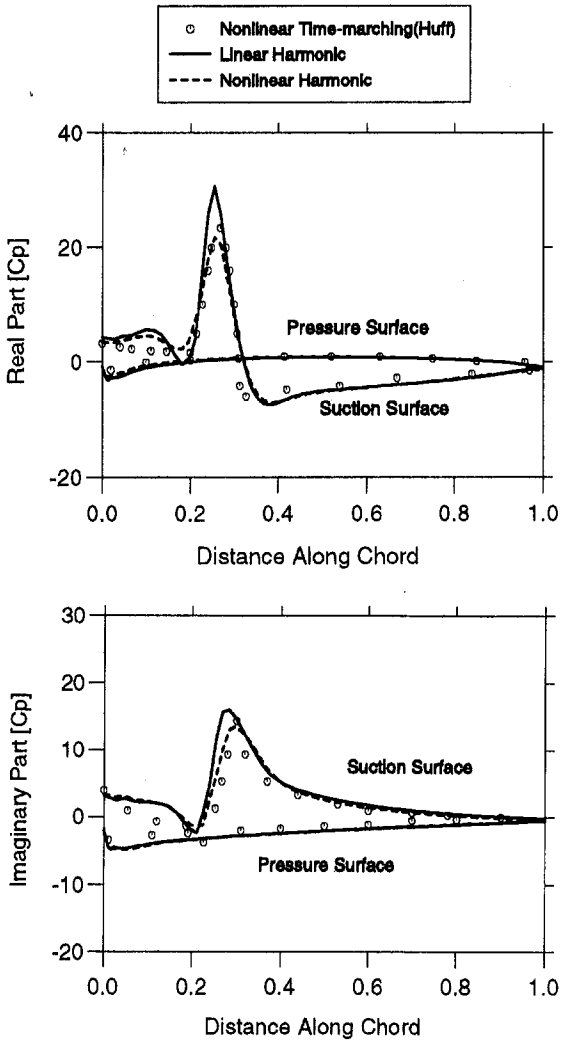

Fig. 7 Unsteady pressure distribution on blade surface

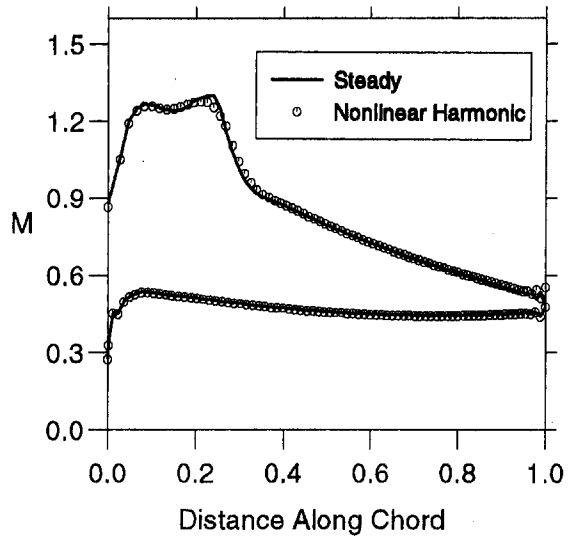

Fig. 6 Isentropic Mach number distribution of tenth standard configuration

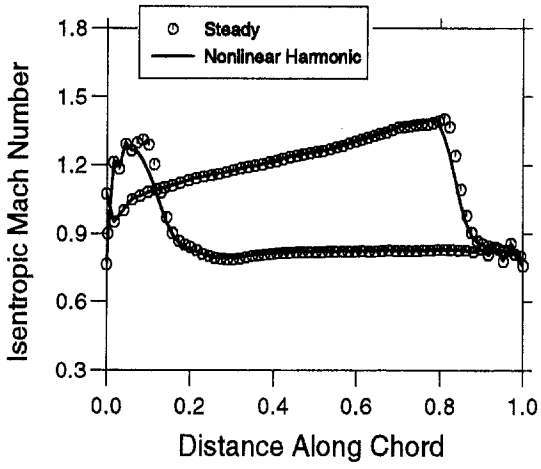

Fig. 8 Isentropic Mach number distribution of a supersonic cascade

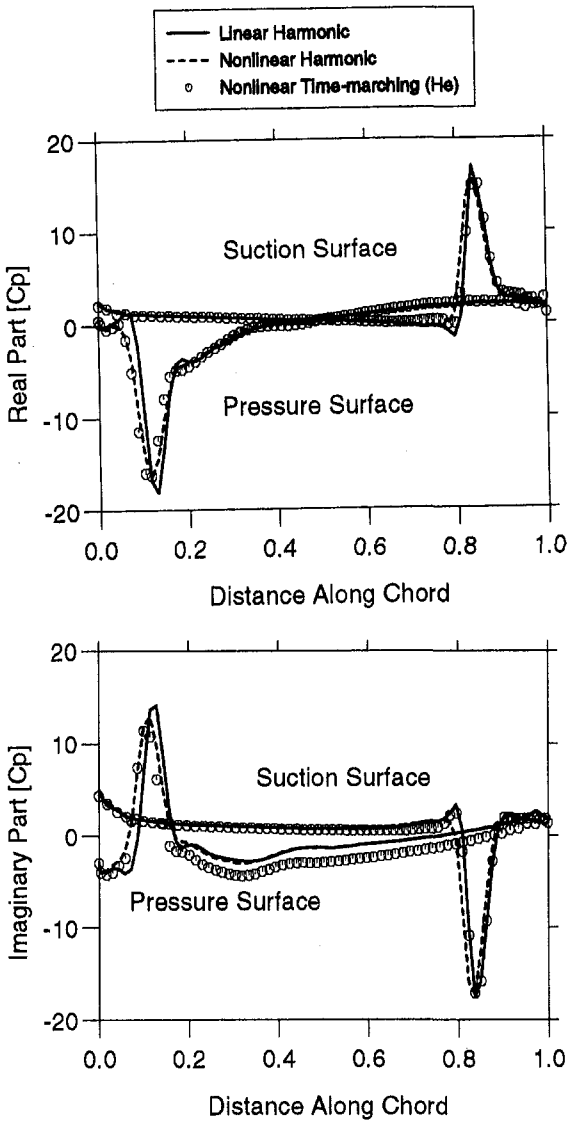

Fig. 9 Unsteady pressure distribution on blade surface

of the steady shock. This is because this transonic patch is not very stable, and the small blockage generated by the unsteadiness will push the steady shock wave forward. The nonlinear harmonic method can capture this nonlinear effect, as shown in Fig. 10. The unsteady pressure distributions found by these three methods are given in Fig. 11. Because the unsteady perturbation in the linear method is based on the steady flow, the shock impulse position generated by the linear method is at downstream of that found by the nonlinear time-marching method. However, the nonlinear harmonic method can improve the results considerably.

Concluding Remarks

First, a quasi-three-dimensional linear harmonic Euler method has been developed for predicting unsteady flows in cascades and channels. The finite-volume time-marching scheme is used to solve both the steady and the perturbation equations. The moving grid is used to avoid extrapolation in the moving blade boundary conditions.

Based on this linear method, a novel nonlinear harmonic Euler method has been developed. The time-averaged flow field is used as the basis of the harmonic perturbations. The "unsteady stress" terms in the time-averaging equations are simultaneously evaluated from the solution of the perturbation equations. The time-averaged equations and perturbation equations are solved in a strongly coupled manner.

Several numerical tests show that the nonlinear harmonic method can considerably improve the results when the nonlinearity is strong. The nonlinear harmonic method typically in-

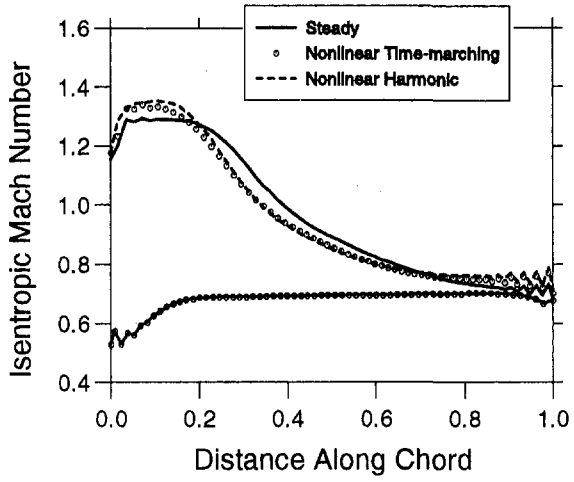

Fig. 10 Steady and time-averaged isentropic Mach number distribution

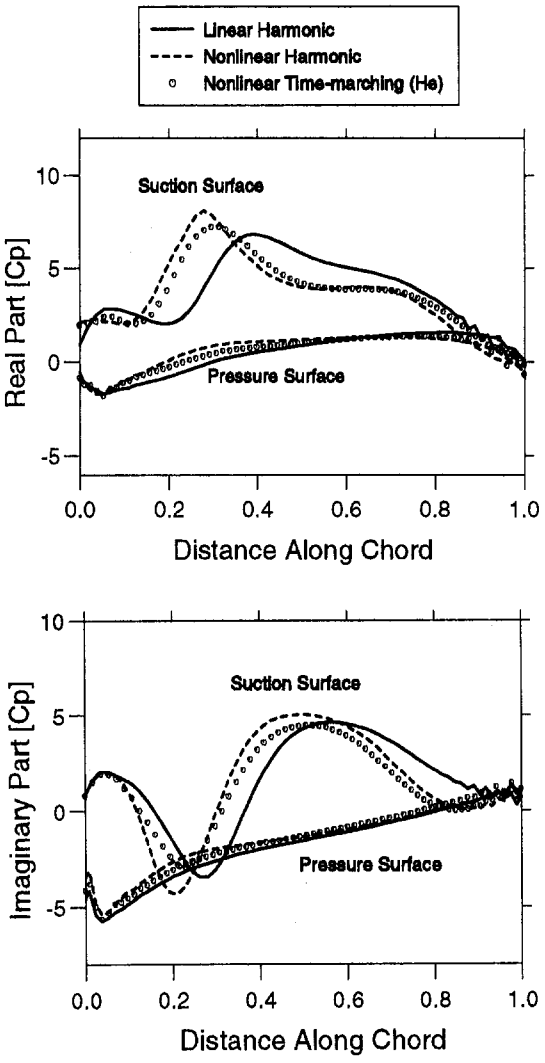

Fig. 11 Unsteady pressure distribution on blade surface

creases 60 percent CPU time compared to the linear harmonic method. Hence, it is still much more efficient than the nonlinear time-marching method.

Acknowledgments

This work is sponsored by European Gas Turbines. Additional support is provided by an ORS award to the first author. The authors wish to acknowledge Mr. R. G. Wells and Dr. Y. S. Li for their advice and continuous interest. The authors also wish to thank Dr. J. Verdon of UTRC for providing the cascade geometry data of the Tenth Standard Configuration.

References

Bölcs, A., and Fransson, T. H., 1986, "Aeroelasticity in Turbomachinery—Comparison of Theoretical and Experimental Cascade Results," Communication du Laboratoire de Thermique Appliquee et de Turbomachines, No. 13, Lausanne, EPEL.

Giles, M. B., 1990, "Non-reflecting Boundary Conditions for the Euler Equations," *AIAA Journal,* Vol. 28, No. 12, pp. 2050–2058.

Hall, K. C., and Crawley, E. F., 1989, "Calculation of Unsteady Flows in Turbomachinery Using the Linearized Euler Equations," *AIAA Journal,* Vol. 27, No. 6, pp. 777–787.

Hall, K. C., Clark, W. S., and Lorence, C. B., 1994, "A Linearized Euler Analysis of Unsteady Transonic Flows in Turbomachinery," ASME JOURNAL OF TURBOMACHINERY, Vol. 116, pp. 477–488.

He, L., 1990, "An Euler Solution for Unsteady Flows Around Oscillating Blades," ASME JOURNAL OF TURBOMACHINERY, Vol. 112, pp. 714–722.

He, L., 1994, "Integration of 2-D Fluid/Structure Coupled System for Calculations of Turbomachinery Aerodynamics/Aeroelastic Instabilities," *International Journal of Comp. Fluid Dynamics,* Vol. 3, pp. 217–231.

He, L., 1996, "I. Modelling Issues for Computation of Unsteady Turbomachinery Flows," VKI Lecture Series "Unsteady Flows in Turbomachines," Mar. 11–15, 1996.

Huff, D. L., and Reddy, T. S. R., 1989, "Numerical Analysis of Supersonic Flow Through Oscillating Cascade Sections by Using a Deforming Grid," AIAA Paper No. 89-2805.

Lindquist, D. R., and Giles, M. B., 1991, "On the Validity of Linearized Unsteady Euler Equations for Shock Capturing," *AIAA Journal,* Vol. 32, No. 1, pp. 46–53.

Ni, R. H., and Sisto, F., 1976, "Numerical Computation of Nonstationary Aerodynamics of Flat Plate Cascade in Compressible Flow," ASME *Journal of Engineering for Power,* Vol. 98, pp. 165–170.

Verdon, J. M., and Caspar, J. R., 1984, "A Linearized Unsteady Unsteady Aerodynamic Analysis for Transonic Cascades," *Journal of Fluid Mechanics,* Vol. 149, pp. 403–429.

Verdon, J. M., 1993, "Review of Unsteady Aerodynamics Methods for Turbomachinery Aeroelastic and Aeroacoustic Applications," *AIAA Journal,* Vol. 31, No. 2.

Whitehead, D. S., 1982, "The Calculation of Steady and Unsteady Transonic Flow in Cascades," Cambridge Univ., Engineering Dept., Rept. CUED/A-Turbo/TR 118, UK.

Prediction of Turbine Blade Vibratory Response Due to Upstream Vane Distress

J. Panovsky

S. M. Carson

GE Aircraft Engines,
Cincinnati, OH 44135

Turbine blades and vanes operate in a hostile environment, which leads to deterioration of these components over time. This paper describes detailed calculations to predict the vibratory response of a high-pressure turbine blade due to the excitation produced by a single distressed upstream vane in a modern turbofan engine. The approach includes detailed computational fluid dynamics (CFD) analysis of the steady flowfield produced by the distressed vane, Fourier decomposition of the flow variables to determine the harmonic content, unsteady CFD analysis to determine the resulting vibratory response of the blade, and crack propagation analysis to determine blade life. Predictions of vibratory stress and threshold crack size are summarized as functions of vane distress level. The results, which indicate that this type of vane distress can indeed be a significant excitation source for the blades, are shown to be in good agreement with engine experience. The method provides, for the first time, a quantitative approach to setting limits for acceptable levels of vane distress in the field.

Introduction

This paper summarizes an approach used to determine the vibratory response of a high-pressure turbine blade due to loss of airfoil material from the upstream vane. The study was prompted by the failure of a set of blades on a modern turbofan engine. Inspection of the engine revealed a significant amount of distress on one vane. The failure scenario envisioned is that this distress sets up a large aerodynamic disturbance, which excites the blade's fundamental bending mode and leads to a high-cycle fatigue (HCF) failure. Failures have occurred on other engines where the only peculiarity has been significant vane distress. On the other hand, some amount of vane distress is fairly common and small amounts are allowed by maintenance manuals. Given the rarity of this type of blade failure, these allowances certainly seem reasonable. The purpose of this study was to quantify the magnitude of the excitation and the resulting vibratory response of the blade, leading to a better understanding of the failure.

The distress of interest here is the loss of a portion of the vane trailing edge region. Figure 1 is a sketch of the geometry under investigation. Experience has shown that this distress progresses slowly over time through oxidation, and not by losing large pieces at erratic intervals. Due to variations in cooling flow, combustor pattern factor, position of the vane relative to fuel nozzles, and operating history, degradation of individual vanes varies significantly even within a given engine. Blockage of a cooling cavity due to a significant event such as bird ingestion can also lead to vane distress. As a result, it is not uncommon to see a single vane with a significant amount of distress while little is shown on the other vanes in the set.

The flowfield is then nonsymmetric since the distress will cause a disruption to the flow beyond that caused by the typical vane. As the downstream blade passes through the wakes and shocks from the vanes, unsteady forces are generated which excite the blades. Assuming there is only a single distressed vane, a once-per-revolution (1E) disturbance will be present in addition to the usual vane passing frequency excitation. The disturbance is primarily due to the increased throat area and the decreased turning because of the missing trailing edge portion. Since this disturbance will be similar to an impulse, it will generate significant higher harmonics in addition to the 1E. The question becomes whether the strength of the 11th or 12th harmonics, which are coincident with the first bending mode of the blade at take-off and cruise speeds, respectively, are strong enough to cause a blade failure in HCF. Figure 2 shows a simplified Campbell Diagram for this blade.

In the analysis that follows, the full range of vane distress is considered, from the nominal case of no distress to a completely missing airfoil. Experience has shown that small amounts of vane distress are acceptable, since there have been no related blade failures. The failure mentioned previously occurred for a larger distress level, corresponding to 40 percent of the vane airfoil chord. But there is also an engine where a completely missing vane airfoil was found during a scheduled maintenance inspection. The challenge is to determine why a 40 percent vane distress leads to a blade failure but a completely missing airfoil does not. The detailed analysis presented here demonstrates that the engine experience to date can be explained through calculation of the excitation strength and the corresponding blade response, plus recognition of the importance of existing low-cycle fatigue cracks in the blade, which were present to some extent for all cases. While the theoretical predictions are shown to be quite accurate, some minor calibration of the final results to experience was required.

Steady Flow Analysis

To quantify the level of the excitation forces, a two-dimensional steady aerodynamic analysis of the vane was conducted using the computational fluid dynamics (CFD) code NOVAK (Holmes et al., 1988; Holmes and Connell, 1989). This code solves the quasi-three-dimensional nonlinear Reynolds-averaged Navier–Stokes equations on an unstructured adaptive grid. The adaptive grid technique densifies the triangular mesh in regions of high gradients, allowing features such as shocks and shear layers to be resolved very well. Turbulent boundary layers were assumed throughout the analysis with an inlet turbulence intensity level of 10 percent. A two-equation $k-\varepsilon$ model was used for turbulence closure. Wall functions were used with quadrilateral cells next to the airfoil surfaces to avoid excessive

Contributed by the International Gas Turbine Institute and presented at the 42nd International Gas Turbine and Aeroengine Congress and Exhibition, Orlando, Florida, June 2–5, 1997. Manuscript received at ASME Headquarters February 1997. Paper No. 97-GT-250. Associate Technical Editor: H. A. Kidd.

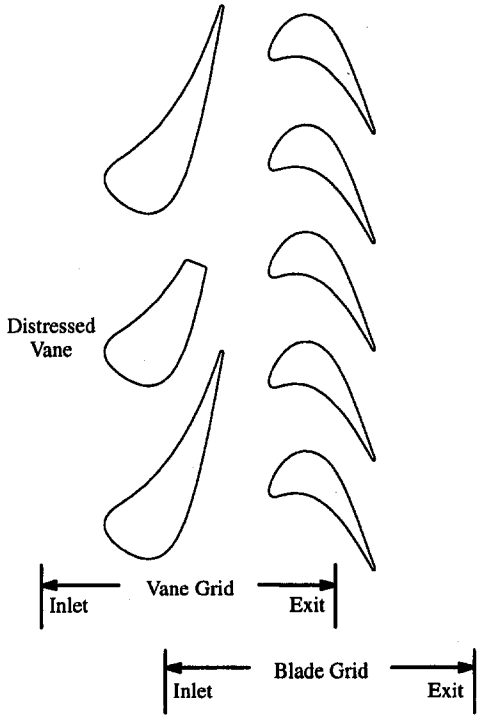

Fig. 1 Schematic of distressed vane (40 percent in this case) and the downstream blades. Extent of computational domains for CFD analyses are also shown.

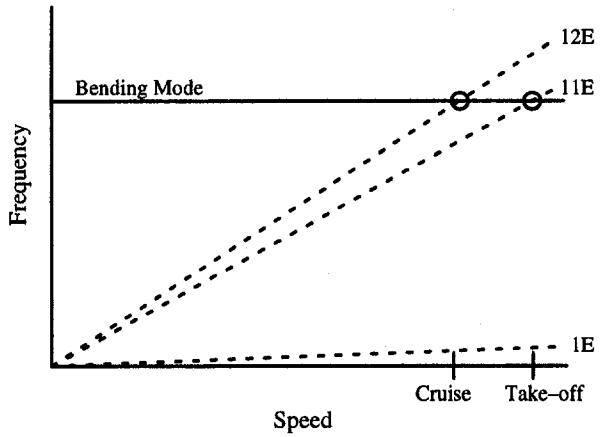

Fig. 2 Campbell diagram for the high-pressure turbine blade

grid. The governing equations are marched to convergence in false time using a Runge–Kutta algorithm.

The distressed vane was placed near the middle of a multipassage computational domain representing the midspan section. Seven passages were found to be the minimum number required for the flow to return to that of a nominal vane at the tangential boundaries, which is critical because of the periodicity conditions enforced there. Four different geometries were considered: nominal (a single passage was used for this baseline case), 20 percent distress, 40 percent distress, and a completely missing airfoil. This is a transonic vane, and the downstream flowfield is characterized by a nearly axial shock emanating from the trailing edge in addition to the viscous wakes. Because of the highly skewed angle of the wakes relative to the axial direction, the phasing of these two excitation sources changes dramatically with axial position.

The primary reason for conducting a viscous analysis is to model the wakes properly. During instrumented engine testing, the bending mode is only excited by low-level random excitation, and so there are few data available to indicate its true response characteristics. One indication of the strength of the harmonics from the vane distress is a comparison with the vane passing strength, which is known to be a strong excitation source. While this is obviously qualitative, it does provide a reasonable guideline.

The square trailing edge geometry used to model the distressed vane introduces unsteady vortex shedding in the wake region. Since the CFD code is solving the unsteady equations of motion to drive the solution to convergence, the inherent unsteadiness of the actual flowfield prevents the CFD analysis from completely converging to a steady-state solution in some cases, but the results are considered adequate. An example of the steady results is given in Fig. 3 in terms of contours of Mach number for the 40 percent distress case. Note the differences in the wake and shock structure for the distressed vane, and the strengthening of the shock on the vane downstream of the distressed vane.

In Fig. 3, also note the behavior of the shock at the grid exit. A constant static pressure was used as the downstream boundary condition, which causes the shock to dissipate rather than pass through the grid exit. The preferred boundary condition would be to set the *average* pressure across the exit to be constant and allow tangential variation of static pressure. This was tried but found to produce convergence difficulties. Note, though, that the grid exit is sufficiently downstream of the blade leading edge (Fig. 1), and the solution at the blade leading edge is considered adequate. Convergence difficulties were more pronounced on the missing airfoil case and only an inviscid solution could be obtained, but it is believed that this is sufficient, as will be discussed later.

Nomenclature

a = speed of sound
a_{th} = threshold crack size
CFD = computational fluid dynamics
C_F = modal force coefficient
c_i = characteristic variables
E = engine order, as on Campbell diagram
F = modal force
G = geometry factor for crack propagation
HCF = high-cycle fatigue
j = imaginary component
K = modal stiffness
K_{th} = threshold stress intensity factor
k_i = axial wave numbers
LCF = low-cycle fatigue
M = Mach number
N = excitation order
n = cycle in decay envelope
P = blade pitch
p = static pressure
Q = modal amplitude
R = radius
r = frequency ratio
t = time
U = rotor speed
u = axial velocity
V = velocity magnitude
v = tangential velocity (absolute)
x = axial coordinate
y = tangential coordinate
β = tangential wave number
δ = modal damping log decrement
γ = mode shape and geometry factor
ζ = modal critical damping ratio
ρ = density
σ = interblade phase angle, vibratory stress
ψ = temporal phase angle
ω = temporal frequency

Subscripts

f = forcing frequency
r = relative velocity

Superscripts

$\sim$ = unsteady component
$\bar{}$ = magnitude

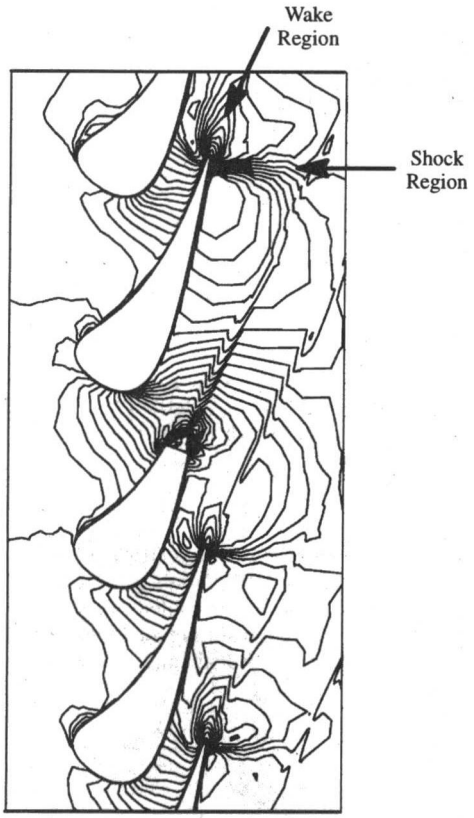

Fig. 3 Example of steady flow analysis: contours of steady Mach numbers shown

One of the main limitations of the current analysis approach is the two-dimensional assumption. Vane distress typically occurs over only a portion of the span, and radial interaction between the distressed and nondistressed portions of the passage is probably substantial. However, three-dimensional viscous multipassage analysis was beyond the scope of this study. As will be shown, the two-dimensional analysis is adequate to identify the salient drivers on blade forced response.

Fourier Analysis

Once the steady vane solutions are complete, the next step is to determine the harmonic excitation seen by the blades. In this case, this was done by interrogating the steady flow solution circumferentially at the plane of the blade leading edge. These data then represent the circumferential variation of each steady flow parameter across the seven-vane domain. To represent the full set of vanes, a nominal passage was defined by a weighted average of the outer of the seven vanes in the CFD solution. This nominal vane was then cloned to define the full set. As an example, Fig. 4 shows the flow angle variation for the first ten passages. Of these, the first seven represent the actual CFD solution while the last three are representative of the nominal repeated passage. The disruption to the flow caused by the distressed vane is obvious. Note that, while only the flow angle is shown, all of the flow parameters—density, pressure, and velocities—were considered and used in the forced response analysis of the blade. While each of these flow parameters has a unique waveform, the example given in Fig. 4 is representative.

The resulting waveforms were then Fourier decomposed to extract the harmonic content. This Fourier analysis was repeated for each of the four distress cases analyzed, and Fig. 5 shows an example of these results, again in terms of flow angle variation. The 42E represents the vane passing excitation, and is the only harmonic present in the nominal case. All other harmonics are generated by the distressed vane stimulus.

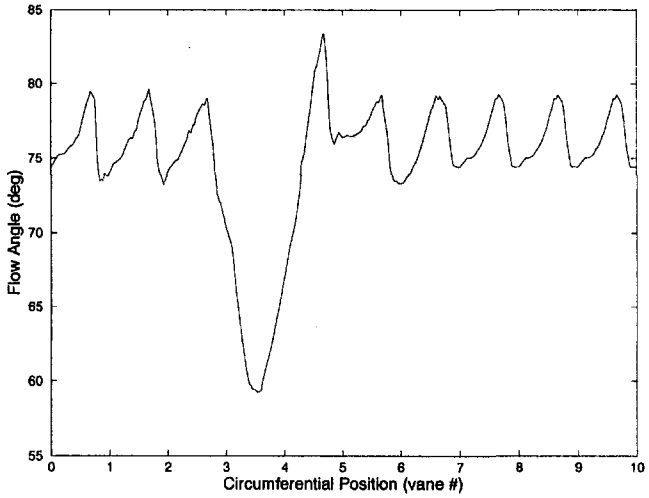

Fig. 4 Example of circumferential variation in a flow parameter, as evaluated at the plane of the blade leading edge

It can be seen that the distressed vane simulation does indeed generate substantial amplitudes in higher harmonics. This in itself is a worthwhile result, because it has often been assumed that the harmonics for this type of disturbance drop off very quickly. The level of excitation generated by the 20 percent distress in these harmonics is small, which is consistent with experience. The 40 percent distress has a significantly higher harmonic content, which is again as expected. The missing airfoil is higher than either of the other cases. The 11E and 12E harmonics, though, are still less than the vane passing strength, and as a result it is difficult to conclude whether there is sufficient strength to cause a blade failure in the bending mode.

Comparisons of the inviscid and viscous solutions for the 20 and 40 percent distress cases indicated that the strength of the 11E and 12E harmonics did not change significantly with the inclusion of viscosity. It was sufficient, then, to conduct viscous analysis only for the nominal case, and run the multipassage distress cases inviscidly. This reduces the complexity of the steady aero analysis significantly.

Unsteady Flow Analysis

To evaluate truly the effect of the vane distress, a forced response analysis of the blade was conducted. This analysis

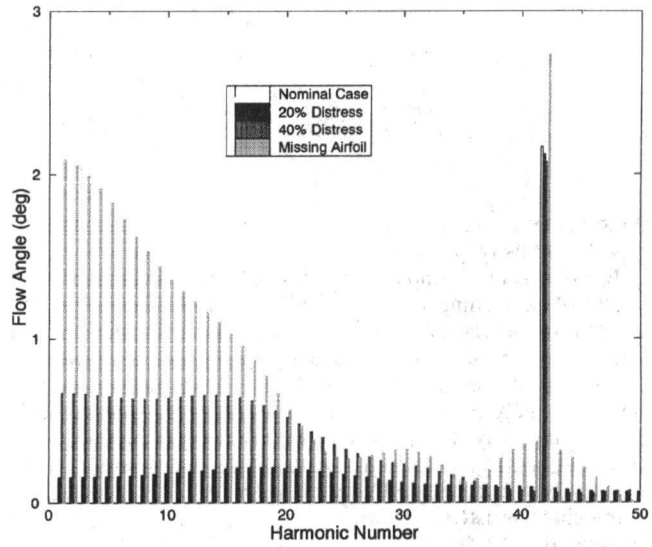

Fig. 5 Example of harmonic content of flow parameters

uses the harmonics from the various flow parameters determined above—for this case, the 11E harmonic in particular—to determine the vibratory response of the blade. The first step in this analysis is to determine the unsteady pressures on the blade and the NOVAK program is again used, but now in its linearized Euler unsteady mode (Holmes and Chuang, 1991). The unsteadiness in the flow is considered to be a small harmonic perturbation from an inviscid nonlinear steady flow, and the resulting equations are linear in the unsteady flow variables. The unsteady equations are solved on the final steady grid using the same numerical algorithm as the steady flow. Boundary conditions for the unsteady solution are based on the two-dimensional formulation of Giles (1988), though only a single Fourier mode was included for these cases.

In unsteady flow problems, it is more convenient to transform the variables from the physical parameters of pressure, velocity, and density to the equivalent set of characteristics. These characteristics are defined by the relations (Giles, 1988; Hall and Crawley, 1989; Lorence, 1991)

$$\begin{Bmatrix} c_1 \\ c_2 \\ c_3 \\ c_4 \end{Bmatrix} = \begin{bmatrix} 1 & 0 & 0 & -\frac{1}{a^2} \\ 0 & \beta u & \beta v_r - \omega & \frac{\beta}{\rho} \\ 0 & \beta v_r - \omega & -\beta u & +\frac{s}{\rho a} \\ 0 & \beta v_r - \omega & -\beta u & -\frac{s}{\rho a} \end{bmatrix} \begin{Bmatrix} \tilde{\rho} \\ \tilde{u} \\ \tilde{v} \\ \tilde{p} \end{Bmatrix} \quad (1)$$

where

$$s = \sqrt{\beta^2(u^2 + v_r^2 - a^2) - 2\beta\omega v_r + \omega^2}$$

The characteristics correspond to entropic, vortical, and downstream and upstream acoustic waves, respectively. Note that the upstream-running acoustic wave is not of interest for this case. These equations are used to calculate the characteristics for each harmonic from the corresponding primitive variables resulting from the Fourier analysis. The transformation can also be written using the tangential velocity in the absolute frame:

$$\begin{Bmatrix} c_1 \\ c_2 \\ c_3 \\ c_4 \end{Bmatrix} = \begin{bmatrix} -a^2 & 0 & 0 & 1 \\ 0 & -\rho a u\frac{\beta}{\omega} & -\rho a v\frac{\beta}{\omega} & -a\frac{\beta}{\omega} \\ 0 & -\rho a v\frac{\beta}{\omega} & +\rho a u\frac{\beta}{\omega} & -a\sqrt{M^2-1}\frac{\beta}{\omega} \\ 0 & +\rho a v\frac{\beta}{\omega} & -\rho a u\frac{\beta}{\omega} & -a\sqrt{M^2-1}\frac{\beta}{\omega} \end{bmatrix} \begin{Bmatrix} \tilde{\rho} \\ \tilde{u} \\ \tilde{v} \\ \tilde{p} \end{Bmatrix} \quad (2)$$

Note that the characteristics have been scaled such that each now has units of pressure.

Recall that the harmonics for the vane solution were obtained at the blade leading edge. This allows the dissipation of the excitation sources to be properly determined by the viscous code. However, it does introduce a complication since the perturbations are defined at the blade grid inlet for the inviscid unsteady analysis. The boundary conditions must be properly phased, plus any decay must be taken into account to get the proper strength and interaction at the blade leading edge. These various grid features are indicated in Fig. 1. The advantage of using characteristics is that this complex scaling decouples and is given directly by the axial wave numbers.

The characteristics can be written in the form

$$c_i = \bar{c}_i e^{j(-\omega t + kx + \beta y)} \quad (3)$$

The temporal frequency ω is known from the vibratory analysis of the blade, while β is the tangential wave number (spatial frequency) of the disturbance and k is the axial wave number. A shift to a new origin

$$x = x' + \Delta x$$
$$y = y' + \Delta y \quad (4)$$

gives

$$c_i = \bar{c}_i e^{j(k\Delta x + \beta\Delta y)} e^{j(-\omega t + kx' + \beta y')} \quad (5)$$

The excitation from the vanes will be seen by the blades as a backward-traveling wave at an interblade phase angle for the blade row corresponding to the 11E (Platzer and Carta, 1988). This defines the tangential wave number

$$\beta = \frac{\sigma}{P} = -\frac{N}{R} \quad (6)$$

The axial wave number is determined by the transformation from primitive to characteristic variables. The transformation requires the solution of an eigenproblem, and the axial wave numbers correspond to the resulting eigenvalues. The wave numbers for the entropic, vortical, and downstream acoustic characteristics are

$$k_1 = k_2 = -\frac{\beta v_r - \omega}{u}$$
$$k_3 = \frac{u(\beta v_r - \omega) + as}{a^2 - u^2} \quad (7)$$

Note that the entropic and vortical characteristics are real while the acoustic characteristic may be complex. From Eq. (5), the entropic and vortical waves propagate without attenuation, so only a phase shift is required to account for changes in axial position. If k_3 is real, this cut-on acoustic wave also propagates without decay. A complex k_3 indicates a cut-off wave, which decays exponentially. Again, the wave numbers can also be expressed in terms of the absolute velocity, which seems to provide more physical insight,

$$k_1 = k_2 = -\frac{v}{u}\beta$$
$$k_3 = -\left[\frac{a^2\sqrt{M^2 - 1} - uv}{a^2 - u^2}\right]\beta \quad (8)$$

Substituting numerical values from the steady flow solution into the expressions for the axial wave numbers shows that all are purely real, so that only a phase shift is required for each. Note that the tangential shift is of no concern because it will be the same for all characteristics. The axial spatial frequencies are much higher for the entropic and vortical characteristics than the acoustic, presumably because of the near-axial orientation of the shock compared to the highly skewed wake. These relative phase shifts can cause the modal force contributions from each characteristic to superpose constructively or destructively.

An initial grid study was conducted to determine the grid resolution required for the incoming waves to propagate from the grid inlet without numerical dissipation. Because of the high spatial frequency of the entropic and vortical waves, a dense grid was required. This grid was then used for subsequent unsteady analyses. For reference, the reduced frequency based on half-chord and exit velocity is about 0.35 for this case.

The linearity of the solutions was exploited by using superposition to reduce the number of solutions required. A separate unsteady analysis was conducted for a unit real perturbation in each characteristic, i.e., a unit 11E perturbation is defined and

at a reference grid point on the inlet boundary the disturbance is in phase with the blade motion. Taking the dot product of the resulting unsteady pressures on the blade surface with the displacements for a unit amplitude in the first bending mode shape and then integrating over the blade surface gives a scalar complex modal force coefficient associated with each characteristic. These modal force coefficients can then be scaled and combined to give the solution to any general case. In particular, the modal force coefficients were scaled to the 11E harmonic for all of the distress levels analyzed. Use of superposition reduces the number of cases to analyze and results in better understanding of the solution.

Vibratory Stress Calculation

The mode shape and vibratory stress distribution for the bending mode were taken from the results of a three-dimensional finite element analysis of the blade. The bending mode is essentially a translation of each radial cross section in the direction normal to the chord. A unit vector in this direction was used when determining the two-dimensional modal force coefficients in the unsteady analysis. The blade is nearly an extrusion of a constant cross section and so an assumption was made that the unsteady pressures on each radial streamline would be the same. It is further assumed that the distress is constant over the span of the vane. The total three-dimensional modal force on the blade can be determined by scaling the two-dimensional modal force coefficients to the actual displacement of the mode shape at each streamline and then integrating up the blade span. Because the two-dimensional modal force coefficient C_F is constant, it can be pulled outside the integral. The integrand is then a function only of known geometry and displacement and can be evaluated, resulting in an expression for the total modal force F of

$$F = \gamma C_F \tag{9}$$

Note that C_F includes the superposition of the phase-shifted modal forces for each of the characteristics. As a result it is a function of the case being analyzed but the mode shape parameter γ is a constant. For each case considered, the total modal force is dominated by the contribution from the downstream acoustic characteristic, indicating that the large shock is the primary excitation source.

The vibratory response can be determined using the single degree of freedom expression for a simple spring-mass-damper modal system at resonance (Vierck, 1979)

$$\bar{Q} = \frac{\bar{F}/K}{2\zeta} \tag{10}$$

Defining the vibratory stress at the critical location from the finite element model as σ^* and using the modal force coefficient, the stress at this location is given by

$$\bar{\sigma} = \frac{\gamma \bar{C}_F}{2K\zeta}\,\sigma^* \tag{11}$$

Because there are no engine data available for a resonance crossing of the bending mode, the value for damping was not explicitly known and was estimated. The primary contribution to the damping is the platform friction damper, and so the estimate was based on the results of bench testing of damper effectiveness. This resulted in a value of $\zeta = 0.016$ (equivalent to a log decrement of 10 percent), a rather large amount of damping, which is indicative of a well-designed friction damper. This value of damping is the total contribution from all sources, including aerodynamic damping, and was assumed to be constant for all excitation levels, a necessary simplification.

Up to this point, a single harmonic has been assumed for the excitation and response. However, because the excitation source is experienced just once per engine revolution, the blade response will actually be a decaying envelope about a sinusoidal wave. The envelope repeats with a frequency of 1E while the enclosed sine wave is at the natural frequency of the blade, in this case 11E. The steady state response is obtained from the generalization of Eq. (10) that includes all of the Fourier terms (Vierck, 1979)

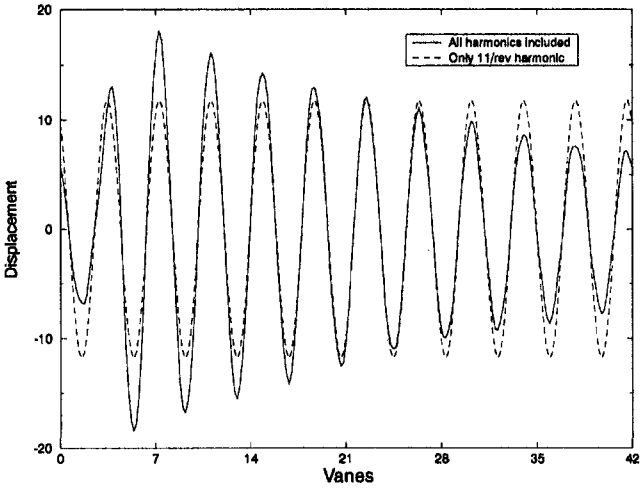

Fig. 6 Comparison of 11E contribution to overall response of system

$$Q = \frac{a_0}{K} + \sum_{n=1}^{\infty} \frac{a_n/K}{\sqrt{(1 - r_n^2)^2 + (2\zeta r_n)^2}} \cos(n\omega_f t - \psi_n) + \sum_{n=1}^{\infty} \frac{b_n/K}{\sqrt{(1 - r_n^2)^2 + (2\zeta r_n)^2}} \sin(n\omega_f t - \psi_n) \tag{12}$$

where a_n and b_n are the Fourier coefficients of the excitation force.

The contribution of the 11E contrasted to the overall response for a representative excitation force is shown in Fig. 6. Obviously, this harmonic dominates the overall response, but inspection shows that the peak value is significantly higher than the 11E magnitude. The decay rate is only a function of the damping level and because of the high damping present there is a substantial difference between the peak response that occurs once per revolution and the 11E content. In the time domain as shown in Fig. 6, the blade is in free decay after responding to the once per revolution excitation force. Using the definition of log decrement

$$\delta = \frac{1}{n} \ln \frac{\bar{Q}_0}{\bar{Q}_n} \tag{13}$$

the amplitude at the end of eleven cycles can be found, and then the average value determined. The ratio of the peak response to the average is found to be 3/2 after some trivial arithmetic, and this average value corresponds to the 11E content. Since the ratio of peak to average magnitude is only a function of the damping constant, it is independent of the form of the excitation force. This indicates that the stress can be determined for a single harmonic at the blade's natural frequency, but then this should be scaled up by 3/2 to obtain the peak stress. This approach, rather than calculating the actual modal forces for all harmonics and using Eq. (12), reduces the effort significantly.

Using Eq. (11) and the 3/2 ratio, the vibratory stresses for the various distress levels can be calculated and these are plotted in Fig. 7 after normalizing by the endurance limit. The four distress levels plotted are nominal (0 percent), the 20 and 40 percent values, and the completely missing airfoil (100 percent). This plot shows that the vane distress under investigation can generate significant vibratory stresses, though it does not appear capable of causing an HCF failure. It is also evident that

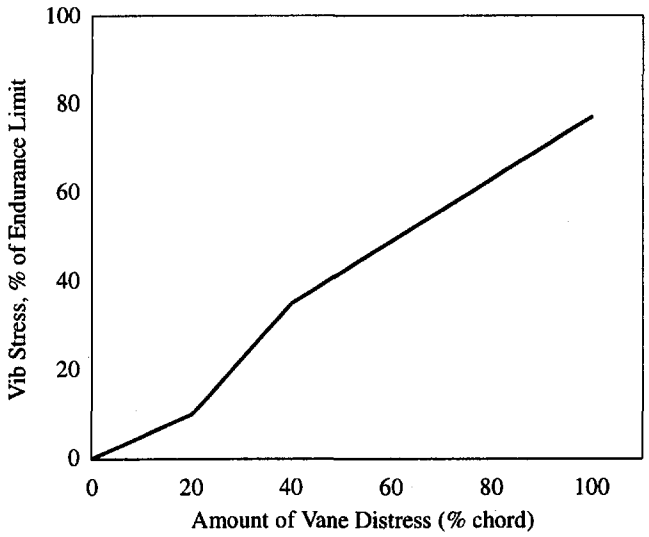

Fig. 7 Vibratory stress predictions for the blade as a function of vane distress level

these results show that the vibratory response should increase as the level of distress increases. Recall that a blade failure occurred for the 40 percent distress but not with a completely missing airfoil.

Crack Propagation Analysis

The blade failure that occurred was due to HCF propagation, but the origin was at a fairly substantial low-cycle fatigue (LCF) crack at the root trailing edge. This LCF crack is caused by the extreme thermal cycling of the blade over its operational life. A simple crack propagation analysis was conducted in which the threshold crack size necessary for a crack to propagate solely due to vibratory stress was determined. The reasoning behind this approach is that crack growth through an LCF mechanism would be slow, while propagation through HCF would lead to virtually instantaneous failure because of the high frequency of the bending mode. The simple crack growth equation (Broek, 1974)

$$K_{th} = G\sigma\sqrt{\pi a_{th}} \tag{14}$$

was used. The threshold stress intensity was estimated based on the data available for the blade material, while G was set to correspond to an edge crack. Equation (14) is solved for a_{th}, and the vibratory stress for each case is substituted. This gives the threshold crack size as a function of vane distress.

The results are summarized in Fig. 8 as the dashed curve, where the crack size has been normalized by *blade* chord. For smaller amounts of distress near 20 percent, a very large existing crack must be present in the blade for the vibratory stress to cause the crack to grow, which is consistent with experience. Actually, a crack this size is not physically possible because the steady stresses would cause tensile overload. At distress levels near 40 percent and beyond, significantly smaller cracks are required for propagation to occur.

Included on this plot is the actual size of the LCF crack that led to the blade failure with 40 percent vane distress, denoted by a horizontal line. Similarly, a line indicating the size of the cracks present in the blades for the "missing airfoil" case is also shown. Considering first the 40 percent distress level, there is very good agreement with the threshold crack size calculated, though the experience lies somewhat above the predicted curve. This can be interpreted as the theoretical results slightly overpredicting the level of vibratory stress. Adjusting the prediction to the data point at 40 percent distress gives the solid curve in Fig. 8. For the "missing airfoil" case, the solid line is above the threshold value for this engine. This latter result explains the reason a failure did not occur on this engine, since crack propagation will not occur unless an LCF crack over 2 percent of the chord in length is present in the blade.

These results may seem inconsistent with the results of Fig. 7, where all the vibratory stresses were below the endurance limit of the material, but HCF data are generated using specimens without LCF cracks. Figure 8 can be used to help set limits of distress that are acceptable for continued operation. The results of this analysis indicate that, for this engine, there must be a combination of vane distress along with existing LCF cracks in the blade for propagation to occur. But with large amounts of distress—those 40 percent and beyond—the crack necessary in the blade is quite small.

Summary and Conclusions

A detailed steady and unsteady forced response analysis has been completed for a high-pressure turbine blade driven by a single distressed upstream vane. The intent of this study was to quantify the strength of this excitation source by determining its ability to drive the primary bending mode of the blade. There are a number of distinct steps in the approach developed, and most of these steps have been studied individually before. But to the authors' knowledge, this is the first systematic application of such tools to this problem. To summarize the steps:

1 Conduct multipassage steady flow analysis of vane.
2 Obtain circumferential variation of flow parameters at blade leading edge plane.
3 Conduct Fourier analysis of flow parameters to obtain harmonic content.
4 Transform to characteristic variables.
5 Calculate corresponding wave numbers.
6 Run finite element analysis to determine mode shape.
7 Run unsteady blade analysis with unit real perturbations.
8 Calculate two-dimensional modal force coefficients.
9 Scale force coefficients to actual harmonic content, using wave numbers to account for phase shifts and attenuation.
10 Integrate up blade span to get total modal force, using appropriate scaling of each section to actual three-dimensional mode shape amplitude.
11 Determine vibratory stress using estimate of modal damping.
12 Calculate threshold size for crack propagation.

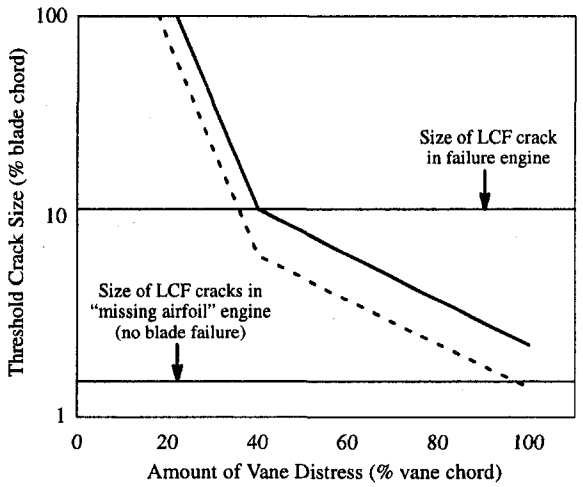

Fig. 8 Threshold crack size for propagation through vibratory stress, as a function of vane distress level

In summary, the approach described here worked well and the predictions are reasonable and consistent with experience. The results show that significant vibratory stresses can be generated by a single distressed vane, and there is also a significant, nearly linear increase in the vibratory excitation and response of the blade as the amount of vane distress increases. The analytical results indicate that a combination of significant vane distress and an existing LCF crack in the blade must be present for propagation through vibratory stress to occur. Use of crack propagation analysis was crucial to providing a reasonable explanation of experience to date.

Acknowledgments

The finite element model and results were provided by Mr. Michael Danowski. Dr. Robert Kielb, Dr. Christopher Lorence, and Dr. Steven Manwaring provided significant technical input for the aeromechanical analysis. We also wish to thank GE Aircraft Engines for permission to publish this paper.

References

Broek, D., 1974, *Elementary Engineering Fracture Mechanics,* Noordhoff International Publishing, Leyden, The Netherlands.

Giles, M. B., 1988, "Non-reflecting Boundary Conditions for the Euler Equations," Computational Fluid Dynamics Laboratory Report CFDL-TR-88-1, Feb.

Hall, K. C., and Crawley, E. F., 1989, "Calculation of Unsteady Flows in Turbomachinery Using the Linearized Euler Equations," *AIAA Journal,* Vol. 27, pp. 777–787.

Holmes, D. G., Lamson, S. H., and Connell, S. D., 1988, "Quasi-3D Solutions for Transonic, Inviscid Flows by Adaptive Triangulation," ASME Paper No. 88-GT-83.

Holmes, D. G., and Connell, S. D., 1989, "Solution of the 2D Navier–Stokes Equations on Unstructured, Adaptive Grids," AIAA Paper No. 89-1932-CP.

Holmes, D. G., and Chuang, H. A., 1991, "2D Linearized Harmonic Euler Flow Analysis for Flutter and Forced Response," *Proc. 6th International Symposium on Unsteady Aerodynamics, Aeroacoustics, and Aeroelasticity of Turbomachines and Propellors,* University of Notre Dame, IN.

Lorence, C. B., 1991, "An Investigation of Three-Dimensional Unsteady Flows in Turbomachinery Using the Linearized Euler Equations," MS Thesis, Duke University.

Platzer, M. F., and Carta, F. O., 1988, "AGARD Manual on Aeroelasticity in Axial-Flow Turbomachines, Vol. 2, Structural Dynamics and Aeroelasticity," SPS Limited.

Vierck, R. K., 1979, *Vibration Analysis,* Harper & Row, New York.

Effects of Surface Roughness on Heat Transfer and Aerodynamic Performance of Turbine Airfoils

N. Abuaf

R. S. Bunker

Corporate Research and Development,
General Electric Company,
Schenectady, NY 12301

C. P. Lee

General Electric Aircraft Engines,
Evendale, OH 45215

Aerodynamic flow path losses and turbine airfoil gas side heat transfer are strongly affected by the gas side surface finish. For high aero efficiencies and reduced cooling requirements, airfoil designs dictate extensive surface finishing processes to produce smooth surfaces and enhance engine performance. The achievement of these requirements incurs additional manufacturing finishing costs over less strict requirements. The present work quantifies the heat transfer (and aero) performance differences of three cast airfoils with varying degrees of surface finish treatment. An airfoil, that was grit blast and Codep coated, produced an average roughness of 2.33 μm, one that was grit blast, tumbled, and aluminide coated produced 1.03 μm roughness, and another that received further postcoating polishing produced 0.81 μm roughness. Local heat transfer coefficients were experimentally measured with a transient technique in a linear cascade with a wide range of flow Reynolds numbers covering typical engine conditions. The measured heat transfer coefficients were used with a rough surface Reynolds analogy to determine the local skin friction coefficients, from which the drag forces and aero efficiencies were calculated. Results show that tumbling and polishing reduce the average roughness and improve performance. The largest differences are observed from the tumbling process, with smaller improvements realized from polishing.

Introduction

Predictions of turbine airfoil metal temperatures depend on reliable knowledge of hot gas and coolant side heat transfer coefficients and bulk temperatures. The external gas side friction and heat transfer are affected by several parameters, which make their accurate predictions quite complicated. Regarding the hot gas side conditions, some of the important physical phenomena to be considered are the free-stream turbulence, the surface roughness, the pressure distribution along the airfoil surface curvature, the upstream local metal temperature distributions, and the laminar-to-turbulent flow transitions (Zerkle and Lounsbury, 1989).

Among these variables, surface roughness increases both the friction factors and the local heat transfer coefficients on surfaces with turbulent boundary layers. In flat plate flows, the relative roughness parameter of pipes (k/R) is replaced by (k/δ), where k is the roughness height, R is the pipe radius, and δ is the boundary layer thickness. In flat plate flows k/δ decreases along the plate. The relative effect of roughness is determined by the relative level of the roughness Reynolds number (Schlichting, 1968) $\mathrm{Re}_{ks} = (V^* k_s/\upsilon)$, where V^* is the friction velocity and equals $\sqrt{\tau_o/\rho}$, k_s is the equivalent sand surface roughness, and υ is the gas kinematic viscosity. When Re_{ks} is less than 5, the flow is considered smooth; when it is larger than 70 the flow is considered to be rough and in between the flow is transitional. In turbulent flows, rough surfaces develop considerably larger skin friction coefficients as compared to smooth surfaces. The same is true for the heat transfer; however, the percentage increase with roughness in heat transfer is smaller than that for the skin friction. Surface roughness also affects the transition from laminar to turbulent flows, causing transition to occur at lower flow Reynolds numbers when compared to smooth walls. There is an extensive collection of data with various rough surface configurations. To compare the results obtained with roughness configurations other than sand roughness, Schlichting (1968) proposed the concept of equivalent sand roughness.

Recently several flat plate heat transfer studies have been reported in which particular roughness types have been used to examine transition and heat transfer coefficients. Hosni et al. (1991) used hemispherical elements of uniform size and regular staggered spacing to determine the effect of surface roughness with zero pressure gradient flows. Chakroun and Taylor (1993) continued to use these same types of surfaces to study heat transfer with mainstream acceleration. Pinson and Wang (1994) measured flat plate heat transfer with various leading edge roughness conditions, using either grits, or cylindrical elements. Barlow et al. (1997) modeled rough surfaces with two distinct element shapes formed by etching of uniform size and spacing, such that all flows were in the fully rough regime of $\mathrm{Re}_{ks} > 70$.

The translation of these rough flat plate experimental results to scaled rough airfoils is not straight forward. Turner et al. (1985) simulated engine type roughness due to depositions and oxidation by attaching abrasive powders to the surfaces of a blade in a stationary cascade. Tarada (1990) proposed a low-Reynolds-number k-epsilon model applicable to flows over rough surfaces to determine skin friction coefficients and flow transitions. The model was first calibrated by comparison with data obtained with deterministic roughness elements and then applied to stochastic (random) surface roughness conditions. Blair (1994) tested roughness effects on a rotating blade surface in a stage-and-a-half, large-scale, ambient temperature annular turbine rig. He used liquid crystals to obtain a "smooth" surface with rms roughness of 0.33 μm and min.-to-max. roughness of 7.6 μm. He also used flat black paint to achieve rms surface roughness of 6.4 μm with min.-to-max. of 51 μm, and also a 600 μm grit size for a very rough surface. The data were compared with four heat transfer correlations applicable to rough surfaces (Dipprey and Saberski, 1963; Kadar and Yaglom, 1972; Seidman, 1978; Han and Delpassand, 1990). These correlations relate the heat transfer coefficients to local Reynolds

Contributed by the International Gas Turbine Institute and presented at the 42nd International Gas Turbine and Aeroengine Congress and Exhibition, Orlando, Florida, June 2–5, 1997. Manuscript received at ASME Headquarters February 1997. Paper No. 97-GT-10. Associate Technical Editor: H. A. Kidd.

numbers, Prandtl number, a roughness parameter, and the skin friction coefficient. Blair used Han's method (1985) for calculating the local friction coefficients as a common input to the four rough surface heat transfer correlations. Guo et al. (1998) measured vane heat transfer in an annular rig using liquid crystals with a reported roughness R_z of 25 μm, and also a smooth surface R_z of less than 1 μm with thin film heat flux gages. R_z is defined as the average peak-to-peak roughness height measured with a profilometer. Hoffs et al. (1996) used liquid crystals to form a rough airfoil surface in a linear vane cascade. Their "natural" crystals were measured as R_a of 7 μm and R_z of 25 μm, and "polished" crystals with R_a of 4 μm and R_z of 15 μm.

The prediction of rough surface friction and heat transfer at present requires the determination of the equivalent sand grain roughness height (k_s). The actual component surface roughness characterization is performed by measuring with a profilometer and specifying an actual roughness height (R_z) or a centerline average value (R_a or CLA). The equivalent sand grain roughness may or may not be similar to any of the measured values and at present there is no universal relation that relates the various surface characterization values. Forster (1967) reported that for machined ground surfaces the relations are $R_z = 5\ R_a$, and $k_s = 2\ R_a$, and for emery paper $R_z = 5\ R_a$ and $k_s = 7\ R_a$. Bammert and Sandstede (1975) present equations for milled surfaces that relate the sand grain roughness to the measured roughness height or centerline averages. For cases when the flow is parallel to the milling grooves, they proposed that $R_z = 5\ k_s$, and when the flow is perpendicular to the grooves $R_z = 2.56\ k_s$. For mechanically produced surfaces these authors suggest that $ks = 2.19\ R_a^{0.877}$. Koch and Smith (1976) estimated that $R_z = 6\ R_a$ for emery paper. Blair (1994) and Boyle (1994) suggested that $k_s = R_z$. Dunn et al. (1994) used $k_s = R_z/0.3$ and Guo et al. (1998) found that $k_s = R_z$ for the best comparison of their experimental data. Bogard et al. (1998) adopted a roughness shape/density parameter of Sigal and Danberg (1990) to characterize vane roughness, and then modeled large-scale, flat plate surfaces to mimic this parameter value. They use cones of uniform size and spacing, measuring heat transfer for a range of flows and turbulence intensities.

Various surface textures result from random finishing processes such as shot peen, vibratory tumbling, abrasive flow, electro discharge machining (EDM), electro chemical machining (ECM), grit blasting, and cast surfaces, which are difficult to characterize by a centerline average and a distance between min. and max. of roughness. Various coatings are also being applied to airfoils on the gas side surface as ceramic insulation layers or for oxidation protection. These coatings tend to be porous and may have surface roughness characteristics that may be different from the metal surface finishing processes. The objective of this work was to conduct experiments with three linear constant section airfoils with varying degrees of surface finish treatment typical of manufacturing processes and to quantify the heat transfer and aero performance differences.

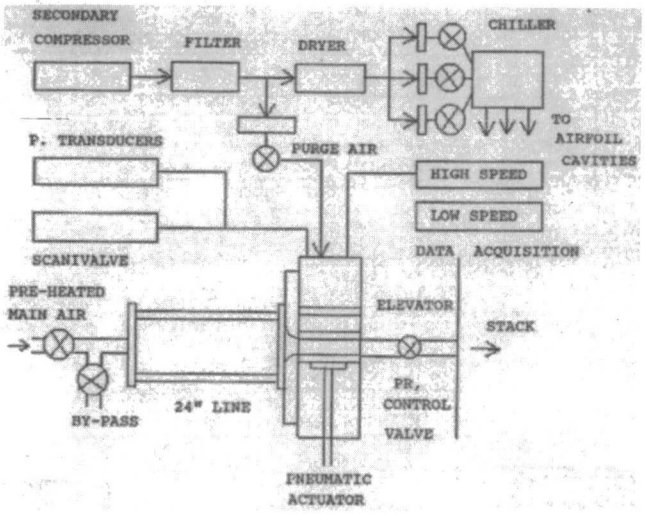

Fig. 1(*a*) Schematic of transient test facility

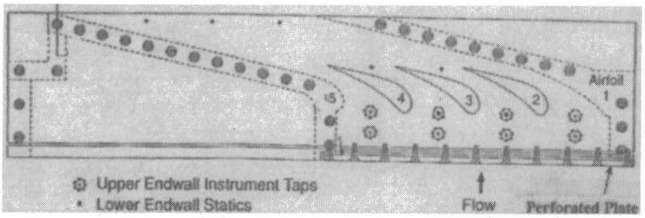

Fig. 1(*b*) Schematic of cascade geometry

Experimental Facility

Apparatus. The test facility used in the present study, and shown in Fig. 1, is fully described by Abuaf et al. (1997), including details of the test methodology, operation and verification testing. The inlet components of the facility include the main air feed line, a flow straightening section, and the pressure containment box, which houses the cascades and elevator. The core of the test apparatus is a transient cascade rig comprised of two linear airfoil cascades, one above the other, housed within a movable elevator assembly. The lower airfoil cascade is known as the dummy cascade, serving the purpose of setting up the desired flow rate, pressure, and temperature to steady conditions prior to initiating a transient test (see below). The upper cascade contains instrumented airfoils for the determination of pressure distributions, and the test airfoil with imbedded thermocouples.

Nomenclature

a = exponential constant
A_x = local airfoil surface area
Bi = Biot number
c_p = specific heat
c_{frx} = rough plate friction coefficient
c_{fsx} = smooth plate friction coefficient
F_D = drag force
h_f = gas side heat transfer coefficient
k = roughness height (designated also as R_z)
k_m = metal thermal conductivity
k_s = equivalent sand grain roughness
l = metal wall thickness
M = total mass flow rate
N = number of vanes
N_o = number of surface regions for each thermocouple
$\mathrm{Nu_{rx}}$ = rough plate Nusselt number
Pr = Prandtl number
P_o, T_o = stagnation pressure and temperature
R = pipe radius
R_a = centerline average roughness (designated also as CLA)
Re = Reynolds number based on exit conditions and axial chord length
$\mathrm{Re_{ks}}$ = roughness Reynolds number
$\mathrm{Re_x}$ = Reynolds number based on distance x and local conditions
R_z = average peak-to-peak roughness
t = time
T_w = wall temperature
v = local velocity
V^* = friction velocity = $\sqrt{\tau_o/\rho}$
x = distance
δ = boundary layer thickness
υ = kinematic viscosity
ρ = density
η = efficiency loss
τ_o = shear stress at the wall

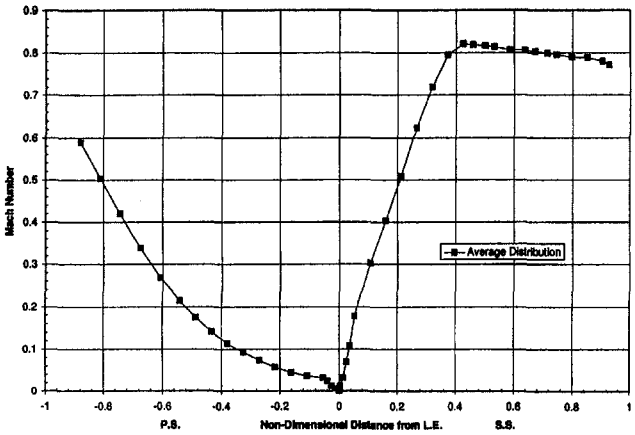

Fig. 2 Plot of average Mach number distributions for a nominal flow rate of 3.62 kg/s (Re = 2.3 × 10^6) as a function of nondimensional distance from the leading edge (L.E.) for the three airfoils A, B, and C investigated

The exit of the cascade section is directed through a back-pressure control valve used to set the overall pressure ratio. The primary flow of the cascades is supplied by a rotary compressor capable of delivering air flow rates of up to 4.53 kg/s at pressures up to 30 atm. A separate natural gas fired heater is used to heat the primary air to the desired level after compression. The cascade containment box is supplied with two secondary sources of air from another house compressor. All secondary air is filtered and metered. A supply of secondary air is used as purge air to pressurize the containment to a level just above the operating inlet pressure of the cascade, thereby preventing cascade bypass leakage flow. This same air also maintains the instrumented cascade at a low temperature until such time as the transient is initiated.

The linear airfoil cascades are representative of typical turbine inlet vanes, with an exit angle of 77.5 deg. Figure 1(*b*) shows the cross-sectional view of the instrumented cascade. Each cascade has five airfoils and four flow passages. Within the instrumented cascade, the central airfoil location is used for the heat transfer test article. The airfoils adjacent to the central location contain surface static pressure instrumentation along the midspan section. These airfoils are present for all testing to monitor the Mach number distributions for the flow passages bounding the center airfoil. The cascade inlet is a rectangular section 28.55 cm wide by 6.1 cm span. While the spanwise profile of the cascade is linear, the flowpath contains a symmetric axial contraction from 6.1 cm to 4.45 cm. The axial chord length of the airfoil geometry is 4.8 cm. The throat diameter is 1.54 cm (minimum geometric airfoil passage width), giving a throat aspect ratio of about 4. Additional instrumentation includes endwall static pressure taps at both inlet and exit to the flow passages, and inlet air thermocouples at each of the flow passages. Approximately 5.08 cm upstream of the cascade is located a perforated plate for the generation of elevated free-stream turbulence intensity. This plate has 42 percent open area with 0.63-cm-dia holes on 0.95 cm centers, and produces 14 percent turbulence intensity at the airfoil leading edge plane. The cascade may be operated under constant pressure ratio condition with Reynolds number varied by a change in pressure level, or the pressure ratio may be adjusted to provide different Mach number distributions. In the present tests, the nominal pressure ratio was set at 1.5, yielding the Mach number distribution shown in Fig. 2.

Heat Transfer Test Airfoils. Three instrumented airfoils were produced and tested for the present study. Because the purpose of this study is to determine the effect of various manufacturing-produced surface finishes on airfoil heat transfer and aerodynamic performance, a specific fabrication and instrumentation method was developed to maintain the external surfaces in the as-manufactured condition. The linear airfoil shape was first cast in Rene 77 material, a high-nickel-content material representative of airfoils in high-performance gas turbines. The solid airfoils were then processed through different polishing and coating steps to produce three external surface finishes. Airfoil A was vapor grit blasted and coated with Codep, an oxidation resistant coating. Airfoil B was vapor grit blasted, tumbled, and then coated with chemical vapor deposited (CVD) aluminide. Airfoil C was vapor grit blasted, tumbled, polished, coated with CVD aluminide, and finally polished again. These three surface finishes represent three different levels of manufacturing effort. Airfoil C obviously required more work and time, but with the goal of producing a smoother finish with less drag and lower heat loads. While such manufactured surfaces are not expected to remain in new condition with airfoil exposed life, many airfoils or regions of airfoils do maintain lower surface roughness if they begin with lower roughness.

Each of the three airfoils was characterized by two surface roughness methods. First, airfoil surface roughness measurements were made with a Perthometer S5P instrument, which scans and records user-selected surface parameters with a cone stylus. Two parameters were measured along spanwise lines at every 1.27 cm around the airfoil perimeters. R_a is the centerline average roughness, and R_z is the average peak-to-peak roughness. Values reported herein are averages of all readings for each airfoil. The processing of Airfoil A resulted in R_a of 2.33 μm with R_z of 14.23 μm. The additional effort required for Airfoil B produced R_a of 1.03 μm with R_z of 6.25 μm. The most highly polished case of Airfoil C resulted in R_a of 0.81 μm with R_z of 5.09 μm. It should be noted here that Airfoil C had differing average roughness levels on the pressure and suction sides with R_a of 0.94 and 0.67 μm, respectively, while Airfoils A and B had similar roughness levels over their entire surfaces. The second surface measurement method used was that of a vertically Scanning Interference Microscope (SIM). This noncontact optical method is further explained, with comparison to stylus profilometry measurements, by Boudreau et al. (1995). Selected regions of the surfaces of all three airfoils were measured with SIM, resulting in R_a values of 2.98, 0.94, and 0.77 μm, respectively, for Airfoils A, B, and C. These readings agree quite well considering the difference between regional mapping and selected line traces. In addition to these measurements, Fig. 3 shows surface micrographs for each airfoil produced by scanning electron microscope. The surface textures are evident, including the effects of coating and polishing, and provide added insight to the heat transfer results.

After the airfoils were finished on the exterior surface, the interior of each airfoil was machined away by wire-Electro Discharge Machining (EDM), leaving a thin-wall airfoil of nominally 1.52 mm wall thickness. The wire-EDM process was adapted to produce a special keyhole groove pattern on the interior surface of the airfoils, as shown in Fig. 4. The grooves are formed such that the 0.508-mm-dia sheaths of the K-type thermocouples are slid into and captured within the grooves, with the cap-grounded junctions located at gas path midspan. The thermocouples are held in place in this manner, while the remaining operation of brazing the thermocouples into the airfoils is completed. To accommodate the cascade vertical motion involved in the transient testing, the stainless steel thermocouple sheathing was transferred to flexible Kapton sheathing via thermocouple splices located several centimeters away from the airfoil. Each airfoil also contains two film cooling cavities, one on each side as seen in Fig. 4, for future testing; but for the present tests these cavities are inactive with no film holes. The inside of each airfoil is sealed against convection or leakage flows. Each airfoil has 32 thermocouples with locations indicated in the results.

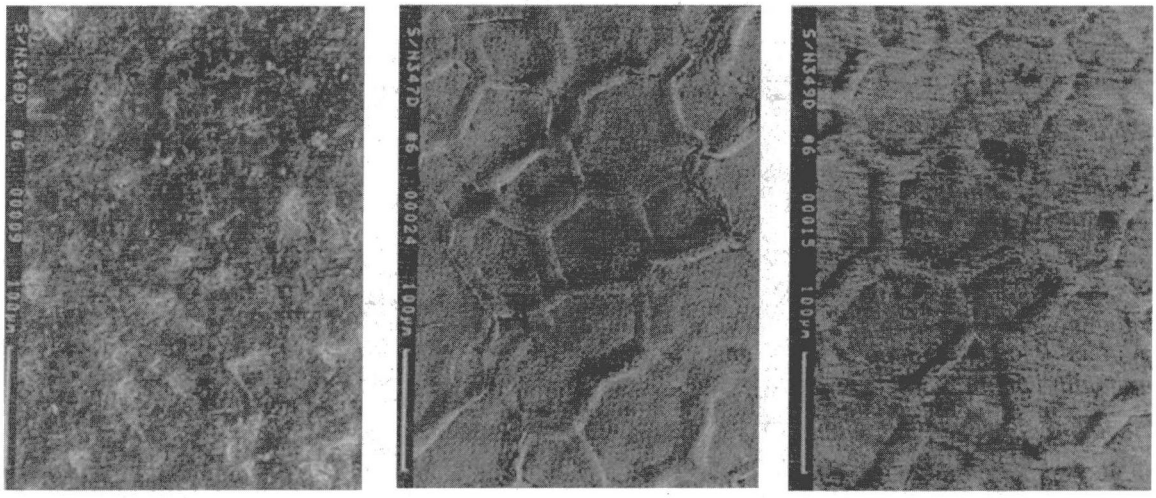

Cast + Vapor Blasted + Codep

Cast + Vapor Blasted + Tumbled + CVD Aluminide

Cast + Vapor Blasted + Tumbled + Polished + CVD Aluminide + Polished

Fig. 3 Surface micrographs from scanning electron microscope

Transient Test Procedure. The present tests derive external airfoil heat transfer coefficients from the temperature–time histories of the recorded embedded thermocouples. A transient test is set up by establishing the desired flow rate, pressure ratio, pressure, and temperature levels through the dummy cascade. At time zero, a transient test is initiated by moving the elevator assembly containing both cascades downward, thereby shuttling the instrumented cascade into the flow. A pneumatic actuator provides assistance to gravity, to force the cascade motion within an interval of 0.1 seconds. This time scale is very small compared to the transient data period of 30 to 60 seconds. A high-speed data acquisition system records the temperature–time histories of all thermocouples on the test article during a transient, while a low-speed system records the main flow conditions and airfoil pressures and temperatures before and after a transient. To convert local temperature data into local heat transfer coefficients, the lumped parameter approximation is used as

$$\frac{T_w(\text{steady state}) - T_w(t)}{T_w(\text{steady state}) - T_w(\text{initial})} = e^{-at}$$

This equation represents a thin-walled section energy balance having negligible radiation and conduction losses, which include the net lateral conduction within the wall and the conduction through the thermocouple leads (Lander et al., 1972). The lumped parameter approximation is usually valid for small values of the Biot number, defined as $\text{Bi} = h_f l/k_m$, and based on the metallic airfoil thin wall thickness (l). T_w(steady state) corresponds to the local steady-state temperature of the metal wall at the end of the transient, T_w(initial) is the local metal wall temperature at time zero, and $T_w(t)$ is the temperature data recorded for a thermocouple at time t. A curve-fitting routine is used to fit an exponential curve to the data, and determine the constant, a, for each thermocouple. As shown in the examples of Fig. 5, the procedure fits the data quite well, with a unique constant determined for each location in each test. The exponential constant is then used to calculate the local heat transfer coefficient

$$a = \frac{h_f}{\rho l c_p}$$

Using the method of Kline and McClintock (1953) for single-sample experimental uncertainties, including both measurement uncertainties of instrumentation and data standard deviations for the tests performed, the uncertainty in the heat transfer coefficients is estimated to be ±8 percent for typical test conditions. The mainstream flow rate uncertainty is about ±1 percent.

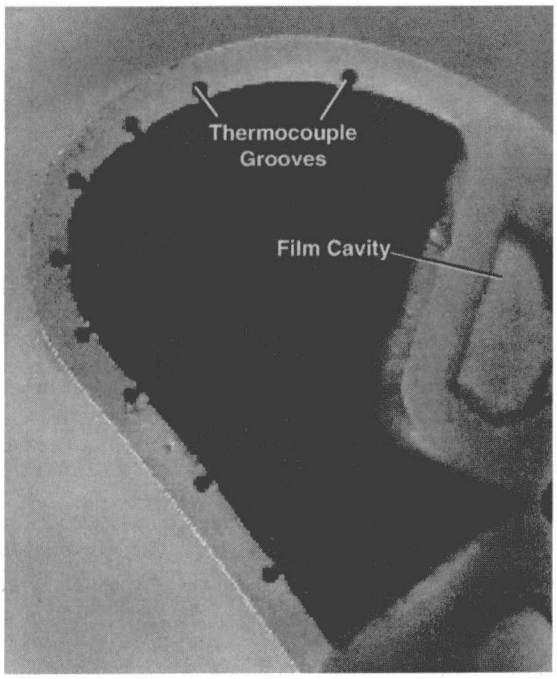

Fig. 4 Detail of thermocouple installation for instrumented airfoils along inside surface of airfoil near leading edge

Experimental Heat Transfer Results

Each of the three prepared airfoils was tested over a range of four Reynolds numbers, based on exit velocity and viscosity and axial chord length, from 6.8×10^5 to 2.3×10^6. In all

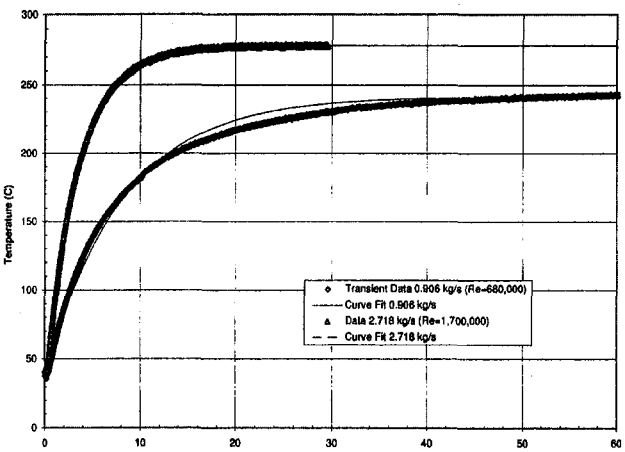

Fig. 5 Typical variation of wall temperature with time recorded during transient tests, and best exponential curve fit

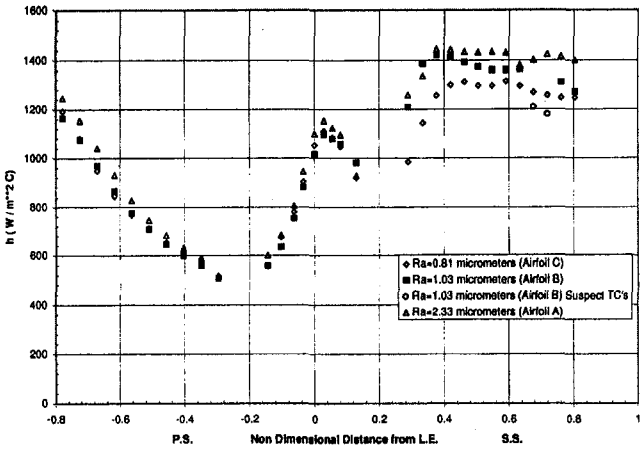

Fig. 7 Comparison of average heat transfer coefficient distributions measured with the transient technique for airfoils A, B, and C having various levels of surface roughness at a nominal flow rate of 1.812 kg/s (Re = 1.2 × 10⁶)

tests, the inlet free-stream turbulence intensity was 14 percent. The typical inlet total temperature was 310°C, while the inlet total pressure varied from 2.5 to 8.85 atm as the Reynolds number was changed. Figure 6 shows the distribution of local heat transfer coefficients for each of the three airfoils at the lowest Re of 6.8×10^5. The data shown here, and in subsequent similar plots, represent the averaged local results from multiple test runs under the same conditions. In some cases, as many as five separate test runs were made with a particular airfoil and Re, but in no case did the variation in results from any two individual tests exceed the estimated experimental uncertainty. Figure 6 indicates that there is virtually no difference in heat transfer anywhere on the airfoil for the three surface finishes. This combination of low Re with a maximum R_a surface roughness of 2.33 μm maintains a hydrodynamically smooth surface condition, though with an elevated inlet turbulence level. The location of suction side transition is the same for each airfoil, just after the inactive film cavity, and corresponds to a local Reynolds number of about 4.5×10^5. Figure 7 shows the averaged heat transfer results for a Re of 1.2×10^6. Here a difference is seen in the distributions, particularly for the suction side. Transition appears to be somewhat earlier for the rougher Airfoils A and B, with a definite increase in heat transfer aft of transition between Airfoils A and C. The pressure side and leading edge regions show no discernible effect of roughness at this Re. Also evident in this figure is that two thermocouples near the end of the suction side of the airfoil are indicating improperly, probably due to incomplete brazing. Figure 8 shows the averaged heat transfer results at Re of 1.7×10^6. The suction side transition location has moved forward for all three airfoils here, with the roughest airfoil beginning first. The distinction between the roughness levels is clearer now. Considering the results of both Figs. 7 and 8, and the multiple tests involved, the pressure side heat transfer is showing a slight increase with the elevated roughness of Airfoil A. The results at the highest Re of 2.3×10^6 are shown in Fig. 9. At this Re, all three airfoils show the effect of very early suction side transition, with a clear progression in heat transfer coefficient magnitude as roughness increases from Airfoil C to Airfoil A. This progression is also noted on the pressure side distribution, with the larger portion attributed to the change from R_a of 1.03 to 2.33 μm.

To compare these airfoil results on the basis of overall heat loading, the individual local heat transfer coefficient distributions for each airfoil and Re were integrated to obtain the area under each distribution. The inactive regions spanning the film cavities were connected by straight lines between the data points. Figure 10 shows the integrated heat loads as a function of exit Reynolds number, with least-squares fits drawn for each airfoil. The integrated heat loads show the progression from no

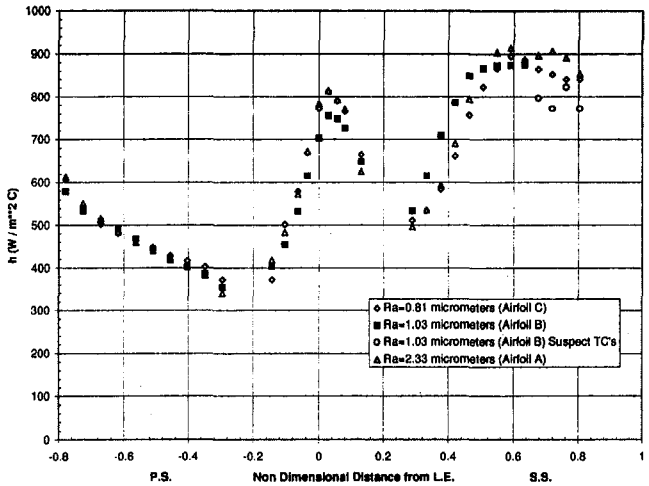

Fig. 6 Comparison of average heat transfer coefficient distributions measured with the transient technique for airfoils A, B, and C having various levels of surface roughness at a nominal flow rate of 0.906 kg/s (Re = 6.8 × 10⁵)

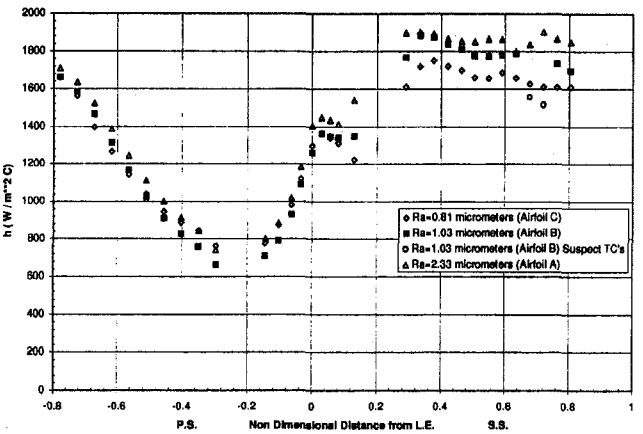

Fig. 8 Comparison of average heat transfer coefficient distributions measured with the transient technique for airfoils A, B, and C having various levels of surface roughness at a nominal flow rate of 2.718 kg/s (Re = 1.7 × 10⁶)

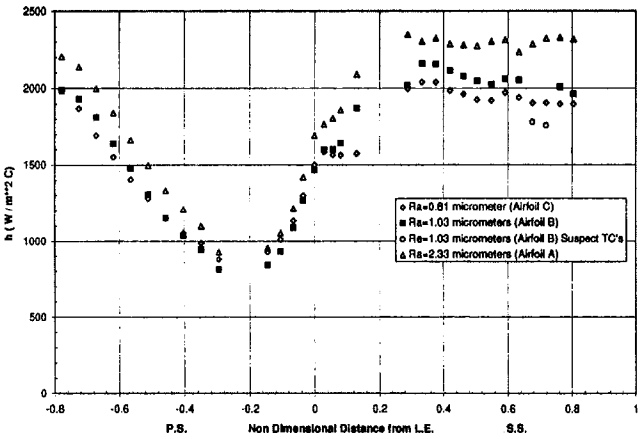

Fig. 9 Comparison of average heat transfer coefficient distributions measured with the transient technique for airfoils A, B, and C having various levels of surface roughness at a nominal flow rate of 3.624 kg/s (Re = 2.3 × 10⁶)

differences at low Re, to a maximum increase of about 15 percent at the highest Re. Most of the increases at higher Re occur between Airfoils A and B, due to the tumbling process and the CVD aluminide coating. Very small but consistent increases are shown between Airfoils B and C, due to the extra polishing steps involved. On the basis of heat load alone, these results would indicate that the added polishing steps, which represent time and cost, add relatively little benefit. On the other hand, major processing steps such as tumbling serve to reduce the heat loads for certain ranges of operating conditions.

Data Analysis

Rough Surface Friction and Heat Transfer Analogy. The local smooth and rough plate friction coefficients were predicted from the following two equations presented by Schlichting (1968) for turbulent boundary layers. The smooth plate, zero-pressure gradient turbulent boundary layer flow, skin friction factor is given by

$$c_{fsx} = \frac{(2)(0.0296)}{\mathrm{Re}_x^{0.2}}$$

This equation is valid for local Reynolds numbers larger than 100,000. To calculate the local friction coefficients for rough surfaces, the following expression can be used:

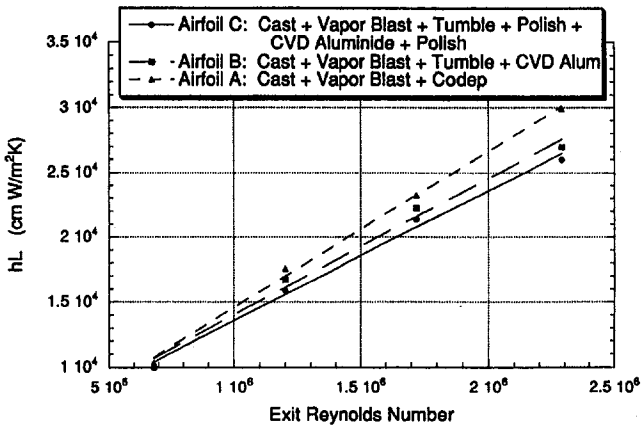

Fig. 10 Comparison of integrated heat transfer coefficients measured along the three airfoils investigated having three distinct levels of surface roughness

$$c_{frx} = \left(2.87 + 1.58 \log\left(\frac{x}{k_s}\right)\right)^{-2.5}$$

In this equation k_s is the equivalent sand roughness. The classical Reynolds analogy relating the friction factor to the local heat transfer cannot be directly applied to rough surfaces. Based on experimental investigations Dipprey and Sabersky (1963) proposed the following expression to relate the heat transfer to friction factors for rough surfaces under zero-pressure gradient conditions,

$$\mathrm{Nu}_{rx} = \frac{0.5\, c_{frx}\, \mathrm{Re}_x\, \mathrm{Pr}}{1 + \sqrt{0.5 c_{frx}}\beta(\mathrm{Re}_{ks}, \mathrm{Pr})}$$

where

$$\mathrm{Re}_{ks} = \frac{V^* k_s}{\upsilon}$$

Dipprey and Sabersky reported that

$$\beta(\mathrm{Re}_{ks}, \mathrm{Pr}) = 5.19\, \mathrm{Re}_{ks}^{0.2}\, \mathrm{Pr}^{0.44} - 8.5$$

This correlation is based on their experimental results with sand grain roughness and was found to be valid in the completely rough regime of $\mathrm{Re}_{ks} > 70$, and the friction velocity was expressed as

$$V^* = \sqrt{\frac{c_{frx}}{2}}\, \upsilon$$

where υ is the local velocity.

Aero Efficiency Calculations for Test Conditions. The data analysis to calculate local friction factors and aero efficiency based on the experimentally measured local heat transfer coefficients for the rough surface airfoils followed a procedure described below:

1 The experimental data recorded and used for each specific test included the centerline average (CLA) surface roughness, the flow rate, the cascade inlet total pressure and temperature (P_o, T_o), and the measured local heat transfer coefficients.

2 With the cascade inlet total pressure and temperature, the density was calculated by the perfect gas equation of state.

3 The local Mach number distributions for each thermocouple location along the pressure and suction side of the airfoil were calculated from the measured static pressure distributions, which were reported above, by using the isentropic equations.

4 The air properties (viscosity, thermal conductivity, specific heat, Prandtl number, and specific heat ratio) were calculated as a function of the local temperatures by using a series of curve fits to the values obtained from air property tables.

5 The local static pressure, temperature, density, sonic velocity, and velocity were calculated at every thermocouple location by using the isentropic equations. With the local flow properties, distance from the leading edge, and air viscosity at the local static temperature, the local Reynolds numbers were calculated for each thermocouple location along the suction and pressure sides of the airfoil:

$$\mathrm{Re}_x = \frac{\rho \upsilon x}{\mu}$$

6 Given the locally measured heat transfer coefficient data from the transient tests conducted at various flow rates and three airfoils with different surface roughness levels, the local Nusselt numbers (based on x) were calculated using the local thermal conductivity of air.

7 Next the local friction coefficients were calculated from the rough surface Nusselt number versus friction coefficient correlation presented above (Dipprey and Sabersky, 1963).

Table 1 Summary of results for efficiency calculations (tests at 3.68 kg/s, Re = 2.3 × 10⁶)

Case 1. k_s = CLA Roughness

Surface Roughness	Pressure Side	Suction Side	Overall	DLoss form 0.81 micrometer * 100
0.81 micrometer	0.99886	0.99368	0.99254	0
1.03 micrometer	0.99876	0.99333	0.99209	-0.045
2.33 micrometer	0.99862	0.99219	0.99081	-0.173

Case 2. k_s = 6.2*CLA Roughness

Surface Roughness	Pressure Side	Suction Side	Overall	DLoss form 0.81 micrometer * 100
0.81 micrometer	0.99876	0.99321	0.99197	0
1.03 micrometer	0.99864	0.99273	0.99137	-0.060
2.33 micrometer	0.99844	0.99121	0.98965	-0.232

Case 3. k_s = 10*CLA Roughness

Surface Roughness	Pressure Side	Suction Side	Overall	DLoss form 0.81 micrometer * 100
0.81 micrometer	0.99873	0.99304	0.99177	0
1.03 micrometer	0.99859	0.99253	0.99112	-0.065
2.33 micrometer	0.99837	0.99087	0.98924	-0.253

Note that in these equations k_s is the equivalent sand roughness and the roughness values quoted for each one of the three airfoils of 0.81, 1.03, and 2.33 μm are the centerline average values measured with a profilometer. In the following calculations we assumed that k_s = constant * CLAroughness. Since the value of the constant is not known, its value was taken to be 1, 6.2, and 10 to investigate its effect in a parametric way. The calculated local friction coefficients were then compared with the smooth surface friction coefficients. If the rough surface friction factor was locally less than the smooth one (because of the low values of the local Reynolds numbers near the leading edge), the local friction factor was set equal to the smooth plate friction factor.

8 Based on the local friction coefficients, the local drag force was calculated for each thermocouple location:

$$F_D = c_{frx} \frac{\rho v^2}{2} A_x$$

In this equation, A_x is the airfoil surface area at the thermocouple location. In calculating this area the interdistance between consecutive thermocouples were taken into account, as well as the height of the airfoil, which was changing from the leading edge to the trailing edge along the suction and pressure sides of the airfoil. This approach neglects the end wall effects and the presence of any secondary flows, since the measurements reported were taken at the pitch line of the airfoil where these effects can be considered to be small.

9 With the calculated local drag forces, the efficiency loss was calculated by using the following expression,

$$\eta = 1 - \frac{\{N \sum_{i=1}^{N_o} (F_{Di} v_i)\}}{M v_{\text{Exit}}^2}$$

In this equation, N is the number of vanes, M is the total mass flow rate, v_{Exit} is the vane exit velocity, and N_o is the number of surface regions corresponding to each thermocouple location.

Typical examples of the calculations are given in Tables 1–4 for the four flow rates (exit Reynolds numbers) and for the three specific surface roughness levels investigated. Figure 11 is a plot of the loss in aero efficiency over the 0.81 μm surface for the two rougher surfaces investigated, as a function of the constant relating the sand grain roughness to the measured representative centerline average surface roughness, for the highest flow Reynolds number of 2.3 × 10⁶ investigated. The aero efficiency loss increases with the constant as one changes it from 1 to 6.2. The increase of the aero loss appears to level off when the constant is increased from 6.2 to 10. The aero loss also increases with the level of the surface finish measured (the centerline average roughness). Figure 12 presents a similar curve for the aero loss as a function of the constant for the

Table 2 Summary of results for efficiency calculations (tests at 2.75 kg/s, Re = 1.7 × 10⁶)

Case 1. k_s = CLA Roughness

Surface Roughness	Pressure Side	Suction Side	Overall	DLoss form 0.81 micrometer * 100
0.81 micrometer	0.999066	0.99486	0.99393	0
1.03 micrometer	0.999008	0.99444	0.99345	-0.048
2.33 micrometer	0.998952	0.99393	0.99288	-0.105

Case 2. k_s = 10*CLA Roughness

Surface Roughness	Pressure Side	Suction Side	Overall	DLoss form 0.81 micrometer * 100
0.81 micrometer	0.998958	0.99433	0.99329	0
1.03 micrometer	0.998872	0.99375	0.99262	-0.067
2.33 micrometer	0.998776	0.99293	0.99170	-0.159

Table 3 Summary of results for efficiency calculations (tests at 1.86 kg/s, Re = 1.2 × 10⁶)

Case 1. k_s = CLA Roughness

Surface Roughness	Pressure Side	Suction Side	Overall	DLoss form 0.81 micrometer * 100
0.81 micrometer	0.999349	0.99626	0.99561	0
1.03 micrometer	0.999330	0.99588	0.99521	-0.040
2.33 micrometer	0.999267	0.99556	0.99483	-0.078

Case 2. k_s = 10*CLA Roughness

Surface Roughness	Pressure Side	Suction Side	Overall	DLoss form 0.81 micrometer * 100
0.81 micrometer	0.999280	0.99589	0.99517	0
1.03 micrometer	0.999248	0.99539	0.99464	-0.053
2.33 micrometer	0.999153	0.99486	0.99401	-0.116

Table 4 Summary of results for efficiency calculations (tests at 0.94 kg/s, Re = 6.8 × 10⁵)

Case 1. k_s = CLA Roughness

Surface Roughness	Pressure Side	Suction Side	Overall	DLoss form 0.81 micrometer * 100
0.81 micrometer	0.999659	0.99771	0.99737	0
1.03 micrometer	0.999654	0.99760	0.99725	-0.012
2.33 micrometer	0.998638	0.99755	0.99719	-0.018

Case 2. k_s = 10*CLA Roughness

Surface Roughness	Pressure Side	Suction Side	Overall	DLoss form 0.81 micrometer * 100
0.81 micrometer	0.999627	0.99749	0.99712	0
1.03 micrometer	0.999616	0.99733	0.99695	-0.017
2.33 micrometer	0.999590	0.99721	0.99680	-0.032

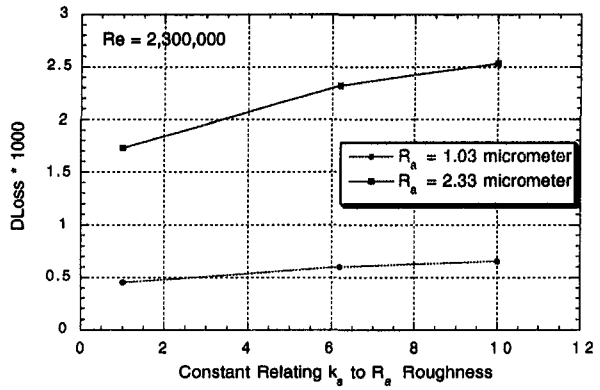

Fig. 11 Plot of the aero efficiency loss over the smooth surface as a function of the constant relating the centerline average to the equivalent sand grain roughness for Re = 2.3 × 10⁶

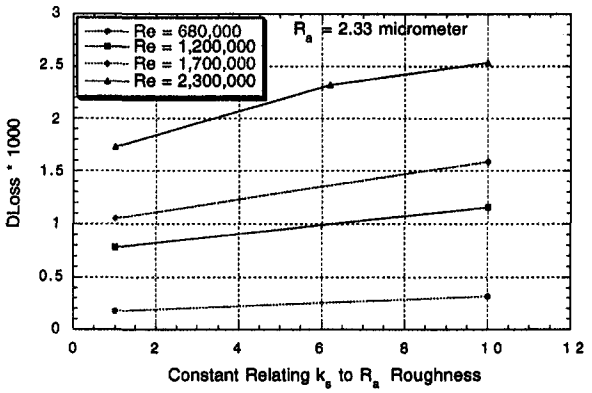

Fig. 12 Plot of the aero efficiency loss over the smooth surface as a function of the constant relating the centerline average to the equivalent sand grain roughness for the roughest surface investigated (2.33 μm)

roughest surface investigated while in this figure the flow Reynolds numbers were used as parameters.

Summary and Conclusions

The present work tried to quantify the heat transfer and aero performance of three cast airfoils with varying degrees of surface finish treatments. The linear airfoils with different degrees of surface finish were used to measure the heat transfer coefficient distributions as a function of flow Reynolds numbers. The measured heat transfer coefficients were used with a rough surface Reynolds analogy to calculate the local skin friction coefficients, the drag forces, and the aero efficiencies. The results showed that: (1) Tumbling and polishing reduces the average roughness and improves performance, (2) the biggest difference is observed between 2.33 and 1.03 μm surface finish, which is due to tumbling, (3) a smaller difference is observed between 1.03 and 0.81 μm surface roughness, which is obtained by hand polishing, (4) a better measure of centerline average roughness is needed to relate skin friction and heat transfer coefficients for rough surfaces, accurate methods should be developed to relate the equivalent sand grain roughness to the representative measurement of the surface finish, (5) in the aero and thermal efficiency calculations the use of a unified approach based on a rough surface Reynolds analogy formulation seems logical.

References

Abuaf, N., Bunker, R., and Lee, P. C., 1997, "Heat Transfer and Film Cooling Effectiveness in a Linear Airfoil Cascade," ASME JOURNAL OF TURBOMACHINERY, Vol. 119, pp. 302–309.

Bammert, K., and Sandstede, H., 1975, "Influences of Manufacturing Tolerances and Surface Roughness of Blades on the Performance of Turbines," ASME Paper No. 75-GT-35.

Barlow, D. N., Kim, Y. W., and Florschuetz, L. W., 1997, "Transient Liquid Crystal Technique for Convective Heat Transfer on Rough Surfaces," ASME JOURNAL OF TURBOMACHINERY, Vol. 119, pp. 14–22.

Blair, M. F., 1994, "An Experimental Study of Heat Transfer in a Large-Scale Turbine Rotor Passage," ASME JOURNAL OF TURBOMACHINERY, Vol. 116, pp. 1–13.

Bogard, D. G., Schmidt, D. L., and Tabbita, M., 1998, "Characterization and Laboratory Simulation of Turbine Airfoil Surface Roughness," ASME JOURNAL OF TURBOMACHINERY, Vol. 120, pp. 337–342.

Boyle R. J., 1994, "Prediction of Surface Roughness and Incidence Effects on Turbine Performance," ASME JOURNAL OF TURBOMACHINERY, Vol. 116, pp. 745–751.

Boudreau, B. D., Raja, J., Sanmreddy, H., and Caber, P. J., 1995, "A Comparative Study of Surface Texture Measurement Using White Light Scanning Interferometry and Contact Stylus Techniques," *Proc. American Society for Precision Engineering 1995 Annual Meeting*, Vol. 12, pp. 120–124, Oct. 15–20.

Chakroun, W., and Taylor, R. P., 1993, "Heat Transfer and Fluid Dynamics Measurements in Accelerated Rough Wall Boundary Layer," ASME Paper No. 93-GT-78.

Dipprey, R. B., and Sabersky, R. H., 1963, "Heat and Mass Transfer in Smooth and Rough Tubes at Various Prandtl Numbers," *Int. J. Heat Mass Transfer*, Vol. 6, pp. 329–353.

Dunn, M. G., Kim, J., Civinskas, K. C., and Boyle, R. J., 1994, "Time-Averaged Heat Transfer and Pressure Measurements and Comparison With Prediction for a Two-Stage Turbine," ASME JOURNAL OF TURBOMACHINERY, Vol. 116, pp. 14–22.

Forster, V. T., 1967, "Performance Loss of Modern Steam Turbine Plant Due to Surface Roughness," *Proc. Instn. Mech. Engrs. 1966–67*, Vol. 181, Pt. 1, pp. 391–405.

Guo, S. M., Jones, T. V., Lock, G. D., and Dancer, S. N., 1998, "Computational Prediction of Heat Transfer to Gas Turbine Nozzle Guide Vanes With Roughened Surfaces," ASME JOURNAL OF TURBOMACHINERY, Vol. 120, pp. 343–350.

Han, L. S., 1985, "Turbulent Flow Over Rough Turbine Airfoils," AFWAL-TR-85-2056, Final Contractor Report, The Ohio State University.

Han, L. S., and Delpassand, M., 1990, "A Heat Transfer Analysis of Rough Turbine Airfoils," WRDC-TR-89-2135, Final Contractor Report, Ohio State University.

Hoffs, A., Drost, U., and Bolcs, A., 1996, "Heat Transfer Measurements on a Turbine Airfoil at Various Reynolds Numbers and Turbulence Intensities Including Effects of Surface Roughness," ASME Paper No. 96-GT-169.

Hosni, M. H., Coleman, H. W., and Taylor, R. P., 1991, "Measurements and Calculations of Rough Wall Heat Transfer in the Turbulent Boundary Layer," *Int. J. Heat Mass Transfer*, Vol. 34, No. 4/5, pp. 1067–1082.

Kadar, B. A., and Yaglom, A. M., 1972, "Heat and Mass Transfer Laws of Fully Turbulent Wall Flows," *Int. J. Heat Mass Transfer*, Vol. 15, pp. 2329–2351.

Kline, S. J., and McClintock, F. A., 1953, "Describing Uncertainties in Single-Sample Experiments," *Mechanical Engineering*, Vol. 75, Jan., pp. 3–8.

Koch, C. C., and Smith, L. H., 1976, "Loss Sources and Magnitudes in Axial Flow Compressors," ASME *Journal of Engineering for Power*, Vol. 98, pp. 411–424.

Lander, R. D., Fish, R. W., and Suo, M., 1972, "External Heat Transfer Distribution on Film Cooled Turbine Vane," *J. Aircraft*, Vol. 9, No. 10, pp. 707–714.

Pinson, M., and Wang, T., 1994, "Effects of Leading Edge Roughness on Fluid Flow and Heat Transfer in the Transitional Boundary Layer Over a Flat Plate," ASME Paper No. 94-GT-326.

Schlichting, H., 1968, *Boundary Layer Theory*, McGraw-Hill, New York.

Seidman, M. H., 1978, "Rough Wall Heat Transfer in a Compressible Turbulent Boundary Layer," AIAA Paper No. 78–163.

Sigal, A., and Danberg, J. E., 1990, "New Correlation of Roughness Density Effect on the Turbulent Boundary Layer," *AIAA Journal*, Vol. 28, No. 3, pp. 554–556.

Tarada, F. H. A., 1990, "Prediction of Rough Wall Boundary Layers Using a Low-Reynolds Number *k*-Epsilon Model," *Int. J. Heat Fluid Flow*, Vol. 11, pp. 331–345.

Turner, A. B., Tarada, F. H. A., and Bayley, F. J., 1985, "Effects of Surface Roughness on Heat Transfer to Gas Turbine Blades," AGARD-CP-390.

Zerkle, R. D., and Lounsbury, R. J., 1989, "Free Stream Turbulence Effect on Turbine Airfoil Heat Transfer," *J. Propulsion*, Vol. 5, No. 1, pp. 82–88.

R. W. Moss
roger.moss@eng.ox.ac.uk

R. W. Ainsworth

T. Garside

Department of Engineering Science,
University of Oxford,
Parks Road,
Oxford, United Kingdom

Effects of Rotation on Blade Surface Heat Transfer: An Experimental Investigation

Measurements of turbine blade surface heat transfer in a transient rotor facility are compared with predictions and equivalent cascade data. The rotating measurements involved both forward and reverse rotation (wake-free) experiments. The use of thin-film gages in the Oxford Rotor Facility provides both time-mean heat transfer levels and the unsteady time history. The time-mean level is not significantly affected by turbulence in the wake; this contrasts with the cascade response to free-stream turbulence and simulated wake passing. Heat transfer predictions show the extent to which such phenomena are successfully modeled by a time-steady code. The accurate prediction of transition is seen to be crucial if useful predictions are to be obtained.

Introduction

The design and development of blade cooling systems is a complex process that is both highly important, since it affects blade life and efficiency, and expensive, because considerable development testing may be required to confirm the accuracy of temperature predictions. One of the largest sources of uncertainty is the prediction of aerofoil external heat transfer rates, and this has led to research into all aspects of boundary layer behavior.

External heat transfer research started over 30 years ago with flat plate and cascade experiments and has since progressed to fully rotating facilities that attempt to reproduce all the unsteady and secondary flow phenomena that would occur in an engine.

Guenette et al. (1989) used an argon/freon mixture to simulate typical combustor gas specific heat ratios in a blowdown rotor facility at MIT. They found that both unsteady and time-mean heat transfer were similar to that in a cascade with simulated wake passing and, using a two-dimensional prediction, achieved a good prediction of Nusselt number at midheight. More recently (Abhari et al., 1992) data from this experiment have been compared with unsteady CFD predictions; the time-mean of the unsteady prediction was found to be very similar to results from a time-steady code. The MIT facility has also been used to measure heat transfer to film-cooled rotor blades (Garg and Abhari, 1996).

Dunn et al. (1989) used a shock tube to supply air to a turbine instrumented with thin film gage inserts. They found large heat flux fluctuations on both pressure and suction surfaces; on the suction surface unsteady transition appeared to occur under the NGV wake.

Hilditch et al. (1994) have developed a large rotating turbine facility that produces engine-representative Mach and Reynolds and uses a turbobrake to maintain an essentially constant speed during a run time of 0.4 second. This facility with its relatively long run-time is capable of taking highly accurate heat transfer measurements on the rotor.

Blair (1994) used a low-speed $1\frac{1}{2}$-stage rotating facility to measure the time-mean heat transfer around a rotor blade and investigate the influence of surface roughness, incidence, and Reynolds number.

Research at Oxford over the last fifteen years has concentrated on understanding unsteady physical phenomena and assessing their importance. The current aerofoil profile was cascade tested by Nicholson et al. (1984). Further cascade testing (Doorly, 1984; Doorly and Oldfield, 1985; Doorly et al., 1989) simulated wake and shock wave passing and showed that this led both to a characteristic AC shock signature, that could be predicted, and to boundary layer transition. The facility was subsequently converted to a rotating turbine, which used the same aerofoil geometry (Dietz and Ainsworth, 1992) and has since generated a large amount of fast-response heat transfer and pressure data. Midheight unsteady heat transfer and pressure data have been compared by Moss et al. (1995) and the pressure data are described by Moss et al. (1997).

Following heat transfer and pressure measurements in the normal, "forward" direction of rotation, the facility was rebuilt to allow rotor testing without any nozzle guide vanes by rotating in the "reverse" direction (Garside et al., 1994). This achieved similar blade-relative conditions to the forward rotation case while providing a very smooth wake-free and shock-free flow over the blades.

Instrumentation

The Oxford Rotor is mounted in a transient turbine test facility based on an isentropic light piston tunnel (Ainsworth et al., 1988). The turbine is a transonic shroudless design of 0.5 m tip diameter with a NGV to blade spacing of 0.346 NGV axial chords. Engine representative Mach and Reynolds numbers are achieved at the nominal design point (Table 1). Prior to a run it is accelerated to 6000 rpm, in vacuum, by an air motor. Compressed air drives a free-sliding piston down the pump tube (Fig. 1), compressing the charge of air in front of it until a suitable pressure and temperature have been reached; a fast-acting annular valve then opens and the air passes through the turbine for 200 ms. The turbine accelerates rapidly to 9500 rpm and the instrumentation system is triggered as it passes through the design condition. The annulus and aerofoil profiles are shown in Fig. 2; there are 36 vanes and 60 blades.

Rotor instrumentation consists of thin-film heat transfer gages (Ainsworth et al., 1989; Hilditch and Ainsworth, 1990; Moss and Ainsworth, 1993) with a 100 kHz response together with subminiature Kulite pressure transducers (Ainsworth et al., 1990; Moss et al., 1997). The heat transfer gages are made by coating the steel blades with an insulating enamel layer, and then painting the gages onto the enamel. This process results in a very smooth blade surface with no roughness or thermal discontinuity at the gage positions. The heat transfer data described in this paper have been produced by a total of 66 thin-film gages located on five blade sections at nominal spanwise

Contributed by the International Gas Turbine Institute and presented at the 42nd International Gas Turbine and Aeroengine Congress and Exhibition, Orlando, Florida, June 2–5, 1997. Manuscript received at ASME Headquarters February 1997. Paper No. 97-GT-188. Associate Technical Editor: H. A. Kidd.

Table 1 Comparison of typical experimental and prediction conditions for the rotor aerofoil

	C_{ax} (mm)	T_{rel}/T_o	Re_{Cax}	β_{rel}	Mn_{2is}
"Design Point"	-	1.138	1.554×10^6	42.75	0.959
Forwards rotation (Allan, 1990)	24.35	1.087	1.402×10^6	40.64	0.9057
Reverse rotation (Garside, 1995)	24.35	1.11	1.339×10^6	44.5	0.77
Cascade (Nicholson et al, 1984)	33.69	1.5	1.554×10^6	42.75	0.931
Cascade (Doorly and Oldfield 1985)	51.9	1.5	1.554×10^6	42.75	0.96
Forwards CFDS (Slater, 1993)	24.35	1.118	1.554×10^6	41.05	0.903
Reverse CFDS (Garside, 1995)	24.35	1.1667	1.554×10^6	43.73	0.855

positions of 5, 10, 50, 90, and 95 percent. A 12 channel slip ring transfers the signals to a 12-bit, 200 kHz A-D system that records these high-frequency signals for 17 ms, during which approximately 90 wake passing cycles occur; annulus wall pressure tappings and stage inlet parameters, used for the definition of the tunnel operating conditions, are recorded by a slower 435 Hz system throughout the test. The data are subsequently processed on a PC using software running under Matlab.

Data Processing

The Oxford rotor facility, in common with most isentropic light piston tunnels, exhibits piston oscillations: the piston and the air on either side of it constitute a mass and spring system and the piston velocity oscillates about some mean level. This induces pressure oscillations in the flow entering the turbine, Fig. 3(*a*). The flow temperature also varies since it is related isentropically to the pressure.

The stage overall pressure ratio, and hence blade exit Mach number, is set by an adjustable "second throat" just downstream of the rotor. In theory, if the filling volume upstream of this throat was negligible, the static pressure at the rotor exit plane would vary in phase with the stage inlet pressure; the pressure *ratio* across the stage (and hence Mach numbers throughout the turbine) would only be a function of $N/\sqrt{T}$. In practice, slight Mach number variations are seen, Fig. 3(*b*), due both to the piston oscillations producing periodic variations in $N/\sqrt{T}$ and to the finite volume upstream of the second throat. These Mach number variations are not important with regard to the data presented here, which are averaged over a period of 17 ms, during which the Mach number is both approximately constant and repeatable from run to run. Variations in Reynolds number corresponding to the fluctuating inlet temperature and pressure are also seen, Fig. 3(*c*). It should be noted that the piston oscillations are at a very low frequency (20 Hz) compared to the flow disturbances produced by wake passing (5 kHz); the blade surface instrumentation has a frequency response in excess of 100 kHz and the presence of 20 Hz oscillations introduces no experimental difficulties whatsoever in the determination of Nusselt or Mach numbers.

The largest manifestation of piston oscillation is its effect on blade surface heat flux. The isentropic flow temperature fluctuations are significant relative to the time-mean gas-to-wall temperature difference, and this causes large fluctuations, of order ±30 percent, in the measured heat flux, Fig. 3(*d*).

Heat flux levels are of little direct value, not only because of these oscillations but because the gas-to-wall temperature difference varies slightly from run to run and is in any case different to levels used in previous cascade tests. The data must therefore be nondimensionalized by converting to Nusselt number. This removes the dependence on temperature difference as shown in Fig. 3(*e*) and one is left only with small random fluctuations due to noise and aliasing: The Nusselt number fluctuations between $t = 0.06$ and 0.18 seconds show an rms/mean level of only 4 percent.

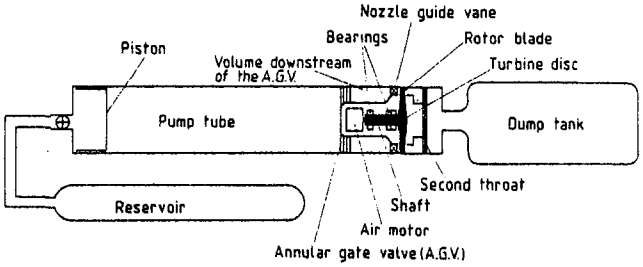

Fig. 1 Layout of the Oxford rotor transient turbine facility

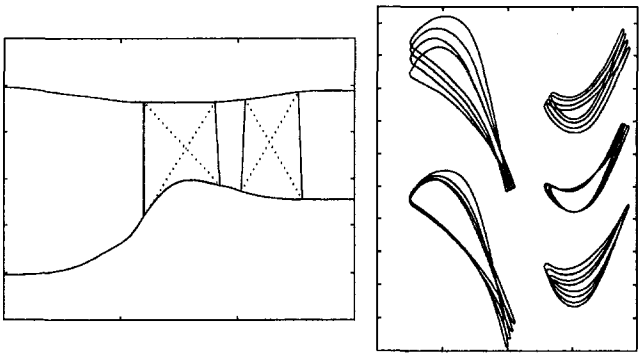

Fig. 2 Annulus cross section and aerofoil profiles (forward rotation tests)

The scaling process by which heat flux is converted to Nusselt number, and allowance is made for Reynolds number and gas-to-wall temperature ratio, is as follows. The heat flux traces are first scaled to correct for any differences between the actual and the design Reynolds number (1.554×10^6), assuming that the boundary layer is turbulent:

$$\dot{q}_{\text{des}} = \dot{q}\left(\frac{1.554 \times 10^6}{\text{Re}}\right)^{0.8}$$

The heat flux is then converted to Nusselt number:

$$\text{Nu} = \left(\frac{\dot{q}_{\text{des}}}{\Delta T}\right)\frac{d}{k}$$

d is axial chord, air conductivity k is evaluated at the relative total gas temperature, and Reynolds number is based on the stage exit conditions:

$$\Delta T = T_{\text{recovery}} - (T_{\text{amb}} + \Delta T_{\text{windage}} + \Delta T_q)$$

where T_{amb} is the ambient temperature (i.e., blade temperature prior to spinning the rotor). $\Delta T_{\text{windage}}$ is the blade temperature rise due to windage as the rotor is accelerated, in the near

Nomenclature

Cax = blade axial chord
f = frequency, Hz
Hade = axial variation in radius of inner or outer casing, i.e., annulus shape; "unhaded" cascade holds aerofoils between parallel walls
M = Mach number
NGV = nozzle guide vane
S = overall perimeter on each surface
T_g = gas temperature
T_w = wall (blade surface) temperature
x = axial distance from leading edge
X = perimeter from stagnation point to transducer

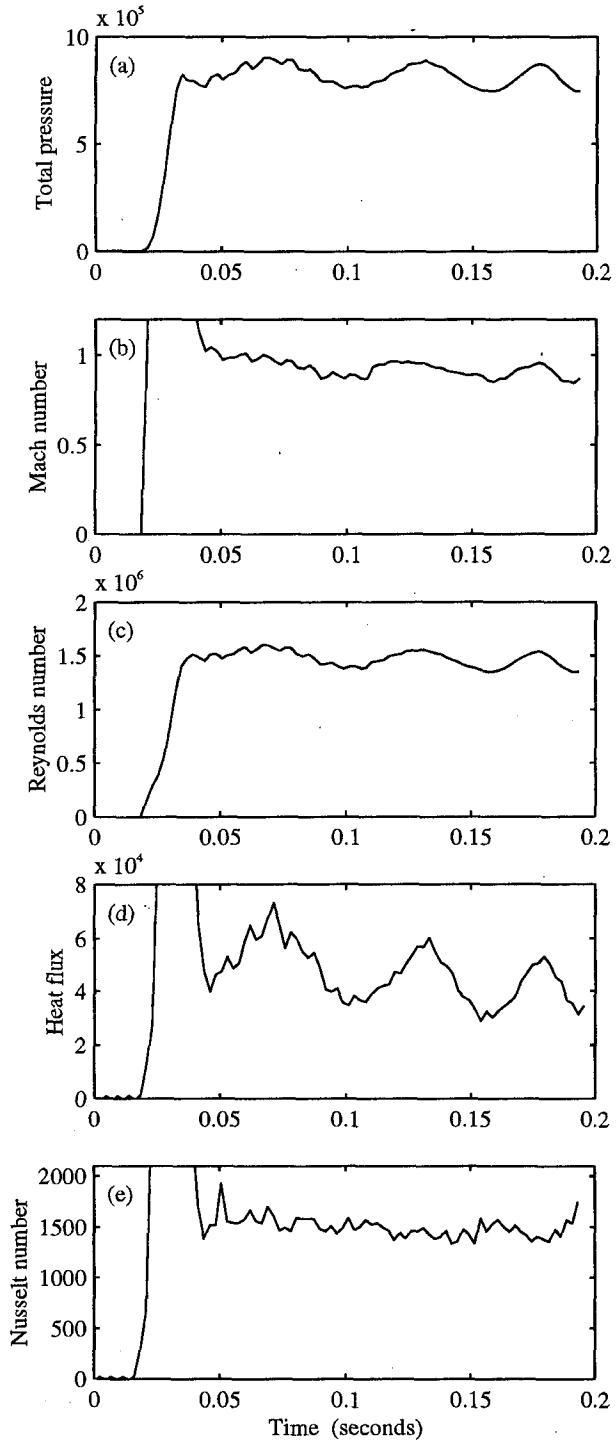

Fig. 3 Time history of (*a*) stage inlet total pressure, (*b*) Reynolds number, based on blade-relative exit conditions, (*c*) blade relative exit Mach number, (*d*) typical heat flux gage signal, (*e*) Nusselt number corresponding to (*d*)

vacuum, prior to firing the tunnel (2K, measured during tunnel commissioning). ΔT_q is the time history of the blade surface temperature rise; it is derived from the gage signal and is typically 7.5 K during the design condition period for a gage with Nu = 1000.

The recovery temperature is obtained from the relative total gas temperature and the Mach number at each gage location assuming a typical (mean of laminar and turbulent) recovery factor of 0.86. All calculations use the instantaneous (as opposed to time-mean) values of Re and ΔT corresponding to each measured $\dot{q}$ value. The Reynolds number correction is small (of order 8 percent) so the correctness of the assumption that the boundary layer is turbulent does not significantly affect the conclusions to be drawn from the comparisons that follow.

This "actual" Nusselt number is then scaled slightly to show the level that would be expected if the test had run exactly at the facility nominal design point relative temperature ratio of 1.138 using the relationship from Fitt et al. (1986): $\mathrm{Nu} = \mathrm{Nu}_i (T_w/T_g)^{-0.25}$ where the subscript i denotes constant properties, i.e.,

$$\mathrm{Nu}_{1.138} = \mathrm{Nu}_{\mathrm{measured}} \left(\frac{T_{g\mathrm{rel}}/T_w}{1.138} \right)^{-0.25}$$

ΔT is typically of order 25K and this makes the measured Nusselt numbers very dependent on the accuracy with which both the gas and blade temperatures can be measured. The validity of the prediction of the ΔT time history used in the conversion from heat flux to Nusselt number may be checked by examining the Nusselt number history throughout the test. Figure 3(*e*) shows that, as expected, the Nusselt number trace is essentially "flat" and this confirms the accuracy of the total temperature measurement. The piston oscillations are actually beneficial in that they enable the quality of the data to be assessed in this manner.

The time history of Nusselt number from each gage is finally converted to a time-mean Nusselt number based on the values over a 17 ms period during which the turbine passes through its design condition. Figures 4 and 5 show the run to run variation in this time mean value, at each gage location, for the forward and reverse rotation experiments, respectively: This shows the reliability of the data and indicates the number of runs (and hence confidence in interpretation) for the data at each point. A line has been drawn through the run-to-run mean value at each gage location and this line will be used for all subsequent comparisons. (Values of Mach and Reynolds number quoted in Table 1 are also mean levels over this period.)

The standard deviation σ of the forward rotation data for those positions that have two or more gages is, on average, given by $\sigma/\mu = 0.095$ where μ is the mean level at each position. Typically one has approximately 3 points per gage and this gives limits of $\pm 0.1\mu$ for an 80 percent confidence limit on the mean value. To this must be added any systematic errors from, for instance, gage calibration. It is estimated that the gage calibration is accurate to ± 1 percent and that the thermocouple measures the stage inlet temperature to ± 1K, which is equivalent, at the forward rotation gas-to-wall temperature ratio, to a

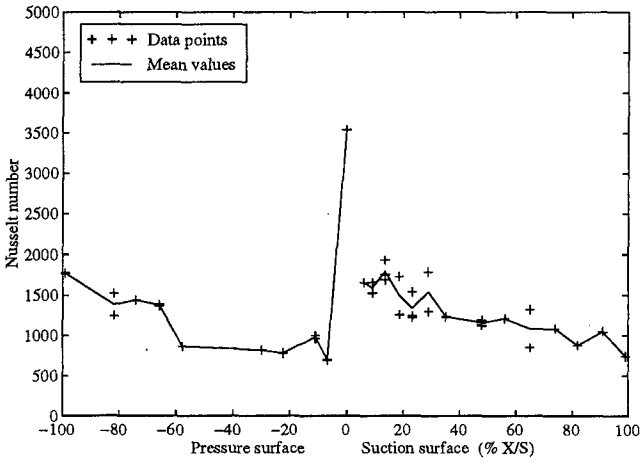

Fig. 4 Run to run Nusselt number scatter in forward rotation tests

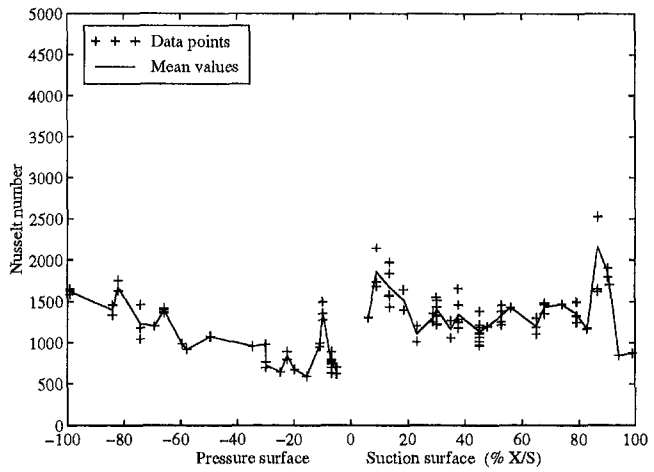

Fig. 5 Run to run Nusselt number scatter in reverse rotation tests

±4 percent uncertainty in $T_g - T_w$. The effective systematic uncertainty in Nusselt number is therefore estimated as ±5 percent and one could thus define the absolute Nusselt number accuracy as being ±15 percent for the average of three data points. (For the reverse rotation data $\sigma/\mu = 0.084$ and there are more data points for each gage, so the confidence limits are slightly smaller.) Note that this predicts the accuracy of the mean at each gage position: It does not imply that one expects all the data points to be within 10 percent of their mean value and, indeed, one can see data in Figs. 4 and 5 where the spread of values approaches ±20 percent. An "overall mean" value of σ/μ has been used above because there is no reason to believe, on the basis of a limited number of data points, that some gages exhibit greater random uncertainty than others. Some of the peaks and troughs in the mean Nusselt number lines in these two figures will be due to errors in this ±15 percent range; only features larger than this can safely be considered to be genuine.

Reverse rotation and cascade Nusselt number data presented in this paper have previously appeared in Garside et al. (1994); the absolute levels shown here differ slightly from the 1994 values as a result of the scaling described above, which should allow more meaningful comparisons to be made.

CFD Prediction Methods

The Rolls-Royce CFDS three-dimensional steady viscous code (based on the Moore Elliptic Flow Program "MEFP," Moore, 1989) was run by Slater (1993, forward rotation) and Garside (1995, reverse rotation) for this turbine geometry. CFDS is a three-dimensional viscous flow solver using a finite volume pressure prediction/correction algorithm and is designed specifically for the solution of turbomachinery flows. It provides a time-steady calculation (as opposed to unsteady, e.g., Unsflo), which is performed in a single frame of reference, i.e., one blade row at a time. It derives turbulent viscosity using either of two turbulence models depending on the distance from the wall: close to the wall the Prandtl–van Driest mixing length model is used, while farther out it uses the Baldwin and Lomax (1978) turbulence model.

Slater used a 88 × 43 × 35 (132440 node) grid for the blade prediction. Garside used a 107 × 41 × 36 grid resolution; the calculation is described in Garside et al. (1994). In each case the final calculation was preceded by calculations using a coarser grid to gain experience regarding convergence and investigate possible grid resolution effects; Slater tried a coarse grid of 58 × 29 × 27 and found that the progression to the fine grid produced a reduction in predicted Nusselt numbers of order 10 percent. There is no proof that the final grid was fine enough to avoid any further grid dependency; in each case the fine grid was the finest possible with the memory available. The fine grid near-wall points were at 0.006 mm from the surface and were chosen to be within the estimated thickness of the laminar sublayer around the leading edge. The maximum grid expansion factor was two.

The input flow parameters used by CFDS include the radial distributions of relative stagnation pressure, temperature, inlet velocity, and inlet static pressure together with an exit static pressure at one point.

The forward rotation prediction used input conditions derived from NGV exit traverses on an annular, continuous flow facility; this used the present turbine components with the rotor removed. These input conditions were modeled in an input generator program using an axisymmetric streamline curvature prediction to ensure that CFDS used a combination of pressure, angle, and velocity distributions compatible with the overall stage mass flow. Probe blockage effects in the continuous flow facility meant that traversing close to the endwalls was not possible. Subsequent CFDS predictions for the NGV row suggest that there was approximately 6 deg of overturning close to the inner endwall: In this region, extrapolation of the traverses on which rotor prediction was based had implied 5 deg of underturning relative to the flow angle at 10 percent span. This uncertainty over the boundary layer swirl means that the results from this prediction should only be considered valid for blade sections at more than 10 percent span. Predictions in the root region will not be presented here.

The reverse rotation input conditions did not include a boundary layer on the annulus walls upstream of the grid input plane at 70 percent blade axial chord from the leading edge. The flow upstream of this plane is accelerating toward the annular contraction where the nozzle guide vanes would traditionally be situated so the endwall boundary layer here is likely to be thin and have little effect on secondary flow within the rotor passage.

Garside (1995) measured a turbulence intensity of 1.5 percent in the parallel inlet annulus (extreme left-hand side of Fig. 2) and estimated that the annulus contraction as the flow approached the rotor in his reverse rotation case would reduce this to 0.5 percent Tu in the absolute frame of reference. The equivalent in the blade-relative frame would be of order 0.4 percent. The pump tube and annular gate valve assembly is the same for both forward and reverse rotation tests so the 1.5 percent level would also exist in the forward rotation case; the acceleration through the nozzle guide vanes would, as in the reverse rotation case, reduce this free-stream intensity to much less than 1 percent. A further estimate of rotor inlet turbulence can be obtained from unsteady velocity data measured by a hot-wire anemometer mounted on a blade leading edge (Sheldrake and Ainsworth, 1995). Figure 6(a) shows the power spectral density $(1/(\bar{M})^2)(d(M')^2/df)$ of the blade-relative Mach number. The wake passing frequency, 5 kHz, and its harmonics can be clearly seen as peaks; these components are effectively the Fourier transform of the periodic component of the vane exit flowfield. The remaining points in the spectral density are produced by random unsteadiness in the flow. Summing the area under the spectral density, with the wake-passing harmonics removed, produces the cumulative energy distribution shown in Fig. 6(b). This distribution must have three components: turbulence in the free stream, turbulence in the NGV wakes, and nonperiodic flow features, such as shock waves, that have slightly different positions from passage to passage. (Shock waves can in fact be clearly seen in the Mach number traces for some passages.) The cumulative energy should therefore be considered very much as an upper limit for the turbulent energy in the flow.

The wake passing harmonics dominate the spectrum at frequencies up to 17 kHz. Taking the sum of the nonharmonic spectral density terms above this limit gives a fractional un-

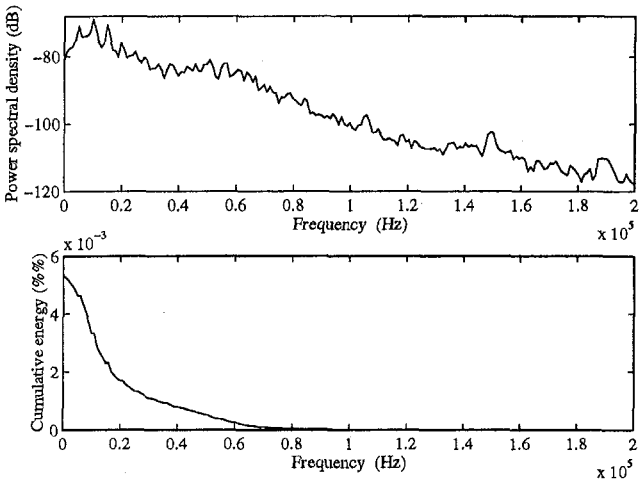

Fig. 6 (*a*) Power spectral density of velocity unsteadiness in relative frame at blade leading edge, (*b*) cumulative energy, excluding wake-passing harmonics, of unsteady intensity

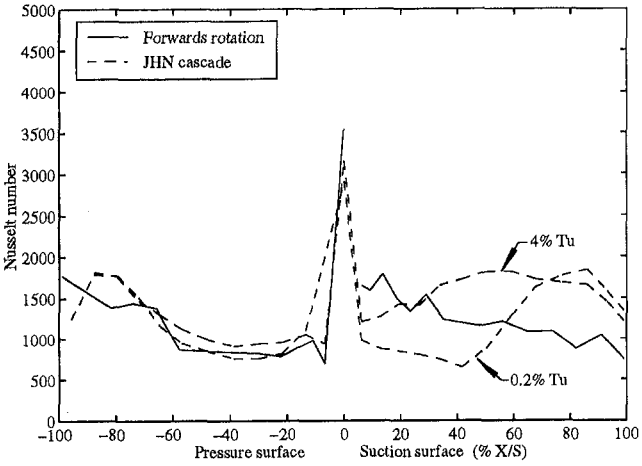

Fig. 7 Midheight forward rotation versus Nicholson's 34 mm chord cascade data

steadiness of 4.5 percent. The mean velocity measured by the wire is 130 m/s so this 17 kHz limit corresponds to a wavelength of 7.6 mm, i.e., roughly half the NGV throat width of 15 mm. One can therefore conclude that the root-mean-square turbulence intensity averaged over a wake passing period must be less than 4.5 percent. Single-sensor measurements in a flowfield of this nature cannot distinguish turbulence from shock waves, but it is nevertheless interesting to define an upper limit in this manner.

The CFDS predictions were performed prior to the hot wire test and various data sets were used with blade inlet turbulence intensities of 0.5, 1, and 2 percent. This was done to investigate the effects of differing turbulent viscosities, over a useful range, rather than an attempt to model a particular experimental flowfield. These various turbulence intensities made little difference to the predictions; differences were, however, seen as a result of specifying alternative blade surface intermittency distributions.

The state of the blade surface boundary layers had to be specified explicitly because CFDS cannot at present predict transition; this was done by specifying an chordwise distribution of intermittency. The forward rotation calculation was run both with a fully turbulent intermittency distribution and with a suction surface intermittency chosen to match the intermittency inferred from Nicholson's fast-response heat flux measurements (labeled as "laminar" in figures here). This prediction should therefore appear similar to the "0.2 percent *Tu*" line in Fig. 7.

The reverse rotation predictions included four different combinations of intermittency and free-stream turbulence in an attempt to study the sensitivity to input parameters and to identify a boundary layer state that would closely match the experimental data. In three of these cases the boundary layers were defined as being fully turbulent over the whole surface, with turbulence intensities of 0.5, 1, and 2 percent, respectively (in each case, the fractional turbulence intensity was assumed constant throughout the grid). The fourth case used an intermittency distribution predicted by a two-dimensional boundary layer code (Forest, 1978), which was turbulent over the pressure surface, and on the suction surface rose from 0 at the leading edge to 0.096 at the trailing edge. The suction surface distribution may be empirically correlated using the formula $\sigma = 0.207(X/S)^3 - 0.14(X/S)^2 + 0.0306X/S - 0.0004$. This "transitional boundary layer" case used a free-stream turbulence intensity of 1 percent.

The CFDS prediction using this intermittency agreed well with the two-dimensional code (Garside, 1995) and this suggests that the MEFP grid had sufficient resolution to produce accurate heat transfer predictions under these conditions.

Experimental Data

Forward Rotation Versus Cascade Tests. Figure 7 compares the forward rotation time-mean Nusselt number line with Nicholson's cascade data. This cascade test used a parallel bar grid to generate the higher (4 percent) turbulence intensity but was, apart from this, a steady flow test (albeit in a transient facility), i.e., without any form of wake passing. Nicholson found that free-stream turbulence caused transition on the *suction surface;* the rotor data show higher heat transfer over the first 20 percent of the surface and lie between the cascade's laminar and turbulent levels thereafter, until the 0.2 percent turbulence cascade test undergoes transition at $x/s = 60$ percent. The rotor and the cascade have slightly different velocity distributions on the suction surface, despite having the same aerofoil profile, because the cascade is two dimensional, while the rotor is haded on the inner wall, as shown in Fig. 2. This comparison is shown not in the expectation that the two tests should give identical results over the whole surface, but rather to investigate whether anything can be learned from the available data.

Figure 8 compares unhaded velocity distributions measured in the blowdown cascade (Mee, 1990) with the rotor mid-height pressure distribution measured by surface-mounted kulites. Rotor Mach number is based on the ratio of surface static pressure to blade-relative total pressure (from a Kulite mounted in a pitot configuration on the blade leading-edge); in each case the average is taken over the 17 ms during which design conditions

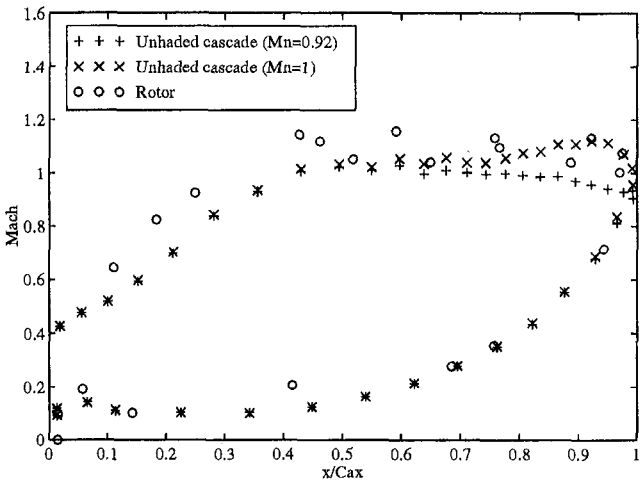

Fig. 8 Effects of hade on Mach number distribution

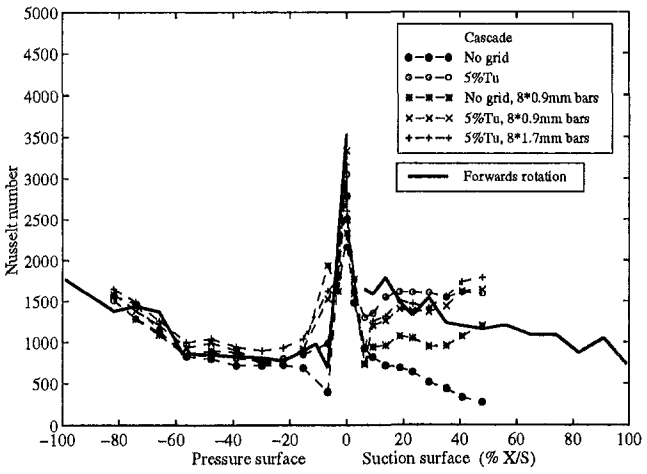

Fig. 9 Midheight forward rotation versus Doorly's 52 mm chord cascade data

pertain. The peaks seen on the suction surface aft of $x/\mathrm{Cax} = 0.4$ appear to be a genuine flow feature induced by local variations in surface curvature. This pressure data is described more fully in Moss et al. (1997).

The rotor has more acceleration over the early suction surface and the higher Reynolds numbers in this region appear to make transition occur earlier. The later transition and more prolonged acceleration in the cascade tests leads to thinner boundary layers and higher (relative to the rotor) heat transfer on the rear suction surface. The confidence limit on pressure ratio based on the rotor kulites is ±1.75 percent so the two points on the early *pressure surface* do not imply that there is any significant difference in velocity distribution here. The excellent pressure surface agreement in Fig. 7 therefore shows that, where the velocity distribution is the same, the two experiments give very similar results. This is a valuable conclusion since it confirms that, despite the complexity of the thin film gages on an enamel substrate, their laser calibration and the in-shaft electronics and slip ring system (Moss and Ainsworth, 1993) the present data do, in fact, agree well with data taken many years previously using completely different instrumentation.

The leading edge Nusselt number can be predicted by considering it to be a laminar boundary layer over a cylinder in crossflow (Kays, 1966): $\mathrm{Nu}_R = 0.81\ \mathrm{Re}_R^{0.5}\ \mathrm{Pr}^{0.4} = 134$ with Re based on mean velocity across the rotor inlet plane; R is cylinder radius. Scaling this for comparison with test data at the nominal design point gives $\mathrm{Nu} = \mathrm{Nu}_R(C_{ax}/R)(1/1.138)^{-0.25} = 4020$. This is slightly larger than the measured forward rotation Nusselt number of 3500 at the leading edge; the discrepancy can be explained in terms of the enamel layer making the leading edge radius larger than the nominal value, but may also be partly due to the distortion of the leading edge flowfield by the presence of the aerofoil behind it; it is not an isolated cylinder.

Figure 9 compares the forward rotation data against Doorly's cascade data. Doorly used rotating bars to produce moving wakes and shock waves that simulated those from an upstream blade row. The bar diameters and bar-to-blade axial spacing were chosen to produce wakes that in terms of width, velocity deficit, and turbulence spectrum would simulate the wake from a nozzle guide vane.

Mechanical considerations limited the smallest possible bar diameter to 0.9 mm; this generated wakes typical of a film-cooled nozzle guide vane, which will be stronger than those expected from the uncooled vanes used in the rotor experiment. (Blade leading edge Kulite measurements of the rotor inlet flowfield, (Moss et al., 1997), do not allow an easy comparison with the discrete wakes produced by the rotating bar experiment: The rotor interacts with the flow field and the Kulite signal cannot easily be compared with that from a small probe behind a bar wake generator.)

In general, his suction surface data show increasing levels of induced unsteadiness leading to increasing intermittency and higher Nusselt numbers; this mimics Nicholson's data. The forward rotation suction surface data show a different trend to these cascade results. The comparison of forward and reverse rotation data (Fig. 11) will show that heat transfer on the early suction surface is insensitive to wake passing and one must conclude that the similarity of the forward rotation and high turbulence cascade heat transfer levels here is not a result of unsteady flow in the turbine: instead, it results from the differences in velocity distribution as discussed in connection with Fig. 7.

The rotor *pressure surface* data agree well with both sets of cascade results. The cascade tests show that wake passing and free-stream turbulence intensities of up to 5 percent have little effect on the time-mean heat transfer here; it is therefore unlikely that the rotor pressure surface Nusselt numbers should differ from these values, and the excellent agreement seen gives confidence in the quality and accuracy of the data.

Doorly and Oldfield (1985) noted the presence of a separation bubble causing low heat transfer at $X/S = 4$ percent on the pressure surface. This can also be seen in the forward rotation data, Fig. 9. The boundary layer state over the rest of the pressure surface proved difficult to characterize but they tentatively defined it as transitional over the $X/S = 20$ to 60 percent range, where a slight heat transfer increase is seen in the presence of free-stream turbulence, and turbulent thereafter. The unsteady reattachment of this separation probably provides the disturbance that keeps it in this state even in the absence of free-stream turbulence. Turbulence studies by Moss and Oldfield (1992) have shown that free-stream turbulence can increase the heat transfer through a turbulent boundary layer. This suggests that the observed increases in pressure surface Nusselt number as free-stream turbulence increases could occur even with a boundary layer that was fully turbulent from $X/S = 20$ percent onwards, i.e., although likely, the present data does not inevitably prove it to be transitional.

Forwards Rotation: Spanwise Variation. Figure 10 shows the spanwise variation in rotor Nusselt numbers for the forward rotation tests. The midheight gages show lower Nusselt number levels than the corresponding gages at any of the other four (5, 10, 90, 95 percent span) sections. In particular, the root, midtip, and tip sections show suction surface Nusselt numbers that are approximately double those at midheight.

The pressure surface midheight and midtip sections show very similar Nusselt number levels. The forward rotation data

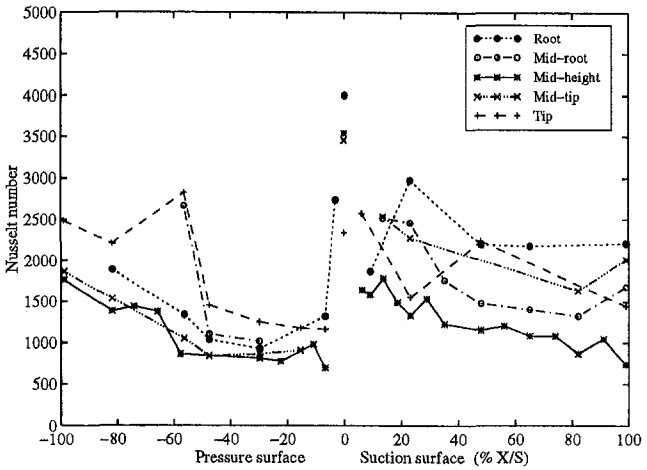

Fig. 10 Forward rotation data at 5, 10, 50, 90, and 95 percent span

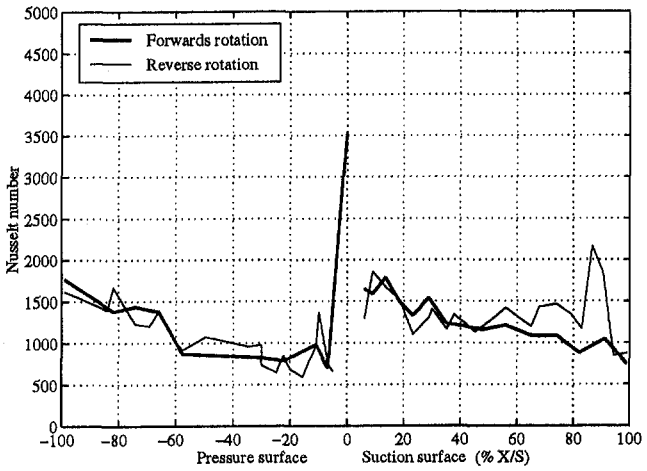

Fig. 11 Forward versus reverse rotor Nusselt numbers at midheight

show an increased level at the tip section, possibly due to the boundary layer being sucked into the overtip gap, and the root and midroot sections show an increase of about 20 percent over the midheight case. The peaks at −58 percent X/S on the tip and midroot sections are not easily explained: In each case, they are points from a single test but there is no reason to suppose that they are unreliable.

The suction surface shows the midheight section as having less heat transfer than any of the root and tip sections: Nusselt numbers generally fall from root to midheight and then start rising again. Up to 40 percent X/S the off-midheight Nusselt numbers are higher than those seen in cascade tests (Fig. 7) and so are presumably not simply the result of transition to a turbulent boundary layer: It seems likely that this results from a horseshoe vortex or overtip flow interaction. On the root section, the continued high Nusselt number on subsequent gages suggests that they are all affected by secondary flow and the horseshoe vortex.

Forward Versus Reverse Rotation Data. Figure 11 compares the forward rotation (Allan, 1990) and reverse rotation data (Garside, 1995) data at midheight.

The mean levels of the two midheight sets of data (obtained by integrating around the whole perimeter) are very close, within 1 percent of each other. The excellent agreement on the pressure surface, which, given the insensitivity to turbulence seen in cascade, would not be expected to show any significant change, seems to confirm that there has been no change in the accuracy of the experiment despite the measurements being taken several years apart.

The forward and reverse rotation results are also very similar on the suction surface up to $X/S = 50$ percent. The Nusselt number levels on the early suction surface imply, as before, transition close to the leading edge. In the reverse rotation case, however, the late suction surface shows a sudden rise in Nusselt number, which appears to imply that some relaminarization has taken place followed, at this point, by a second transition, possibly due to the lower blade-relative exit Mach number under reverse rotation producing an adverse pressure gradient in this region.

The similarity of the forward and reverse rotation Nusselt numbers suggests that the rotor suction surface boundary layer is predominantly turbulent and that the differences in Nusselt number between high turbulence cascade and rotor are due to differences in velocity distribution, and to transition occurring earlier on the rotor, rather than to differences in intermittency.

Reverse Rotation Data: Spanwise Variation. Figure 12 shows the spanwise variation of Nusselt numbers from the reverse rotation tests. The root section provided very few data points and has not been included here. The midtip and midheight sections show very similar levels, though the suspected transition seen on the rear suction surface at the midheight section is, if present, not clearly shown at midtip due to a lack of detail here. The suction surface Nusselt numbers show a steady rise in level that appears different to the fall seen on the forward rotation midheight data though, as seen in Fig. 11, the difference in level is only appreciable beyond the 65 percent chord position.

It is also interesting to note that the midroot Nusselt numbers are lower than at midheight on the suction surface and higher on the pressure surface, whereas in the forward rotation case both surfaces showed an increase toward the root. This may be due to the reversal in the direction of the passage vortex, but is also likely to be influenced by differences in the blade inlet angle in this region. The reverse rotation experiment simulates forward rotation blade relative inlet angles to ±3 deg at all sections above 10 percent span, but in the root region the absence of NGV secondary flows leads to a much larger discrepancy in inlet angle.

The fact that the off-midheight data show significant differences between the forward and reverse rotation tests in spite of the similarity of the midheight data confirms the importance of rotation and three-dimensional effects with regard to the prediction of heat transfer over the whole blade.

Influence of Unsteady Phenomena

The thin film gages have a frequency response of order 100 kHz and thus show a characteristic "wake passing" signature. Moss et al. (1995) showed that the fluctuations could be reasonably well predicted by a model that assumed a constant heat transfer coefficient together with a relative total temperature that varied isentropically with the blade surface static pressure as measured by embedded Kulite pressure transducers. Figure 13 compares a typical heat flux trace with such a prediction. The heat flux fluctuations are a significant fraction of the mean level because the gas-to-wall temperature ratio (Table 1) is small in the blade-relative frame. Similar predictions for other midheight gages (Fig. 14) show rms levels close to those measured at most positions around the blade surface. (Two gages disagree with this explanation: D09, which is downstream of the separation bubble and presumably experiences unsteady reattachment, and B06, which is currently unexplained.)

The explanation of the unsteady heat flux in terms of a gas temperature fluctuation implies that wake-induced unsteady transition is relatively insignificant, if indeed it occurs at all, in this turbine. This explains why the forward and reverse rotation tests show such similar time-mean Nusselt numbers at mid-

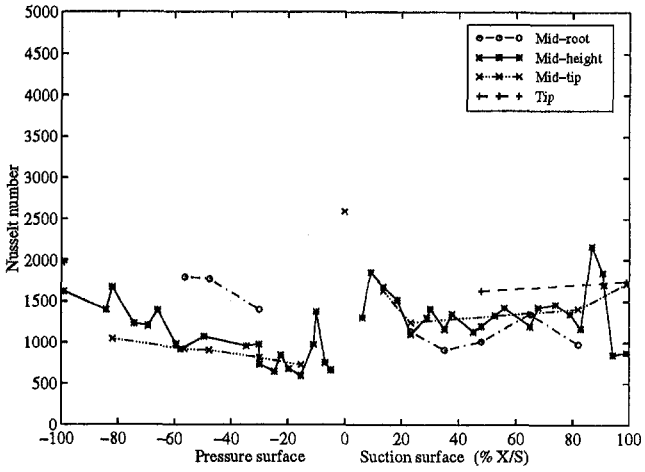

Fig. 12 Reverse rotation data at 10, 50, 90, and 95 percent span

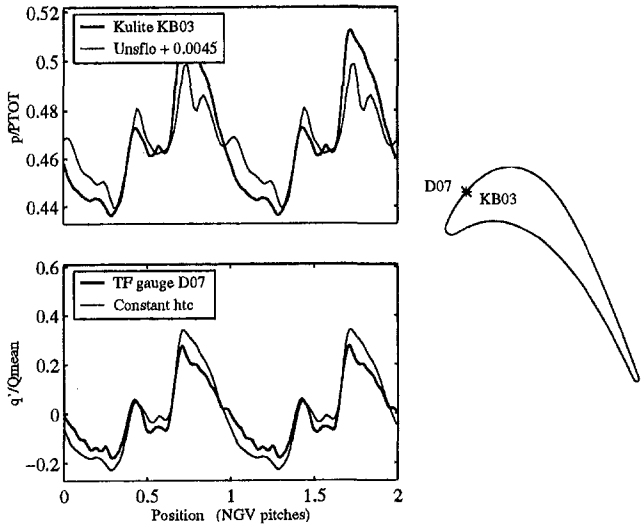

Fig. 13 Forward rotation unsteady heat flux may be explained in terms of gas temperature fluctuations (Moss et al., 1995)

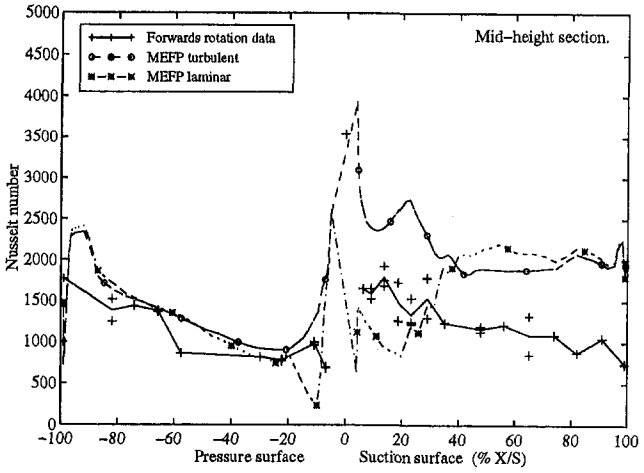

Fig. 15 Forward rotation data versus CFDS: 50 percent span

height. It has also proved possible to predict the heat flux fluctuation on the suction surface crown of the midroot section (Moss et al., 1997) in a similar fashion: This implies that the increased heat flux toward the root in the forward rotation case results from relatively steady three-dimensional flows rather than wake-induced transition.

The differences in suction surface Nusselt numbers and susceptibility to turbulence between the rotor and cascade appears to be due to the differences in velocity distribution. The wake strength in the forward rotation test may be less than that produced in the rotating bar cascade test but, even, so, a considerable disturbance still exists (Moss et al., 1997). The fact that the forward and reverse rotation data are *so* similar on the early suction surface, and that the mean level here is higher than in cascade, implies that transition occurs very early on this surface with the "haded" velocity distribution and, in turn, that even a much stronger wake, e.g., from a cooled NGV, would probably have little effect on the Nusselt number distribution for this aerofoil.

The absence of any wake-induced increase in heat transfer is most unexpected; prior to this work it was widely supposed that turbulence in the NGV wakes would cause unsteady transition (Mayle, 1991) or produce periodic enhancement above the normal turbulent level. These differences between cascade and rotor measurements highlight the value of rotor testing. The present data provides a most rigorous and valuable test case: If unsteady phenomena do not affect heat transfer, sophisticated-time-steady codes such as CFDS should be able to predict heat transfer to a high degree of accuracy. It is anticipated that the present work will lead to greatly enhanced capabilities in this respect. Different aerofoil profiles, conversely, might indeed show sensitivity to wake-induced transition; it is hoped that further prediction work based on the cascade conditions will reveal more precisely the reasons for their sensitivity to turbulence.

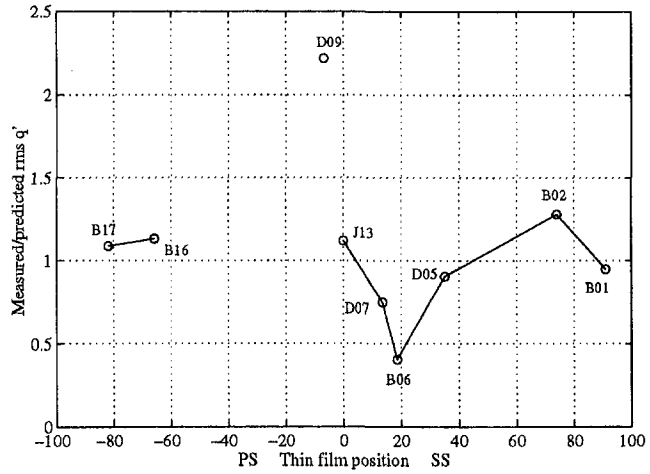

Fig. 14 Ratio of measured AC component of heat flux to that predicted from measured pressures

Comparisons With CFDS

Forward Rotation Data Versus CFDS. Figure 15 compares the midheight forward rotation data with CFDS. The pressure surface prediction agrees reasonably well with the data, with CFDS typically overpredicting by approximately 10 percent. The suction surface prediction, however, is nearly double the measured level; it is actually close, from $X/S = 30$ percent onward, to the turbulent level measured in cascade. This overprediction may indicate that, though the grid resolution was adequate for a laminar boundary layer, a finer grid would have been preferable for the turbulent case. The CFDS-predicted Nusselt number distributions also show more spatial unsteadiness than one might expect; it is not yet known whether these peaks and troughs are a realistic product of the velocity distribution or whether they simply imply a grid resolution problem.

At the midtip section (Fig. 16) the CFDS prediction overpredicts by approximately 20 percent on the pressure surface. Three of the four suction surface gages agree well with the predicted turbulent level, while the gage at $X/S = 82$ percent is 40 percent below the predicted level; this is, however, only a single data point.

At the tip section (Fig. 17) the pressure surface prediction is approximately 20 percent low. There is also one point at $X/S = 57$ percent that defies explanation, being nearly double the predicted level. The suction surface measurements at $X/S = 5$, 48, and 99 percent agree well with the turbulent CFDS. The measured dip at $X/S = 22$ percent may indicate that transition is occurring in the $X/S = 20$–40 percent region, i.e., rather later than shown for the "laminar" prediction.

Reverse Rotation Data Versus CFDS. Figure 18 compares reverse rotation measurements at 10 percent span with the CFDS prediction at this section. The measured pressure surface Nusselt numbers are approximately 50 percent above the midheight values but the CFDS predicted level is about 10

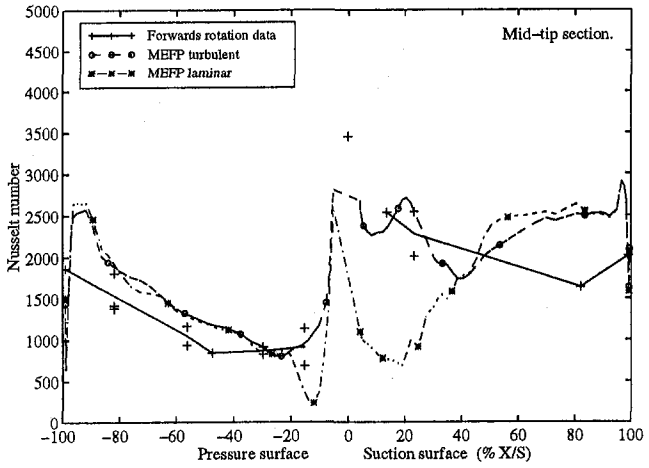

Fig. 16 Forward rotation data versus CFDS: 90 percent span

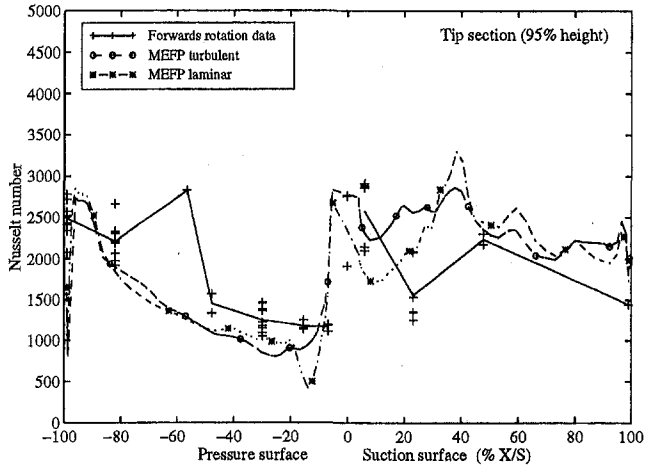

Fig. 17 Forward rotation data versus CFDS: 95 percent span

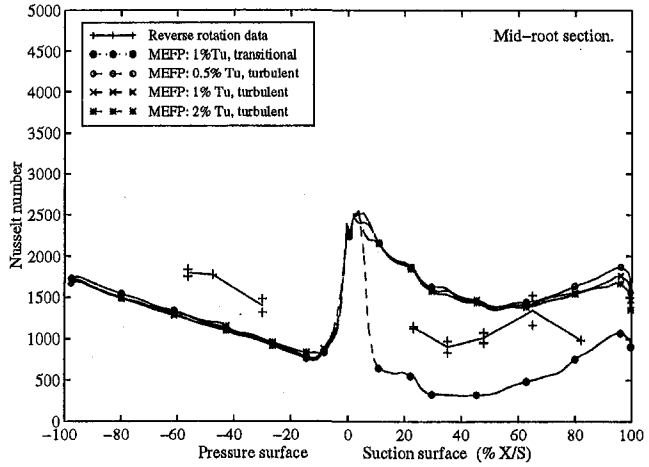

Fig. 18 Reverse rotation data versus CFDS: 10 percent span

percent lower than at midheight. The midheight data and turbulent prediction are, as expected, similar to the forward rotation case, but the midroot section shows an increase relative to the forward case that is not predicted.

On the suction surface the predicted Nusselt numbers are 10–20 percent lower than at midheight, which may be due to the horseshoe vortex entraining endwall fluid and thickening the boundary layer here. As at midheight, the suction surface measurements lie between the predicted transitional and turbulent levels.

Comparing the midheight and midroot data shows some evidence of secondary flow effects, in that the root measurements have higher pressure surface and lower suction surface values than at midheight.

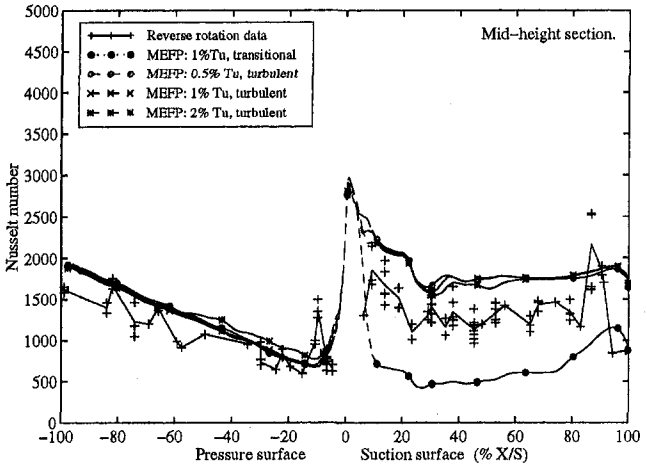

Fig. 19 Reverse rotation data versus CFDS: 50 percent span

Figure 19 compares the reverse rotation data with a CFDS prediction of Nusselt numbers at midheight. On the suction surface, there is a great difference between the CFDS predictions with turbulent boundary layers and that with a transitional boundary layer, with the experimental data about halfway between the two. It is clear that some way of accurately predicting the boundary layer state is essential if accurate predictions in this region are to be achieved. On the pressure surface, however, the choice of boundary layer state has little effect on the prediction, which is approximately 25 percent above measured levels.

Figure 20 shows the corresponding data at 90 percent span. The predicted pressure surface level is close to the midheight value until $X/S = 60$ percent, when it rises more rapidly; this could be due to a thinning of the boundary layer resulting from the overtip leakage. The experimental data is lower than at midheight: If the experimental facility experienced a relatively small degree of overtip leakage it is conceivable that the passage vortex would carry the shroud ring boundary layer onto the pressure surface with a corresponding low level of heat flux,

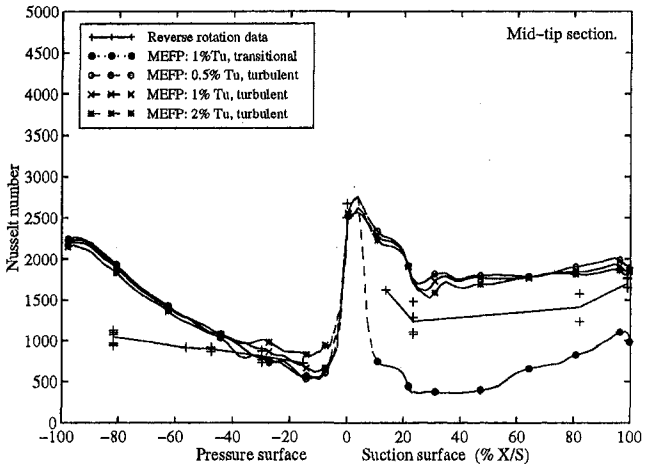

Fig. 20 Reverse rotation data versus CFDS: 90 percent span

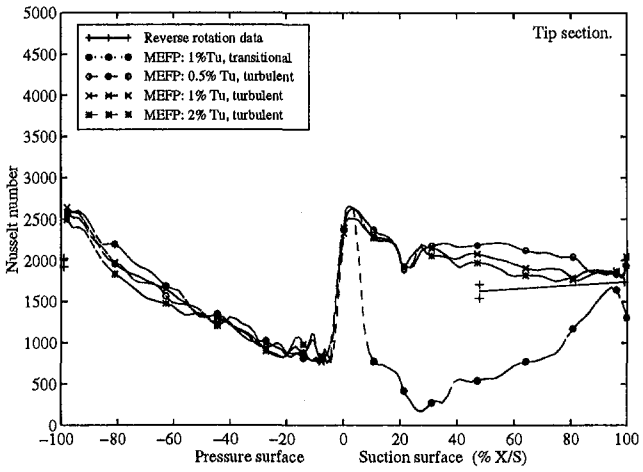

Fig. 21 Reverse rotation data versus CFDS: 95 percent span

though there is no actual evidence that this occurs; conversely, one may infer that CFDS has simply overpredicted the tip leakage flow.

On the suction surface there are only a limited number of experimental points, but they do show very similar Nusselt numbers to the midheight gages. The CFDS prediction is very similar to that at midheight; although the predicted levels differ from the measured data, it is encouraging that the trends in heat transfer when comparing different spanwise sections are similar to those seen experimentally.

Figure 21 shows the data from the tip (95 percent) section. There are few usable gages here but the data seem to confirm the general trend seen at 50 and 90 percent height of the suction surface data being approximately 25 percent below predicted levels.

Conclusions

At midheight, the forward and reverse rotation Nusselt numbers are very similar. This was most unexpected as, hitherto, suction surface intermittency had been thought to depend strongly on wake-induced transition.

On the pressure surface, both sets of rotor data resemble cascade measurements.

Suction surface measurements differ from cascade values in two ways. First, the blade is found to lie between the cascade laminar and turbulent levels. Second, the cascade time-mean heat transfer was very sensitive to changes in inlet turbulence level and in this respect behaves differently from the blade.

The similarity of the forward and reverse rotation Nusselt numbers suggests that the rotor suction surface has a turbulent boundary layer and that the differences in Nusselt number between high turbulence cascade and rotor are due to differences in velocity distribution, and to transition occurring earlier on the rotor, rather than to differences in intermittency.

The unsteady component of each heat transfer signal was well predicted in terms of a constant heat transfer coefficient and temperature fluctuations arising isentropically from the unsteady static pressure field. This prediction describes an AC fluctuation that does not affect the time-mean level and hence explains why, despite the large fluctuations seen in the forward rotation data, the time-mean level is the same as from the reverse rotation test.

Since the time-mean heat flux is unaffected by unsteady effects, the present data provide an invaluable test case for the time-steady CFD and boundary layer codes currently used for turbine design. The unsteady pressure and heat flux data captured during these tests should also prove useful in the development of three-dimensional unsteady methods; although time-steady methods may be sufficient for heat transfer prediction, unsteady codes are essential for predicting unsteady flow phenomena in the quest for increased aerodynamic efficiency.

The forward rotation data show heat transfer enhancement of up to 100 percent in the root and tip regions and, as at midheight, this appears to be a steady-state condition. The reverse rotation tests show smaller changes and different trends at the off-midheight sections. These rotational effects show the need for three-dimensional predictions; the combination of cascade, forward, and reverse rotation data provides a unique test case for the accurate modeling of rotational terms in such codes.

CFDS overpredicts the midheight pressure surface heat flux by approximately 20 percent; it is, nevertheless, still a usefully accurate method here. On the suction surface the solution is very dependent on the intermittency distribution chosen. Possible solutions straddle the experimental points, but are either 50 percent high (turbulent) or 50 percent too low (transitional). The fact that CFDS overpredicts Nusselt numbers for a turbulent boundary layer on the suction surface may indicate that even 130,000 nodes are insufficient for accurate heat transfer calculations of this kind. The choice and assessment of CFD codes for heat transfer prediction is, together with their memory requirements, a topic of continual interest. It is hoped that the comparisons presented here will provide a useful record of the state of the art.

Acknowledgments

The authors would like to thank Rolls-Royce plc, the Defence Research Agency (Pyestock), the Ministry of Defence and the Department of Trade and Industry for their support of this work.

References

Abhari, R. S., Guenette, G. R., Epstein, A. H., and Giles, M. B., 1992, "Comparison of Time-Resolved Turbine Rotor Blade Heat Transfer Measurements and Numerical Calculations," ASME JOURNAL OF TURBOMACHINERY, Vol. 114, pp. 818–827.

Ainsworth, R. W., Schultz, D. L., Davies, M. R. D., Forth, C. J. P., Hilditch, M. A., Oldfield, M. L. G., and Sheard, A. G., 1988, "A Transient Flow Facility for the Study of the Thermofluid Dynamics of a Full Stage Turbine Under Engine Representative Conditions," ASME Paper No. 88-GT-144.

Ainsworth, R. W., Allen, J. L., Davies, M. R. D., Doorly, J. E., Forth, C. J. P., Hilditch, M. A., Oldfield, M. L. G., and Sheard, A. G., 1989, "Developments in Instrumentation and Processing for Transient Heat Transfer Measurements in a Full Stage Model Turbine," ASME JOURNAL OF TURBOMACHINERY, Vol. 111, pp. 20–27.

Ainsworth, R. W., Dietz, A. J., and Nunn, T. A., 1991, "The Use of Semi-Conductor Sensors for Blade Surface Pressure Measurement in a Model Turbine Stage," ASME *Journal of Engineering for Gas Turbines and Power,* Vol. 113, pp. 261–268.

Allan, W. D. E., 1990, "Heat Transfer and Instrumentation Studies on Rotating Turbine Blades in a Transient Flow Facility," DPhil thesis, University of Oxford.

Baldwin, B. S., and Lomax, H., 1978, "Thin Layer Approximation and Algebraic Model for Separated Turbine Flows," AIAA Paper No. 78-257.

Blair, M. F., 1994, "An Experimental Study of Heat Transfer in a Large Scale Turbine Rotor Passage," ASME JOURNAL OF TURBOMACHINERY Vol. 116, pp. 1–13.

Dietz, A. J., and Ainsworth, R. W., 1992, "Unsteady Pressure Measurements on the Rotor of a Model Turbine Stage in a Transient Flow Facility," ASME Paper No. 92-GT-156.

Doorly, D. J., 1984, "A Study of the Effect of Wake-Passing on Turbine Blades," DPhil Thesis, University of Oxford.

Doorly, D. J., and Oldfield, M. L. G., 1985, "Simulation of Wake Passing in a Stationary Turbine Rotor Cascade," AIAA *Journal of Propulsion and Power,* Vol. 1, No. 4, p. 316.

Doorly, D. J., Oldfield, M. L. G., and Scrivener, C. T. J., 1989, "Wake Passing in a Turbine Rotor Cascade," AGARD CP390 pp. 7.1–7.18.

Dunn, M. G., Seymour, P. J., Woodward, S. H., George, W. K., and Chupp, R. E., 1989, "Phase-Resolved Heat Transfer Measurements on the Blade of a Full-Scale Rotating Turbine," ASME JOURNAL OF TURBOMACHINERY, Vol. 111, pp. 8–19.

Fitt, A. D., Forth, C. J. P., Robertson, B. A., and Jones, T. V., 1986, "Temperature Ratio Effects in Compressible Turbulent Boundary Layers," *Int. J. Heat Mass Transfer,* Vol. 29, No. 1, pp. 159–164.

Forest, A. E., 1978, "Engineering Predictions of Transitional Boundary Layers," AGARD CP 224.

Garg, V. K., and Abhari, R. S., 1996, "Comparison of Predicted and Experimental Nusselt Number for a Film-Cooled Rotating Blade," ASME Paper No. 96-GT-223.

Garside, T., Moss, R. W., Ainsworth, R. W., Dancer, S. N., and Rose, M. G., 1994, "Heat Transfer to Rotating Turbine Blades in a Flow Undisturbed by Wakes," ASME Paper No. 94-GT-94.

Garside, T., 1995, "The Heat Transfer and Aerodynamic Performance of a Rotating Turbine in the Absence of Upstream Nozzle Guide Vane Wakes," DPhil thesis, University of Oxford.

Giles, M. B., 1988, "Calculation of Unsteady Wake-Rotor Interaction," AIAA *Journal of Propulsion and Power,* Vol. 4, pp. 356–362.

Guenette, G. R., Epstein, A. H., Giles, M. B., Haimes, R., and Norton, R. J. G., 1989, "Fully Scaled Transonic Turbine Rotor Heat Transfer Measurements," ASME JOURNAL OF TURBOMACHINERY, Vol. 111, pp. 1–7.

Hilditch, M. A., and Ainsworth, R. W., 1990, "Unsteady Heat Transfer Measurements on a Rotating Turbine Blade," ASME Paper No. 90-GT-175.

Hilditch, M. A., Fowler, A., Jones, T. V., Chana, K. S., Oldfield, M. L. G., Ainsworth, R. W., Hogg, S. I., Anderson, S. J., and Smith, G. C., 1994, "Installation of a Turbine Stage in the Pyestock Isentropic Light Piston Facility," ASME Paper No. 94-GT-277.

Kays, W. W., 1966, *Convective Heat and Mass Transfer,* McGraw-Hill, New York.

Mayle, R. E., 1991, "The Role of Laminar–Turbulent Transition in Gas Turbine Engines," ASME JOURNAL OF TURBOMACHINERY, Vol. 113, pp. 509–537.

Mee, D. J., Baines, N. C., Oldfield, M. L. G., and Dickens, T. E., 1992, "An Examination of the Contributions to Loss on a Transonic Turbine Blade in Cascade," ASME JOURNAL OF TURBOMACHINERY, Vol. 114, pp. 155–162.

Moss, R. W., and Ainsworth, R. W., 1993, "A Transient Measuring Technique for Heat Transfer to Metallic Aerofoils," *Proc. Eurotherm 32, Heat Transfer in Single Phase Flows,* Oxford.

Moss, R. W., Sheldrake, C. D., Ainsworth, R. W., Smith, A. D., and Dancer, S. N. D., 1995, "Unsteady Pressure and Heat Transfer Measurements on a Rotating Blade Surface in a Transient Flow Facility," AGARD CP571, pp. 22.1–22.11.

Moss, R. W., Ainsworth, R. W., and Sheldrake, C. D., 1997, "The Unsteady Pressure Field Over a Turbine Blade Surface: Visualization and Interpretation of Experimental Data," ASME Paper No. 97-GT-474.

Moss, R. W., and Oldfield, M. L. G., 1992, "Measurements of the Effect of Freestream Turbulence Length Scale on Heat Transfer," ASME Paper No. 92-GT-244.

Nicholson, J. H., Forest, A. E., Oldfield, M. L. G., and Schultz, D. L., 1984, "Heat Transfer Optimized Turbine Rotor Blades—An Experimental Study Using Transient Techniques," ASME *Journal of Engineering for Gas Turbines and Power,* Vol. 106, pp. 173–181.

Sheldrake, C. D., and Ainsworth, R. W., 1995, "The Use of Hot-Wires Applied to Aerodynamic Measurements in a Model Turbine Stage," presented at the First European Conference on Turbomachinery Fluid Dynamic and Thermodynamic Aspects, Nuremberg.

Slater, J. T. D., 1993, "Three-Dimensional Aerodynamic Studies of a Turbine Stage in a Transonic Flow Facility," DPhil Thesis, University of Oxford.

Influence of Gap Leakage Downstream of the Injection Holes on Film Cooling Performance

Y. Yu

M. K. Chyu

Department of Mechanical Engineering,
Carnegie Mellon University,
Pittsburgh, PA 15213

This study investigated a practical but never exploited issue concerning the influence of flow leakage through a gap downstream on the film cooling performance with discrete-hole injection. A heat transfer system as such can be categorized as either a three-temperature or a four-temperature problem, depending on the direction of leakage through the gap. To characterize a three-temperature-based film cooling system fully requires knowledge of both local film effectiveness and heat transfer coefficient. A second film effectiveness is necessary for characterizing a four-temperature problem. All these variables can be experimentally determined, based on the transient method of thermochromic liquid crystal imaging. Although the overall convective transport in the region is expected to be dependent on the blowing ratios of the coolants, the mass flow ratio of the two injectants, and the geometry, the current results indicated that the extent of flow injection or extraction through the gap has significant effects on the film effectiveness and less on the heat transfer coefficient, which is primarily dominated by the geometric disturbance of gap presence.

Introduction

Film cooling is one of the most effective methods for thermal control of gas turbine components subjected to intensive heat load. Its effectiveness for the cooling of turbine blades and vanes is well known (Goldstein, 1971), and expected to extend further, as the operating temperature of future gas turbines increases for higher performance. As a result of recent success in the developments of advanced combustors, the temperature profile at a combustor exhaust has become more uniform and flattened. Such a desirable temperature profile, however, presents a substantial thermal penalty to those components exposed to the edges of the flattened temperature profile. Thus film cooling is often implemented to protect the endwalls immediately downstream of the combustor and ahead of the first-stage vane. The turbine structure in this region usually consists of several individual components instead of one single piece. This type of assembly almost always produces a gap, formed in the junction of different components to accommodate thermal expansion for different operating conditions. Usually no seal is implemented in the gap to separate the hot passage gas to the flow outside, so that a leakage flow through the gap can be induced radially, when the static pressure across the gap is different. Depending on the pressure differential, the leak through the gap may flow either into or out of the turbine gas passage, presenting an uncertain issue, which further complicates the problem.

The primary objective of this research is to characterize the film cooling performance experimentally in a region affected by the presence of a gap between mating surfaces. A test section, as sketched in Fig. 1, consists of a row of five discrete holes with a 30-deg injection angle, followed by a transverse gap on a flat surface, constructed to house the research. While a study of this nature has not been found in the open literature, the transport phenomena involved here have two key contributing factors: One is the film cooling with discrete, inclined holes, and the other is the convective transport over a discontinuous surface. The transport features for the latter are considered to be similar to those with flow over a deep cavity. The heat and momentum transfer in the vicinity of a rectangular cavity is dominated by a highly turbulent shear layer initiated at the top, sharp corner of the downstream-facing wall (upstream sidewall) (Chyu and Goldstein, 1986; Chyu et al., 1987; Chyu and Schwarz, 1990). Depending on the approaching flow conditions and cavity geometry, the shear layer can have profound effects on the heat transfer over the surface downstream to the cavity. One intriguing and important aspect based on the current setup lies on the interaction of the coolant injected upstream with the flow disturbance associated with the gap.

Early studies of film cooling are focused mainly on the film effectiveness (η) or the adiabatic wall temperature, T_{aw}. To estimate the heat transfer accurately on a film-cooled surface requires knowledge of the local heat transfer coefficient (h), in addition to the film effectiveness (Erikson and Goldstein, 1974). In general, these two parameters, η and h, of a given system are determined separately from different experiments and often under different test conditions. In an attempt to develop a measurement technique that is capable of revealing both parameters simultaneously, Vedula and Metzger (1991) introduced a transient approach based on the thermography of thermochromic liquid crystals. The framework of such an approach is commonly termed the "three-temperature problem" since the heat transfer from a film cooled wall is collectively determined by temperatures of the mainstream, the injectant, and the wall. The liquid crystal thermography technique results in two algebraic equations that are dominated by error functions for both η and h. Recently Ekkad et al. (1995a, 1997b) employed the same approach to study the film cooling with compound angle injections. Instead of using liquid crystals, Chyu and Hsing (1996) extended the transient principle to determine both parameters, based on the fluorescence images of a thermographic phosphor. The current research employs the transient liquid crystal technique originated by Vedula and Metzger (1991). Similar to the aforementioned studies, the present study neglects the effect of density difference between the mainflow and injectants.

Contributed by the International Gas Turbine Institute and presented at the 41st International Gas Turbine and Aeroengine Congress and Exhibition, Birmingham, United Kingdom, June 10–13, 1996. Manuscript received at ASME Headquarters February 1996. Paper No. 96-GT-175. Associate Technical Editor: J. N. Shinn.

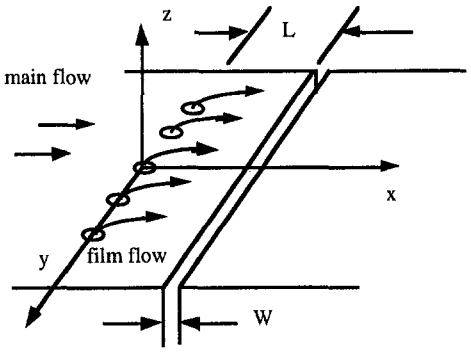

Fig. 1 Gap located downstream of film injection holes

Understandably, the three-temperature problem remains valid both for the case of no leakage flow and leak drawn from the film-cooled boundary layer through the gap. This notion, however, is no longer justifiable in the case of gap leakage injected into the test section. The additional temperature scale associated with the secondary injectant through the gap makes the system a "four-temperature problem." As a highlight of this paper, the experimental implementation and fundamental principle for determining the film cooling performance in a "four-temperature" system are described as follows.

Transient Liquid Crystal Technique for Multiple-Temperature Systems

One essential aspect of the transient measurement technique for convective heat transfer system is to facilitate a means to acquire and record the temporal variation of local surface temperatures over the test region of interest. In the present study this is achieved by spraying a thin layer of encapsulated chiral nematic thermochromic liquid crystal (TLC) on the test surface as a temperature indicator.

If the test surface of a uniform initial temperature is suddenly exposed to the heated flow with a temperature of T_m, the magnitude of the time-varying surface temperature, T_w, is governed by transient heat conduction penetrating into a semi-infinite solid. Assuming the heat conduction is primarily one dimensional (in z direction), the governing equation is:

$$k\frac{\partial^2 T}{\partial^2 z} = \rho C_p \frac{\partial T}{\partial t} \tag{1}$$

If the wall material including the test surface is initially at a uniform temperature T_i at all depths, then the initial and boundary conditions can be described as:

$$-k\left.\frac{\partial T}{\partial z}\right|_{z=0} = h(T_w - T_r) \tag{2}$$

$$T|_{z=\infty} = T_i \tag{3}$$

$$T|_{\tau=0} = T_i \tag{4}$$

Here the convective heat transfer coefficient, h, is defined as:

$$h = \frac{q}{T_w - T_r} \tag{5}$$

where q is the heat transfer per unit area per unit time from the gas stream to the surface. T_r is the local reference temperature.

The solution of Eq. (5), obtained from Laplace transform, is:

$$\frac{T_w - T_i}{T_r - T_i} = 1 - \exp\left[\frac{h^2\alpha\tau}{k^2}\right]\operatorname{erfc}\left[\frac{h\sqrt{\alpha\tau}}{k}\right] \tag{6}$$

Here T_i is the initial temperature of the test section prior to the test, and it is usually equal to the ambient air temperature and can be measured by thermocouples. The values α and k are the thermal properties of the test material (Plexiglas) and are available from the manufacturer. In a conventional two-temperature convection situation, the reference temperature T_r is simply equal to T_m, which is the flow mixed-mean temperature in the test channel, and can be obtained from reading of a thermocouple located at the mainstream. The value of the local heat transfer coefficient can thus be determined by measuring the time, τ, required for the surface temperature to reach a prescribed value, T_w, displayed by the color of the TLC applied on the test surface.

Three-Temperature System. The foregoing discussion, however, is inapplicable in the case of film cooling where the predominant convection feature is governed by three temperatures. Here the reference temperature T_r is a function of the supply temperatures of the two interacting streams and the level of mixing that occurs between them; hence it is also an unknown, in addition to h. Since T_r must be equal to the wall temperature when heat flux $q = 0$, T_r is often termed the adiabatic wall temperature, T_{aw}.

It is understandable that both T_r and h can be determined by simultaneously solving two equations of form Eq. (6). The two equations are individually obtained from two different test conditions. Provision for the two different conditions in the present study is achieved by performing two closely related experiments. The two tests use the same flow conditions; however, one uses heated film injection and the other uses either less heated or unheated (at ambient temperature) injection. While the mainstream is always heated, its heating level varies

Nomenclature

c_p = fluid specific heat
D = injection hole diameter
D_h = channel hydraulic diameter
h = convective heat transfer coefficient
k = test surface thermal conductivity
M = blowing ratio = $(\rho V)_f/(\rho V)_m$
m = injectant mass flow rate
L = distance from the center of the injection hole to the upstream rim of the gap
q = heat flux
Re = Reynolds number = $\rho V D_h/\mu$
t = test elapsed time
T = local temperature
V = local mean flow velocity
W = gap width
x = streamwise distance downstream from the center of the injection hole
y = spanwise distance from the center of the injection hole
z = axis perpendicular to the test surface
α = thermal diffusivity of the test rig
η = film cooling effectiveness
μ = dynamic viscosity of fluid
ρ = fluid density
τ = time

Subscripts

1 = first coolant, injected from the discrete holes
2 = second coolant, injected from the transverse gap
aw = adiabatic wall
f = secondary film flow
i = initial values at $t = 0$
m = mainstream
r = local reference temperature
w = local surface

with different test conditions. In general, the mainstream temperature cannot be too high, so the color evolution of TLC may be too rapid to be discerned. On the other hand, the heating level cannot be too low so that the over-long experiment violates the one-dimensional heat conduction model (Yu, 1994). In the current tests, the mainstream temperature is maintained at about 70°C, and a heated film flow has a temperature around 60 to 65°C. The temperature of a less heated film flow is about 0 to 10°C above the room temperature.

The two different aforementioned tests result in two governing equations for h and T_r:

$$\frac{T_w - T_{i1}}{T_{r1} - T_{i1}} = 1 - \exp\left[\frac{h^2\alpha\tau_1}{k^2}\right] \text{erfc}\left[\frac{h\sqrt{\alpha\tau_1}}{k}\right] \quad (7)$$

$$\frac{T_w - T_{i2}}{T_{r2} - T_{i2}} = 1 - \exp\left[\frac{h^2\alpha\tau_2}{k^2}\right] \text{erfc}\left[\frac{h\sqrt{\alpha\tau_2}}{k}\right] \quad (8)$$

Assuming a constant thermal property and that the turbulent convection is governed predominantly by flow dynamics rather than thermal conditions, the values of h and T_r obtained from the current experiment are deemed to be the unique solution to the prescribed film cooling conditions. This notion leads to the conclusion that T_{r1} and T_{r2} are related and therefore represent only one unknown.

Since true step changes in applied flow temperatures are not realizable, in actual experiments an additional complication is introduced and the reference temperature is a function of time. This complication can be accounted for by modifying the equation through use of superposition and Duhamel's theorem. The actual gradual change is obtained through a series of steps. The solution is represented as:

$$T_w - T_i = \sum_{i=1}^{N} U(\tau - \tau_i)\Delta T_r \quad (9)$$

where:

$$U(\tau - \tau_i) = 1 - \exp\left[\frac{h^2\alpha(\tau - \tau_i)}{k^2}\right] \times \text{erfc}\left(\frac{h\sqrt{\alpha(\tau - \tau_i)}}{k}\right) \quad (10)$$

Here the equation is cast in terms of time-varying T_r, which is an unknown, but related to T_m and T_f, which are both measurable quantities. Such a relation is based upon the definition of film effectiveness, η, expressed as:

$$\eta = \frac{(T_m - T_{aw})}{(T_m - T_f)} \quad (11)$$

or

$$T_r = T_{aw} = (1 - \eta)T_m + \eta T_f \quad (11a)$$

Hence the increment of T_r can be written as:

$$\Delta T_r = (1 - \eta)\Delta T_m + \eta\Delta T_f \quad (12)$$

Equation (9) now transforms into

$$T_w - T_i = \sum_{i=1}^{N} U(\tau - \tau_i)[(1 - \eta)\Delta T_m + \eta\Delta T_f] \quad (13)$$

Two equations of this form, obtained from two closely related experiments, must be solved for the two unknowns, h and η.

Four-Temperature System. As stated earlier, the convective heat transfer in a four-temperature system is governed by four independent temperatures: the wall temperature, the mainstream temperature, and two injected coolant temperatures. As in the three-temperature problem, both h and T_r (or T_{aw}) are unknowns that must be resolved. To formulate T_r, it is convenient and rational to define two new parameters: the first reference temperature, T_{r1}, and the second reference temperature, T_{r2}, in form of Eq. (11a), i.e.,

$$T_{r1} = (1 - \eta_1)T_m + \eta_1 T_{f1} \quad (14)$$

and:

$$T_{r2} = (1 - \eta_2)T_m + \eta_2 T_{f2} \quad (15)$$

where η_1 and η_2 are the film effectiveness for the first and second injection (holes and gap), respectively. Similar to Eq. (11), they are defined as:

$$\eta_1 = \frac{(T_m - T_{r1})}{(T_m - T_{f1})} \quad (16)$$

$$\eta_2 = \frac{(T_m - T_{r2})}{(T_m - T_{f2})} \quad (17)$$

Hence the T_r can be expressed as

$$T_r = T_{r1} + T_{r2} - T_m = (1 - \eta_1 - \eta_2)T_m + \eta_1 T_{f1} + \eta_2 T_{f2} \quad (18)$$

The physical meaning of T_{r1} can be considered as the mixing temperature of the mainstream and the first (upstream) film flow when $T_{f2} = T_m$. The difference between this temperature and the wall temperature is the driving potential of the heat transfer under the condition of $T_{f2} = T_m$. On the other hand, T_{r2} can be viewed similarly for the second film flow when $T_{f1} = T_m$.

Once the heat transfer coefficient h and the driving temperature T_r are determined, the heat flux can be calculated using:

$$q = h(T_r - T_w) \quad (19)$$

According to the foregoing discussion, there are three unknowns, i.e., h, T_{r1}, and T_{r2} (or h, η_1, and η_2) to be resolved by experiment. Similar to the approach for the three-temperature problem, these variables can be determined by simultaneously solving three equations of form Eq. (6). Hence, in addition to Eqs. (7) and (8) for the three-temperature case, one more equation needs to be established, i.e.,

$$\frac{T_w - T_{i3}}{T_{r3} - T_{i3}} = 1 - \exp\left[\frac{h^2\alpha\tau_3}{k^2}\right] \text{erfc}\left[\frac{h\sqrt{\alpha\tau_3}}{k}\right] \quad (20)$$

The subscript 3 on T_r represents the third test condition. A three-test scheme was designed under the following three conditions: (1) mainstream, first film flow, and second film flow all heated; (2) the heated mainstream, the heated first film flow and the "cold" second film flow (cold means flow is unheated, same as the room temperature); and (3) the heated main flow, the heated second film flow, and the "cold" first film flow. Conceptually this arrangement leads to the best possible results for the four temperature problems using the current experimental method (Yu, 1994).

To account for the lack of true step-change in the temperature fields, all three governing equations must be cast in the form of Eqs. (9) and (10), which involve a series of step changes in reference temperature, ΔT_r. According to Eq. (18),

$$\Delta T_r = (1 - \eta_1 - \eta_2)\Delta T_m + \eta_1\Delta T_{f1} + \eta_2\Delta T_{f2} \quad (21)$$

Experimental Apparatus and Procedures

Figure 2 shows a schematic of the experimental apparatus. The mainstream and two injected coolant flows are supplied from laboratory compressed air. After metering, the flows are

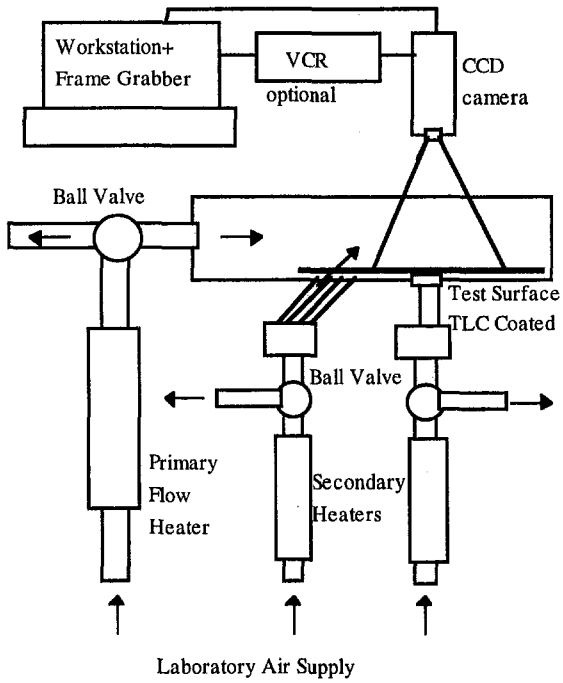

Fig. 2 Test section with liquid crystal imaging system

routed to individual auto-transformer controlled tubular in-line heaters, where their temperatures can be accurately controlled to the levels desired. All flows are initially diverted away from the test section via three-way ball valves installed in the pipe lines, until the start of the experiment.

The TLC used in the study displays colors in response to temperature changes as a result of lattice reorientation of the crystals. The nominal temperatures for this TLC formula are at 38.4, 39.1, and 42.5°C for red, green, and blue colors respectively.

The green color display of the TLC is used as an indication of the surface temperature during the tests. The green color indication of the TLC has been carefully calibrated; the repeatability of the temperature indication is within ±0.15°C.

A test is started by switching the flow control valves. The three-way ball valves used to direct flow directions are switched simultaneously. Film flows are routed into the test section by way of secondary flow tubes. The automated data acquisition system is initiated at the time when the valve positions are switched. The data acquisition system employs a color CCD camera and a UNIX-based image processing system on a SUN workstation; it records the times of transition of the TLC from colorless to green over a domain designated downstream of the injection holes. Meanwhile, time-varying temperatures of both the mainstream and the injectants are recorded using thermocouples and an automated data acquisition system.

The test section consists of a Plexiglas rectangular duct 152.4 mm wide and 95.25 mm high. As shown in Fig. 1, five coolant injection holes are located in the upstream section of the test surface. These five equally spaced injection holes have the same diameter, D = 6.4 mm, and their axes are inclined at 30 deg relative to the mainstream direction. The distance between the adjacent holes is three times the injection hole diameter. To facilitate a comparative study on the effects of gap leakage on the film cooling characteristics, the present test matrix consists of a wide range of combinations of different flow rates through the film cooling holes and gap downstream. The entire test matrix is listed in Table 1. A negative value in the secondary mass flow ratio (M_2) suggests that the flow is extracted from the test channel through the gap, while a positive M_2 implies that the gap flow is injected into the channel. In addition to variations in flow rate, two different gap sizes, i.e., W/D = 1 and 3, are included in the test matrix. The mainstream Reynolds number, based on the hydraulic diameter of the channel, is maintained the same at 46,600 for all test cases.

Results and Discussion

The automated liquid crystal imaging system has provided test results with very remarkable spatial resolution. Each image frame consists of 200 × 150 = 30,000 pixel data. While two-dimensional color contours are readily available in the present system, line plots are chosen here for result presentation, due mainly to ease of direct comparison among different cases. Most of the following figures and discussion are based on the experimental result along the centerline of the injection holes.

First Effectiveness. Figure 3 shows the streamwise first effectiveness distribution along the centerline of the injection holes in the cases of first blowing ratio M_1 = 0.5 with positive second blowing ratio ($M_2 > 0$). The case of W = 0 and M_2 = 0 represents an uninterrupted film cooling without gap presence. Data of such a reference case agree well with those of discrete hole injection, reported in the literature (Vedula and Metzger, 1991). The trend for the values of effectiveness downstream of the gap to be slightly higher (up to 50 percent) than those without the gap is significant. The only exception is the case of W/D = 3, and m_2/m_1 = 150 percent, where the effectiveness is lower in the area immediately downstream of the gap. However, it recovers and displays the same trend as the others at about 6D downstream of the gap. It can be concluded that the flow boundary layer with such a relatively low first blowing

Table 1 Test matrix

Test No	W/D	M_1	M_2	m2/m1
A11	0	0.0	0.0	--
A21	0	0.5	0.0	--
A31	0	1.0	0.0	--
B11	1	0.0	0.0	--
B12	1	0.0	+0.084	--
B13	1	0.0	+0.126	--
B21	1	0.5	0.0	0
B22	1	0.5	+0.084	100%
B23	1	0.5	+0.126	150%
B24	1	0.5	-0.042	-50%
B25	1	0.5	-0.084	-100%
B26	1	0.5	-0.126	-150%
B31	1	1.0	0.0	0%
B32	1	1.0	+0.084	50%
B33	1	1.0	+0.126	75%
B34	1	1.0	-0.042	-25%
B35	1	1.0	-0.084	-50%
B36	1	1.0	-0.126	-75%
C11	3	0.0	0.0	--
C12	3	0.0	+0.028	--
C13	3	0.0	+0.042	--
C21	3	0.5	0.0	0%
C22	3	0.5	+0.028	100%
C23	3	0.5	+0.042	150%
C24	3	0.5	-0.014	-50%
C25	3	0.5	-0.028	-100%
C26	3	0.5	-0.042	-150%
C31	3	1.0	0.0	0
C32	3	1.0	+0.028	50%
C33	3	1.0	+0.042	75%
C34	3	1.0	-0.014	-25%
C35	3	1.0	-0.028	-50%
C36	3	1.0	-0.042	-75%

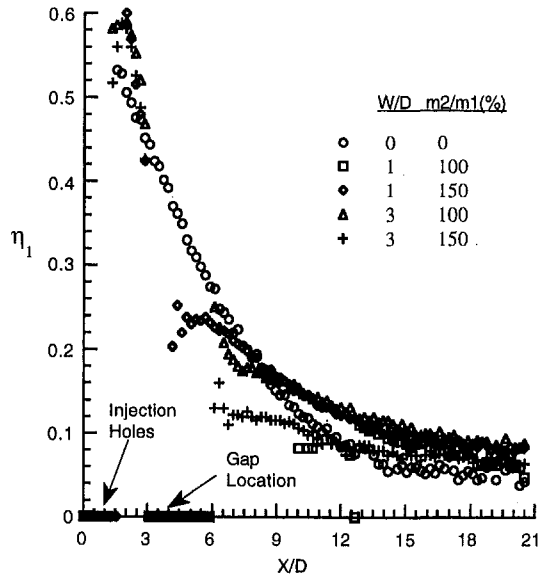

Fig. 3 Distributions of first effectiveness, $M_1 = 0.5$

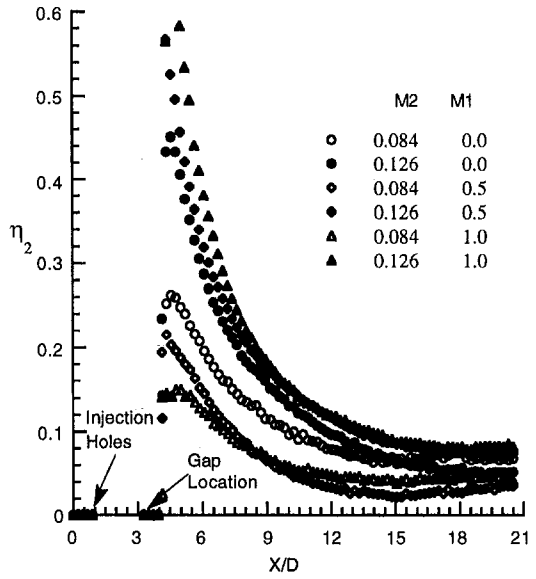

Fig. 5 Distributions of second film effectiveness, $W/D = 1$

ratio is generally quite stable, and a mild addition of coolant injected out of the gap promotes better film protection. However, a relatively stronger secondary injection from the gap appears to lift the film boundary layer away from the wall, reducing film effectiveness in the downstream vicinity of the gap. This phenomenon seems to be the dominating feature, so that the influence of difference in gap size seems to be somewhat insignificant.

Figure 4 shows the streamwise effectiveness distribution for the cases with a first blowing ratio of 1.0. Compared to the previous case ($M_1 = 0.5$) the film effectiveness for the baseline case without gap present has lower values in the near region downstream of the film cooling holes, and higher values further downstream. The stronger injectant momentum associated with higher injection rate tends to elevate the coolant away from the wall in the near-hole region, but it induces better film protection as the coolant entrains back to the boundary layer sufficiently downstream to the injection hole. Apparently the current blowing ratio ($M_1 = 1.0$) has already exceeded its corresponding optimal value under the present test conditions. The other significant difference, as compared to the case of lower injection rate ($M_1 = 0.5$), is that the secondary injection from a gap generally results in a lower film effectiveness than that of the reference case without the gap. Such a trend is more pronounced in the near-gap region and gradually diminished toward downstream. This is evidenced by the fact that virtually all the values of η_1 for $X/D > 10$ become quite comparable to those without secondary injection. The only exception is the case of $W/D = 3$ and $m_2/m_1 = 0.75$, which represents the strongest secondary injection over the widest gap overall. The values of η_1 are substantially lower than those of the other cases, and the influence of gap flow on the film effectiveness persists more than 15 hole diameters ($6 < x/D < 21$) downstream from the gap. This observation is attributable to the combination of strong coolant lifting and excessive turbulence generation associated with the injection from a wide gap.

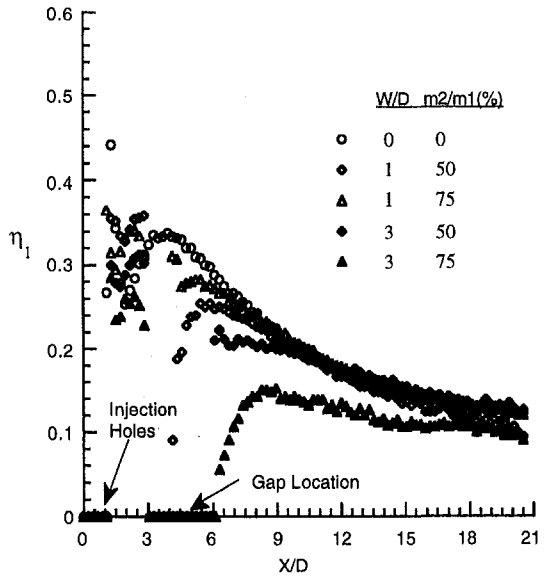

Fig. 4 Distributions of first film effectiveness, $M_1 = 1.0$

Second Effectiveness. While the foregoing discussion has demonstrated that the first film is affected by the second injection from a gap downstream, the nature of the second-coolant effectiveness is, in fact, also influenced by the first injection upstream. Figures 5 and 6 show the spanwise-averaged, streamwise-resolved second effectiveness for the case of $W/D = 1$ and 3, respectively. For $W/D = 1$, an increase in the first blowing rate reduces the second-coolant effectiveness when the second-to-first coolant mass flow ratio is moderate, i.e., $m_2/m_1 = 0.5$ ($M_2 = 0.084$). The second injectant from the gap apparently lacks sufficient momentum to penetrate into the boundary layer established jointly by the first film flow and the mainstream. The additional disturbance induced by the upstream injection may further enhance turbulence mixing locally and temper the second effectiveness in the region. Such a trend however, reverses as the second-to-first coolant mass flow ratio is higher, $m_2/m_1 = 1.0$ ($M_2 = 0.126$). The second injectant, with a greater m_2/m_1 ratio, is more capable of penetrating deeper into the boundary layer, or even escaping to the mainstream. A stronger blowing rate in first injection can suppress the second injectant from such an overshoot and hence promote the effectiveness. For $W/D = 3$, the general trend revealed in Fig. 6 is quite similar to that observed in Fig. 5. Note that the mass flow rates from the second injectant between these two figures are correspondingly equal, hence the second blowing ratio, M_2, for the cases shown in Fig. 6 are only $\frac{1}{3}$ of that in Fig. 5.

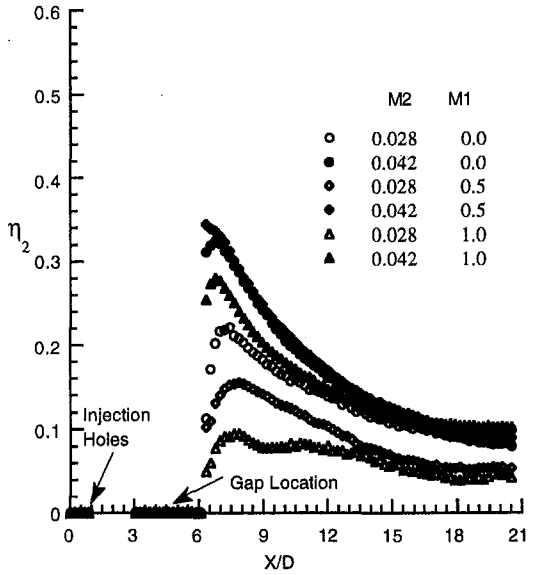

Fig. 6 Distributions of second film effectiveness, $W/D = 3$

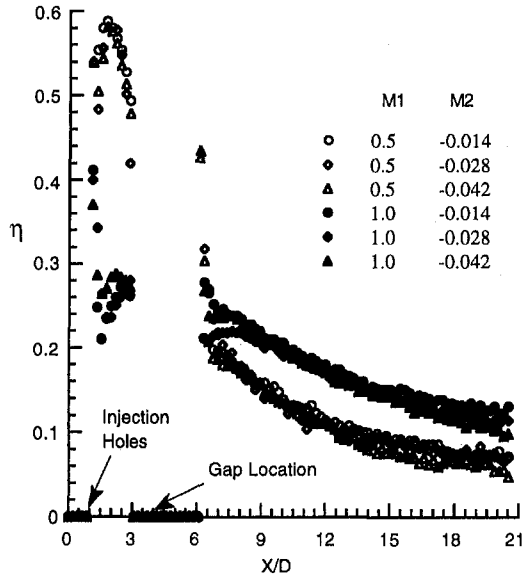

Fig. 8 Distributions of film effectiveness, $W/D = 3$, $M_2 < 0$

A comparison of the results between the two figures reveals that such a factor of 3 difference in M_2 has a moderate influence on the values of η_2. This appears to be caused by the unevenly distributed velocity profile which is sheared by the crossflow over a relatively wide gap at the exit of second injection. The velocity profile is expected to be slanting with a higher local magnitude toward downstream side of the gap; hence the actual difference in M_2 is less than a factor of 3.

Effectiveness in a Three-Temperature System. An opposing case to the dual-coolant injection occurs when the flow leaks out of the mainstream through the gap downstream to the film cooling injection holes. In reality this can happen when the pressure inside the hot-gas pass is greater than the static pressure outside. Figures 7 and 8 exhibit the distributions of film effectiveness for the cases of $W/D = 1$ and 3, respectively. Note that the present situation is a three, instead of four-temperature problem, and only one effectiveness, η, as given in Eq. (11) is defined. The negative values associated with M_2 in these figures signify flow depletion through the gap. An interesting trend revealed in Fig. 7 is that the values of η vary little with different depletion rates (M_2) for the cases of moderate film blowing ratio, $M_1 = 0.5$. The situation changes for the cases with a higher blowing ratio, $M_1 = 1.0$, as the characteristics of η are more sensitive to the variation of M_2. The value of η increases as the depletion rate increases from $M_2 = -0.042$ to -0.084; however, it decreases as the magnitude of M_2 increases further to -0.126. This phenomenon appears to be closely related to the nature of boundary layer with film cooling under a high-blowing-ratio condition. A moderate level of flow extraction may drag the coolant, which is otherwise lifted toward the film-protected surface. Such an effect apparently dominates in the regime of M_2 less than 0.084 in magnitude. However, an excessive flow extraction ($M_2 = -0.126$) may overly deplete the coolant injected upstream and reduce the film effectiveness. The results shown in Fig. 8 for $W/D = 3$ have a basic trend similar to that of the moderate blowing ratio, $M_1 = 0.5$, when $W/D = 1$. The magnitudes of η are determined primarily by M_1 and virtually independent of M_2.

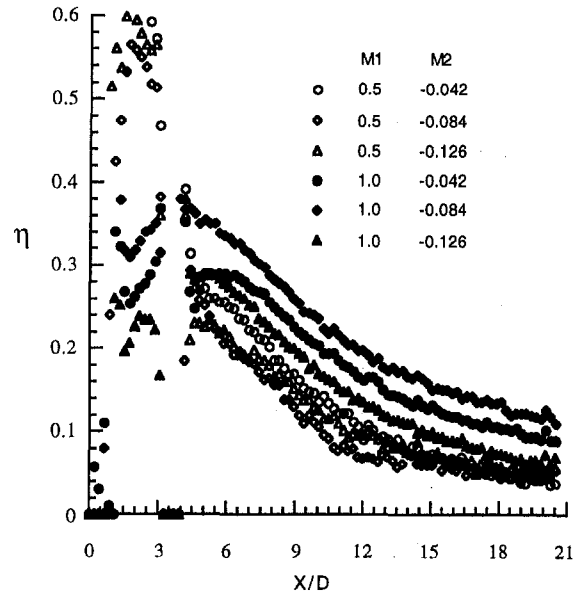

Fig. 7 Distributions of film effectiveness, $W/D = 1$, $M_2 < 0$

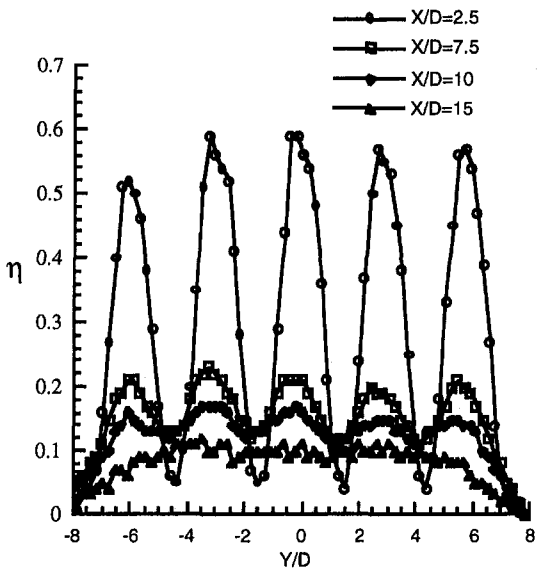

Fig. 9 Spanwise effectiveness distributions; $M_1 = 0.5$, $M_2 = 0.0$, $W/D = 1$

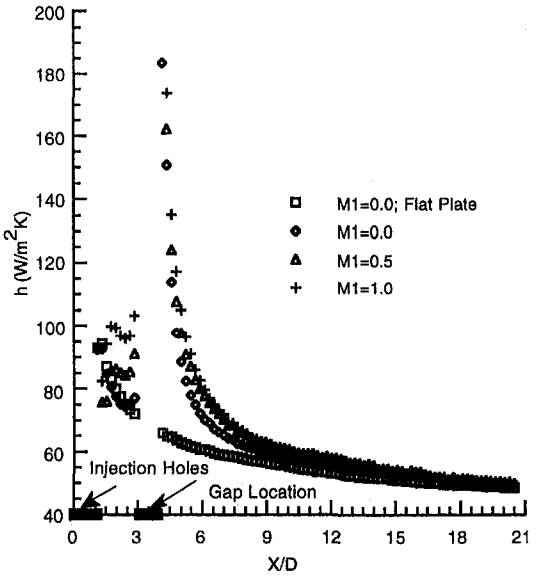

Fig. 10 Distributions of heat transfer coefficient; $W/D = 1$, $M_2 = 0$

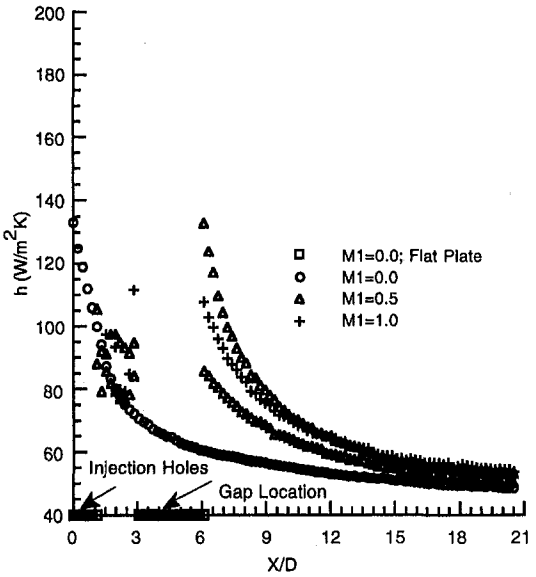

Fig. 12 Distributions of heat transfer coefficient; $W/D = 3$, $M_2 = +0.126$

Figure 9 shows the spanwise distributions of the first effectiveness at four different streamwise locations. The values of the film effectiveness exhibit strong variations across the span and eventually becomes nonexistent at $x/D = 15$. The data overall display an excellent symmetry, which further demonstrates the quality of the present experimental technique, immediately downstream of the injection holes ($x/D = 2.5$). Such an effect diminishes substantially with the streamwise coordinate.

Heat Transfer Coefficient. In addition to film effectiveness, knowledge of the local heat transfer coefficient, h, is equally important for determining the heat transfer over a film protected surface. Figures 10 to 12 show the sample results of h distribution for $M_2 = 0$, -0.126, and $+0.126$, respectively. A baseline case, plotted in each figure, is the corresponding heat transfer coefficient over a flat plate without film cooling and gap present. In virtually all cases, notable disturbance, either by flow injection or suction or by geometric discontinuity with gap, elevates the heat transfer coefficient to be higher than the baseline case. As a collective evidence based on all the results obtained from the current study, the geometric disturbance caused by the gap presence is the most dominating factor on the heat transfer coefficient. The influence of M_1 on the values of h appears to be insignificant for the cases without gap flow (Fig. 10) and with flow extraction (Fig. 11). However, for the cases with injected gap-flow (Fig. 12), a four-temperature problem, the distributions of h downstream of the gap are more dependent on M_1, as h increases with M_1. Since the trends described above also prevail for other cases of different M_2 values, the influence of M_2 on the heat transfer coefficient is the least significant, at least within the present test range.

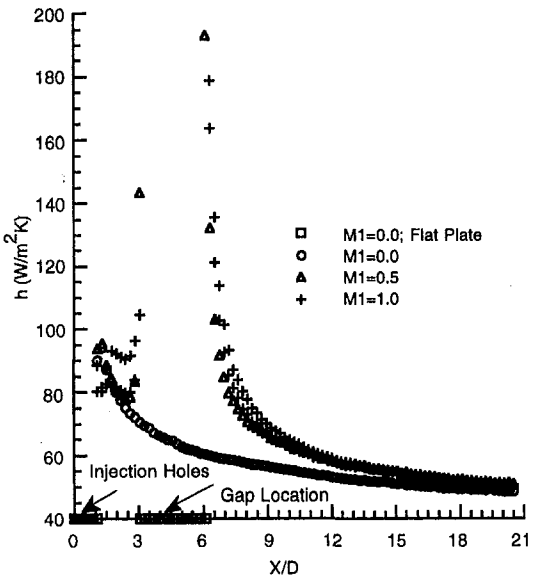

Fig. 11 Distributions of heat transfer coefficient; $W/D = 3$, $M_2 = -0.126$

Conclusions

Using a transient liquid crystal imaging system, the present study has acquired detailed distributions of both the local film effectiveness and heat transfer coefficient on a film-cooled surface with a transverse gap present downstream of the injection holes. One intriguing feature associated with the present geometry is that the system becomes a four-temperature problem when an additional temperature scale is introduced to the working flow associated with the injectant from the gap. Experimental results obtained from the current study have led to the following conclusions: Interaction between the two injectants appears to be relatively strong for the four-temperature problem as compared to the three-temperature problem. For a moderate level of film cooling ($M_1 = 0.5$), the combined presence of the gap and its injectant promotes the first effectiveness downstream of the gap. The effect is less significant for a wider gap. This trend reverses with a higher level of first blowing ratio at $M_1 = 1.0$, where the second injectant reduces the magnitude of the first effectiveness. The second effectiveness can also be affected by the first film injectant upstream, particularly for the cases with moderate levels of second injection. In this case, an increase in the first blowing ratio generally elevates the values of second effectiveness. However, this trend, again, reverses for the cases with higher second blowing ratios.

Flow extraction through the gap, a three-temperature problem, generally increases the film effectiveness over the protected wall. The mechanism of flow suction retains the coolant which is otherwise lifted near the protected surface. However, excessive extraction may overly deplete the coolant in the region and demote the film effectiveness.

The values of local heat transfer coefficient downstream of the gap for all cases studied are significantly enhanced as com-

pared to those without gap present. Measured data suggest that, at least within the present test range, the geometric disturbance, i.e., the presence of the gap, rather than flow disturbance, is primarily responsible for such a phenomenon. The effects of both injectants on the characteristics of heat transfer coefficient are insignificant.

Acknowledgments

This work was initiated by the first author (Y. Yu) and his former doctoral thesis advisor, the late Professor Darryl E. Metzger, at Arizona State University. The project was then continued at Carnegie Mellon University supported, in part, by the U.S. Department of Energy's Advanced Turbine System (ATS) Program. Both authors would like to express their deepest appreciation for the mentorship that Professor Metzger offered throughout the years. The authors would also like to thank Drs. Dan Fant and Lawrence P. Golan, who manage the ATS program at South Carolina Energy R&D Center.

References

Chyu, M. K., and Goldstein, R. J., 1986, "Local Mass Transfer in Rectangular Cavities With Separated Turbulent Flow," *Heat Transfer 1986,* Vol. 3, Hemisphere Publication, pp. 1065–1070.

Chyu, M. K., Metzger, D. E., and Hwan, C. L., 1987, "Heat Transfer in Shrouded Rectangular Cavities," *J. Thermophysics and Heat Transfer,* Vol. 1, pp. 247–252.

Chyu, M. K., and Schwarz, S. G., 1990, "Effects of Bottom Injection on Heat Transfer and Fluid Flow in Rectangular Cavities," *J. Thermophysics and Heat Transfer,* Vol. 4, pp. 521–526.

Chyu, M. K., and Hsing, Y. C., 1996, "Use of a Laser-Induced Fluorescence Thermal Imaging System for Film Cooling Heat Transfer Measurement," ASME Paper No. 96-GT-430.

Ekkad, S. V., Zapata, D., and Han, J.-C., 1997a, "Heat Transfer Coefficients Over a Flat Surface With Air and CO_2 Injection Through Compound-Angle Hole Using a Transient-Liquid-Crystal Image Method: Part I," ASME JOURNAL OF TURBOMACHINERY, Vol. 119, pp. 580–586.

Ekkad, S. V., Zapata, D. and Han, J.-C., 1997b, "Film Cooling Effectiveness Over a Flat Surface With Air and CO_2 Injection Through Compound-Angle Hole Using a Transient-Liquid-Crystal Image Method: Part II," ASME JOURNAL OF TURBOMACHINERY, Vol. 119, pp. 587–593.

Eriksen, V. L., and Goldstein, R. J., 1974, "Heat Transfer and Film Cooling Following Injection Through Inclined Circular Holes," ASME *Journal of Heat Transfer,* Vol. 96, pp. 235–240.

Goldstein, R. J., 1971, "Film Cooling," *Advances in Heat Transfer,* Academic Press, New York, Vol. 7, pp. 321–379.

Vedula, R. J., and Metzger, D. E., 1991, "A Method for the Simultaneous Determination of Local Effectiveness and Heat Transfer Distributions in Three Temperature Convection Situations," ASME Paper No. 91-GT-345.

Yu, Y., 1994, "Film Cooling Measurements With a Transverse Gap Downstream of the Injection Holes," Ph.D. dissertation, Arizona State University.

Adiabatic Wall Effectiveness Measurements of Film-Cooling Holes With Expanded Exits

M. Gritsch

A. Schulz

S. Wittig

Lehrstuhl und Institut für Thermische Strömungsmaschinen, Universität Karlsruhe (T.H.), Kaiserstr. 12, 76128 Karlsruhe, Germany

This paper presents detailed measurements of the film-cooling effectiveness for three single, scaled-up film-cooling hole geometries. The hole geometries investigated include a cylindrical hole and two holes with a diffuser-shaped exit portion (i.e., a fan-shaped and a laid-back fan-shaped hole). The flow conditions considered are the crossflow Mach number at the hole entrance side (up to 0.6), the crossflow Mach number at the hole exit side (up to 1.2), and the blowing ratio (up to 2). The coolant-to-mainflow temperature ratio is kept constant at 0.54. The measurements are performed by means of an infrared camera system, which provides a two-dimensional distribution of the film-cooling effectiveness in the near field of the cooling hole down to x/D = 10. As compared to the cylindrical hole, both expanded holes show significantly improved thermal protection of the surface downstream of the ejection location, particularly at high blowing ratios. The laidback fan-shaped hole provides a better lateral spreading of the ejected coolant than the fan-shaped hole, which leads to higher laterally averaged film-cooling effectiveness. Coolant passage crossflow Mach number and orientation strongly affect the flowfield of the jet being ejected from the hole and, therefore, have an important impact on film-cooling performance.

Introduction

Increasing the lifetime of gas turbine blades can be achieved by cooling the blades effectively. Typically, this cooling process involves film-cooling of the blade surface. In an attempt to improve the cooling process, recent attention has been given to contouring the hole geometry. Film-cooling holes with a diffuser-shaped expansion at the exit portion of the hole are believed to improve the film-cooling performance on a gas turbine blade. The increased cross-sectional area at the hole exit compared to a standard cylindrical hole leads to a reduction of the mean velocity and, thus, of the momentum flux of the jet exiting the hole. Therefore, the penetration of the jet into the mainflow is reduced, resulting in an increased cooling efficiency. Furthermore, lateral expansion of the hole provides an improved lateral spreading of the jet, leading to a better coverage of the airfoil in lateral direction and a higher laterally averaged film-cooling efficiency.

Recent studies have shown that expanding the exit of the cooling hole improves film-cooling performance relative to a cylindrical hole. Overall improvements in adiabatic effectiveness were found for laterally expanded holes (Goldstein et al., 1974) as well as for forward-expanded holes (Makki and Jakubowski, 1986). Schmidt et al. (1996a) and Sen et al. (1996) compared a cylindrical hole to a forward-expanded hole, both with compound angle injection. Although the spatially averaged effectivenesses for the cylindrical and forward-expanded holes were the same, a larger lateral spreading of the forward expanded jet was found. Haller and Camus (1984) performed aerodynamic loss measurements on a two-dimensional transonic cascade. Holes with a spanwise flare angle of 25 deg were found to offer significant improvements in film-cooling effectiveness without any additional loss penalty. Liess (1975) studied the effect of the external crossflow Mach number on the film-cooling parameters. Mach numbers up to 0.9 were employed. Using the mainflow recovery temperature as reference temperature, no measurable effect on film-cooling effectiveness was found.

However, no studies are present in the open literature examining the effect of transonic external crossflow Mach numbers for discrete hole film-cooling in the near-hole region. Despite the fact that film-cooling holes are fed from supply passages in most gas turbine applications, there aren't any studies discussing the effect of coolant supply passage Mach number and orientation on film-cooling performance.

Flowfield measurements performed by Thole et al. (1998) showed that jet penetration as well as velocity gradients in the mixing region were significantly reduced for holes with expanded exits as compared to a cylindrical hole at the same blowing rate. Peak turbulence levels were found downstream of the hole exit for the cylindrical hole and in the hole exit plane for the expanded holes. Numerical studies performed by Giebert et al. (1997) were able to predict the general flow features of coolant ejection through diffuser-shaped holes. Discharge coefficient measurements presented by Gritsch et al. (1998) for the same hole geometries tested in the present paper showed that the discharge coefficient for all geometries strongly depends on the flow conditions (crossflows at hole inlet and exit, and pressure ratio). The discharge coefficient of both expanded holes was found to be higher than that of the cylindrical hole, particularly at low pressure ratios and with a hole entrance crossflow applied. The effect of the additional layback on the discharge coefficient was negligible.

This paper presents the film-cooling effectiveness results of a comprehensive film-cooling study conducted at the University of Karlsruhe. Two-dimensional distributions of the film-cooling effectiveness in the near-field of a single, scaled-up film-cooling hole with and without exit expansions were measured by means of an infrared camera system. The flow parameters investigated are typical for real film-cooling applications. Mach numbers both in the main channel and in the coolant supply passage, and the blowing ratio were varied in a wide range. Moreover, the effect of the orientation of the coolant supply passage with respect to the mainflow direction was investigated.

Experimental Apparatus and Measuring Technique

The present investigation was carried out in a continuous flow wind tunnel. The air supply was furnished by a high-

Contributed by the International Gas Turbine Institute and presented at the 42nd International Gas Turbine and Aeroengine Congress and Exhibition, Orlando, Florida, June 2–5, 1997. Manuscript received at ASME Headquarters February 1997. Paper No. 97-GT-164. Associate Technical Editor: H. A. Kidd.

Table 1 Operating conditions of the film-cooling test rig

Internal Temperature	T_{tc}	290 K
Blowing ratio	M	0.25 ... 2
Temperature ratio	T_{tc}/T_{tm}	0.54
Pressure ratio	p_{tc}/p_m	1 ... 2
Internal Mach number	Ma_c	0, 0.3, 0.6
External Mach number	Ma_m	0.3, 0.6, 1.2
Internal Reynolds number	Re_{Dc}	up to $2.5 \cdot 10^5$
External Reynolds number	Re_{Dm}	up to $1.3 \cdot 10^5$
Boundary layer thickness	δ_{99}/D	0.5
External turbulence level	Tu_m	<2 %
Internal turbulence level	Tu_c	1 %

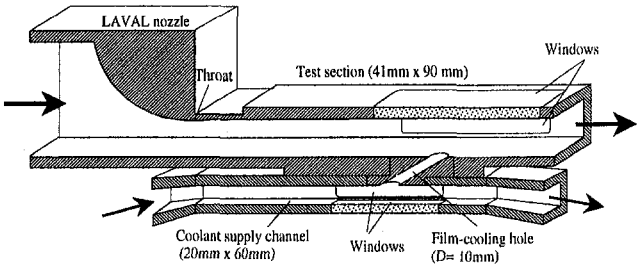

Fig. 1 Film-cooling test section

pressure, high-temperature (HPHT) test facility. The coolant-to-mainflow temperature ratio was 0.54 and kept constant for all test cases, which can be assumed to be representative for typical gas turbine applications. The operating conditions are shown in Table 1. Further details of the test rig design, the flow conditions, and on preliminary testing were given by Wittig et al. (1996).

The film-cooling test rig consists of a primary loop representing the external flow and a secondary loop representing the internal flow (see Fig. 1).

Primary Loop. The air supplied by the HPHT test facility passes a metering orifice and flow straighteners before entering the test section through a LAVAL nozzle. The test section is 90 mm in width and 41 mm in height. For the supersonic flow case, the height of the test section was reduced to 32 mm. The top wall opposite to the film-cooling hole exit had a sapphire window required for surface temperature measurements using an infrared (IR) camera system.

A zero streamwise pressure gradient was set in the test section by adjusting the position of the upper test section wall. For the subsonic flow cases, the position of the top wall was adjusted for each blowing ratio considered. Contrary to the subsonic flow cases, this procedure was performed for the supersonic flow cases ($Ma_m = 1.2$) at zero coolant ejection ($M = 0$) and the position of the top wall was kept for all blowing ratios investigated. With coolant ejected, the pressure distribution was of course strongly altered by the formation of shock waves in the test section.

Secondary Loop. Flow for the secondary loop is provided by the HPHT test facility, too. However, the total pressure in the secondary loop can be set independently from the primary loop. The flow in the secondary loop is driven by an additional blower. Thus, the Mach number can be set by adjusting the volume flow rate circulating in the secondary loop. The cross-sectional area at the film-cooling hole is 60 mm in width and 20 mm in height. Due to a "closed-loop" design of the secondary loop, the flow rate through the film-cooling hole is obtained directly, independently of the crossflow rate. Very accurate measurements of the flow rate through the film-cooling hole were achieved.

The orientation of the coolant supply passage with respect to the mainflow direction could be set within $\beta = 0$ deg (parallel flow) to 90 deg (perpendicular flow) to account for the various flow configurations in cooled airfoils in relation to film-cooling holes as discussed by Hay et al. (1983).

Film-Cooling Hole Geometries Tested. All tests were carried out using single, scaled-up film-cooling holes with an inclination angle of $\alpha = 30$ deg. All holes were sharp edged and the interior surfaces were aerodynamically smooth. In total, three hole geometries (a cylindrical hole and two holes with an expanded exit portion) were tested (see Fig. 2). The diameter of the cylindrical hole and the diameter of the cylindrical inlet section of the expanded holes was 10 mm. The length-to-diameter ratio L/D was 6 for all hole geometries. The lateral expansion angle of both expanded holes was 14 deg, resulting in a hole width of 30 mm at the hole exit. The forward expansion angle of the laid-back fan-shaped hole was 15 deg, resulting in a hole length of 40 mm at the hole exit. The exit-to-entry area ratio of the fan-shaped and laid-back fan-shaped hole were 3.0 and 3.1, respectively (areas perpendicular to hole axis).

The hole geometries were decided in cooperation with the industrial partners involved in the present research program. The chosen geometry of the expanded holes is in agreement with the suggestion of Hay and Lampard (1995) that the length of the cylindrical section at the hole entrance of the expanded holes should be at least two hole diameters. This is to allow the flow to reattach before entering the expanded section and, therefore, to improve the diffusion of the flow. A large expansion angle would lead to an improved lateral coverage of the ejected film but flow separation in the diffuser section of the hole could occur. Therefore, the chosen expansion angle must be seen as a compromise.

For the fan-shaped and the laid-back fan-shaped hole, the calculation of the blowing ratio was based on the inlet cross-sectional area of these holes. Thus, the blowing ratio of the shaped holes can be directly compared to those of the cylindrical

Nomenclature

D = film-cooling hole diameter
DR = coolant-to-mainflow density ratio
I = coolant-to-mainflow momentum flux ratio
L = film-cooling hole length measured along the hole centerline axis
M = blowing ratio
Ma = Mach number
Re_D = Reynolds number based on hole diameter
T_t = total temperature
T_{Rec} = recovery temperature
Tu = turbulence intensity
x = streamwise distance from downstream edge of the film-cooling hole
z = lateral distance from centerline of the film-cooling hole
α = angle of hole inclination
β = angle of coolant supply passage orientation with respect to the mainflow direction
δ_{99} = boundary layer thickness, 99 percent point
η = local film-cooling effectiveness
$\bar{\eta}$ = laterally averaged film-cooling effectiveness

Subscripts

AW = adiabatic wall conditions
c = internal flow conditions
CL = centerline
m = external flow conditions

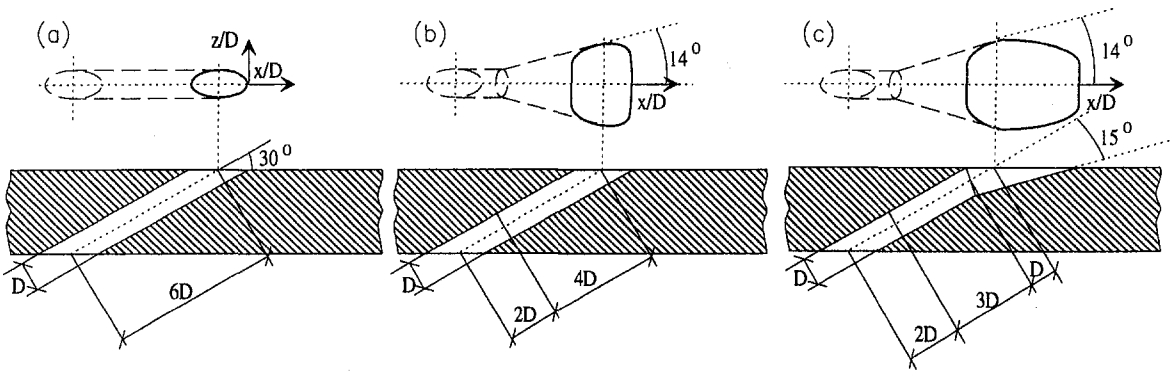

Fig. 2 *Cylindrical, fan-shaped, and laid-back fan-shaped film-cooling hole geometries*

hole. The same blowing ratio is synonymous with same amount of coolant ejected if the mainflow conditions remain unchanged. This makes it more convenient to evaluate the effect of contouring the hole.

Each hole geometry was tested for a matrix of three internal Mach numbers (Ma_c = 0.0, 0.3, 0.6) and three external Mach numbers (Ma_m = 0.3, 0.6, 1.2) over a range of blowing ratios.

Adiabatic Wall Temperature Measurements. The test plate used for measuring adiabatic wall temperatures consisted of a high-temperature plastic material (TECAPEK) with a thermal conductivity of 0.2 W/mK and a maximum operating temperature of about 570 K. Surface temperatures were measured using both thermocouples placed on the surface of the test plate and an AGEMA 870 IR camera system. The IR camera system provided a two-dimensional distribution of the temperature on the plate surface. The image of the test plate surface was digitized into an array of 140 × 140 pixels. Accounting for the optical setup used with the IR camera, a spatial resolution 0.8 mm × 0.8 mm per pixel could be achieved. The test plate surface was covered by black paint of a well-known emissivity of 0.95. The thermocouples placed on the plate surface were used for an in situ calibration of the IR camera system to increase the accuracy of the temperature measurements. Details of the in situ calibration procedure were given by Martiny et al. (1996).

Since mainflow Mach numbers up to 1.2 were considered in the present study, viscous dissipation and compressibility effects cannot be neglected. Therefore, the definition of the local film-cooling effectiveness η was based on the mainflow recovery temperature as a reference temperature

$$\eta(x/D, z/D) = \frac{T_{AW}(x/D, z/D) - T_{Rec,m}}{T_{tc} - T_{Rec,m}}$$

The mainflow recovery temperature was measured on the test plate at a location not affected by the coolant ejection.

Results and Discussion

Preliminary tests were performed to check results of the present facility against previously published data presented by Sinha et al. (1991), Schmidt et al. (1996a), and Schmidt et al. (1996b). These references were chosen since the cylindrical hole geometries they used at high density ratios were similar to those applied in the present study.

	α	L/D	DR	Ma_m
Present study	30°	6	1.85	0.3
Schmidt et al. (1996a)	35°	4	1.6	<0.1
Schmidt et al. (1996b)	30°	6	2.0	<0.1
Sinha et al. (1991)	35°	1.75	1.6, 2.0	<0.1

Figure 3 illustrates the good agreement between the present results and previously published data in terms of centerline effectiveness at moderate as well as high blowing ratios. The deviations of the different studies in the near-hole region at the moderate blowing ratio are believed to be due to differences in the experimental setup (i.e., hole inclination, hole length-to-diameter ratio, density ratio, and boundary layer thickness), which would be most apparent close to the hole. At high blowing ratio, all studies indicate that the coolant jet is detached from the surface, resulting in a very low effectiveness.

The main contributions to uncertainty in measuring the film-cooling effectiveness were due to variations in blowing ratio (δM = 2 percent). As pointed out by Schmidt et al. (1996a) the jet position relative to the wall is very sensitive to slight variations of the blowing ratio at high blowing ratios. Other uncertainty contributions include thermocouple measurements for coolant and recovery temperatures. As shown by Martiny et al. (1996) the maximum deviation of the temperatures measured by means of the IR camera system from the temperatures of the surface thermocouples was less than 1.5 K. Combining these uncertainties results in an average uncertainty of 1.5 percent for the local and laterally averaged film-cooling effectiveness. The maximum uncertainty was calculated to be 8 percent. The uncertainty in setting the external and internal Mach number was within 3 percent and in setting the temperature ratio was 1.5 percent.

The results of the present investigation will be presented in terms of two-dimensional effectiveness distributions, streamwise and spanwise variations of the local effectiveness as well as streamwise variation of laterally averaged effectiveness. As a baseline case, a mainflow Mach number of Ma_m = 0.6 and a

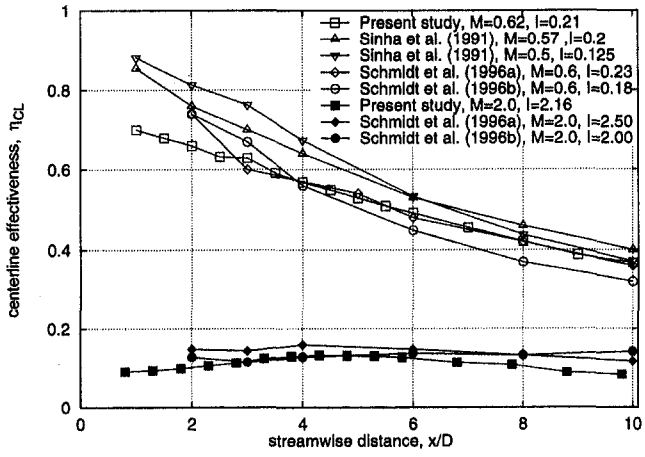

Fig. 3 *Comparison of present results to published data*

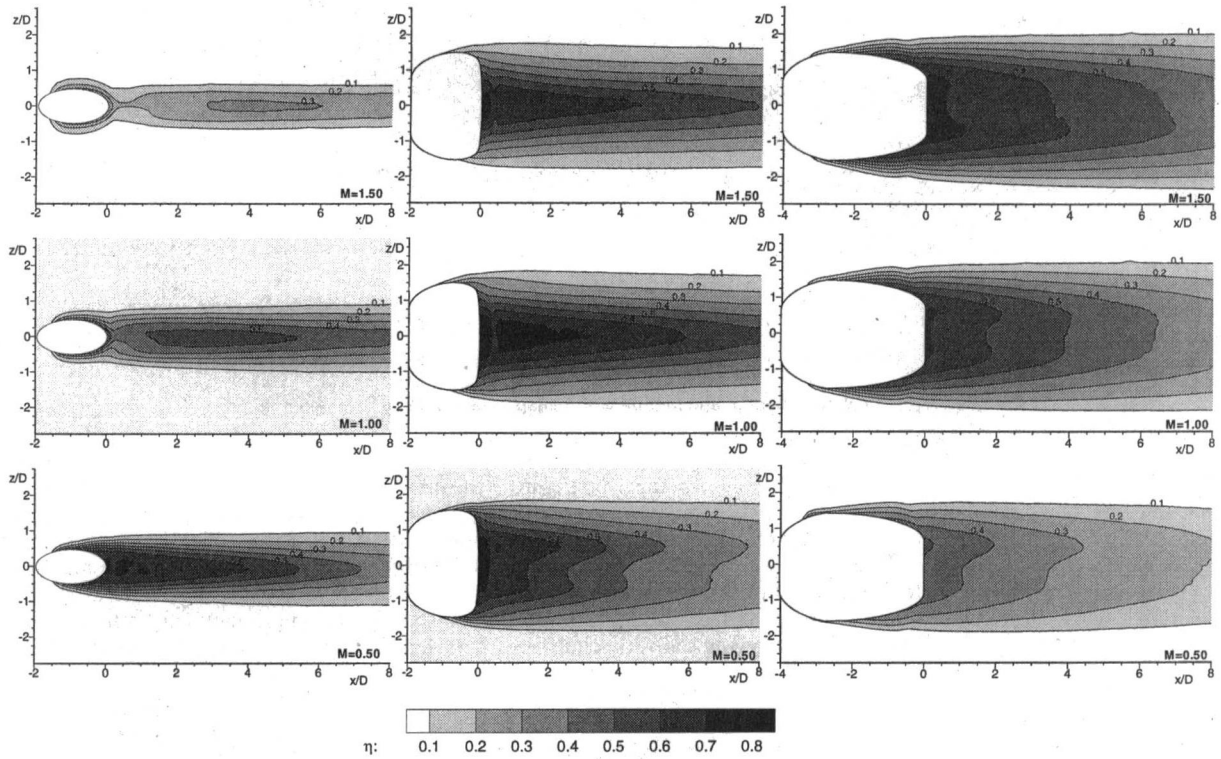

Fig. 4 Local effectiveness η for the cylindrical, fan-shaped, and laid-back fan-shaped hole at $Ma_m = 0.6$, $Ma_c = 0.0$, and $\beta = 0$ deg

coolant supply passage crossflow Mach number of $Ma_c = 0.0$ (i.e., plenum condition) were chosen from the test matrix. For this flow configuration, the effect of hole geometry and blowing ratio will be shown. Furthermore, the effect of the mainflow Mach number, the coolant supply passage crossflow Mach number as well as the coolant supply passage orientation on film-cooling performance will be presented for all hole geometries and compared to the baseline case.

Two-Dimensional Effectiveness Distribution. Figure 4 shows the two-dimensional distribution of the film-cooling effectiveness derived from IR camera images downstream of the baseline cylindrical hole, the fan-shaped hole, and the laid-back fan-shaped hole for three blowing ratios ($M = 0.5$, 1.0, and 1.5). For the cylindrical hole the jet was found to be detached from the surface at the high blowing ratio ($M = 1.5$), resulting in a poor effectiveness. Decreasing the blowing ratio increases the effectiveness since the penetration of the jet into the mainflow is reduced. The lateral spreading of the jet is very poor. For the fan-shaped hole, only a small separation zone was found in the vicinity of the hole exit for high blowing ratios indicated by a slight decrease of effectiveness. The spreading of the jet is much better compared to the cylindrical hole, but most of the jet is still ejected along the centerline, resulting in large gradient in lateral direction, at least for high blowing ratios. For the laid-back fan-shaped hole, the centerline effectiveness is lower compared to the fan-shaped hole. On the other hand, improved spreading of the cooling film compared to the fan-shaped hole was found. The nonsymmetric character of the flow exiting both shaped holes will be discussed later.

Effect of Hole Shape

Local Effectiveness. Figure 5 presents centerline effectiveness for all three hole geometries, confirming the conclusions drawn from the two-dimensional effectiveness images. Figure 6 shows the lateral distribution of effectiveness at $x/D = 6$. The lateral expansion of the jet ejected from the cylindrical hole is small compared to both expanded holes, as one would expect. The fan-shaped hole provides a high centerline effectiveness, but effectiveness decreases rapidly off-centerline. Increasing the blowing ratio has only a small impact on effectiveness at $z/D > 1.25$. For the laid-back fan-shaped hole, centerline effectiveness is lower compared to the fan-shaped hole, but the spreading of the jet is better, which leads to improved off-centerline effectiveness.

Figure 7 presents centerline effectiveness plotted versus blowing ratio at streamwise locations $x/D = 2$, 6, and 10. Maximum centerline effectiveness for the cylindrical hole occurs at low blowing ratios; further increasing the blowing ratio leads to jet separation and, therefore, drastically reduced effectiveness. Maximum centerline effectiveness for the fan-shaped hole was found at a blowing ratio of about unity. Further increasing the blowing ratio leads only to a slight reduction of effectiveness. For the laidback fan-shaped hole no maximum

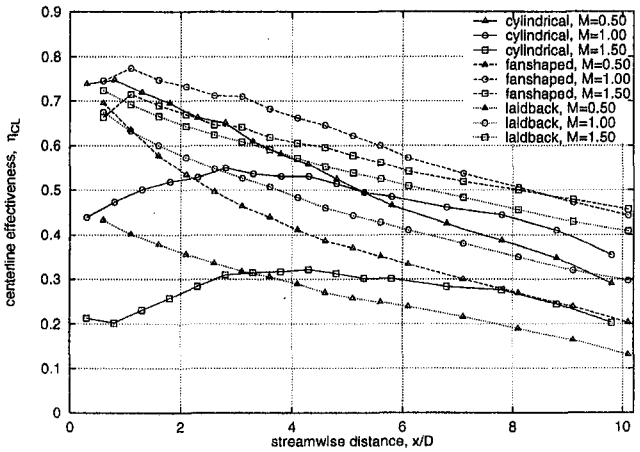

Fig. 5 Centerline effectiveness η_{CL} for the three holes tested at $Ma_m = 0.6$, $Ma_c = 0.0$, and $\beta = 0$ deg

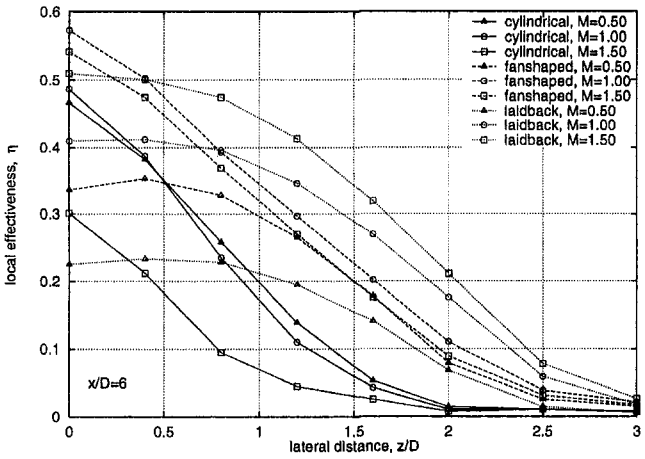

Fig. 6 Local lateral effectiveness η for the three holes tested at Ma_m = 0.6, Ma_c = 0.0, and β = 0 deg

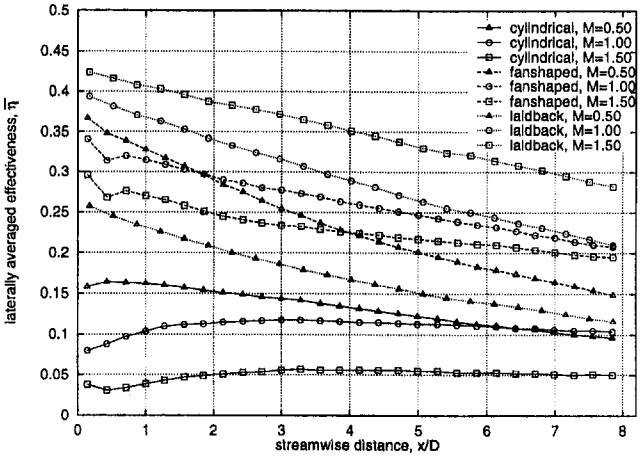

Fig. 8 Laterally averaged effectiveness $\bar{\eta}$ for the three holes tested at Ma_m = 0.6, Ma_c = 0.0, and β = 0 deg

effectiveness was found. Centerline effectiveness increases for all blowing ratios within the range considered.

Laterally Averaged Effectiveness. To account for the lateral spreading of the jet, local film-cooling effectiveness values were averaged across the lateral range covered by the IR camera ($z/D = \pm 2.75$) resulting in laterally averaged effectiveness

$$\bar{\eta}(x/D) = \frac{1}{5.5}\int_{-2.75}^{2.75} \eta(x/D, z/D)d(z/D)$$

Figure 8 presents the laterally averaged film-cooling effectiveness plotted versus streamwise distance for the three hole geometries. Due to the fact that the jet ejected from the cylindrical hole penetrates far into the mainflow and the lateral spreading of the film downstream of the cooling hole is very limited, the film-cooling performance at a high blowing ratio is poor. For both expanded holes, effectiveness decreases monotonously with streamwise distance from the hole for all blowing ratios considered. The superiority of the expanded holes as compared to the cylindrical hole is clearly demonstrated.

The differences between the fan-shaped and the laidback fan-shaped hole are shown in Fig. 9 where laterally averaged effectiveness is plotted versus blowing ratio. Additionally performed temperature measurements showed a streamwise increase of the surface temperature in the laid-back portion of the laid-back fan-shaped hole. This is obviously due to mixing of hot mainflow and coolant jet in the laid-back portion of the hole, which is exposed to the hot mainflow, revealing lower laterally averaged effectiveness as compared to the fan-shaped hole at low blowing ratios. For elevated blowing ratios, however, the performance of the laidback fan-shaped hole is better because of the limited lateral spreading of the jet ejected from the fan-shaped hole.

Effect of Crossflow Mach Number at Hole Exit. Most previous film-cooling studies using flat test plates applied relatively low-speed mainflows and, therefore, didn't match enginelike conditions. To evaluate the effect of crossflow Mach number at the hole exit, the three test geometries were tested at three blowing ratios (M = 0.5, 1.0, 1.5) for three external crossflow Mach numbers (Ma_m = 0.3, 0.6, 1.2). It is the first time that the effect of a supersonic crossflow on discrete hole flat plate film-cooling effectiveness was investigated.

The results for the cylindrical hole (Fig. 10(a)) show that the laterally averaged film-cooling effectiveness is hardly affected by the crossflow Mach number for the subsonic test cases (Ma_m = 0.3 and 0.6) at all blowing ratios investigated, which corresponds to the findings of Liess (1975). The minor differences are due to run-to-run variations of the blowing ratio, as discussed above. For the supersonic case (Ma_m = 1.2), however, the laterally averaged effectiveness was found to be increased as compared to the subsonic test cases. Two reasons can be identified for this behavior. The first reason is the drastically altered flowfield for the case of jet injection into a supersonic crossflow as discussed in previous studies (e.g., Spaid and Zu-

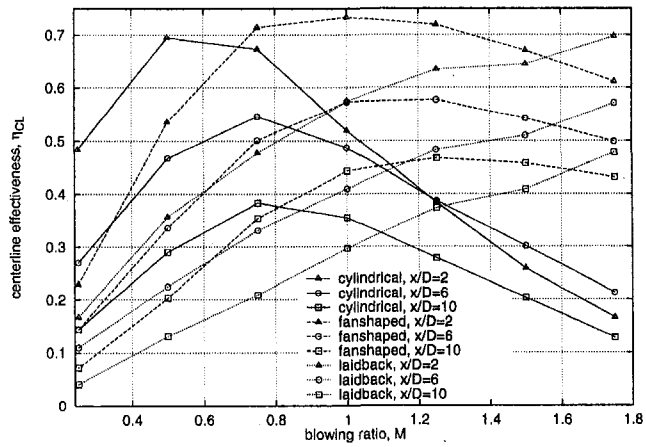

Fig. 7 Effect of blowing ratio M on centerline effectiveness η_{CL} for the three holes tested at Ma_m = 0.6, Ma_c = 0.0, and β = 0 deg

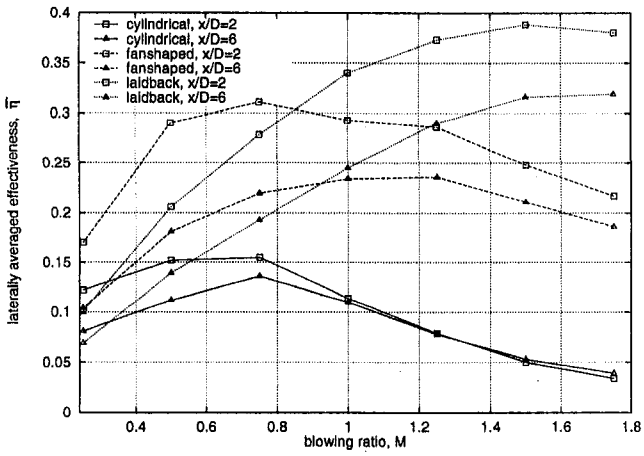

Fig. 9 Effect of blowing ratio M on laterally averaged effectiveness $\bar{\eta}$ for the three holes tested at Ma_m = 0.6, Ma_c = 0.0, β = 0 deg

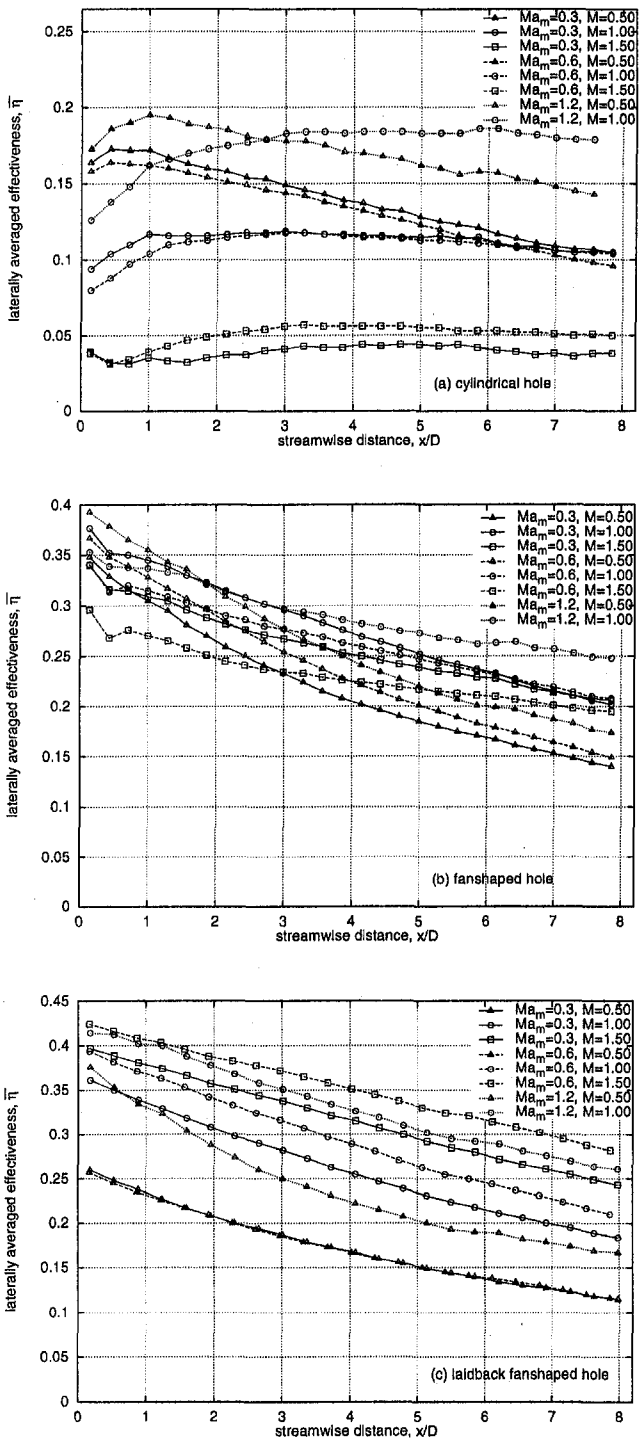

Fig. 10 Effect of mainflow Mach number Ma_m on the laterally averaged effectiveness $\bar{\eta}$ for the three holes tested at $Ma_c = 0.0$ and $\beta = 0$ deg

koski, 1968). The jet acts as an obstacle to the crossflow, causing the generation of a bow shock upstream of the injection location. Approaching the bow shock, the boundary layer faces a positive pressure gradient, which leads to a separation of the boundary layer from the surface. At the separation location an additional weak shock is formed. Downstream of the injection location, the combined jet and crossflow is forced back to the surface by means of a recompression shock. Obviously, the shock-induced pressure field turns the ejected jet rapidly into a flow parallel to the surface. Therefore, film-cooling effectiveness is increased compared to subsonic test cases. This holds true particularly for higher blowing ratios since in these cases the lift-off of the jet is impeded by the shock-induced pressure field. Additionally, the second reason, the change in crossflow Mach number of course affects the local recovery temperature of the flow. A reduced Mach number in the vicinity of the injection location leads to a slightly increased film-cooling effectiveness since the calculation of the effectiveness is based on the recovery temperature of the undisturbed crossflow. However, this effect is rather small because the reduction of the Mach number is small since the speed of the undisturbed crossflow is close to sonic.

For the expanded holes (Fig. 10(b) and 10(c)) the penetration into the mainflow is not that pronounced as for the cylindrical hole as shown earlier (Thole et al., 1998). Therefore, the effect of a supersonic crossflow on film-cooling performance as described above is evident, but not as pronounced as for the cylindrical hole. For these holes, the results of the subsonic test cases differ somewhat, too. Two main reasons can be identified for this behavior. First, for the $Ma_m = 0.6$ test cases, an increased pressure ratio is needed to apply the same blowing ratio as compared to the $Ma_m = 0.3$ test cases. Laser light sheet flow visualization showed that the pressure ratio across the hole affects the coolant distribution in the hole exit plane: the higher the pressure ratio, the more coolant is ejected at the hole centerline. Lateral spreading is reduced. This is particularly true for the fan-shaped hole at high blowing ratios. Second, further experiments, which are not presented here in detail, revealed that the jet tends to separate from one of the side walls in a certain low-pressure-ratio range in the diffuser section of the hole, as indicated by Fig. 4. The skewed cooling film ejected from the hole leads to a reduced laterally averaged film-cooling effectiveness. This behavior was found for the fan-shaped at low blowing ratios as well as for the laidback fan-shaped for all blowing ratios. This effect is mainly dominated by the relatively large expansion angle of these holes. This is, however, only a temporary phenomenon since at even lower pressure ratios the flow becomes attached to both side walls, which is the range the diffuser operates at its best.

Effect of Coolant Crossflow Mach Number and Orientation. Thus far, none of the film-cooling studies reported have investigated the effect of crossflow at the hole entrance. A plenum, widely used to feed the film-cooling holes, is not necessarily a correct means to represent the internal coolant supply passage of an airfoil. To evaluate the effect of coolant supply passage crossflow, three representative crossflow conditions were chosen from the test matrix. These comprise coolant passage Mach numbers $Ma_c = 0.0$ (i.e., plenum condition) and $Ma_c = 0.6$. For the $Ma_c = 0.6$ case two different orientations of the coolant passage with respect to the mainflow were considered: parallel ($\beta = 0$ deg) and perpendicular ($\beta = 90$ deg).

For the cylindrical hole (Fig. 11(a)), at the low blowing ratio applied, no effect of the flow conditions at the hole entrance was found. At elevated blowing ratios, however, cooling performance is significantly affected. As pointed out by Thole et al. (1997), the flow conditions at the hole entrance govern the jet velocity and turbulence intensity distribution in the hole exit plane. Measurements reported showed that for the case of high coolant passage crossflow Mach number, a separation region is formed at the windward side of the hole entrance, shifting the coolant jet to the leeward side. The jet is ejected from the hole on the leeward side at a shallow flow angle. For the case of plenum condition, however, a separation region is formed at the leeward side of the hole entrance, shifting the coolant jet to the windward side. The jet is ejected from the hole more on the windward side at a rather steep flow angle. This causes enhanced mixing with the hot crossflow and leads to a reduced film-cooling effectiveness, as shown in Fig. 11(a). Rotating the coolant supply passage to a perpendicular position keeps the jet closer to the wall, particularly at high blowing ratios,

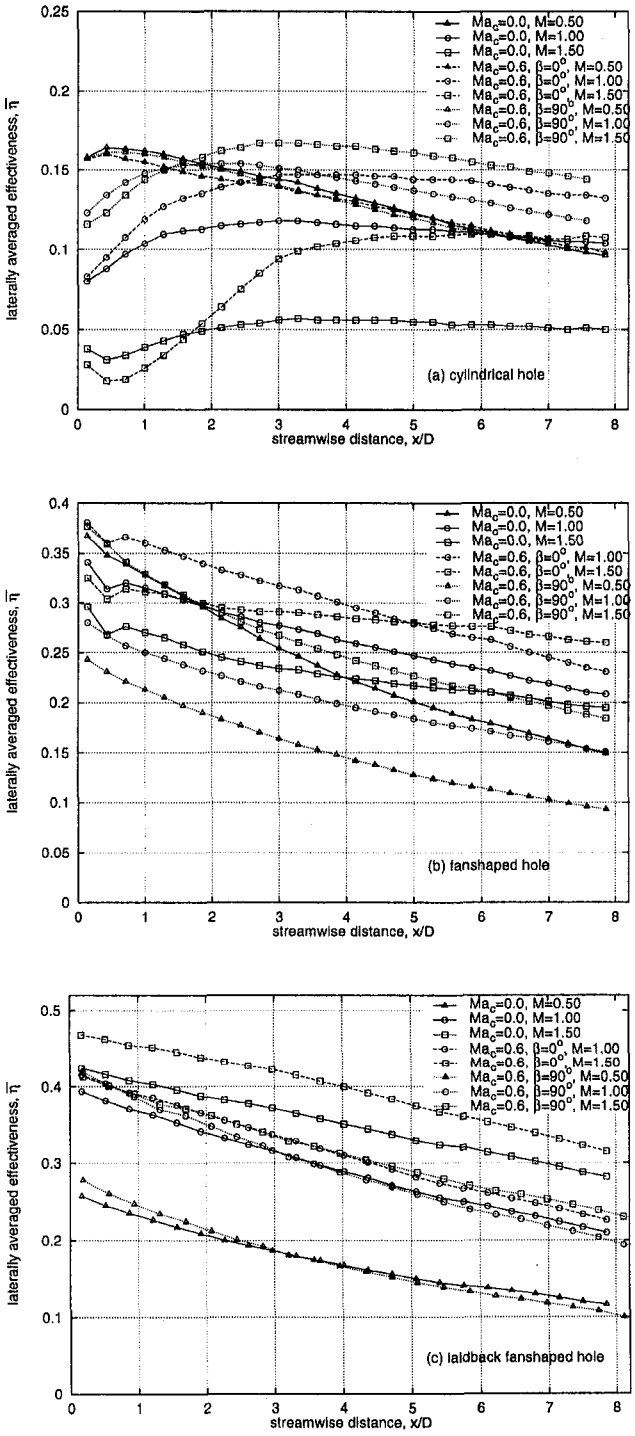

Fig. 11 Effect of coolant supply passage Mach number Ma_c and orientation β on the laterally averaged effectiveness $\bar{\eta}$ for the three holes tested at Ma_m = 0.6

leading to an improved lateral spreading as well as to an increased maximum effectiveness.

For the fan-shaped hole (Fig. 11(*b*)) the effect of the coolant passage crossflow Mach number is not as pronounced as for the cylindrical hole. The trend holds true that the film-cooling effectiveness is improved for the high-Mach-number crossflow in the coolant passage. The effect of rotating the coolant supply passage to a perpendicular position is contrary to the cylindrical hole. Effectiveness is rather reduced since the flow entering the diffuser section of the hole is highly disturbed, resulting in a poor performance of the diffuser and, therefore, a reduced lateral spreading of the jet. For the laid-back fan-shaped hole (Fig. 11(*c*)) only at the high blowing ratio an effect of coolant crossflow Mach number and orientation could be detected.

Figure 12 shows the two-dimensional effectiveness distribution for the case of the coolant passage being rotated to a perpendicular position with respect to the mainflow. Coolant supply approach is from down to top. As can be seen, the maximum effectiveness either occurs on the upstream side with respect to the coolant flow approach (i.e., for the cylindrical and the laid-back fan-shaped hole) resulting from a "reflection" of the jet inside the hole or on the downstream side (i.e., for the fan-shaped hole). Further experiments showed that only for the cylindrical hole is the location of the maximum strongly dependent on blowing ratio. The general trend was that for high blowing ratios the maximum occurs on the downstream side and moves to the upstream side as the blowing ratio is reduced. For both expanded holes, the position of the maximum was not affected by the blowing ratio within the range considered.

Conclusions

An experimental investigation was conducted to determine the effect of hole geometry, including a cylindrical hole and two holes with a diffuser-shaped exit portion on film-cooling performance. At the hole exit side, crossflow Mach numbers up to 1.2 were considered. Additionally, the effect of internal coolant supply channel Mach number and orientation was investigated. The results showed that:

- Holes with expanded exits show significantly improved film-cooling effectiveness as compared to a cylindrical hole, particularly at high blowing ratios.

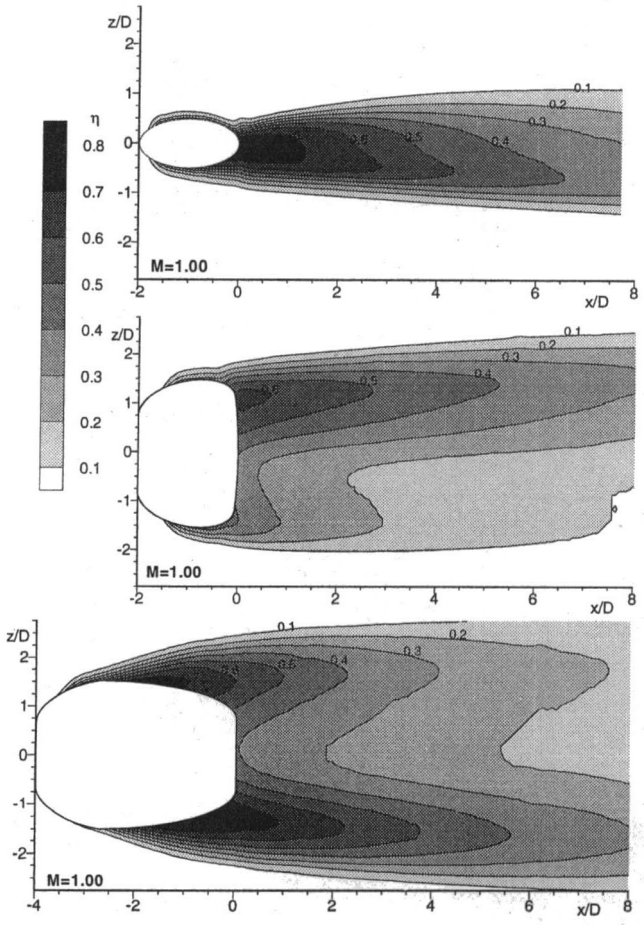

Fig. 12 Local effectiveness η at Ma_m = 0.6, Ma_c = 0.6, M = 1.0, and β = 90 deg: (*a*) cylindrical, (*b*) fan-shaped, (*c*) laid-back fan-shaped hole (coolant flow approach from down to top)

- The laid-back fan-shaped hole provides a better lateral spreading of the jet as compared to the fan-shaped hole and, therefore, leads to increased laterally averaged effectiveness, particularly at high blowing ratios.
- Transonic crossflow at hole exit side drastically alters the flowfield in the vicinity of the ejection location. Film-cooling effectiveness is increased as compared to subsonic flow cases, particularly for the cylindrical hole.
- Coolant crossflow Mach number and orientation have a strong impact on film-cooling performance in the near-hole region. Therefore, crossflow at the hole entrance side has to be taken into account when modeling film-cooling at engine representative conditions.

Acknowledgments

This study was partly funded by the European Union through grant by the Brite Euram program "Investigation of the Aerodynamics and Cooling of Advanced Engine Turbine Components" under Contract No. AER2-CT92-0044.

References

Giebert, D., M. Gritsch, A. Schulz, and S. Wittig, 1997, "Film-Cooling From Holes With Expanded Exits: A Comparison of Computational Results With Experiment," ASME Paper No. 97-GT-163.

Goldstein, R., E. Eckert, and F. Burggraf, 1974, "Effects of Hole Geometry and Density on Three-Dimensional Film Cooling," *Int. J. Heat Mass Transfer,* Vol. 17, pp. 595–607.

Gritsch, M., A. Schulz, and S. Wittig, 1998, "Discharge Coefficient Measurements of Film-Cooling Holes With Expanded Exits," ASME JOURNAL OF TURBOMACHINERY, Vol. 120, this issue, pp. 557–563.

Haller, B., and J. Camus, 1984, "Aerodynamic Loss Penalty Produced by Film Cooling Transonic Turbine Blades," ASME *Journal of Engineering for Gas Turbines and Power,* Vol. 106, pp. 198–205.

Hay, N., D. Lampard, and S. Benmansour, 1983, "Effect of Crossflows on the Discharge Coefficient of Film Cooling Holes," ASME *Journal of Engineering for Power,* Vol. 105, pp. 243–248.

Hay, N., and D. Lampard, 1995, "The Discharge Coefficient of Flared Film Cooling Holes," ASME Paper No. 95-GT-15.

Liess, C., 1975, "Experimental Investigation of Film Cooling With Ejection From a Row of Holes for the Application to Gas Turbine Blades," ASME *Journal of Engineering for Power,* Vol. 97, pp. 21–27.

Makki, Y., and G. Jakubowski, 1986, "An Experimental Study of Film Cooling From Diffused Trapezoidal Shaped Holes," AIAA Paper No. 86-1326.

Martiny, M., R. Schiele, M. Gritsch, A. Schulz, and S. Wittig, 1996, "In Situ Calibration for Quantitative Infrared Thermography," in: *QIRT'96 Eurotherm Seminar No. 50,* Stuttgart, Germany, Sept. 2–5.

Schmidt, D., B. Sen, and D. Bogard, 1996a, "Film Cooling With Compound Angle Holes: Adiabatic Effectiveness," ASME JOURNAL OF TURBOMACHINERY, Vol. 118, pp. 807–813.

Schmidt, D., B. Sen, and D. Bogard, 1996b, "Effect of Surface Roughness on Film Cooling," ASME Paper No. 96-GT-299.

Sen, B., D. Schmidt, and D. Bogard, 1996, "Film Cooling With Compound Angle Holes: Heat Transfer," ASME JOURNAL OF TURBOMACHINERY, Vol. 118, pp. 800–806.

Sinha, A., D. Bogard, and M. Crawford, 1991, "Film Cooling Effectiveness Downstream of a Single Row of Holes With Variable Density Ratio," ASME JOURNAL OF TURBOMACHINERY, Vol. 113, pp. 442–449.

Spaid, F., and E. Zukoski, 1968, "A Study of the Interaction of Gaseous Jets From Transverse Slots With Supersonic External Flows," *AIAA Journal,* Vol. 6, pp. 205–212.

Thole, K., M. Gritsch, A., Schulz, and S. Wittig, 1997, "Effect of a Crossflow at the Entrance to a Film-Cooling Hole," ASME *Journal of Fluids Engineering,* Vol. 119, pp. 533–540.

Thole, K., M. Gritsch, A. Schulz, and S. Wittig, 1998, "Flowfield Measurements for Film-Cooling Holes With Expanded Exits," ASME JOURNAL OF TURBOMACHINERY, Vol. 120, pp. 327–336.

Wittig, S., A. Schulz, M. Gritsch, and K. Thole, 1996, "Transonic Film-Cooling Investigations: Effects of Hole Shapes and Orientations," ASME Paper No. 96-GT-222.

Discharge Coefficient Measurements of Film-Cooling Holes With Expanded Exits

M. Gritsch

A. Schulz

S. Wittig

Lehrstuhl und Institut für Thermische Strömungsmaschinen, Universität Karlsruhe (T.H.), Kaiserstr. 12, 76128 Karlsruhe, Germany

This paper presents the discharge coefficients of three film-cooling hole geometries tested over a wide range of flow conditions. The hole geometries include a cylindrical hole and two holes with a diffuser-shaped exit portion (i.e., a fan-shaped and a laidback fan-shaped hole). The flow conditions considered were the crossflow Mach number at the hole entrance side (up to 0.6), the crossflow Mach number at the hole exit side (up to 1.2), and the pressure ratio across the hole (up to 2). The results show that the discharge coefficient for all geometries tested strongly depends on the flow conditions (crossflows at hole inlet and exit, and pressure ratio). The discharge coefficient of both expanded holes was found to be higher than of the cylindrical hole, particularly at low pressure ratios and with a hole entrance side crossflow applied. The effect of the additional layback on the discharge coefficient is negligible.

Introduction

Correctly sizing film-cooling holes is critical in achieving the necessary cooling for gas turbine nozzle guide vanes and rotor blades. High blowing rates can result in inefficient use of turbine working fluid, as well as reduced cooling effectiveness because of jet detachment. Low blowing rates also result in reduced cooling effectiveness and blade areas with high thermal loads. Discharge coefficients, needed to determine actual film-cooling blowing ratios and momentum flux ratios, are dependent on hole geometry as well as inlet and exit flow conditions.

Most of the data that have been presented in the literature with regard to discharge coefficients of film-cooling holes have been reported by researchers at the University of Nottingham, i.e., studies by Hay et al. (1983, 1994a, b), and Hay and Lampard (1995). Based on their results, the discharge coefficient scaled best with the total coolant-to-static mainstream pressure ratio. They found discharge coefficients to be strongly dependent on internal crossflow conditions with only weak dependence on external crossflow conditions within the range considered. A review of published data on discharge coefficients for film-cooling applications was given recently by Hay and Lampard (1998).

The geometry of the film-cooling holes has received recent attention in attempts to optimize the film-cooling parameters (e.g., Goldstein et al., 1974; Makki and Jakubowski, 1986; Schmidt et al., 1996; Sen et al., 1996). Haller and Camus (1984) performed aerodynamic loss measurements on a two-dimensional transonic cascade. Holes with a spanwise flare angle of 25 deg were found to offer significant improvements in film-cooling effectiveness without any additional loss penalty. Film-cooling holes with a diffuser-shaped expansion at the exit portion of the hole are believed to improve the film-cooling performance on a gas turbine blade. The increased cross-sectional area at the hole exit compared to a standard cylindrical hole leads to a reduction of the mean velocity and, thus, of the momentum flux of the jet exiting the hole. Therefore, the penetration of the jet into the mainflow is reduced, resulting in an increased cooling efficiency. Furthermore, lateral expansion of the hole provides an improved lateral spreading of the jet, leading to a better coverage of the airfoil in the spanwise direction and a higher spanwise averaged film-cooling efficiency.

Flowfield measurements performed by Thole et al. (1998) showed that jet penetration as well as velocity gradients in the mixing region were significantly reduced for holes with expanded exits as compared to cylindrical holes at the same blowing rate. Peak turbulence levels were found downstream of the hole exit for the cylindrical hole and in the hole exit plane for the expanded holes. In a companion paper (Gritsch et al., 1998), film-cooling effectiveness measurements are presented for the same hole geometries as investigated in the present paper. Both expanded holes show significantly improved thermal protection as compared to the cylindrical hole. The laidback fan-shaped hole provides a better lateral spreading of the film ejected from the hole than the fan-shaped hole, which leads to higher laterally averaged film-cooling effectiveness.

So far, only Hay and Lampard (1995) have reported on discharge coefficients for shaped cooling holes. They investigated cylindrical holes with a lateral expansion angle of 12.5 deg (flared holes) and holes with an additional layback of 7.5 deg. It was found that the discharge coefficient of flared holes is higher than for cylindrical holes. The layback did not further increase the discharge coefficient. However, they concentrated on very moderate mainflow Mach numbers up to 0.3 and did not report on any discharge coefficients for a film-cooling hole exposed to crossflows at both the hole entrance and exit side.

This study presents discharge coefficients for three hole geometries tested over a wide range of enginelike flow conditions. These comprise external Mach numbers up to 1.2, internal Mach numbers up to 0.6, and pressure ratios across the film-cooling hole up to 2. The hole geometries chosen for the present study are two holes with a cylindrical inlet portion and a diffuser-shaped exit portion and, for reasons of comparison, a cylindrical hole. One of the holes with the diffuser-shaped exit portion is additionally expanded in the mainflow direction by a layback. Since a wide range of flow conditions is covered by the present study, the data can be used either to derive correlations (Gritsch et al., 1997) or to validate CFD codes (Giebert et al., 1997).

Experimental Apparatus

The present investigation was carried out in a continuous flow wind tunnel at the Institut für Thermische Strömungsmaschinen (ITS), Karlsruhe. Details of the experimental facility can be found in Wittig et al. (1996). The air supply was furnished by a high-pressure, high-temperature (HPHT) test facility. The film-

Contributed by the International Gas Turbine Institute and presented at the 42nd International Gas Turbine and Aeroengine Congress and Exhibition, Orlando, Florida, June 2–5, 1997. Manuscript received at ASME Headquarters February 1997. Paper No. 97-GT-165. Associate Technical Editor: H. A. Kidd.

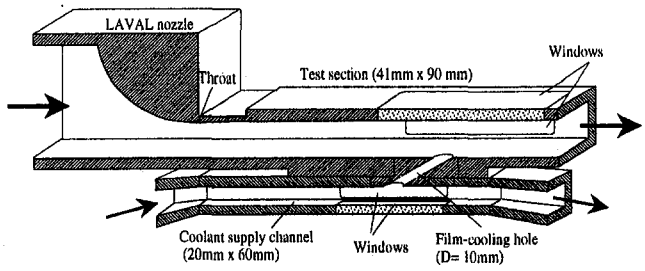

Fig. 1 Film-cooling test section

cooling test rig consists of a primary loop representing the external flow and a secondary loop representing the internal flow of an airfoil (see Fig. 1).

Primary Loop. The air supplied by the HPHT test facility passes a metering orifice and flow straighteners before it enters the test section through a LAVAL nozzle. The test section is 90 mm in width and 41 mm in height. For supersonic flow conditions the height is reduced to 32 mm. Using an adjustable upper wall, a zero pressure gradient in streamwise direction is set in the test section.

Preliminary tests were performed to evaluate the effect of the coolant-to-mainflow temperature ratio on the discharge coefficient. No measurable effect of temperature ratio on discharge coefficient was found in the range of $0.54 < T_{tc}/T_{tm} < 1$ as long as the external Mach number is matched. Therefore, the reported measurements were conducted with a mainflow temperature being equal to the coolant flow temperature of about 290 K.

Secondary Loop. Flow for the secondary loop is also provided by the HPHT test facility. However, the total pressure in the secondary loop can be set independently from the primary loop. The flow in the secondary loop is driven by an additional blower. Thus, the Mach number can be set by adjusting the volume flow rate circulating in the secondary loop. The cross-sectional area at the film-cooling hole is 60 mm in width and 20 mm in height. Due to a "closed loop" design of the secondary loop, the flow rate through the film-cooling hole is obtained directly, independently of the crossflow rate as presented by Wittig et al. (1996). Therefore, very accurate measurements of the flow rate through the film-cooling hole, which are imperative for an exact determination of the discharge coefficient, were achieved.

For all tests presented in the present paper, primary and secondary loop were parallel to each other, representing a flow condition usually found in the midportion of nozzle guide vanes.

Film-Cooling Hole Geometries Tested. All tests were carried out using single scaled-up film-cooling holes with an inclination angle of $\alpha = 30$ deg. In total, three hole geometries (one cylindrical hole and two expanded holes) were tested (see Fig. 2). All holes were sharp edged and the internal surfaces were aerodynamically smooth. The diameter of the cylindrical hole and the diameter of the cylindrical inlet section of the expanded holes was 10 mm. The length-to-diameter ratio L/D was 6 for all hole geometries. The lateral expansion angle of both expanded holes was 14 deg, resulting in a hole width of 30 mm at the hole exit. The forward expansion angle of the laidback fan-shaped hole was 15 deg, resulting in a hole length of 40 mm at the hole exit. The exit-to-entry area ratio of the fan-shaped and laidback fan-shaped hole were 3.0 and 3.1, respectively (areas perpendicular to hole axis).

The hole geometries were decided in cooperation with the industrial partners involved in the present research program. The chosen geometry of the expanded holes is in agreement with the suggestion of Hay and Lampard (1995) that the length of the cylindrical section at the hole entrance of the expanded holes should be at least two hole diameters. This is to allow the flow to reattach before entering the expanded section and, therefore, to improve the diffusion of the flow. A large expansion angle would lead to an improved lateral coverage of the ejected film, but flow separation in the diffuser section of the hole could occur. Therefore, the chosen expansion angle must be seen as a compromise.

Each hole geometry was tested for a matrix of three internal Mach numbers ($Ma_c = 0.0, 0.3, 0.6$) and four external Mach numbers ($Ma_m = 0.0, 0.3, 0.6, 1.2$) over a range of pressure ratios $1 < p_{tc}/p_m < 2$. Moreover, each hole geometry was tested

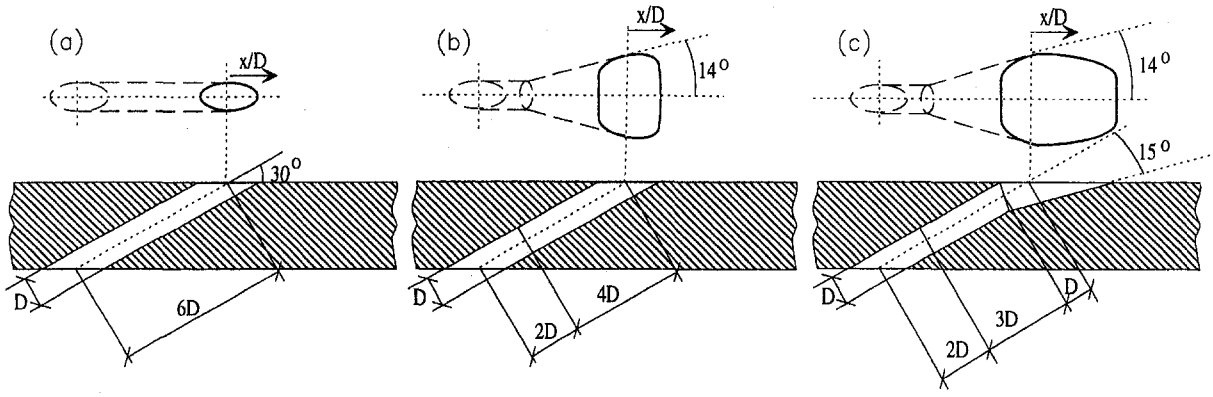

Fig. 2 Cylindrical, fan-shaped, and laidback fan-shaped film-cooling hole geometries

Nomenclature

C_D = discharge coefficient
D = film-cooling hole diameter
L = film-cooling hole length measured along the centerline axis
Ma = Mach number
$\dot{m}$ = mass flow rate through the film-cooling hole
p = static pressure
p_t = total pressure
R = gas constant
Re_D = Reynolds number based on film-cooling hole diameter
T_t = total temperature
Tu = turbulence intensity
α = angle of hole inclination
κ = ratio of specific heats

Subscripts

c = internal flow conditions
m = external flow conditions

Table 1 Operating conditions of the film-cooling test rig

Internal pressure	p_{tc}	up to 2 Bars
Internal Temperature	T_{tc}	290 K
Pressure ratio	p_{tc}/p_m	1 ... 2
Temperature ratio	T_{tc}/T_{tm}	1
Internal Mach number	Ma_c	0 ... 0.6
External Mach number	Ma_m	0 ... 1.2
Internal Reynolds number	Re_{Dc}	up to $2.5 \cdot 10^5$
External Reynolds number	Re_{Dm}	up to $2.1 \cdot 10^5$
Internal turbulence intensity	Tu_c	1 %
External turbulence intensity	Tu_m	<1.5 %

at four pressure ratios: p_{tc}/p_m = 1.1, 1.25, 1.4, 1.6 over a range of internal Mach number Ma_c = 0.0 to 0.6 with no external crossflow applied (Ma_m = 0.0). The operating conditions considered for the present investigation are shown in Table 1.

Definition of the Discharge Coefficient

The discharge coefficient C_D is the ratio of actual mass flow rate to ideal mass flow rate through the film-cooling hole. The ideal mass flow rate is calculated assuming an isentropic one-dimensional expansion from the total pressure in the secondary loop p_{tc} to the static pressure in the primary loop p_m. This leads to

$$C_D = \frac{\dot{m}}{p_{tc}\left(\frac{p_m}{p_{tc}}\right)^{(\kappa+1)/2\kappa}\sqrt{\frac{2\kappa}{(\kappa-1)RT_{tc}}\left(\left(\frac{p_{tc}}{p_m}\right)^{(\kappa-1)/\kappa}-1\right)}\frac{\pi}{4}D^2}$$

For the fan-shaped and the laidback fan-shaped holes, the discharge coefficient was based on the ideal mass flow rate through a cylindrical hole having the same diameter as the inlet section of the shaped holes. Thus, the discharge coefficient of the expanded holes can be directly compared to those of the cylindrical holes. This makes it more convenient to evaluate the effect of contouring the hole, but is a deviation from the classic definition of the discharge coefficient.

The total pressure and temperature in the coolant channel were measured $1D$ upstream of the cooling hole inlet with a probe located $2D$ off channel centerline. The static pressure in the mainstream was measured at the side wall $10D$ upstream of the hole exit for the subsonic flow case and at the top wall opposite the hole exit for the supersonic flow case.

Estimates of Accuracy

Uncertainties were estimated following the procedure given by Kline and McClintock (1953). The uncertainty in the values of C_D primarily resulted from the uncertainty in measuring the actual flow rate through the film-cooling hole and the uncertainty in determing the ideal flow rate. Due to the fact that the secondary loop was designed as a closed loop, the actual flow rate could be measured for all flow cases directly using a standard orifice leading to an uncertainty of 2.5 percent except for very low mass flow rates. The uncertainty in determining the ideal flow rate was calculated to be much less than 2 percent, except for very low pressure ratios. Overall, the uncertainty in the values of C_D was found to be less than 2 percent in most of the cases considered, increasing for low pressure ratios and mass flow rates up to 4.5 percent.

Results and Discussion

Cylindrical Hole. Although discharge coefficients of a 30 deg inclined cylindrical hole have been reported before by others, they will be presented here for two reasons. First, the studies conducted before only document a limited range of operational

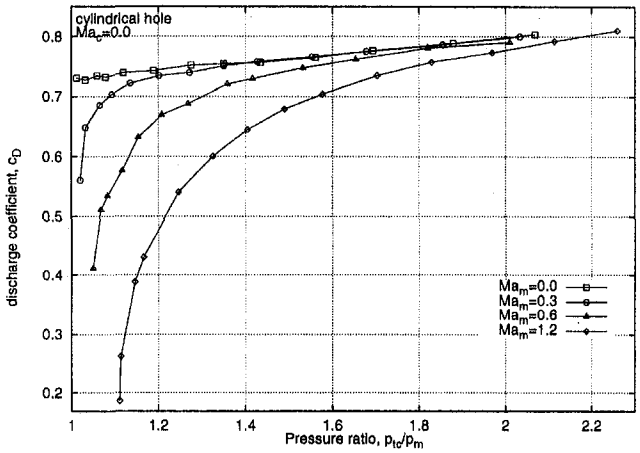

Fig. 3 Discharge coefficient C_D of the cylindrical hole at Ma_c = 0.0

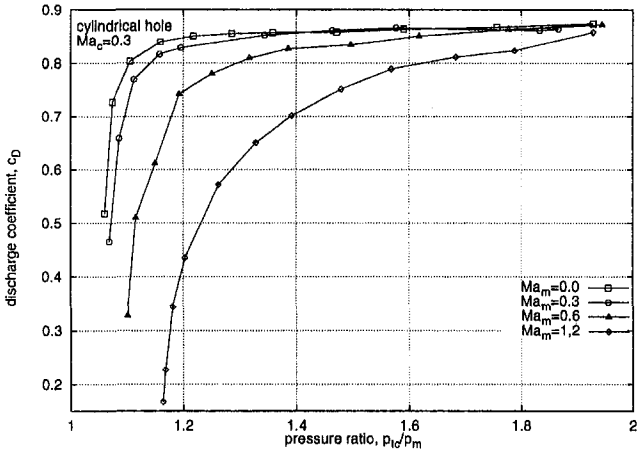

Fig. 4 Discharge coefficient C_D of the cylindrical hole at Ma_c = 0.3

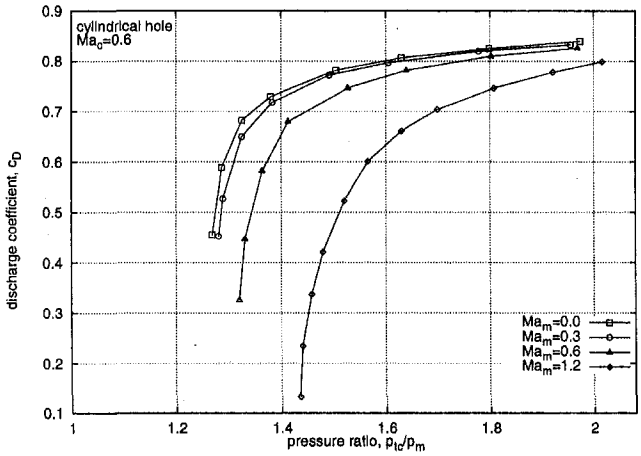

Fig. 5 Discharge coefficient C_D of the cylindrical hole at Ma_c = 0.6

conditions, particularly when the crossflow Mach numbers were quite moderate. Therefore, in the present study discharge coefficients of a 30 deg inclined cylindrical hole were measured over a wide range of crossflow Mach numbers. Second, it will serve as a baseline case to compare the discharge coefficients of the expanded holes to.

For zero external and internal crossflow only a weak dependence of the discharge coefficient C_D on the pressure ratio

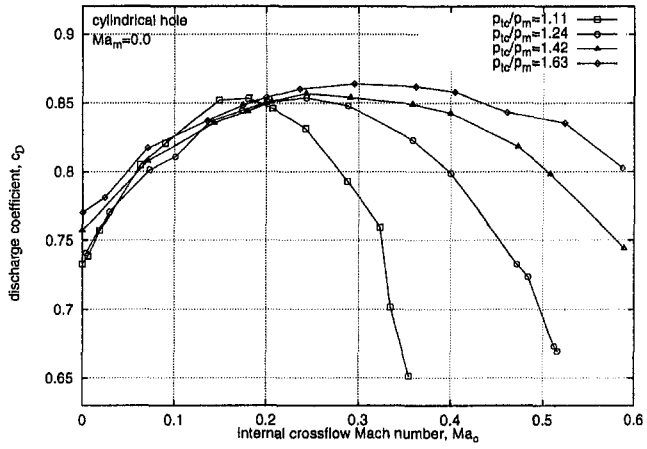

Fig. 6 Discharge coefficient C_D of the cylindrical hole: effect of internal crossflow Mach number Ma$_c$

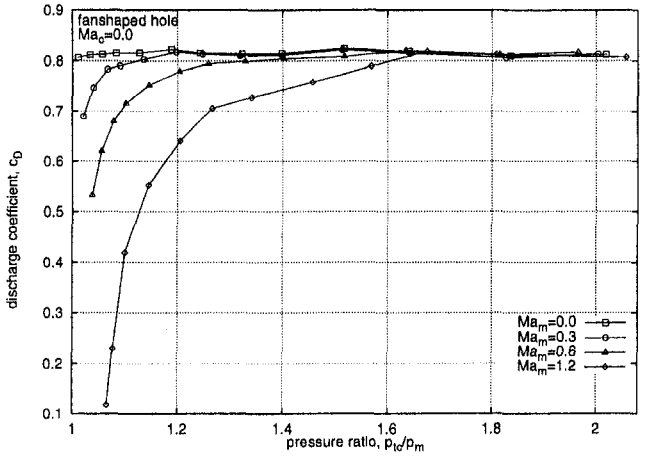

Fig. 7 Discharge coefficient C_D of the fan-shaped hole at Ma$_c$ = 0.0

p_{tc}/p_m was found (Fig. 3). There is a slight increase of the discharge coefficient C_D of about 10 percent when the pressure ratio p_{tc}/p_m is raised from 1 to 2. This effect, which doesn't occur for incompressible flows (Lichtarowicz et al., 1965) is believed to be due to a pressure ratio effect on the cross-sectional area of the vena contracta formed at the hole inlet and was reported by others before (e.g., Jackson, 1963; Hay et al., 1994b).

Figures 3–5 show the effect of external crossflow Mach number. While the internal crossflow Mach number was kept constant four different external Mach numbers (Ma$_m$ = 0, 0.3, 0.6, and 1.2) were tested over a range of pressure ratios $1 < p_{tc}/p_m < 2$. The effect of external crossflow is to decrease the discharge coefficient C_D. This effect is more pronounced at low pressure ratios and high external crossflow Mach numbers Ma$_m$. At high pressure ratios and low external crossflow Mach numbers, however, the discharge coefficient is almost not affected by the external crossflow. This effect is independent of the internal crossflow Mach number. Previous studies have reported only a negligible effect of the external crossflow Mach number since they investigated only a very limited range of external crossflow Mach numbers. Note that higher pressure ratios are required to have positive coolant flow through the hole as the internal crossflow Mach number Ma$_c$ is increased.

Figure 6 presents the effect of internal crossflow Mach number on the discharge coefficient for the case of no external crossflow. For each pressure ratio an internal crossflow Mach number exists for which the discharge coefficient C_D is at an optimum. This internal crossflow Mach number Ma$_{c,opt}$ is lower, the lower the pressure ratio. However, the level of optimum discharge coefficient is almost not affected by the pressure ratio.

As clearly indicated by flowfield measurements inside the cooling hole, reported by Thole et al. (1997), the size and location of the separation region at the entrance of the cooling hole strongly depend on the crossflow Mach number at the hole entrance side. For the case of no crossflow at the hole entrance side, a separation region was found at the downstream edge of the cooling hole. This separation region moves to the upstream edge of the hole for an elevated crossflow Mach number Ma$_c$ = 0.5. For a medium Mach number Ma$_c$ = 0.3, most of the jet was found in the center of the hole, indicating that the effect of the separation region is very small, if there is a separation region at all. This is proved by the drastically decreased turbulence levels inside the hole of the Ma$_c$ = 0.3 flow case as compared to the Ma$_c$ = 0 and Ma$_c$ = 0.5 flow cases. Those findings were confirmed by the present discharge coefficient measurements. The peak value discharge coefficient occurs at a crossflow Mach number Ma$_{c,opt}$ for which the flow enters the hole without jet separation taking place. If a crossflow Mach

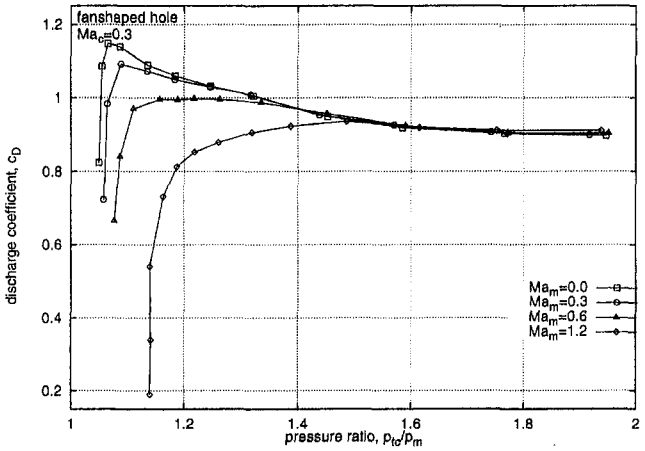

Fig. 8 Discharge coefficient C_D of the fan-shaped hole at Ma$_c$ = 0.3

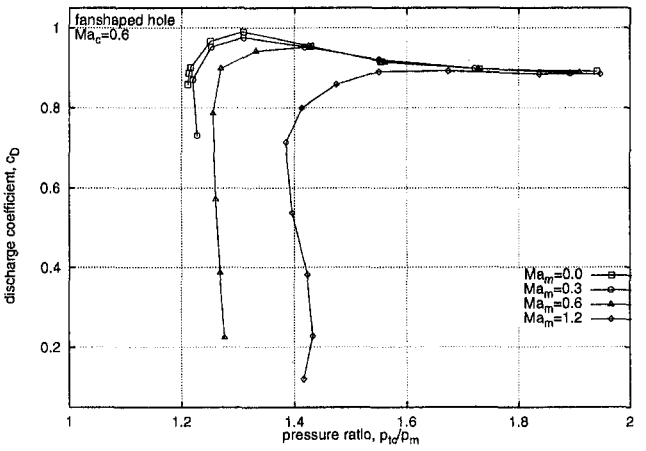

Fig. 9 Discharge coefficient C_D of the fan-shaped hole at Ma$_c$ = 0.6

number applied is lower than Ma$_{c,opt}$ jet separation occurs at the downstream edge of the hole inlet; if it is higher than Ma$_{c,opt}$ jet separation occurs at the upstream edge of the hole inlet, both producing additional losses and, therefore, resulting in decreased discharge coefficients.

Fan-Shaped Hole. Figures 7–10 present the discharge coefficient measurements for the fan-shaped hole. For the zero external and internal crossflow case the discharge coefficient

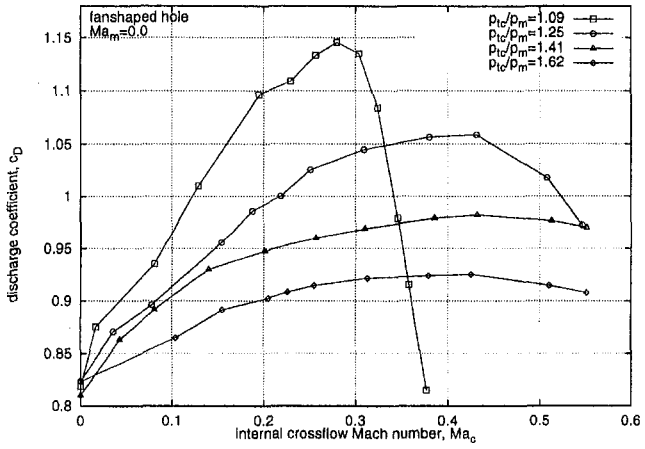

Fig. 10 Discharge coefficient C_D of the fan-shaped hole: effect of internal crossflow Mach number Ma_c

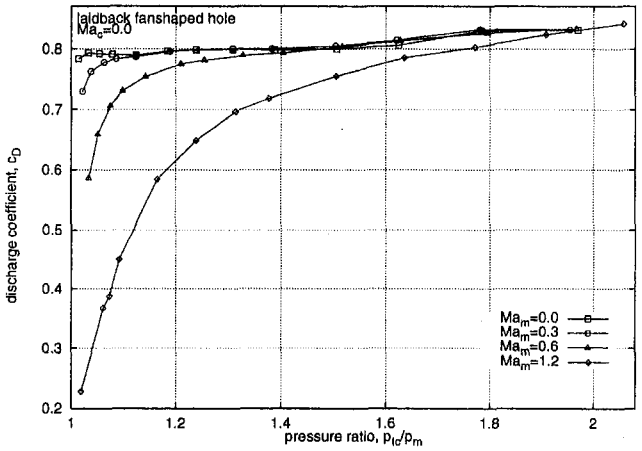

Fig. 11 Discharge coefficient C_D of the laidback fan-shaped hole at $Ma_c = 0.0$

was found to be almost independent of the pressure ratio, indicating that the flow through the hole is choked even at low pressure ratios. With an external crossflow applied, two flow regimes can be identified. For high pressure ratios the external crossflow doesn't affect the discharge coefficient at all. For low pressure ratios, however, external crossflow leads to decreased discharge coefficients. The reduction of the discharge coefficient is more pronounced at elevated crossflow Mach numbers. This extends the findings of Hay and Lampard (1995), who reported that external crossflow has no effect on the discharge coefficient since they only investigated crossflow Mach numbers up to 0.3.

With internal crossflow applied the behavior of the fan-shaped hole differs significantly from the cylindrical hole. For low pressure ratios, the discharge coefficient was found to be increased as compared to high pressure ratios. Discharge coefficients exceeding unity were measured indicating that the actual flow rate through the hole is even higher than the ideal flow rate through a cylindrical hole with the same inlet cross-sectional area due to pressure recovery in the diffuser section of the hole. The peak discharge coefficient of the $Ma_c = 0.3$ case occurring at a pressure ratio of 1.07 is 40 percent increased compared to the case of zero internal crossflow. Further increasing of the pressure ratio leads to a decrease of the discharge coefficient, reaching a plateau value for high pressure ratios, being about 10 percent increased compared to the zero internal crossflow case.

This clearly demonstrated that the diffuser section of the hole operates best in the low pressure ratio range resulting in a high pressure recovery and, thus, high discharge coefficients. For elevated pressure ratios the flow entering the diffuser section separates from the diffuser walls reducing the pressure recovery and the discharge coefficients. Obviously, for the zero crossflow case a separation region at the downstream edge at the hole inlet leads to a highly disturbed flow entering the diffuser section of the hole. In this case no pressure recovery can be detected.

The effect of internal crossflow is much more pronounced than reported by Hay and Lampard (1995). They found only a very weak increase in discharge coefficient of about 5 percent for an internal Mach number of 0.3. A possible explanation is that the length of the cylindrical inlet portion of the hole is $2D$ in the present study compared to $4D$ in their study. In the present case, the flow expanding behind the inlet vena contracta might enter the diffuser-shaped section of the hole as a diverging streamtube, which supports the diffusing process and, therefore, leads to drastically elevated discharge coefficients.

For very low pressure ratios and high internal crossflow Mach numbers ($Ma_c = 0.6$), an effect was identified occurring due to the fact that the flow rate through the hole is extremely

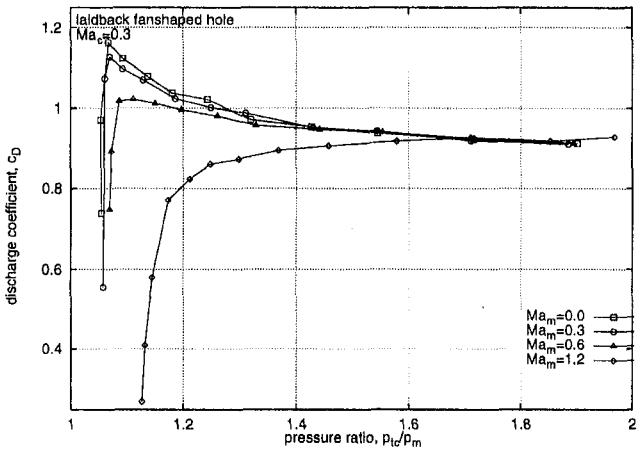

Fig. 12 Discharge coefficient C_D of the laidback fan-shaped hole at $Ma_c = 0.3$

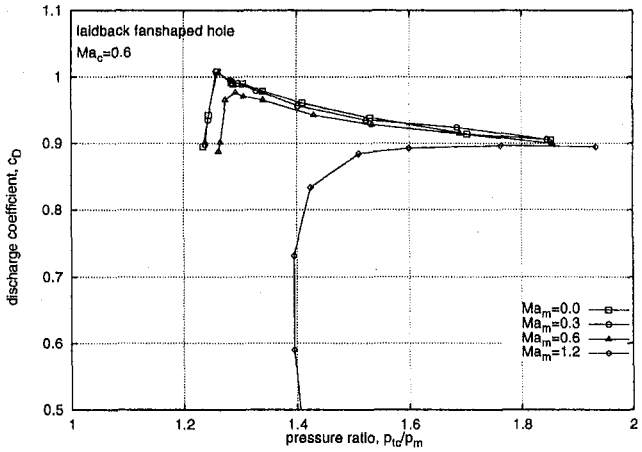

Fig. 13 Discharge coefficient C_D of the laidback fan-shaped hole at $Ma_c = 0.6$

sensitive to the pressure ratio applied, which becomes obvious by the steep gradient of the discharge coefficient. Additionally, the flow through the hole itself affects the pressure in the coolant supply channel, since an incremental increase of the pressure ratio results in a drastic increase of the discharge coefficient and mass flow rate through the hole. The increase of the mass

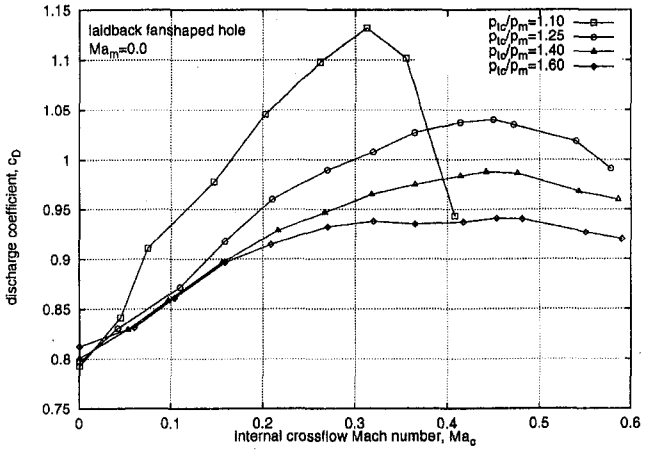

Fig. 14 Discharge coefficient C_D of the laidback fan-shaped hole: effect of internal crossflow Mach number Ma_c

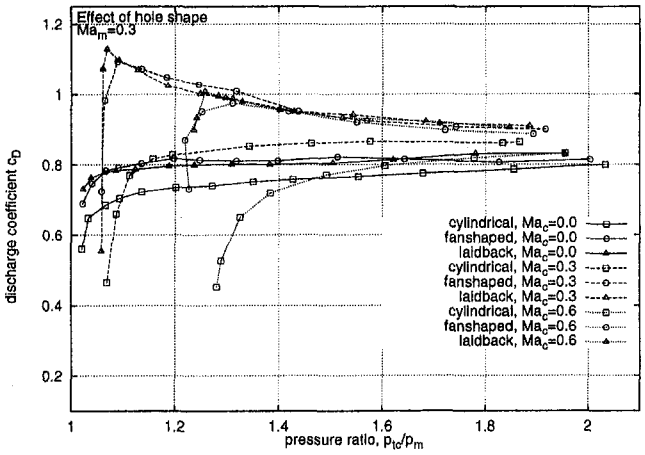

Fig. 16 Effect of hole shape at Ma_m = 0.3

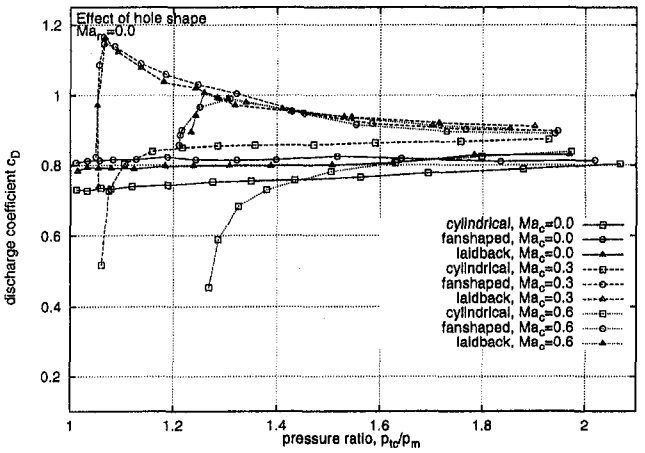

Fig. 15 Effect of hole shape at Ma_m = 0.0

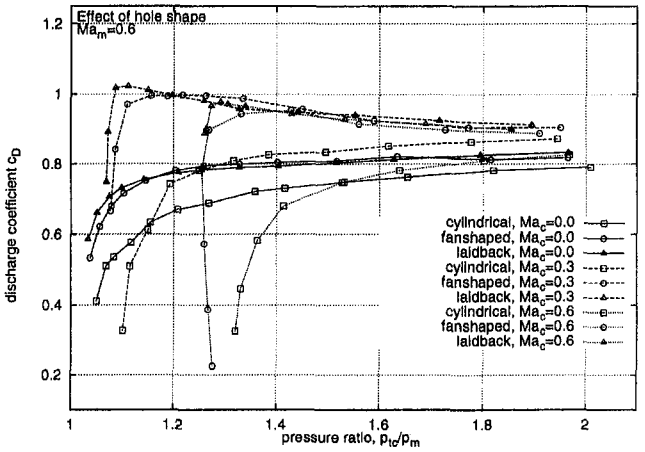

Fig. 17 Effect of hole shape at Ma_m = 0.6

flow rate, however, reduces the pressure in the coolant supply channel causing a double bend of the curves. This leads to an unstable flow regime in this pressure ratio range. Since this unstable flow regime occurs in a pressure range close to that of optimum diffuser performance, caution must be noted to designers in this area. A design may perform well at one point, but may be disastrous at another.

Figure 10 illustrates that the discharge coefficient is strongly affected by both pressure ratio and internal crossflow Mach number. The peak value of the discharge coefficient is higher, the lower the pressure ratio. For each pressure ratio an optimum internal crossflow Mach number can be identified to reduce losses at the hole entrance, thus leading to high discharge coefficients.

Laidback Fan-Shaped Hole. Figures 11–14 present the discharge coefficient measurements for the laidback fan-shaped hole. It was found that adding an additional forward expansion to the hole only slightly affects the behavior of the hole geometry in terms of discharge coefficient. Of course, the layback doesn't play an important role for the jet–crossflow interaction at the hole inlet and for the jet diffusion in the laterally expanded portion of the hole. The results of the present study show, that the altered jet-crossflow regime at the exit of the laidback fan-shaped hole doesn't affect the discharge coefficient, as compared to the fan-shaped hole.

Effect of Hole Geometry on the Discharge Coefficient. Figures 15–18 present a comparison of the discharge coefficients for all hole geometries considered in the present study.

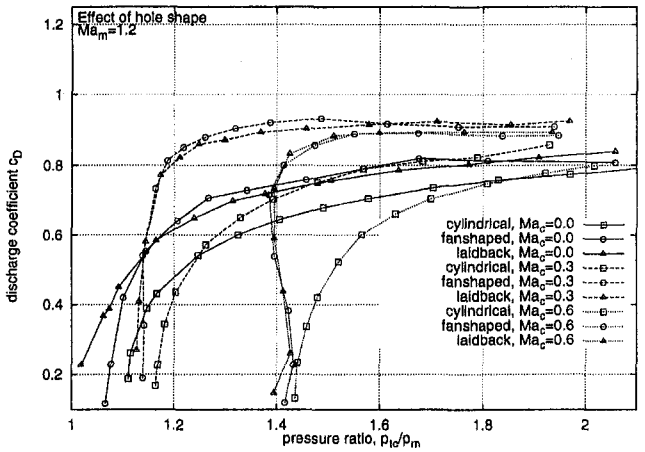

Fig. 18 Effect of hole shape at Ma_m = 1.2

For zero external and internal crossflow, the discharge coefficient was up to 10 percent increased for the expanded holes compared to the cylindrical hole. With an internal crossflow applied, a profound increase of the discharge coefficient for both expanded holes as compared to the cylindrical hole was found. In this case, at low pressure ratios the discharge coefficient C_D is more than 50 percent increased compared to the cylindrical hole and more than 40 percent increased compared

to the expanded holes without internal crossflow. This is due to the pressure recovery taking place in the diffuser section of the hole. It can be seen very clearly that this flow regime only exists for low pressure ratios. At elevated pressure ratios, the pressure recovery is reduced, leading to a moderate decrease of the discharge coefficient with pressure ratio. These findings hold true for all external crossflow Mach numbers considered.

The discharge coefficient C_D for the laidback fan-shaped hole was found to be very close to the fan-shaped hole for all cases investigated. This was already indicated by the flowfield measurement reported by Thole et al. (1998) who showed that the flowfields of both expanded holes were very similar. However, as presented in a companion paper (Gritsch et al., 1998), the laidback fan-shaped hole offers improved thermal protection as compared to the fan-shaped hole due to the better lateral spreading of the film being ejected from the hole.

Conclusions

A study was performed to acquire discharge coefficients of holes with expanded exits over a wide range of hole inlet crossflow Mach numbers, hole exit crossflow Mach numbers, and pressure ratios across the hole. Additionally, a cylindrical hole was tested as a basis of comparison. It can be concluded from this study that

1 Discharge coefficients of all hole geometries investigated strongly depend on the flow configuration (i.e., combination of internal crossflow Mach number, external crossflow Mach number, and pressure ratio).
2 Discharge coefficients of both expanded holes are higher than of the cylindrical hole with the same flow conditions applied. This effect is more pronounced at low pressure ratios and with an internal crossflow applied.
3 Minimum pressure losses and, thus, optimum discharge coefficients for both expanded holes will be achieved by applying:

   - low pressure ratios to avoid jet separation in the diffuser section of the hole, and
   - an internal crossflow Mach number adjusted to the pressure ratio to avoid jet separation at the hole entrance (Figs. 10 and 14).

   But caution must be noted to designers for the case of off-design operation at even lower pressure ratios due to the steep gradients in this area.

4 The performance of the fan-shaped and the laidback fan-shaped hole in terms of discharge coefficient is very similar.
5 High external crossflow Mach numbers at the hole exit lead to significantly reduced discharge coefficients, particularly at low pressure ratios for all geometries.
6 For the cylindrical hole optimum discharge coefficients are (almost) independent of the pressure ratio (Fig. 6).

Acknowledgments

This study was partly funded by the European Union through a grant by the Brite Euram program "Investigation of the Aerodynamics and Cooling of Advanced Engine Turbine Components" under Contract No. AER2-CT92-0044.

References

Giebert, D., M. Gritsch, A. Schulz, and S. Wittig, 1997, "Film-Cooling From Holes With Expanded Exits: A Comparison of Computational Results With Experiment," ASME Paper No. 97-GT-163.

Goldstein, R., E. Eckert, and F. Burggraf, 1974, "Effects of Hole Geometry and Density on Three-Dimensional Film Cooling," *Int. J. Heat Mass Transfer,* Vol. 17, pp. 595–607.

Gritsch, M., A. Schulz, and S. Wittig, 1997, "A Method of Correlating the Discharge Coefficient of Film-Cooling Holes With Crossflows at Hole Entry and Exit," presented at the Thirteenth International Symposium on Airbreathing Engines, Sept. 8–12, Chattanooga, TN.

Gritsch, M., A. Schulz, and S. Wittig, 1998, "Adiabatic Wall Effectiveness Measurements of Film-Cooling Holes With Expanded Exits," ASME JOURNAL OF TURBOMACHINERY, Vol. 120, this issue, pp. 549–556.

Haller, B., and J. Camus, 1984, "Aerodynamic Loss Penalty Produced by Film Cooling Transonic Turbine Blades," ASME *Journal of Engineering for Gas Turbines and Power,* Vol. 106, pp. 198–205.

Hay, N., S. Henshall, and A. Manning, 1994a, "Discharge Coefficients of Holes Angled to the Flow Direction," ASME JOURNAL OF TURBOMACHINERY, Vol. 116, pp. 92–96.

Hay, N., and D. Lampard, 1995, "The Discharge Coefficient of Flared Film Cooling Holes," ASME Paper No. 95-GT-15.

Hay, N., and D. Lampard, 1998, "Discharge Coefficient of Turbine Cooling Holes: A Review," ASME JOURNAL OF TURBOMACHINERY, Vol. 120, pp. 314–319.

Hay, N., D. Lampard, and S. Benmansour, 1983, "Effect of Crossflows on the Discharge Coefficient of Film Cooling Holes," ASME *Journal of Engineering for Power,* Vol. 105, pp. 243–248.

Hay, N., D. Lampard, and A. Khaldi, 1994b, "The Coefficient of Discharge of 30° Inclined Film Cooling Holes With Rounded Entries or Exits," ASME Paper No. 94-GT-180.

Jackson, R., 1963, "The Compressible Discharge of Air Through Small Thick Plate Orifices," *Applied Scientific Research,* Vol. A13, pp. 241–248.

Kline, S., and F. McClintock, 1953, "Describing Uncertainties in Single-Sample Experiments," *Mechanical Engineering,* Vol. 75, Jan., pp. 3–8.

Lichtarowicz, A., R. Duggins, and E. Markland, 1965, "Discharge Coefficients for Incompressible Noncavitating Flow Through Long Orifices," *Journal of Mechanical Engineering Science,* Vol. 7, pp. 210–219.

Makki, Y., and G. Jakubowski, 1986, "An Experimental Study of Film Cooling From Diffused Trapezoidal Shaped Holes," AIAA Paper No. 86-1326.

Schmidt, D., B. Sen, and D. Bogard, 1996, "Film Cooling With Compound Angle Holes: Adiabatic Effectiveness," ASME JOURNAL OF TURBOMACHINERY, Vol. 118, pp. 807–813.

Sen, B., D. Schmidt, and D. Bogard, 1996, "Film Cooling With Compound Angle Holes: Heat Transfer," ASME JOURNAL OF TURBOMACHINERY, Vol. 118, pp. 800–806.

Thole, K., M. Gritsch, A. Schulz, and S. Wittig, 1998, "Flowfield Measurements for Film-Cooling Holes With Expanded Exits," ASME JOURNAL OF TURBOMACHINERY, Vol. 120, pp. 327–336.

Thole, K., M. Gritsch, A. Schulz, and S. Wittig, 1997, "Effect of a Crossflow at the Entrance to a Film-Cooling Hole," ASME *Journal of Fluids Engineering,* Vol. 119, pp. 327–336.

Wittig, S., A. Schulz, M. Gritsch, and K. Thole, 1996, "Transonic Film-Cooling Investigations: Effects of Hole Shapes and Orientations," ASME Paper No. 96-GT-222.

Measurements of Heat Transfer Coefficients and Friction Factors in Passages Rib-Roughened on All Walls

M. E. Taslim

T. Li

Department of Mechanical Engineering,
Northeastern University,
Boston, MA 02115

S. D. Spring
GE Aircraft Engines,
Lynn, MA 01910

A liquid crystal technique was used to measure heat transfer coefficients in twelve test sections with square and trapezoidal cross-sectional areas representing blade midchord cooling cavities in a modern gas turbine. Full-length ribs were configured on suction side as well as pressure side walls while half-length ribs were mounted on partition walls between adjacent cooling cavities. Ribs were in staggered arrangements with a nominal blockage ratio of 22 percent and an angle of attack to the mainstream flow, α, of 90 deg. Heat transfer measurements were performed on the roughened walls with full-length as well as half-length ribs. Nusselt numbers, friction factors, and thermal performances of all geometries are compared. The most important conclusion of this study is that the roughening of the partition walls enhances the heat transfer coefficients on those walls but, more importantly, enhances heat transfer coefficients on the primary walls considerably.

Introduction

Various methods have been developed over the years to keep turbine blade metal temperatures below critical levels. A main objective in turbine blade cooling design is to achieve maximum heat transfer coefficients while minimizing the coolant flow rate. One such method is to route coolant air through serpentine passages within the airfoil and convectively remove heat from the blade. The coolant is then ejected either at the tip of the blade, through the cooling slots along the trailing edge or the cooling holes on the airfoil surface. Heat transfer coefficients in the cooling passages can be increased by roughening their walls. One such method, used over the past thirty years in internal cooling passages, is to mount ribs on the channel walls. These ribs, also called turbulators, increase the level of mixing of the cooler core air with the warmer air close to the channel wall, thereby enhancing the cooling capability of the passage.

Geometric parameters such as channel aspect ratio (AR), rib height-to-passage hydraulic diameter or blockage ratio (e/D_h), rib angle of attack (α), the manner in which the ribs are positioned relative to one another (in-line, staggered, crisscross, etc.), rib pitch-to-height ratio (S/e) and rib shape (round versus sharp corners, fillets, rib aspect ratio (AR_r), and skewness toward the flow direction) have pronounced effects on both local and overall heat transfer coefficients. Some of these effects have been studied by different investigators, such as Abuaf and Kercher (1994), Burggraf (1970), Chandra et al. (1988), Chandra and Han (1989), Han (1994), Han et al. (1978, 1985, 1992), Hwang and Liou (1995), Metzger et al. (1983, 1990), Taslim and Spring (1988a, b), Taslim et al. (1991, 1995), Webb et al. (1971), and Zhang et al. (1994). The available data in the open literature, however, are mostly for the cases in which the square or rectangular cooling cavities are roughened on two opposite walls adjacent to the blade suction and pressure sides. Experimental data on heat transfer and pressure drop for the leading and trailing edge cooling cavities are previously reported by these and other investigators. This report, however, concentrates on the midchord cooling cavities. These cavities, as shown in Fig. 1 for a typical modern blade, have cross-sectional areas that can be simulated by square, rectangular, or trapezoidal shapes. These midchord cavities are conventionally rib-roughened on the primary walls (pressure and suction sides). In this study, in an effort to enhance the heat transfer coefficients further on the primary walls, ribs are also mounted on the partition walls. It will be shown that the mere presence of the ribs on the partition walls causes considerable enhancement in heat transfer coefficient on the primary walls. The combination of ribs on the primary as well as partition walls alters the flow field in the channel and promotes the level of mixing of the cooler core air with the warmer near-wall air. It should be noted that enhancing the heat transfer coefficients on the partition walls may change the metal temperature gradients and consequently the thermal stresses on those walls. However, the benefits gained on the pressure and suction sides usually overshadow any effects from these changing thermal gradients. Proper positioning of the ribs on the partition walls is another important issue. Since these and other authors' previous work in this area showed that a staggered rib arrangement is a preferred orientation, it was decided to mount the ribs on the primary walls in a staggered arrangement. A pitch-to-height ratio of 8.5 was chosen as an optimum value presented by these and other investigators for ribs with 90 deg angle of attack. Ribs on the partition walls, however, span half of the partition width and originate from the pressure and suction sides in an alternative fashion, as shown in Fig. 3. The main objective of this study was to measure and compare the heat transfer coefficient as well as the friction factors for two channels of square and trapezoidal cross-sectional areas roughened on two, three, or four walls with twelve different rib geometries. With the increasing demand for high levels of heat transfer coefficient in cooling cavities, the ribs on the partition walls offer a great bonus both in terms of added heat transfer area, and (by altering the flow field) producing high levels of heat transfer enhancement on all passage walls.

Test Sections

Figures 2 and 3 show schematically the layouts, rib geometries, and cross-sectional areas of the two test sections. Table 1

Contributed by the International Gas Turbine Institute and presented at the 41st International Gas Turbine and Aeroengine Congress and Exhibition, Birmingham, United Kingdom, June 10–13, 1996. Manuscript received at ASME Headquarters February 1996. Paper No. 96-GT-355. Associate Technical Editor: J. N. Shinn.

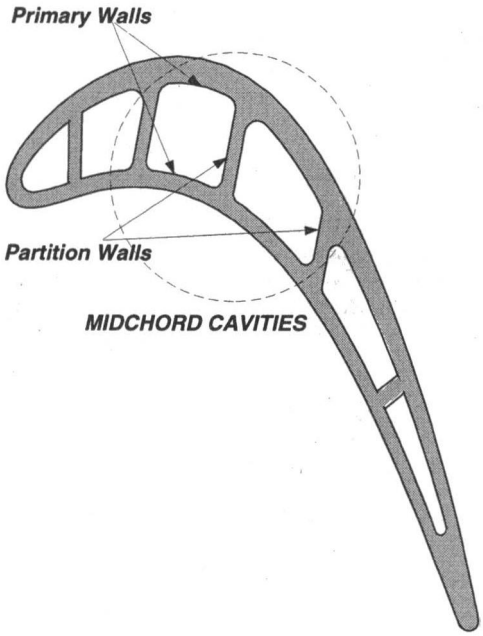

Fig. 1 Schematic of a cooled blade

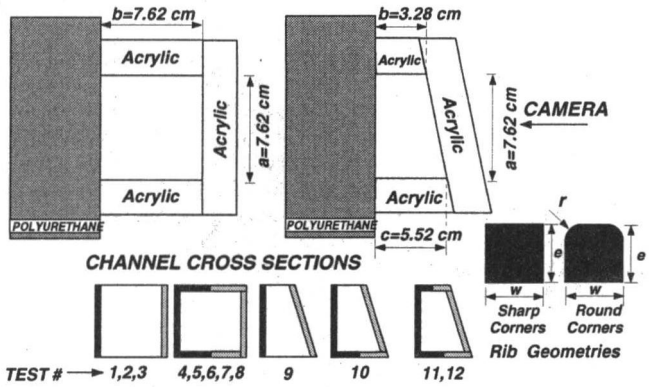

Fig. 2 Channel cross-sectional and rib geometries

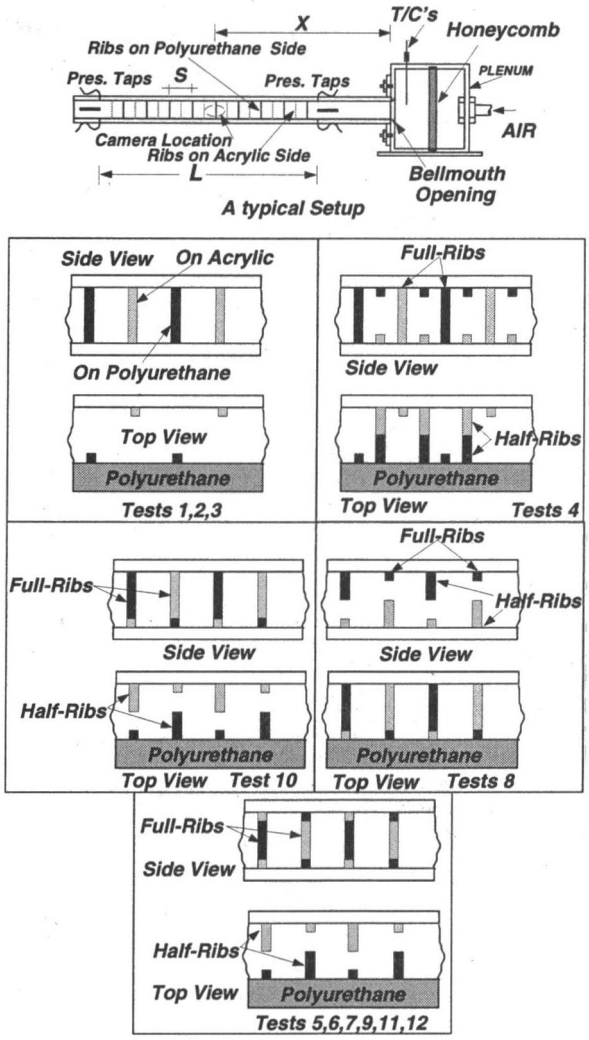

Fig. 3 Schematic of a test setup and rib arrangements

contains the specifications of the twelve rib geometries tested in this investigation. A liquid crystal technique was employed to measure the heat transfer coefficients between pairs of ribs in these test sections (Moffat, 1990). In this technique, the most temperature-sensitive color displayed by the liquid crystals is chosen as the reference color corresponding to a known temperature. By sensitive variation of the Ohmic power to a constant heat flux thin foil heater beneath the liquid crystals, the reference color is moved from one location to another such that the entire area between two ribs is eventually covered with the reference color at constant flow conditions. This process results in a series of photographs, each corresponding to a certain location of the reference color. The area covered by the reference color for each photograph is then measured and an area-weighted average heat transfer coefficient is calculated along

Nomenclature

a = channel straight sidewall (Fig. 2)
b = channel width (Fig. 2)
c = channel base (Fig. 2)
A = cross-sectional area without ribs
AR = channel aspect ratio ($=b/a$ for rectangular, $(b + c)/2a$ for trapezoidal)
AR_t = rib aspect ratio (e/w)
D_h = hydraulic diameter based on the cross-sectional area without ribs = $4A/P$
e = rib height
$\bar{f}$ = Darcy friction factor = $\Delta P(D_h/L)/(1/2\rho U_m^2)$
$\bar{f}_s$ = Darcy friction factor in an all-smooth-wall channel
h = average heat transfer coefficient between a pair of ribs
k = air thermal conductivity
L = length of the roughened portion of the test section
$\overline{\mathrm{Nu}}$ = average Nusselt number between a pair of ribs = hD_h/k
$\overline{\mathrm{Nu}}_s$ = Nusselt number in a smooth passage
P = channel perimeter without ribs
r = rib rounded corner radius
Re = Reynolds number = $\rho U_m D_h/\mu$
S = rib pitch (center-to-center)
T_f = film temperature = $0.5(T_s + T_m)$
T_m = air mixed mean temperature
T_s = surface temperature
U_m = air mean velocity
w = rib width
X = distance between camera and test section entrance
α = angle of attack
μ = air dynamic viscosity
ΔP = pressure differential across the roughened portion of the test section
ρ = air density

Table 1 Geometric specifications

Test	e (mm)	r/e	e/D_h	S/e	AR	AR_t	Remarks
1	16.61	0.0	0.218	8.5	1.0	1.0	Ribs on two walls, base
2	16.61	0.191	0.218	8.5	1.0	1.0	Ribs on two walls
3	16.61	0.191	0.218	8.62	1.0	1.47	Ribs on two walls
4	16.61	0.191	0.218	8.5	1.0	1.0	Ribs on four walls
5	16.61	0.191	0.218	8.5	1.0	1.0	Ribs on four walls, nom.
6	15.49	0.256	0.203	9.11	1.0	0.87	Ribs on four walls, min.
7	17.73	0.224	0.233	7.97	1.0	1.0	Ribs on four walls, max.
8	16.61	0.191	0.218	8.5	1.0	1.0	Ribs on four walls
9	12.11	0.164	0.218	8.5	Trapezoid	1.0	Ribs on two walls, base
10	12.11	0.164	0.218	8.5	Trapezoid	1.0	Ribs on three walls
11	12.11	0.164	0.218	8.5	Trapezoid	1.0	Ribs on four walls, nom.
12	11.23	0.212	0.202	9.16	Trapezoid	0.87	Ribs on four walls, min.
$\alpha = 90°$ for all tests							

with the iso-Nu contours (contours of constant Nusselt number). Details of this process are explained in the procedure section. Among the advantages of liquid crystal thermography is to depict the flow "footprints" and local values of heat transfer coefficient on the surface under investigation. This simultaneous "flow visualization" enhances the understanding of the underlying physics and helps the investigator in interpretation of the results. Furthermore, unexpected asymmetries in flow are revealed as well as the slightest heat and flow leaks, nonuniformities in surface heat flux, imperfections associated with the attachment of the heater to the test section surface, and nonuniformities in wall material thermal conductivity. Coolant air, supplied by a compressor to a 0.95 m^3 storage tank, was circulated through an air filter, to a water-to-air heat exchanger, and through a second air filter to remove any residual water vapor and oil. A pressure regulator downstream of the second filter was used to adjust the flow rate. The air then entered a critical venturi-meter for mass flow measurement, to a plenum equipped with a honeycomb flow straightener, and then to the test section via a bellmouth opening.

As shown in Fig. 2, two test channels simulating two typical cooling cavities in the midchord region of a blade were used. The first one with a length of 147.3 cm, had a 7.62 cm by 7.62 cm square cross-sectional area. The second one with a length of 116.8 cm, had a trapezoidal cross-sectional area with the two bases and height of 5.52 cm, 3.28 cm and 7.62 cm, respectively. Three walls of these channels were made of 1.27-cm-thick clear acrylic plastic. The fourth wall, on which the heaters and liquid crystal sheets were attached and all measurements were taken, was made of a 5-cm-thick machinable polyurethane slab. This wall, for all cases tested, had a fixed width of 7.62 centimeters. Ribs were also machined out of acrylic plastic using numerically controlled milling machines and glued onto different walls in accordance with the rib arrangements shown in Figs. 2 and 3. Ribs on the primary walls were of full length, spanning the entire width of the channel, and were always in a staggered arrangement. Ribs on the secondary walls (partitions between adjacent cooling cavities), however, were of half length, spanning half of the channel width and were tested for both in-line and staggered arrangements. The choice of half ribs on the partition walls was based on (a) these authors' past observation, with liquid crystals, of high heat transfer coefficients downstream of a short rib where the vortices shed from the rib tip, roll over the surface, and bring the cooler core air in contact with warmer near-wall air, and (b) a pressure drop advantage compared to full-length ribs. Whether longer or shorter ribs on the partition walls would have been superior or inferior, they were not tested in the present study and are left to be investigated by future investigators. Ribs in all tests were positioned at an angle of 90 deg to the axial flow direction. The entrance region of all test sections was left smooth to produce well-established hydrodynamic and thermal boundary layers. Heat transfer measurements were performed for an area between a pair of ribs in the middle of the roughened zone corresponding to an X/D_h of about 14. Four 7.62 cm × 27.94 cm custom-made etched-foil heaters with a thickness of 0.15 mm were placed on the polyurethane wall where measurements were taken using a special double-stick 0.05-mm-thick tape with minimal temperature deformation characteristics. A detailed construction sketch of the heaters is shown in El-Husayni (1991). The heaters covered the entire test section length including the smooth entry length. However, they did not extend over the actual rib surface nor on the acrylic plastic sidewalls. Thus the reported heat transfer coefficients are the averages over the wall surface area between a pair of ribs and this area was used for the calculation of heat flux in data reduction. The heat transfer coefficients on the rib surfaces are reported by other investigators such as Metzger et al. (1988), and Taslim and Wadsworth (1997). As for having only one heated wall, it is noted that an experimental investigation by El-Husayni et al. (1994) on heat transfer in a rib-roughened channel with one, two, and four heated walls showed that, in a stationary roughened channel, the heat transfer coefficient is not significantly sensitive to the number of heated walls, i.e., the variation in heat transfer coefficient was within the reported experimental uncertainty of ±8 percent. Encapsulated liquid crystals sandwiched between a mylar sheet and a black paint coat, collectively having a thickness of 0.127 mm, were then placed on the heaters. Static pressure taps, located one-half rib pitch upstream of the first rib and one-half rib pitch downstream of the last rib, measured the pressure drop across the rib-roughened test section. The reported friction factor is the overall passage average, $\bar{f}$, and not just the roughened surfaces. The test sections were covered on all sides by 5-cm-thick styrofoam sheets to minimize heat losses to the environment, except for a small window on the opposite wall at the location where photographs of liquid crystals were taken. The radiational heat loss from the heated wall to the unheated walls as well as losses to ambient air were taken into consideration when heat transfer coefficients were calculated. A 35-mm programmable camera, in conjunction with proper filters and background lighting to simulate daylight conditions, was used to take photographs of isochrome patterns formed on the liquid crystal sheet. Surface heat flux in the test section was generated by the heaters through a custom-designed power supply unit. Each heater was individually controlled by a variable transformer.

Procedure

Before testing, the liquid crystal sheets were calibrated in a water bath to attain uniform isochromes on a small piece of the liquid crystal sheet used in this investigation. The temperature corresponding to each color was measured with a precision thermocouple and photographs were taken at laboratory conditions simultaneously to simulate closely the actual testing environment. A reference color along with its measured temperature of 36.9°C was chosen for the experiments. It should be noted that all possible shades of the selected reference color did not indicate a temperature variation of more than 0.3°C. Therefore, the maximum uncertainty in wall temperature measurement was ±0.15°C. A contact micromanometer with an accuracy of 0.025 mm of water column measured the pressure differential across the rib-roughened channel. A critical venturi-meter, with choked flow for all cases tested, measured the total mass flow rate entering the test section. With the known surface heat flux along the test section and application of the energy balance from the test section inlet to the camera location, the air-mixed mean temperature was calculated, taking into account the small heat losses through the test section walls to ambient air. For a typical test Reynolds number, at a constant mass flow rate, the lowest heat flux was induced by adjusting the heater power until the first band of reference color was observed on the liquid crystal sheet in the area of interest. Each heater was adjusted individually to ensure a uniform heat flux over the entire tested surface. At thermal equilibrium a photograph was taken and data recorded. Power to the heaters was then increased such that the reference color moved to a location next to the previous one

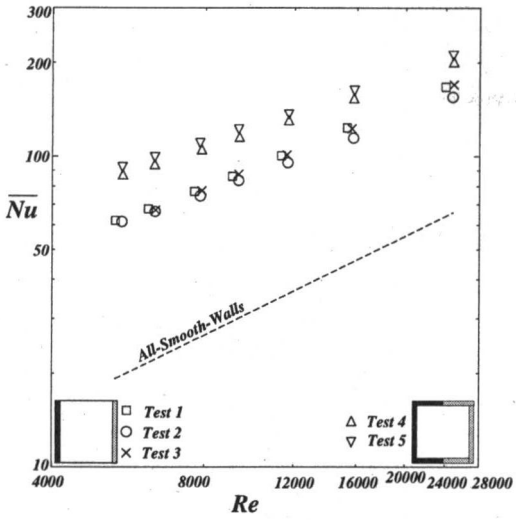

Fig. 4 Comparison of Nusselt numbers for tests 1–5

(higher heat transfer coefficient) and another photograph was taken. This procedure was repeated until the entire surface between a pair of ribs was covered by the reference color at one time or another. The process was then repeated for the range of test Reynolds numbers. Each photograph was digitized in order to measure the area covered by the reference color. This was done by using a magnetic tablet and a commercial software package installed on a computer. Once the areas were measured, an area-weighted average heat transfer coefficient was calculated. For verification of the liquid crystal technique accuracy, an all-smooth-wall channel has been tested with heaters on one wall. The heat transfer coefficient results (Taslim, 1990) were within 5 percent of the Dittus–Boelter (1930) correlation. Previous results (Taslim et al., 1991) of various geometry roughened channels using the same technique compared favorably with those of Metzger et al. (1990). Experimental uncertainties, following the method of Kline and McClintock (1953), were estimated to be ±6 and ±8 percent for the heat transfer coefficient and friction factor, respectively.

Results and Discussion

Local average heat transfer coefficient results for an area between a pair of ribs corresponding to X/D_h of 14 for twelve rib geometries in two channels are compared with the all-smooth-wall channel Dittus–Boelter (1930) correlation:

$$\overline{\mathrm{Nu}_s} = 0.023\ \mathrm{Re}^{0.8}\ \mathrm{Pr}^{0.4}$$

With this correlation, the enhancement in rib-roughened heat transfer coefficients can be readily evaluated. The thermal performance, based on the same pumping power, is given by:

$$(\overline{\mathrm{Nu}}/\overline{\mathrm{Nu}}_s)/(\bar{f}/\bar{f}_s)^{1/3}$$

(Han et al., 1985), where $\bar{f}_s$ is the *all-smooth-wall* friction factor from Moody (1944). It should be noted that the thermal performances reported here do not include the contribution of the heat transfer coefficients on the rib surfaces. Rib thermal performance data are reported by the first author (Taslim and Wadsworth, 1997) and can be combined with the present data to determine the overall thermal performances. Air properties for Nusselt and Reynolds number calculations are based on the local film temperature, T_f, for all cases.

Figure 4 combines the results of five rib arrangements in a single channel. A baseline test of square sharp corner ribs on two opposite primary walls (geometry 1 in Table 1) against which four other arrangements are compared was run first. With a high rib blockage ratio of 0.218, typical of small gas turbines, great enhancement in heat transfer coefficient is achieved when compared with the all-smooth-wall heat transfer coefficient also presented in that figure. A problem facing the designer of these cooling cavities, however, is the gradual wearing of the core die. Relatively sharp-edged ribs, cast at the beginning of a core die life span, eventually deteriorate to rounded corner ribs as the die wears. This change in rib profile will affect the flow pattern, which in turn decreases the heat transfer performance of the rib accompanied with a decrease in the pressure drop. Test 2 is identical to Test 1 in all aspects except that the rib top corners are rounded to an r/e of 0.191 (Table 1). A decrease in the Nusselt number ranging from 1 percent at the lowest Reynolds number and 7 percent at the highest Reynolds number was measured. All other ribs tested in this investigation had rounded corners, as shown in Table 1. Test 3 deals with a rib geometry similar to that of Test 2 except that the rib width is reduced such that the rib aspect ratio is increased to 1.47. Earlier investigations by these authors (Taslim et al., 1997) showed that the tall and thin ribs performed better than square (AR_t = 1) or short and wide ($AR_t < 1$) ribs from a heat transfer point of view. The same behavior is observed here. Test 4 was the first trial in mounting ribs on the partition walls. As shown in Fig. 2, half-length ribs initiating, alternatively, from the primary walls and extending to the partition walls' centerline were mounted on the partition walls. Heat transfer coefficients, measured on a primary wall, increased by a remarkable 35 percent as shown in Fig. 4. This increase is attributed to a dramatic change in the flow field as was evidenced by the liquid crystal displays shown in Fig. 5. In Test 5, the arrangement of the half-length ribs on the partition walls was changed to a configuration that was believed to perform better, thermally, by promoting higher levels of mixing. The configuration of ribs for this test, shown in Fig. 2, which was chosen for the rest of the tests, further increased the heat transfer coefficient by about 5 percent (over Test 4). Thus, the mere presence of the half-length ribs on the partition walls increased the heat transfer coefficients on the primary walls by about 40 percent. This finding offers a relatively easy solution to those cases in which the blade cooling designer needs high heat transfer coefficients in midchord cavities to meet blade life requirements when the necessary pressure drop is available.

Representative iso-Nu contours for tests 2, 4, and 5 at one Reynolds number are shown in Fig. 5. The solid black ribs are those mounted on the liquid crystal wall and the half-length ribs originating from it. The shaded areas represent the ribs

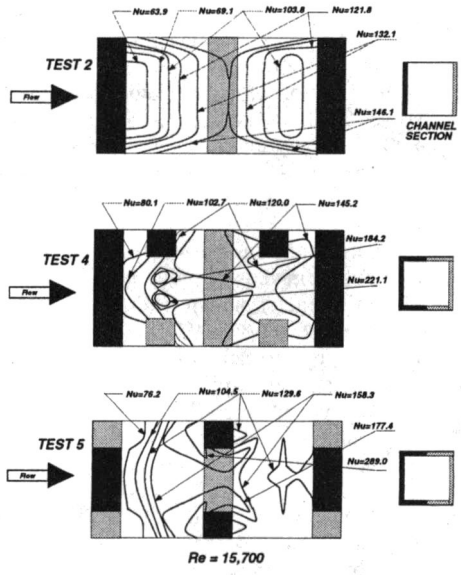

Fig. 5 Comparison of iso-Nu contours for Tests 2, 4, and 5

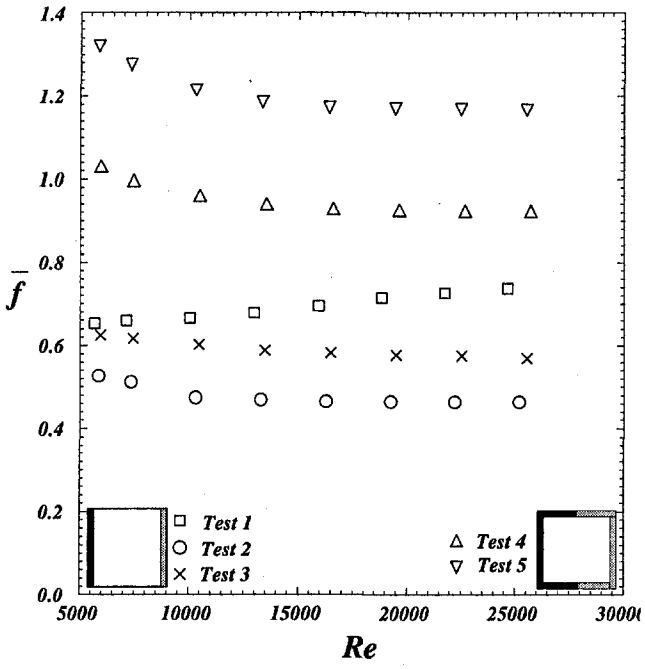

Fig. 6 Comparison of friction factors for Tests 1–5

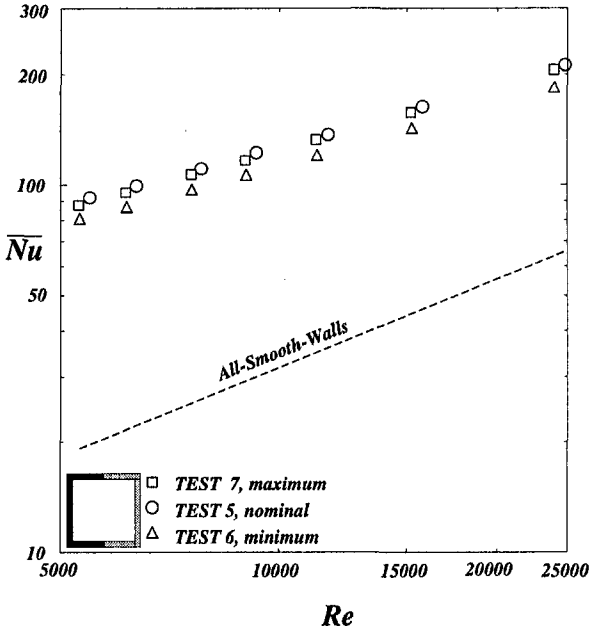

Fig. 7 Effects of manufacturing tolerances on Nusselt number

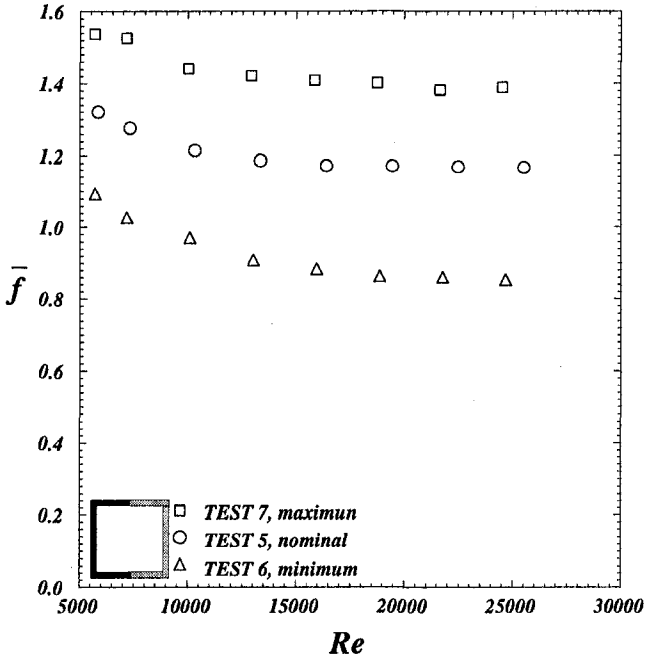

Fig. 8 Effects of manufacturing tolerances on friction factor

mounted on the opposite wall (acrylic) and the half-length ribs originating from it. Iso-Nu contours for Test 4 are typical for 90 deg staggered ribs on two opposite walls, i.e., starting from a relatively low value in the rib wake region, it reaches its maximum near the point of the flow re-attachment and decreases again close to the downstream rib. However, when half-length ribs were mounted on the partition walls (Tests 4 and 5), the iso-Nu contour pattern changed dramatically with high values on Nusselt numbers where vortices are shed from the edges of the ribs on the partition walls. Friction factors for these tests are compared in Fig. 6. As expected for 90 deg ribs, higher heat transfer coefficients are accompanied with higher friction factors.

In tests 5, 6, and 7, the rib dimensions were varied so as to represent typical manufacturing variations that may exist due to real blade casting processes. Test 5, with a blockage ratio of 0.218 and a pitch-to-height ratio of 8.5, represents the nominal geometry. The choice of 8.5 for the pitch-to-height ratio is based on these and other investigators' optimum value. Test 6 with a blockage ratio of 0.203 (a 7 percent reduction from nominal) and a pitch-to-height ratio of 9.11 represents the minimum rib geometry. The 9.11 ratio, which deviates from the optimum value, is based on the fact that the distance between the ribs (pitch, S) is not affected by the manufacturing tolerances; thus, a reduction in rib height, e, increases the pitch-to-height ratio, S/e. For the same reason the rib aspect ratio, e/w, reduces to 0.87. The combined effects of lower blockage ratio, lower rib aspect ratio (short and wide), and possible deviation of pitch-to-height ratio from optimum cause a reduction in rib heat transfer coefficient and friction factor shown in Figs. 7 and 8. Test 7 in Table 1 with a blockage ratio of 0.233 (a 7 percent increase from nominal) and a pitch-to-height ratio of 7.97 represents the maximum rib geometry. No significant change in heat transfer coefficient was observed, although the friction factors are higher than those of nominal case. It is speculated that the combined effects of higher blockage ratio and nonoptimum pitch-to-height ratio resulted in almost the same level of heat transfer coefficients as the nominal case.

Heat transfer coefficients on the partition walls, roughened with half-length ribs, are compared with those on the primary walls, roughened with full-length ribs, in Fig. 9. It is noted that the heat transfer coefficients on the partition walls have been enhanced to a level of about 94 percent of those on the primary walls. This is a considerable increase compared to the conventional practice of leaving the partition walls smooth. Liquid crystal displays for this experiment showed regions of high heat transfer coefficient around the tip of half-length ribs where shed vortices scrub over the channel surface.

Figure 10 shows the heat transfer results for all tests performed in the trapezoidal test section (tests 9–12 in Table 1). Test 9, which is the trapezoidal test section with full-length ribs on two opposite primary walls, serves as the baseline test against which other rib geometries are compared. Similar to the tests with the square channel, there was an increase of about 20 percent in the heat transfer coefficient on the primary walls

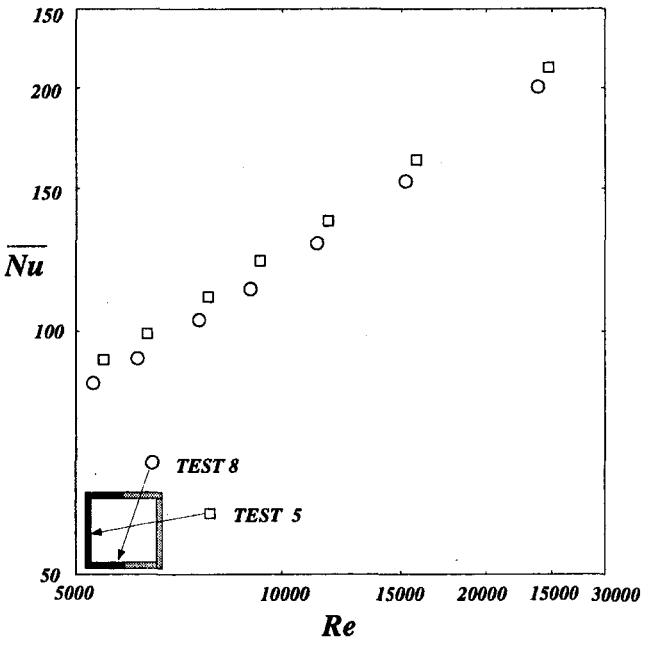

Fig. 9 Comparison of Nusselt numbers on the full- and half-rib walls

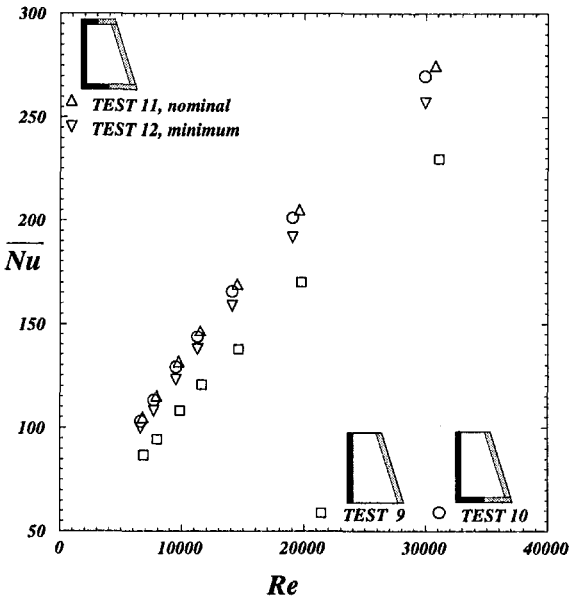

Fig. 10 Comparison of Nusselt numbers for four rib geometries in the trapezoidal channel

when half-length ribs were mounted on the bases of the trapezoidal test section. There was a small difference of about 1.6 percent in heat transfer coefficients between the tests 10 and 11. This is attributed to the fact that, in this trapezoidal test section, flow is biased toward the bigger base, thus roughening the smaller base, does not show much contribution to the enhancement of heat transfer coefficient on the primary walls. A lower blockage ratio rib (Test 12, e/D_h = 0,202) representing the blueprint minimum rib geometry shows a lower heat transfer coefficient than those of the nominal rib geometry (Test 11, e/D_h = 0.218) as expected. Representative iso-Nu contours for tests 9, 10, and 11 are shown in Fig. 11. It is noted that in contrast to Test 2, the iso-Nu contours for Test 9 are not spanwise symmetric due to the trapezoidal shape of the channel cross-section. Again, mounting the half-length ribs on the partition walls alters the flow field considerably and promotes the

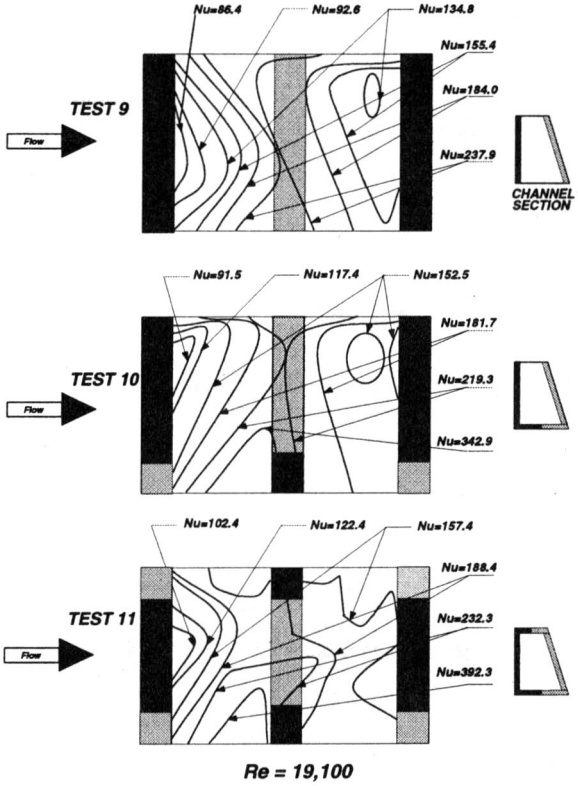

Fig. 11 Comparison of iso-Nu contours for Tests 9, 10, and 11

mixing of the cooler core air with the warmer near-wall air, thus lowering the boundary layer temperature and increasing the heat transfer. Friction factors for these tests are shown in Fig. 12. The trend of friction factors is in line with the Nusselt numbers presented in Fig. 10.

Figure 13 compares the thermal performances of all twelve geometries tested. Of particular interest are tests 4, 5, 10, and 11 in which half-length ribs were mounted on partition walls. These geometries not only produced much higher heat transfer coefficients compared to their corresponding baseline tests

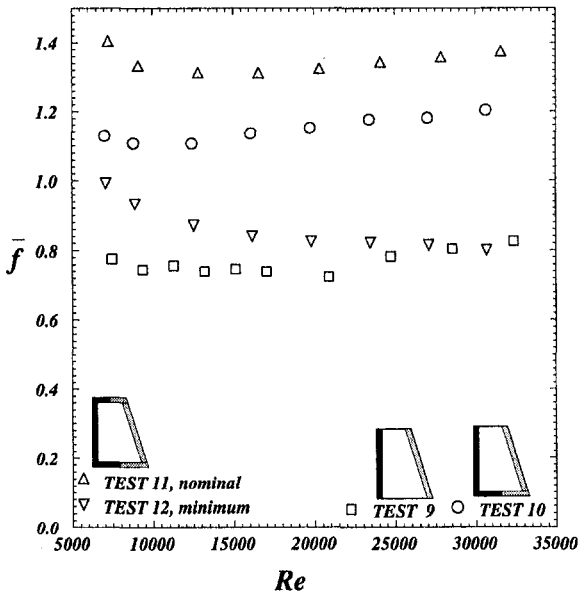

Fig. 12 Comparison of friction factors for four rib geometries in the trapezoidal channel

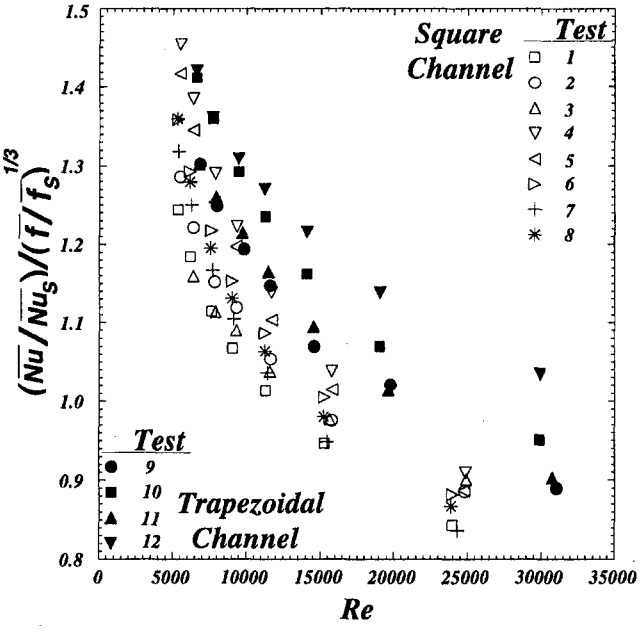

Fig. 13 Thermal performance comparisons for all geometries

(Tests 1 and 9), but their thermal performances are also higher than those of baseline tests, proving, once again, the usefulness of ribs on partition walls. It is also noted that the solid symbols representing the results of the trapezoidal test section are generally above the open symbols. This behavior is due to the fact that, for the same blockage and pitch-to-height ratios, ribs on opposite or adjacent walls in the trapezoidal test sections were relatively closer to each other thus communicating more effectively from a heat transfer point of view as can be deduced from Figs. 4 and 10.

Conclusions

A total of twelve rib geometries were tested in two channels with square and trapezoidal cross sections representing mid-chord cooling cavities in small aircraft engines. The most important conclusion of this study is that the roughening of the partition walls enhances the heat transfer coefficients on those walls but, more importantly, enhances heat transfer coefficients on the primary walls considerably. This heat transfer coefficient enhancement is accompanied by an increase in overall channel friction factor. However, the net effect is an increase in the channel's thermal performance.

References

Abuaf, N., and Kercher, D. M., 1994, "Heat Transfer and Turbulence in a Turbulated Blade Cooling Circuit," ASME JOURNAL OF TURBOMACHINERY, Vol. 116, pp. 169–177.

Burggraf, F., 1970, "Experimental Heat Transfer and Pressure Drop With Two Dimensional Turbulence Promoters Applied to Two Opposite Walls of a Square Tube," *Augmentation of Convective Heat and Mass Transfer,* A. E. Bergles and R. L. Webb, eds., ASME, New York, pp. 70–79.

Chandra, P. R., Han, J. C., and Lau, S. C., 1988, "Effect of Rib Angle on Local Heat/Mass Transfer Distribution in a Two-Pass Rib-Roughened Channel," ASME JOURNAL OF TURBOMACHINERY, Vol. 110, pp. 233–241.

Chandra, P. R., and Han, J. C., 1989, "Pressure Drop and Mass Transfer in Two-Pass Ribbed Channels," *Journal of Thermophysics,* Vol. 3, No. 3, pp. 315–319.

Dittus, F. W., and Boelter, L. M. K., 1930, *Publications in Engineering,* Vol. 2, No. 13, University of California, Berkeley, CA, pp. 443–461.

Dutta, S., and Han, J. C., 1994, "Effect of Model Orientation on Local Heat Transfer in a Rotating Two-Pass Smooth Triangular Duct," presented at the ASME Winter Annual Meeting.

El-Husayni, H. A., 1991, "An Experimental Investigation of Heat Transfer Coefficients in Stationary and Orthogonally Rotating Smooth and Rib-Roughened Test Sections Heated on One, Two and Four Walls," M.S. Thesis, Mechanical Engineering Department, Northeastern University, Boston, MA.

El-Husayni, H. A., Taslim, M. E., and Kercher, D. M., 1994, "An Experimental Investigation of Heat Transfer Coefficients in a Spanwise Rotating Channel With Two Opposite Rib-Roughened Walls," ASME JOURNAL OF TURBOMACHINERY, Vol. 113, pp. 75–82.

Han, J. C., Glicksman, L. R., and Rohsenow, W. M., 1978, "An Investigation of Heat Transfer and Friction for Rib Roughened Surfaces," *International Journal of Heat and Mass Transfer,* Vol. 21, pp. 1143–1156.

Han, J. C., 1984, "Heat Transfer and Friction in Channels With Two Opposite Rib-Roughened Walls," ASME *Journal of Heat Transfer,* Vol. 106, No. 4, pp. 774–781.

Han, J. C., Park, J. S., and Lei, C. K., 1985, "Heat Transfer Enhancement in Channels With Turbulence Promoters," ASME *Journal of Engineering for Gas Turbines and Power,* Vol. 107, No. 1, pp. 628–635.

Han, J. C., Zhang, Y. M., and Lee, C. P., 1992, "Influence of Surface Heat Flux Ratio on Heat Transfer Augmentation in Square Channels With Parallel, Crossed, and V-Shaped Angled Ribs," ASME JOURNAL OF TURBOMACHINERY, Vol. 114, pp. 872–880.

Hwang, J., and Liou, T., 1995, "Effect of Permeable Ribs on Heat Transfer and Friction in a Rectangular Channel," ASME JOURNAL OF TURBOMACHINERY, Vol. 117, pp. 265–271.

Kline, S. J., and McClintock, F. A., 1953, "Describing Uncertainty in Single-Sample Experiments," *Mechanical Engineering,* Vol. 75, Jan, pp. 3–8.

Metzger, D. E., Fan, C. S., and Pennington, J. W., 1983, "Heat Transfer and Flow Friction Characteristics of Very Rough Transverse Ribbed Surfaces With and Without Pin Fins," *Proc. ASME–JSME Thermal Engineering Joint Conference,* Vol. 1, pp. 429–436.

Metzger, D. E., Chyu, M. K., and Bunker, R. S., 1988, "The Contribution of On-Rib Heat Transfer Coefficients to Total Heat Transfer From Rib-Roughened Surfaces," *Transport Phenomena in Rotating Machinery,* J. H. Kim, ed., Hemisphere Publishing Co.

Metzger, D. E., Fan, C. S., and Yu, Y., 1990, "Effects of Rib Angle and Orientation on Local Heat Transfer in Square Channels With Angled Roughness Ribs," *Compact Heat Exchangers: A Festschrift for A. L. London,* Hemisphere Publishing Co., pp. 151–167.

Moffat, R. J., 1990, "Experimental Heat Transfer," *Proc. 9th Int. Heat Transfer Conf.,* Vol. 1, pp. 187–204.

Moody, L. F., 1944, "Friction Factors for Pipe Flow," *Transactions of ASME,* Vol. 66, p. 671.

Taslim, M. E., and Spring, S. D., 1988a, "An Experimental Investigation of Heat Transfer Coefficients and Friction Factors in Passages of Different Aspect Ratios Roughened With 45° Turbulators," *Proc. ASME National Heat Conference,* Houston, TX.

Taslim, M. E., and Spring, S. D., 1988b, "Experimental Heat Transfer and Friction Factors in Turbulated Cooling Passages of Different Aspect Ratios, Where Turbulators Are Staggered," Paper No. AIAA-88-3014.

Taslim, M. E., 1990, "Application of Liquid Crystals in Heat Transfer Coefficient Measurement," *Proc. IEEE ELECTRO^R/90,* Boston, MA.

Taslim, M. E., Bondi, L. A., and Kercher, D. M., 1991, "An Experimental Investigation of Heat Transfer in an Orthogonally Rotating Channel Roughened With 45° Criss-Cross Ribs on Two Opposite Walls," ASME JOURNAL OF TURBOMACHINERY, Vol. 113, pp. 346–353.

Taslim, M. E., and Spring, S. D., 1994, "Effects Turbulator Profile and Spacing on Heat Transfer and Friction in a Channel," *AIAA J. of Thermophysics and Heat Transfer,* Vol. 8, No. 3, pp. 555–562.

Taslim, M. E., and Wadsworth, C. A., 1997, "An Experimental Investigation of the Rib Surface-Averaged Heat Transfer Coefficient in a Rib-Roughened Square Channel," ASME JOURNAL OF TURBOMACHINERY, Vol. 119, pp. 381–389.

Taslim, M. E., Li, T., and Spring, S. D., 1995, "Experimental Study of the Effects of Bleed Holes on Heat Transfer and Pressure Drop in Trapezoidal Passages With Tapered Turbulators," ASME JOURNAL OF TURBOMACHINERY, Vol. 117, pp. 281–289.

Webb, R. L., Eckert, E. R. G., and Goldstein, R. J., 1971, "Heat Transfer and Friction in Tubes With Repeated-Rib-Roughness," *Int. J. Heat Mass Transfer,* Vol. 14, pp. 601–617.

Zhang, Y. M., Gu, W. Z., and Han, J. C., 1994, "Heat Transfer and Friction in Rectangular Channels With Ribbed or Ribbed-Grooved Walls," ASME *Journal of Heat Transfer,* Vol. 116, pp. 58–65.

45 deg Staggered Rib Heat Transfer Coefficient Measurements in a Square Channel

M. E. Taslim

A. Lengkong

Department of Mechanical, Industrial, and Manufacturing Engineering, Northeastern University, Boston, MA 02115

For high-blockage ribs with large heat transfer areas, commonly used in small gas turbine blades, the rib heat transfer is a significant portion of the overall heat transfer in the cooling passages. Three staggered 45 deg rib geometries corresponding to blockage ratios of 0.133, 0.167, and 0.25 were tested in a square channel for pitch-to-height ratios of 5, 8.5, and 10, and for two distinct thermal boundary conditions of heated and unheated channel walls. Comparisons were made between the surface-averaged heat transfer coefficients and friction factors for 45 deg ribs, and 90 deg ribs reported previously. Heat transfer coefficients of the furthest upstream rib and that of a typical rib located in the middle of the rib-roughened region were also compared. It was concluded that: (a) For the geometries tested, the rib average heat transfer coefficient was much higher than that for the area between the ribs. (b) Except for two cases corresponding to the highest blockage ribs mounted at pitch-to-height ratios of 8.5 and 10 for which the heat transfer results of 45 deg ribs were very close to those of 90 deg ribs, 45 deg ribs produced higher heat transfer coefficients than 90 deg ribs. (c) At pitch-to-height ratios of 8.5 and 10, all 45 deg ribs produced lower friction factors than 90 deg ribs. However, when they were brought closer to each other ($S/e = 5$), they produced higher friction factors than 90 deg ribs. (d) Heat transfer coefficients for the two smaller rib geometries ($e/D_h = 0.133$ and 0.167) did not vary significantly with the pitch-to-height ratio in the range tested. However, the heat transfer coefficient for the high blockage rib geometry increased significantly as the ribs were brought closer to each other. (e) Under otherwise identical conditions, ribs in the furthest upstream position produced lower heat transfer coefficients than those in the midstream position. (f) Rib thermal performance decreased with the rib blockage ratio. For both angles of attack, the smallest rib geometry in the midstream position and at a pitch-to-height ratio of 10 had the highest thermal performance, and the highest blockage rib in the furthest upstream position produced the lowest thermal performance.

Introduction

Various cooling methods have been developed over the years to ensure that gas turbine blade metal temperatures are maintained at a level consistent with airfoil design life. The objective in turbine blade cooling is to achieve maximum internal heat transfer coefficients while minimizing the coolant flow rate. One such method is to route coolant air through serpentine channels within the airfoil and convectively remove heat from the blade. The coolant is then ejected either at the tip of the blade, through the cooling slots along the trailing edge, or film holes on the airfoil surface. Heat transfer coefficients in the cooling passages can be increased by roughening their walls. One such method, used over the past 25 years in gas turbine blade and nozzle internal cooling passages, is to cast ribs on the airfoil-contour opposite channel walls. These ribs, also called turbulators, increase the level of mixing of the cooler core air with the warmer air close to the channel wall and restart the boundary layer after flow reattachment between ribs resulting in enhanced heat transfer coefficients.

Geometric parameters such as channel aspect ratio (AR), rib height-to-passage hydraulic diameter (e/D_h) or blockage ratio, rib angle of attack (α), the manner in which the ribs are positioned relative to one another (in-line, staggered, criss-cross, etc.), rib pitch-to-height ratio (S/e) and rib shape (round versus sharp corners, fillets, rib aspect ratio (AR_r), and skewness toward the flow direction) have pronounced effects on both local and overall heat transfer coefficients. Some of these effects were studied by different investigators such as Abuaf et al. (1986), Burggraf (1970), Chandra (1987), Chandra and Han (1989), Han (1984), Han et al. (1978, 1985, 1992), Metzger et al. (1983, 1988, 1990), Taslim et al. (1988a, b, 1991a, b, 1994, 1996), Webb et al. (1971). Considerable data are available on the heat transfer coefficient on the passage surface between the ribs. However, the heat transfer coefficients on the surface of the ribs themselves have not been investigated to the same extent.

Several investigators have studied the flow and heat transfer associated with the ribs in rib-roughened channels. Solntsev et al. (1973) conducted an experimental investigation on heat transfer in the vicinity of sudden two- and three-dimensional steps of circular and square cross-sectional areas mounted on a flat surface in an open channel. They reported enhancements in heat transfer coefficient for a range of Reynolds numbers between 10^4 to 10^5. Berger and Hau (1979) used an electrochemical analogue technique to measure mass/heat transfer on square ribs as well as on the wall surface between the ribs in a pipe. For a blockage ratio (e/d) of 0.0364 and a range of Reynolds numbers between 10,000 and 25,000, they varied the rib pitch-

Contributed by the International Gas Turbine Institute and presented at Turbo Asia '96, Jakarta, Indonesia, November 5–7, 1996. Manuscript received at ASME Headquarters July 1996. Paper No. 96-TA-9. Associate Technical Editor: J. W. Shinn.

to-height ratio from 3 to 10. At the Reynolds number of 10^4, they showed enhancements, compared to smooth channels, in mass (heat) transfer on the ribs in the order of 4.4 and 5.2 for pitch-to-height ratios of 10 and 7, respectively. Metzger et al. (1988) used a thermal transient technique to examine the contribution of the rib heat transfer to the overall heat transfer of a rib-roughened wall with variations in rib angle of attack and pitch. Square ribs representing a blockage ratio of 0.14 were mounted on only one wider side of a 0.154 aspect ratio rectangular channel. The main conclusions were that heat transfer on the rib surface significantly contributed to the overall rib-roughened wall heat transfer and this contribution mainly depended on the rib pitch-to-height spacing, with very little effect from the rib angle. Lockett and Collins (1990) used a holographic interferometry technique to measure heat transfer coefficient in a 0.25 aspect ratio rectangular channel. Square ribs with both sharp and round top corners representing a blockage ratio, e/D_h, of 0.067 and a pitch-to-height ratio of 7.2 were mounted on one of the wider sides of the channel, perpendicular to the flow direction. They reported overall enhancements in heat transfer of up to 2.24 for the Reynolds number of 7400. Liou et al. (1991) performed numerical as well as experimental investigation of turbulent flow in a 4:1 aspect ratio rectangular channel roughened on two opposite wider sides with square ribs in an in-line arrangement perpendicular to the flow direction. The rib blockage ratio, e/D_h, was 0.081 and four pitch-to-height ratios of 5, 10, 15, and 20 were examined at a fixed Reynolds number of 33,000. Two-dimensional Navier–Stokes equations in elliptic form in conjunction with the $k-\epsilon$ turbulence model were solved numerically and a holographic interferometry technique was used in the experimental part. They reported an enhancement in heat transfer on the rib surface of 3.1. Sato et al. (1992) investigated the flow characteristics and heat transfer in a rectangular channel with a total of 20 square ribs on two opposite walls in staggered, in-line, and quarter-pitch-shift arrangements. The channel aspect ratio was 0.2 and the ribs, mounted on the two wider sides of the channel, had a blockage ratio of 0.12. Details of the flow and heat transfer over a typical rib-roughened section (including the rib surface) well downstream of the first rib were presented. They concluded that the staggered arrangement had a better heat transfer performance than the other two arrangements. Dawes (1994) solved the three-dimensional Navier–Stokes equations in a rotating cylindrical serpentine passage roughened with square ribs. Rib blockage, e/d, and pitch-to-height ratios were 0.2 and 10, respectively. Results of this work were compared with other numerical and experimental works. Liou and Hwang (1993) also used the holographic interferometry technique to measure the heat transfer coefficient in a rectangular channel of 0.25 aspect ratio with three rib shapes including a square rib geometry mounted on two opposite wider sides in an in-line arrangement perpendicular to the flow direction. They tested four pitch-to-height ratios of 8, 10, 15, and 20, all with a blockage ratio of 0.08, for a range of Reynolds numbers between 7800 and 50,000. The heat transfer coefficient was measured over the ribs as well as the wall surfaces between the ribs. They reported overall heat transfer coefficient enhancements on the order of 2.2 and 2.7 for semi-cylindrical and square ribs, respectively. Taslim and Wadsworth (1997) reported on the rib surface-averaged heat transfer coefficients in a square channel. Thirteen rib geometries including three blockage ratios and four pitch-to-height ratios were tested. Sharp corner ribs were mounted on two opposite walls of the channel at a 90 deg angle with respect to the flow direction in a staggered arrangement. A major conclusion of their study was that the rib surface-average heat transfer coefficient was much higher than that for the area between the ribs (h_{floor}). Therefore, the contribution of the ribs to the overall heat transfer in a rib-roughened passage is significant. They showed that for a typical rib arrangement the $h_{\text{rib}} A_{\text{rib}}$ can be as high as 33 to 53 percent of $h_{\text{overall}} A_{\text{total}}$. Other conclusions were that (a) for sharp-edged ribs, a pitch-to-height ratio of 8.5 produced the highest heat transfer coefficient, and (b) heat transfer coefficient on ribs in the furthest upstream position was lower than that on the midchannel ribs. Korotky and Taslim (1998) tested the same rib geometries with rounded corners to investigate the rounding effects of rib corners on heat transfer coefficient and friction factor. They concluded that the general effect of rounding was a decrease in midstream rib heat transfer coefficient and an increase for the ribs in the furthest upstream position.

In small gas turbine blades and nozzles with small cooling passages and relatively large ribs, the rib surfaces comprise a large portion of the passage heat transfer area. Therefore, an accurate account of the heat transfer coefficient on the rib surfaces is critical in the overall design of the airfoil cooling sys-

Nomenclature

a = channel height (Fig. 1)
b = channel width (Fig. 1)
A = channel cross-sectional area without ribs = ab
A_{floor} = wall heat transfer area between two ribs
A_{rib} = rib total heat transfer area (three sides)
A_{total} = total heat transfer area = $A_{\text{rib}} + A_{\text{floor}}$
AR = channel aspect ratio = b/a
AR_t = rib aspect ratio = e/w
D_h = hydraulic diameter based on the smooth cross section = $4A/P = a$
e = rib height
$\bar{f}$ = Darcy friction factor = $\Delta P(D_h/L)/(1/2\rho U_m^2)$
$\overline{f_s}$ = Darcy friction factor in an all-smooth-wall channel
h_{floor} = average heat transfer coefficient on the wall surface between a pair of ribs
h_{overall} = overall average heat transfer coefficient on a rib and on the wall surface between a pair of ribs
h_{rib} = rib average heat transfer coefficient = $q/(T_s - T_m)$
i = current through the heater inside the copper rib
k = air thermal conductivity
L = length of the rib-roughened portion of the test section
m = air mass flow rate
$\overline{\text{Nu}}$ = rib-averaged Nusselt number = $h_{\text{rib}}D_h/k$
$\overline{\text{Nu}_s}$ = average Nusselt number in a smooth channel
P = channel perimeter without ribs
Pr = Prandtl number
q = net heat flux from the copper rib three surfaces = $(vi - Q_{\text{loss}})/A_{\text{rib}}$
Q_{loss} = heat losses from the copper rib by radiation and conduction
Re = Reynolds number = $\rho U_m D_h/\mu$
S = rib pitch (center-to-center)
T_f = film temperature = $0.5(T_s + T_m)$
T_m = air mixed mean temperature at copper rib location
T_s = copper rib surface temperature
U_m = air mean velocity
v = voltage drop across the heater inside the copper rib
w = rib width
X = distance between the instrumented rib and test section entrance (Fig. 1)
α = angle of attack
ΔP = pressure drop across the rib-roughened portion of the test section
μ = air dynamic viscosity
ρ = air density

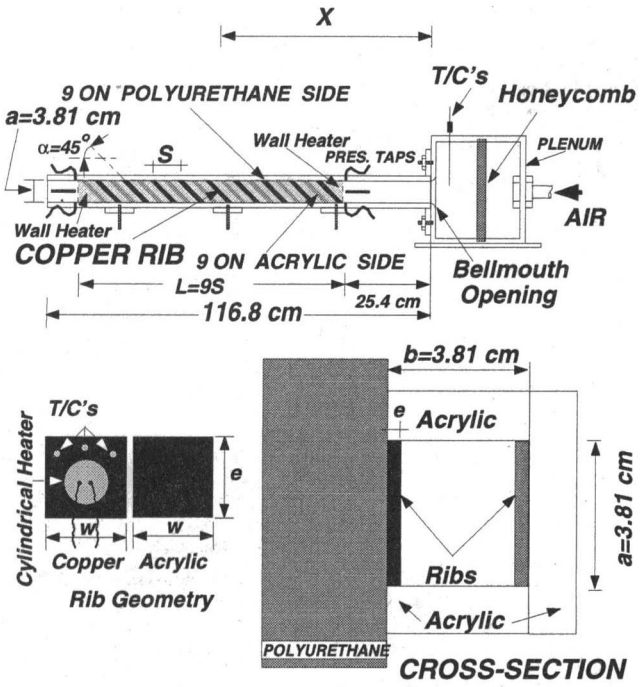

Fig. 1 Schematic of a typical test section

tem. The objective of this investigation was, while isolating the ribs from the wall surface thermally: (*a*) to measure the overall heat transfer coefficient on the rib surface, (*b*) to study the effects of pitch-to-height ratio (S/e) and blockage ratio (e/D_h), (*c*) to study the effects rib orientation (furthest upstream position or in the middle of the channel rib-roughened portion) have on the rib surface heat transfer coefficient, and (*d*) to compare 45 deg angle-of-attack results with previous 90 deg angle measurements.

Test Sections

All test sections, with a length of 116.84 cm, had a square 3.81 cm by 3.81 cm cross-sectional area. Three walls of these channels were made of 1.27-cm-thick clear acrylic plastic. The fourth wall, on which the surface heaters and instrumented copper rib were mounted and all measurements were taken, was made of a 7.62-cm-thick machinable polyurethane slab. Figure 1 shows schematically the layout and cross-sectional area of a typical test section. Eighteen ribs of square cross section with sharp corners were symmetrically staggered on the polyurethane wall and its opposite acrylic wall (nine on each) at 45 deg angle of attack to the air flow. Rib geometry details are shown in Table 1. The entrance region of all test sections was left smooth to simulate the cooling passage in the dovetail region of a gas turbine blade. All ribs but one were machined out of acrylic plastic and were mounted on the walls using a special double-stick 0.05-mm-thick tape with minimal temperature deformation characteristics. The instrumented rib on which all measurements were taken was machined out of copper. Inside this copper rib, a 60 Ω cylindrical electric heater was installed using a highly conductive silver glue. The heater, which ran the full length of the rib, was mounted as centrally as possible. Also installed in the copper rib were three calibrated thermocouples to measure the surface temperature. These three thermocouples were equally spaced over the length of the rib with their beads close to the rib surface. Their temperature readings were found to be the same within a fraction of a degree. For data reduction, the average of the three temperatures was used. Copper rib surfaces were polished to minimize the radiational heat losses from the copper rib to the unheated wall. Rib heat transfer coefficient

Table 1 Specifications

Test	e(mm)	e/Dh	S/e	X (cm)	X/Dh	Remarks
1	9.525	0.25	5	60.96	16	Midstream
2	9.525	0.25	8.5	60.96	16	Midstream
3	9.525	0.25	10	60.96	16	Midstream
4	9.525	0.25	8.5	28.58	7.5	Upstream
5	6.35	0.167	5	59.06	15.5	Midstream
6	6.35	0.167	8.5	59.06	15.5	Midstream
7	6.35	0.167	10	59.06	15.5	Midstream
8	6.35	0.167	8.5	37.47	9.83	Upstream
9	5.08	0.133	5	60.96	16	Midstream
10	5.08	0.133	8.5	60.96	16	Midstream
11	5.08	0.133	10	60.96	16	Midstream
12	5.08	0.133	8.5	43.69	11.47	Upstream
Dh=3.81 cm, AR = 1, ARt = e/w = 1, α = 45°, 9 Ribs on Each Side						
Sharp-Corner Staggered Ribs for all Geometries						

measurements were performed for two distinct rib locations. First, the copper rib was mounted in the middle of the rib-roughened portion of the channel (fifth rib) and other eight acrylic plastic ribs were arranged on each side with the desired rib pitch-to-height ratio. Second, the copper rib was moved to the furthest upstream position and the other eight ribs were mounted downstream of it. Table 1 shows the rib location from the channel entrance, X, for each geometry. Two 3.81 cm × 30.48 cm × 5.39 cm × 26.67 cm trapezoidal custom-made etched-foil heaters with a thickness of 0.15 mm were placed on the polyurethane wall abutting both sides of the copper rib using the same special double-stick tape. With a 45-deg side, these

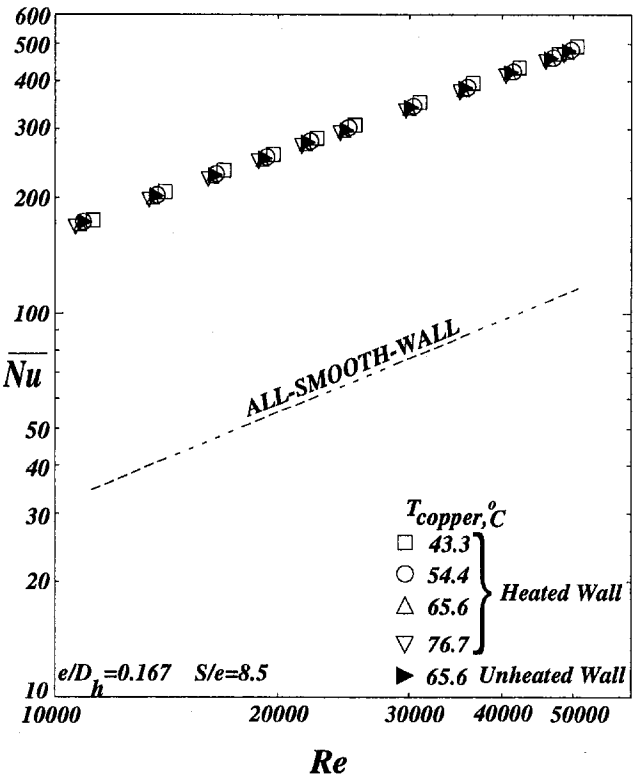

Fig. 2 Rib average Nusselt number for a range of rib surface temperature

heaters were laid snugly on both sides of the copper rib and were actuated in those tests termed as "Heated Wall" in Fig. 2. The air mixed mean temperature, T_m, was calculated from an energy balance between the channel inlet and copper rib location. The test section was covered on all sides by 5-cm-thick styrofoam sheets to minimize the heat losses to the environment. Surface heat flux in the test section was generated by the heaters through a custom-designed power supply unit. Each heater was individually controlled by a variable transformer. Thermocouples were calibrated using ice water and boiling water reference points prior to testing. For a typical test run, the Reynolds number was set by precisely fixing the air mass flow rate. The heat flux was induced by adjusting heater power until the copper rib reached the desired temperature. Enough time was given so that the system came to thermal equilibrium, at which time data was recorded. Power to the copper rib was then increased to gather data at a higher surface temperature. This procedure was repeated for all copper temperatures and flow rates. Static pressure taps were mounted on all three acrylic plastic walls of the test section to measure the pressure drop across the rib-roughened portion of the test section. A contact micromanometer with an accuracy of 0.025 mm of water column measured the pressure differences between the static pressure taps. A critical venturimeter, with choked flow for all cases tested, measured the air mass flow rate entering the test section. The reported friction factor is the overall passage average, $\bar{f}$, and not just the rib-roughened surfaces. Details of the experimental apparatus and test procedures are reported by Lengkong (1996). The radiational heat loss from the heated rib (and wall) to the unheated walls as well as losses to ambient air were taken into consideration when heat transfer coefficients were calculated. The reported heat transfer coefficients are the averages over the rib surfaces and not that of wall surfaces between the ribs. The heat transfer coefficients on the roughened walls for various geometries are reported by those investigators mentioned in the Introduction section. Experimental uncertainties, following the method of Kline and McClintock (1953), were determined to be ±8 and ±6 percent for the heat transfer coefficient and friction factor, respectively.

Results and Discussion

Heat transfer as well as friction factor results for the twelve 45 deg rib geometries are compared with those of 90 deg ribs in Figs. 3–16. The Dittus–Boelter (1930) correlation for an all-smooth-wall channel ($\overline{Nu}_s = 0.023\ Re^{0.8}\ Pr^{0.4}$) is plotted on Fig. 2. With this correlation, the enhancement (relative to smooth walls) in rib-roughened heat transfer coefficients is readily evaluated. The thermal performance based on the same pumping power was derived by Gee and Webb (1980) as $(\overline{Nu}/\overline{Nu}_s)/(\bar{f}/f_s)^{1/3}$, where f_s is the all-smooth-wall friction factor from Moody (1944). Air properties for Nusselt and Reynolds number calculations are based on the local film temperature, T_f, for all cases.

Figure 2 shows the Nusselt versus Reynolds numbers for the medium rib geometry corresponding to a blockage ratio, e/D_h, of 0.167 and a pitch-to-height ratio, S/e, of 8.5. Copper rib temperature is varied from 43.3°C to 76.7°C with no change in the measured heat transfer coefficient. This lack of effect of the copper surface temperature on heat transfer coefficient continued for all geometries examined. Furthermore, this insensitivity of the measured heat transfer coefficient to the rib surface temperature supports the accuracy of our accounting for the heat losses to the ambient air and radiational losses from the heated copper rib to the unheated surrounding walls. Shown in Fig. 2 are also the results of two tests of identical geometries for which the foil heaters were on and off, respectively. The difference in the Nusselt number was well below the experimental uncertainties, indicating that the thermal boundary layer, being interrupted repeatedly by the ribs, did not affect the heat transfer. It

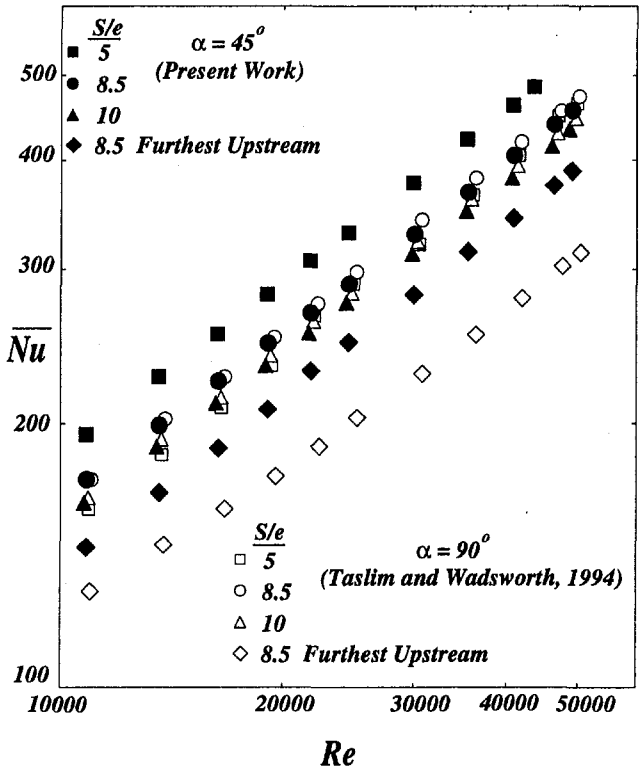

Fig. 3 Rib average Nusselt number for a range of pitch-to-height ratios, $e/D_h = 0.25$

would appear that the mixing phenomenon was the dominant driving force for the high levels of heat transfer coefficient. As for having only one heated wall, it is noted that an experimental investigation by El-Husayni et al. (1994) on heat transfer in a rib-roughened channel with one, two, and four heated walls showed that, in a stationary roughened channel, the heat transfer coefficient was not significantly sensitive to the number of heated walls, i.e., the variation in heat transfer coefficient was within the reported experimental uncertainty of ±8 percent.

To investigate the effects pitch-to-height ratio have on rib heat transfer and channel overall friction factor, a 9.525 mm square rib geometry was tested for three pitch-to-height ratios of 5, 8.5, and 10 (geometries 1–3 in Table 1) the results of which are shown in Fig. 3. Also shown in Fig. 3 are the rib heat transfer results for an S/e of 8.5 when the instrumented copper rib was mounted in the furthest upstream position (geometry 4 in Table 1). The open symbols on that figure are the results of 90 deg ribs, reported previously by Taslim and Wadsworth (1997). Several observations are made. First, the heat transfer coefficient for the furthest upstream rib was considerably lower than that for the rib in the middle of the rib-roughened region, indicating that upstream ribs and those staggered on the opposite wall contribute significantly to the very high level of heat transfer enhancement of downstream ribs by interrupting the flow and diverting its direction thus promoting high levels of mixing. Second, for these ribs of high blockage ratio, the pitch-to-height ratio of 5 produced the highest heat transfer coefficient and as the pitch-to-height ratio increased, the heat transfer coefficient decreased. Secondary flows in the form of swirls along the angled ribs, especially for these relatively big ribs, are believed to be responsible for high levels of heat transfer coefficients compared with those for the 90 deg ribs. These secondary flows are stronger when angled ribs are brought closer to each other as is seen for the pitch-to-height ratio of 5. Third, in the midstream position, the heat transfer coefficients of 45 and 90 deg ribs are very close for pitch-to-height ratios of 8.5 and 10. However, 45 deg ribs produce much

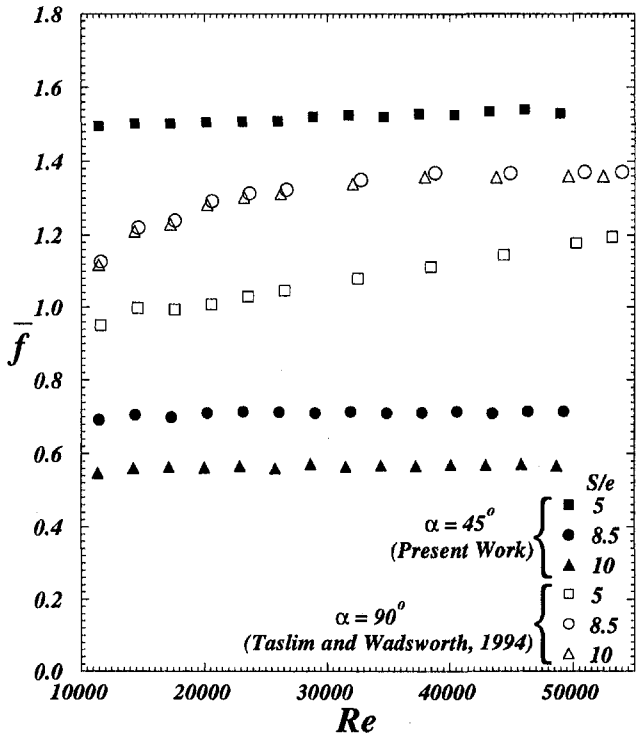

Fig. 4 Channel average friction factor for a range of pitch-to-height ratios, e/D_h = 0.25

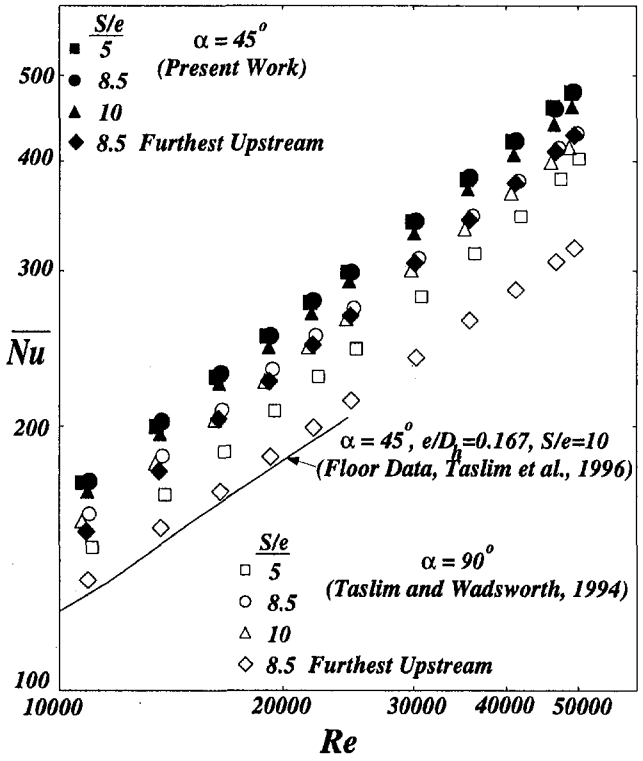

Fig. 5 Rib average Nusselt number for a range of pitch-to-height ratios, e/D_h = 0.167

higher heat transfer coefficients in the furthest upstream position and also in the midstream position when the pitch-to-height ratio is 5. Secondary flows associated with the angled ribs are responsible for this remarkable difference. Friction factors for these geometries are shown in Fig. 4. While 45 deg ribs at pitch-to-height ratios of 8.5 and 10 produced lower pressure drops and consequently lower friction factors compared to 90 deg ribs, *S/e* of 5 represented a reversed trend. Following the discussion of the heat transfer results, formation of strong secondary flows along the 45 deg ribs produces higher pressure drops and higher heat transfer coefficients while in case of 90 deg ribs, if ribs are positioned too close to each other, with the formation of a recirculating bubble in the cavity between the ribs, the flow may totally skip that cavity, thus producing a lower friction factor.

The next series of four tests, shown in Fig. 5, corresponded to a rib blockage ratio of 0.167 three of which (test geometries 5–7 in Table 1) were performed for pitch-to-height ratios of 10, 8.5, and 5 with the instrumented copper rib mounted in the middle of the rib-roughened region. The fourth test represents the heat transfer results when the copper rib was mounted in the furthest upstream position (geometry 8 in Table 1). Also shown in Fig. 5 are the heat transfer results for the area between the ribs (called floor heat transfer coefficient by some investigators) reported by Taslim et al. (1996). It can be seen that the rib average heat transfer coefficient is much higher than that for the area between the ribs (h_{floor}). Therefore, the contribution of the ribs to the overall heat transfer in a rib-roughened passage is significant. It is also seen that these lower blockage ratio 45 deg ribs perform superior to their 90 deg counterparts for all pitch-to-height ratios, and both in midstream and furthest upstream positions. Again, the secondary flows associated with the angled ribs are believed to be responsible for this difference. This trend is repeated once again for the next rib geometry of still lower blockage ratio to be discussed shortly. Similar to the rib geometry discussed previously, the midstream ribs produced higher Nusselt numbers than that in the furthest upstream position. From a comparison between Figs. 3 and 5, it is observed that the Nusselt number for the 45 deg ribs is much less dependent on the pitch-to-height ratio for these smaller ribs and it will continue to be the case for the next rib geometry of lower blockage ratio. The pitch-to-height ratio of 10 produced the lowest midstream heat transfer coefficient for both 45 and 90 deg ribs, indicating that the optimum spacing for rib heat transfer coefficient is generally lower than that for the heat transfer

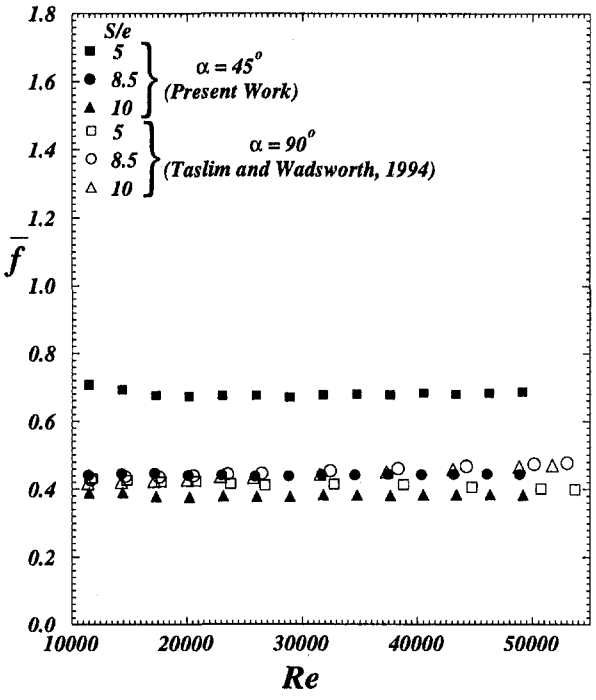

Fig. 6 Channel average friction factor for a range of pitch-to-height ratios, e/D_h = 0.167

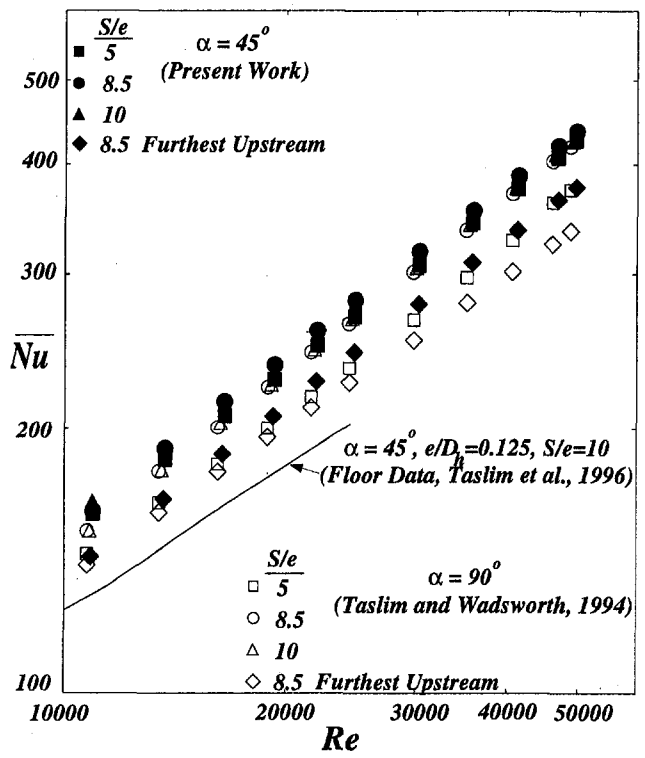

Fig. 7 Rib average Nusselt number for a range of pitch-to-height ratios, $e/D_h = 0.133$

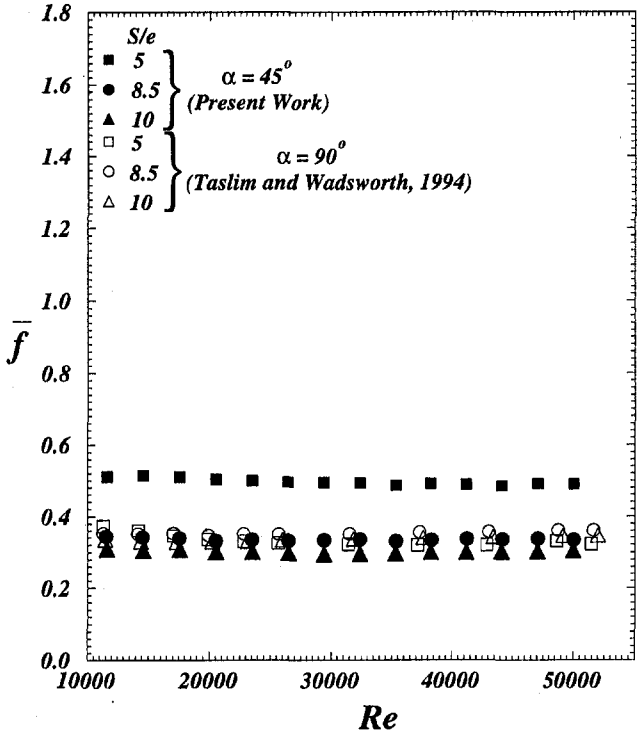

Fig. 8 Channel average friction factor for a range of pitch-to-height ratios, $e/D_h = 0.133$

coefficient on the area between the ribs. This trend is observed for several rib geometries tested and reported previously (Taslim and Wadsworth, 1997; Korotky and Taslim, 1998). The friction factors for these tests are shown in Fig. 6 and trends, discussions, and physical reasoning are similar to that of Fig. 4, i.e., (*a*) lower pressure drops (friction factors) for the 45 deg ribs at pitch-to-height ratios of 8.5 and 10, and (*b*) higher friction factors for the 45 deg ribs when the pitch-to-height ratio is reduced to 5.

The next four tests, shown in Fig. 7, corresponded to a yet smaller rib blockage ratio of 0.133. The first three tests (geometries 9–11 in Table 1) were performed for pitch-to-height ratios of 5, 8.5, and 10 with the instrumented copper rib mounted in the middle of the rib-roughened region. The fourth test represents the heat transfer results for the copper rib mounted in the furthest upstream position (geometry 12 in Table 1). Floor heat transfer results (Taslim et al., 1996) for a blockage ratio of 0.125, the closest geometry that could be found in open literature, are also shown for comparisons. Several observations are made. Similar to the previously discussed rib geometry, 45 deg rib results for this small blockage ratio are higher than those for the 90 deg ribs at all pitch-to-height ratios. Again, the rib in the furthest upstream position produced a lower heat transfer coefficient than those in the midstream position. The difference, however, is not as remarkable as that for the higher blockage ribs shown in Figs. 3 and 5 since the secondary flows are not as strong as those for the high blockage ribs. An optimum pitch-to-height ratio for these relatively small ribs is between 8.5 and 10, similar to that for the 90 deg ribs. The corresponding friction factors for this rib geometry are shown in Fig. 8. The trend is similar to those of higher blockage ratio ribs. 45 deg ribs with a pitch-to-height ratio of 5 have consistently produced the highest pressure drop, which is not always accompanied with higher heat transfer coefficients, indicating high levels of form drag when 45 deg ribs are brought too close to each other.

Figure 9 combines the results of all three rib geometries in the furthest upstream position at S/e of 8.5. First, it is observed that the rib heat transfer coefficients for the 45 deg ribs in the furthest upstream position are higher than those for the 90 deg ribs for the three blockage ratios tested. We attributed this behavior to the formation of secondary flows along the angled

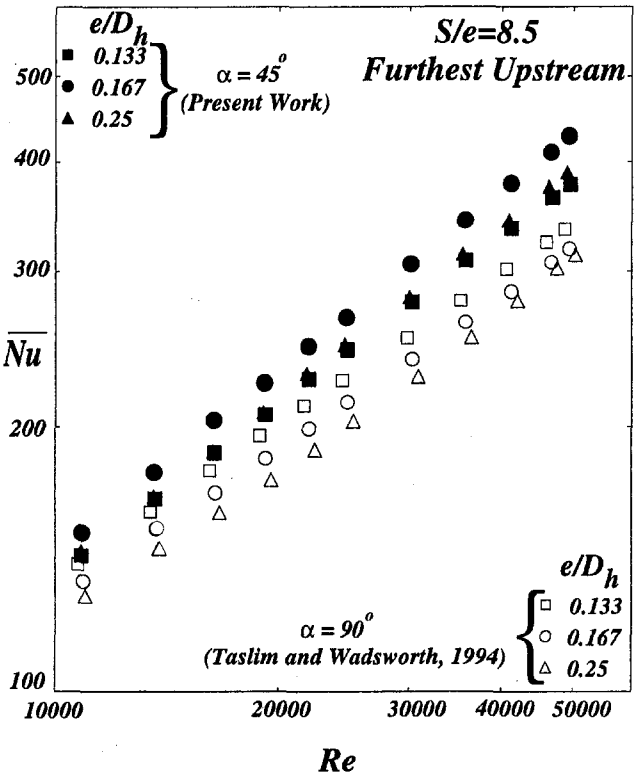

Fig. 9 Rib average Nusselt number of the farthest upstream rib for a range of blockage ratios

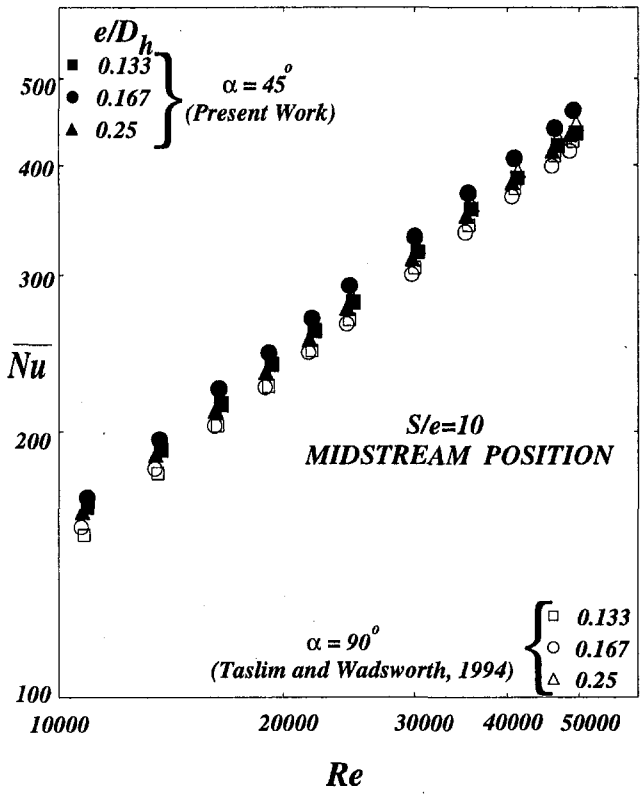

Fig. 10 Rib-averaged Nusselt number for a range of blockage ratios, $S/e = 10$

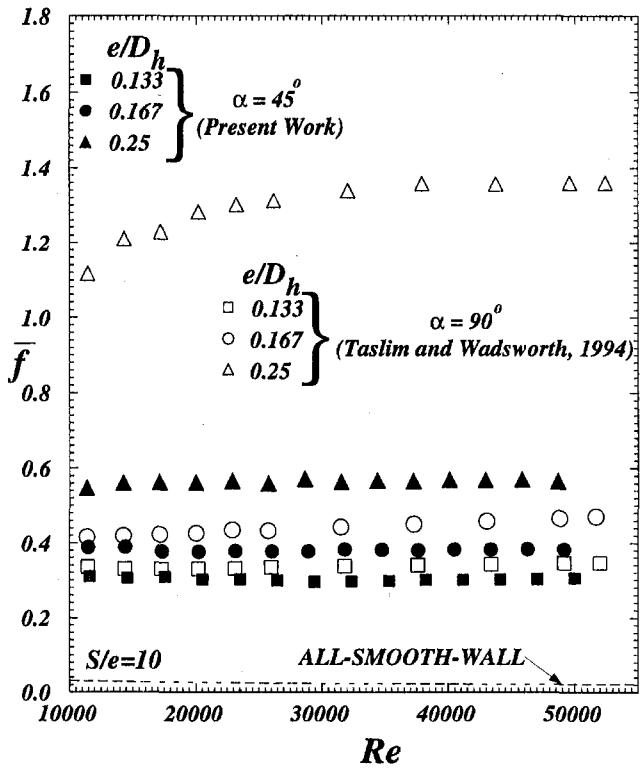

Fig. 11 Channel average friction factor for a range of blockage ratios, $S/e = 10$

ribs in our discussion of the results for each rib geometry. Second, while the 90 deg ribs show a decrease in Nusselt number with an increase in blockage ratio, the 45 deg ribs show an optimum blockage ratio of 0.167. Not benefiting from the effects of the ribs on the opposite wall, it is speculated that this behavior is due to the change of flow pattern over different ribs. In other words, for the 90 deg ribs in the extreme case, recirculating bubbles may form on both the back and top surfaces of the big rib, reducing the contribution of the rib top surface to heat transfer, known to be major for square ribs with sharp corners by all investigators mentioned above. For the smallest 90 deg rib, the top surface is in contact with the core air, thus higher heat transfer coefficients are produced. When the ribs are angled, a combination exists of the secondary flows and the recirculating bubbles, mentioned above, that act in opposite ways and, depending on the strength of each phenomenon, the overall rib heat transfer coefficient varies. There is a better flow adherence to the smaller angled ribs but the secondary flows are not as strong as those for higher blockage ratio ribs. On the other hand, high blockage angled ribs produce strong secondary flows, which are accompanied with the separation of the main flow from the top and back surfaces. This combination results in a lower heat transfer coefficient than that for the medium size rib for which a proper combination of the two effects produces the highest heat transfer coefficient.

Figures 10 and 11 compare the midchannel rib heat transfer coefficient and channel friction factors for three blockage ratios at one pitch-to-height ratio of 10. In contrast with the heat transfer coefficient on the area between a pair of ribs, which is highly affected by the blockage ratio, the rib heat transfer coefficient did not show as strong a dependency on the blockage ratio for $S/e = 10$. However, as ribs were brought closer to each other by reducing the pitch-to-height ratio, rib heat transfer coefficient was more and more affected by the blockage ratio (Figs. 12 and 14). It is noted that for the pitch-to-height ratios of 10 and 8.5 (Figs. 10 and 12) the 45 deg rib with the blockage ratio of 0.167 produced the highest heat transfer coefficients. However, as the ribs were brought closer to each other ($S/e = 5$, Fig. 14), the high blockage ratio rib ($e/D_h = 0.25$) produced the highest heat transfer coefficient. The corresponding friction

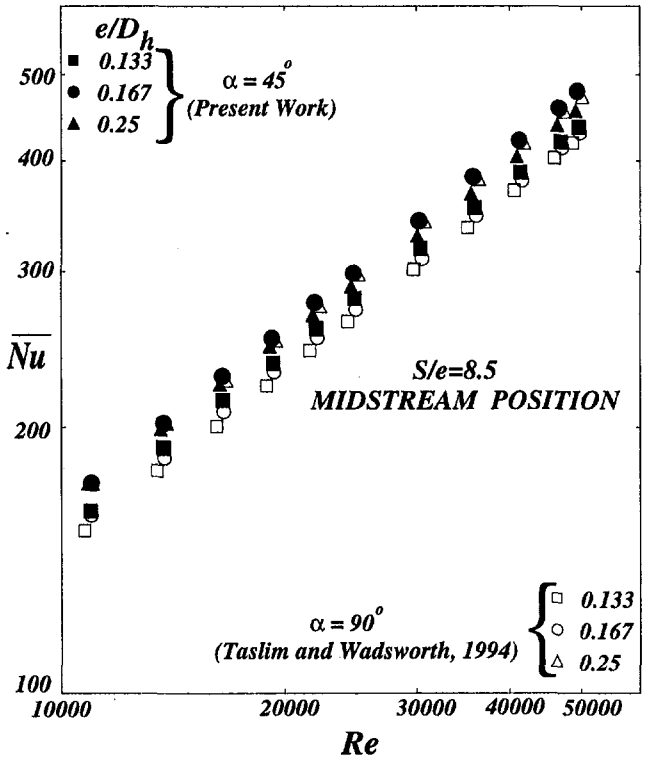

Fig. 12 Rib-averaged Nusselt number for a range of blockage ratios, $S/e = 8.5$

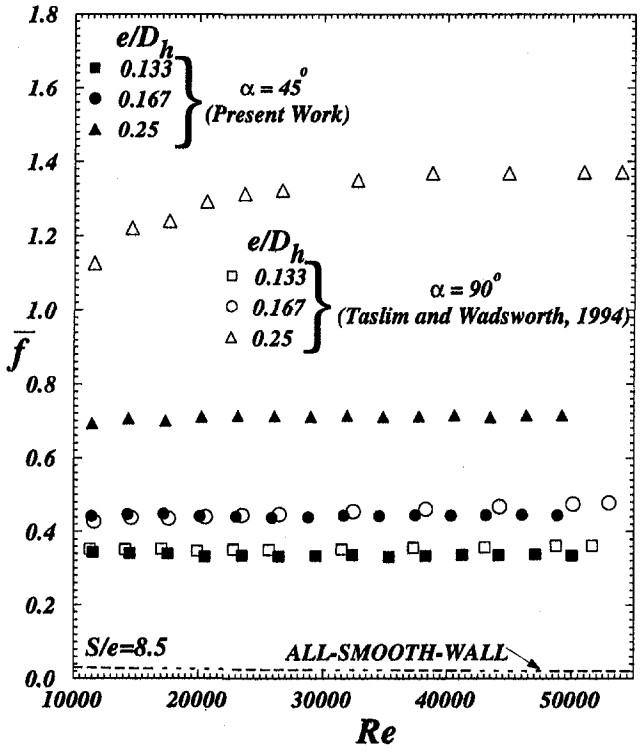

Fig. 13 Channel-averaged friction factor for a range of blockage ratios, S/e = 8.5

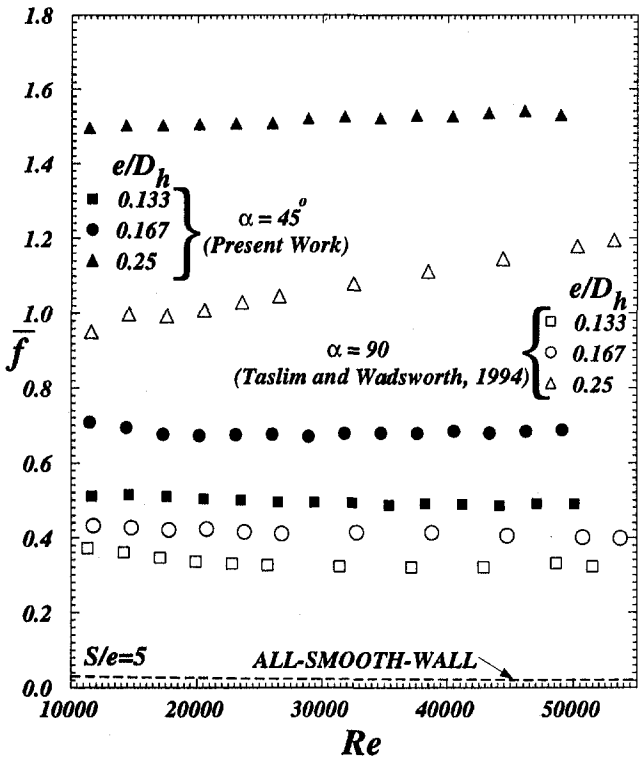

Fig. 15 Channel-averaged friction factor for a range of blockage ratios, S/e = 5

factors for S/e of 8.5 and 5 are shown in Figs. 13 and 15. An inspection of Figs. 11, 13, and 15 reveals that, for pitch-to-height ratios of 10 and 8.5, angled ribs produce lower friction factors than 90 deg ribs. However, when the ribs are brought closer to each other (S/e = 5, Fig. 15), 45 deg ribs have higher friction factors than those of 90 deg for all blockage ratios. As we discussed before, these high friction factors are accompanied with high heat transfer coefficients and the secondary flows generated by angled ribs are believed to be responsible for high levels of friction factors and Nusselt numbers.

Figure 16 shows the variation of Nusselt number with the rib spacing for the 45 and 90 deg ribs. The results are for a typical

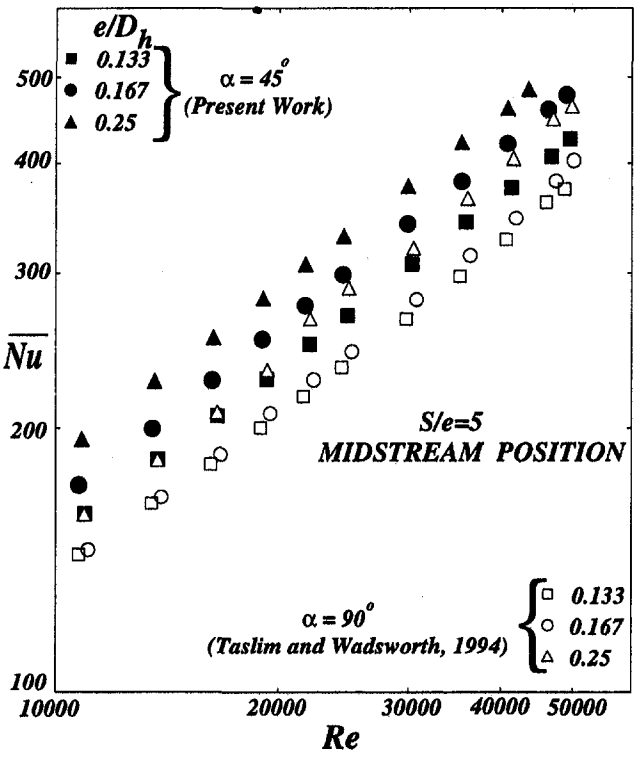

Fig. 14 Rib-averaged Nusselt number for a range of blockage ratios, S/e = 5

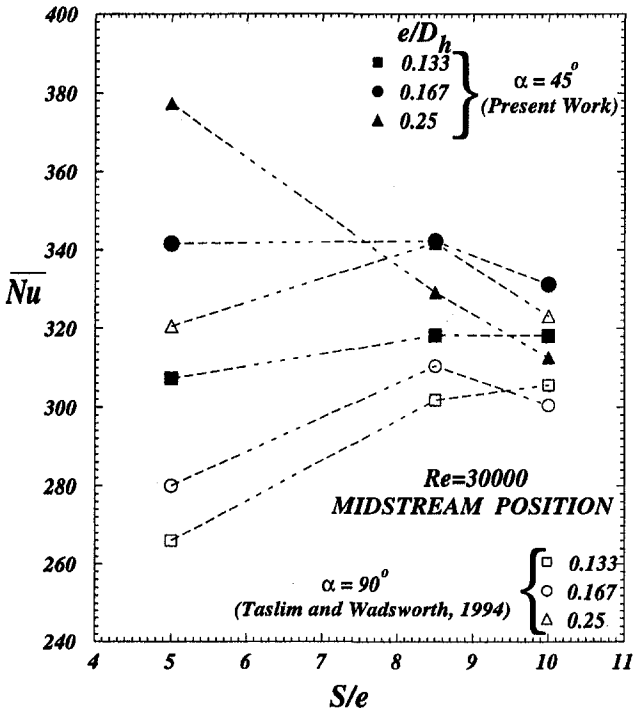

Fig. 16 Rib-averaged Nusselt number versus pitch-to-height ratio for all blockage ratios

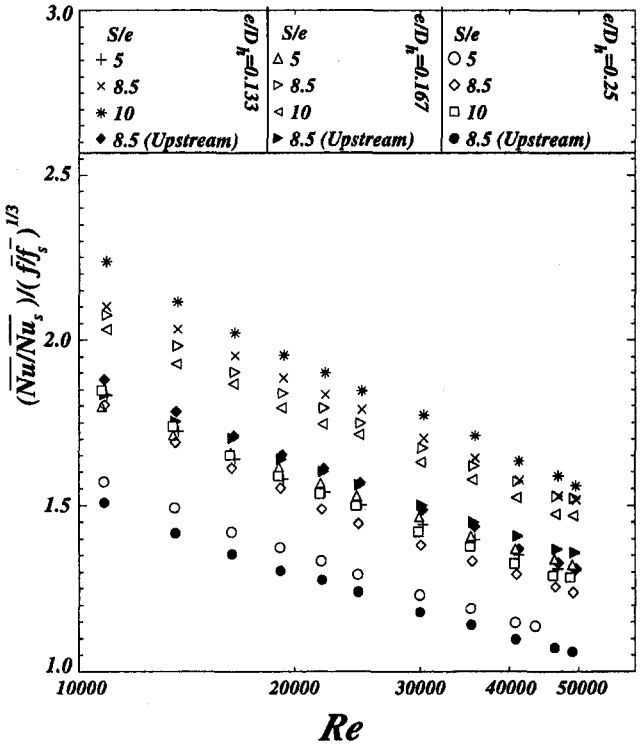

Fig. 17 Rib thermal performances of the twelve geometries

Reynolds number of 30,000 and for the ribs in the midstream position. The two smaller 45 deg ribs show very little sensitivity to the pitch-to-height ratio. However, the high blockage 45 deg rib is very sensitive to the pitch-to-height ratio and as the ribs are separated further from each other, the heat transfer coefficient decreases considerably. In our discussion of heat transfer coefficients for this rib geometry, we attributed this behavior to the strength of the secondary flow for each case. In contrast, the 90 deg ribs of all three blockages show almost similar behavior and the two larger rib geometries tend to have an optimum pitch-to-height ratio of 8.5. Low spacing for 90 deg ribs resembles a cavity-driven flow between the ribs that causes a decrease in the heat transfer coefficient (Metzger et al., 1988).

Finally, the thermal performances of all geometries tested are compared in Fig. 17. It should be noted that the thermal performances reported here do not include the contribution of the heat transfer coefficient on the surface area between the ribs, h_{floor}. Thermal performance data for the surface area between the ribs are reported by the first author (Taslim et al., 1996) and can be combined with the present data to determine the overall thermal performances. It is seen that as the blockage ratio increases, the rib thermal performance decreases. For all geometries tested, the maximum and minimum thermal performances corresponded to the smallest rib ($e/D_h = 0.133$) with a pitch-to-height ratio of 10 and the biggest rib ($e/D_h = 0.25$) in the furthest upstream position, respectively. For the blockage ratios of 0.167 and 0.25, the furthest upstream ribs had the lowest thermal performances. This was expected since, for the same channel average friction factor, the furthest upstream rib had a lower heat transfer coefficient than that in the middle of the rib-roughened region. For the small ribs, however, the pitch-to-height ratio of 5 showed the lowest thermal performance, indicating that the pressure drop for that geometry was mainly due to form drag and not skin friction, which is responsible for high levels of heat transfer coefficients.

Conclusions

Major conclusions of this study are:

1 For the geometries tested, the rib-averaged heat transfer coefficient was much higher than that for the area between the ribs. For high blockage ribs with large heat transfer areas, commonly used in small gas turbines, the rib heat transfer is a significant portion of the overall heat transfer in the cooling passages.

2 Except for two cases corresponding to the highest blockage ribs mounted at pitch-to-height ratios of 8.5 and 10 for which the heat transfer results of 45 deg ribs were very close to those of 90 deg ribs, in the remaining ten cases, 45 deg ribs produced higher heat transfer coefficients than 90 deg ribs.

3 At pitch-to-height ratios of 8.5 and 10, all 45 deg ribs produced lower friction factors than 90 deg ribs. However, when they were brought closer to each other ($S/e = 5$), they produced higher friction factors than 90 deg ribs.

4 Heat transfer coefficients for the two smaller rib geometries ($e/D_h = 0.133$ and 0.167) did not vary significantly with the pitch-to-height ratio in the range tested. However, the heat transfer coefficient for the high blockage rib geometry increased significantly as the ribs were brought closer to each other.

5 Under otherwise identical conditions, ribs in the furthest upstream position produced lower heat transfer coefficients than those in the midstream position.

6 Rib thermal performance decreased with the rib blockage ratio. While the smallest rib geometry in the midstream position and at a pitch-to-height ratio of 10 had the highest thermal performance, the highest blockage rib in the furthest upstream position produced the lowest thermal performance. These trends were identical for 45 and 90 deg ribs.

References

Abuaf, N., Gibbs, R., and Baum, R., 1986, "Pressure Drop and Heat Transfer Coefficient Distributions in Serpentine Passages With and Without Turbulence Promoters," *Proc. Eighth International Heat Transfer Conference,* C. L. Tien, V. P. Carey, and J. K. Ferrel, eds., pp. 2837–2845.

Berger, F. P., and Hau, K. F., 1979, "Local Mass/Heat Transfer Distribution on Surfaces Roughened With Small Square Ribs," *International Journal of Heat and Mass Transfer,* Vol. 22, pp. 1645–1656.

Burggraf, F., 1970, "Experimental Heat Transfer and Pressure Drop With Two Dimensional Turbulence Promoters Applied to Two Opposite Walls of a Square Tube," *Augmentation of Convective Heat and Mass Transfer,* A. E. Bergles and R. L. Webb, eds., ASME, pp. 70–79.

Chandra, P. R., 1988, "Effect of Rib Angle on Local Heat/Mass Transfer Distribution in a Two Pass Rib-Roughened Channel," ASME JOURNAL OF TURBOMACHINERY, Vol. 110, pp. 233–241.

Chandra, P. R., and Han, J. C., 1989, "Pressure Drop and Mass Transfer in Two-Pass Ribbed Channels," AIAA *Journal of Thermophysics,* Vol. 3, No. 3, pp. 315–319.

Colburn, A. P., 1933, "A Method of Correlating Forced Convection Heat Transfer Data and a Comparison With Fluid Friction," *Trans. A.I.Ch.E.,* Vol. 29, pp. 174–210.

Dawes, W. N., 1994, "The Solution-Adaptive Numerical Simulation of the Three-Dimensional Viscous Flow in the Serpentine Coolant Passage of a Radial Inflow Turbine Blade," ASME JOURNAL OF TURBOMACHINERY, Vol, 116, pp. 141–148.

Dittus, F. W., and Boelter, L. M. K., 1930, University of California, Berkeley, CA, Publications in Engineering, Vol. 2, p. 443.

El-Husayni, H. A., Taslim, M. E., and Kercher, D. M., 1994, "An Experimental Investigation of Heat Transfer Coefficients in a Spanwise Rotating Channel With Two Opposite Rib-Roughened Walls," ASME JOURNAL OF TURBOMACHINERY, Vol. 113, pp. 75–82.

Gee, D. L., and Webb, R. L., 1980, "Forced Convection Heat Transfer in Helically Rib-Roughened Tubes," *International Journal of Heat and Mass Transfer,* Vol. 23, pp. 1127–1136.

Han, J. C., Glicksman, L. R., and Rohsenow, W. M., 1978, "An Investigation of Heat Transfer and Friction for Rib Roughened Surfaces," *International Journal of Heat and Mass Transfer,* Vol. 21, pp. 1143–1156.

Han, J. C., 1984, "Heat Transfer and Friction in Channels With Two Opposite Rib-Roughened Walls," ASME *Journal of Heat Transfer,* Vol. 106, No. 4, pp. 774–781.

Han, J. C., Park, J. S., and Lei, C. K., 1985, "Heat Transfer Enhancement in Channels With Turbulence Promoters," ASME *Journal of Engineering for Gas Turbines and Power,* Vol. 107, pp. 628–635.

Han, J. C., Zhang, Y. M., and Lee, C. P., 1992, "Influence of Surface Heat Flux Ratio on Heat Transfer Augmentation in Square Channels With Parallel, Crossed, and V-Shaped Angled Ribs," ASME JOURNAL OF TURBOMACHINERY, Vol. 114, pp. 872–880.

Kline, S. J., and McClintock, F. A., 1953, "Describing Uncertainty in Single-Sample Experiments," *Mechanical Engineering,* ASME, Vol. 75, Jan., pp. 3–8.

Korotky, G. J., and Taslim, M. E., 1998, "Rib Heat Transfer Coefficient Measurements in a Rib-Roughened Square Passage," ASME JOURNAL OF TURBOMACHINERY, Vol. 120, pp. 376–385.

Lengkong, A., 1996, "An Experimental Investigation of Surface-Averaged Rib Heat Transfer Coefficient in a Square Passage Roughened With 45 deg Ribs," M.S. Thesis, Department of Mechanical, Industrial and Manufacturing Engineering, Northeastern University, Boston, MA.

Liou, T. M., Hwang, J. J., and Chen, S. H., 1991, "Turbulent Heat Transfer and Fluid Flow in a Channel With Repeated Rib Pairs," *Proc. ASME/JSME Thermal Eng.,* Vol. 3, pp. 205–212.

Liou, T. M., and Hwang, J. J., 1993, "Effects of Ridge Shapes on Turbulent Heat Transfer and Friction in a Rectangular Channel," *International Journal of Heat and Mass Transfer,* Vol. 36, pp. 931–940.

Lockett, J. F., and Collins, M. W., 1990, "Holographic Interferometry Applied to Rib-Roughness Heat Transfer in Turbulent Flow," *International Journal of Heat and Mass Transfer,* Vol. 33, pp. 2439–2449.

Metzger, D. E., Fan, C. S., and Pennington, J. W., 1983, "Heat Transfer and Flow Friction Characteristics of Very Rough Transverse Ribbed Surfaces With and Without Pin Fins," *Proc. ASME–JSME Thermal Engineering Joint Conference,* Vol. 1, pp. 429–436.

Metzger, D. E., Chyu, M. K., and Bunker, R. S., 1988, "The Contribution of On-Rib Heat Transfer Coefficients to Total Heat Transfer From Rib-Roughened Surfaces," *Transport Phenomena in Rotating Machinery,* J. H. Kim, ed., Hemisphere Publishing Co.

Metzger, D. E., Fan, C. S., and Yu, Y., 1990, "Effects of Rib Angle and Orientation on Local Heat Transfer in Square Channels With Angled Roughness Ribs," *Compact Heat Exchangers: A Festschrift for A. L. London,* Hemisphere Publishing Co., pp. 151–167.

Moody, L. F., 1944, "Friction Factors for Pipe Flow," *Trans. ASME,* Vol. 66, p. 671.

Sato, H., Hishida, K., and Maeda, M., 1992, "Characteristics of Turbulent Flow and Heat Transfer in a Rectangular Channel With Repeated Rib Roughness," *Exp. Heat Transfer,* Vol. 5, pp. 1–16.

Solntsev, V. P., Luzhanskii, B. E,, and Kryukov, V. N., 1973, "An Investigation of Heat Transfer in the Turbulent Separation Zones in the Vicinity of Sudden Steps," *Heat Transfer—Soviet Research,* Vol. 5, No. 2, pp. 122–128.

Taslim, M. E., and Spring, S. D., 1988a, "An Experimental Investigation of Heat Transfer Coefficients and Friction Factors in Passages of Different Aspect Ratio Roughened With 45° Turbulators," *Proc. ASME National Heat Conference,* Houston, TX.

Taslim, M. E., and Spring, S. D., 1988b, "Experimental Heat Transfer and Friction Factors in Turbulated Cooling Passages of Different Aspect Ratios, Where Turbulators are Staggered," Paper No. AIAA-88-3014.

Taslim, M. E., Rahman, A., and Spring, S. D., 1991a, "An Experimental Investigation of Heat Transfer Coefficients in a Spanwise Rotating Channel With Two Opposite Rib-Roughened Walls," ASME JOURNAL OF TURBOMACHINERY, Vol. 113, pp. 75–82.

Taslim, M. E., Bondi, L. A., and Kercher, D. M., 1991b, "An Experimental Investigation of Heat Transfer in an Orthogonally Rotating Channel Roughened With 45° Criss-Cross Ribs on Two Opposite Walls," ASME JOURNAL OF TURBOMACHINERY, Vol. 113, pp. 346–353.

Taslim, M. E., and Spring, S. D., 1994, "Effects of Turbulator Profile and Spacing on Heat Transfer and Friction in a Channel," AIAA *J. Thermophysics and Heat Transfer,* Vol. 8, No. 3, pp. 555–562.

Taslim, M. E., and Wadsworth, C. M., 1997, "An Experimental Investigation of the Rib Surface-Averaged Heat Transfer Coefficient in a Rib-Roughened Square Passage," ASME JOURNAL OF TURBOMACHINERY, Vol. 119, pp. 381–389.

Taslim, M. E., Li, T., and Kercher, D. M., 1996, "Experimental Heat Transfer and Friction in Channels Roughened With Angled, V-Shaped, and Discrete Ribs on Two Opposite Walls," ASME JOURNAL OF TURBOMACHINERY, Vol. 118, pp. 20–28.

Webb, R. L., Eckert, E. R. G., and Goldstein, R. J., 1971, "Heat Transfer and Friction in Tubes With Repeated-Rib-Roughness," *International Journal of Heat and Mass Transfer,* Vol. 14, pp. 601–617.

Effect of Rib Height and Pitch on the Thermal Performance of a Passage Disturbed by Detached Solid Ribs

Tong-Miin Liou

Woei-Jiunn Shuy

Yu-Houe Tsao

Department of Power Mechanical Engineering, National Tsing Hua University, Hsinchu, Taiwan 30043

Laser holographic interferometry and pressure measurements are presented for the effects of rib-to-duct height ratio (H/2B), rib pitch-to-height ratio (Pi/H), and Reynolds number (Re) on the spatially periodic–fully developed turbulent heat transfer and friction in a rectangular duct of width-to-height ratio of 4:1 with an array of ribs detached from one wall at a clearance to rib-height ratio of 0.38. The ranges of H/2B, Pi/H, and Re examined were 0.13 to 0.26, 7 to 13, and 5×10^3 to 5×10^4, respectively. The difference in the H/2B dependence of the thermal performance between the detached and attached solid-rib array is documented. H/2B = 0.17 and Pi/H = 10 are found to provide the best thermal performance for the range of parameters tested. Compact heat transfer and friction correlations are developed. Additionally, it is found that heat transfer augmentation with a detached solid-rib array is superior to with a detached perforated-rib array, and the mechanism responsible for the difference is revealed by the complementary flow visualization results.

Introduction

Spatially periodic flow interruption generated by rib arrays mounted on the walls is an extensively used means for augmentation of heat transfer in many practical applications such as heat exchangers, electronic cooling devices, cooling panels of a scramjet inlet, and turbine blade cooling passages (Burggraf, 1970; Han et al., 1978; Bergles, 1988; Liou and Hwang, 1992; Liou et al., 1992, 1993; Acharya et al., 1993; Chang and Mills, 1993; Taslim and Wadsworth, 1994). To remove the local heat transfer deterioration in the rear concave corners of the attached solid ribs, attached permeable ribs (Hwang and Liou, 1994) and detached solid ribs (Fujita et al., 1978; Marumo et al., 1985; Suzuki et al., 1993a, b; Liou and Wang, 1995; Liou et al., 1995) have been proposed and proved to be effective by researchers. The present study intends to further investigate if the permeable rib array positioned at a small distance from one wall can attain a better thermal performance than the detached solid rib array.

For spatially periodic solid ribs positioned at a small distance from one wall, Kawaguchi et al. (1985) studied the effect of streamwise pitches of circular cylinders arranged in a line on the flat plate heat transfer enhancements using thermocouples. They found that the pitch-to-cylinder diameter ratios (Pi/H) of 12.5 and 25 for the range of $6.25 < Pi/H < \infty$ investigated resulted in the optimum thermal performance. Oyakawa et al. (1986) investigated how the rib shapes (different shapes of band plate) and detached distances affect the heat transfer from the wall in the fully developed region of a rectangular duct with staggered ribs using thermocouples. The band plate with I shape was found to provide best thermal performance and the optimal clearance ratio (C/H = detached distance/rib height) was about 0.3. Karniadakis et al. (1988) performed a numerical study of unsteady two-dimensional flow at Reynolds numbers ranging from 100 to 525 in a plane channel with a detached circular cylinder array. Heat transfer enhancement was attributed to strongly nonparallel finite-amplitude Tollmien–Schlichting waves, which act as effective heat exchangers between the heated wall and bulk fluid. For duct flows with a staggered array of circular cylinders, Yao et al. (1987, 1989) experimentally found that an almost consistently repeatable state was attained thermally and hydrodynamically after the first three cylinders and that an averaged Nusselt number more than three times larger relative to that in the smooth duct flow can be achieved. In addition, the distribution of the thermocouple measured local Nusselt number was found to be similar in shape for the Reynolds number (Re) range of 8×10^3 to 6×10^4.

For the papers quoted above, no data have been reported for turbulent heat transfer and friction in a duct with a detached square-rib array. Liou and Wang (1995) and Liou et al. (1995), therefore, performed such a study using laser holographic interferometry (LHI) in developing and fully developed flow regions, respectively, for $5 \times 10^3 \leqq \mathrm{Re} \leqq 5 \times 10^4$ and $0 \leqq C/H \leqq 1.5$. The significant information they reported is that there exists a critical clearance ratio, $C/H = 0.38$, above which the heat transfer augmentation is mainly achieved by the enhanced forced convection and turbulent transport along the heated wall. Below this ratio, the heat transfer augmentation is attributable to the extended surfaces provided by the square ribs and the approach of the separated shear layer from the rib top toward the heated wall.

For attached permeable rib arrays, Tanasawa et al. (1983) measured the heat transfer coefficients for turbulent flows in a channel with perforated plate arrays mounted on two opposite walls in an in-line fashion by resistance heating method and thermocouple technique. Their results showed that surfaces with perforated plate arrays provided better thermal performance at a constant pumping power than those with slitted plate arrays and fence arrays. Ichimiya and Mitsushiro (1988) studied the heat transfer characteristics in a parallel plate duct with porous rib array mounted on one insulated wall, which is opposite to the heated smooth wall. The mean heat transfer coefficient distribution measured by thermocouple technique was found to be two to four times that of the smooth duct, whereas friction factor measurements showed a decrease to two thirds to one fourth of the solid rib array. Recently, Hwang and Liou (1994,

Contributed by the International Gas Turbine Institute and presented at the 41st International Gas Turbine and Aeroengine Congress and Exhibition, Birmingham, United Kingdom, June 10–13, 1996. Manuscript received at ASME Headquarters February 1996. Paper No. 96-GT-490. Associate Technical Editor: J. N. Shinn.

1995) employed the LHI to investigate the effect of permeable rib arrays in in-line and staggered arrangements on the periodically fully developed turbulent heat transfer in a rectangular channel. The effect of rib open area ratio (β) was examined and a criterion of rib permeability was proposed. In addition, the permeable ribbed geometry provides a higher thermal performance than the solid-type ribbed one, and the best thermal performance occurs as $\beta = 0.44$.

The present paper addresses the following: (1) For duct flows with a detached rectangular-rib array, the effects of rib-to-duct height ratio (or rib height to duct hydraulic diameter ratio) and rib pitch-to-height ratio on the thermal performance of solid-type ribs have not been explored in the past and are, therefore, examined in the present paper. (2) The difference in the heat transfer characteristics between the detached solid-type and perforated rib array has also not been studied in open literature and thus is investigated in the present study. The fluid dynamic mechanism responsible for the difference will be revealed through flow visualization. (3) There is lacking of semi-empirical correlations of spatially periodic heat transfer and friction in terms of rib-to-duct height ratio, rib pitch-to-height ratio, and Reynolds number for a rectangular duct disturbed by an array of detached rectangular solid-type ribs. Such correlations are developed in the present work and may be helpful for the design of compact heat exchangers or cooling panels used in a scramjet inlet.

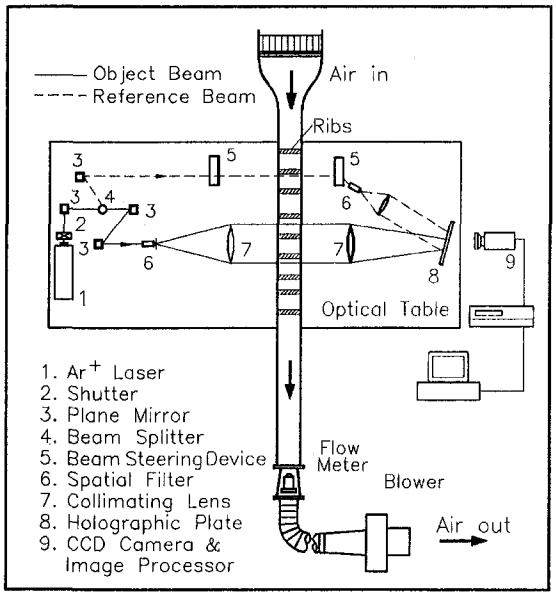

Fig. 1 Schematic drawing of overall test system

Test Facility and Conditions

Flow System. An open-loop airflow circuit was adopted as the flow system, as shown schematically in Fig. 1. The airflow was drawn from a temperature-controlled room into the test section through a settling chamber and a nozzlelike contraction to provide a fairly uniform flow with turbulence intensity less than 1 percent in the test section inlet. The uniformity of the flow and turbulence level were checked by LDV measurements (Liou et al., 1993). After traversing the test section, air flowed through a flow straightener and a flowmeter, and was then exhausted by a 3 hp centrifugal blower.

Flow Field Temperature Measurement. The optical setup of the real-time LHI in the present work is depicted in Fig. 1 and is similar to that described in Liou et al. (1995). Please refer to this earlier paper for more detail. A 3-W argon-ion laser with 514.5 nm (green) line provided the coherent light source. A module consisted of a holographic film plate holder and a liquid gate was used to attain in-place development of the film plate as required for real-time holographic interferometry. The photographic emulsion 8E56, made by Agfa-Gevaert Ltd., was found to be a suitable recording material for combining a good compromise between light sensitivity and resolution. The instantaneous interference field was digitized by a CCD camera, which allows 512 pixel resolution with 256 gray levels per pixel, and recorded on a VHS videocassette recorder for storage and further image processing.

Test Section. Figure 2 depicts the coordinate system, construction, and dimension of the test section. The test duct was 1150 mm long and had a rectangular cross section of 160 mm by 40 mm (YZ plane). The solid-type or perforated aluminum rectangular ribs of 5.2 mm in width were positioned at a distance C from the bottom wall and at an angle-of-attack of 90 deg. Thermofoils of thickness 0.18 mm conducted heat to the top and bottom walls (stainless-steel sheet, 0.3 mm in thickness) were adhered uniformly between the stainless steel plates and 30-mm-thick Bakelite plates and could be controlled electrically

Nomenclature

A = half-width of channel
B = half-height of channel
C = clearance between rib and wall
c_p = specific heat at constant pressure
De = hydraulic diameter $= 4B/(1 + B/A)$
f = Darcy friction factor
H = rib height
h = heat transfer coefficient
k_f = air conductivity
m = mass flow rate
n = number of rib perforations
Nu = local Nusselt number
$\overline{\mathrm{Nu}}$ = average Nusselt number
$\overline{\mathrm{Nu}}_p$ = average Nusselt number in a rib pitch
$\overline{\mathrm{Nu}}_s$ = average Nusselt number for smooth duct (at same mass flow rate)
$\overline{\mathrm{Nu}}_s^*$ = average Nusselt number for smooth duct (at same pumping power)
P = pressure
Pi = rib pitch
Pr = Prandtl number
Q = quantity of heat given to air from duct entrance to considered cross section
q_{conv} = local convective heat transfer flux from wall
Re = Reynolds number
T = temperature of air
T_b = local bulk mean temperature of air
T_{in} = air temperature at duct inlet (i.e., room temperature)
T_w = local wall temperature
$\overline{T}_b$ = average bulk mean temperature of air
$\overline{T}_w$ = average wall temperature
U = axial mean velocity
W = rib width
X = axial coordinate ($X = 0$ at inlet reference, Fig. 2)
X_N = axial coordinate ($X = 0$ at rib rear edge, Fig. 2)
Y = transverse coordinate, Fig. 2
Z = spanwise coordinate, Fig. 2
β = open-area ratio of perforated rib $= (n\pi\phi^2)/(2AH)$
ϕ = radius of perforation
λ = wavelength of laser beam
ρ = air density

Subscripts

N = rib index
r = reference
w = wall

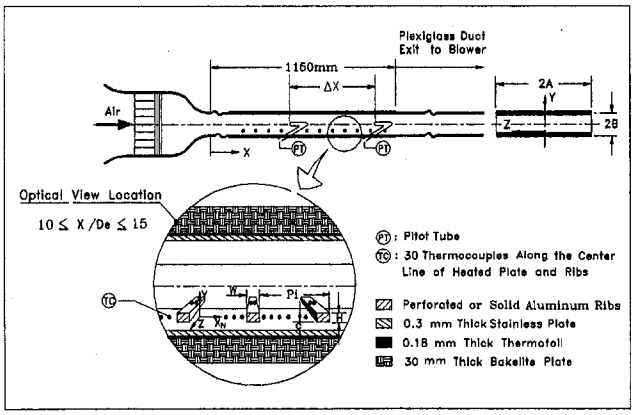

Fig. 2 Coordinate system, construction, and dimension of test duct

by a 60 W d.c. power supply. The Bakelite plates were used to prevent heat loss from the back sides of the heated stainless plates. A thin layer of glue (0.13 mm thick or less) served at each of the above-mentioned interfaces to ensure good contact. The thermal resistance of the glue may be neglected (less than 1 percent). The side walls of the entire heated test duct were made of plexiglass plates to provide optical access for LHI measurements. The construction of the detached-ribbed wall is displayed in detail in Fig. 2.

Wall Temperature and Centerline Pressure Measurement. As shown in Fig. 2, the interferograms were taken at the region of $10 \le X/De \le 15$. The region of optical view was instrumented with 30 copper-constantan thermocouples along the centerline ($Z = 0$) of the heated bottom wall for wall temperature measurements. The junction beads (0.15 mm in diameter) were carefully embedded into the wall, and then ground flat to ensure that they were flush with surfaces. The wall temperature signals were transferred to a Yokogawa DA-2500 hybrid recorder, and then sent to a PC-AT for data storage and further processing. Two Pitot tubes inserted from the side wall at $X/De = 9.8$ and 13.1 were used to measure the centerline static pressure drop for the spatially periodic regions.

Test Conditions. The clearance between the detached ribs and bottom wall is fixed at $C/H = 0.38$ since the previous study indicated the maximum heat transfer and thermal performance enhancement attained by the solid-type ribs at this C/H value (Liou et al., 1995). The parameters investigated include the rib height to duct hydraulic diameter ($De = 64$ mm) ratio, $H/De = 0.081$, 0.106, and 0.162 (or rib-to-duct height ratio, $H/2B = 0.13$, 0.17, and 0.26), rib pitch-to-height ratio, $Pi/H = 7$, 10, and 13, and Reynolds number (based on the hydraulic diameter and cross-sectional bulk mean velocity of the ribbed duct) from 5×10^3 to 5×10^4. Since the present study is interesting in periodic fully developed heat and friction characteristics in ribbed ducts, the temperature and pressure drop data are taken in the range $10 \le X/De \le 15$ and $9.8 \le X/De \le 13.1$, respectively. The spatially hydrodynamic and thermal periodicity in these regions has been verified in our previous work (Liou et al., 1995; Liou and Wang, 1995), and thus is not elaborated on in the present work.

Since LHI is based on the integral of the change in spanwise refractive index, the two dimensionality of spanwise temperature profile of the flow field is examined by the thermocouple probing. Figure 3 shows an example of wall temperature distribution in the Z direction at various Reynolds numbers. The scatter in spanwise direction is typically less than 5.7 percent of the duct spanwise average temperature. Another source of error results from the presence of density gradients normal to light beam. By using the interferometry error analysis suggested in Goldstein (1976), the resulting errors in the fringe (or temperature) shift due to the end effect associated with deviation from two dimensionality and refraction effect associated with normal density gradient are 8 and 4.2 percent, respectively.

Data Analysis. The temperature field can be obtained from LHI interferograms through the following expression for a two-dimensional incompressible flow (Hauf and Grigull, 1970)

$$S_i - S_{i-1} = T_r \cdot \rho_r \cdot G_d \cdot 2A\left(\frac{1}{T_{s_i}} - \frac{1}{T_{s_{i-1}}}\right)\Big/\lambda \qquad (1)$$

where $S_i - S_{i-1}$ is the fringe shift, S_i the fringe order, and G_d the Gladstone–Dale constant.

The local Nusselt number of the heated surface is defined as:

$$\mathrm{Nu} = -(dT/dY)_w \cdot D_e/(T_w - T_b) \qquad (2)$$

where T_w is read from the thermocouple output and T_b is calculated from an energy balance, $T_b = T_{in} + Q/(m \cdot c_p)$ with $Q = \int_0^X [k_f \cdot (dT/dY)_w \cdot 2A] \cdot dX$. The maximum uncertainty of Nu is estimated to be less than 8.1 percent for all examined cases by the uncertainty estimation method of Kline and McClintock (1953).

The average Nusselt number for the spatially periodic region is evaluated as:

$$\overline{\mathrm{Nu}}_p = q_{\mathrm{conv}} \cdot D_e/[k_f \cdot (\bar{T}_w - \bar{T}_b)] \qquad (3)$$

where q_{conv} is estimated by subtracting the heat loss from the supplied electrical input and $\bar{T}_w$ is the average wall temperature along the lower ribbed wall in a pitch module. The maximum uncertainty of $\overline{\mathrm{Nu}}_p$ is estimated to be less than 9.8 percent. The average Nusselt number for fully developed turbulent flow in smooth circular tubes correlated by Dittus and Boelter (1930), $\overline{\mathrm{Nu}}_s = 0.023 \cdot \mathrm{Re}^{0.8} \cdot \mathrm{Pr}^{0.4}$, is used to normalize the local and average Nusselt number in the present study.

The Darcy friction factor of the periodically fully developed flow is expressed as:

$$f = [(-\Delta P/\Delta X) \cdot D_e]/(\rho \cdot U^2/2) \qquad (4)$$

where $\Delta P/\Delta X$ is evaluated by taking the ratio of the pressure difference and the distance of two successive Pitot tubes. A maximum 7.3 percent uncertainty of f is estimated.

Results and Discussion

Local Nusselt Number. The local heat transfer coefficient distribution of the heated wall can be calculated from the whole-field coolant temperature distribution provided by the LHI inter-

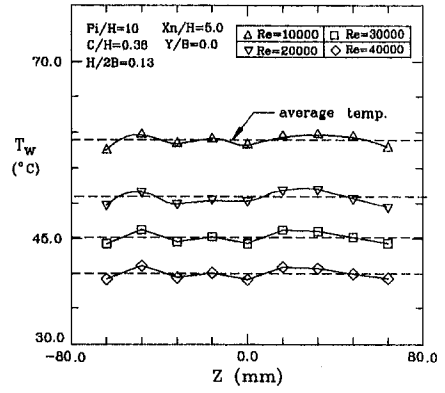

Fig. 3 Spanwise wall temperature distribution at various Reynolds numbers

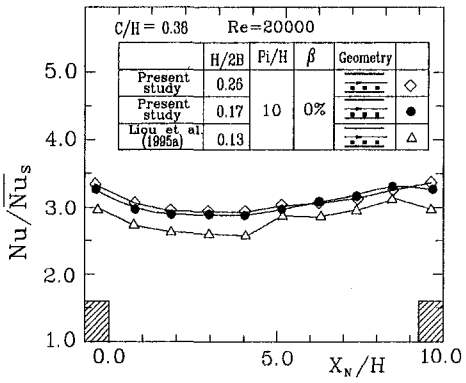

Fig. 4 Distributions of local Nusselt number ratio along the heated wall for different $H/2B$

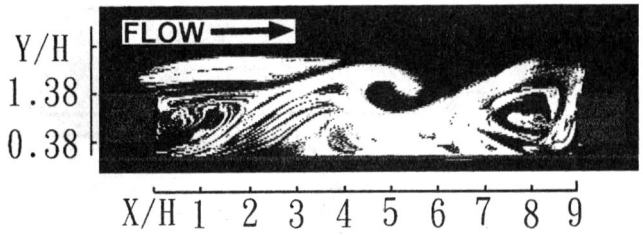

Fig. 6 Flow pattern of smoke-streak visualization for Re = 2300, C/H = 0.38, $H/2B$ = 0.13, Pi/H = 10, and β = 0 percent

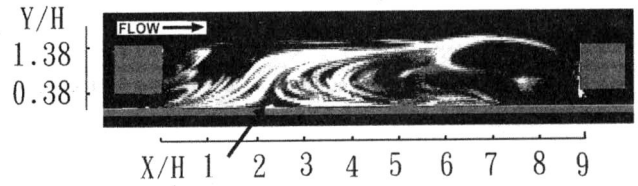

Fig. 7 Flow pattern of smoke-streak visualization for Re = 2300, C/H = 0.38, $H/2B$ = 0.13, Pi/H = 10, and β = 44 percent

ferograms and is shown in Fig. 4 for various $H/2B$ and fixed values of β = 0 percent, C/H = 0.38, Pi/H = 10, and Re = 2×10^4. In general, higher values of $\overline{Nu}/\overline{Nu}_s$ occur at about X_N/H = 8.5 close to the rib's bottom front corner and at the half-rib width $X_N/H = -0.5$ beneath the rib. At these two locations both the temperature gradient and mean velocity gradient are steep due to an approach of the shear layer to the wall by sudden contraction of the flow around the rib's bottom corner and to the enhanced forced convection of the flow's acceleration through the gap. For $H/2B \leqq 0.17$ (or $H/De \leqq 0.106$), the local level of heat transfer enhancement ($\overline{Nu}/\overline{Nu}_s > 1$) generally increases as $H/2B$ increases from 0.13 to 0.17 (or H/De from 0.081 to 0.106). Beyond $H/2B$ = 0.17 the level of $\overline{Nu}/\overline{Nu}_s$ increases only slightly with increasing H/De, with an exception at $6.2 < X_N/H < 9$. This dependence of $\overline{Nu}/\overline{Nu}_s$ on H/De was also found by Sparrow and Tao (1984) for Sherwood number in a duct with attached circular ribs.

For the case of perforated ribs, $H/2B$ = 0.17 and β = 44 percent, Fig. 5 depicts that the level of local Nusselt number ratio along the wall in one pitch module is markedly lower than the corresponding case of solid-type ribs, $H/2B$ = 0.17 and β = 0 percent, especially for the interrib region. The fluid dynamic mechanism responsible for the difference in the local heat transfer distributions between the aforementioned detached solid-type ribs and perforated ribs may be revealed from the complementary flow visualization results shown in Figs. 6 and 7, although the photographs were taken at a lower Reynolds number. Immediately behind the detached ribs with β = 0 percent, Fig. 6 shows the presence of recirculating flow, i.e., wake behind the bluff body. The wake is asymmetric due to the rather different distances between the rib and two opposite walls. The wall jet issuing from the gap between the the rib and bottom wall proceeds downstream and expands upward. Part of wall-jet fluids meets with the fluid stream separated from the rib top rear corner at the wake's rear end. These two fluid streams with different velocities form a shear layer, which rolls up into a vortex and subsequently grows and sheds downstream until the front edge of the next rib. In contrast, for the case of perforated ribs (Fig. 7), a part of the fluid passes through the rib and exits from the rear face of the rib in the form of multijets, as indicated by saw-shaped smoke-streak pattern or interferometric fringes (Fig. 8, taken at Re = 2×10^4) immediately behind the rib. Note that the interferometric fringes represent lines of constant temperature. The wake behind the rib is thus broken up. The multijets behind the rib, the fluid stream separated from the rib top rear corner, and the above-mentioned wall jet form a thicker and complex mixing layer downstream of X/H = 2 to 3. No noticeable roll-up and shedding phenomena were observed during most of the time. Occasionally, the vortex roll-up would occur close to the next rib and thus no enough space for shedding. A distinct difference between Figs. 6 and 7 in the smoke-streak patterns along the rib-top line (Y/H = 1.38) is clearly visible. The presence of vortex shedding for the detached solid-type ribs promotes the mixing of cold core fluids with the hot near-wall fluids and hence leads to a higher level of $\overline{Nu}/\overline{Nu}_s$ distribution, as compared with the perforated-rib case, which lacks of unsteady vortex shedding. On the other hand, the interaction of the multijets behind the perforated ribs contributes a local maximum $\overline{Nu}/\overline{Nu}_s$ at half-rib distance downstream of the rib (X_N/H = 0.5), which is not found for the detached solid-

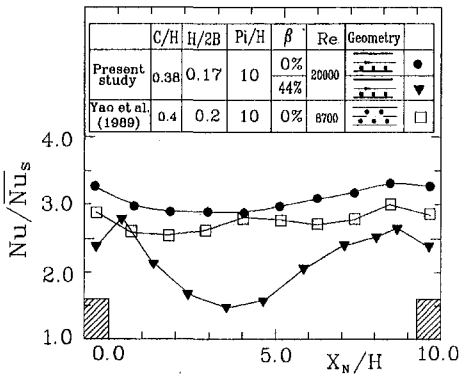

Fig. 5 Comparison of local Nusselt number ratio distributions along the heated wall for different β and geometric arrangements

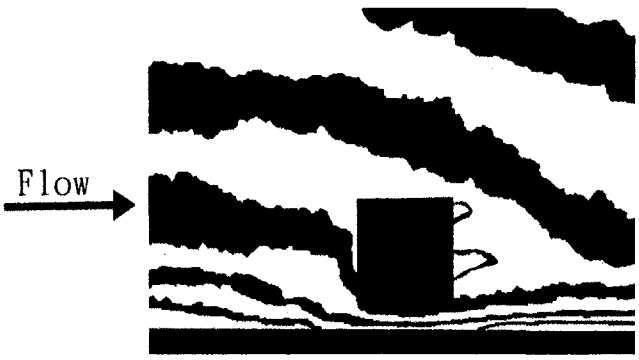

Fig. 8 Example of holographic interferogram for Re = 2×10^4, C/H = 0.38, H/De = 0.081, Pi/H = 10, and β = 44 percent

type ribs; however, the level is not greater than that for solid ribs.

One previous result (Yao et al., 1989) in open literature with closest C/H, $H/2B$, and β but different Reynolds number and geometric arrangement is also shown in Fig. 5 for reference. Both cases of $\beta = 0$ percent generally provide higher levels of $\overline{Nu}/\overline{Nu}_s$ than the case of $\beta = 44$ percent for the reason given above. The differences between the present result of $\beta = 0$ percent and the data of Yao et al. are mainly due to different Re, rib shape (rectangular versus circular), rib arrangement (one-side-roughened duct versus a staggered arrangement), and duct width-to-height ratio (4:1 for the present work versus 8:1 for the work of Yao et al. (1989)).

Average Nusselt Number and Friction Factor. The average Nusselt number ratio for the detached solid-type ribbed duct flows with three values of $H/2B$ is plotted in Fig. 9(a) as a function of Reynolds number. It is seen that the average heat transfer coefficient ratio $\overline{Nu}_p/\overline{Nu}_s$ is weakly affected by the rib-to-duct height ratio $H/2B$. The $H/2B = 0.17$ case attains a slightly higher $\overline{Nu}_p/\overline{Nu}_s$ for most of the Re range tested. This trend for the duct flows with detached solid-type ribs (H/De = 0.081, 0.106, and 0.162; $C/H = 0.38$) is different from that observed for the duct flows with attached solid-type ribs. Han (1984; H/De = 0.021, 0.042, and 0.063; in-line ribs), Liou and Hwang (1992; H/De = 0.063, 0.081, and 0.106; in-line ribs), and Taslim and Wadsworth (1997; H/De = 0.133, 0.167, and 0.25; staggered ribs) reported that both the average friction factor (Fig. 9(b)) and Stanton number or Nusselt number (Fig. 9(b)) increase with increasing H/De for attached solid-type ribbed duct flows ($C/H = 0$ and $Pi/H = 10$). For $C/H = 0$ the increase of $\overline{Nu}_p$ with increasing rib height is due to the increased rib heat transfer surface area, turbulence intensity, and flow acceleration through the in-line rib contraction or additionally due to increased diversion of flow towards ribs on the opposite wall for staggered ribs. In contrast, for $C/H = 0.38$ of the present case our previous study (Liou et al., 1995) indicated that the heat transfer from the rib surface to the core fluid was insignificant and the forced convection enhancement in the gap between the rib base and the heated wall as well as turbulent transport enhancement played the main role for the overall heat transfer augmentation. Consequently, for $C/H = 0.38$, the increasing rib height does not effectively lead to increased rib heat transfer surface area. Moreover, as rib height H is increased, the overall blockage increases to accelerate flow through the gap; nevertheless, the gap C also increases to offset the acceleration since the ratio $C/H = 0.38$ is fixed. In other words, because the ratio $C/H = 0.38$ is fixed, the increasing rib height does not effectively enhance the flow acceleration through the gap. The increasing rib height does promote turbulence; however, it also results in larger amount of lower speed wake fluids. It is these factors responsible for the weak dependence of $\overline{Nu}_p/\overline{Nu}_s$ on $H/2B$ for the present case of $C/H = 0.38$. With the values presented in Fig. 9(a) the dependence of the average Nusselt number on the rib height and Reynolds number for the duct flows with detached solid-type ribs can be further correlated by an equation of the form

$$\overline{Nu}_p/\overline{Nu}_s = 1 + 22.16 \cdot Re^{-0.23} \cdot (H/2B)^{0.05} \quad (5 \times 10^3 \le Re \le 5 \times 10^4) \quad (5)$$

where the constants are obtained by curve fitting, based on a least-squares method through the measured data. The average deviations of the experimental data from this equation are ±2.4, 1.1, and 1.8 percent for $H/2B$ = 0.13, 0.17, and 0.26, respectively.

For the same reason discussed in the section of local heat transfer coefficient, Fig. 9(a) shows that the corresponding case for the detached perforated ribs ($\beta = 44$ percent) gives rise to a significant lower $\overline{Nu}_p/\overline{Nu}_s$ enhancement, as compared with the detached solid-type ribs. Quantitatively, the level of heat transfer augmentation of the detached perforated and solid-type ribbed duct over the smooth one is approximately 0.75–1.75 and 1.60–2.75 times $\overline{Nu}_s$, respectively, for the test range of Re and $H/2B = 0.17$, as depicted in Fig. 9(a).

Because the ribs disturb the core flow significantly, the rib-type heat transfer augmentor also increases the friction loss. Figure 9(a) also shows the Reynolds number dependence of average friction factor for periodic fully developed duct flows with three rib-to-duct height ratios. All the curves depict a decrease of f with increasing Re, an increase of f with increasing rib height, and a decrease of f with increasing β for the range of parameters tested. It may be interesting to point out that while trend of heat transfer with rib height differs for attached and detached solid ribs, the friction factor trend remains the same (Figs. 9(a, b)). Quantitatively, Fig. 9(a) indicates that for $H/2B = 0.17$ the detached solid-type ribs increase the friction loss approximately 5.7–6.6 and 1.4–1.7 times over those of the smooth wall case and the detached perforated-rib case, respectively, for the test ranges of C/H, Pi/H, and Re. The effects of the Reynolds number ($5 \times 10^3 \le Re \le 5 \times 10^4$) and the solid-rib height on the average friction factor for the present test conditions can be correlated by the following expression:

$$f = 10.23 \cdot Re^{-0.33} \cdot (H/2B)^{0.49} \quad (6)$$

The average deviations of the measured data from the correlation are ±2.8, 12.0, and 3.6 percent for $H/2B$ = 0.13, 0.17, and 0.26, respectively.

Thermal Performance. As addressed in Introduction, the effect of $H/2B$ on the thermal performance of a duct flow with detached rectangular solid ribs has not been studied in the past. Figure 10 allows such a study by comparing the average heat transfer coefficient for a duct with detached solid ribs of various heights with that for a smooth duct at a constant pumping power which is proportional to $f^{1/3} \cdot Re$. In Fig. 10 $\overline{Nu}_s^*$ is the average Nusselt number for a smooth duct with the flow rate at which the pumping power is the same as that obtained in the ribbed duct and its correlation had been described in detail by Liou and Hwang (1992). The improvement in $\overline{Nu}_p$ of the duct with detached solid ribs is significant and approximately 1.8 to 2.1 times that of $\overline{Nu}_s^*$ for the ranges of Reynolds number and rib height investigated. Among the rib heights studied, $H/2B$ = 0.17 provides the best thermal performance at a constant pumping power.

For a duct with attached ($C/H = 0$) perforated ($\beta \neq 0$) ribs on two opposite walls, Hwang and Liou (1994) reported that ribs with open-area ratio $\beta = 44$ percent gave the best thermal performance among the β range investigated. It is interesting to find out whether the detached perforated rib array can perform better than the detached solid rib array. An additional measurement for a duct with a perforated rib array ($H/2B = 0.17$) detached a distance of $C/H = 0.38$ from one wall was therefore performed and the result is also included in Fig. 10 for comparison. It is seen that $\overline{Nu}_p/\overline{Nu}_s^*$ performance enhancement for a detached perforated ribbed duct is less pronounced and decreases with increasing pumping power at a faster rate (from 1.9 to 1.3 times that of $\overline{Nu}_s^*$) than that (from 2.1 to 1.8 times that of $\overline{Nu}_s^*$) for a detached solid-type ribbed duct. Moreover, the detached solid-type rib array with $H/2B = 0.17$ achieves the best thermal performance among the $H/2B$ range examined.

Effect of Rib Pitch. For spatially periodic duct flows with attached solid-type ribs in an in-line arrangement, the effect of rib pitch was investigated by Han (1984) for Pi/H = 10, 20, and 40 and by Liou and Hwang (1992a) for Pi/H = 10, 15, and 20. Both works reported a decrease of average Stanton number or Nusselt number and friction factor with increasing Pi/H for H/De = 0.021–0.106. Taslim and Wadsworth (1997)

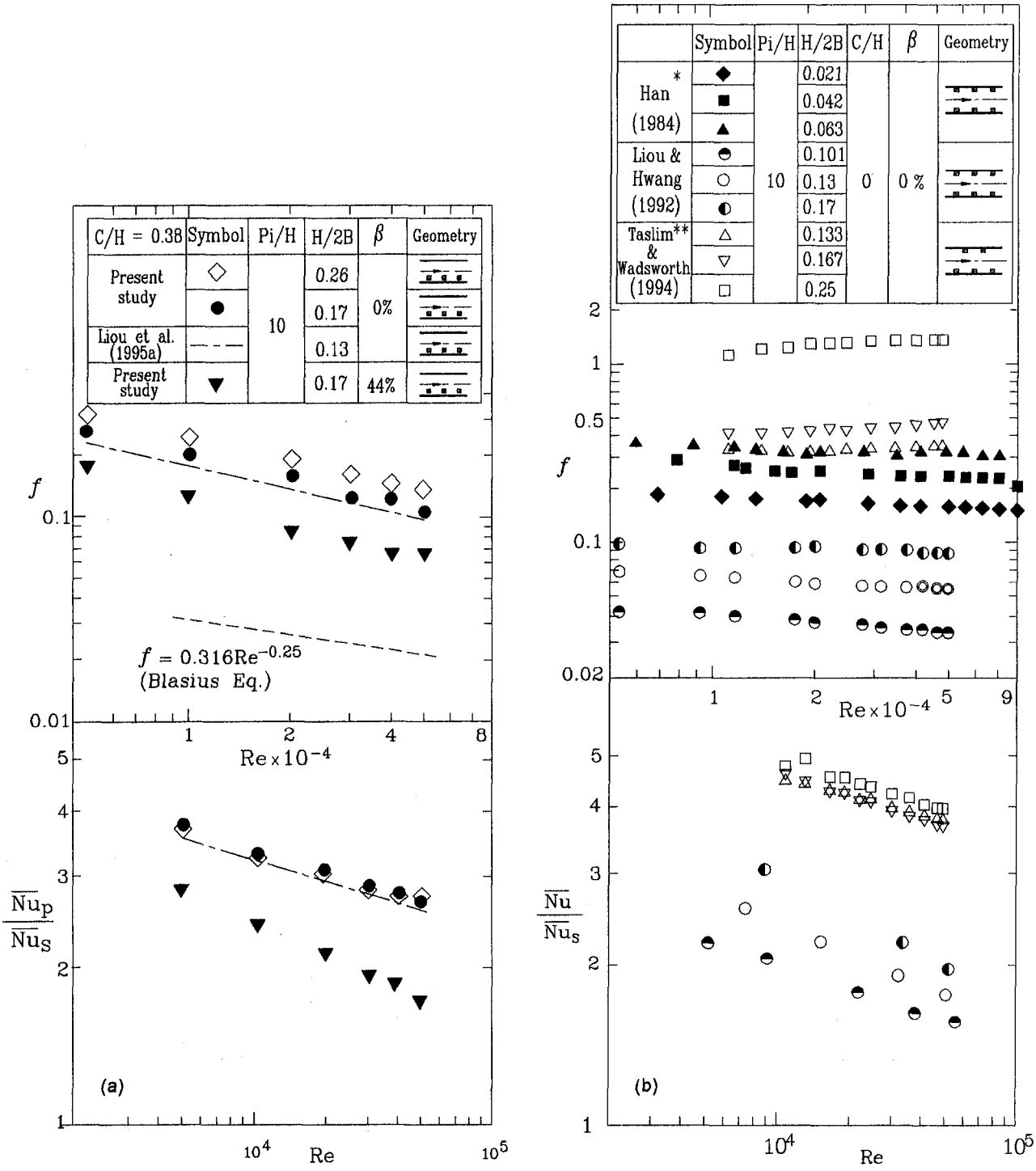

Fig. 9 Average Nusselt number ratio and friction factor versus Reynolds number: (*a*) comparison between authors' works; (*b*) comparison between works of various researchers (* ribs mounted on four walls; ** all acrylic ribs but one copper rib)

performed a similar study with ribs in a staggered arrangement, a pitch range of $Pi/H \leqq 10$ (or 5, 8.5, and 10), and $H/De = 0.133–0.25$. They found that $Pi/H = 8.5$ produced higher heat transfer coefficient, $Pi/H = 10$ had the highest thermal performance at a constant pumping power for $H/De = 0.133$, and thermal performance of higher H/De did not change significantly with Pi/H. From the results of $Pi/H \leqq 10$ and $Pi/H \geqq 10$ reported in the past, a rib pitch-to-height ratio of 10 seems to be an appropriate choice for heat transfer enhancement in a duct flow with attached solid-type rectangular ribs. It is now interesting to know whether a similar conclusion can be obtained for the present detached solid-type rectangular ribs. Figures 11 and 12 depict the average Nusselt number ratio and friction factor versus Reynolds number, respectively, for the detached solid-type ribs with $Pi/H = 7$, 10, and 13. Both figures show that $\overline{Nu}_p/\overline{Nu}_s$ and f decrease with increasing Pi/H, a result similar to that reported by Han (1984) and Liou and Hwang (1992) for the attached solid-type ribs. Owing to the opposite effect of Pi/H on the $\overline{Nu}_p/\overline{Nu}_s$ augmentation and f reduction, a thermal performance analysis at a constant pumping power is worthwhile and the result is plotted in Fig. 13. It appears that the moderate value of $Pi/H = 10$ gives a slightly

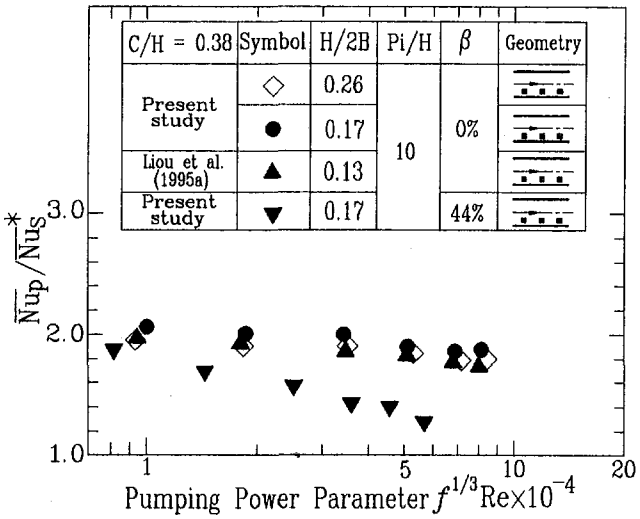

Fig. 10 Thermal performance comparison at a constant pumping power

better thermal performance at a constant pumping power among the Pi/H explored.

Semi-empirical correlations for the dependence of average Nusselt number and friction factor can be obtained from Figs. 11 and 12 and expressed by the following forms

$$\overline{Nu}_p/\overline{Nu}_s = 1 + 2.89 \cdot Re^{-0.04} \cdot (Pi/H)^{0.01} \quad (7)$$

$$f = 8.43 \cdot Re^{-0.32} \cdot (Pi/H)^{-0.38} \quad (8)$$

The maximum deviations of the measured data from Eqs. (7) and (8) are within 5.4 and 4.5 percent, respectively.

Conclusions

Laser holographic interferometry and pressure measurements of spatially periodic–fully developed turbulent fluid flow under the conditions examined in the present paper indicate that for a rectangular rib array detached from one wall, the duct flow with solid-type ribs attains a higher thermal performance than the duct flow with perforated ribs. The complementary flow visualization further reveals that the main controlling mechanism for this trend is the presence and absence of vortex shedding in the interrib region for the former and latter cases, respectively. Among the three rib heights investigated the detached solid-rib array with $H/2B = 0.17$ (or $H/De = 0.106$) provides the best thermal performance at both constant pumping power and constant flow rate. This present result of the detached solid rib array is different from that of the attached solid rib array for which the thermal performance at a constant flow rate (i.e., average Nusselt number) increases with increasing rib height, as reported in the past for the appropriate range of rib heights. Not benefiting from the effects of extended rib surface area with increasing rib height on the heat transfer augmentation for the detached rib array provides the rationale for this difference.

As for the effect of rib pitch, $Pi/H = 10$ is found to give the highest thermal performance at a constant pumping power among the three rib pitches examined. Moreover, compact correlations of the friction and average heat transfer coefficients for duct flows with a detached solid-rib array are obtained for

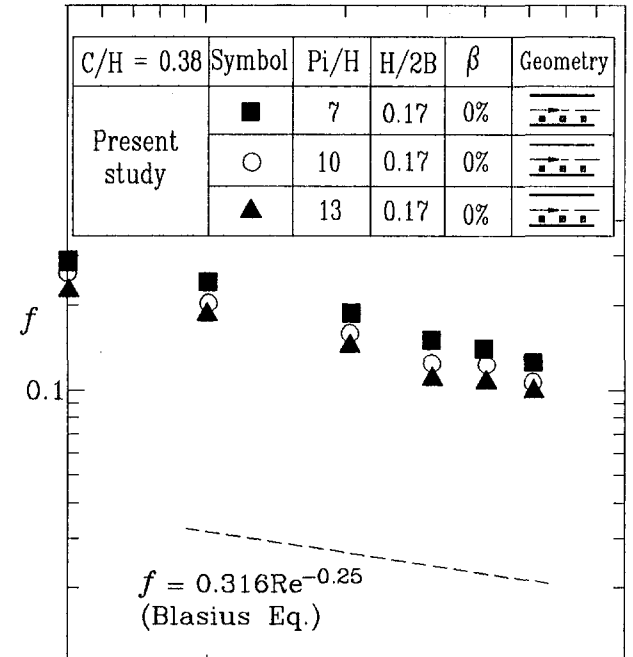

Fig. 12 Average friction factor versus Reynolds number for $H/2B = 0.17$

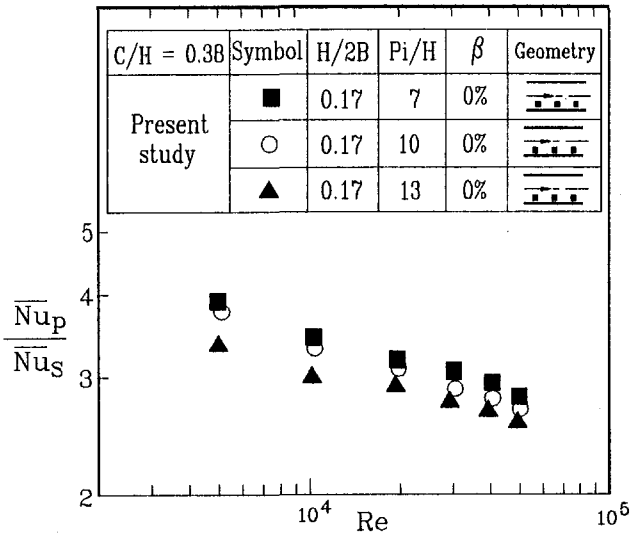

Fig. 11 Average Nusselt number ratio versus Reynolds number for $H/2B = 0.17$

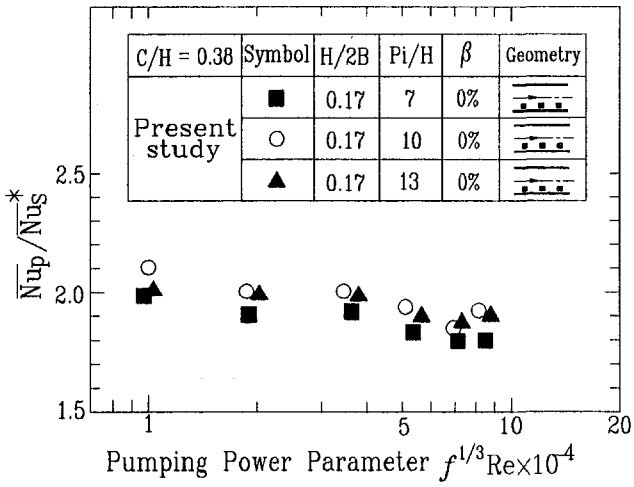

Fig. 13 Thermal performance comparison at a constant pumping power for $H/2B = 0.17$

the first time. For the duct flow with a detached solid rib array of $H/De = 0.106$ and $Pi/H = 10$ the thermal performance at a constant flow rate and a constant pumping power over the smooth duct flow can attain values as high as 160 to 275 percent and 90 to 110 percent, respectively, for the range of Reynolds number tested.

Acknowledgments

Support for this work was provided by the National Science Council of the Republic of China under contract No. NSC82-0401-E007-289.

References

Acharya, S., Dutta, S., Myrum, T. A., and Baker, R. S., 1993, "Periodically Developed Flow and Heat Transfer in a Ribbed Duct," *International Journal of Heat and Mass Transfer,* Vol. 36, No. 8, pp. 2069–2082.

Burggraf, F., 1970, "Experimental Heat Transfer and Pressure Drop With Two-Dimensional Discrete Turbulence Promoters Applied to Two Opposite Walls of a Square Tube," *Augmentation of Convective Heat and Mass Transfer,* E. E. Bergles and R. L. Webb, eds., ASME, New York, pp. 70–79.

Bergles, A. E., 1988, "Some Perspectives on Enhanced Heat Transfer-Second-Generation Heat Transfer Technology," ASME *Journal of Heat Transfer,* Vol. 110, pp. 1082–1096.

Chang, B. H., and Mills, A. F., 1993, "Turbulent Flow in a Channel With Transverse Rib Heat Transfer Augmentation," *International Journal of Heat and Mass Transfer,* Vol. 36, No. 6, pp. 1159–1169.

Dittus, F. W., and Boelter, L. M. K., 1930, *Publications on Engineering,* Vol. 2, University of California at Berkeley, p. 443.

Fujita, H., Takahama, H., and Yamahsita, R., 1978, "Forced Convection Heat Transfer on a Plate With a Cylinder Inserted in the Boundary Layer," *Heat Transfer—Jap. Res.,* Vol. 7, pp. 69–78.

Goldstein, R. J., 1976, "Optical Measurement of Temperature," *Measurements in Heat Transfer,* 2nd ed., Eckert, E. R. G., and Goldstein, R. J., eds., Hemisphere, Washington, DC, pp. 241–294.

Han, J. C., Glicksman, L. R., and Rohsenow, W. M., 1978, "An Investigation of Heat Transfer and Friction of Rib-Roughened Surfaces," *International Journal of Heat and Mass Transfer,* Vol. 21, No. 8, pp. 1143–1156.

Han, J. C., 1984, "Heat Transfer and Friction in Channels With Two Opposite Rib-Roughened Walls," ASME *Journal of Heat Transfer,* Vol. 106, No. 4, pp. 774–781.

Hauf, W., and Grigull, U., 1970, "Optical Methods in Heat Transfer," *Advances in Heat Transfer,* Vol. 6, J. P. Hartnett and T. F. Irvine, Jr., eds., Academic, New York, pp. 133–136.

Hwang, J. J., and Liou, T. M., 1994, "Augmented Heat Transfer in a Rectangular Channel With Permeable Ribs Mounted on the Wall," ASME *Journal of Heat Transfer,* Vol. 116, pp. 912–920.

Hwang, J. J., and Liou, T. M., 1995, "Heat Transfer and Friction in a Rectangular Channel With Perforated Ribs Staggeringly Mounted on Two Opposite Walls," ASME *Journal of Heat Transfer,* Vol. 117, No. 4.

Ichimiya, K., and Mitsushiro, K., 1988, "Enhancement of the Heat Transfer of Wide Temperature Range in a Narrow Passage," *Proc. Experimental Heat Transfer, Fluid Mechanics, and Thermodynamics,* Shah, R. K., Ganic, E. N., and Yang, K. T., eds., Dubrovnik, Yugoslavia, pp. 659–664.

Karniadakis, G. E., Mikic, B. B., and Patera, A. T., 1988, "Minimum Dissipation Transport Enhancement by Flow Destabilization: Reynolds' Analogy Revisited," *Journal of Fluid Mechanics,* Vol. 192, pp. 365–391.

Kawaguchi, Y., Suzuki, K., and Sato, T., 1985, "Heat Transfer Promotion With a Cylinder Array Located Near the Wall," *International Journal of Heat and Fluid Flow,* Vol. 6, No. 4, pp. 249–255.

Kline, S. J., and McClintock, F. A., 1953, "Describing Uncertainties on Single-Sample Experiments," *Mechanical Engineering,* Jan., pp. 3–8.

Liou, T. M., and Hwang, J. J., 1992, "Turbulent Heat Transfer Augmentation and Friction in Periodic Fully Developed Channel Flows," ASME *Journal of Heat Transfer,* Vol. 114, pp. 56–64.

Liou, T. M., Hwang, J. J., and Chen, S. H., 1992, "Turbulent Transport Phenomena in a Channel With Periodic Rib Turbulators," AIAA *Journal of Thermophysics and Heat Transfer,* Vol. 6, No. 3, pp. 513–521.

Liou, T. M., Wu, Y. Y., and Chang, Y., 1993, "LDV Measurements of Periodic Fully Developed Main and Secondary Flows in a Channel With Rib-Disturbed Walls," ASME *Journal of Fluids Engineering,* Vol. 115, pp. 109–114.

Liou, T. M., Wang, W. B., and Chang, Y. J., 1995, "Holographic Interferometry Study of Spatially Periodic Heat Transfer in a Channel With Ribs Detached From One Wall," ASME *Journal of Heat Transfer,* Vol. 117, pp. 32–39.

Liou, T. M., and Wang, W. B., 1995, "Laser Holographic Interferometry Study of Developing Heat Transfer in a Duct With a Detached Rib Array," *International Journal of Heat and Mass Transfer,* Vol. 38, No. 1, pp. 91–100.

Marumo, E., Suzuki, K., and Sato, T., 1985, "Turbulent Heat Transfer in a Flat Plate Boundary Layer Disturbed by a Cylinder," *International Journal of Heat and Fluid Flow,* Vol. 6, No. 4, pp. 241–248.

Oyakawa, K., Shinzato, T., and Mabuchi, I., 1986, "Effect on Heat Transfer Augmentation of Some Geometric Shapes of a Turbulence Promoter in a Rectangular Duct," *Bulletin of JSME,* Vol. 29, No. 256, pp. 3415–3420.

Sparrow, E. M., and Tao, W. O., 1984, "Symmetric Versus Asymmetric Periodic Disturbance at the Walls of a Heated Flow Passage," *International Journal of Heat and Mass Transfer,* Vol. 27, pp. 2133–2144.

Suzuki, H., Inoue, Y., Nishimura, T., Fukutani, K., and Suzuki, K., 1993a, "Unsteady Flow in a Channel Obstructed by a Square Rod (Crisscross Motion of Vortex)," *International Journal of Heat and Fluid Flow,* Vol. 14, pp. 2–9.

Suzuki, H., Fukutani, K., Takishita, T., and Suzuki, K., 1993b, "Flow and Heat Transfer Characteristics in a Channel Obstructed by a Square Rod Mounted in Asymmetric Positions," *Proc. 6th International Symposium on Transport Phenomena in Thermal Engineering,* Seoul, Korea, pp. 353–358.

Tanasawa, T., Nishio, S., Takano, K., and Tado, M., 1983, "Enhancement of Forced Convection Heat Transfer in a Rectangular Channel Using Turbulence Promoters," *Proc. ASME–JSME Thermal Engineering Joint Conference,* pp. 395–402.

Taslim, M. E., and Wadsworth, C. M., 1997, "An Experimental Investigation of the Rib Surface-Average Heat Transfer Coefficient in a Rib-Roughened Square Passage," ASME JOURNAL OF TURBOMACHINERY, Vol. 119, pp. 381–389.

Yao, M., Nakatani, M., and Suzuki, K., 1987, "An Experimental Study on Pressure Drop and Heat Transfer in a Duct With a Staggered Array of Cylinders," *Proc. ASME–JSME Thermal Engineering Joint Conference,* by Marto, P. J., and Tanasawa, I., eds., Vol. 5, pp. 189–196.

Yao, M., Nakatani, M., and Suzuki, K., 1989, "Flow Visualization and Heat Transfer Experiments in a Duct With a Staggered Array of Cylinders," *Experimental Thermal and Fluid Science,* Vol. 2, pp. 193–200.

Heat Transfer in a Two-Pass Internally Ribbed Turbine Blade Coolant Channel With Cylindrical Vortex Generators

R. G. Hibbs

S. Acharya[1]

Y. Chen

D. E. Nikitopoulos

T. A. Myrum

Mechanical Engineering Department,
Louisiana State University,
Baton Rouge, LA 70803

The effect of vortex generators on the mass (heat) transfer from the ribbed passage of a two-pass turbine blade coolant channel is investigated with the intent of optimizing the vortex generator geometry so that significant enhancements in mass/heat transfer can be achieved. In the experimental configuration considered, ribs are mounted on two opposite walls; all four walls along each pass are active and have mass transfer from their surfaces but the ribs are nonparticipating. Mass transfer measurements, in the form of Sherwood number ratios, are made along the centerline and in selected interrib modules. Results are presented for Reynolds number in the range of 5000 to 40,000, pitch to rib height ratios of 10.5 and 21, and vortex generator-rib spacing to rib height ratios of 0.55 and 1.5. Centerline and spanwise-averaged Sherwood number ratios are presented along with contours of the Sherwood number ratios. Results indicate that the vortex generators lead to substantial increases in the local mass transfer rates, particularly along the side walls, and modest increases in the average mass transfer rates. The vortex generators have the effect of making the interrib profiles along the ribbed walls more uniform. Along the side walls, vortices that characterize the vortex generator wake are associated with significant mass transfer enhancements. The wake effects and the levels of enhancement decrease somewhat with increasing Reynolds number and decreasing pitch.

Introduction

Since the power output of a gas turbine engine depends on the turbine inlet temperature, one of the primary goals in the development of advanced turbine systems is to explore more effective methods of heat removal from the turbine blades. This paper deals with the flow and heat transfer in the internally ribbed coolant channels of a gas turbine blade and aims to examine heat transfer enhancement brought about by placing vortex generators above the ribs in the coolant passages. This expected enhancement is based on observations made in flow past ribs (Acharya et al., 1991) in which it was shown that the separated shear layer behind the rib was characterized by large-scale vortical structures, and that these structures could be manipulated by introducing an external perturbation into the flow in order to promote mixing behind the rib. Greater mixing and shear layer growth behind the ribs is expected to lead to enhancement in surface heat transfer. In this paper the vortex street behind a cylindrical vortex generator mounted above the rib will be used as the external perturbation, and its effect on the heat transfer from the ribbed surface will be examined. The long-term goal of the study is to examine the heat transfer behavior for this geometry under rotating conditions. However, in this paper, only stationary coolant channel results are reported.

Numerous experimental investigations reporting the local and average heat transfer behavior in ribbed channels are available in the literature (e.g., Sparrow and Tao, 1983; Han and Zhang, 1991; Acharya et al., 1993, 1995a, b). In general, these studies consistently report significant heat transfer enhancement due to the ribs, with peak heat transfer values in the vicinity of reattachment and just upstream of the rib. A number of studies have also reported flow measurements in ribbed channels in order to explain the observed heat transfer behavior. Humphrey and Whitelaw (1979) have shown that the ribs induce a strong generation of turbulent kinetic energy as well as gradients in Reynolds stresses, which result in a normal-stress-driven secondary flow. Developing flow characteristics in a ribbed duct show that the interaction of shear layers formed by consecutive ribs results in an increase in turbulent kinetic energy (Liou et al., 1990). Karniadakis et al. (1988) performed a numerical study, and using the Reynold's analogy of momentum and heat transfer, showed that heat transfer rate increases with flow instability. Acharya et al. (1994) have reported measurements of velocity and heat transfer past a surface mounted rib, and have shown the correlation between the surface heat transfer and near-wall turbulence levels.

In recent years, more effective heat removal techniques have been explored. A half-delta-wing geometry has been shown to generate longitudinal vortices embedded in the boundary layer in such a way that heat transfer dominates over momentum transfer (Wroblewski and Eibeck, 1991). With this vortex generator geometry, it was shown that the maximum heat transfer occurred at low Reynolds numbers (Garimella and Eibeck, 1991). A small fencelike geometry placed opposite a ribbed wall was shown to reduce the occurrence of local hot spots in the fully developed region by inducing a more uniform heat transfer distribution (Hung and Lin, 1992). A cylindrical vortex generator placed above and parallel to the ribs in a duct has been shown to increase heat transfer significantly at low Reynolds numbers (Myrum et al., 1992). Further investigations with the cylindrical vortex generators have shown that the local streamwise distributions of heat transfer are more uniform, but are

[1]Corresponding author.

Contributed by the International Gas Turbine Institute and presented at the 41st International Gas Turbine and Aeroengine Congress and Exhibition, Birmingham, United Kingdom, June 10–13, 1996. Manuscript received at ASME Headquarters February 1996. Paper No. 96-GT-474. Associate Technical Editor: J. N. Shinn.

restricted to the interrib region immediately downstream of the generator (Myrum et al., 1993). A later, more extensive study of the effects of cylindrical vortex generators has shown that heat transfer enhancement can be attributed to the enhancement of near-wall turbulence (Myrum et al., 1996). It is believed that this increased turbulence is the result of the interaction of the wake downstream of the cylinder and the separated shear layer downstream of the rib (Myrum and Acharya, 1994).

The above-mentioned studies of Acharya, Myrum, and coworkers with cylindrical vortex generators have shown significant heat transfer enhancement at low Reynolds numbers. These studies have, however, been performed in a two-dimensional rectangular geometry. The present investigation will study the effect of this vortex generator geometry in a square-sectioned, ribbed duct over a range of Reynolds numbers. This geometry is more representative of a gas turbine coolant channel. The flow is three dimensional with secondary flows expected to have some effect on the flow structure. To the authors' knowledge, no studies on the effect of cylindrical vortex generators in a square-sectioned duct have been made.

Experiments

The experiments are performed in a test apparatus designed for the study of mass transfer (sublimation of naphthalene) in a rotating duct that simulates the coolant channels of a turbine blade. Mass transfer measurements permit the acquisition of detailed local distributions of the Sherwood number, which can then be converted to Nusselt numbers using the heat–mass transfer analogy.

Apparatus. An overall schematic of the experimental setup is shown in Fig. 1. Compressed air is used as the working fluid for all experiments in order to simulate the operational parameters in a turbine engine more closely. The air is taken from large, exterior reservoirs in order to minimize flow disturbances caused by the compressor. A concentric bore orifice plate is used to measure the mass flow rate in the meter run. A regulator is used to maintain a constant supply pressure in the meter run. Test section and meter run pressures are measured using mechanical pressure gages that have a 2.5 psi (17.2 kPa) resolution, and are controlled independently with gate valves located downstream of both the meter run and test section. Naphthalene-laden exhaust air is directed through flexible tubing to a fume hood.

The aluminum alloy test section consists of a 2.75 in. (69.85 mm) tapered settling chamber; a frame that supports eight removable wall frames; and a removable 180 deg bend. These major components are secured in a flange-like manner, using O-rings between all parts to prevent air leakage. When assembled, the test section forms 1 × 1 × 12 in. (25.4 × 25.4 × 304.8 mm) long inlet and outlet sections 1.5 in. (38.1 mm)

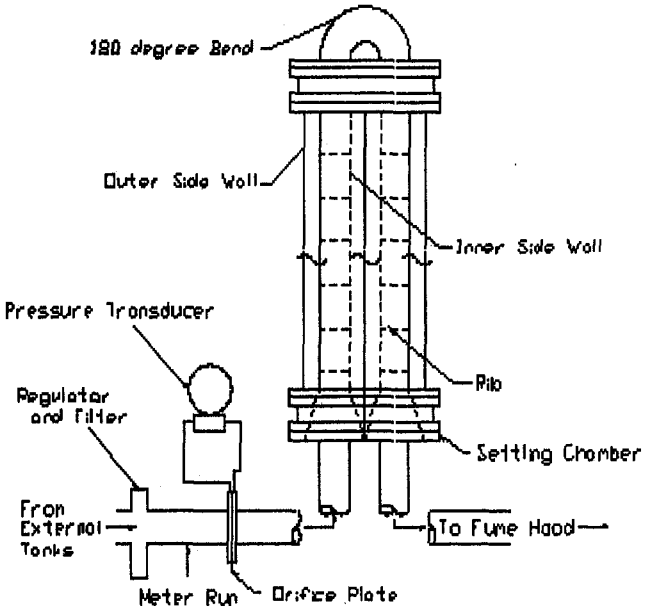

Fig. 1 Schematic of experimental apparatus

apart that are connected by the 180 deg, 1 × 1 in. (25.4 × 25.4 mm) square cross-sectional bend. The aluminum ribs are 0.1 × 0.1 × 1.0 in. (2.54 × 2.54 × 25.4 mm) long and have holes on either end for mounting (Fig. 2). Steel, 0.025 in. (0.635 mm) diameter music wire is inserted into these holes to secure them to the side walls of the test section. The ribs are mounted only on opposite walls and are not coated with naphthalene. The vortex generators (rods) are made from 0.078 in. (1.98 mm) diameter steel music wire. The rods are positioned in the test section by means of small aluminum brackets that allow for variation of rib-rod spacing.

Detailed surface profiles of the cast surfaces are required for local mass transfer results. These profiles are obtained by moving the walls under a fixed, linear variable differential transducer (LVDT) type profilometer. A bidirectional traversing table is securely mounted to the platform of a milling machine. The plates are secured to a 0.625 in. (15.875 mm) thick tooling aluminum plate, which is fixed to the traversing table. This mounting plate has been machined with an assortment of pin supports and machine screw taps to ensure the walls not only lie flat on the plate, but also are mounted in the same location for all scans. A custom written program run on a personal computer is used to control the motion of the traversing table through micro-step drive motors with a 0.00005 in. (0.00127 mm) step size.

Nomenclature

d = vortex generator diameter, ft
D = hydraulic diameter of test section, ft
D_{n-a} = binary diffusion coefficient for naphthalene-air, ft^2/s
e = rib height, ft
h_m = local mass transfer convection coefficient, ft/s
m'' = local mass flux, $lb_m/ft^2/s$
N = local augmentation number, defined in Eq. (8)
N_o = local Sherwood number ratio, defined in Eq. (7)
Nu = local Nusselt number
P = rib pitch, ft
Pr = Prandtl number
p_w = wall vapor pressure of naphthalene, lb/ft^2
Re = test section Reynolds number
s = rod-rib clearance, ft
Sc = Schmidt number of naphthalene–air
Sh = local Sherwood number
$\overline{Sh}_{CL}$ = centerline average Sherwood number for entire duct
Sh_o = fully developed Sherwood number
T_w = wall temperature, R
x = streamwise coordinate, ft
y, z = cross stream coordinates, ft
δ = local sublimation depth, ft
Δt = time of experiment, s
ν = viscosity of air, ft^2/s
$\rho_b(x)$ = local bulk vapor density of naphthalene, lb_m/ft^3
ρ_s = density of solid naphthalene, lb_m/ft^3
ρ_w = wall vapor density of naphthalene, lb_m/ft^3

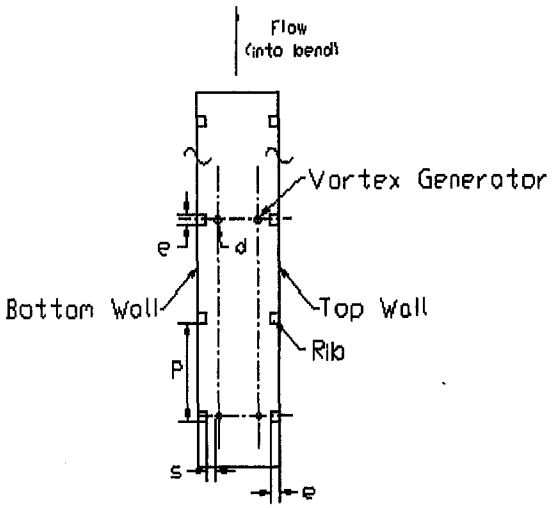

Fig. 2 Schematic of test section showing geometric notation

Procedure. Fresh, 99 percent pure naphthalene crystals are melted in a heavy-walled glass beaker with an electric heating element. The clean test section walls are clamped to stainless steel plates, which have been polished to a mirrorlike finish. Molten naphthalene is quickly poured into the hollow cavity of the plate frame to fill completely the region between the walls. The cast plates stand for at least eight hours in a fume hood to attain thermal equilibrium with the laboratory.

Each wall is then separated from the casting plate and mounted to the mounting plate for scanning. After scanning, the plates are stored in an air-tight container, saturated with naphthalene vapor, to hinder natural sublimation until the test section is assembled.

Test section assembly is begun by first inserting the two inner side walls and then attaching the bend. Any ribs or vortex generators are then attached to these walls and the two outer side walls are mounted. The alignment of all ribs and vortex generators is checked before the four top and bottom walls are assembled. After the experiment is over, the test section is disassembled and the walls are placed in the storage container until they are scanned again.

Data Reduction. Mass flow rate in the meter run is calculated from measurements of temperature, pressure, and differential pressure using standard equations for concentric bore orifice meters (Stearns et al., 1951; Miller, 1989).

Naphthalene sublimation depth is calculated from the two surface profiles for each wall. Each profile is normalized with respect to a reference plane computed from three points scanned on the aluminum surface of the walls. The difference between the normalized profiles gives the local sublimation depth.

The local mass flux m'' at each location is calculated from the following expression:

$$m'' = \rho_s \delta / \Delta t \tag{1}$$

where ρ_s is the density of solid naphthalene, δ is the local sublimation depth, and Δt is the duration of the experiment. Vapor pressure at the wall p_w is calculated from the following equation (Sogin and Providence, 1958):

$$\log_{10}(p_w) = A - B/T_w \tag{2}$$

where A and B are constants (11.884 and 6713, respectively) and T_w is the absolute wall temperature. Wall vapor density ρ_w is then calculated using the perfect gas law. Bulk vapor density of naphthalene $\rho_b(x)$ is obtained by mass conservation balances of naphthalene from the inlet ($x = 0$) to the streamwise location (x).

The local mass transfer convection coefficient h_m is then calculated as follows:

$$h_m = m''/(\rho_w - \rho_b(x)) \tag{3}$$

The binary diffusion coefficient D_{n-a} for naphthalene sublimation in air is taken as the ratio of the kinematic viscosity of air ν to the Schmidt number for naphthalene–air (Sc = 2.5). The local Sherwood number Sh is then calculated by:

$$\mathrm{Sh} = h_m D/D_{n-a} = h_m D\mathrm{Sc}/\nu \tag{4}$$

where D is the hydraulic diameter of the test section. Sherwood number results presented in this study have been scaled with a correlation adapted from McAdams (1954) for fully developed smooth wall pipe flow:

$$\mathrm{Sh}_o = 0.023\ \mathrm{Re}^{0.8}\mathrm{Sc}^{0.4} \tag{5}$$

where Re is the duct Reynolds number.

Comparison of heat transfer and mass transfer results is done through the use of the heat–mass transfer analogy (Sogin, 1958):

$$\mathrm{Nu} = \mathrm{Sh}(\mathrm{Pr}/\mathrm{Sc})^{0.4} \tag{6}$$

where Nu is the Nusselt number and Pr is the Prandtl number of air. To facilitate comparison between mass and heat transfer results, a Sherwood number ratio, N_o, is defined as follows:

$$N_o = \mathrm{Sh}/\mathrm{Sh}_o = \mathrm{Nu}/\mathrm{Nu}_o \tag{7}$$

where Nu_o is the correlated fully developed Nusselt number, analogous to Sh_o. An augmentation number N is used to show mass transfer augmentation for tests involving vortex generators. It is defined as follows:

$$N = \mathrm{Sh}_{\mathrm{rib-rod}}/\mathrm{Sh}_{\mathrm{rib}} \tag{8}$$

where $\mathrm{Sh}_{\mathrm{rib\text{-}rod}}$ is the Sherwood number with the vortex generators installed and $\mathrm{Sh}_{\mathrm{rib}}$ is the Sherwood number for the baseline. Both local (N_o, N) and area-averaged ($\overline{N_o}$, $\overline{N}$) results are compared in this manner. Area-averaging is performed over the region between consecutive ribs.

Uncertainty. Uncertainties for all computed values are estimated using the second-power equation method (Kline and McClintock, 1953). The estimates for these experiments are comparable to previously reported values for both heat transfer and mass transfer studies, but are believed to be conservative.

Volume flow rate and duct Reynolds number (Re) uncertainties are estimated to be less than 10 percent for Re > 6000. The reported resolution of the LVDT is 0.00005 in. (0.00127 mm) while the analog-to-digital (A/D) board is reported to have an accuracy of 0.000078 in. (0.002 mm) in a 12 kHz acquisition rate, 16-bit resolution mode. Experimental tests of accuracy and repeatability for the entire acquisition system indicate a sublimation depth uncertainty of 0.00015 in. (0.0038 mm). Sublimation depths are maintained at about 0.006 in. (0.152 mm) by varying the duration of the experiment. This target depth was selected to minimize uncertainties in both depth measurement and changes in duct cross section area. These uncertainties were found to be 1 and 3 percent, respectively. The resulting experimental duration was between 90 min for Re = 30,000 and 180 min for Re = 5,000.

Vapor density uncertainty based on measured quantities is negligible for both wall and bulk values. Overall uncertainty in Sherwood number calculation is about 8 percent and varies slightly with Reynolds number (<1 percent).

Experimental Results

The experiments reported in this paper were performed with ribbed top and bottom walls and smooth side walls. Measurements were made for the following parameters (see Fig. 2 for

notation): rib height-to-hydraulic diameter ratio, $e/D = 0.1$, and vortex generator (rod) diameter-to-rib height ratio, $d/e = 0.78$. Rods are placed above all the ribs for $P/e = 21$, and over every other rib, beginning with the first one in the duct, for rib pitch-to-rib height ratio, $P/e = 10.5$. For $s/e = 0.55$, rods are placed in both the inlet and outlet sections, but for $s/e = 1.0$ and 1.5, rods are placed only in the inlet section. Four different Reynolds numbers: 5000, 10,000, 30,000, and 40,000 were investigated for the rib only baseline and each of the three rod clearance ratios.

Along the centerline of each plate, 120 points are measured and these are used for the calculation of the bulk naphthalene vapor density. This method assumes a uniform cross-stream mass transfer distribution, which will later be shown to be inaccurate. However, the difference between cross-stream-averaged sublimation depth and local centerline sublimation depth corresponds to a negligible difference in bulk vapor density in the inlet duct, and does not exceed about 5 percent at the end of the outlet duct. To obtain more detailed measurements in both the developing and fully developed regions of the walls, profile measurements on a 30×28 (streamwise $\times$ transverse) uniform grid are made in selected interrib regions. Close to the plate edges, the spherical tip of the LVDT often rides on the aluminum edge of the wall, giving erroneous data. For this reason, the contours presented do not always cover the entire width of the plate.

Rib-Only Baseline Measurements. Figure 3 shows the centerline Sherwood number ratio in the inlet (radially outward leg) and the outlet (radially inward leg) sections for the rib-only baseline case at a Reynolds number of 5000 and both pitch ratios tested. Along the ribbed top and bottom walls periodic fully developed profiles are obtained after only a few interrib modules for both $P/e = 10.5$ (Fig. 3(a)) and $P/e = 21$ (Fig. 3(b)). Asymmetry between the top and bottom walls is present for most of the inlet, and is due to the asymmetry in the inlet flow profile. The asymmetry appears mainly in the value of peak Sherwood number ratio and does not affect the overall behavior. For $P/e = 10.5$ (Fig. 3(a)), peak Sherwood number ratios are typically between 4.5 and 5.5 in the inlet and between 4.5 and 5.0 in the outlet. For $P/e = 21$ (Fig. 3(b)), these values decrease to about 4 in both inlet and outlet ducts. These peak values remain nearly constant throughout the length of the section. The profiles typically have two peaks, one that occurs nearly 4–6 rib heights downstream of the rib and corresponds to reattachment, and the other that occurs just upstream of each rib and corresponds to a corner eddy upstream of the rib. The later region is quite small and is often missed by the 120 point center line scan for $P/e = 10.5$. These observations are consistent with those reported in the literature (e.g., Acharya et al., 1995a).

The centerline profiles for the smooth side walls at $P/e = 10.5$ (Fig. 3(a)) qualitatively resemble the asymptotically decaying profiles (to fully developed values) observed for a smooth surface. However, a careful inspection shows small periodic undulations in the profile with the peaks in the vicinity of the ribs. These peaks are more visible for the larger pitch ratio and appear to correlate directly with the peaks in the turbulence intensity profiles reported by Acharya et al. (1994). Sherwood number ratios for the inlet are in the range of 2–5 for $P/e = 10.5$ and in the range of 1.5–2 for $P/e = 21$ over most of the plate. This nearly twofold enhancement of centerline mass transfer over the purely smooth walls can be attributed to an increase in the turbulence levels caused by the ribs. The profiles in the outlet section show that immediately past the bend the Sherwood numbers along the outer wall are higher than those along the inner wall. This is presumably due to the effect of secondary flows induced by the bend and leads to a noticeable asymmetry between opposing walls in the first interrib module past the bend.

Detailed contours of Sherwood number ratio in selected developing and periodic fully developed regions of the inlet and outlet ducts for the baseline case at $P/e = 10.5$ are shown in Fig. 4. These regions are presented as though the test section were unfolded. The developing region is depicted by the first interrib space and the fully developed region is depicted by the second to last interrib space, which is far enough upstream of the bend that its influence is not prominent. The asymmetry between opposing walls in the developing region, noted earlier in the centerline profiles, is also evident in the contours. Asymmetry is dampened downstream, indicating that the flow field induced in a rib-roughened duct quickly overwhelms the history of the inlet field. The fully developed mass transfer on the top and bottom walls clearly shows regions of separation, reattachment, redevelopment, and recirculation that, as noted earlier, have been previously reported in the literature based on centerline values. Sherwood number ratio in most of the separated region downstream of a rib is in the range of 2 to 3. A peak value in the vicinity of 4.5–5 occurs near the point of flow reattachment, and in the fully developed region, this peak is relatively uniform in the spanwise direction. Sherwood number ratios expectedly decrease downstream of reattachment. Just upstream of the rib appears to be a small but energetic eddy that, in the transverse direction, spans most of the rib and extends about one rib height upstream of the rib. Sherwood number ratios as high as 5 are noted in this region.

The Sherwood number ratios for the smooth side walls show similar asymmetry in the developing region. Contours in the fully developed region clearly show a periodically fully developed distribution on the outer wall. Local mass transfer near the ends of the ribs is very high ($N_o = \mathrm{Sh}/\mathrm{Sh}_o = 5$), but is restricted to the near vicinity of the rib. These localized regions of high mass transfer near the ribs correlate spatially with the peaks in the streamwise turbulence intensity measured in the vicinity of the ribs (Acharya et al., 1993, 1994, 1995a). Sherwood number ratios in the midspan regions of the smooth walls are of the order of 2. This mass transfer enhancement on the side walls extends up to nearly 4 rib heights toward the midspan of the plate, and is believed to result from an increase in turbulence levels caused by the ribs.

Top and bottom wall symmetry is excellent in the outlet duct. Comparison of the inner and outer walls clearly shows the effects of the bend. Higher Sherwood numbers are observed on the outer surface relative to the values on the inner wall. Secondary flows induced by the bend are expected to drive the flow toward the outer wall, resulting in higher Sherwood numbers along these walls as observed here.

Mass transfer distributions in the fully developed region of the outlet duct resemble those from the inlet duct, except that the peak values along the ribbed walls are 15–25 percent lower. The mass transfer distribution on the side walls is also similar to that in the inlet, but the region of augmentation ($N_o > 1$) is restricted to only about two rib heights.

Rib-Vortex Generator (Rod) Measurements. Centerline mass transfer distribution for both the rib-only baseline and the $s/e = 0.55$ rib-vortex generator spacing at $P/e = 21$ and $\mathrm{Re} = 5000$ is shown in Fig. 5. Mass transfer in the inlet duct is noticeably enhanced by the presence of vortex generators. In particular, the peak value upstream of each rib is consistently 1.5–2 times greater than the baseline rib-only values. In the first two interrib spaces, the profiles are similar in shape to the baseline profile, with the reattachment location appearing to be roughly at the same location (5–6 rib heights downstream of the rib). From the third interrib module onward, the interrib Sherwood number profiles for the rib-rod cases appear to be more uniform, and suggests a delayed reattachment (10–15 rib heights downstream of the rib). However, these more uniform Sherwood numbers are generally higher than the rib-only values, and particularly so in the later regions of the interrib mod-

ule. Presumably the rods enhance the interrib turbulence intensities and provide an overall increase in the mass (heat) transfer from the ribbed surface.

The outlet centerline Sherwood number distribution indicates that the enhancement of local mass transfer is not as pronounced as in the inlet. However, the same trends of generating a more uniform Sherwood number distribution in the interrib modules can be observed.

Centerline mass transfer distribution along the side walls in both the inlet and outlet sections show that vortex generators induce considerable enhancement (nearly 2–2.5 the rib-only value). It is believed that this enhancement is due to the vortices shed behind the base of the rods and the associated increases in the turbulence levels. Overall, the presence of the rods seems to merely increase the local mass transfer distribution, without altering the trends. Similar mass transfer behavior is seen in the outlet section.

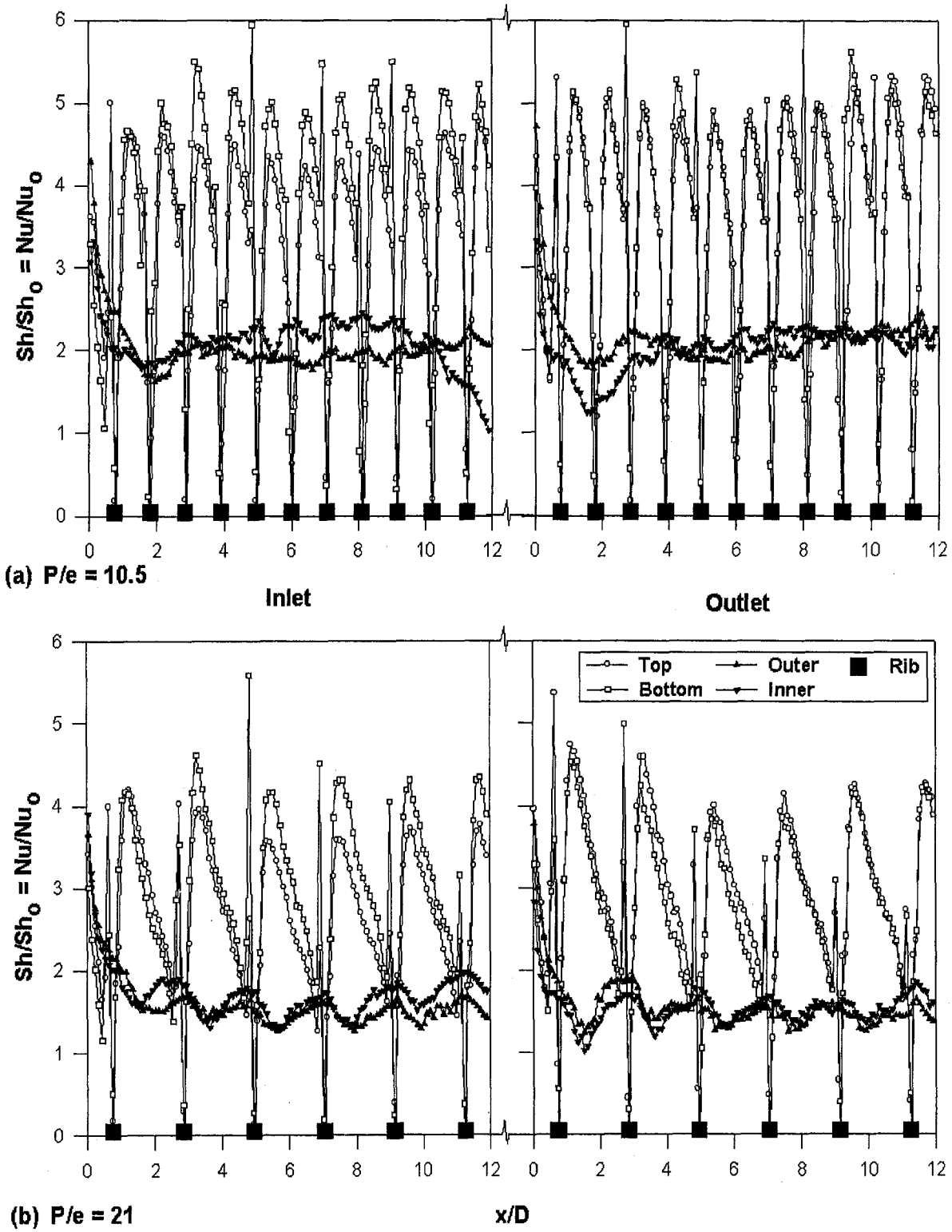

Fig. 3 Effect of rib pitch ratio on centerline mass transfer ratio, Re = 5000

Figure 6 presents the results at the lowest and highest Reynolds numbers studied (Re = 5000 and 40,000) and for the same *P/e* and *s/e* values as in Fig. 5. Only the fully developed region (the last interrib module in each section) is shown. The results, in the form of a mass transfer augmentation number, $N = Sh_{rib\text{-}rod}/Sh_{rib}$, are presented for each of the four walls in the inlet and outlet sections. At the lower Re value, mass transfer enhancement of the order of 50 percent is obtained along the smooth inner and outer walls with peak enhancement as high as 80 percent. Along the ribbed top wall, there is an initial degradation for up to six rib heights followed by a substantial increase in mass transfer with peak *N*-values reaching 1.75. For Re = 40,000, the behavior is similar, with centerline mass transfer along the smooth side walls enhanced by nearly 50 percent due to the presence of the vortex generators. Along the ribbed bottom wall of the inlet passage, the centerline *N*-values show about a 20 percent average increase in mass transfer, with a peak increase of nearly 40 percent. It is worth noting that these

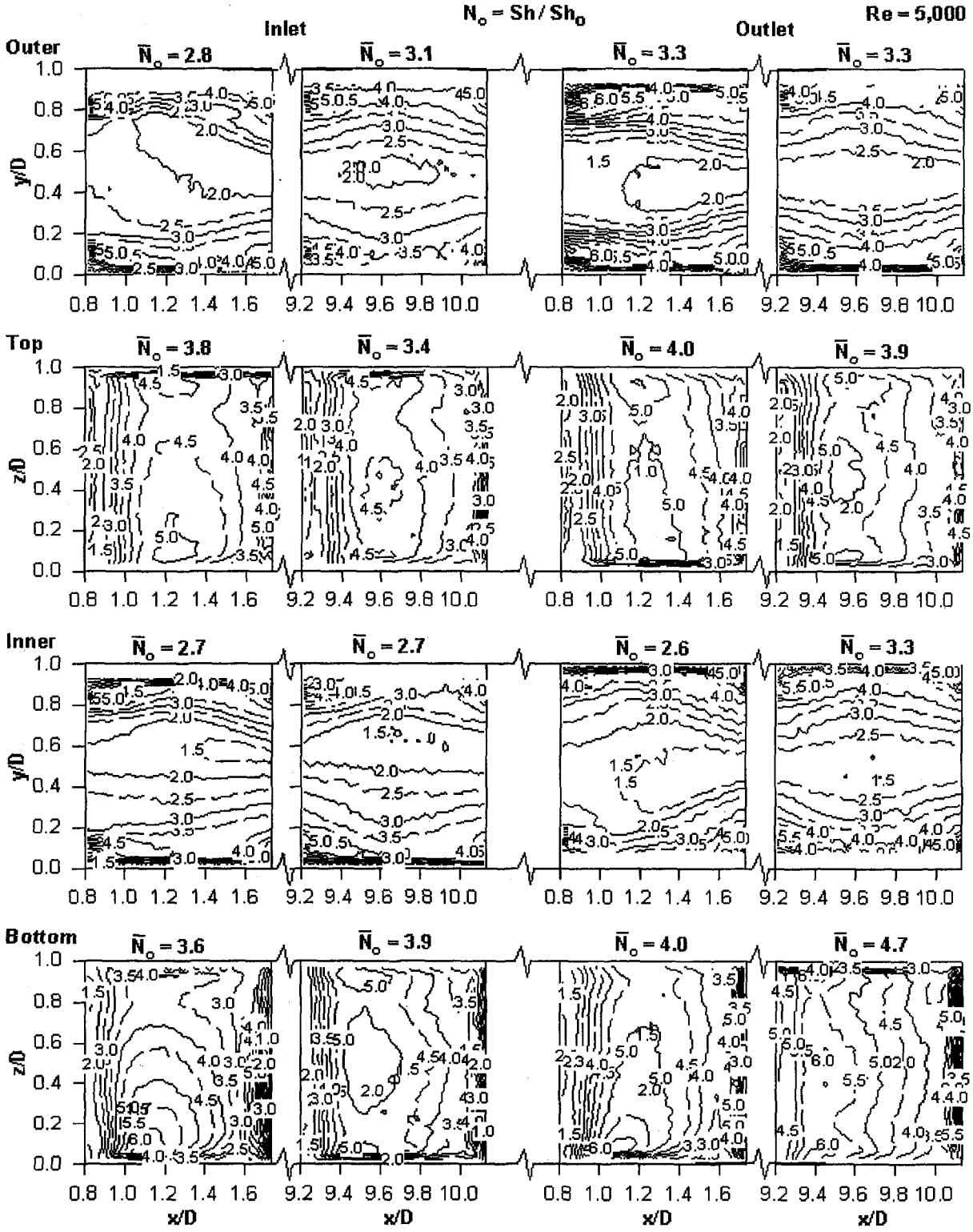

Fig. 4 Detailed mass transfer ratio in selected regions of the rib only baseline case, Re = 5,000, *P/e* = 10.5

increases are primarily downstream of eight rib heights from the rib, and that the maximum enhancement generally occurs just ahead of the rod-rib pair downstream. Along the top ribbed wall enhancement levels are similar to those along the bottom ribbed wall. In the outlet passage, enhancement in the ribbed wall mass transfer is observed over most of the streamwise extent of the inter rib module, with a peak enhancement of nearly 50 percent for the bottom ribbed wall.

To highlight the effects of the spanwise variations in the enhancements induced by the vortex generator, spanwise-averaged augmentation numbers are also presented for Re = 40,000. Spanwise-averaged profiles of the mass transfer augmentation number, as expected, have a smoother appearance than the centerline profiles. Spanwise-averaged values for the side walls are consistent with the centerline, with average enhancements along the side walls that are typically of the order of 50 percent except

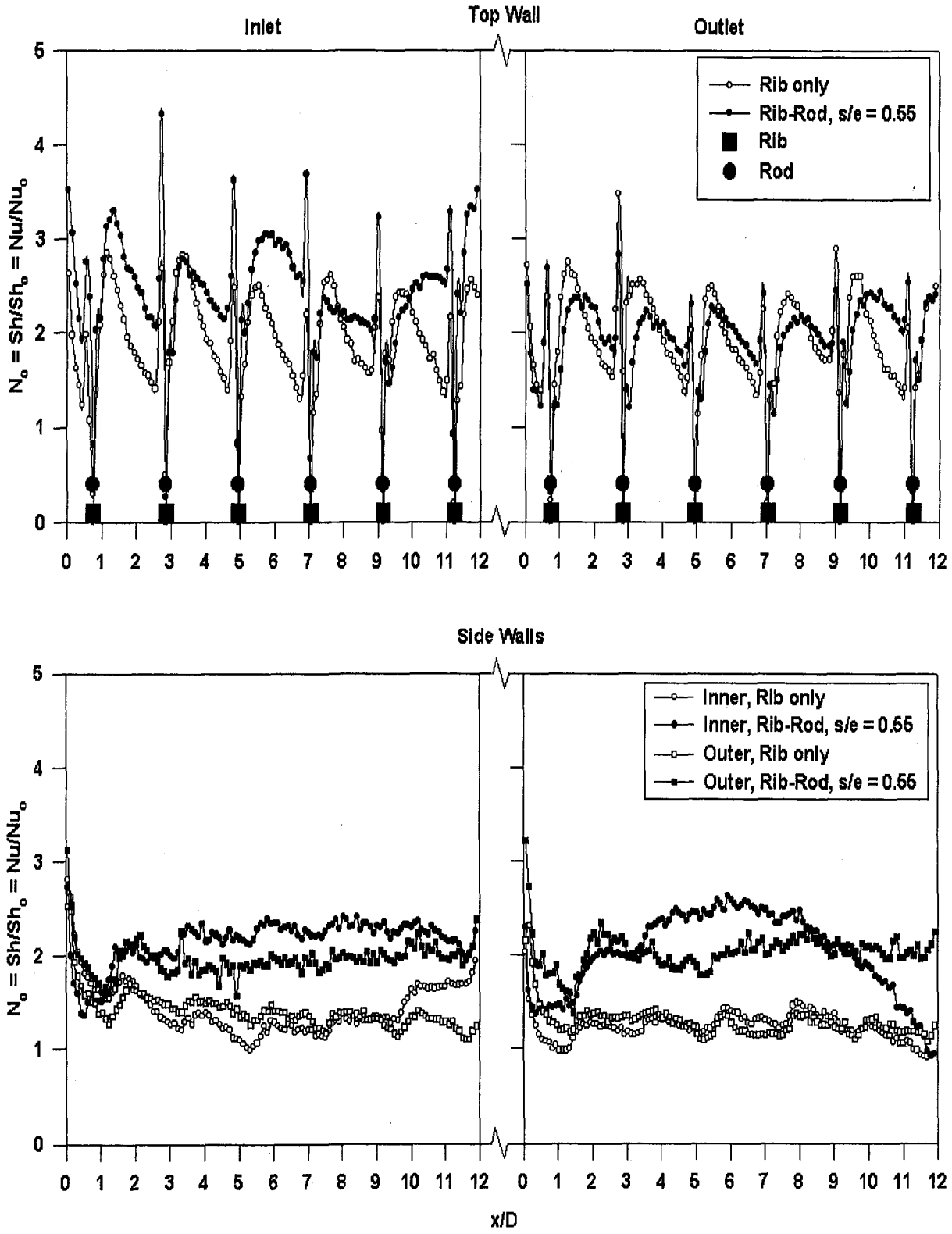

Fig. 5 Effect of vortex generators on centerline mass transfer ratio, Re = 5,000, P/e = 21, s/e = 0.55

for the inner wall of the inlet duct where the enhancements are somewhat lower. For the ribbed walls, the enhancement levels are somewhat lower in the outflow passage.

Contours of the local mass transfer augmentation numbers in a fully developed interrib region for all the walls is shown in Fig. 7 for Re = 5000, P/e = 21, and s/e = 0.55. As seen in Fig. 5, there is enhancement in the second half of the interrib region, and degradation in the first half. It is clear from Fig. 7 that on the top wall the enhancement (peak value of N is nearly 2) is greater than the degradation (minimum value is around 0.6), corresponding to a net average enhancement of nearly 10 percent, and that the spanwise profile is fairly uniform. Near the outer and inner walls, high values of N are noted. Along the bottom ribbed wall, the enhancement levels are lower, with an average degradation of

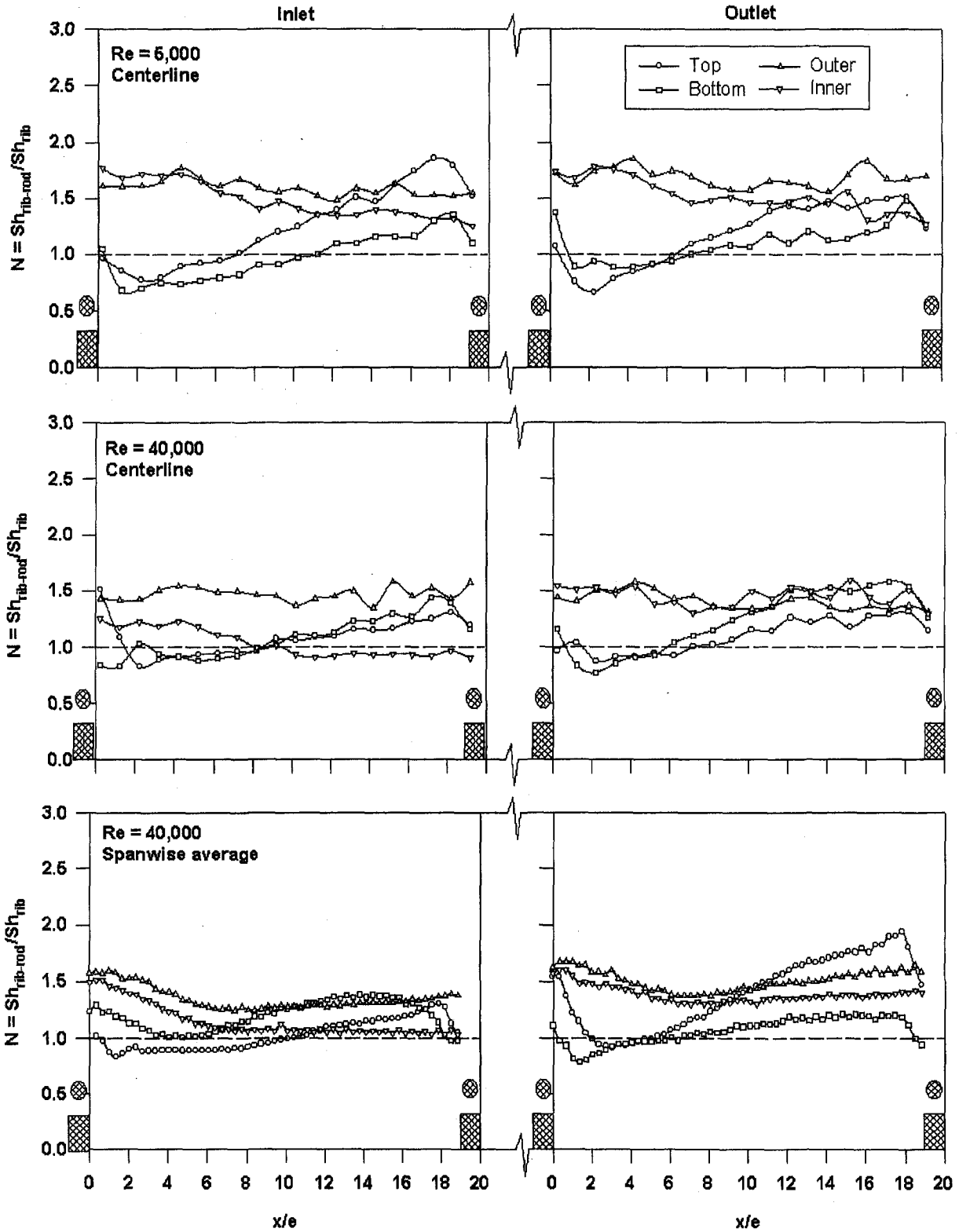

Fig. 6 Effect of Reynolds number on centerline mass transfer ratio in the fully developed regions, P/e = 21, s/e = 0.55

nearly 10 percent. The smooth side walls show significant enhancements (values of N as high as 2.75 can be seen) with the peak values centered in the wake of the vortex generator. The traces of N in the two wakes behind the vortex generators show that they are deflected away from the rib as the flow emerges from the rib-rod interspace. The two wakes appear to merge downstream (at approximately 10 rib heights downstream of the rod); the wake effect on local mass transfer can be seen to persist through the entire interrib module and corresponds to about a 40 percent enhancement in average mass transfer. An average over all four walls indicates an enhancement of nearly 40 percent.

Figure 8 shows the local behavior at the lower $P/e = 10.5$. Observations similar to those noted above can be made. Along the ribbed walls local regions of mass transfer degradation and enhancement can be seen, but overall the enhancement levels and coverage exceed the degradation. Mass transfer degradation

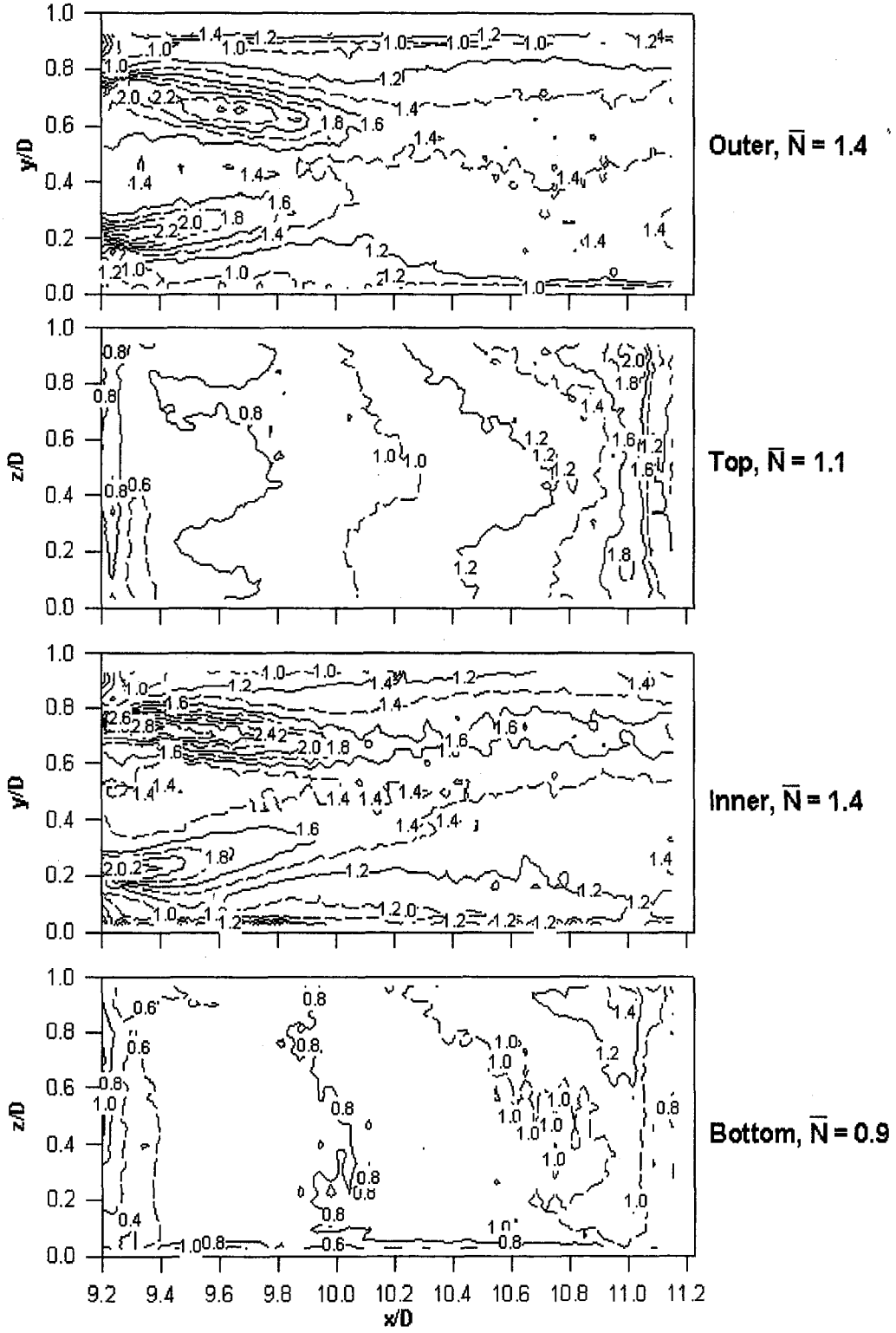

Fig. 7 Detailed mass transfer augmentation number in the fully developed region of the inlet duct, Re = 5000, $P/e = 21$, $s/e = 0.55$

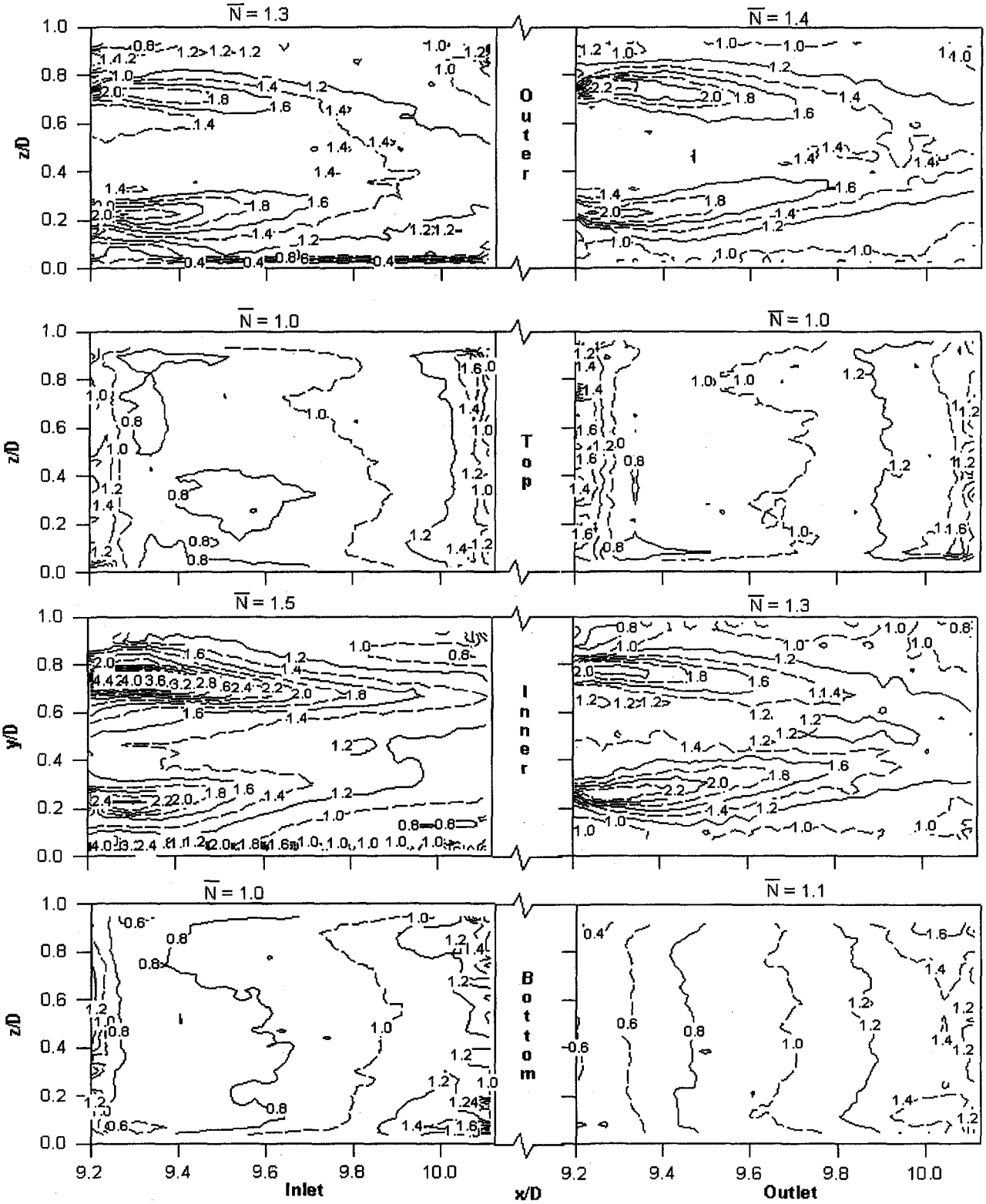

Fig. 8 Detailed mass transfer augmentation number in the fully developed regions, Re = 5000, P/e = 10.5, s/e = 0.55

levels are typically 20 percent, while enhancements levels are typically in the 20–40 percent range. Average mass transfer augmentation along the bottom wall is about unity in the inlet and increases to about 1.1 in the outlet.

Mass transfer contours for the side walls again clearly show the effect of vortex shedding behind the rods. In the wake region behind the rods, significant mass transfer enhancement is present. The "distinct" wake regions behind the rods on the outer wall seem to extend to about five rib heights and show local enhancement of up to 100 percent before the two wake regions combine. In the region after the two wakes have combined, mass transfer enhancement is about 20–40 percent. The inner wall seems to benefit more from the rods than the outer wall. The contours for the inner wall indicate that the wakes combine later and that enhancement is much greater—over 300 percent. Mass transfer near the centerline of both side walls

is enhanced, even in the region between the wakes. Average enhancement for the side walls is approximately 40 percent over the entire interrib space. In order to rationalize the benefits of the vortex generators at $P/e = 10.5$, it should be noted that while along the top and bottom walls the enhancement levels are not significant, they are quite high along the side walls (nearly 40 percent) and overall lead to substantial increase in heat transfer.

Local mass transfer contours for $s/e = 1.5$ and Re = 10,000 and 30,000 are shown in Fig. 9. Enhancement at higher Reynolds numbers is somewhat smaller than the enhancement at the lower Reynolds numbers, with the higher Reynolds number showing average augmentation numbers about 5–10 percent lower than those for the lower Reynolds number. It is believed that the shear layers formed by the ribs and rods are much thinner at higher Reynolds numbers and thus do not influence the flow as much as they do at lower Reynolds numbers. For the ribbed walls, local degradation up to 20 percent and local enhancement levels up to 40 percent are noted. The surface area with enhancement is again much larger than the area where degradation occurs. Along the side walls maximum enhancement levels are in the range of 2–2.8, but they are much more localized. Unlike the flow at lower Reynolds numbers, the merging of the two wakes is not apparent along the smooth walls of

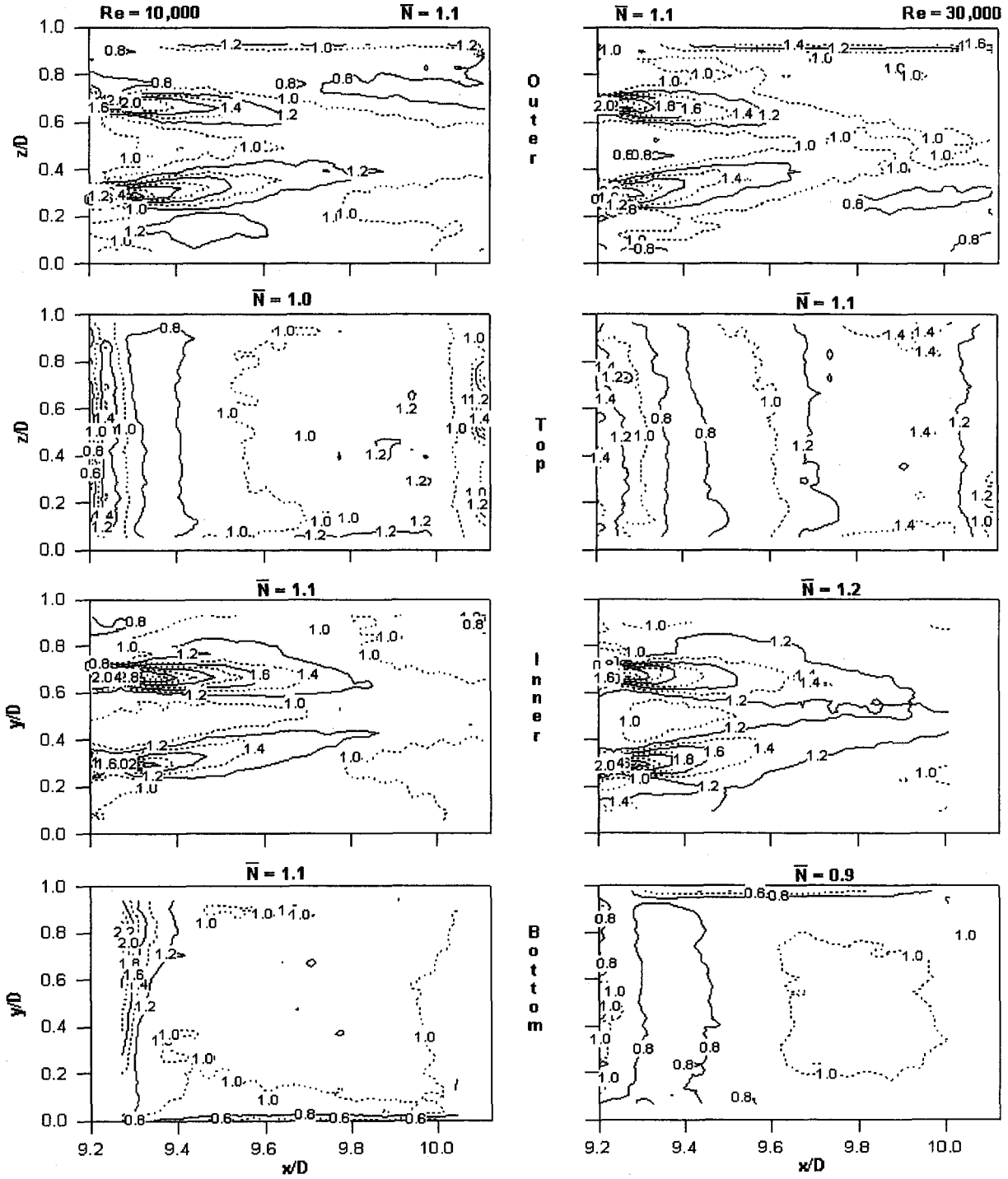

Fig. 9 Effect of Reynolds number on mass transfer augmentation number in the fully developed region of the inlet duct, $P/e = 10.5$, $s/e = 1.5$

the inlet passage. In fact, in the midspan regions, the augmentation number is typically unity, indicating no enhancement. Along the inner wall of the outflow passage, some wake interference can, however, be observed.

Concluding Remarks

An experimental study is made to measure the local Sherwood numbers in the internally ribbed passages of a square turbine blade coolant channel with a radially outward flow leg and a radially inward flow leg. The primary objective of the study is to examine whether cylindrical vortex generators placed above the ribs can be used to enhance mass transfer from the surfaces. Measurements of the mass transfer include centerline and spanwise-averaged profiles of Sherwood number ratios and corresponding contours in the developing and periodically developed regions. The following main conclusions are obtained.

1 Baseline rib-only results confirm the reported peaks in the Sherwood number in the vicinity of reattachment and just upstream of the rib where a strong corner vortex is formed. Along the smooth side walls, significant enhancement is obtained with the peak occurring in the vicinity of the rib. This peak correlates with the measured location of maximum turbulence intensity.

2 For the higher pitch case ($P/e = 21$), significant enhancement due to the vortex generators is obtained along the ribbed walls in the developing region of the inflow passage. In the periodically developed region, the profile is more uniform, with degradation in the initial separated region and enhancement in the later regions of the inter rib module. The enhancement levels and coverage substantially exceed the corresponding degradation quantities. Along the smooth walls, the vortices in the wake of the vortex generator are associated with high levels of mass transfer enhancement. The wakes from each vortex generator are deflected away from the rib, and appear to merge downstream. The wake effect is seen to decrease somewhat with Reynolds number.

3 Spanwise-averaged profiles in the developed regions indicate an average 50 percent increase in the mass transfer from the side walls due to the vortex generators. Along the ribbed walls the average enhancement levels are lower. Local enhancement levels can be substantially higher—reaching values in the vicinity of 300 percent along the side walls.

4 For the lower pitch ($P/e = 10.5$), the general behavior is the same as that for $P/e = 21$. Enhancement levels are somewhat lower and the wake interference and merging effects along the side walls are weaker.

5 Future studies are directed at optimizing the vortex generator geometry and making measurements under rotating conditions.

Acknowledgments

This research was performed under a subcontract from the South Carolina Energy Research and Development Center to Louisiana State University (93-01-SR015). The contract monitors were Dr. Daniel Fant and Dr. Larry Golan. Their help is gratefully acknowledged.

References

Acharya, S., Myrum, T., and Inamdar, S., 1991, "The Effect of Subharmonic Flow Pulsation in a Ribbed Pipe: Flow Visualization and Pressure Measurements," *AIAA Journal*, Vol. 29, No. 9, pp. 1390–1400.

Acharya, S., Dutta, S., Myrum, T., and Baker, R. S., 1993, "Periodically Developed Flow and Heat Transfer in a Ribbed Duct," *Int. J. Heat Mass Transfer*, Vol. 36, No. 8, pp. 2069–2082.

Acharya, S., Dutta, S., Myrum, T., and Baker, R. S., 1994, "Turbulent Flow Past a Surface Mounted Rib," ASME *Journal of Fluids Engineering*, Vol. 116, No. 2, pp. 238–246.

Acharya, S., Myrum, T., Sinha, S., and Qiu, X., 1995a, "Developing and Periodically Developed Flow, Temperature and Heat Transfer in a Ribbed Duct," *Proc. ASME/JSME Thermal Engg. Conf.*, Vol. 1, pp. 303–312; also *Int. J. Heat Mass Transfer*, Vol. 40, No. 2, pp. 461–480.

Acharya, S., Myrum, T. A., and Dutta, S., 1995b, "Heat Transfer in Turbulent Flow Past a Surface Mounted Two-dimensional Rib," presented at the ASME Intl. Mech. Engg. Conf. and Expo., San Francisco, Nov.

Durst, F., Founti, M., and Obi, S., 1988, "Experimental and Computational Investigation of the Two-Dimensional Channel Flow Over Two Fences in Tandem," ASME *Journal of Fluids Engineering*, Vol. 110, pp. 48–54.

Garimela, S. V., and Eibeck, P. A., 1991, "Enhancement of Single Phase Convective Heat Transfer From Protruding Elements Using Vortex Generators," *Int. J. Heat Mass Transfer*, Vol. 34, No. 9, pp. 2431–2433.

Han, J. C., and Zhang, P., 1991, "Effect of Rib-Angle Orientation on Local Mass Transfer Distribution in a Three-Pass Rib-Roughened Channel," ASME JOURNAL OF TURBOMACHINERY, Vol. 113, pp. 123–130.

Humphrey, J. A. C., and Whitelaw, J. H., 1979, "Turbulent Flow in a Duct With Roughness," in: *Turbulent Shear Flows 2*, Bradbury et al., eds., Springer-Verlag, Berlin, pp. 174–188.

Hung, Y. H., and Lin, H. H., 1992, "An Effective Installation of Turbulence Promoters for Heat Transfer Augmentation in a Vertical Rib-heated Channel," *Int. J. Heat Mass Transfer*, Vol. 35, No. 1, pp. 29–42.

Karniadakis, G. E., Mikic, B. B., and Patera, A. T., 1988, "Minimum-Dissipation Transport Enhancement by Flow Destabilization: Reynolds' Analogy Revisited," *J. Fluid Mech.*, Vol. 192, pp. 365–391.

Kline, S. J., and McClintock, F. A., 1953, "Describing Uncertainties in Single-Sample Experiments," *Mech. Engineering*, Vol. 75, Jan., pp. 3–8.

Liou, T. M., Chang, Y., and Hwang, D. W., 1990, "Experimental and Computational Study of Turbulent Flows in a Channel With Two Pairs of Turbulence Promoters in Tandem," ASME *Journal of Fluids Engineering*, Vol. 112, pp. 302–310.

McAdams, W., 1954, *Heat Transmission*, 3rd ed., McGraw-Hill, New York.

Miller, R. W., 1989, *Flow Measurement Engineering Handbook*, 2nd ed., McGraw-Hill, New York.

Myrum, T. A., Acharya, S., Inamdar, S., and Mehrotra, A., 1992, "Vortex Generator Induced Heat Transfer Augmentation Past a Rib in a Heated Duct Air Flow," ASME *Journal of Heat Transfer*, Vol. 114, pp. 280–284.

Myrum, T. A., Qiu, X., and Acharya, S., 1993, "Heat Transfer Enhancement in a Ribbed Duct Using Vortex Generators," *Int. J. Heat Mass Transfer*, Vol. 36, No. 14, pp. 3497–3508.

Myrum, T. A., and Acharya, S., 1994, "Enhanced Heat Transfer in Ribbed Ducts Using Vortex Generators," Final Report, GRI-94/0256.

Myrum, T. A., Acharya, S., Sinha, S., and Qiu, X., 1996, "Flow and Heat Transfer in a Ribbed Duct With Vortex Generators," ASME *Journal of Heat Transfer*, Vol. 118, pp. 294–300.

Sogin, H. H., and Providence, R. I., 1958, "Sublimation From Disks to Air Streams Flowing Normal to Their Surfaces," *Transactions of the ASME*, Vol. 80, pp. 61–69.

Sparrow, E. M., and Tao, W. Q., 1983, "Enhanced Heat Transfer in a Flat Rectangular Duct With Streamwise-Periodic Disturbances at One Principal Wall," ASME *Journal of Heat Transfer*, Vol. 105, pp. 851–861.

Stearns, R. F., Johnson, R. R., Jackson, R. M., and Larson, C. A., 1951, *Flow Measurement With Orifice Meters*, D. van Nostrand Co., Inc., Toronto.

Wroblewski, D. E., and Eibeck, P. A., 1991, "Measurements of Turbulent Heat Transport in a Boundary Layer With an Embedded Streamwise Vortex," *Int. J. Heat Mass Transfer*, Vol. 34, No. 7, pp. 1617–1631.

Zukauskas, A., 1994, "Enhancement of Forced Convection Heat Transfer in Viscous Fluid Flows," *Int. J. Heat Mass Transfer*, Vol. 37, Suppl. 1, pp. 207–212.

A Fast-Response High Spatial Resolution Total Temperature Probe Using a Pulsed Heating Technique

D. R. Buttsworth

T. V. Jones

Department of Engineering Science,
University of Oxford,
Parks Road,
Oxford, United Kingdom

This paper discusses the operation of a fast-response total temperature probe based on transient thin film heat flux gage technology. The probe utilizes two thin film gages located close to the stagnation point of a hemispherically blunted fused quartz cylinder. Development of the present total temperature probe was motivated by the need for a fast-response device with a high spatial resolution. The diameter of the probe was 2.8 mm and the two films were separated by a distance of less than 1 mm. Measurement of the flow total temperature requires the films to operate at different temperatures. In the present work, the temperature difference was generated using a current pulse (approximately 70 mA with a duration of around 1 s) to heat one of the thin film resistance gages. With this technique, temperature differences between the hot and cold films of around 120 K were achieved. The interpretation of the transient surface temperature measurements is discussed, and the validity and utility of the technique are demonstrated with reference to total temperature and convective heat transfer coefficient measurements in a compressible free jet. The results demonstrate that accurate total temperature and convective heat transfer coefficient measurements with high spatial and temporal resolution can be obtained with the present device.

Introduction

Probe measurements continue to play a significant role in the testing and development of gas turbine engines (e.g., Smout and Cook, 1996). Thermocouple probes are routinely used as they can provide a simple, robust, reasonably accurate, and relatively cheap temperature measurement. However, a major disadvantage of thermocouple probes is their relatively poor frequency response, which limits their ability to measure temperature variations associated with typical turbomachinery blade passing events. Such high-frequency information (around 10 kHz) is needed to characterize the operation of gas turbines properly and thereby achieve improved performance either directly, or with the aid of CFD codes that have been calibrated against such measurements. Many attempts have been made to compensate thermocouple temperature measurements for the effects of thermal inertia (e.g., Boutrif and Thelliez, 1995). However, the accuracy of the compensated measurements diminishes with increasing frequency, and thus, there exist practical limits beyond which compensated measurements become unreliable.

Thin wire anemometry is possible in an experimental turbomachinery environment. However, constant current anemometers, like thermocouple devices, suffer from frequency response problems, and cannot successfully measure high-frequency components without compensation. Compensation techniques have been used to measure turbulent fluctuations in a relatively low-speed environment (Bremhorst and Graham, 1990). Cold wire compensation has also been examined with a view to possible turbomachinery applications (Denos and Sieverding, 1997). However, even with compensation, such measurements have a limited bandwidth (around 10 kHz). In contrast, constant-temperature anemometers typically have a much higher frequency response (around 100 kHz) because the wire is not required to reach thermal equilibrium with the gas stream. However, exposed thin wire techniques can suffer from breakage problems, and the wires should ideally be cleaned and calibrated regularly because of contamination problems (e.g., Lomas, 1986). Furthermore, the interpretation of the measurements obtained with exposed thin wire devices can become prohibitively complicated in unsteady compressible flows.

To overcome many of these difficulties, the aspirating probe was developed by Ng and Epstein (1983). This probe has since found application in a number of compressor and turbine experiments (e.g., Alday et al., 1993; Van Zante et al., 1995; Suryavamshi et al., 1998). The aspirating probe can, in principle, measure relatively high-frequency fluctuations in both the total temperature and the total pressure. For the original design, Ng and Epstein (1983) estimated the probe frequency response to be above 20 kHz, and, in a later application (Suryavamshi et al., 1998), frequencies as high as 40 kHz were observed in spectral analyses of the measured signals. However, little information is available on the probe response roll-off as this limiting frequency is approached. Van Zante et al. (1995) have noted that the bandwidth of the aspirating probe is likely to be somewhat restrictive in some turbomachinery applications, and furthermore, it gives results that are flow angle sensitive for off-axis flows beyond ± 12.5 deg (Alday et al., 1993). By itself, the dual-wire aspirating probe cannot independently measure temperatures in compressible flows of varying composition without the addition of a third wire at a different overheat ratio, or a total pressure transducer operating in parallel with the aspirating probe. (In a varying composition flow, the heat transfer from a constant-temperature hot wire located upstream of a choked orifice is a function of the flow total pressure, total temperature, and the gas composition; Ninnemann and Ng, 1992).

Recently, a total temperature probe based on transient thin film heat transfer gage technology was demonstrated (Butts-

Contributed by the International Gas Turbine Institute and presented at the 42nd International Gas Turbine and Aeroengine Congress and Exhibition, Orlando, Florida, June 2–5, 1997. Manuscript received at ASME Headquarters February 1997. Paper No. 97-GT-301. Associate Technical Editor: H. A. Kidd.

worth and Jones, 1998). This probe utilized two hemispherical quartz probes operating at different temperatures in order to measure the flow total temperature in a variety of compressible flows. Similar versions of this total temperature probe concept have since been used downstream of a high-pressure turbine stage (Buttsworth et al., 1998) and in a planar transonic turbine cascade (Cascallen et al., 1997). This thin film total temperature probe holds a number of advantages over the aspirating probe, including (*i*) a significantly higher bandwidth; (*ii*) robust construction; (*iii*) elimination of the need for a heat transfer law calibration; and (*iv*) ease of operation in compressible flows of arbitrary composition.

Successful operation of the thin film total temperature probe relies on the assumption that the flow seen by the heated and the unheated thin films is identical. If unsteady total temperature fluctuations are adequately characterized in terms of rms values, or if the unsteady flow is sufficiently periodic, then local total temperature fluctuations can be obtained by traversing the hot and cold films, which may be separated by a significant distance (Buttsworth and Jones, 1996). In general, however, for instantaneous time-resolved total temperature measurements, it is desirable to locate the hot and cold films as close as possible in order to resolve small-scale fluctuations accurately. The minimum film separation in previous applications has been approximately 3 mm (Buttsworth et al., 1998; Cascallen et al., 1997), which is of the same order as the spatial resolution of aspirating probe measurements. However, improvements in the spatial resolution of the thin film total temperature probe are possible, and it is the purpose of the current paper to demonstrate one of these techniques.

Probe Design and Operation

Principles of Operation. The transient heat flux measured by a thin film gage at the stagnation point of a probe can be written

$$q = h(T_t - T_w) \tag{1}$$

Therefore, it is possible to determine the convective heat transfer coefficient and the flow total temperature using two nominally identical transient heat flux probes operated at two different surface temperatures. That is,

$$h = \frac{q_1 - q_2}{T_{w2} - T_{w1}} \tag{2}$$

$$T_t = T_{w1} + q_1 \frac{T_{w2} - T_{w1}}{q_1 - q_2} \tag{3}$$

In essence, Eq. (3) describes the operation of the fast-response total temperature probe, which has been the subject of other investigations (Buttsworth and Jones, 1996; Buttsworth et al., 1998). The total temperature probe described in the present work again utilizes Eq. (3); however, instead of operating two probes at different temperatures, a single probe with two films at different temperatures is used.

Physical Details. A photograph and sketch of the total temperature probe are given in Fig. 1. The probe is essentially a hemispherically blunted cylinder with a radius of approximately 1.4 mm. The probe substrate is fused quartz, and two platinum thin films (of the dimensions given in Fig. 1) are located close to the stagnation point. The electrical leads for the thin films are a low resistance silver paint.

At room temperature, the resistances of the "hot" and "cold" films are approximately 44 Ω and 58 Ω, respectively, and the coefficients of resistance of the hot and cold films were determined (using a water calibration bath) to be 2.25×10^{-3} and 2.38×10^{-3} K^{-1}, respectively. Based on the dimensions shown in Fig. 1, the films lie within approximately 25 deg of the probe stagnation point.

Pulsed Heating Technique. In order to generate a significant temperature difference between the two films, a relatively large current (around 70 mA) is driven through the hot film. The cold film was operated in the usual transient thin film manner with a constant current of approximately 15 mA. However, in order to avoid a significant temperature rise at the cold film (which is in close proximity to the hot film), the hot film heating current is applied approximately 1 s before the flow commences. An example of the hot and cold film temperatures during this pulsed heating process is given in Fig. 2. It is clear

Nomenclature

A, B, C = coefficients describing convective heat flux distribution
c = specific heat of the substrate, $J \cdot kg^{-1} \cdot K^{-1}$
c_p = specific heat of the flow, $J \cdot kg^{-1} \cdot K^{-1}$
Ch = Chapman-Rubesin parameter
d = displacement or distance relative to the jet centerline
D = diameter of the probe
h = convective heat transfer coefficient, $W \cdot m^{-2} \cdot K^{-1}$
k = conductivity of the flow or substrate, $W \cdot m^{-1} \cdot K^{-1}$
K = stagnation point velocity gradient
M = Mach Number
Nu = Nusselt number
p = pressure
Pr = Prandtl number
q = surface heat transfer rate, $W \cdot m^{-2}$
Q = heat transfer per unit volume, $W \cdot m^{-3}$
r = radial coordinate from center of the probe
r = recovery factor = $Pr^{0.5}$ for a laminar flow
R = radius of the probe, radius of curvature
R = specific gas constant, $J \cdot kg^{-1} \cdot K^{-1}$
R_0 = heat penetration radius
t = time, usually from the start of the heat transfer
T = temperature, K
T_r = flow recovery temperature
T_t = flow total temperature
u = flow velocity
x = distance from injection, or around probe from stagnation point
α = thermal diffusivity of substrate material = $k/\rho c$, $m^2 \cdot s^{-1}$
γ = ratio of specific heats
θ = angle from either stagnation point or thin film location, rad
μ = viscosity, Pa · s
ρ = density of the flow or substrate material

Subscripts

e = boundary layer edge
f = value at the temperature sensing film
l = heat transfer in lateral direction
n = heat transfer normal to the probe surface
pit = pitot pressure
t = total (convective) heat transfer
w = value at probe surface (local film value)
1 = hot probe
2 = cold probe
∞ = value in the undisturbed free stream

Superscripts

o, i, ii = successive approximations in the lateral conduction correction

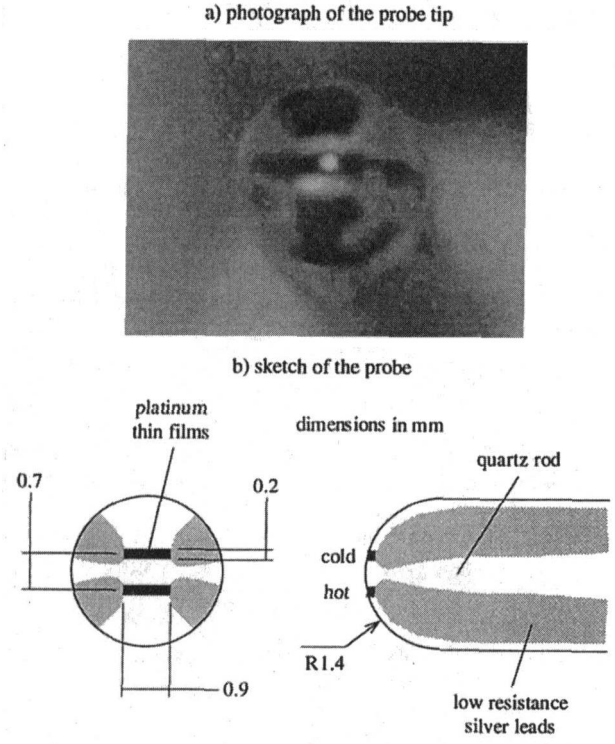

Fig. 1 Configuration of the total temperature probe

that after a delay of around 50 ms, the temperature of the cold film begins to increase due to the lateral conduction of heat away from the hot film (Fig. 2). However, the temperature difference between the two films remains constant at around 120 K from approximately 200 ms after the start of the heating.

Hot film temperature measurements are obtained using the configuration shown in Fig. 3. For convenience, the hot film current is obtained using the constant current supplies from two heat transfer analogue units (Oldfield et al., 1982) operated in parallel. Prior to a run, the film bypass switch remains closed. The offset voltage (see Fig. 3) is chosen so that when the bypass switch is opened, the amplified film voltage signal falls within the voltage range of the A/D unit. On opening the bypass switch, the magnitude of the current supply (which changes slightly with the addition of the extra film resistance), is determined by measuring the voltage drop across the known resistance. (The film bypass switch remains open for the duration of run.) The hot film temperature is thus determined from the film current and voltage measurements, the coefficient of resistance, and the measured ambient resistance of the film.

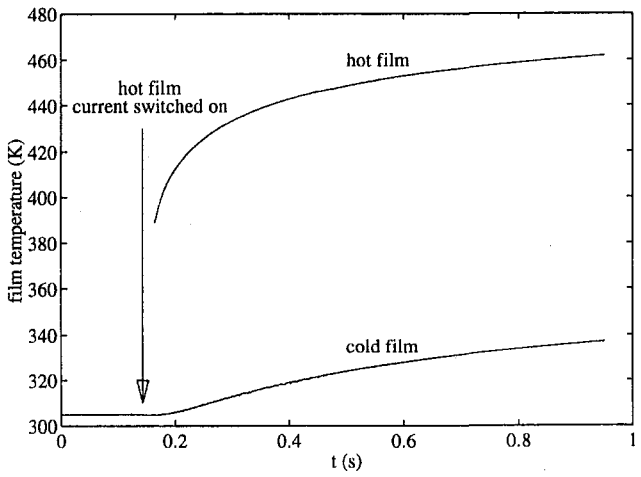

Fig. 2 Temperature measurements from the hot and cold films during the prerun pulsed heating

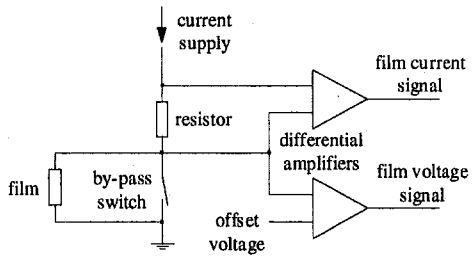

Fig. 3 Arrangement for film heating with simultaneous film temperature measurement

Stagnation Point Flow. In principle, the present temperature probe measures the flow *total temperature,* rather than a *recovery temperature,* because the flow velocity at the probe stagnation point is negligible. Thus, the measured transient heat flux is driven by the difference between the flow total temperature and the local film temperature. However, due to the finite film dimensions, transient heat flux measurements cannot be obtained exactly at the stagnation point. It is therefore important to quantify the influence that off-stagnation point operation will have on the total temperature measurements.

The boundary layer heat transfer process at locations away from the stagnation point will be driven by the difference between a flow recovery temperature and the wall temperature. Since it may be assumed that the flow at the edge of the boundary layer undergoes an isentropic acceleration around the hemisphere, the recovery temperature may be written

$$\frac{T_r}{T_t} = r + (1 - r)\cdot\left(\frac{p_e}{p_{pit}}\right)^{(\gamma-1)/\gamma} \tag{4}$$

Using the measured variation of static pressure around hemispheres (e.g., Korobkin and Gruenewald, 1957), it is possible to evaluate Eq. (4), giving the results shown in Fig. 4. For the limiting case of hypersonic flow ($M \rightarrow \infty$, which is also shown in Fig. 4), the variation of static pressure near the stagnation point was obtained from the Newtonian approximation,

$$\frac{p_e}{p_{pit}} = \cos^2\theta \tag{5}$$

which has been verified experimentally (e.g., Kemp et al., 1959).

In the present work, the thin film gages were within 25 deg of the stagnation point, and thus the measured temperature (an integrated temperature between 0 and 25 deg in Fig. 4) will certainly be within 1 percent of the flow total temperature. Therefore, it appears reasonable to claim that the probe measures the flow *total* temperature.

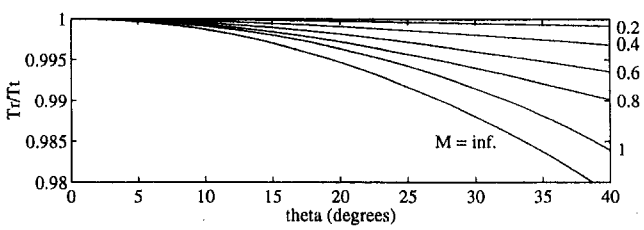

Fig. 4 Predicted variation of flow recovery temperature around the probe for different Mach number flows

Lateral Conduction Effects. Although there is only a slight variation in the recovery temperature close to the stagnation point (Fig. 4), the convective heat flux around the probe can vary significantly due to lateral variations in both the convective heat transfer coefficient, and the surface temperature of the probe. Lateral variations in the convective heat flux will alter the lateral temperature gradients and thus give rise to additional lateral conduction effects. To determine the magnitude of the lateral conduction, the heat diffusion equation for a hemispherical substrate with constant thermal properties is written,

$$k\frac{\partial^2 T}{\partial r^2} + k\frac{2}{r}\frac{\partial T}{\partial r} + k\frac{2}{r^2}\frac{\partial^2 T}{\partial \theta^2} = \rho c\frac{\partial T}{\partial t} \tag{6}$$

The third term on the left-hand side of Eq. (6) can be equated to the lateral heat transfer per unit volume,

$$Q_l = k\frac{2}{r^2}\frac{\partial^2 T}{\partial \theta^2} \tag{7}$$

The normal heat transfer per unit volume will then be given by

$$Q_n = k\frac{\partial^2 T}{\partial r^2} + k\frac{2}{r}\frac{\partial T}{\partial r} \tag{8}$$

with the total (convective) heat transfer per unit volume being simply,

$$Q_t = \rho c\frac{\partial T}{\partial t} \tag{9}$$

To obtain the total convective heat flux at the surface, Eq. (9) can be integrated between the surface, $r = R$ and the location corresponding to the heat penetration depth, $r = R_0$. That is,

$$q_t = \int_{R_0}^{R} Q_t \cdot dr = \rho c\int_{R_0}^{R}\frac{\partial T}{\partial t}\,dr \tag{10}$$

To obtain the total lateral heat conduction per unit surface area, Eq. (7) can be similarly integrated,

$$q_l = \int_{R_0}^{R} Q_l \cdot dr = 2k\int_{R_0}^{R}\frac{1}{r^2}\frac{\partial^2 T}{\partial \theta^2}\,\mathrm{dr} \tag{11}$$

Assuming the heat penetrates only a small distance relative to the radius of curvature (i.e., for $R_0 \approx R$), Eq. (11) may be written

$$q_l = \frac{2\alpha}{R^2}\int_{R_0}^{R}\rho c\frac{\partial^2 T}{\partial \theta^2}\,dr \tag{12}$$

Now the temperature at any point in the substrate can be written

$$T(t) = \int_0^t \frac{\partial T}{\partial \tau}\,d\tau \tag{13}$$

Thus, by substituting Eq. (13) into Eq. (12) and changing the order of integration, the lateral conduction per unit of surface area is

$$q_l = \frac{2\alpha}{R^2}\int_0^t \frac{\partial^2}{\partial \theta^2}\int_{R_0}^{R}\rho c\frac{\partial T}{\partial \tau}\,dr\cdot d\tau \tag{14}$$

which, with the aid of Eq. (10), can therefore be written

$$q_l = \frac{2\alpha}{R^2}\int_0^t \frac{\partial^2 q_t}{\partial \theta^2}\cdot d\tau \tag{15}$$

It is assumed that the convective heat flux distribution can be modeled reasonably well by a parabolic distribution such as,

$$\frac{q_t(\theta)}{q_f} = A + B\theta + C\theta^2 \tag{16}$$

(which is a good approximation in the case of a hemisphere with a sensibly uniform surface temperature distribution; Schultz and Jones, 1973). Therefore,

$$q_l = 4C\cdot\frac{\alpha}{R^2}\int_0^t q_f\cdot d\tau \tag{17}$$

Provided the lateral conduction remains a small fraction of the total convective heat flux, the actual value of q_f can be approximated in the first instance (q_f^o), by the value inferred from the direct (one dimensional) analysis of the measured temperature history. Thus, a better estimate (q_f^i) of the total convective heat flux at the film can be written,

$$q_f^i = q_f^o - 4C\cdot\frac{\alpha}{R^2}\int_0^t q_f^o\cdot d\tau \tag{18}$$

If necessary, Eq. (18) can be used in an iterative manner until convergence is achieved (e.g., for the next estimate of the actual convective heat flux at the film (q_f^{ii}), q_f^i would replace q_f^o within the integral on the right-hand side of Eq. (18)).

Compressible Free Jet Experiments

Apparatus and Flow Conditions. As a demonstration of the pulsed total temperature probe technique, experiments were performed using the free jet arrangement shown in Fig. 5. The contoured Mach 4 injection nozzle had a throat diameter of 9.42 mm and was designed using the method of characteristics. The nozzle exit diameter was 29.5 mm and the lip thickness was 0.5 mm. The injection nozzle was located in the test section of the University of Oxford gun tunnel facility. Either nitrogen or hydrogen was supplied to the Mach 4 nozzle from a Ludwieg tube, which was initially at room temperature. Prior to a run, the working section was evacuated to approximately 1.2 kPa, and the slug of gas in the Ludwieg tube was isolated from the working section by a fast-acting valve.

The probe (initially located above the centerline of the free jet) was driven across the jet (at a speed of approximately 1.7 $\mathrm{m\cdot s^{-1}}$) after the fast-acting valve was opened (see Fig. 6). The Ludwieg tube filling pressure was chosen so that when the probe traversed the free jet, the static pressure measured close to the exit of the Mach 4 nozzle was approximately the same as the initial background static pressure in the test section. It was difficult to achieve a perfect match between the injection static pressure and the static pressure of the air within the test section because the jet flow caused a pumping effect, which lowered the test section static pressure.

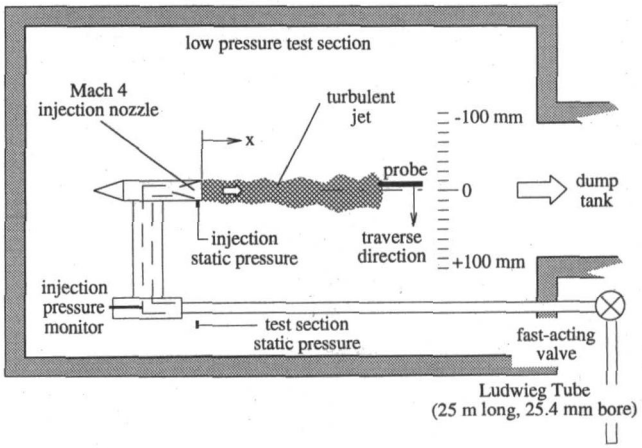

Fig. 5 Illustration of the experimental arrangement for the compressible free jet experiments (not to scale)

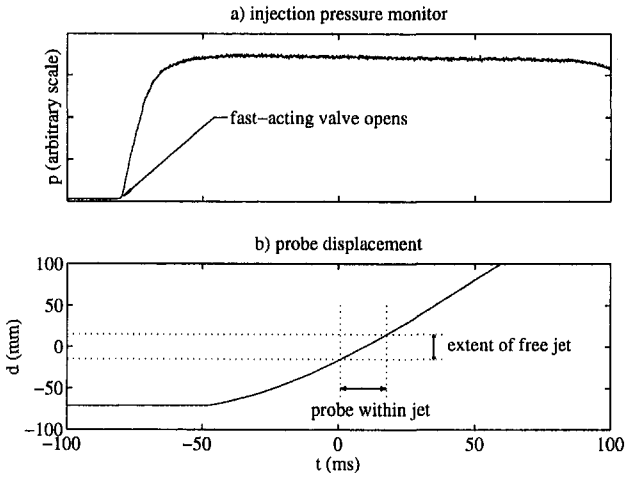

Fig. 6 Typical facility measurements for a nitrogen injection run (traverse at $x = 3$ mm)

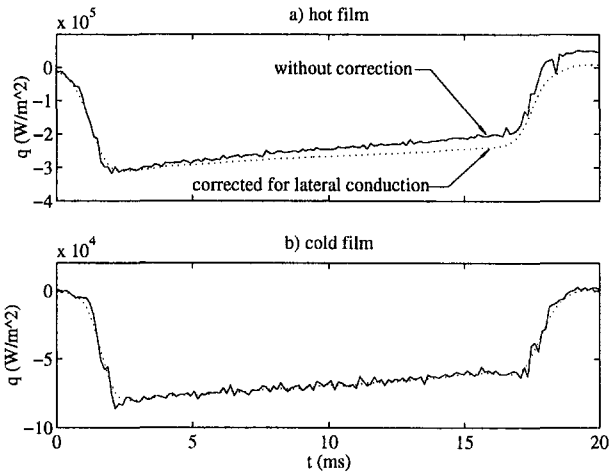

Fig. 8 Heat flux measurements derived from the temperature histories shown in Fig. 7 (hydrogen injection, traverse at $x = 3$ mm)

Analysis. Temperature measurements from the hot and the cold films for the case of hydrogen injection with a probe traverse at $x = 3$ mm are given in Fig. 7. It will be noticed that both the hot and cold film temperatures are increasing (due to the ohmic heating of the hot film) immediately prior to the probe entering the free jet. The heat diffusion equation that governs the operation of transient thin film heat flux gages is linear. Thus, the temperature change of interest (the temperature change due to the convective heat flux) is obtained by determining the temperature rise due to ohmic heating (the dotted line) and subtracting this from the measured film temperature history (the solid line).

Convective heat transfer rates are determined for the hot and cold films using a finite difference routine, which analyzed the temperature difference histories discussed above. (The finite difference routine was originally developed to account accurately for variable thermal property and curvature effects. Although the temperature changes and the time scales are not large enough in the present experiments for such effects to be significant, the finite difference routine still provided a convenient method of analysis.) For the temperature measurements in Fig. 7, the resulting convective heat transfer rate data are presented in Fig. 8.

In the case of the hot film, the convective heat flux level on the lower side of the free jet appears to be positive (see the solid line in Fig. 8(a) in the region, $t > 18$ ms). This apparent convective heat flux arose due to lateral conduction effects. To correct the measurements for lateral conduction effects, the value of C in Eq. (18) is chosen so that the corrected value of convective heat flux returns to zero when the probe reaches the lower jet boundary (see the dotted line in Fig. 8(a)). For the hot film, the necessary value of C varied from run to run but was generally around -3, whereas for the cold film, very little correction was required at all (see Fig. 8(b)).

The need to correct the results for lateral conduction arises because the temperature gradients associated with the pulsed heating technique give rise to significant lateral gradients in the convective heat flux. The *direct* effects of the temperature gradients associated with the pulsed heating are eliminated by only analyzing the temperature changes associated with the convective heating as discussed previously. However, it is the induced convective heat flux gradients that generate the additional temperature gradients responsible for the lateral conduction effects.

Successful operation of the pulsed total temperature probe is verified by a number of consistency checks. First, the flow total temperature measured by the probe is very close to the anticipated level (Fig. 9). Furthermore, values of the convective heat transfer coefficient, indicated by an individual analysis of temperature and heat flux histories from hot and cold films, are in close agreement. (Analysis of the nitrogen and hydrogen measurements at $x = 3$ mm indicates individual values of h from the hot and cold films within ± 2 percent of the mean value.) These results indicate that the basic operating principles and transient heat transfer analysis are valid. Finally, because the indicated total temperature (Fig. 9) remains essentially constant with time, it is concluded that the lateral conduction correction is indeed reasonable.

Results. Measurements of the convective heat transfer coefficient (obtained using Eq. (2)) at equal distances either side of the jet centerline were averaged to give the results in Fig.

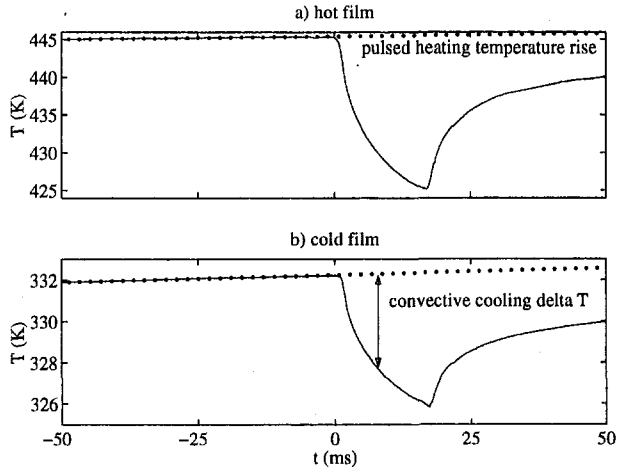

Fig. 7 Measurements of the hot and the cold film temperatures (hydrogen injection, traverse at $x = 3$ mm)

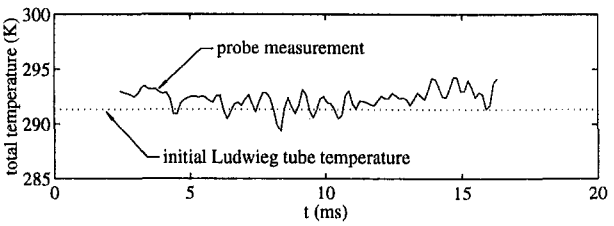

Fig. 9 Total temperature measurement (the solid line) for hydrogen injection with the probe traverse at $x = 3$ mm

10. (Thus, the results in Fig. 10 are symmetric). The results for both the nitrogen and hydrogen injection demonstrate the usual form of spreading anticipated for a jet flow. The core flow region appears to be entrained into the mixing layer somewhat earlier in the case of the hydrogen injection. It may also be observed that the magnitude of the convective heat transfer coefficient for the hydrogen jet was significantly larger than for the nitrogen jet (note that the scale in part (b) is five times larger than the scale in part (a)).

The steady convective heat transfer coefficient at the stagnation point of a hemisphere can be expressed as

$$\mathrm{Nu} = 0.763\ \mathrm{Pr}^{0.4}\ \mathrm{Re}^{0.5}\mathrm{Ch}^{0.1}\sqrt{\frac{KD}{u_\infty}} \tag{19}$$

where

$$\mathrm{Nu} = \frac{hD}{k_e},\quad \mathrm{Pr} = \frac{c_p\mu_e}{k_e},\quad \mathrm{Re} = \frac{\rho_e u_\infty D}{\mu_e},$$

$$K = \frac{du_e}{dx},\quad \mathrm{Ch} = \frac{\rho_w\mu_w}{\rho_e\mu_e} \tag{20}$$

On evaluating this expression for nitrogen and hydrogen flows with the same total pressure and temperature, it is found that $h_{H2}/h_{N2} \approx 5.0$. Probe measurements in the core flow of the jet (Fig. 10 at x = 3 mm) indicate a ratio very close to this value. Thus, in future experiments, it will be possible to use convective heat transfer coefficient measurements from the total temperature probe to determine the composition of a binary gas mixture, provided independent measurements of pitot pressure and static pressure are available. Likewise, the convective heat transfer coefficient measurements could also be used (with a calibration such as Eq. (19)) to determine other flow properties such as the mass flux ($\rho_\infty u_\infty$) in a manner similar to such measurement obtained using thin wire anemometry.

Total temperature measurements from the present experiments are given in Fig. 11. The results demonstrate that at each traverse location, the total temperature remains virtually constant across the majority of the jet width. In each case, the measured temperature was approximately equal to the ambient temperature of the gas in the Ludwieg tube. Total temperature results have not been presented for the outer regions of the free jets, since in these regions, the convective heat flux from both the hot and cold probes approaches zero. The present method cannot be used to determine the temperature in a static fluid, or in an environment in which the convective heat flux from both the hot and cold probes is close to zero, because in such cases, the second term in Eq. (3) approaches infinity. Thus, when the convective heat flux at both films approaches zero, even a small amount of noise on either the hot or cold heat flux signal will result in large (erroneous) total temperature fluctuations. There is no such restriction on measurement of the probe's convective heat transfer coefficient since the hot and cold film convective heat fluxes appear only in the numerator of Eq. (2).

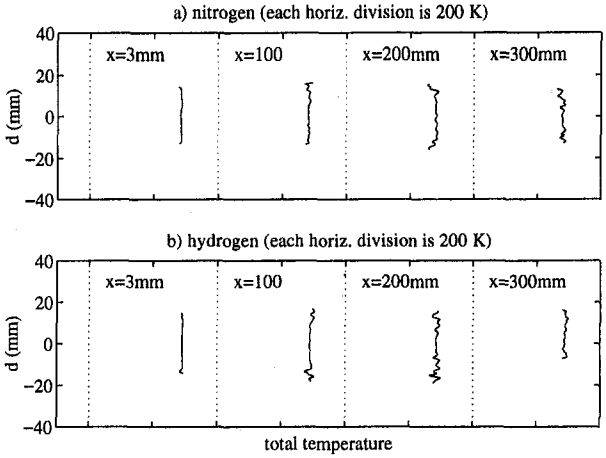

Fig. 11 Total temperature results

As a demonstration of the probe's capacity for fluctuation measurements in high-speed turbulent flow, the probe was again operated in the free jet, this time with both films at approximately the same temperature. Figure 12 presents the fluctuating component of the heat flux measurements from both of the films. These signals were obtained directly from the electrical analogues of the heat transfer process (Oldfield et al., 1982). These heat transfer analogues have a −3 dB point around 85 kHz. In principle however, measurements at even higher frequencies are possible with the present device because, for typical gas turbine flow conditions, the stagnation point boundary layer will respond in a quasi-steady manner to fluctuations at frequencies well beyond 100 kHz. The measurements in Fig. 12 indicate that occasionally, there are small differences between the two heat flux signals. These differences may be attributed to the finite separation of the two films. However, there is generally a very good correlation between the heat flux signals from the two films. Thus, it is anticipated that useful turbulence measurements may be obtained with the probe.

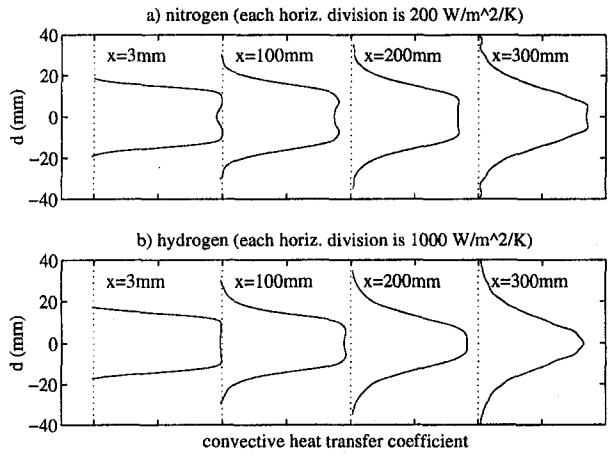

Fig. 10 Convective heat transfer coefficient results

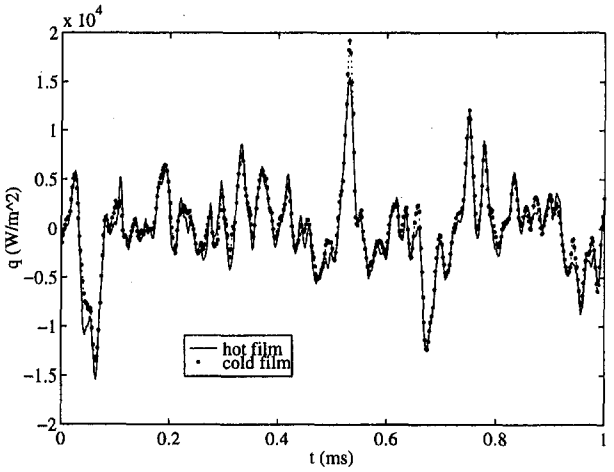

Fig. 12 Example of the high-frequency component of the heat flux signals from the total temperature probe

Conclusions

The present work demonstrates a technique that can be used to measure the flow total temperature in situations where fast-response (around 100 kHz) and high spatial resolution (around 1 mm) measurements are required. The total temperature device utilizes two transient thin film heat flux gages located close to the stagnation point of a hemispherically blunted fused quartz probe. The required temperature difference between the two films is generated using a pulsed ohmic heating technique. Transient heating effects associated with the pulsed ohmic heating do not inhibit the analysis of the transient temperature changes associated with the convective heat transfer. However, it is necessary to correct the transient convective heat flux measurements for lateral conduction effects. A procedure to achieve this correction has been developed and is shown to yield accurate results. High-speed turbulent free jet experiments demonstrate that accurate total temperature and convective heat transfer coefficient measurements having a high temporal and spatial resolution can be obtained using the present device.

Acknowledgments

Thanks are due to Trevor Godfrey for his skill and care in manufacturing the total temperature probe.

References

Alday, J., Osborne, D. J., Morris, M. B., Ng, W., and Gertz, J., 1993, "Flow Randomness and Tip Losses in Transonic Rotors," ASME Paper No. 93-GT-189.

Boutrif, M. S., and Thelliez, M., 1995, "Determination of Flow Temperature by Using the Two Thermocouples Experimental Technique. Application for the Exhaust Flow Gas Engine," *Revue Generale de Thermique,* Vol. 34, No. 400–401, pp. 263–271.

Bremhorst, K., and Graham, L. J. W., 1990, "A Fully Compensated Hot/Cold Wire Anemometer System for Unsteady Flow Velocity and Temperature Measurements," *Meas. Sci. Technol.,* Vol. 1, pp. 425–430.

Buttsworth, D. R., Jones, T. V., and Chana, K. S., 1998, "Unsteady Total Temperature Measurements Downstream of a High Pressure Turbine," ASME JOURNAL OF TURBOMACHINERY, in press.

Buttsworth, D. R., and Jones, T. V., 1998, "A Fast-Response Total Temperature Probe for Unsteady Compressible Flows," ASME *Journal of Engineering for Gas Turbines and Power,* in press.

Carscallen, W. E., Hogg, S. I., Gostelow, J. P., and Buttsworth, D. R., 1997, "Time Resolved Total Temperature Measurements in Transonic Turbine Vane Wake Flows," AGARD 81st Fluid Dynamics Panel Symposium on Advanced Aerodynamic Measurement Technology, Sept., Seattle, WA.

Denos, R., and Sieverding, C. H., 1997, "Assessment of the Cold Wire Resistance Thermometer for High-Speed Turbomachinery Applications," ASME JOURNAL OF TURBOMACHINERY, Vol. 119, pp. 140–148.

Kemp, N. H., Rose, P. H., and Detra, R. W., 1959, "Laminar Heat Transfer Around Blunt Bodies in Dissociated Air," *J. Aero/Space Sci.,* Vol. 26, pp. 421–430.

Korobkin, I., and Gruenewald, K. H., 1957, "Investigation of Local Laminar Heat Transfer on a Hemisphere for Supersonic Mach Numbers at Low Rates of Heat Flux," *J. Aeronautical Sci.,* Vol. 24, pp. 188–194.

Lomas, C. G., 1986, *Fundamental of Hot Wire Anemometry,* Cambridge University Press.

Ninnemann, T. A., and Ng, W. F., 1992, "A Concentration Probe for the Study of Mixing in Supersonic Shear Flows," *Experiments in Fluids,* Vol. 13, pp. 98–104.

Ng, W. F., and Epstein, A. H., 1983, "High-Frequency Temperature and Pressure Probe for Unsteady Compressible Flows," *Rev. Sci. Instrum.,* Vol. 54, No. 12, pp. 1678–1683.

Oldfield, M. L. G., Burd, H. J., and Doe, N. G., 1982, "Design of Wide-Bandwidth Analogue Circuits for Heat Transfer Instrumentation in Transient Wind Tunnels," *Proc. 16th Symp. of International Centre for Heat and Mass Transfer,* Hemisphere Publishing, pp. 233–257.

Schultz, D. L., and Jones, T. V., 1973, "Heat-Transfer Measurements in Short-Duration Hypersonic Facilities," AGARDograph No. 165.

Smout, P. D., and Cook, S. C., 1996, "Simple Instrumentation Rake Designs for Gas Turbine Engine Testing," ASME Paper No. 96-GT-32.

Suryavamshi, N., Lakshminarayana, B., and Prato, J., 1998, "Aspirating Probe Measurements of the Unsteady Total Temperature Field Downstream of an Embedded Stator in a Multistage Axial Flow Compressor," ASME JOURNAL OF TURBOMACHINERY, Vol. 120, pp. 156–169.

Van Zante, D. E., Suder, K. L., Strazisar, A. J., and Okiishi, T. H., 1995, "An Improved Aspirating Probe for Total-Temperature and Total-Pressure Measurements in Compressor Flows," ASME JOURNAL OF TURBOMACHINERY, Vol. 117, pp. 642–649.

A High-Temperature Assessment of Air-Cooled Unsteady Pressure Transducers

D. G. Ferguson

P. C. Ivey

School of Mechanical Engineering,
Cranfield University,
Bedfordshire, United Kingdom

This paper discusses the problem of measuring unsteady pressure in a high-temperature environment using standard transducers. Commercially available cooling adapters for these transducers use water as the cooling medium to provide thermal protection. This arrangement is suitable only for some test bed applications and not suitable for integration into in-flight active control systems. An assessment of the cooling effectiveness of a commercial water-cooled adapter using air as the cooling medium is presented using an experimentally validated finite element heat transfer model. The assessment indicates survival of an air-cooled transducer, itself rated to 235°C, at source flow temperatures up to 800°C.

Introduction

There is a continuing need to have an accurate measurement of unsteady pressure in environments whose temperature far exceeds that of the maximum operating temperature of the current commercially available high-temperature transducers. Such a measurement has application for safety monitoring of gas turbine engines, both test bed and in-flight engines, and validation of numerical models, especially in the turbomachinery field. There are three approaches to the problem: develop a transducer to survive at the required temperature, mount the transducer remote from the environment, and compensate for the degradation in the measurement or thermally protect the in situ transducer. At present, the approach using thermal protection has been identified as the most cost effective and with the greatest potential for transducer survival at temperatures typical of a gas turbine engine.

Ferguson and Ivey (1995) assessed the extent of thermal protection given to a transducer using two commercially available water cooling adapters when measuring the unsteady pressure of a high-temperature flow. Survival of a transducer, rated up to 235°C, was proven at 600°C and it was indicated that there was great potential for survival at still higher temperatures using water cooling. The use of water as a cooling medium is acceptable, to an extent, for test bed applications, but for possible future integration into an in-flight active control system for a gas turbine aero-engine the cooling medium is required to be air.

A gas is rarely favored as a coolant because of its inferior heat transfer properties relative to liquid and, as a result, little evidence of its use can be found in the open literature. However, Harman (1968) used hydrogen or helium to cool the strain gages in a rocket combustion chamber. However, to achieve sufficient cooling, a shield of coolant over the front of the strain gage was required. Consequently the accuracy of the unsteady pressure measurement could be compromised by this "film cooling" technique.

There was therefore a need to conduct a high-temperature assessment of an air-cooled unsteady pressure transducer suitable for application in a gas turbine engine.

Method

The main objective of this study was an assessment of air as a cooling medium for thermally protecting commercially available pressure transducers. For use in high-temperature environments, typical of that experienced in gas turbine engines, a better understanding of the heat transfer process inside the cooling adapter was required. A Finite Element heat transfer model of the cooling adapter, validated by a detailed experimental study, satisfied this requirement. The model simulated cooling using both water and air as the coolant and was flexible to allow parametric studies over a wide range of differing conditions and applications. A commercially available transducer (Kulite XTE-190) and its cooling adapter were used for the validation study.

Modeling

Geometric Modeling. It was decided to include the hot gas, the pipe wall of the test rig, the cooling adapter, the coolant and the surrounding atmosphere within the problem domain to be analyzed. It was anticipated that all these aspects would have some influence on the heat transfer processes to be modeled.

The cooling adapter was assumed to be axisymmetric in a circumferential direction and symmetric about an axis running longitudinally through the transducer. Refer to Fig. 1 for the complete solution domain.

The model only considered one half of one "slice" of the cooling adapter. This greatly reduced the time and computational resource required for both the model creation and analysis.

The grid density was increased at all surfaces where boundary effects occur (boundaries between metal, coolant, and the hot gas) to increase the accuracy of the prediction where the largest thermal gradients were expected. In addition, the sides of adjacent "boundary" elements were superimposed onto the actual problem boundary, defining a mathematical boundary at the geometric boundary. This style of grid density definition is almost universally accepted as a requirement to accommodate for the large changes in material properties and characteristics at these locations (see Patankar (1978) and Taylor et al. (1992)).

Mathematical Modeling. The phenomenon under investigation, heat transfer, is well understood. It has three specific modes: conduction, convection, and radiation. The time constraint placed on the development of the model meant that it was assumed that the effect of radiation would be relatively small and could be neglected (a simple study of this application showed that radiated heat was less than 10 percent of the total heat transferred into the cooling adapter) and that a steady-state model was felt sufficient to fulfill the objectives within this

Contributed by the International Gas Turbine Institute and presented at the 42nd International Gas Turbine and Aeroengine Congress and Exhibition, Orlando, Florida, June 2–5, 1997. Manuscript received at ASME Headquarters February 1997. Paper No. 97-GT-6. Associate Technical Editor: H. A. Kidd.

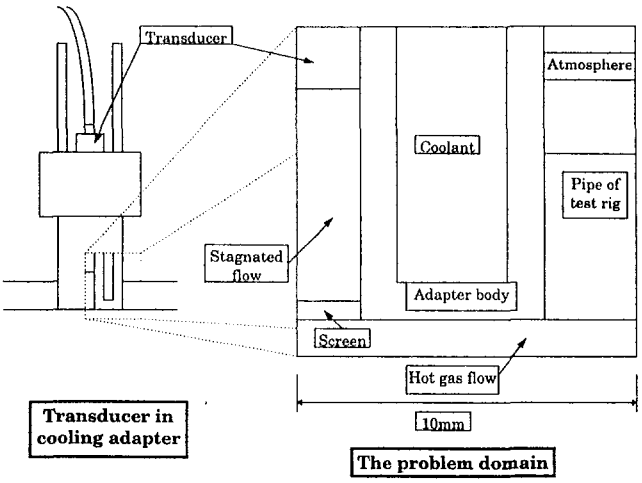

Fig. 1 Problem domain

research program. The governing equation for the two remaining modes of heat transfer is as follows (from Patankar, 1978):

$$-\rho u \frac{\partial T}{\partial x} + \rho v \frac{\partial T}{\partial y} + kx \frac{\partial^2 T}{\partial x^2} + ky \frac{\partial^2 T}{\partial y^2} + \bar{Q} = 0 \qquad (1)$$

where the first two terms are for convection, the second two for conduction, and the final represents a heat source. k is the thermal conductivity of a material, ρ is the fluid density and u and v are fluid velocities in the x and y directions, respectively.

Using the Galerkin weighted-residual method (see El-Zafrany, 1994), an integral equation can be derived from Eq. (1). Integrating using the integration by parts theorem, the second-order differential equations can be reduced to first-order differential equations with the penalty of introducing boundary integral terms as follows:

$$\iint_\Omega \delta T \frac{\partial g}{\partial (x/y)}\, dxdy \equiv \oint_\Gamma \delta T g (l/m) d\Gamma - \iint_\Omega \frac{\partial (\delta T)}{\partial x}\, g dxdy = 0 \qquad (2)$$

where Ω is the domain, Γ is the domain boundary, and

$$l = \frac{dy}{d\Gamma}, \quad m = -\frac{dx}{d\Gamma}, \quad g = k\frac{\partial T}{\partial x}, \quad k\frac{\partial T}{\partial y} \qquad (2a)$$

There are three possible conditions for the boundary integral (Γ), where the boundary temperature T is prescribed (Γ_T), or is insulated so that the temperature gradient normal to the boundary is zero (Γ_q), or there is a heat flux to the fluid (Γ_f) governed as follows:

$$-k\frac{\partial T}{\partial n} = h(T - T_\alpha) \qquad (3)$$

where T_α is the temperature of the bulk fluid into which the heat is transferring, n is a vector normal to the boundary, and h is called the "film coefficient," which encompasses both conduction and convection (conjugate heat transfer) away from the boundary.

Using Eq. (3) as the boundary integral expression and integrating again, the variational statement is derived. This expresses the variation of temperature over the whole problem domain.

The approximate trial function solution for the temperature, T, for each node of a single element of the whole domain is as follows:

$$T(x, y) = \sum_{i=1}^{nn} T_i N_i(x, y) \qquad (4)$$

where i is the node number, nn is the total number of nodes in the element, and N denotes the node interpolation function. Substituting the trial function solution, Eq. (4), into the variational statement and, for the purpose of reporting clarity considering the first term of the variational statement (convection) only, collecting terms gives

$$-\sum_{i=1}^{nn} \iint_{\text{element}} \rho \delta T_i N_i \left(u \frac{\partial N_i}{\partial x} + v \frac{\partial N_j}{\partial y} \right) T_j dxdy \equiv -\delta T' KCT \qquad (5)$$

This is the variation of temperature, due to convection, over a particular element where δT is a matrix of the order $1 \times n$. $[\delta T_1, \delta T_2, \ldots \delta T_n\}$, T is a matrix of the order $n \times 1$ $[T_1, T_2, \ldots T_n]$ and KC is the convection matrix of the element ($n \times n$) as follows,

$$KC_{ij} = \iint_{\text{element}} \rho N_i \left(u \frac{\partial N_i}{\partial x} + v \frac{\partial N_j}{\partial y} \right) dxdy \qquad (6)$$

Following the same procedure as Eqs. (5) and (6) for the remaining domain terms in the variational statement (conduction term (K), heat source term (N_q) and boundary heat transfer terms (C and N_α) the following matrix expression can be derived:

$$\delta T'[(-K - KC - C)T + N_\alpha + N_q] = 0 \qquad (7)$$

Rearranging Eq. (7) gives,

$$(K + KC + C)T = N_\alpha + N_q \qquad (8)$$

Equation (8) is the generic element equation indicating the variation of temperature over an element, T is the temperature that is required in the solution, $(K + KC + C)$ is the "stiffness" or proportionality matrix of the element and represents the three types of heat transfer under consideration; conduction (K), convection (KC), and boundary or conjugate heat transfer (C). N_q is a heat source term that can be neglected in this analysis and N_α is a term related to the boundary heat transfer. The only remaining requirement was to recognize what forms of heat transfer will take place in which element. The explicit element equation could then be derived for each element including only the terms relevant to the material and its position in the domain. For example, only conduction occurs in the solid metal of the cooling adapter walls (matrix Eq. (8) becomes $KT = 0$) but conduction and boundary heat transfer occurs at the solid/fluid boundary where the metal adapter meets the coolant (Eq. (8) becomes $[K + C]T = N_\alpha$).

All the variables within the analysis can be prescribed at start, or were numerically approximated during the analysis, except for two. The two that could not easily be prescribed were associated with the boundary heat transfer to and from a moving fluid. They were the heat transfer or film coefficient, h, and the bulk material temperature T_α.

The problem of estimating these values, h in particular, is one faced by all authors investigating conjugate heat transfer. The normal procedure followed is to perform a separate Computational Fluid Dynamics (CFD) analysis of the fluid flow in the domain in the first place. From this the bulk gas or liquid temperature and the heat transfer coefficients near the boundaries at any place can be derived. The information from the CFD analysis is then used as the boundary conditions for a finite element analysis to derive the temperature distribution across the whole domain. An example of this procedure is given by Lebail and Popp (1993). This procedure is lengthy because it involves two separate analyses and is also somewhat inaccurate. Russell et al. (1993) have highlighted discrepancies between CFD and experimental analyses. The error is based on the use

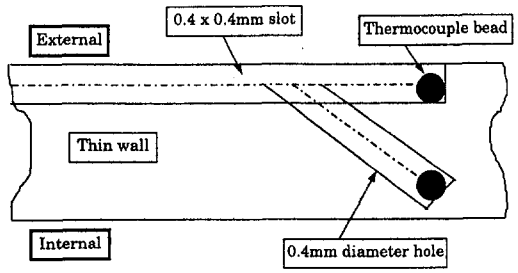

Fig. 2 Method of surface temperature measurement

of a "near-wall function" to approximate the heat transfer in the boundary layer based on flow conditions and empirical relationships derived from generic experimental data.

Time was not available here for an additional CFD analysis of the coolant and hot gas flow. Instead it was decided to use "typical" generic heat transfer coefficients given by Bayley et al. (1972) for certain material interfaces and approximate the bulk material temperatures based on the position within the problem domain relative to the hot gas and coolant inlet (the prescribed boundary conditions).

Using a prescribed value for h limits the application of the model. The pressures experienced in a modern gas turbine are an order of magnitude higher than those used in the test rig for model validation. The greater pressures would increase the heat transferred from the hot gas to the cooling adapter. To appreciate this, the model has two "setups": an engine setup and a test rig setup where the prescribed value for heat transfer coefficient are based on the differing flow conditions of the hot gas in each case. The test rig setup was used for the model validation process.

Experimental Validation

Some form of validation of all finite element models is required at certain conditions before the results from other conditions can be used with any confidence. The extent of the accuracy of the model, due to the nature and number of assumptions and approximations used, can be assessed by the validation process. The extent of the model's accuracy, when known, can then be accounted for when results are interpreted.

Several standard fundamental mathematical tests were carried out successfully on the model initially, but this analysis was totally novel and as a result no relevant experimental data were available for validation. A specific experiment therefore had to be designed. The task was to produce a similar temperature distribution across the cooling adapter experimentally, as created by the model. The comparison of model output and experimental data formed the model validation.

Experimental Apparatus. The test rig used was an in-line combustor rig, compressed air passed through the combustor where it was heated to the required temperature. It then flowed past the transducer in a cooling adapter that was mounted in a boss in the side of the pipe about ten pipe diameters downstream from the combustor exit. The heated air then exited to atmosphere. The rig capabilities were as follows: mass flow rate, up to 1.5 kg/s; maximum pressure, 317.2 kPa g; temperature range, ambient up to 800°C.

The cooling adapter was machined to allow thermocouple measurement of the temperature distribution. From the temperature contours indicated by the output of the model, it was decided that measurements of temperature would ideally be taken at many places on the inner and outer walls of the coolant chamber, the temperature of the coolant at different heights, and the temperature of the "stagnated" flow in front of the transducer. The measurement of the wall temperatures in thin-walled components was done in accordance with Rolls-Royce Instrumentation Standards and Techniques (1988) normally applied to the measurement of surface temperatures of cooled turbine blades. The method was as shown in Fig. 2 and was used for the measurements on all the coolant chamber walls. However, no measurements could be taken on the inside wall because the machining required was physically impossible. It was assumed that the validation of the prediction of heat transfer across the outer and lower walls of the coolant chamber would be sufficient.

Each slot for the thermocouple lead out had to be machined in a different circumferential position to be physically feasible. The temperatures were expected to be relatively axisymmetric and so, for ease of validation, all measurements were assumed to appear all in the same plane. The coolant temperatures were achieved by "hanging" the thermocouples in the coolant at different heights in a very thin-walled tube to maintain its position. The temperature of the stagnated flow, in the recess in front of the transducer, was measured in similar way. The Kulite XTE-190 transducer was replaced by a stainless steel blank to prevent any chance of damage to it. All the positions where temperature was experimentally derived are shown in one plane with respect to the finite element problem domain in Fig. 3.

The specification of the chosen thermocouples was as follows: "K" Type, 0.25 mm diameter, accuracy ± 1 percent or better up to 500°C, maximum operating temperature 820°C.

The data acquisition system used a multiplexer providing 16 differential analogue input channels into one analogue input channel on a data acquisition board fitted to a 486 PC. The multiplexer included cold-junction sensing and compensation for thermocouples, and internal gain of the low voltage output. Each run was stored straight to the hard disk of the PC.

Three variables for the validation were studied at two values. These were: the mass flow rate (0.089 and 0.124 kg/s) and the temperature (500 and 800°C) of the source air flow (the hot gas) and the flow rate of the two different coolants (water at 8.28 and 12.48 kg/s and air at 0.000161 and 0.000321 kg/s).

At each experimental condition, when the source flow temperature had settled at the required value, each thermocouple output was sampled ten times over a period of one minute and saved to disk. During this time the relevant information to calculate coolant and source flow mass flow rates were recorded in accordance with BS 1042. For information, the test rig pipe external temperature was also recorded. The entire experimental procedure was conducted twice and compared to ensure that no erratic results were used. After the testing was complete the ten outputs from each thermocouple were averaged for each different test condition to give one temperature for each thermocouple

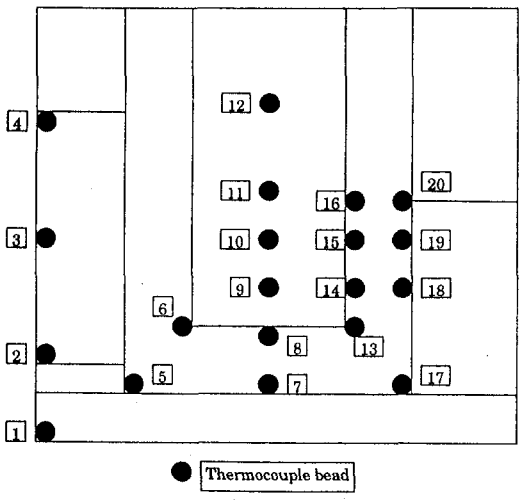

Fig. 3 Temperature measurement locations

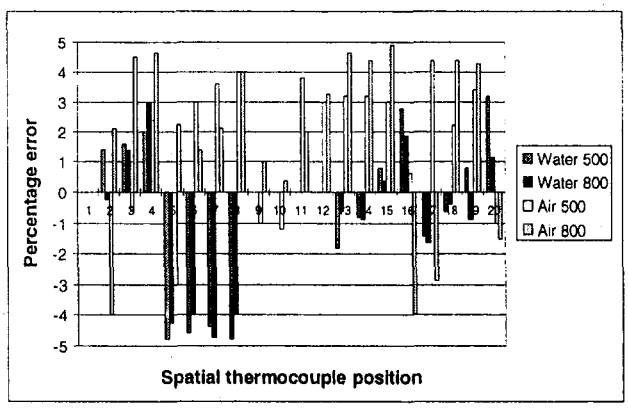

Fig. 4 Error in model predictions against experimental data

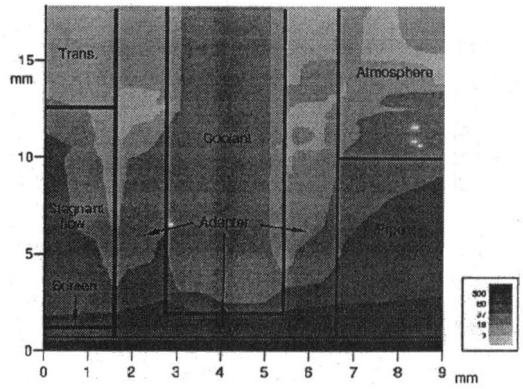

Fig. 6 Water cooling at 800°C source flow

to reduce scatter in the results from minor fluctuations in the experimental values.

Data Comparison

A simple comparison was then made between the relevant experimental data and the spatially equivalent nodal temperature predicted by the model for each of the four conditions modeled (water-cooled at 500 and 800°C source flow and air-cooled at 500 and 800°C source flow).

Good qualitative agreement was immediately found, but to gain some quantitative agreement required more boundary conditions to be prescribed in the model. For the cases using water as a coolant, a greater number of coolant nodes had to be prescribed at coolant inlet temperature. For the cases using air as the coolant, the external pipe temperature of the test rig had to be prescribed. The two values required (water coolant inlet temperature and pipe external temperature) had been taken during testing and so were readily available.

A summary of the discrepancy found between the temperatures predicted by the model and the experimental temperatures is shown in Fig. 4. The discrepancy is plotted as a percentage of the source flow temperature boundary condition (500 or 800°C).

The temperature predicted by the model matched the experimental temperature to within ±5 percent of the source flow temperature. It was assumed that, using the model, it was possible to predict any temperature in the domain to within ±5 percent or less of the source flow temperature (±25°C for 500°C source flow and ±40°C for 800°C source flow).

Although this error tolerance may appear large, it was felt that appreciating the assumptions inherent in the model (no time for an additional CFD investigation of the coolant and using "typical" heat transfer coefficients) and the future use of the model in the research program, this tolerance was acceptable and would not negate the conclusions of the study.

Results

Experimental data were already available at 500°C source flow temperature. A source flow of 800°C was considered typical of the rear stages of an advanced high-pressure compressor. Air and water were used in the assessment to highlight differences between the effectiveness of the two media used in the same configuration.

Water as the Coolant. Figure 5 shows the temperature distribution for the analysis at 500°C source flow temperature with water as the coolant at a temperature of 10°C.

The predicted maximum transducer temperature was 21°C (measured at 28°C). The model predicts that the majority of the heat transferred into the screen of the adapter was passed into the coolant rather than up the recess to the transducer. Heat from the pipe of the test rig was prevented from transferring into the cooling adapter, leaving its outside wall relatively cool. The heat transferred into the inside wall of the cooling adapter appeared to be transferred into the coolant and away from the transducer. The overall impression is of very effective cooling of the transducer and evidence of localized cooling of the test rig pipe.

Figure 6 shows the temperature distribution for the analysis at 800°C source flow temperature with water as the coolant.

The predicted maximum transducer temperature was 38°C (measured at 53°C). The model predicts almost the same phenomena as at 500°C, but a general increase in temperature of the cooling adapter was evident. The temperature of the stagnated flow in the recess in front of the transducer and the inside wall of the cooling adapter appeared to be rising more quickly than other areas.

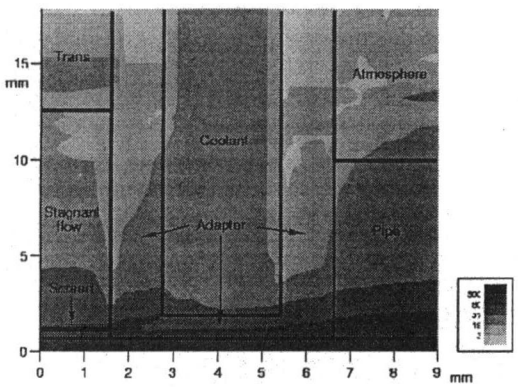

Fig. 5 Water cooling at 500°C source flow

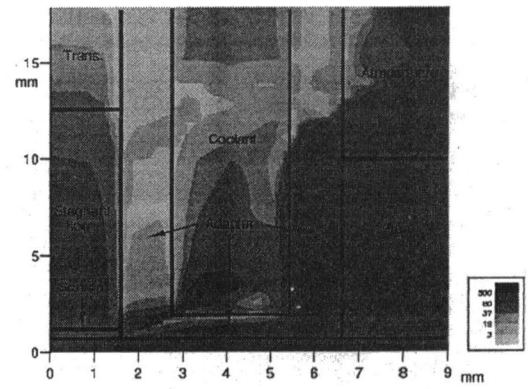

Fig. 7 Air cooling at 500°C source flow

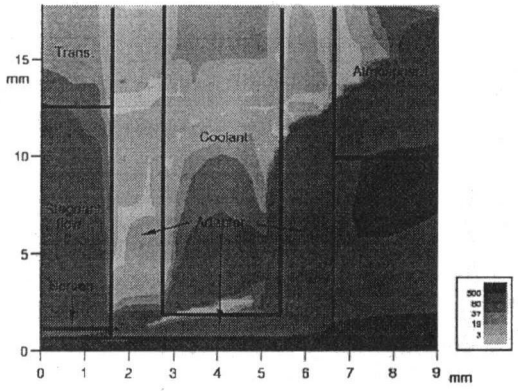

Fig. 8 Air cooling at 800°C source flow

Air as the Coolant. Figure 7 shows the temperature distribution for the analysis at 500°C source flow temperature with air as the coolant at 20°C.

The predicted maximum transducer temperature was 64°C (measured at 54°C). The cooling appears less effective; the heat appears reluctant to transfer into the coolant and was guided into the inside wall of the cooling adapter. Heat from the pipe of the test rig was transferred easily into the cooling adapter. The heat transferred into the screen was transferred more readily through the stagnated flow in the recess in front of the transducer than in the water-cooled case. The cooling adapter was at a generally higher temperature than the water-cooled case; this was most apparent in the outside wall of the cooling adapter. There was no evidence of localized cooling of the test rig and the general impression is reasonable cooling of the transducer, but less efficient than water cooling.

Figure 8 shows the temperature distribution for the analysis at 800°C source flow temperature with air as the coolant.

The predicted maximum transducer temperature was 198°C (measured at 182°C). The model again predicts almost the same phenomena as seen at the lower source flow temperature, but a general rise in the temperature within the problem domain was seen. The effectiveness of the transducer cooling was greatly reduced, there was an alarming increase in the heat transferred through the stagnated flow in the recess in front of the transducer, raising the temperature of the transducer itself to a dangerous level.

It is important to note that the use of a recessed transducer, to achieve sufficient cooling and allow survival at such high environment temperatures, has a detrimental effect on its measuring capability. The recess created has a first resonant frequency at about 10 kHz, severely reducing the measurement bandwidth of the transducer, quoted as 100 kHz by its manufacturer.

Conclusions

The model output can be summarized as follows:

- The primary heat path to the transducer was through the stagnated flow in the recess in front of the transducer. Heat transfer along this path was increased when air was the cooling medium and further increased at higher source flow temperatures.
- A rise in source flow temperature showed little change in general heat transfer characteristics except a general rise in domain temperatures. However, the increase in temperature of the adapter recess and transducer was at a higher relative rate.

The validated model confirmed that, using a commercially available design, water as a cooling medium was far better at protecting the transducer from the high-temperature environment.

When air was used as the coolant in the water-cooling adapter, the transducer diaphragm temperature was predicted as 198°C and experimentally measured as 182°C at a source flow temperature of 800°C, confirming survival of the transducer in an environment at this temperature. (The transducer is rated up to 235°C.) Survival at this temperature using a simplistic design of cooling adapter and air as the coolant was very encouraging, but the rise in predicted transducer temperature between 500 and 800°C source flow temperatures (64°C to 198°C) indicated that 800°C is very near the survival limit of this configuration.

The main concern was the ease with which heat from the hot gas passes up the stagnated flow in the recess in front of the transducer. This appeared to be by far the most dangerous heat path, even more so as the temperature of the source flow is increased.

Acknowledgments

The authors would like to acknowledge the UK Engineering and Physical Sciences Research Council and Rolls-Royce plc as project sponsors, and Rolls-Royce plc for permission to publish, and to thank P. Loftus and R. Stevenson of Rolls-Royce, and J. Yost for the guidance received during the course of this study.

References

Anon., 1900, "Measurement of Fluid Flow in Closed Conduits, Part 1—Pressure Differential Devices," Paper No. BS1042.

Bayley, F. J., Owen, J. M., and Turner, A. B., 1972, *Heat Transfer,* Nelson, UK.

El-Zafrany, A., 1994, "Finite Element Method for Engineering Analysis," M Sc Lecture Notes, School of Mechanical Engineering, Cranfield University, England, Sept.

Ferguson, D., and Ivey, P. C., 1995, "Unsteady Pressure Measurement in a High Temperature Environment Using Water Cooled Fast Response Pressure Transducers," ASME Paper No. 95-GT-345.

Harman, H. S., 1968, "Pressure Transducers for Environmental Extremes," NASA TM X-53743.

LeBail, F., and Popp, M., 1993, "Numerical Analysis of High Aspect Ratio Cooling Passage Flow and Heat Transfer," AIAA Paper No. 93-1829.

Patankar, S. V., 1978, "A Numerical Method for Conduction in Composite Materials, Flow in Irregular Geometries and Conjugate Heat Transfer," presented at the 6th International Heat Transfer Conference, Toronto, Canada, Aug.

Rolls-Royce, 1988, "Instrumentation Standards and Techniques: Surface Temperature Measurement," IST 02.13.

Russell, L. M., Hippensteele, S. A., Poinsatte, P. E., Thurman, D. E., and Simonyi, P. S., 1993, "Measurements and Computational Analysis of Heat Transfer and Flow in a Simulated Turbine Blade Internal Cooling Passage," AIAA Paper No. 93-1797.

Taylor, C., Xia, J. Y., Medwell, J. O., and Morris, W. D., 1992, "Numerical Representation of Heat Transfer Into Turbine Blade Cooling Ducts," STAR 9218, Feb.

A New Model for Free-Stream Turbulence Effects on Boundary Layers

R. J. Volino
Mechanical Engineering Department,
U.S. Naval Academy,
Annapolis, MD 21402-5042

A model has been developed to incorporate more of the physics of free-stream turbulence effects into boundary layer calculations. The transport in the boundary layer is modeled using three terms: (1) the molecular viscosity, ν; (2) the turbulent eddy viscosity, ϵ_T, as used in existing turbulence models; and (3) a new free-stream-induced eddy viscosity, ϵ_f. The three terms are added to give an effective total viscosity. The free-stream-induced viscosity is modeled algebraically with guidance from experimental data. It scales on the rms fluctuating velocity in the free stream, the distance from the wall, and the boundary layer thickness. The model assumes a direct tie between boundary layer and free-stream fluctuations, and a distinctly different mechanism than the diffusion of turbulence from the free-stream to the boundary layer assumed in existing higher order turbulence models. The new model can be used in combination with any existing turbulence model. It is tested here in conjunction with a simple mixing length model and a parabolic boundary layer solver. Comparisons to experimental data are presented for flows with free-stream turbulence intensities ranging from 1 to 8 percent and for both zero and nonzero streamwise pressure gradient cases. Comparisons are good. Enhanced heat transfer in higher turbulence cases is correctly predicted. The effect of the free-stream turbulence on mean velocity and temperature profiles is also well predicted. In turbulent flow, the log region in the inner part of the boundary layer is preserved, while the wake is suppressed. The new model provides a simple and effective improvement for boundary layer prediction.

Introduction

Free-stream turbulence can have a strong effect on the behavior of a boundary layer. Elevated free-stream turbulence tends to cause early transition from laminar to turbulent flow and can lead to higher skin friction and heat transfer coefficients. Highly disturbed flows are found in many applications including gas turbine engines, where free-stream turbulence intensities (FSTI) as high as 20 percent are possible. Given the strong effects that free-stream turbulence can have, accurate turbulence and transition models that incorporate these effects are needed for improved prediction and design. Existing turbulence models handle the FSTI in a number of ways. The simplest models do not account for the free-stream turbulence explicitly. They cannot, therefore, predict elevated heat transfer or skin friction in high FSTI boundary layers. Included are integral methods and zero-equation partial differential equation solvers, which use a mixing length model for closure of the momentum equation. Higher order turbulence models, such as two-equation $k-\epsilon$ models, provide a means for including the free-stream turbulence effect. Equations are derived for the turbulent kinetic energy and dissipation rate, and the free-stream turbulence conditions are supplied as boundary conditions for these equations. Although these equations are derived exactly, several terms must be modeled empirically for implementation. Turbulence is modeled as entering the boundary layer from the free stream through a diffusion process. This turbulence then raises the level of transport in the boundary layer, resulting in higher skin friction and heat transfer coefficients. It also leads to boundary layer transition.

Two-equation models must produce the correct qualitative end results. Turbulence is put into the boundary layer, and this will tend to cause transition and higher skin friction and heat transfer. The mechanism by which the turbulence enters the boundary layer in existing models may not be correct, however. If the mechanism is not correct, the constants in the models may still be tuned to give good predictions in some flows, but there is no reason to expect the models to be robust over all conditions. It is also questionable whether continued work with such models will lead to improvement, particularly in the area of transition. Increasing the FSTI in a $k-\epsilon$ simulation will correctly move transition upstream, but current models are still often poor predictors of transition (Mayle, 1991). This is evidenced by the comparisons in Savill (1992). Existing models generally predict transition starting too far upstream and with too short a transition zone.

Recent work suggests that diffusion may not be the primary mechanism by which free-stream turbulence influences the boundary layer. Volino and Simon (1994) considered transitional boundary layers under both low (0.6 percent) and high (8 percent) FSTI conditions. They documented spectra of the fluctuating streamwise velocity, u', the fluctuating normal component of velocity, v', and the turbulent shear stress, $-u'v'$, at several positions in the boundary layer and in the free stream. In the pre- and early-transitional boundary layers they found that the peak energy in the boundary layer u' spectra occurred at the same frequency as the peak in the free-stream v' spectra. This was observed under both high and low FSTI conditions. The boundary layer u' fluctuations were believed to be caused by the "splat mechanism" proposed by Bradshaw (1994). In the splat mechanism, free-stream eddies buffet the boundary layer. A negative v' fluctuation in the free stream compresses the boundary layer momentarily, forcing high-speed fluid from the outer region closer to the wall. This results in a positive u' fluctuation in the boundary layer. The free stream acts directly on the boundary layer. The mechanism does not involve turbulence diffusion. The splat mechanism consists mainly of "inactive motions," i.e., motions that do not lead to turbulent trans-

Contributed by the International Gas Turbine Institute and presented at the 42nd International Gas Turbine and Aeroengine Congress and Exhibition, Orlando, Florida, June 2–5, 1997. Manuscript received at ASME Headquarters February 1997. Paper No. 97-GT-122. Associate Technical Editor: H. A. Kidd.

port. Once the free-stream eddy passes, the boundary layer rebounds to its original state, with little net effect. This compression and release of the boundary layer may, however, lead to some turbulent mixing. Under high FSTI conditions, Volino and Simon (1994, 1997b) found significant levels of $-u'v'$ in the upstream, pretransitional boundary layer, and it occurred at the frequencies of the peak v' in the free-stream unsteadiness. This upstream $-u'v'$ was of lower energy and lower frequency than the $-u'v'$ in the fully turbulent boundary layer downstream. The upstream $-u'v'$ still had an impact on the upstream boundary layer, however, influencing the mean velocity and temperature profiles and enhancing the skin friction and heat transfer (Volino and Simon, 1997a).

Moss and Oldfield (1996) provide more direct evidence of the effect of the free-stream on the boundary layer. They considered FSTI up to 12 percent, recording simultaneous traces of instantaneous free-stream velocity and instantaneous wall heat flux. The correlation coefficient between the unsteady velocity and heat flux was as high as 50 percent. The spectra of the two signals were similar at low wavenumbers, but at higher wavenumbers the heat flux appeared unaffected by the free stream. Instantaneous Nusselt numbers fluctuated between a low level similar to that seen in low-FSTI turbulent boundary layers and a high level, which was up to 100 percent higher. The transition between the two levels occurred at a low frequency, which was associated with the free-stream turbulence. Smaller, higher frequency fluctuations within the heat flux signal were associated with turbulence within the boundary layer. Velocity spectra taken in the free stream and near the wall were nearly identical, suggesting that free-stream eddies were "penetrating right through the velocity-defect part of the boundary layer." The turbulent eddy structure of the boundary layer was believed to be dominated by high free-stream turbulence, and this was believed to be the main heat transfer enhancing mechanism.

Thole and Bogard (1996) considered boundary layers with FSTI ranging from 10 to 20 percent. At low wavenumbers they found that the free-stream u' spectra and the boundary layer spectra down to $y^+ = 15$ were nearly identical. At higher wavenumbers the FSTI level had little effect on the near-wall spectra. At 12 percent FSTI the near-wall spectra exhibited a double peak, with the lower frequency peak matching the peak frequency in the free-stream spectra. The higher frequency peak was associated with boundary layer generated turbulence.

Mayle and Schultz (1997) developed a "laminar kinetic energy" equation for pretransitional flows, and showed that pressure fluctuations, not diffusion, are the primary mechanism for turbulence entering the boundary layer.

The studies described above all suggest a direct link between free-stream and boundary layer fluctuations. They also show a distinct frequency separation between fluctuations induced by the free stream and fluctuations generated within the boundary layer by near-wall production. Although the $u'v'$ correlation is lower in the free-stream-induced fluctuations than in the boundary-layer-generated turbulence, the free stream has a significant and direct role in enhancing heat transfer. The diffusion mechanism used in current turbulence models does not appear to be supported by the experimental results.

In the present study a new method is proposed to model the direct link between the free-stream and boundary layer. A model is developed, as motivated by the experimental data, and then tested against several experimental data sets.

Turbulence Model

The two distinct scales observed in the experimental data suggest a separate treatment of the boundary-layer-generated and free-stream-induced turbulence. For modeling purposes, the two scales are assumed independent of each other except for their mutual influence and dependence on the mean streamwise velocity profile. The effect of the near-wall-generated turbulence is captured with an existing turbulence model. A new model is developed below for the free-stream effect.

The "splat mechanism" proposed by Bradshaw (1994) and discussed by Volino and Simon (1994) suggests that the level of free-stream-induced u' fluctuations in a boundary layer should depend on the level of v' fluctuations, a characteristic length, $l_{v'}$, associated with these fluctuations, and the mean velocity gradient, dU/dy. A v' fluctuation transports a packet of fluid some distance $l_{v'}$ across the mean streamwise velocity gradient, resulting in a fluctuation $u' \propto l_{v'} dU/dy$. The spectral results of Volino and Simon (1994) suggest that the turbulent transport induced by these fluctuations varies with the magnitude of the u' fluctuations.

The magnitude of the free-stream-induced v' fluctuations in the boundary layer can be inferred from an experimental v' profile in a high FSTI flow. Figure 1 shows a typical example from Volino and Simon (1997b). The value of v' drops from a maximum near the wall to a minimum at $y/\delta = 0.25$, before rising to the free-stream value. The near-wall peak can be associated with near-wall turbulence production. The decrease from the free stream to $y/\delta = 0.25$ suggests that the free-stream effect

Nomenclature

A = dimensionless coefficient in ϵ_f model
A^+ = coefficient in Van Driest damping model
b = dimensionless coefficient in ϵ_f model
C_f = skin friction coefficient
c = dimensionless coefficient in ϵ_f model
FSTI = free-stream turbulence intensity $= [(u'^2 + v'^2 + w'^2)/3U_\infty^2]^{0.5}$
G = transition model parameter
H = shape factor $= \delta^*/\theta$
K = acceleration parameter $= (\nu/U_\infty^2)(dU_\infty/dx)$
k = turbulent kinetic energy
$l_{v'}$ = mixing length for v' fluctuations
$\mathrm{Pr_t}$ = turbulent Prandtl number
q_o = wall heat flux
$\mathrm{Re_x}$ = Reynolds number based on distance from leading edge
Re_θ = momentum thickness Reynolds number
$\mathrm{Re}_{\theta t}$ = momentum thickness Reynolds number at transition start
St = Stanton number
T = temperature
U = mean streamwise velocity
u^+ = local velocity in wall coordinates $= U/u_\tau$
u' = fluctuating component of streamwise velocity
u_τ = friction velocity
v' = fluctuating component of velocity normal to wall
w' = fluctuating component of spanwise velocity
x = streamwise coordinate
y = coordinate normal to the wall
y^+ = distance from wall in wall coordinates $= yu_\tau/\nu$
α = thermal diffusivity
δ = boundary layer thickness
δ^* = displacement thickness
ϵ = turbulence dissipation rate
ϵ_f = free-stream induced viscosity
ϵ_H = total thermal diffusivity
ϵ_M = total viscosity
ϵ_T = turbulent viscosity
ν = kinematic viscosity
θ = momentum thickness

Subscripts

∞ = free-stream
f = free-stream induced

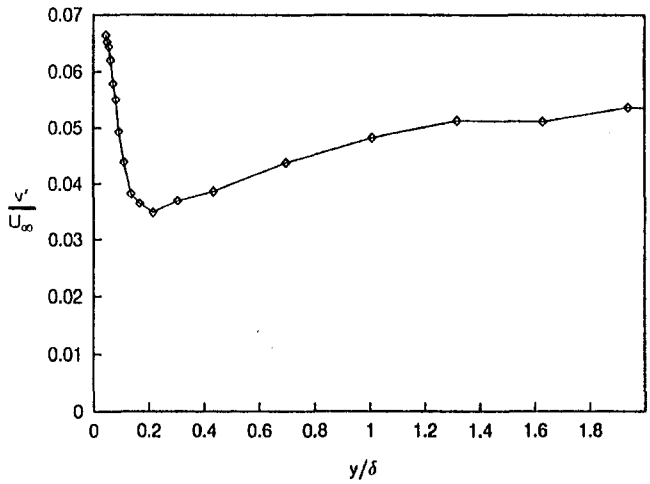

Fig. 1 Typical v' profile from a high FSTI boundary layer

diminishes as the boundary layer is penetrated and the wall is approached. This effect should approach zero at the wall. The free-stream-induced v' is assumed to scale with the distance from the wall, y, and inversely with the boundary layer thickness, δ.

If the length scale $l_{v'}$ is assumed to scale with v', y, and δ, this argument suggests the following form for the free-stream-induced shear stress, $-u'v'_f$:

$$-u'v'_f = Av'_\infty \frac{y^b}{\delta^c}\frac{dU}{dy} \tag{1}$$

where A, b, and c are dimensionless constants. To be dimensionally correct, $c = b - 1$. The form of Eq. (1) suggest a free-stream-induced eddy viscosity of the form:

$$\epsilon_f = Av'_\infty \frac{y^b}{\delta^{b-1}} = Av'_\infty \delta\left(\frac{y}{\delta}\right)^b \tag{2}$$

The value of v'_∞ may be allowed to vary in the streamwise direction to model the decay of the free-stream turbulence. In the present study, however, most of the experimental comparison cases showed only a small variation in v'_∞ with position, so v'_∞ was assumed constant at an upstream value for all calculations. The constants A and b are determined empirically. For two-dimensional boundary layers on flat walls with grid-generated turbulence and FSTI < 8 percent, $A = 0.41$ and $b = 2.5$ were determined based on a best overall fit to the laminar and turbulent Stanton number data of Blair (1982, 1983). In laminar boundary layers ϵ_f is assumed to act in combination with the molecular viscosity, ν. In turbulent boundary layers it is assumed to act in combination with the molecular viscosity and turbulent viscosity, ϵ_T. This is discussed further below.

The development above, although guided by experimental observations, is recognized as speculative. Its utility is demonstrated by the model's ability to improve the match of calculations to experimental data.

Implementation of the Model

The free-stream eddy viscosity proposed in Eq. (2) is independent of the near-wall turbulence model (e.g., $k-\epsilon$ or mixing length) and the computational method used in a simulation. In this study the new free-stream model (henceforth referred to as the FS model) is implemented along with a mixing length turbulence model. Since a mixing length model alone has no way of incorporating free-stream effects, use of one provides a clear and relatively simple test of the FS model. Computations are done using the TEXSTAN code referenced in Kays and Crawford (1993). TEXSTAN is an updated version of the STAN5 code presented by Crawford and Kays (1976). It is a two-dimensional, parabolic boundary layer code based on the Patankar and Spalding (1970) method. The mixing length model included in the TEXSTAN code, which includes the Van Driest (1956) near-wall damping model with a variable A^+ parameter, is utilized. Details are available in Kays and Crawford (1993).

The total viscosity, ϵ_M, used in the solution of the momentum equation is the sum of the molecular, turbulent, and free-stream contributions:

$$\epsilon_M = \nu + \epsilon_T + \epsilon_f \tag{3}$$

where ϵ_T is provided by the mixing length model. In laminar flows this reduces to

$$\epsilon_M = \nu + \epsilon_f \tag{4}$$

The energy equation is solved using the total thermal diffusivity, ϵ_H, where

$$\epsilon_H = \alpha + (\epsilon_T + \epsilon_f)/\mathrm{Pr}_t \tag{5}$$

and Pr_t is the turbulent Prandtl number. A variable Pr_t model recommended by Kays and Crawford (1993) is used. Heat transfer calculations depend strongly on the choice of Pr_t. The Kays and Crawford model produces good agreement with near-wall ($y^+ < 100$) mean temperature profile data, in wall coordinates, at all of the FSTI considered in this study, independent of whether the FS model is in use. Changing the Pr_t model produced changes in the slope and magnitude of the mean temperature profiles in the inner part of the boundary layer, which were not supported by the experimental data. The Kays and Crawford (1993) model is, therefore, used in all computations in this study.

Transition Model. Although development of a transition model is not the purpose of this paper, a transition model was needed for evaluation of the FS model in transitional and early turbulent boundary layers. The most reliable models currently available depend on empirical correlations for transition start and end. Transition was initiated in the present calculations by turning on ϵ_T when the momentum thickness Reynolds number, Re_θ, exceeded the value given by a correlation. Park and Simon (1987) recommended use of the Abu-Ghannam and Shaw (1980) correlation:

$$\mathrm{Re}_{\theta t} = 163 + \exp(6.91 - \mathrm{FSTI}) \tag{6}$$

for transition start with mixing length models. Schmidt and Patankar (1991) also used this correlation in the development of their "Production Term Modification" (PTM) $k-\epsilon$ transition model, which provides improved transition prediction over standard $k-\epsilon$ calculations. Mayle (1991) stated that the lower limit of 163 on $\mathrm{Re}_{\theta t}$ in Eq. (6) is artificial and proposed the equation

$$\mathrm{Re}_{\theta t} = 400(\mathrm{FSTI})^{-5/8} \tag{7}$$

This is similar to the correlation

$$\mathrm{Re}_{\theta t} = 460(\mathrm{FSTI})^{-0.65} \tag{8}$$

given by Hourmouziadis (1989). Recognizing that the correlations were developed for different ranges of FSTI, Eqs. (6) and (8) were used for cases with FSTI less than and greater than 4.5 percent, respectively. Additionally, transition was not allowed to begin if the acceleration parameter K was above 3×10^{-6}, as suggested by Mayle (1991). This last restriction has no effect at low FSTI, since the strong acceleration suppresses the growth of the boundary layer, keeping Re_θ below $\mathrm{Re}_{\theta t}$. At high FSTI, however, where $\mathrm{Re}_{\theta t}$ is itself low, the restriction can move transition start downstream.

TEXSTAN provides for a gradual transition with the mixing length model by modifying the Van Driest (1956) damping

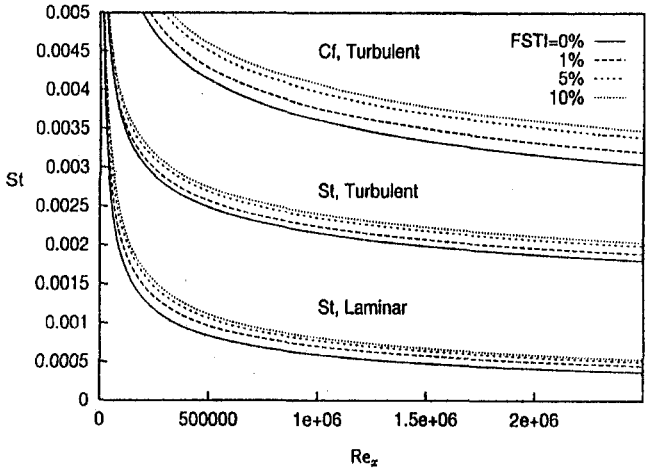

Fig. 2 FS model Stanton number and skin friction coefficient predictions for unaccelerated flow on a flat plate

term. This is accomplished by setting the A^+ term to 300 at the start of transition, then allowing it to gradually decrease to its equilibrium value ($A^+ = 25$ for unaccelerated flow) at the end of transition. This was found still to produce too abrupt a transition, so a further modification was implemented. In the range $\mathrm{Re}_{\theta t} < \mathrm{Re}_\theta < 2.667\ \mathrm{Re}_{\theta t}$ (with the 2.667 factor coming from the Abu-Ghannam and Shaw, 1980, model for transition length), Eqs. (3) and (5) were modified to

$$\epsilon_M = \nu + G\epsilon_T + \epsilon_f \tag{9}$$

$$\epsilon_H = \alpha + (G\epsilon_T + \epsilon_f)/\mathrm{Pr}_t \tag{10}$$

with

$$G = (\mathrm{Re}_\theta - \mathrm{Re}_{\theta t})/(1.667 * \mathrm{Re}_{\theta t}) \tag{11}$$

This might be thought of as a crude intermittency model. Although G does not match the shape of typical intermittency distributions (e.g., Abu-Ghannam and Shaw, 1980), it does vary smoothly with Re_θ, increasing from zero to one, as does the intermittency.

Initial Conditions. All computations were started at $x = 0.0001$ m ($\mathrm{Re}_x \approx 100$) with a Blasius velocity profile and a uniform temperature profile. The boundary layer thickness was set to 4×10^{-5} m using a nonuniform grid with forty points. Testing with different starting profiles and finer grids showed that results were independent of the initial conditions and grid to within 0.5 percent.

Results

The behavior of the model is demonstrated with a series of runs simulating air flow with a constant $U_\infty = 20$ m/s and $T_\infty = 300$ K along a 2-m-long plate. The wall boundary condition was a constant heat flux of 200 W/m^2. Simulations were run with 0, 1, 5, and 10 percent FSTI. Skin friction coefficient and Stanton number results are presented in Fig. 2 for simulations with the boundary layer assumed turbulent from the leading edge. At zero FSTI the model reduces to the standard mixing length model, and the results agree with correlations presented in Kays and Crawford (1993). At 1 percent FSTI, both C_f and St are about 5 percent above the zero FSTI conditions. At 10 percent FSTI, C_f and St are 15 percent above the zero turbulence results. Also shown in Fig. 2 are Stanton numbers for the same cases, but with laminar flow (ϵ_T set to zero). At $\mathrm{Re}_x = 2.5 \times 10^6$, 25 and 45 percent enhancements in St are seen for the 1 and 10 percent FSTI cases, respectively. Although laminar flow under these conditions would not be observed in practice, similar results would be expected in strongly accelerated, high FSTI flows, where extended laminar and transition regions would be present even under high FSTI conditions. Examples of such cases from Blair (1982) and Volino and Simon (1997a) are presented below.

The effect of the free-stream turbulence on the mean streamwise velocity profiles is shown in Fig. 3 for fully laminar and fully turbulent simulations. Profiles are presented in wall coordinates at $\mathrm{Re}_x = 0.5 \times 10^6$ (Re_θ between 400 and 600) for the laminar runs and at $\mathrm{Re}_x = 2.5 \times 10^6$ (Re_θ between 4700 and 5400) for the turbulent simulations. The free-stream turbulence causes the laminar profiles to deviate from the zero FSTI, Blasius profile, and suppresses the wake in the turbulent profiles, in agreement with experimental data (e.g., Blair, 1983). Similar results are observed in the mean temperature profiles. The log region of the turbulent profiles is unaffected by the free stream, in agreement with experimental results such as those of Thole and Bogard (1996). This lends support to the form of ϵ_f given by Eq. (2).

Comparison to Experimental Data. These results exhibit the correct trends, but a comparison to experimental data is needed to validate the model quantitatively. Data from flat and concave-curved wall cases, and from accelerated and unaccelerated flows were chosen. Free-stream turbulence levels up to 8 percent were considered. All experimental results are for flows of room temperature air along walls with constant flux heating downstream of a short unheated starting length. Attention is focused on Stanton number data and mean velocity and temperature profiles.

Unaccelerated Flow Over Flat Walls. Blair (1983) considered unaccelerated flow along a flat wall with $U_\infty = 30$ m/s and $q_o = 880$ W/m^2 downstream of a 4.3-cm-long unheated starting length. Data are tabulated in Blair (1981a). Free-stream turbulence intensities of 1.3, 2.6, 6.4, and 7.6 percent were generated with grids. Experimental Stanton number data are compared to calculated results in Fig. 4(*a*). The same data are compared to standard mixing length calculations (ϵ_f set to zero) in Fig. 4(*b*). The free-stream turbulence has only a small effect in the laminar region in these flows, and the laminar data are well predicted in both sets of calculations. In the turbulent region, the FS model provides an improved match to the data. For the 1.3 percent FSTI case, the standard model predicts St about 5 percent too low, while the FS model is about 2 percent too high. The standard model provides a better prediction of the 2.6 percent FSTI case, but the experimental data show the wrong trend with FSTI for this case, with St below the level of the 1.3

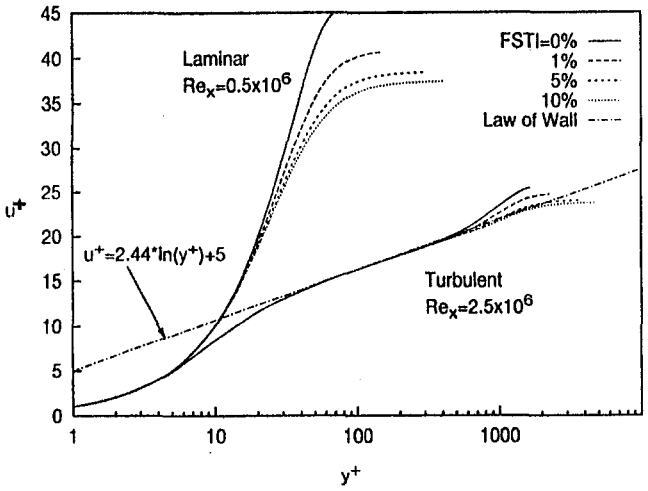

Fig. 3 FS model velocity profile predictions for unaccelerated flow on a flat plate

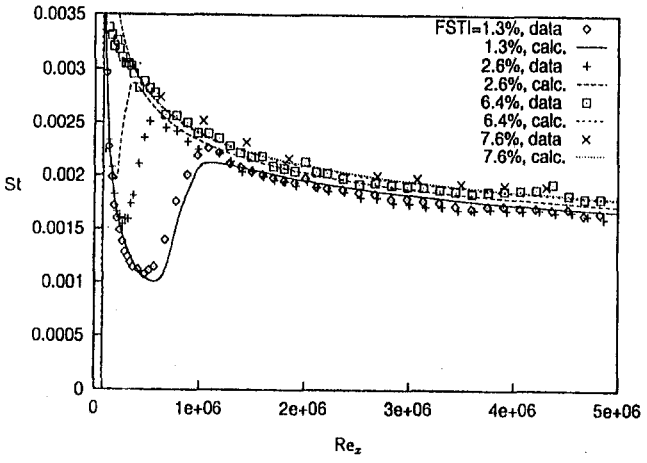

(a) FS Model

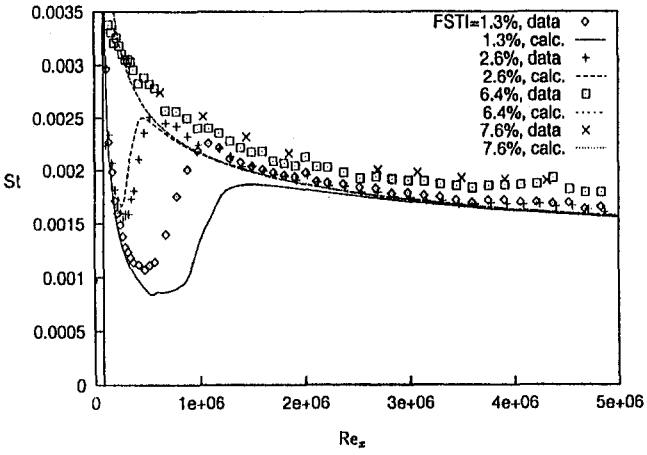

(b) Standard Mixing Length Model

Fig. 4 Comparison of Stanton number predictions to unaccelerated flow data of Blair (1983)

percent case. At the 6.4 and 7.6 percent FSTI levels, the standard model predicts Stanton number between 10 and 14 percent too low, while the FS model predicts St within 2 percent of the data. Schmidt and Patankar (1991) provide comparisons to these data sets with their $k-\epsilon$, PTM model. Their results are nearly identical to those of Fig. 4(a), both in the prediction of transition (expected since both are based on the Abu-Ghannam and Shaw, 1980, model) and in the prediction of heat transfer enhancement due to the FSTI effect.

Figure 5 shows comparisons of mean velocity and temperature profile data to the FS and standard mixing length calculations for a typical location from the fully turbulent zone of the 6.4 percent FSTI case. The FS model provides a clear improvement. The elevated FSTI leads to faster growth of the boundary layer, which is well captured. The wall temperature is predicted to within 1 percent of the wall-to-free-stream difference by the FS model, while the standard model prediction was 13 percent high. The shape factor, H, from the measured velocity profile was 1.33, while the values predicted by the FS and standard models were 1.29 and 1.42 respectively.

Accelerated Flow Over Flat Walls. Blair (1982) considered flow over a flat wall subject to favorable pressure gradients. Data are tabulated in Blair (1981b). At a constant acceleration parameter $K = 0.2 \times 10^{-6}$ and inlet $U_\infty = 15.9$ m/s, cases with 1 and 2 percent FSTI were considered. At a constant $K = 0.75 \times 10^{-6}$ and inlet $U_\infty = 10.1$ m/s, cases with 2 and 5 percent FSTI were documented. In all four cases the wall heat flux was approximately 500 W/m^2. Stanton number calculations using the FS and standard mixing length models are compared to the data in Fig. 6. At $K = 0.2 \times 10^{-6}$ and 1 percent FSTI (Fig. 6(a)), the models are comparable in the laminar region, predicting the data to within about 8 percent. Both models predict too late a transition. At $K = 0.2 \times 10^{-6}$ and 2 percent FSTI, the FS model is clearly better. It matches the laminar data, predicts the transition well, and is about 4 percent low in the turbulent region. The standard mixing length model is 12 percent low in the laminar and turbulent regions and predicts a late transition. At $K = 0.75 \times 10^{-6}$ and 2 percent FSTI (Fig. 6(b)) the FS model matches the data to within about 3 percent in the laminar and transition regions while the standard model is about 15 percent low in the laminar region and predicts a late transition. At 5 percent FSTI the FS model is about 9 percent low in the turbulent region, while the standard model is about 18 percent low.

Schmidt and Patankar (1988, 1991) also simulated these accelerated cases with their PTM model. At the lower K, they predict the 1 percent FSTI case well, including the transition. In the 2 percent FSTI case, their result is nearly identical to the prediction of the FS model in Fig. 6(a). At $K = 0.75 \times 10^{-6}$ with 2 percent FSTI, the PTM model predicts Stanton numbers 20 percent low in the laminar region and transition about 0.3

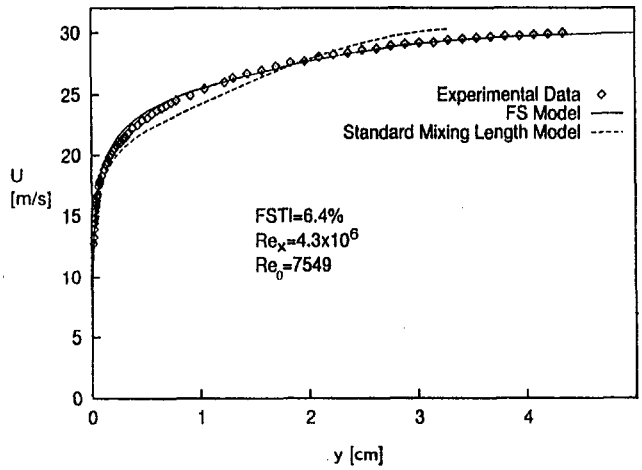

(a) Velocity Profile

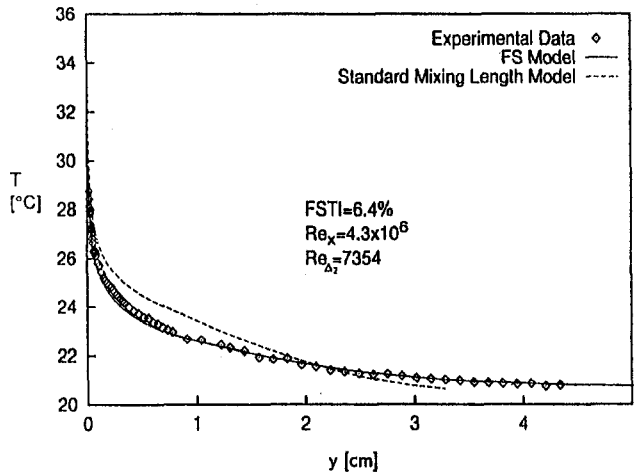

(b) Temperature Profile

Fig. 5 Comparison of calculated profiles to unaccelerated flow data of Blair (1983)

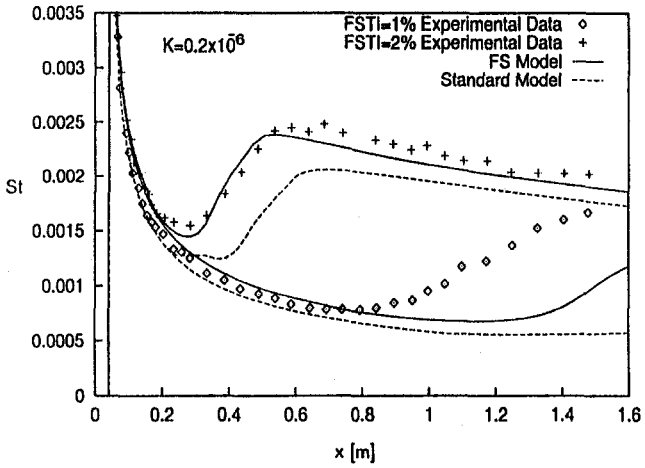

(a) K=0.2×10^{-6}

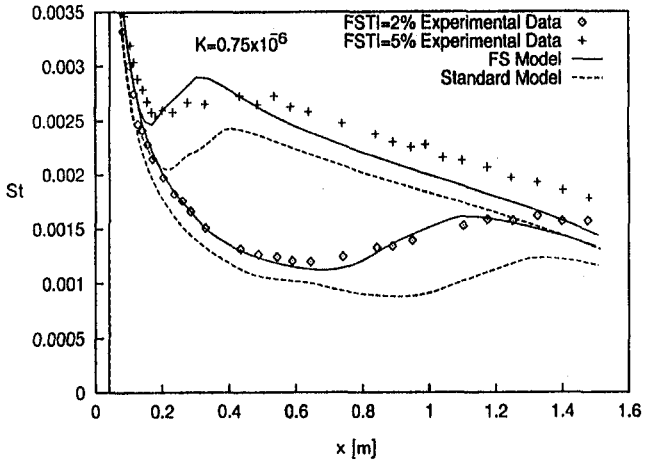

(b) K=0.75×10^{-6}

Fig. 6 Comparison of FS model and standard mixing length Stanton number predictions to accelerated flow data of Blair (1982)

m too far upstream. Schmidt and Patankar (1991) noted low St predictions in the laminar region of other strongly accelerated flows. At 5 percent FSTI the PTM model produces results very similar to those of the FS model in Fig. 6(b).

In summation, for the flat wall cases considered here, the new model is a clear improvement over the standard mixing length model. It correctly predicts the effects of free-stream turbulence. The model behaves very similarly to the more complex PTM $k-\epsilon$ model and in some cases produces a better result.

Modeling of Curvature Effects. To demonstrate an extension of the FS model, the effects of streamwise curvature are considered. Streamwise concave curvature is inherently destabilizing and can lead to higher heat transfer rates. Kestoras and Simon (1995) stated that when concave curvature and high FSTI are combined, the free-stream eddies are able to penetrate closer to the wall than in a flat wall flow, resulting in significantly higher turbulent transport within the boundary layer. They studied an 8 percent FSTI flow moving from a concave wall onto a flat recovery wall, and measured an almost immediate drop in turbulence within the boundary layer as the flow moved onto the flat wall. This rapid recovery further suggests that the effect of the free stream on the boundary layer is a direct one and not due to turbulent diffusion.

If the enhanced transport in concave-wall boundary layers is in part due to a closer penetration of free-stream eddies toward the wall, an adjustment of the profile of ϵ_f might capture the effect. To maintain the level of ϵ_f at the edge of the boundary layer while increasing the effect within the boundary layer, the constant b in Eq. (2) can be lowered while the constant A is held fixed. Kim et al. (1992) investigated boundary layers with 8 percent FSTI along both a flat wall and a concave wall with a constant radius of curvature of 1 m. In the turbulent region of the flow, an FS model simulation of the flat wall case produced Stanton numbers in agreement with the experimental data to within 5 percent. For the concave wall case, it was found that changing the constant b to 1.5 produced a good match to the turbulent flow data. The 8 percent FSTI alone (with b set to the 2.5 flat wall value) produced an 11 percent rise in Stanton number above a zero FSTI calculation, and the curvature effect (b set to 1.5 with FSTI = 8 percent) produced an additional 16 percent increase, for a total rise of 27 percent over a zero FSTI flat wall flow.

To test the concave wall model, accelerated flow data acquired by Volino and Simon (1995, 1997a) along the same 1 m radius of curvature wall used in the Kim et al. (1992) study were considered. The following three cases were simulated, all with a nominal 8 percent FSTI at the inlet to the test section:

Case	Inlet U_∞	Acceleration	Wall heat flux
1	7.5 m/s	$K = 0.75 \times 10^{-6}$ constant	76 W/m^2
2	9.6 m/s	$dU_\infty/dx = 28$ s^{-1} constant	380 W/m^2
3	4.9 m/s	$dU_\infty/dx = 13.6$ s^{-1} constant	180 W/m^2

The mixing length turbulence model, as described above, was used for the calculations with no additional curvature correction. Stanton numbers for the three cases are presented in Fig. 7. The transition is not well predicted in Case 1, but the calculated results are within 4 percent of the data at the downstream stations. The calculated results are 17 percent higher than those from a flat wall simulation with the FS model, and 28 percent higher than those predicted with the standard mixing length model. The calculations for Cases 2 and 3 are in good agreement with the data in all regions of the flow. Stanton numbers are well above the values predicted by a flat-wall FS calculation or the standard mixing length model. Volino and Simon (1995) stated that the curvature effect in these cases was probably small, since the acceleration kept the boundary layer thin. The present computations suggest that the curvature effect may have actually been large. An experiment on a flat wall under the FSTI and acceleration conditions of Case 3 would be an interesting check of this result. Cases 2 and 3 include extended nonturbulent regions due to the strong acceleration, which delays the start of transition in spite of the high FSTI. In this "disturbed laminar" region, the FS model correctly predicts a rise in Stanton numbers by as much as 65 percent above a laminar calculation. Figure 8 shows temperature profiles from two stations of Case 3. At the upstream station the flow is pretransitional ($\epsilon_T = 0$). All deviation from laminar behavior is due to the free-stream effect. The profile shape, boundary layer thickness, and wall temperature are all well predicted. At the downstream station the flow is fully turbulent. As at the upstream station, the calculated profile matches the data well, and represents a substantial improvement over the standard mixing length model.

Discussion

These results suggest the usefulness of the FS model. In the cases considered, results were good and comparable to those produced with a $k-\epsilon$ model. The FS model holds advantages over existing $k-\epsilon$ models. When used in conjunction with a mixing length model, it is less computationally intense. The FS model is also simpler, and is believed to model the physics

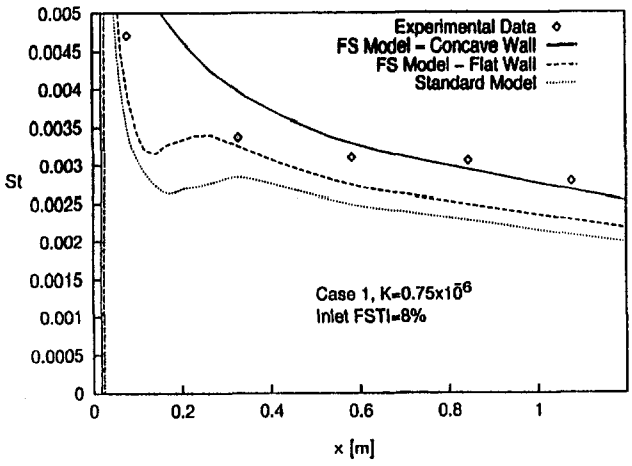

(a) Case 1

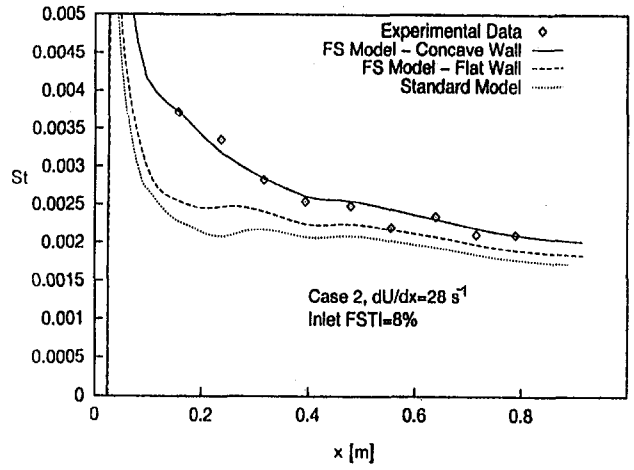

(b) Case 2

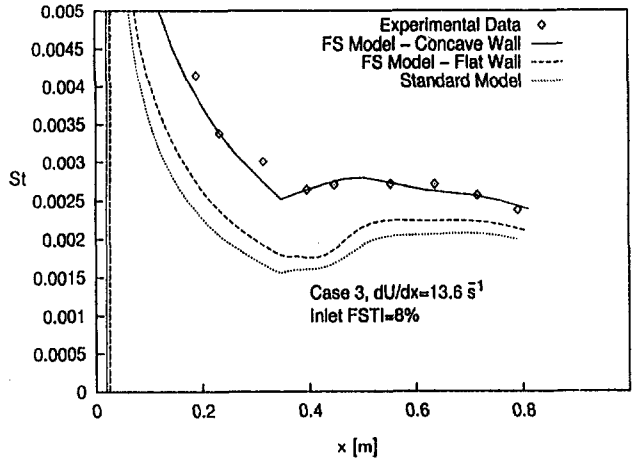

(c) Case 3

Fig. 7 Comparison of FS model and standard mixing length Stanton number predictions to accelerated, concave wall data of Volino and Simon (1995)

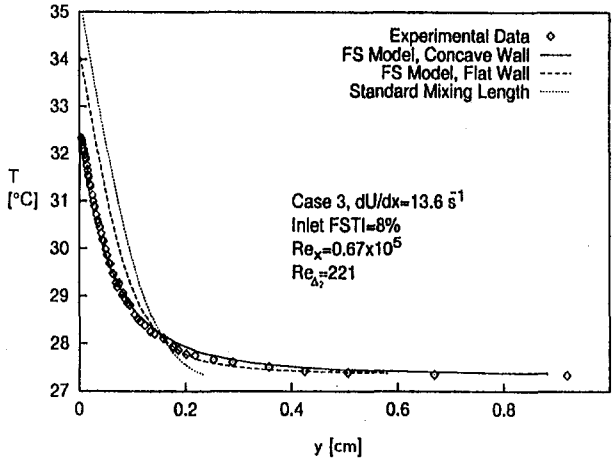

(a) Laminar Region

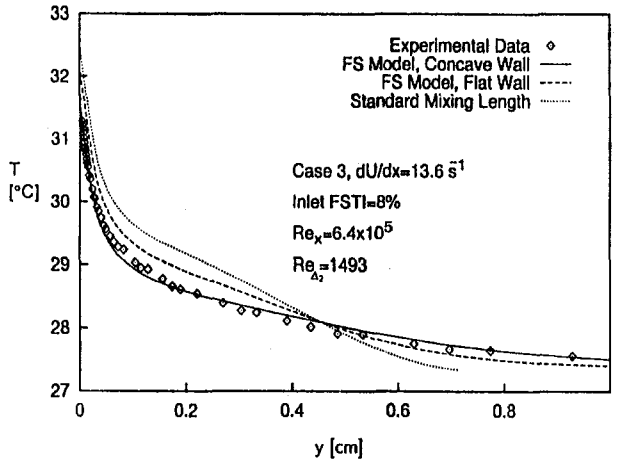

(b) Turbulent Region

Fig. 8 Comparison of FS model and standard mixing length temperature profile predictions to accelerated, concave wall data of Volino and Simon (1995)

of the free-stream–boundary-layer interaction better than the diffusion model assumed in $k-\epsilon$ computations. The location of the start of calculations is less important with the FS model than with standard models since the problem of allowing sufficient distance for diffusion of turbulence into the boundary layer is not an issue. Regardless of the comparison to $k-\epsilon$ models, mixing length models are still the models of choice in many Navier–Stokes calculations (Lakshminarayana, 1996) and the FS model provides a straightforward means of incorporating free-stream effects into these calculations.

While the comparisons presented above are generally good, they are limited. The purpose of the present work is to introduce the model and demonstrate its utility. Further work is still needed. All comparisons were to flows with grid-generated turbulence in which the integral length scale based on v'_∞ was 1 to 3 times the boundary layer thickness. Several investigators (e.g., Hancock and Bradshaw, 1989) have concluded that both free-stream intensity and length scale are important, and that large free-stream eddies have a greater effect on the boundary layer than smaller scale eddies. One or both of the constants in Eq. (2) might be a function of the free-stream integral length scale. Comparison to flows with different types of free-stream turbulence are needed.

The curvature correction presented above demonstrates the utility of the FS model and the way it may be modified based on an understanding of the flow. What one can say about the correction is, however, limited since the flows considered were all from the same test wall at the same nominal FSTI. One might speculate that the constant b in Eq. (2) is a function of the radius of the curvature of the wall and possibly the free-

stream turbulence level, but only further comparisons will confirm or deny this.

A final point is that the cases chosen for comparison were deliberately selected as relatively simple cases in which a mixing length calculation would be possible. No attempt was made, for example, to simulate an adverse pressure gradient flow, where a mixing length calculation would most likely fail, with or without the FS model correction. The FS model is in no way limited, however, to implementation with a mixing length model. If the FS model does capture the physics of the free-stream effect better than a conventional diffusion model, it may prove a useful addition to higher order turbulence models.

Conclusions

The FS model has been introduced and successfully tested in comparisons to a range of experimental data sets. The model is based on experimental observations, which suggest a direct link between free-stream turbulence and turbulent transport in the boundary layer. This is believed to be an improvement over the diffusion mechanism assumed in existing higher order turbulence models. The FS model can be used in combination with any existing turbulence model, and provides a means for incorporating free-stream turbulence effects into mixing length calculations. Further testing and development of the model are warranted.

References

Abu-Ghannam, B. J., and Shaw, R., 1980, "Natural Transition of Boundary Layers—The Effects of Turbulence, Pressure Gradient and Flow History," *J. Mech. Eng. Sci.,* Vol. 22, No. 5, pp. 213–228.

Blair, M. F., 1981a, "Final Data Report—Vol. I—Velocity and Temperature Profile Data for Zero Pressure Gradient, Turbulent Boundary Layers," United Technologies Research Center Report No. R81-914388-15.

Blair, M. F., 1981b, "Final Data Report—Vol. II—Velocity and Temperature Profile Data for Accelerating, Transitional Boundary Layers," United Technologies Research Center Report No. R81-914388-16.

Blair, M. F., 1982, "Influence of Free-Stream Turbulence on Boundary Layer Transition in Favorable Pressure Gradients," ASME *Journal Engineering for Power,* Vol. 104, pp. 743–750.

Blair, M. F., 1983, "Influence of Free-Stream Turbulence on Turbulent Boundary Layer Heat Transfer and Mean Profile Development, Part I, Experimental Data, Part II, Analysis of Results," ASME *Journal of Heat Transfer,* Vol. 105, pp. 33–47.

Bradshaw, P., 1994, "Turbulence: The Chief Outstanding Difficulty of Our Subject," *Exp. in Fluids,* Vol. 16, pp. 203–216.

Crawford, M. E., and Kays, W. M., 1976, "STAN5—A Program for Numerical Computation of Two-Dimensional Internal and External Boundary Layer Flows," NASA CR 2742.

Hancock, P., and Bradshaw, P., 1989, "Turbulence Structure of a Boundary Layer Beneath a Turbulent Free-Stream," *J. Fluid Mech.,* Vol. 205, pp. 45–76.

Hourmouziadis, J., 1989, "Aerodynamic Design of Low Pressure Turbines," AGARD Lecture Series, 167.

Kays, W. M., and Crawford, M. E., 1993, *Convective Heat and Mass Transfer,* 3rd ed., McGraw-Hill, New York.

Kestoras, M. D., and Simon, T. W., 1995, "Effects of Free-Stream Turbulence Intensity on a Boundary Layer Recovering From Concave Curvature Effects," ASME JOURNAL OF TURBOMACHINERY, Vol. 117, pp. 240–247.

Kim, J., Simon, T. W., and Russ, S. G., 1992, "Free-Stream Turbulence and Concave Curvature Effects on Heated Transitional Boundary Layers," ASME *Journal of Heat Transfer,* Vol. 114, pp. 338–347.

Lakshminarayana, B., 1996, *Fluid Dynamics and Heat Transfer of Turbomachinery,* Wiley, New York.

Mayle, R. E., 1991, "The Role of Laminar-Turbulent Transition in Gas Turbine Engines," ASME JOURNAL OF TURBOMACHINERY, Vol. 113, pp. 509–537.

Mayle, R. E., and Schultz, A., 1997, "The Path to Predicting Bypass Transition," ASME JOURNAL OF TURBOMACHINERY, Vol. 119, pp. 405–411.

Moss, R. W., and Oldfield, M. L. G., 1996, "Effect of Free-Stream Turbulence on Flat-Plate Heat Flux Signals: Spectra and Eddy Transport Velocities," ASME JOURNAL OF TURBOMACHINERY, Vol. 118, pp. 461–467.

Park, W., and Simon, T. W., 1987, "A Test of the MLH Models for Prediction of Convex-Curved Transitional Boundary Layer Heat Transfer Behavior," *Proc. 1987 ASME–JSME Thermal Engineering Joint Conference,* Vol. 3, pp. 349–360.

Patankar, S. V., and Spalding, D. B., 1970, *Heat and Mass Transfer in Boundary Layers,* 2nd ed., Intertext, London.

Savill, A. M., 1992, "A Synthesis of T3 Test Case Predictions," *Numerical Simulation of Unsteady Flows and Transition to Turbulence,* O. Pironneau et al., eds., Cambridge University Press, pp. 404–442.

Schmidt, R. C., and Patankar, S. V., 1988, "Two-Equation Low-Reynolds-Number Turbulence Modeling of Transitional Boundary Layer Flows Characteristic of Gas Turbine Blades," NASA CR 4145.

Schmidt, R. C., and Patankar, S. V., 1991, "Simulating Boundary Layer Transition With Low-Reynolds-Number $k-\epsilon$ Turbulence Models, Part I—An Evaluation of Prediction Characteristics, Part 2—An Approach to Improving the Predictions," ASME JOURNAL OF TURBOMACHINERY, Vol. 113, pp. 10–26.

Thole, K. A., and Bogard, D. G., 1996, "High Freestream Turbulence Effects on Turbulent Boundary Layers," ASME *Journal of Fluids Engineering,* Vol. 118, pp. 276–284.

Van Driest, E. R., 1956, "On Turbulent Flow Near a Wall," *J. Aero. Sci.,* Vol. 23, pp. 1007–1011.

Volino, R. J., and Simon, T. W., 1994, "Transfer Functions for Turbulence Spectra," *Unsteady Flows in Aeropropulsion,* ASME AD-Vol. 40, pp. 147–155.

Volino, R. J., and Simon, T. W., 1995, "Measurements in Transitional Boundary Layers Under High Free-Stream Turbulence and Strong Acceleration Conditions," NASA CR 198413.

Volino, R. J., and Simon, T. W., 1997a, "Boundary Layer Transition Under High Free-Stream Turbulence and Strong Acceleration Conditions: Part 1—Mean Flow Results," ASME *Journal of Heat Transfer,* Vol. 119, pp. 420–426.

Volino, R. J., and Simon, T. W., 1997b, "Boundary Layer Transition Under High Free-Stream Turbulence and Strong Acceleration Conditions: Part 2—Turbulent Transport Results," ASME *Journal of Heat Transfer,* Vol. 119, pp. 427–432.